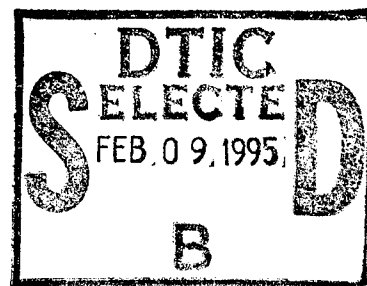


REPORT DOCUMENTATION PAGE			Form Approved OMB No. 0704-0188	
Public reporting burden for this collection of information is estimated to average 1 hour per response, including the time for reviewing instructions, searching existing data sources, gathering and maintaining the data needed, and completing and reviewing the collection of information. Send comments regarding this burden estimate or any other aspect of this collection of information, including suggestions for reducing this burden, to Washington Headquarters Services, Directorate for Information Operations and Reports, 1215 Jefferson Davis Highway, Suite 1204, Arlington, VA 22202-4302, and to the Office of Management and Budget, Paperwork Reduction Project (0704-0188), Washington, DC 20503.				
1. AGENCY USE ONLY (Leave blank)	2. REPORT DATE December 1994	3. REPORT TYPE AND DATES COVERED Final 1 May 94-31 Oct 94		
4. TITLE AND SUBTITLE Sixth International Symposium on Long-Range Sound Propagation		5. FUNDING NUMBERS DAAH04-94-G-0039		
6. AUTHOR(S) Henry E. Bass (principal investigator)				
7. PERFORMING ORGANIZATION NAME(S) AND ADDRESS(ES) University of Mississippi University, MS 38677		8. PERFORMING ORGANIZATION REPORT NUMBER		
9. SPONSORING/MONITORING AGENCY NAME(S) AND ADDRESS(ES) U.S. Army Research Office P.O. Box 12211 Research Triangle Park, NC 27709-2211		10. SPONSORING/MONITORING AGENCY REPORT NUMBER ARO 32664.1-GS-CF		
11. SUPPLEMENTARY NOTES The views, opinions and/or findings contained in this report are those of the author(s) and should not be construed as an official Department of the Army position, policy, or decision, unless so designated by other documentation.				
12a. DISTRIBUTION/AVAILABILITY STATEMENT Approved for public release; distribution unlimited.		12b. DISTRIBUTION CODE		
13. ABSTRACT (Maximum 200 words) Papers presented at the Sixth International Symposium on Long-Range Sound Propagation, 12-14 June 1994, at Chateau Laurier Hotel, Ottawa, Canada.				
14. SUBJECT TERMS Sound Propagation, Turbulence, Meteorology, Ground Impedance, Infrasound			15. NUMBER OF PAGES 514	
			16. PRICE CODE	
17. SECURITY CLASSIFICATION OF REPORT UNCLASSIFIED	18. SECURITY CLASSIFICATION OF THIS PAGE UNCLASSIFIED	19. SECURITY CLASSIFICATION OF ABSTRACT UNCLASSIFIED	20. LIMITATION OF ABSTRACT UL	





National Research Council
Canada

Institute for
Microstructural Sciences

Conseil national de recherches
Canada

Institut des
sciences des microstructures

ARO 32664.1-GS-CF

Sixth International Symposium on Long-Range Sound Propagation

Proceedings of a symposium held at the
Château Laurier Hotel
Ottawa, Canada
12-14 June 1994

19950206 049

Canada



National Research Council
Canada

Institute for
Microstructural Sciences

Conseil national de recherches
Canada

Institut des
sciences des microstructures

Sixth International Symposium on Long-Range Sound Propagation

Compiled by
David I. Havelock
Michael R. Stinson
National Research Council
Ottawa ON, CANADA

Proceedings of a symposium held at the
Château Laurier Hotel
Ottawa, Canada
12-14 June 1994

Sponsored by
National Research Council
University of Mississippi
US Army Research Office

Canada

DTIC QUALITY INSPECTED 8

PREFACE

The Sixth International Symposium on Long Range Sound Propagation was held 12-14 June 1994 at the Chateau Laurier Hotel in Ottawa, Canada. The programmes of the earlier symposia, held in 1981 (Mississippi), 1984 (New Orleans), 1988 (Mississippi), and 1990 (NASA Langley), each contained about 25 papers. The Fifth International Symposium on Long Range Sound Propagation, held two years ago in Milton Keynes, England, had a programme containing 38 papers. The programme of the present Symposium contains 35 papers. Again, research and interest in the area of atmospheric sound propagation shows no signs of diminishing. The topics covered at the present meeting included sonic booms, detection of acoustic signatures, the effects of meteorology and ground on sound propagation, and there were two papers on infrasound. The Sixth Symposium clearly shows the shift in emphasis over recent years from studies primarily devoted to the effects of finite ground impedance to more and more studies of the effects of refraction and atmospheric turbulence. In fact, half the total number of papers in these Proceedings are concerned with meteorological effects.

As with previous symposia, the purpose of the meeting was to exchange information on current research, identify areas needing additional work, and coordinate activities as much as possible. Attendees at the meeting included representatives from most groups with active research programs in the area of atmospheric sound propagation. The meeting was divided into eight short sessions: nonlinear propagation, sources, turbulence in the atmosphere I and II, acoustical modelling, meteorology, ground topography and impedance, ground impedance and infrasound. The symposium ended with an open discussion and plans for a future meeting in 1996. These proceedings contain a list of attendees with addresses and a compilation of the presentations made at the symposium.

The hosts would like to express their appreciation to the participants for attending and for sharing their knowledge and expertise and to Libby Cauthen for assistance during the meeting.

Gilles A. Daigle

National Research Council
Ottawa, ON K1A 0R6
Canada

Henry E. Bass

National Center for Physical Acoustics
University of Mississippi
University, MS 38677
USA

Keith Attenborough

Faculty of Technology
The Open University
Milton Keynes MK7 6A
England

Accession For	
NTIS GRA&I	<input checked="checked" type="checkbox"/>
DTIC TAB	<input type="checkbox"/>
Unannounced	<input type="checkbox"/>
Justification	
By	
Distribution/	
Availability Codes	
Dist	Avail and/or Special
A-1	

CONTENTS

PREFACE	iii
ATTENDEES	ix
SUNDAY 12 JUNE 1994	
<u>NONLINEAR PROPAGATION</u> (chair: Keith Attenborough)	
Nonlinear aeroacoustics: Experimental evidence from the F-4C. Wayne R. Lundberg	1
Asynchronous ensemble averaging: A travel-time-corrected averaging method for transient waves in random media. Alan R. Wenzel	21
Atmospheric effects on the risetime and waveshape of sonic booms. Richard Raspet, Henry E. Bass and Patrice Boulanger	41
Effect of stratification of the atmosphere on sonic boom propagation. Robin O. Cleveland, Mark F. Hamilton and David T. Blackstock	59
<u>SOURCES</u> (chair: Michael R. Stinson)	
Fast Field Program compared to helicopter field data. John M. Noble	77
Propagation near the ground from a fixed jet engine source. Keith Attenborough, Cyrus Chinoy and Reginald Lambert	88
Acoustic helicopter classification. Ton van Koersel, Martijn Miedema and Chris Nieuwenhuize	108
Acoustic characterization of ricochets. J. van der Haven, H.A. van Hoof, H.C.A. Romijn, M.G.A. Ruizenaar	115
Acoustical characteristics of the Mother of All Speakers. James M. Sabatier	123

MONDAY 13 JUNE 1994

TURBULENCE IN THE ATMOSPHERE I (chair: Henry E. Bass)

The effects of density and humidity fluctuations on sound propagation and scattering in the turbulent atmosphere. 142
V. Mellert, V. Ostashev and R. Wandelt

Aspects of sound field fluctuations in a refractive shadow. 152
David I. Havelock, Michael R. Stinson and Gilles A. Daigle

Propagation of low frequencies in the presence of a sound speed gradient. 167
A.J. Cramond and C.G. Don

A new approach in predicting sound propagation outdoors. 168
K.M. Li, S. Taherzadeh and K. Attenborough

TURBULENCE IN THE ATMOSPHERE II (chair: C.G. Don)

Estimation of linear sound speed gradients associated to general meteorological conditions. 181
A. L'Espérance, G.A. Daigle and Y. Gabillet

Long-term average sound transfer through the atmosphere: Predictions based on meteorological statistics and numerical computations of sound propagation. 209
Erik M. Salomons, Frank H.A. van den Berg and Hans E.A. Brackenhoff

The meteorological influence on the atmospheric absorption for horizontal and vertical sound propagation. 229
Conny Larsson

Sound propagation in a spatially inhomogeneous medium. 241
K.M. Li

ACOUSTICAL MODELLING (chair: Louis C. Sutherland)

A qualitative approach of atmospherical effects on long range sound propagation. 251
V. Zouboff, Y. Brunet, M. Bérengier and E. Sechet

Sound propagation through a turbulent atmosphere: Influence of the turbulence model.	270
D. Juvé, Ph. Blanc-Benon and P. Chevret	
Simulation of scattering by turbulence into a shadow region using the GF-PE method.	283
Michael R. Stinson, David I. Havelock and Gilles A. Daigle	
Calculation of average turbulence effects on sound propagation based on the Fast Field Program formulation.	296
Richard Raspet and Wenliang Wu	
The effect of turbulence and irregular terrain on outdoor sound propagation.	315
Xiao Di and Kenneth E. Gilbert	
 <u>METEOROLOGY</u> (chair: David I. Havelock)	
Sound scattering by scalar and vector random fields.	334
V. Mellert, V. Ostashev and R. Wandelt	
Index-of-refraction and profile-curvature statistics derived from large-eddy simulations.	348
D. Keith Wilson	
Conclusions pertinent to acoustical scattering by atmospheric turbulence using a turbulence ensemble model.	357
Harry J. Auvermann, George H. Goedecke and Michael D. DeAntonio	
Problems with creeping waves in a non-linear sound speed gradient.	371
C.G. Don	

TUESDAY 14 JUNE 1994

GROUND TOPOLOGY AND IMPEDANCE (chair: D. Juvé)

A new generalised terrain parabolic equation (GT-PE).	385
M. West and R.A. Sack	
Application of the parabolic approximation method to sound propagation above ground with impedance variations.	394
Marta Galindo	

Influence of ground roughness on outdoor sound. Keith Attenborough	408
Investigations into point source propagation in the frequency domain and in the time domain. Karsten Bo Rasmussen and Stoyan Yotov	423
Evaluation of the Noise Assessment and Prediction System (NAPS). Robert O. Olsen, John M. Noble and Richard Okrasinski	438
 <u>GROUND IMPEDANCE AND INFRASOUND</u> (chair: Gilles A. Daigle)	
Methodology of ground impedance measurement using the two- microphone technique. C. Peng and J.A. Lines	447
Review of ground impedance for grass surfaces - Delany and Bazley revisited. Louis C. Sutherland	460
Infrasonic observations and modeling of the Minor Uncle high explosive event. Rodney Whitaker, Susan D. Noel and Wayne R. Meadows	480
Infrasonic observations of the Northridge, California, earthquake. J. Paul Mutschlecner and Rodney W. Whitaker	498

LIST OF ATTENDEES

Keith Attenborough
Engineering Mechanics
The Open University
Walton Hall
Milton Keynes MK7 6AA
England

Georges Audet
Tactical Surveillance Group
Armaments Division
Defense Research Establishment Valcartier
2459, Pie XI Blvd., North (PO Box 8800)
Courcelette, Québec, G0A 1R0
CANADA

Harry J. Auvermann
US Army Research Laboratory
Battlefield Environment Directorate
White Sands Missile Range, NM 8802-
5501
USA

Gordon Baird
Deptment of Physics and Astronomy
University of Mississippi
University, MS 38677
USA

Henry Bass
National Center for Physical Acoustics
University of Mississippi
University, MS 38677

Michel Bérengier
LCPC-Centre de Nantes
BP 19-F
44340 Bouguenais
FRANCE

Robin Cleveland
Applied Research Labs.
University of Texas at Austin
P.O. Box 8029
Austin, TX 78713-8029
USA

Andrew Cramond
Department of Physics
Monash University
Clayton Victoria 3168
AUSTRALIA

Charles Don
Department of Physics
Monash University
Clayton, Victoria 3168
AUSTRALIA

Gilles Daigle
Institute for Microstructural Sciences
National Research Council
Ottawa ON K1A 0R6
CANADA

Xiao Di
Department of Acoustics
Pennsylvania State University
University Park, PA 16801
USA

Marta Galindo
The Acoustics Laboratory
Technical University of Denmark
Building 352
DK-2800 Lyngby - DENMARK

Kenneth C. Gilbert
Applied Research Laboratory
Pennsylvania State University
University Park, PA 16801
USA

Scott Hansen
Department of Acoustics
Pennsylvania State University
University Park, PA 16801
USA

David Havelock
Institute for Microstructural Sciences
National Research Council
Canada ON K1A 0R6

Daniel Juvé
Département d'acoustique
École Centrale de Lyon
36, avenue Guy de Collongue
BP 163
69131 Ecully Cedex
FRANCE

Conny Larsson
Department of Meteorology
Uppsala University
Box 516
S-751 20 Uppsala
SWEDEN

André L'Espérance
Département de génie mécanique
Université de Sherbrooke
Sherbrooke (Québec) J1K 2R1
CANADA

Dr Kai Ming Li
Engineering Mechanics Department
The Open University
Walton Hall
Milton Keynes, MK7 6AA
U.K.

Francis Lortie
CAE Electronics Ltd.
C.P. 1800 Saint-Laurent
Québec H4L 4X4
CANADA

Wayne R. Lungberg
Armstrong Laboratory Noise Effects
Branch
AL/OEbn
2610 Seventh St.
Wright-Patterson AFB, OH 45433-7901
USA

Paul Mutschlecner
EES-5
Los Alamos National Laboratory
Los Alamos, NM 87545
USA

John Noble
US Army Research Laboratory
Battlefield Environment Directorate
ATTN: AMSRL BE-S
White Sands Missile Range, NM 88002
USA

Vladimir Ostashev
Physical Science Laboratory
New Mexico State University
Box 30002 - Anderson Hall
Las Cruces, New Mexico 88003-0002
USA

Chaoying Peng
Silsoe Research Institute
Silsoe, Bedford
MK45 4MS
U.K.

Rony Philippe
Tactical Surveillance Group
Armaments Division
Defense Research Establishment Valcartier
2459, Pie XI Blvd., North (PO Box 8800)
Courcellette, Québec, G0A 1R0
CANADA

Karsten Bo Rasmussen
Acoustics Laboratory
Technical University of Denmark
Building 352
DK-2800 Lyngby
DENMARK

Richard Raspet
Dept. of Physics and Astronomy
University of Mississippi
University, MS 38677
USA

Karl Reichard
Graduate Program in Acoustics
Pennsylvania State University
State College, PA 16804
USA

James M. Sabatier
National Center for Physical Acoustics
Coliseum Drive
University, MS 38677
USA

Erik M. Salomons
TNO Institute of Applied Physics
Stieltjesweg 1
P.O. Box 155
2600 AD Delft
THE NETHERLANDS

Michael R. Stinson
Institute for Microstructural Sciences
National Research Council
Ottawa ON K1A 0R6
CANADA

Lou Sutherland
27803 Longhill Drive
Rancho Palos Verdes, CA 90274
USA

Shahram Taherzadeh
Dept. of Engineering Mechanics
The Open University
Walton Hall
Milton Keynes, MK7 6AA
ENGLAND

Ton van Koersel
P.O. Box 90804
2508 JG The Hague
Oude Waalsdorperweg 63
2597 AK The Hague, The Netherlands

Ralf Wandelt
Carl von Ossietzky Universität
Fachbereich Physik
Postfach 2503
26111 Oldenburg
GERMANY

Keith Wilson
Dept. of Meteorology
503 Walker Bldg.
Penn State University
University Park, PA 16802
USA

Rodney Whitaker
EES-5 MSF665
LANL
Los Alamos, NM 87545
USA

Alan R. Wenzel
Applied Acoustics Branch
Mail Stop 460
NASA Langley Research Center
Hampton, VA 23681-0001
USA

Martin West
Department of Applied Acoustics
University of Salford
UK

Vadim Zouboff
Laboratoire Regional des Ponts et
Chaussée
23, avenue de l'Amiral-Chauvin
BP 69
49136 Les Ponts-de-Cé Cedex
FRANCE

Nonlinear Aeroacoustics: Experimental Evidence from the F-4C

Wayne R. Lundberg
Armstrong Laboratory Noise Effects Branch
Wright-Patterson AFB, OH, USA

ABSTRACT

An analysis of the USAF flight noise database (NOISEBANK) was conducted in comparison to the proposed American National Standards Institute Model for Prediction of the Attenuation of Sound by the Atmosphere (pANSI S1.26-9X). The best noise propagation data available was determined to be that from the F-4C near vertical emission. This data had small standard deviations and no interference from background noise. A near windless condition permitted an accurate atmospheric temperature and humidity profile to be reconstructed using a ground heating model. The atmospheric profile was layered to facilitate a complete implementation of the pANSI model. Discrepancies up to 35 dB SPL were observed between the linear pANSI model and third octave band measurements up to 10 kHz over a 400m range. The measured discrepancies could only be explained by nonlinear acoustic propagation mechanisms. A formulation applicable in the frequency domain was derived from earlier work on Outdoor Propagation of Finite-Amplitude Noise [1]. The nonlinear formulation used to modify the pANSI model also incorporated atmospheric variables. Empirical fitting using the effective source radius and relative amplitudes allowed the discrepancies to be reduced to less than 3 dB 1/3 OB SPL at all far-field distances.

INTRODUCTION

This study was begun in 1991 in an effort to validate an atmospheric attenuation model which could replace the SAE ARP 866A Atmospheric Absorption Model [2] in USAF Armstrong Laboratory Noise Effects Branch (AL/OEBN) noise analysis and prediction programs [3,4,5]. Initially, the impact of the existing ANSI S1.26-78 Standard [6] on AL/OEBN noise predictions was evaluated for 15 aircraft representing four major engine types. Those aircraft were the F-4, C-135A, T-38, F-15, C-135B, F-111F, KC-10A, T-43, C-5A, KC-135R, A-10A, C-7, C-130E, OV-10 and C-23. The Sound Exposure

Level (SEL) versus distance curves predicted by the ANSI standard did not agree well with the established SAE model, particularly for the pure jet engined aircraft.

A revised ANSI model had been proposed which accommodates the effect of rapidly increasing atmospheric absorption on third octave band level predictions at high frequencies. The pANSI S1.26-9x model [7] is identical to that contained in ISO 9613-1. The pANSI model was used in a more detailed analysis in comparison to AL/OEBN in-flight noise measurements for six aircraft. The F-4C, C-135A, F-111F, KC-10A, KC-135R and A-10A were chosen because low-altitude data were available for use in the analysis. The analysis was accomplished for both homogeneous and inhomogeneous atmospheres. Neither approach resulted in acceptable agreement between predictions and measurements.

A nonlinear attenuation model was developed which essentially eliminated the discrepancies. The analysis as presented here includes only the F-4C for the following reasons: there were flight noise measurements at many altitudes; the measurement day was calm, which reduced deviations due to turbulence and allowed the atmospheric profile to be modeled with certainty. The pilot was able to reproduce his power setting and altitude on subsequent flights which minimized any normalization error; the aircraft has two engines close together which minimized the near-field effects generated. The F-4C flight noise measurements therefore give the clearest example of the nonlinear propagation effect witnessed in aircraft noise.

FLIGHT NOISE MEASUREMENT ANALYSIS

The measured atmospheric conditions for the six aircraft under study were plotted in Figure 1. Percent molar concentration, %h, of water vapor was used to measure humidity because the standard models of atmospheric absorption are dependent on this term. The molar concentrations and temperatures were subdivided into groups consistent with the technique used by L.C. Sutherland [8] to support the existing ANSI Standard. The F-4C measurements were 12.8 °C and 0.71 %h. Seven reference weather conditions are plotted which were used to assess the impact of the proposed pANSI standard.

Each aircraft's dataset was comprised of one or more engine power settings and two or more altitudes. The noise generated by aircraft engines is quite sensitive to power setting so the datasets were subdivided accordingly for comparative analysis. The total attenuation in each third octave band was calculated by the level difference spectrum method using measured SPLs averaged over 1/8 to 1/2 second intervals after propagation from different altitudes. Atmospheric attenuations were then calculated by correcting for spherical spreading loss.

One or more flights were conducted at each distinct aircraft/engine/power setting/altitude/atmospheric

condition. Each flight's noise was measured by one to three microphones directly under the flight path. A third octave band spectral time history was derived from the analog recordings using measurement system calibration techniques. Corrections were made for background noise, but such corrections had virtually no influence on the analysis of F-4C noise data.

The foregoing flight noise measurement data reduction techniques are standardized procedures used by AL/OEBN. The programs used in flight noise measurement analysis, Omega5 & 6 [3], are routinely capable of normalizing the maximum A-weighted SPL spectrum to U.S. Standard Day conditions at 1000 ft altitude and a fixed airspeed. The Omega5 flight noise measurement analysis program was modified for the purposes of this study. The modified program incorporated the pANSI Standard and allowed the reference altitude, airspeed, temperature, relative humidity and atmospheric pressure to be specified by the user. In all cases, these reference values were specified to be the average of their respective measurements. Flight altitudes were "averaged" using the Inverse Root-Mean Inverse Square (IRMIS) technique [9, see Perceived Mean Altitude] to correctly account for spherical spreading. The corrections incorporated in the unweighted reference spectra were relatively small, by design.

The emission angle associated with the maximum A-weighted SPL spectrum varies considerably with flight altitude. This complicating factor was not accounted for during the analyses using a homogeneous atmosphere. The Omega5 program was further modified to select the SPL spectrum at a near-vertical emission angle as well as to incorporate a layered, inhomogeneous atmosphere.

RESULTS DERIVED USING A HOMOGENEOUS ATMOSPHERE

It is important to establish the extent to which airbase environmental noise predictions would be affected by changing the atmospheric attenuation model applied. Such an impact study was conducted using the pANSI model in a homogeneous atmosphere only. The AL/OEBN flight noise prediction model, Omega10 [10], was modified during the course of this study to incorporate the pANSI model without including a technique to estimate atmospheric inhomogeneities. The Omega10 model applies an atmospheric attenuation model in the same way as the flight noise analysis program. It has the further capability to adjust for significant power setting changes using a set of linear interpolation rules. The Omega10 model uses a duration correction function [11] to predict SELs from maximum A-weighted SPLs. This function estimates the effective duration of a flight noise event from the distance between the observer and the aircraft's point of closest approach (or slant range).

The impact of the pANSI model was assessed in three ways: the effect on NOISEFILE (USAF standard) noise

reference spectra (Figures 2&3); the effect on predicted SEL vs distance curves at standard day (Figure 4); the effects on predicted SEL vs distance curves at seven non-standard day conditions (Figure 5). Figure 2 shows a nominal impact on the Training Route power setting (98% RPM) reference spectrum at high frequencies due to the proposed ANSI standard. The reference spectra at Takeoff and Afterburner power settings are given in Figure 3 to show the strong influence of the aircraft's power setting relative to the Training Route spectrum.

The Standard Day SEL vs. distance curves given in Figure 4 showed a significant discrepancy at close range for Takeoff Power which is exemplary of the effect seen at all higher power settings. This result was ascribed to the pANSI model's increased atmospheric absorption coefficients over those obtained using the SAE methodology. The increased coefficients affect the SELs near the source because they were extrapolated backward from the 1000 ft reference distance. Seven non-standard day conditions were used to be consistent with those selected by P. Joppa in a previous study [12] of the proposed atmospheric attenuation methodology. A plot of SEL difference vs. distance curves was generated (Figure 5) to more clearly illustrate the impact of applying the pANSI model at these non-standard day conditions. It is evident that the overall impact on predicted SELs is quite dependant on atmospheric conditions. The most severe effect occurred at high temperature and humidity which would be relevant to environmental noise predictions in a climate like that in Puerto Rico or Panama.

A scientific analysis was conducted to compare the pANSI model's predictions to measured flight noise data. The technique used in Reference 8 was employed in Figure 6 to plot the ratio of measured to predicted absorption losses (M/P ratio). Such plots require that the reader be aware of the fact that the total atmospheric absorption loss increases rapidly at high frequencies. The random variation of measured atmospheric attenuation was fairly constant with frequency, being characterized by a standard deviation of about 1-2 dB SPL. These two factors combined to produce a large scatter in the M/P ratio at frequencies up to 3 kHz and limited scatter above. Some of the M/P ratio scatter was ascribed to the fact that the emission angle of the noise generating the $SPL_{A,max}$ varied with altitude. Emission angle was measured from the direction of flight to the direction of sound propagation. A further complicating factor was that a homogeneous atmosphere having ground-level temperature and humidity was assumed.

The measured results nonetheless showed a consistent divergence away from predictions at high frequency. These divergences, although apparently small in terms of the M/P ratio, represent discrepancies in Sound Pressure Level of up to 40 dB. However, the aforementioned systematic errors coupled to render these results inconclusive.

INHOMOGENEOUS ATMOSPHERIC MODEL

A model which allowed estimation of the atmospheric variables at flight altitudes was adapted for the purposes of this analysis and for more general application to environmental noise prediction problems. The considerations of boundary-layer meteorology generally assume that both mechanical and convective turbulence are present.

Although this assumption was true of most flight noise measurement days, fortunately it was not true on 19 October 88, the day of the F-4C flight noise measurements. These measurements were taken in the early afternoon of a calm day. The lack of mechanical turbulence allowed a mildly superadiabatic temperature lapse rate, $\gamma_T = -11.8$ °C/km, to form. This superadiabatic lapse rate was apparent from the evening Rawindesonde observation (RAOB) which was taken six miles away at the Huber Heights launch station. The evening's measured lapse rate was used with the hourly ground-level temperatures to reconstruct an applicable atmospheric profile. This method resulted in a relatively accurate atmospheric profile estimation. It was shown that the change in predicted total third octave band atmospheric absorption due to atmospheric inhomogeneity was limited to ~7 dB.

The more generally applicable method of estimating an atmospheric profile required consideration of the effect that the sun's heat has on surface-layer temperature profiles [13]. The sun effectively only heats the ground, whose temperature increase is then convected upward with some mechanical assistance due to turbulence. It was thus a simple matter to estimate a temporally-varying profile based on a morning RAOB and hourly ground-level temperatures and assuming a dry adiabatic lapse rate, as shown in Figure 7. However, validated models of lapse rate exist only under dry or saturated humidity conditions.

An empirical model suitable for application at any humidity condition was developed for use in this study. A simple relationship between humidity and lapse rate was derived from those RAOBs collected at Huber Heights which were associated with the flight noise measurement days under study. The relation:

$$\begin{aligned} \gamma_T &= 12 - 0.06286 (RH), & RH > 35\% \\ \gamma_{T, dry} &= 9.8, & RH < 35\% \end{aligned} \quad (1)$$

was applied to estimate atmospheric lapse rate for most measurement days analyzed. It agrees with the existing models for dry and 10 °C saturated humidity conditions. Profiles of relative humidity were estimated using a simple interpolation scheme. Further scientific development of an applicable model is indicated, although the overall impact on environmental noise predictions may be minimal.

RESULTS DERIVED USING AN INHOMOGENEOUS ATMOSPHERE

The F-4C flight noise data was reanalyzed using a mildly superadiabatic lapse rate atmospheric profile. The flight measured noise spectra nearest vertical emission were normalized to their respective altitudes and the measured average atmospheric condition. A revised prediction of third octave band absorption was calculated and the M/P ratio plotted in Figure 8. The data plotted in Figure 8 is similar, but not identical to, that in Figure 6. The refined analysis significantly reduced the scatter in the measured spectral data. The measured attenuations were again consistently smaller than predictions at higher frequencies, tending toward one-half the predicted absorption values.

A clearer representation of the comparison between measurements and predicted third octave band SPL vs. distance curves was generated in Figure 9. Here the predicted curves were calculated using the level difference method based on the 82.6m measured SPLs. Discrepancies up to 35 dB SPL were evident. It was clear that none of the factors considered as a part of the linear theory could explain such systematic discrepancies.

NONLINEAR ATMOSPHERIC ATTENUATION MODEL

A Nonlinear atmospheric attenuation model was derived from an earlier successful theory [1]. It will here be considered as an extension of the pANSI model into the high-amplitude acoustics regime. No re-formulation of the pANSI model in an inhomogeneous atmosphere was required; only the variables and outputs from the pANSI model were used.

Specifically, a total effective attenuation coefficient due to atmospheric absorption, α_1 , was calculated from the total absorption predicted by the pANSI model divided by the propagation distance. The third octave band center frequency, f , was used to calculate the frequency dependance of Nonlinear effects instead of the (unknown) representative frequency involved in the band attenuation correction function [12]. Ground level temperature and humidity conditions were used in conjunction with the Ideal Gas Law to calculate the atmospheric density dependance of Nonlinear effects. Further simplifying assumptions associated with the existing Nonlinear propagation theory were used.

The expression used for predicting the propagated sound pressure of second harmonic nonlinear acoustic waves, p_2 , is given by [1, Eq. A-21]:

$$p_2 = p_{1r} \frac{r_r}{r} e^{-4\alpha_1(r-r_r)} \sqrt{a^2 + \frac{\sigma^2}{4} I_{22}^2 + a\sigma I_{22} \cos\phi} \quad (2)$$

where α_1 is the attenuation coefficient in nepers/meter.

The expression under the square root was simplified by

assuming that the relative phase of the second harmonic was zero, $\phi=0$. Formula 2 was converted to give the Sound Pressure Level in decibels at the receiver by:

$$L_2 = L_{1r} + 20 \log_{10} \left(\frac{r_r}{r} \right) - 4\alpha_1 (r - r_r) + 20 \log \left(a + \frac{\sigma}{2} I_{22} \right) \quad (3)$$

where the first three terms are those commonly applied to linear theoretical predictions since $\alpha_2 = 4\alpha_1$ for air. Only the last term in this expression needed evaluation. The integral I_{22} is associated with the contribution of the second order solution to the second harmonic and is given by [1, Eq. A-9a]:

$$I_{22} = \int_{r_0}^r \frac{e^{2\alpha_1 (r' - r_0)}}{r'} dr' \quad (4)$$

which was evaluated numerically by series expansion.

The expression for the nonlinear distortion range variable when ordinary absorption is not important is [1, Eq. 2-1]: $\sigma = \beta \epsilon k r_r \ln(r/r_0)$. Here $\beta = (\gamma + 1)/2 = 1.2$ is the coefficient of nonlinearity which is considered constant in air, $k = 2\pi f/c_0$ is the wave number, $c_0 = 335.1\sqrt{T/273.15}$ is the ambient speed of sound, $\epsilon = p_{1r}/\rho_0 c_0^2$ is the dimensionless source amplitude with $\rho_0 = P/RT$ the ambient air density. The atmospheric pressure P was expressed in micropascals, T in degrees Kelvin and R is the universal gas constant.

The reference distance r_r was dissociated from the effective source radius r_0 in this formulation since they were very different measures in typical aeroacoustics applications. Since the reference distance, r_r , sound pressure, $p_{1r} = 10^{(L_{1r}/20)}$, and the atmospheric variables were given, only two adjustable parameters, a and r_0 remain. The effective source radius, r_0 , is the distance at which nonlinear effects begin and the relative amplitude, a , is the ratio of linear to nonlinear amplitudes at the reference distance. Both may be derived from measurements when, as in this case, no theoretical description of the source exists.

RESULTS DERIVED USING A NONLINEAR ATTENUATION MODEL

The reference distance was taken to be 82.6m (271 ft) and the associated measured sound level spectrum was used as input to the model. The values of r_0 and a were adjusted to arrive at the improved fit to the measured noise spectral data. The results were plotted for comparison in Figure 10.

A further method of comparison was used to clarify the effect of atmospheric absorption models on predictions of aeroacoustic spectra. The measured normalized spectra at each flight altitude were plotted in Figure 11. The

spectrum at 325m (1068 ft) was then used as a reference and the level difference spectrum method applied to predict spectra at 82.6m. Four predicted spectra were then plotted in Figure 12 using four different atmospheric attenuation models: the SAE ARP 866A; the existing ANSI Standard; the proposed pANSI Standard (ISO 9613-1 plus band correction); and the pANSI model with a Nonlinear extension. These results explain why the F-4C Takeoff Power SEL vs distance curve in Figure 4 had an anomolous increase. The extended model's predicted spectrum also concisely demonstrated the improvement in the attenuation model achieved in this study.

CONCLUSIONS

A thorough analysis of USAF aircraft flight noise measurements was conducted in comparison to the pANSI S1.26-199x model for prediction of attenuation of sound by the atmosphere. Although a number of complicating factors exist, none could explain discrepancies between the theoretical model and experimental data.

A simplified Nonlinear Acoustic propagation model was developed to extend the pANSI model to include high-amplitude sources. The extended pANSI model significantly improved the comparison to measured flight noise data from the F-4C.

The discrepancy at high frequency between the SAE ARP 866A model and the pANSI S1.26-199x was explained. The SAE model was developed using a flight noise dataset including high-amplitude data from Stage I aircraft engines, whereas the pANSI model was based on laboratory measured acoustic data. Preliminary results from the A-10, a much quieter Stage III aircraft, indicated that it did not produce the discrepancy attributed to nonlinear propagation.

A general formulation of the extended pANSI model applicable to all aircraft engine power settings has not yet been derived. The parameters of the model are dependant on source noise characteristics and could only be determined experimentally.

REFERENCES

- [1] D.A. Webster and D.T. Blackstock, "Experimental Investigation of Outdoor Propagation of Finite-Amplitude Noise", NASA CR-2992 (ARL-TR-78-31), National Aeronautics and Space Administration, August 1978.
- [2] --- "Standard Values of the Atmospheric Absorption as a Function of Temperature and Humidity for Use in Evaluating Aircraft Flyover Noise", Aerospace Recommended Practice 866A, Soc. of Automot. Eng., 1975.
- [3] H.T. Mohlman, "Computer Programs (Omega5, 6 & 8) for Processing Measured Aircraft Flyover/Runup Noise Data for USAF Community Noise Prediction Procedures

(NOISEMAP/ NOISEFILE)", UDR-TR-82-49, University of Dayton Research Institute, April 1982.

- [4] D.E. Bishop and W.J. Galloway, "Community Noise Exposure Resulting from Aircraft Operations: Acquisition and Analysis of Aircraft Noise and Performance Data", AMRL-TR-73-107 (AD# A017741), Armstrong Laboratory, August 1975.
- [5] C.L. Moulton, "Air Force Procedure for Predicting Aircraft Noise around Airbases: Noise Exposure Model (NOISEMAP) Technical Report", AL-TR-1992-0059 (AD# A255769), Armstrong Laboratory, May 1992.
& "...User's Manual", AAMRL-TR-90-011 (AD# A223162), February 1990.
- [6] --- "American National Standard Method for the Calculation of the Absorption of Sound by the Atmosphere", ANSI S1.26-1978 (ASA 23-1978), American Natl. Stand. Inst., Inc., June 1978.
- [7] --- "Attenuation of Sound During Propagation Outdoors. Part 1: Calculation of the Absorption by the Atmosphere", ISO DIS 9613-1:199x (proposed ANSI S1.26-199x), Draft presented to the SAE A-21S6 Sound Propagation Subcommittee, 31 October 1991.
- [8] L.C. Sutherland, "Review of Experimental Data in Support of a Proposed New Method for Computing Atmospheric Absorption Losses", DOT-TST-75-87, U.S. Dept. Transp., May 1975.
- [9] W.R. Lundberg, "Analysis of Measured Environmental Noise Levels:...", AL-TR-1991-0097 (AD#A244805), Armstrong Laboratory, June 1991.
- [10] H.T. Mohlman, "Computer Programs for Producing Single-Event Aircraft Noise Data for Specific Engine Power and Meteorological Conditions for Use with USAF Community Noise Model (NOISEMAP)", AFAMRL-TR-83-020 (AD#A127419), Armstrong Laboratory, April 1983.
- [11] J.D. Speakman, "Effect of Propagation Distance on Aircraft Flyover Sound Duration", AFAMRL-TR-81-28 (AD# A099694), Armstrong Laboratory, May 1981.
- [12] P. Joppa, "Development of a Simplified Method for Calculation of Atmospheric Absorption of Aircraft Noise in One-third Octave Bands", Minutes of the SAE A-21S6 Sound Propagation Subcommittee, 18 October 1990.
- [13] --- "The Use of the Skew T, Log P Diagram in Analysis and Forecasting", AWS/TR-79/006 revised (AD# A221842), Air Weather Service, March 1990.

Meteorology for 120 Flights by 6 Aircraft

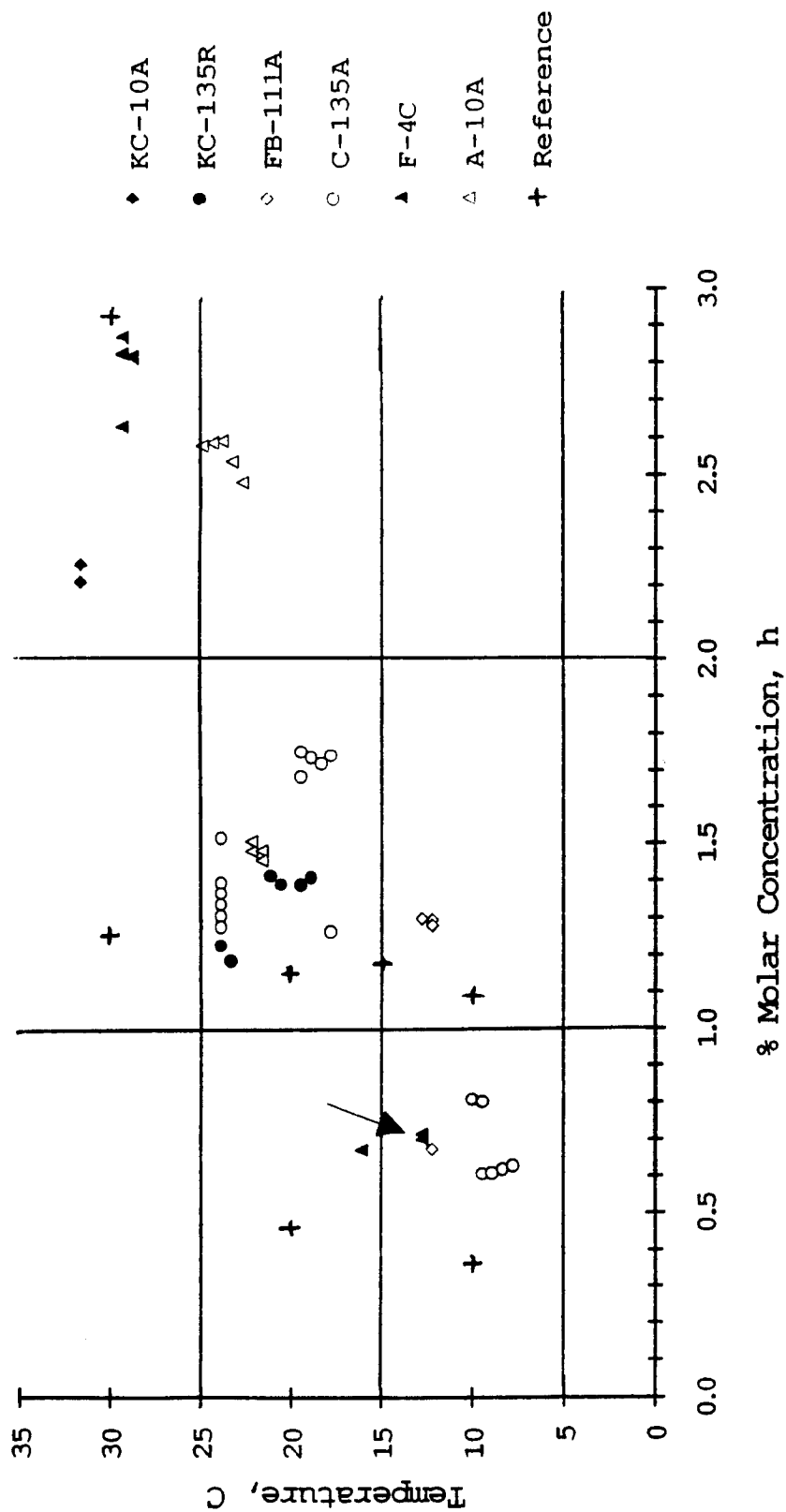


Figure 1.

Comparison of Measured Reference Spectra F-4C in Traffic P. & Training Rte Power

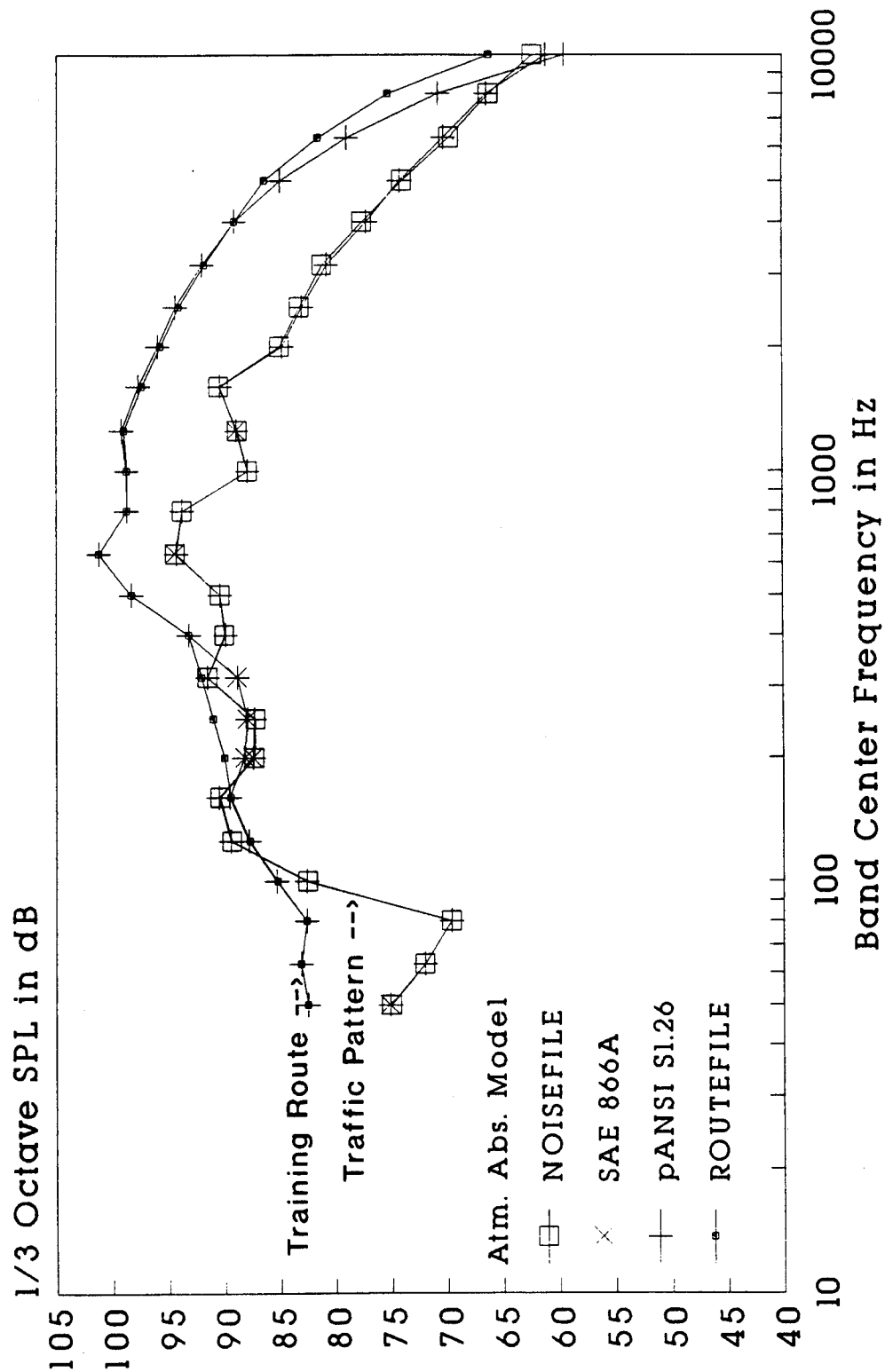


Figure 2. Impact of pANSI Model on NOISEFILE Reference Spectra

Comparison of Measured Reference Spectra F-4C in A/B, Approach and Takeoff Power

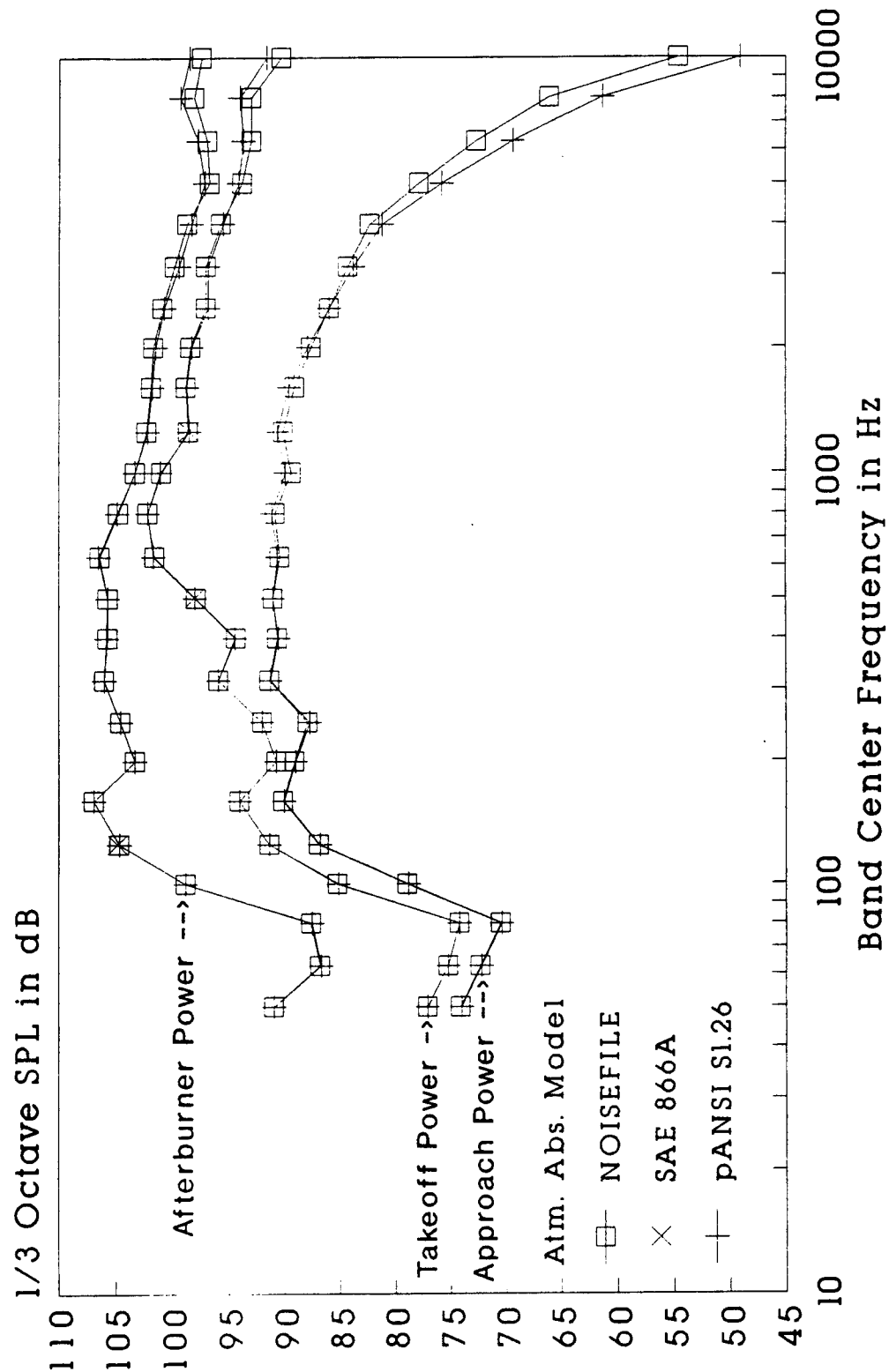


Figure 3. Impact of pANSI Model on NOISEFILE Reference Spectra

pANSI Std vs SAE ARP F-4C - 2 J79 Jet engines

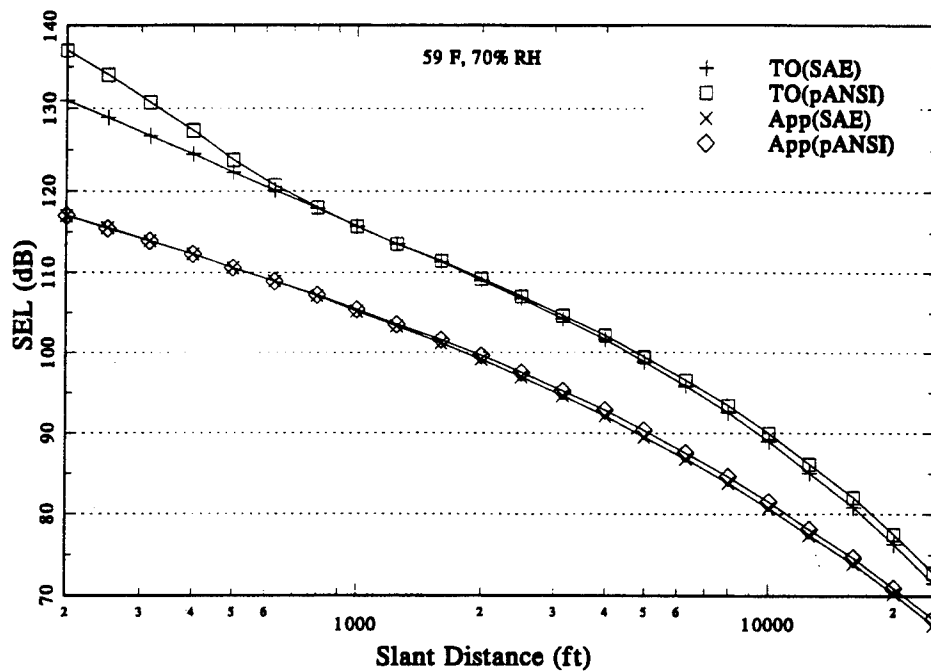


Figure 4. Impact of pANSI Model on SEL Predictions for Homogeneous Standard Day Conditions.

pANSI Std vs SAE ARP F-4C - 2 J79 Jet engines

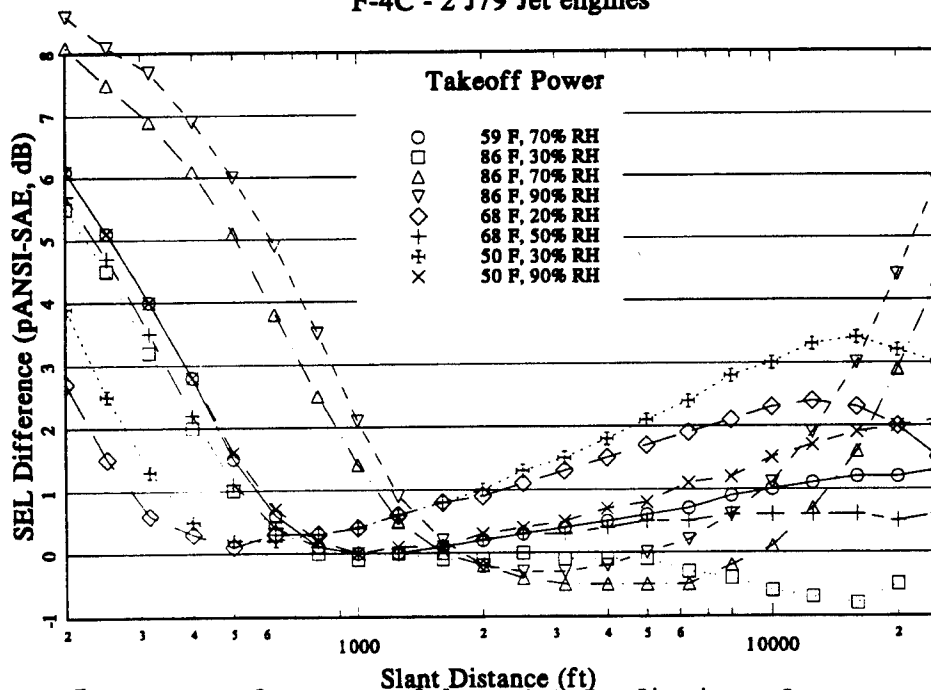


Figure 5. Impact of pANSI Model on SEL Predictions for Seven Homogeneous Reference Meteorological Conditions.

Ratio of Absorption Losses Measured/pANSI Prediction

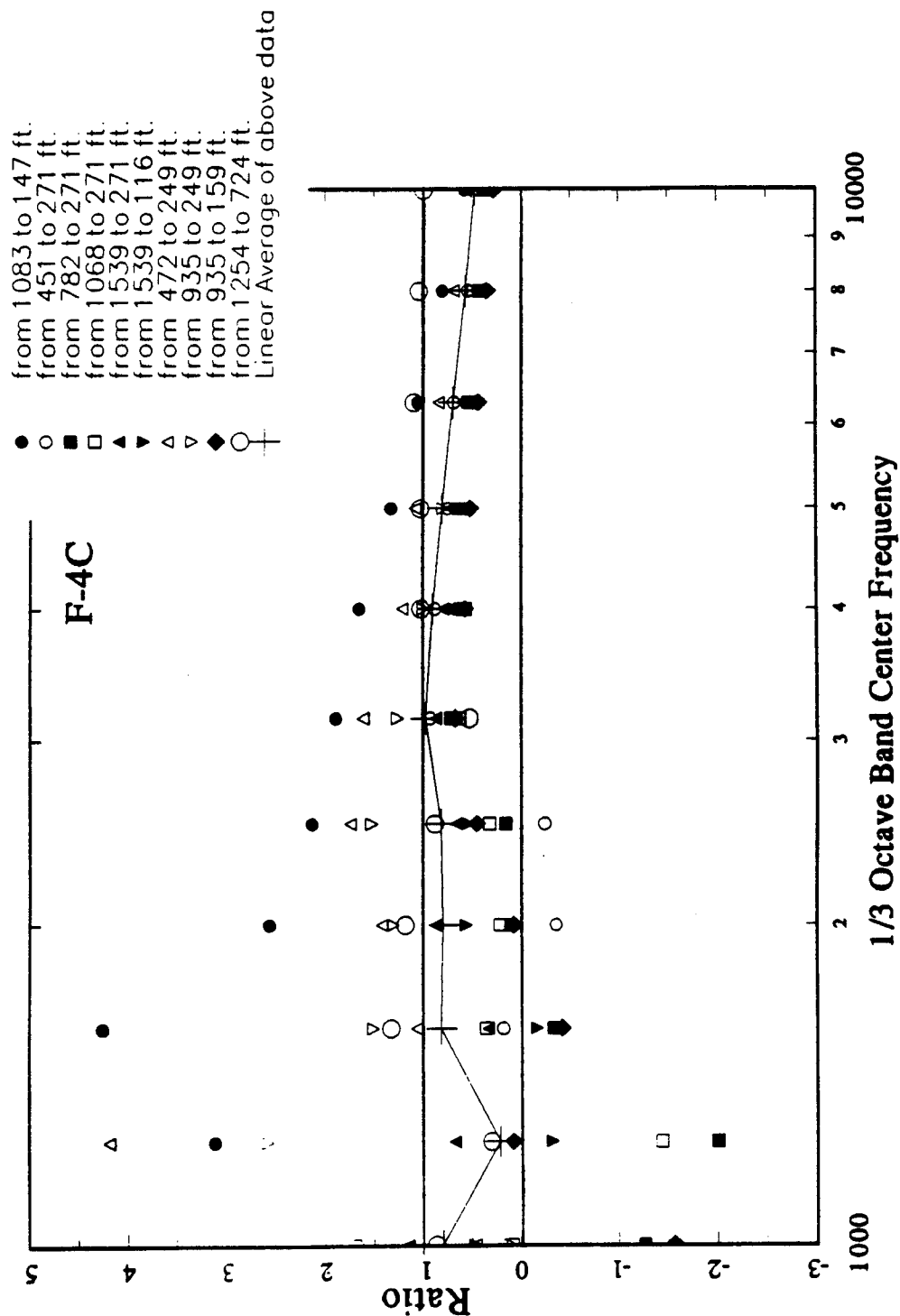
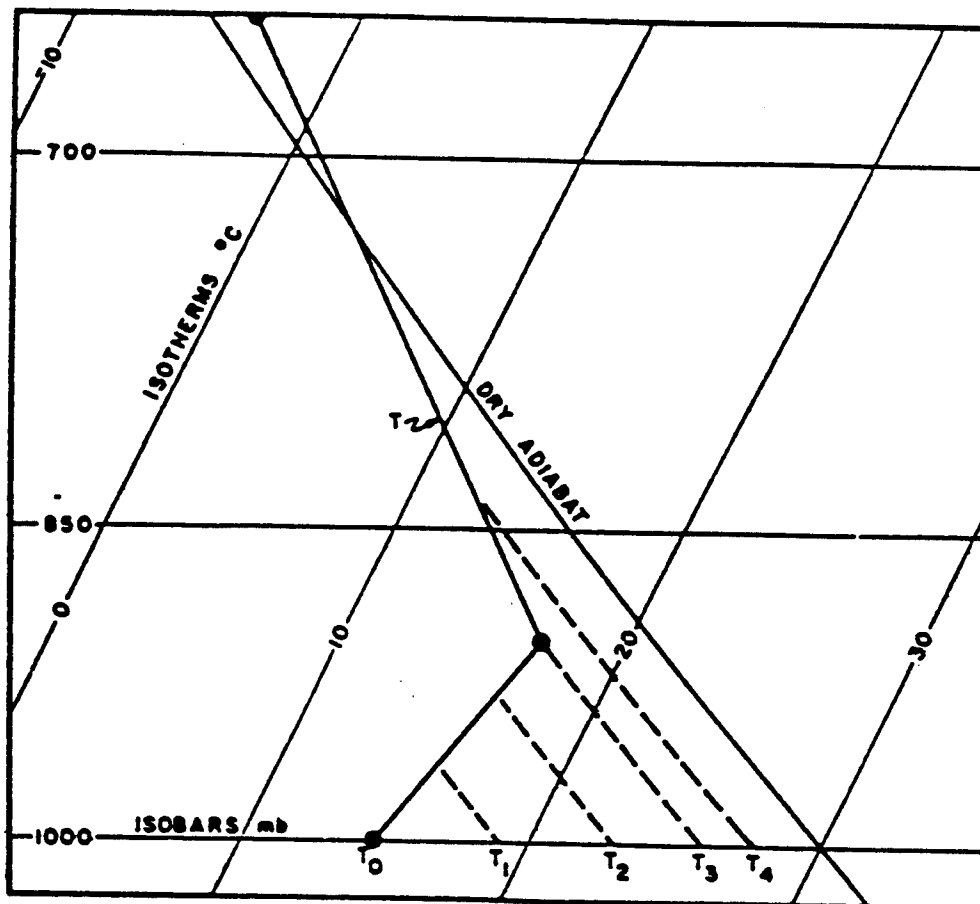


Figure 6. The pANSI Model's Predictions for a Homogeneous Atmosphere Compared to F-4C Flight Noise Attenuations Measured at AL_{max} .



from AWS/TR-79/006 revised 3/90; "Use of the Skew T, Log P Diagram in
AD# A221 842 Analysis and Forecasting"

Figure 7. The Successive Changes of the Temperature Lapse
Rate Due to Solar Heating of the Ground with Time.

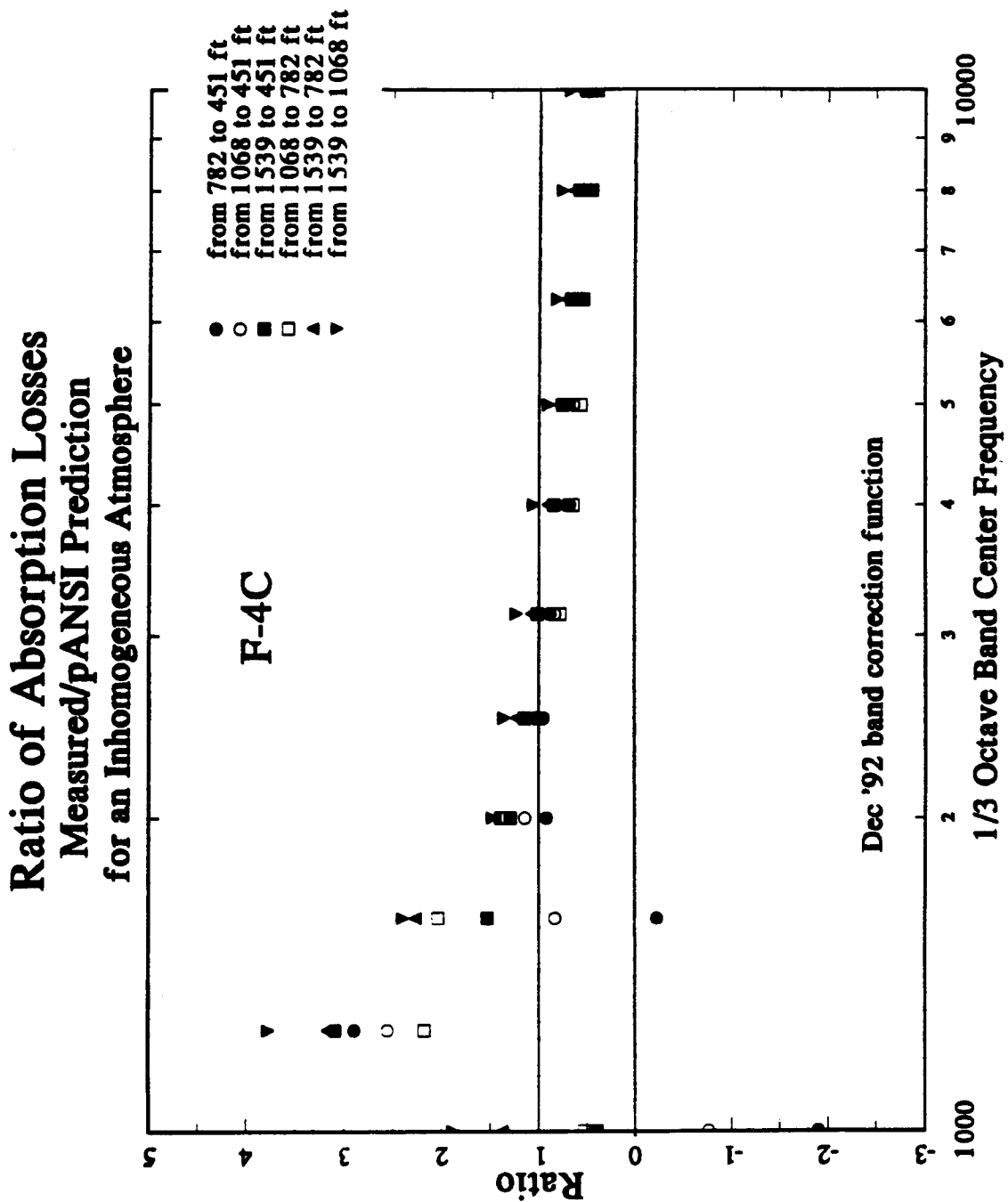


Figure 8. The pANSI Model's Predictions for an Inhomogeneous Atmosphere Compared to Aircraft Flight Noise Attenuations Measured near Vertical Emission.

Measured SPLs for F-4C at 98% RPM
at 90 degree emission angle

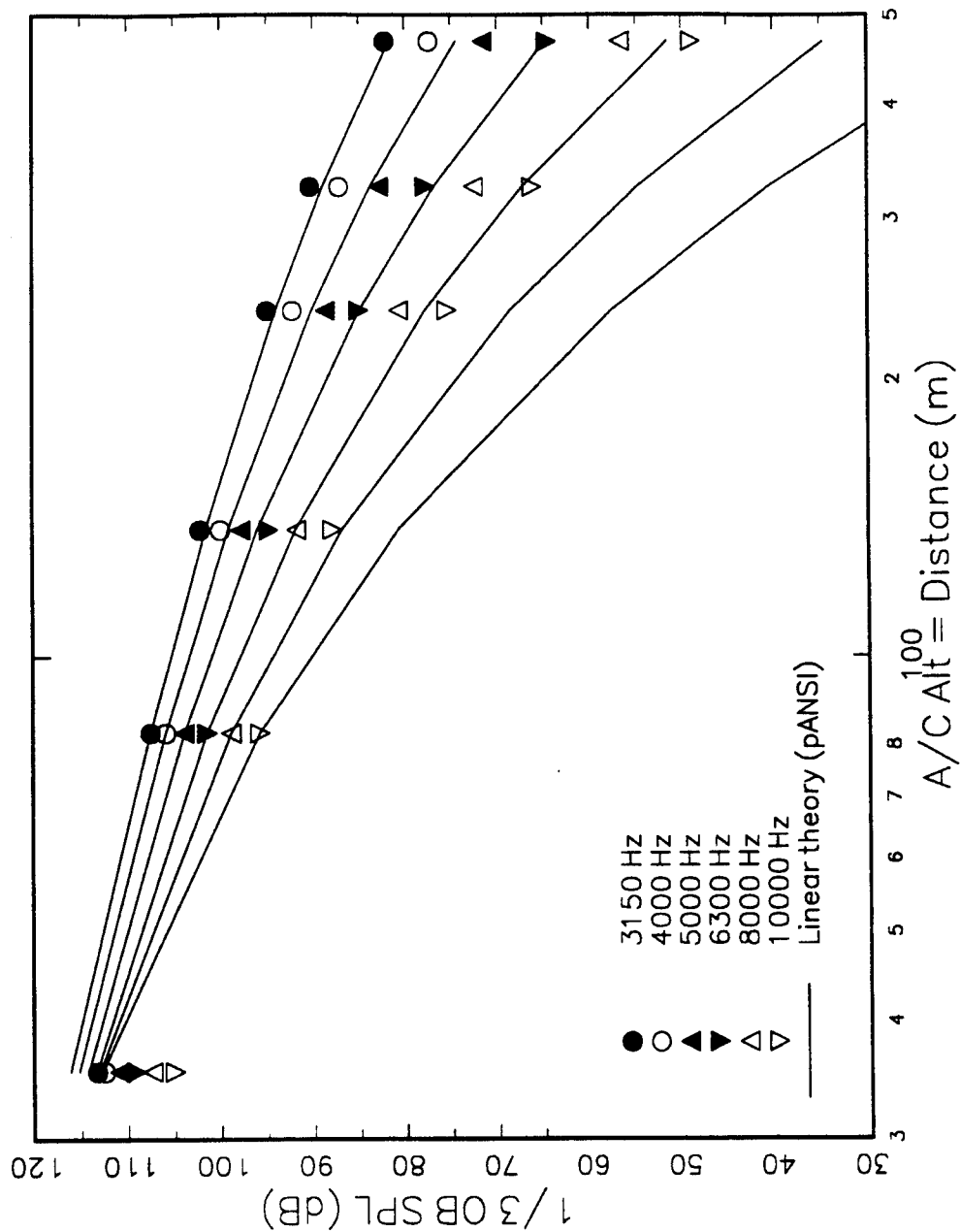


Figure 9. The pANSI Model's Predicted SPL vs Distance Curves in an Inhomogeneous Atmosphere Compared to F-4C Measured SPLs near Vertical Emission.

Measured SPLs for F-4C at 98% RPM
at 90 degree emission angle

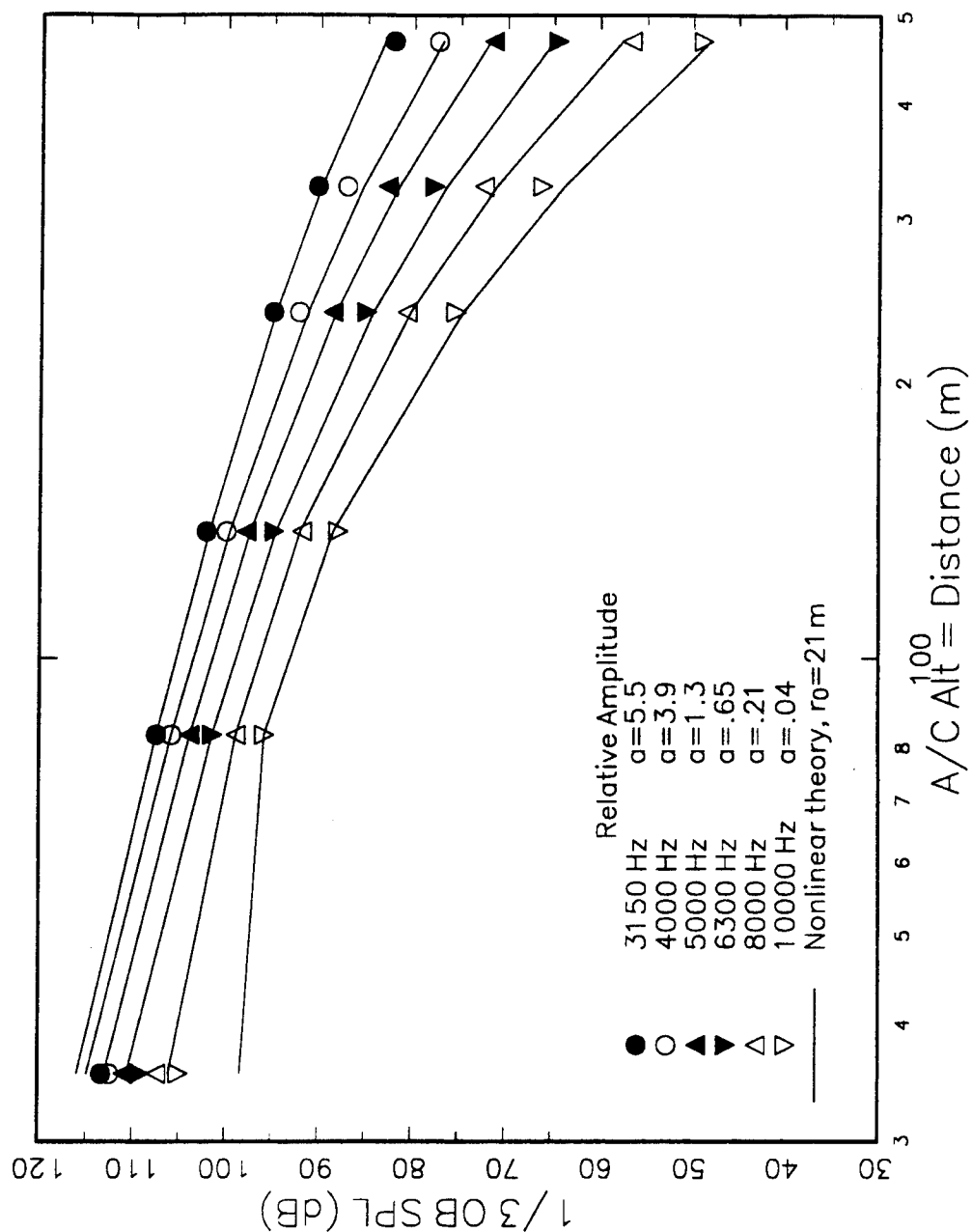


Figure 10. The Nonlinear Extension of the pANSI Model's Predicted SPL vs Distance Curves in an Inhomogeneous Atmosphere Compared to F-4C Measured SPLs near Vertical Emission.

F4-C Measured spectra at 6 altitudes (vertical emission)

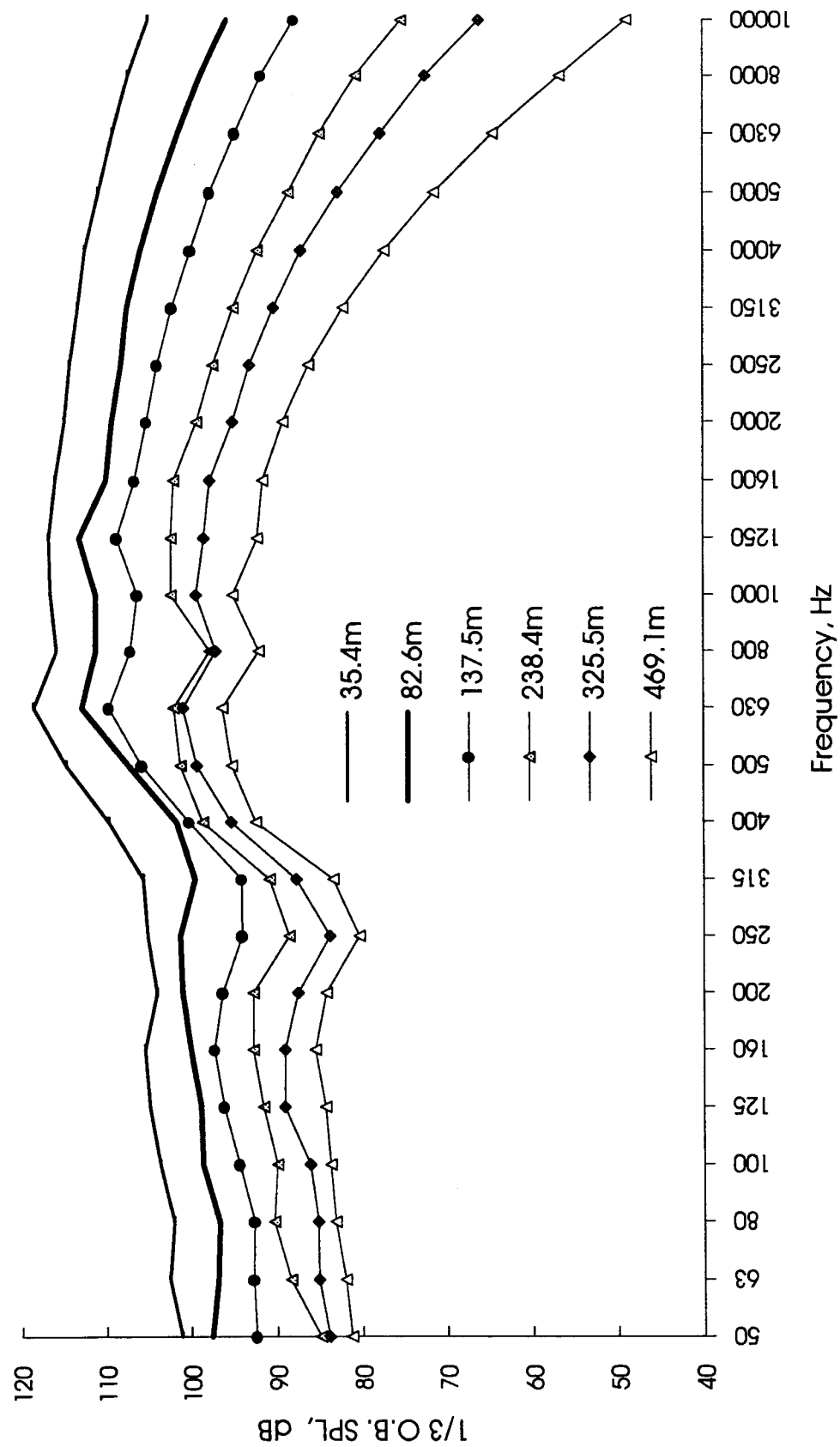


Figure 11.

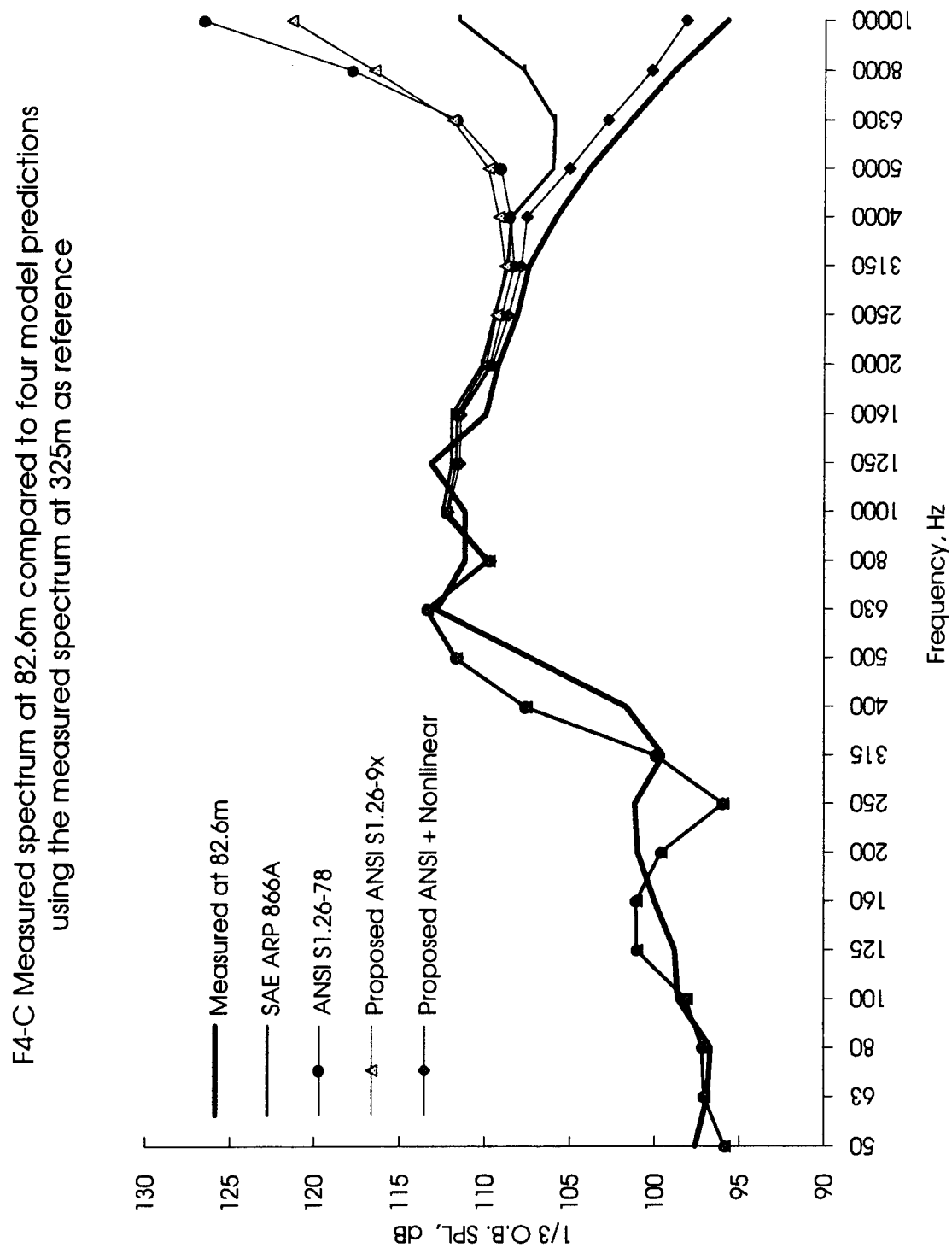


Figure 12.

Asynchronous Ensemble Averaging: A Travel-Time-Corrected
Averaging Method for Transient Waves in Random Media

Alan R. Wenzel
Fluid Mechanics and Acoustics Division
NASA Langley Research Center
Hampton, VA 23681-0001

ABSTRACT

A travel-time-corrected averaging procedure, intended for the study of propagation of transient waves in a random medium, is described. The procedure, called asynchronous ensemble averaging, is designed to eliminate certain spurious effects that arise when ordinary (synchronous) averaging is performed on an ensemble of waves that has become dispersed due to random travel times among the various members of the ensemble. Results obtained by applying asynchronous averaging to a relatively simple problem involving propagation of transient waves in a one-dimensional random medium are contrasted with corresponding results obtained using synchronous averaging. The advantages of asynchronous averaging are pointed out. It is shown that, for the case of sonic-boom propagation in the atmospheric boundary layer, random travel-time effects are likely to be important, and hence a travel-time-corrected averaging procedure is required, whenever the propagation path length is of the order of 5000 ft. or greater.

INTRODUCTORY REMARKS

The adoption of a stochastic, rather than a deterministic, approach in the analysis of any complicated physical phenomenon entails, of necessity, giving up precise but unreliable information about individual realizations in favor of less precise but more reliable information about ensemble averages. In the case of wave propagation--particularly transient wave propagation--in a random medium, a mechanism is at work which tends to exacerbate this loss of information about individual realizations. This mechanism is illustrated in the first figure.

1. AN ENSEMBLE OF WAVES

Figure 1 shows three members of an ensemble of transient waves, all of which have the same form; namely, that of a step-function pulse with amplitude W_0 . For simplicity, the waves are supposed to be propagating in a somewhat artificial medium which is such that only the propagation speeds of the waves are affected and consequently differ from one another in a random manner--the waveforms themselves are unaffected and hence remain identical.

As indicated in the figure, because of the variation in propagation speeds, the waves have become dispersed. The figure, incidentally, actually shows waveform signatures, which are graphs of the wave function (e.g., acoustic pressure, particle velocity) vs. time as recorded at a fixed observation point, and therefore illustrates dispersion in time.

As a consequence of the variation in propagation speeds among the various members of the ensemble, the travel time of each wave from source to receiver, and hence the arrival time of the wave at the receiver, will vary randomly across the ensemble. (The arrival times τ_1 , τ_2 , and τ_3 of the three waves shown in the figure are indicated.)

The expression shown at the top of the figure describes mathematically the ensemble of wave-function signatures. The symbol w denotes the wave function, which is written as a function of t only, since the observer is assumed to be at a fixed position in space. The quantity W_0 is the amplitude, H denotes the Heaviside unit step function, and τ is the arrival time. This last quantity is, as mentioned, assumed to be a random variable.

Suppose now that the ensemble average of these waves were to be calculated in the usual way; that is, with t fixed (fixed across the ensemble, that is). It's easy to visualize what the result will look like, even without doing any calculations. If the value of t at which the average is being carried out is so small that none of the waves of the ensemble has reached the observer by that time, then the ensemble average will be zero. If, on the other hand, t is so large that all of the waves of the ensemble have arrived at the observer by that time, then the ensemble average will be equal to W_0 . For intermediate values of t the average will be somewhere between zero and W_0 , depending on how many waves have reached the observer by that time.

The averaging procedure described above, in which every member of the ensemble of waves is sampled at the same time in forming the average, is referred to here as synchronous ensemble averaging.

It's clear, in view of the above remarks, that a plot of the synchronous-averaged waveform will generally be a smooth curve, starting at zero for some small value of t and increasing to the value W_0 for some large value of t . It's clear also that this waveform will generally bear no resemblance to the form of any individual wave. This discrepancy between the ensemble-averaged wave and the individual waves making up the ensemble arises solely as a

consequence of averaging over an ensemble of waves that has become dispersed due to random travel times among the various members of the ensemble. This phenomenon is referred to here as spurious distortion.

The spurious-distortion effect can also be demonstrated by means of a simple mathematical argument. The details are given on the next figure.

2. SYNCHRONOUS AVERAGING

The sketch in Figure 2 shows what the graph of the probability distribution function of the arrival times (i.e., the arrival times associated with the ensemble of waves discussed above) might look like. The symbol F denotes the distribution function; s , the independent variable, has the dimension of time.

The first equation defines the function F : It is, for every value of s , simply the probability that the arrival time is less than s .

It's clear that the graph of F must have, generally, the form shown on the sketch: It must be zero for all values of s that are less than some minimum value, say τ_- , of the arrival time, and it must be equal to unity for all values of s that are greater than some maximum value, say τ_+ , of the arrival time. For s between τ_- and τ_+ F must be a non-decreasing function taking on values between zero and one.

The precise shape of the curve shown in the figure depends, of course, on the extent to which the waves making up the ensemble have become dispersed by the time they reach the observation point. The function F thus depends also on the propagation path length; however, that dependence is not explicitly indicated here.

To calculate the ensemble-averaged wave function in terms of the function F , start with the same formula for the wave function that was shown in Fig. 1. This is the second formula in Fig. 2. The right-hand side of this expression is a function of the random variable τ ; therefore, in order to carry out the calculation, one can use a formula from probability theory that expresses the expectation of a function of a random variable in terms of the distribution function of the random variable. That formula is shown on the third line of Fig. 2. The symbol \bar{w}_s denotes the synchronous average of w .

The integral on the right-hand side of this expression is evaluated by noting that the Heaviside function vanishes when its argument is negative, and that $F(-\infty)$ is zero, which leads to the highlighted formula.

This result shows that, apart from the constant factor W_0 , the synchronous-averaged wave has a form identical to that of the function F . What is remarkable about this result is that the function F , and therefore the ensemble-averaged waveform, has no relation whatever to any individual wave of the ensemble. It is, instead, determined solely by the spread in travel times of the waves.

This result confirms mathematically what has already been shown heuristically; namely, that, as a consequence of dispersion due to random travel times, the (synchronous) ensemble-averaged waveform may be distorted to such an extent that it no longer resembles the form of any individual wave.

The ultimate consequence of the spurious-distortion effect (as it has been referred to here) is therefore to render the ensemble-averaged waveform irrelevant insofar as the form of any individual wave is concerned. For the

applied scientist, this poses certain difficulties. Individual waves are, after all, what the physicist or engineer is most often concerned with. Individual electromagnetic waves, for example, not ensemble averages, are what carry information along a transmission line, and individual sonic booms, not ensemble averages, are what cause annoyance and structural damage. It's to the advantage of the applied scientist, therefore, that his ensemble averages reflect, as accurately as possible, individual waveforms.

Spurious distortion has long been recognized as an undesirable consequence of the standard ensemble-averaging procedure, and a number of techniques have been proposed for overcoming it. Crow, for example, in his analysis of sonic-boom propagation [1], adopted the expedient of simply dropping from his approximate expression for the scattered field the term (which he called the phase-shift term) that gives rise to what has here been called spurious distortion. Wu [2] did something similar in discarding the forward-scatter term from his expansion of the wave field. Plotkin and George [3] took an even more drastic step in dropping the entire first-order scattering term from their double-scatter approximation of the wave field, in an attempt to eliminate the spurious-distortion effect. The hazard of such wholesale elimination of inconvenient terms from the analysis is, of course, that it may lead to an unacceptable error in the final expression for the wave field. This is exemplified in the case of the analysis of Plotkin and George [3], wherein the discard of all of the single-scatter terms leads to the loss of some important single-backscatter contributions to the wave field.

A different approach to this problem was taken by Burridge, et al. [4], who avoided the problem entirely by basing their analysis on spatial averages rather than on ensemble averages. That approach, however, is feasible only when a suitable relation exists between the relevant length scales associated with the particular phenomenon under study. (In their case, the characteristic length scale of the medium was assumed small compared to a typical wave length.)

Other investigators, such as Pierce [5], have treated the problem of spurious distortion in a manner which (like the method proposed herein) takes explicit account of travel-time variations among the members of the ensemble of waves. Sato [6] and Stanke and Burridge [7] have attempted to incorporate this idea into a systematic procedure by introducing the travel time explicitly into the wave equation at the outset. The drawback of this type of approach is that it generally leads to equations for the wave field that are more complicated than the standard wave equation.

The method proposed herein, like those mentioned in the preceding paragraph, is based on the idea of including the travel time explicitly in the analysis as a random variable. In order to avoid the complexities inherent in the treatments described in [6] and [7], however, the travel time is introduced at a later stage in the analysis, rather than at the outset.

The method is described in detail in the next two sections.

3. AN ENSEMBLE OF WAVES II

Figure 3 shows the same ensemble of waves that was shown in Fig. 1, except that here a time interval r , relative to the arrival time, has been marked off on each waveform. The time interval r is to be regarded as a fixed parameter (fixed across the ensemble, that is) for purposes of ensemble averaging.

The essential feature of the averaging method proposed here is that each wave is sampled at the time r , relative to its arrival time, in order to form the ensemble average. Thus, each wave is sampled at the time $\tau + r$, where τ is the arrival time for that wave.

Sampling in this way is equivalent to, in effect, sliding each waveform along the time axis until its arrival time coincides with the origin, and then sampling at a fixed time in order to form the ensemble average. The result of this procedure is to eliminate the influence of travel-time induced dispersion on the ensemble average, which is the mechanism underlying spurious distortion.

Sampling each wave at a fixed time relative to its arrival time entails sampling each wave at a different absolute time (since the waves generally have different arrival times) in order to form the ensemble average. For this reason, the averaging method proposed here is referred to as asynchronous ensemble averaging.

The analytical procedure by which asynchronous averaging is applied to the ensemble of waves being considered here is described on the next figure.

4. ASYNCHRONOUS AVERAGING

The first formula in Fig. 4 is the same formula for the ensemble of waves that was shown in Fig. 1, and for which the (synchronous) ensemble average was calculated using the distribution function of the travel time. The procedure for obtaining the asynchronous average of this ensemble is actually somewhat easier to carry out than was the calculation of the synchronous average.

The first step is to replace t by $\tau + r$ (the travel time plus the time relative to onset at which the average is being formed). This yields the result shown on the third line. Note that, since $t - \tau = r$, the travel time τ has disappeared from the right-hand side, leaving only a function of r , which is determinate. Inasmuch as the randomness has disappeared from this expression, the ensemble-averaging process is trivial--it just returns the same function again. The result is shown highlighted, where \bar{w}_a denotes the asynchronous-averaged wave function.

A plot of \bar{w}_a as a function of r is sketched at the bottom of the figure. Note that asynchronous averaging has removed the random travel-time effect from the ensemble average. Since this was, in this case, the only effect acting to distort the waveform of the averaged wave, asynchronous averaging returns simply the original step-function waveform.

Asynchronous averaging has thus eliminated entirely the spurious-distortion effect.

Generalizing the procedure described above leads to the following recipe for applying asynchronous averaging to the study of wave propagation in random media:

- (1) Obtain an analytic solution (generally approximate), by whatever method is appropriate, for each member of the ensemble. In other words, first solve the problem as if it were deterministic.
- (2) Wherever the time variable t appears in the solution, replace it by $\tau + r$, where τ is the travel time and r is the time relative to onset (assumed fixed across the ensemble) at which the ensemble average is to be formed. (The travel time must generally be obtained by means of a separate calculation.)
- (3) Carry out the ensemble average.

The procedure outlined above for applying asynchronous averaging involves an additional step (step 2), as compared to the corresponding procedure for synchronous averaging. For this reason, and because step 3 (the carrying out of the ensemble average) is likely to be more complicated as a result of step 2 than it would be otherwise, asynchronous averaging is generally a somewhat more complicated procedure than is synchronous averaging. There are, however, exceptions to this rule. The situation treated just above is a case in point: Because the term $t - \tau$ appears explicitly in the expression for the wave function (the

first line in Fig. 4), when t is replaced by $\tau + r$, prior to carrying out the asynchronous-averaging process, this term reduces to just r , which is determinate. As a consequence, the entire right-hand side of this expression becomes determinate, which, of course, renders the ensemble-averaging procedure trivial.

Something similar occurs when the wave function is expressed in terms of a wave-front expansion. That approach is suitable when information on the wave function is sought only in a region near the wave front. (See [8], p. 236.) In that case the wave function can be expanded as a sum of terms, each of which has the same form as the term on the right-hand side of the first equation in Fig. 4, except that H is a function of more general form (i.e., more general than a step function, but still determinate), while W_0 is generally a random function of the spatial coordinate. When the substitution of $\tau + r$ for t is made, as described above, the function H again becomes determinate, leaving W_0 as the only random function remaining in the expression. The asynchronous ensemble-averaging process is then much easier to carry out than is synchronous averaging, since it involves only the single function W_0 instead of the product of W_0 and H .

An important case in which asynchronous averaging does in fact turn out to be more complicated than synchronous averaging is that in which an approximation to the wave function is sought in the form of an expansion in powers of a small parameter measuring the magnitude of the variations in the refractive index of the medium. This type of perturbation approach is appropriate when the medium is inhomogeneous, but only weakly so.

The procedure by which asynchronous averaging is applied to this case is described on the next three figures.

5. PERTURBATION METHOD

The problem under consideration here; namely, propagation of transient waves in a one-dimensional, weakly inhomogeneous random medium, is set out on the upper part of Fig. 5a. The key parameters appearing here are the wave function w , the sound speed c , which is assumed to be a random function of the spatial coordinate; also c_0 , a constant reference sound speed, μ , a random function with zero mean and unit variance, and ϵ , the standard deviation of the index of refraction of the medium, which is assumed to be small. Letter superscripts denote derivatives.

Regardless of whether synchronous or asynchronous averaging is used, the analysis is based on the assumption that w has an expansion in powers of ϵ as written out on the third equation line. Shown on the following two lines are, for future reference, expressions for the travel time τ , and its mean and fluctuating parts; namely, $\bar{\tau}$ and $\epsilon\tau_1$, respectively.

Synchronous averaging of the wave function is, in this case, a straightforward procedure: One simply averages the expansion for w with both x and t held fixed. The result appears on the bottom line of Fig. 5a. Here \bar{w}_s denotes the synchronous-averaged wave function. The first-order term does not appear in this expansion, since it is linear in the random function μ and hence averages to zero.

The asynchronous-averaging procedure for this case is described on Figs. 5b and 5c.

The first step in calculating the asynchronous ensemble average of the wave function for this case is, following the general procedure set out previously, to replace t by $\tau + r$ in the expansion of w , where r is a fixed (across the ensemble) time parameter. The result is shown on the first equation line of Fig. 5b.

The ensemble average of the resulting expression for w can not, in general, be calculated directly. This is because the coefficients w_0 , w_1 , w_2 , etc. appearing on the right-hand side are functions of τ , which is a random variable. Ensemble averaging of these coefficients can not therefore be carried out without information on the distribution function of τ --information that is generally not available. That the higher-order coefficients w_1 , w_2 , etc. are themselves random functions complicates matters further.

An alternative approach is to write the quantity $\tau + r$ as shown on the third equation line of Fig. 5b (using the expression for τ given on Fig. 5a). Next, that expression is used to substitute for the quantity $\tau + r$ in each of the coefficients w_0 , w_1 , w_2 , etc., which are then expanded in powers of ϵ . That procedure is described mathematically on the lower half of Fig. 5b. The resulting expression for w is the one that begins on the last line of Fig. 5b and is continued on Fig. 5c. Averaging it yields the last equation in Fig. 5c, which is an expression for \bar{w}_A , the asynchronous-averaged wave function, in terms of known or calculable quantities.

Comparing the expression for \bar{w}_A given in Fig. 5c with

the one for \bar{w}_s , the corresponding synchronous-averaged result that appears in Fig. 5a, reveals (after terms of order ϵ^3 are dropped from both expressions) that the former contains two more terms on the right-hand side than does the latter. These are the second and third terms on the right-hand side of the last equation in Fig. 5c. (Note that t is simply a parameter in the expression for \bar{w}_s , while $\tau + r$ plays an analogous role in the expression for \bar{w}_n .) Thus, correcting for travel-time effects requires in this case the calculation of two additional terms in the expression for the ensemble-averaged wave function.

6. SONIC BOOM

The last figure (Fig.6) shows the derivation of an order-of-magnitude estimate of the propagation distance at or beyond which random travel-time effects are important in the case of sonic-boom propagation in the atmospheric boundary layer. The calculation is based on the one-dimensional model described in the previous section.

As indicated on the first equation line, travel-time effects are deemed important whenever the standard deviation of the travel time exceeds the magnitude of the smallest time scale of the wave, which in the case of a sonic boom is the rise time. Based on parameter values typical of sonic-boom propagation in the atmospheric boundary layer (rise time δ about 1 msec; nominal sound speed c_0 about 1000 ft/sec; index-of-refraction standard deviation ϵ about 1/1000), an estimate of 5000 ft. is obtained for the critical propagation distance. As it happens, this is approximately equal to the boundary-layer height (under typical daytime conditions).

Inasmuch as sonic booms generally originate much higher in the atmosphere than the top of the boundary layer, they must, of necessity, propagate through the entire boundary layer before reaching the ground. It follows, in view of the above calculation, that, under typical daytime conditions, these booms will be subject to appreciable travel-time effects, and that these effects must be taken into account in any theoretical study of the statistics of sonic-boom signatures as received at ground level.

REFERENCES

1. Crow, S.C. J. Fluid Mech. 37 (1969) 529-563
2. Wu, R.-S. Wave Motion 4 (1982) 305-316
3. Plotkin, K.J. and George, A.R. J. Fluid Mech. 54 (1972) 449-467
4. Burridge, R. et al. Wave Motion 10 (1988) 19-44
5. Pierce, A.D. J. Acoust. Soc. Am. 49 (1971) 906-924
6. Sato, H. J. Acoust. Soc. Am. 71 (1982) 559-564
7. Stanke, F., and Burridge, R. J. Acoust. Soc. Am. 93 (1993) 36-41
8. Whitham, G.B. Linear and Nonlinear Waves. Wiley 1974

AN ENSEMBLE OF WAVES

$$w(t) = W_0 H(t - \tau)$$

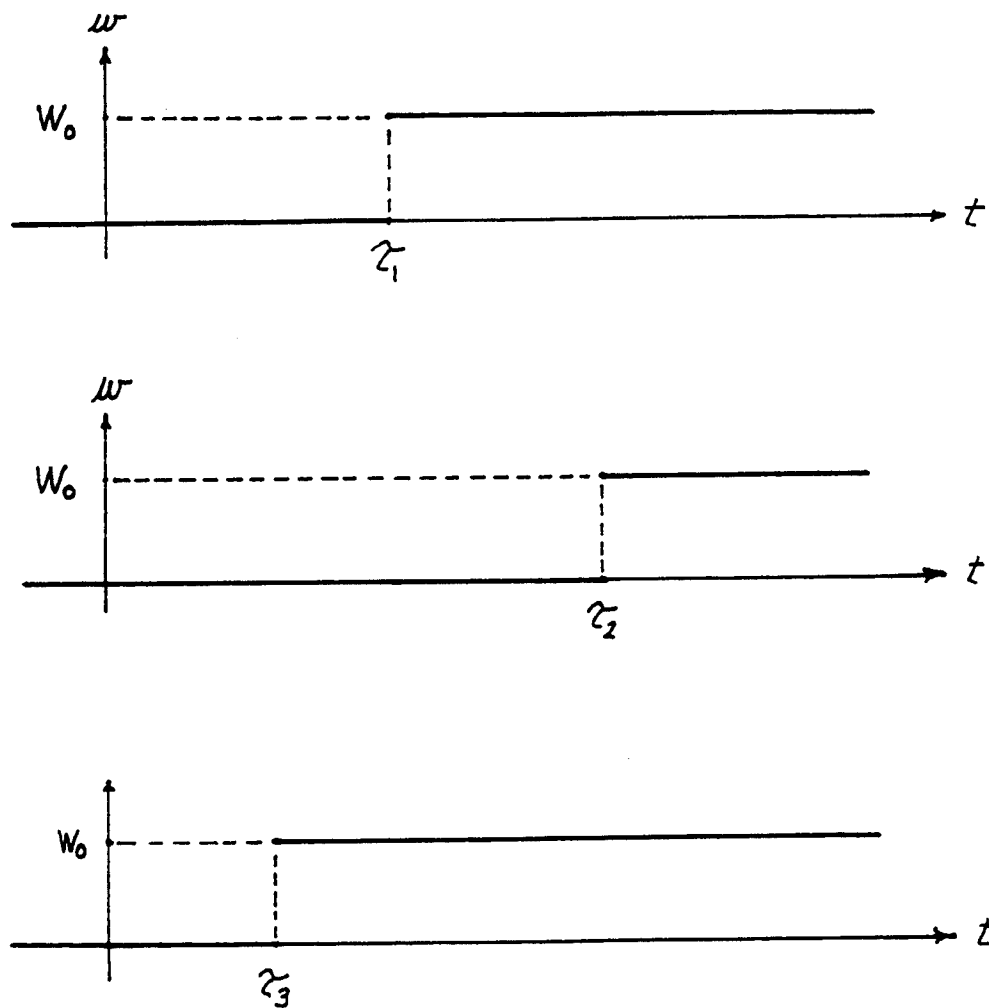
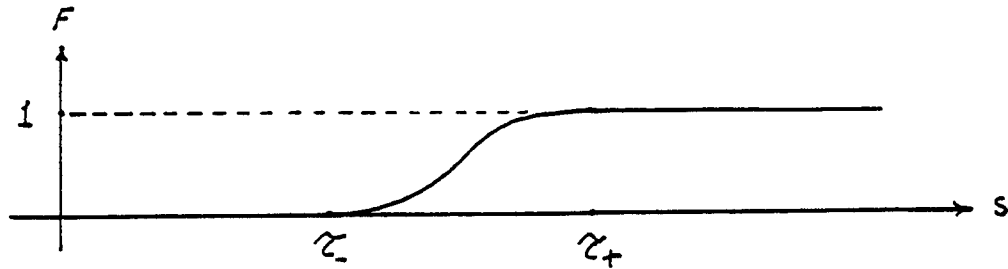


FIG. 1

SYNCHRONOUS AVERAGING



$$F(s) = \text{Pr} \{ z < s \}$$

$$w(t) = W_0 H(t - z)$$

$$\bar{w}_s(t) = W_0 \langle H(t - z) \rangle = W_0 \int_{-\infty}^{+\infty} H(t - s) dF(s)$$

$$= W_0 \int_{-\infty}^t dF(s) = W_0 [F(t) - F(-\infty)]$$

$$\bar{w}_s(t) = W_0 F(t)$$

FIG. 2

AN ENSEMBLE OF WAVES II

$$w(t) = W_0 H(t - \tau)$$

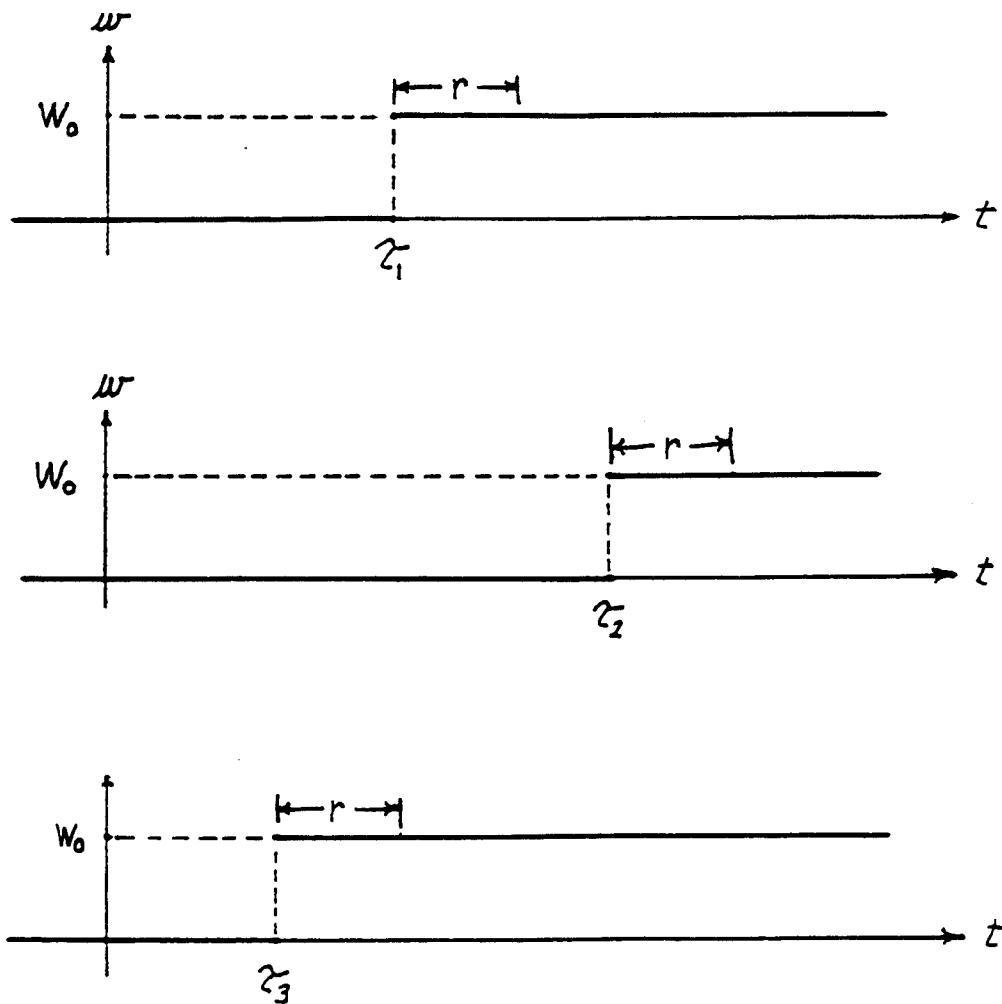


FIG. 3

ASYNCHRONOUS AVERAGING

$$w(t) = W_0 H(t - \tau)$$

$$t = \tau + r \Rightarrow t - \tau = r$$

$$w(\tau + r) = W_0 H(r)$$

$$\bar{w}_A(r) = W_0 H(r)$$

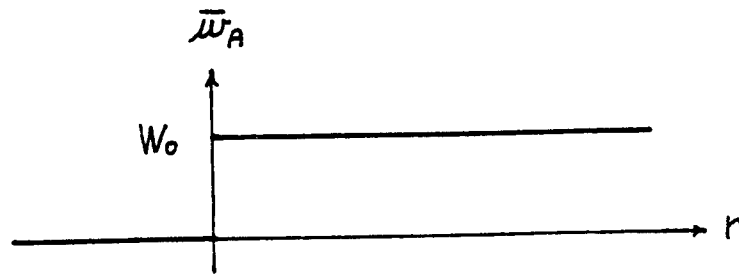


FIG. 4

PERTURBATION METHOD I

Waves in a weakly inhomogeneous medium:

$$c^{-2} w^{tt} - w^{xx} = f \quad ; \quad t > 0, \quad -\infty < x < +\infty$$

$$c(x) = \frac{c_0}{1 + \epsilon \mu(x)} \quad ; \quad \langle \mu \rangle = 0, \quad \langle \mu^2 \rangle = 1$$

$$w(x, t; \epsilon) = w_0(x, t) + \epsilon w_1(x, t) + \epsilon^2 w_2(x, t) + \dots$$

$$\tau = \int_0^x \frac{dy}{c(y)}$$

$$\tau = \tau_0 + \epsilon \tau_1 \quad ; \quad \tau_0 = \frac{x}{c_0}, \quad \tau_1 = \frac{1}{c_0} \int_0^x \mu(y) dy$$

Synchronous averaging:

$$\bar{w}_s(x, t; \epsilon) = w_0(x, t) + \epsilon^2 \langle w_2(x, t) \rangle + \dots$$

FIG. 5a

PERTURBATION METHOD II

Asynchronous averaging: $t = \tau + r$,

$$\begin{aligned} w(x, \tau + r; \epsilon) &= w_0(x, \tau + r) + \epsilon w_1(x, \tau + r) \\ &+ \epsilon^2 w_2(x, \tau + r) + \dots \end{aligned}$$

$$\tau + r = \tau_0 + r + \epsilon \hat{z}_1$$

$$\begin{aligned} w_0(x, \tau + r) &= w_0(x, \tau_0 + r + \epsilon \hat{z}_1) = w_0(x, \tau_0 + r) \\ &+ \epsilon \hat{z}_1 w_0^t(x, \tau_0 + r) + \frac{1}{2} \epsilon^2 \hat{z}_1^2 w_0^{tt}(x, \tau_0 + r) + O(\epsilon^3) \end{aligned}$$

$$\begin{aligned} w_1(x, \tau + r) &= w_1(x, \tau_0 + r + \epsilon \hat{z}_1) = w_1(x, \tau_0 + r) \\ &+ \epsilon \hat{z}_1 w_1^t(x, \tau_0 + r) + O(\epsilon^2) , \end{aligned}$$

$$w_2(x, \tau + r) = w_2(x, \tau_0 + r + \epsilon \hat{z}_1) = w_2(x, \tau_0 + r) + O(\epsilon)$$

$$w(x, \tau + r; \epsilon) = w_0(x, \tau_0 + r) + \epsilon \hat{z}_1 w_0^t(x, \tau_0 + r)$$

FIG. 5b

PERTURBATION METHOD III

$$\begin{aligned}
 & + \frac{1}{2} \epsilon^2 \hat{z}_1^2 \mathcal{W}_0^{tt}(x, z_0 + r) + \epsilon \mathcal{W}_1(x, z_0 + r) \\
 & + \epsilon^2 \hat{z}_1 \mathcal{W}_1^t(x, z_0 + r) + \epsilon^2 \mathcal{W}_2(x, z_0 + r) + \mathcal{O}(\epsilon^3)
 \end{aligned}$$

$$\begin{aligned}
 \bar{\mathcal{W}}_A(x, r; \epsilon) &= \mathcal{W}_0(x, z_0 + r) + \frac{1}{2} \epsilon^2 \langle \hat{z}_1^2 \rangle \mathcal{W}_0^{tt}(x, z_0 + r) \\
 &+ \epsilon^2 \langle \hat{z}_1 \mathcal{W}_1^t(x, z_0 + r) \rangle + \epsilon^2 \langle \mathcal{W}_2(x, z_0 + r) \rangle + \mathcal{O}(\epsilon^3)
 \end{aligned}$$

FIG. 5c

SONIC BOOM

Travel-time - corrected averaging necessary when

$$\langle (\tau - \tau_0)^2 \rangle^{1/2} \gtrsim \delta, \text{ or } \epsilon \langle \tau_1^2 \rangle^{1/2} \gtrsim \delta.$$

$$\langle \tau_1^2 \rangle = \frac{1}{c_0^2} \left\langle \left[\int_0^x \mu(y) dy \right]^2 \right\rangle \approx \frac{2lx}{c_0^2}; \quad x \gg l$$

$$\frac{\epsilon}{c_0} \sqrt{2lx} \gtrsim \delta, \quad x \gtrsim \frac{1}{2l} \left(\frac{\delta c_0}{\epsilon} \right)^2$$

Sonic boom: $\delta \approx 10^{-3}$, $c_0 \approx 10^3$, $\epsilon \approx 10^{-3}$,
 $l \approx 10^2$

$$x \gtrsim 5000 \text{ ft.}$$

FIG. 6

ATMOSPHERIC EFFECTS ON THE RISE TIME AND WAVESHAPE OF SONIC BOOMS

Richard Raspet, Henry E. Bass and Patrice Boulanger
Department of Physics and Astronomy
University of Mississippi
University, MS 38677

ABSTRACT

Accurate prediction of human response to sonic booms from proposed HSCT aircraft depends on a knowledge of the waveshape and risetime of the boom at the ground. In previous work, we have developed a numerical technique to predict the combined effects of molecular absorption and finite wave distortion on the sonic boom as it propagates from the aircraft to the top of the turbulent boundary layer. We have more recently developed a scattering center based model to calculate the effects of turbulence on the sonic boom waveform as it propagates through this boundary layer. Calculations have been performed using single scales of turbulence and compared to measurements at Edwards AFB in the late 1960s. A model of the atmosphere involving two scales each for convective and mechanical turbulence has been developed and fit to meteorological data collected during JAPE 2. Scattering calculations employing this model underpredict the number of unperturbed waveforms. In order to develop a more realistic model of the atmosphere, the JAPE 2 meteorological data has been fit to a von Karman spectrum. Results of scattering using this multi-scale model will be presented. The combination of finite wave effects with turbulent scattering predictions includes the principle effects of the atmosphere on the sonic boom from the HSCT.

INTRODUCTION

The prediction of the average environmental impact of the HSCT requires accurate modeling of the processes affecting the sonic boom waveform and risetime. We have used the enhanced Anderson algorithm to predict the risetime and waveshape of sonic booms under non-turbulent conditions. This method can also be used to predict the risetime and waveshape at the top of the turbulent planetary boundary layer.

The enhanced Anderson algorithm includes all finite wave effects and the vibrational relaxation effects of N_2 , O_2 , and CO_2 in combination with atmospheric H_2O . This algorithm has been compared to data from sonic explosions¹ and sonic booms² and has been tested against measurements of high intensity ballistic waves from rifles and from tank guns³. In addition, the results of this calculation for quasi steady shocks agree with the results from the enhanced Burgers' Equation^{4,5}.

Figure 1 presents the results of the application of the enhanced Anderson algorithm to a predicted HSCT waveform. We emphasize that the key parameter in determining the risetime of the sonic boom is the absolute humidity.

Under turbulent conditions, the risetime of sonic booms are scattered and are occasionally as large as ten times the risetime calculated from vibrational relaxation considerations. It is clear that turbulence is the cause of the increased risetime and peculiar waveforms observed. Analytic techniques have been used to estimate the increase in average risetimes^{7, 8, 9} and to calculate perturbed waveforms due to focusing and defocusing of the waves by turbulence¹⁰. In such calculations, it is usually necessary to assume a single strength and turbulence scale representative of the atmospheric turbulence. The largest turbulence effects are usually identified when the largest scales are chosen as typical.

We have chosen a different approach to calculating the effects of turbulence on sonic boom risetimes and waveforms based on a simple scattering center-based theory. The scattering center-based method accurately predicted the effects of turbulence on the coherence of continuous wave signals above natural ground surfaces¹¹.

METHOD

The scattering center-based technique resolves atmospheric fluctuations into a sum of discrete spherically symmetric Gaussian "turbules". The total effect of the atmosphere is then calculated by summing up the scattering amplitudes. See Figure 2. The scattered amplitudes are calculated using the first Born approximation. If the complex pressure at the receiver is written as:

$$\vec{p}^B(\vec{r}) = \vec{p}_o(\vec{r}) + \sum_{i=1}^N \vec{\psi}_i^B \quad (1)$$

where the superscript B refers to the first Born approximation, $\vec{p}_o(\vec{r})$ is the unperturbed spherical wave, and N is the number of turbules, then

$$\vec{\psi}_i^B = \frac{\sqrt{\pi}}{2} q_i k^2 s^3 \frac{e^{ik(r_{st} + r_{tr})}}{r_{st} + r_{tr}} \left[\frac{1}{1 - ia} \right] e^{-Ck^2 s^2/4} \quad (2)$$

where

$$C = (1 - \cos \theta_o)^2 + \sin^2 \theta_o \left[\frac{1}{1 - ia} \right] \quad (3)$$

and

$$a = \frac{ks^2}{2} \left[\frac{1}{r_{st}} + \frac{1}{r_{tr}} \right] \quad (4)$$

s defines the $1/e^2$ contour of the turbule, q_i is the index of refraction profile strength, and θ_o is the scattering angle. The geometry is indicated in Figure 3.

The initial research on continuous wave propagation, modeled the atmosphere as a random sum of identical turbules. This single scale calculation was extended to impulse propagation with promising results.¹² The impulse is Fourier transformed into the frequency domain and the total scattered component at each frequency is calculated. Then the inverse Fourier transform yields the time domain waveform. The single scale calculation (s = 10m, 30m or 100m) with a fluctuating index of refraction of $\langle \mu^2 \rangle = 10 \times 10^{-6}$ predicted spiked and rounded waveforms and predicted risetimes as large as 10 ms. These results encouraged us to analyze the results of the JAPE-2 tests^{13,14} using the scattering center-based model.

ANALYSIS OF JAPE-2 DATA

The JAPE-2 tests consisted of simultaneous measurement of sonic boom characteristics and meteorological measurements. The wind and temperature fluctuations were measured at heights up to 30m using sonic anemometers and hot wire anemometers. The sonic boom data was analyzed by Willshire, Garber and DeVilbiss¹⁴ and provided as computer files. The turbulence data was analyzed by Bass, Boulanger, Olsen and Chintawongvanich¹⁵.

a.) Two Scale Model

Examination of the data showed that a single scale model of the atmosphere could not fully describe the turbulence above the ground. The time correlation of the fluctuation quantities was fit to a two scale model. See Figure 4. Table I displays the results of the analysis for a moderately turbulent day during JAPE-2.

Table I. Example of the Two Scale Model Applied to Atmospheric Data

	Wind driven 1	Wind driven 2	Temp. driven 1	Temp. driven 2
Size (meters)	117	11	74	8
Number of Eddies	1	90	1	233
$\langle \mu^2 \rangle$	$0.54 \cdot 10^{-5}$	$0.25 \cdot 10^{-5}$	$0.5 \cdot 10^{-6}$	$0.4 \cdot 10^{-6}$

The scattering calculation was performed by summing the results of four calculations - one for each scale size. The input waveform to the scattering calculation was an N-wave propagated from the flight altitude to the top of the turbulent layer using the enhanced Anderson algorithm. The results of the Anderson algorithm agree moderately with the measurements taken under low turbulence conditions. See Table II.

Table II. Comparison of Measured and Predicted Waveform Parameters for the T-38

	Measurements for the low turbulence case	Calculations using the Anderson algorithm
Peak overpressure (psf)	0.71	0.88
Risetime (ms)	0.32	0.33

Figure 5 compares the results of the measurement and prediction for T-38 overflights under moderate turbulence conditions. Although the scattering center model produces a wide distribution of risetimes, it does not predict the shift of the histogram maximum to 2 ms; rather the maximum remains at the unperturbed value of 0.3 ms. It is believed that this is due to the use of two relatively large scales to represent the atmospheric turbulence. The scattering from large turbules is predominantly in the forward direction, and large turbules are relatively sparse, so that it is easy to "miss" the receiver with the scattered wave. The four scale model does, however, represent a significant improvement over the single scale model.

b.) von Karman Spectrum Model

The fit of the autocorrelation to two scales rather than one, improved the prediction of risetimes significantly. The high occurrence of unperturbed risetimes indicated that smaller and intermediate scales were needed to fully describe the scattering of sonic booms by turbulence.

De Wolf¹⁶ presented a technique for simulation of a turbulent atmosphere obeying the von Karman spectrum in terms of the number density of turbules.

The general form of a 3-D von Karman spectrum is given in terms of frequency by:

$$\phi(f) = \frac{a f^2}{(f^2 + b)^{\frac{11}{6}}} \quad (5)$$

where:

$$a = 4\pi\gamma C_\epsilon^2 \left(\frac{c}{2\pi}\right)^{2/3} \quad (6)$$

and

$$b = \left(\frac{c}{2\pi L_o}\right)^2 \quad (7)$$

The coefficients a and b are determined by fitting a function $\phi(f)$ through the measured spectra. See Figure 6.

The fit parameters are then used to determine $n(s)$, the number density of turbules of size s needed to model the fluctuating atmosphere. De Wolf's model was originally developed to predict second moments of a scattered field and therefore is designed to reproduce only second moments of the fluctuation fields. Higher moments must be accurately represented to express the temporal characteristics of an impulse. De Wolf used an index of refraction maximum for each turbule of ± 1.0 and employed a very sparse distribution. We have varied the product of q_i^2 and $n(s)$ until the model distribution approximates the measured second and fourth moments $\langle \mu^2 \rangle = 9.6 \times 10^{-6}$, $\langle \mu^4 \rangle = 2.5 \times 10^{-10}$. The variation of calculated $\langle \mu^2 \rangle$ with number of turbules and q_i^2 is shown in Table III.

Table III. Calculate $\langle \mu^2 \rangle$ and $\langle \mu^4 \rangle$ as a Function of Number of Turbules

Number of Turbules	Percentage of Volume	q_i^2	$\langle \mu^2 \rangle$	$\langle \mu^4 \rangle$
42000	8	1.5×10^{-4}	1.2×10^{-5}	1.0×10^{-9}
63000	12	1.0×10^{-4}	1.1×10^{-5}	1.0×10^{-9}
95000	18	6.7×10^{-5}	1.0×10^{-5}	6.9×10^{-10}
127000	24	5.0×10^{-5}	1.1×10^{-5}	5.5×10^{-10}
254000	48	2.5×10^{-5}	9.9×10^{-6}	4.4×10^{-10}

The turbulence spatial and size distribution for each realization is determined by Monte Carlo methods. The index of refraction fluctuations along a straight line has been compared to the corresponding measured values and exhibit similar fluctuation scales and displacement.

The second improvement to the scheme was the use of the measured height of the Planetary Boundary Layer in the calculation. Figure 7 displays the temperature versus height curve for one flight during JAPE-2. One sounding is taken with the tethersonde going up and the inversion height is 400m, the other trace is the tethersonde coming down 30 minutes later and the inversion height is at 670m. The turbulent layer thickness at the time of the later sonic boom measurement was extrapolated from this as 750m.

The results of this calculation for 20 realizations are displayed in Figure 8. The maximum occurrence risetime shows a shift away from the non-turbulent risetime of 0.3 ms. The smaller and intermediate scales of turbulence have a significant effect on the risetimes of sonic booms. It is clear, however, that the shift is not large enough to match the measured data in Figure 5a.

CONCLUSION

The enhanced Anderson algorithm provides a good prediction of waveshape and risetime of the HSCT at the top of the Planetary Boundary Layer.

The scattering center-based model can be extended to predict distorted wave shapes and longer risetimes. At this stage, the scattering based model does not predict long enough average risetimes, but does show that smaller and intermediate scales are important in increasing the average risetimes.

The larger scales are the source of the dramatically distorted waveforms, but are not the source of the shift in average risetimes. The scattering center-based calculation allows the quantitative investigation and modeling of the turbulence effects discussed qualitatively by Crow, Plotkin and George, and Pierce.

REFERENCES

1. Bass, H. E.; and Raspet, Richard: Vibrational relaxation effects on the atmospheric attenuation and risetimes of explosion waves. *J. Acoust. Soc. Am.*, vol. 64, 1978, pp. 1208-1210.
2. Bass, H. E.; Ezell, J.; and Raspet, R.: Effect of vibrational relaxation on risetime of shock waves in the atmosphere. *J. Acoust. Soc. Am.*, vol. 74, 1983, pp. 1514-1517.
3. Bass, H. E.; Layton, B. A.; Bolen, L. N.; and Raspet, R.: Propagation of medium strength shock waves through the atmosphere. *J. Acoust. Soc. Am.*, vol. 82, 1987, pp. 306-310.
4. Bass, Henry E.; and Raspet, Richard: Comparison of sonic boom risetime prediction techniques. *J. Acoust. Soc. Am.*, vol. 91, 1992, pp. 1761-1768.
5. Kang, J.; and Pierce, A. D.: Contribution of molecular relaxation to rise time of sonic booms. *J. Acoust. Soc. Am.*, Supp. 1, vol. 85, 1989, p. S81.
6. Raspet, Richard; and Bass, Henry E.: Comparison of Shock Rise Time Prediction Techniques. AIAA 13th Aeroacoustics Conference, Tallahassee, FL, Oct. 22-24, 1990.
7. Crow, S. C.: Distortion of sonic bangs by atmospheric turbulence. *J. Fluid Mech.*, vol. 37, 1969, pp. 529-563.
8. Plotkin, Kenneth J.; and George, A. R.: Propagation of weak shock waves through turbulence. *J. Fluid Mech.*, vol. 54, 1972, pp. 449-467.
9. Pierce, A. D.: Statistical theory of atmospheric turbulence effects on sonic boom rise times. *J. Acoust. Soc. Am.*, vol. 49, 1971, pp. 906-924.
10. Pierce, Allan D.: Spikes on sonic boom pressure waveforms. *J. Acoust. Soc. Am.*, vol. 44, 1968, pp. 1052-1061.
11. McBride, Walton E.; Bass, Henry E.; Raspet, Richard; and Gilbert, Kenneth E.: Scattering of sound by atmospheric turbulence: A numerical simulation above a complex impedance boundary. *J. Acoust. Soc. Am.*, vol. 90, 1991, pp. 3314-3325.
12. Raspet, Richard; Bass, Henry E.; Yao, Lixin; Boulanger, Patrice; and McBride, Walton E.: Statistical and numerical study of the relationship between turbulence and sonic boom characteristics. *J. Acoust. Soc. Am.*, Revised manuscript submitted, March, 1994.
13. Kennedy, Bruce W.; Willshire, Jr., William L.; and Olsen, Robert O.: Sonic Boom Propagation Test. The Bionetics Corporation, Las Cruces, NM, Sept., 1991.

14. Willshire, Jr., William L.; Garber, Donald P.; and DeVilbiss, David W.: Flight test measurements of the effect of turbulence on sonic boom peak overpressure and rise time. *J. Acoust. Soc. Am.*, vol. 92, 1992, p. 2329.
15. Bass, Henry E.; Boulanger, Patrice; Olsen, Robert; and Chintawongvanich, Prasan: Sonic Boom Propagation Test - Low Level Turbulence Report. Physical Acoustics Research Group Report, University of Mississippi, Feb., 1993.
16. De Wolf, D. A.: A random-motion model of fluctuation in a nearly transparent medium. *Radio Science*, vol. 18 (2), 1983, pp. 138-142.

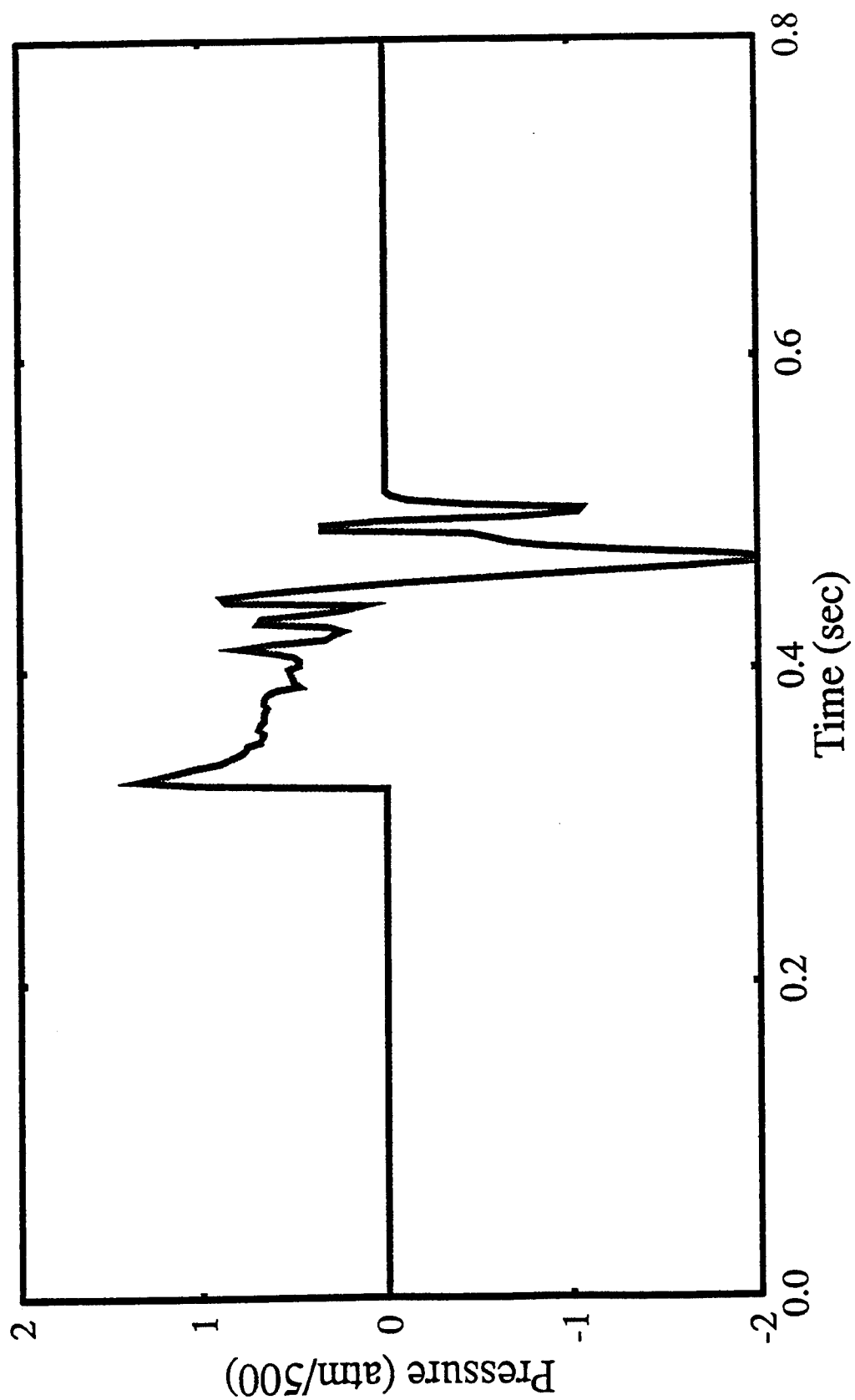


Figure 1a. Predicted HSCT waveform close to the aircraft.

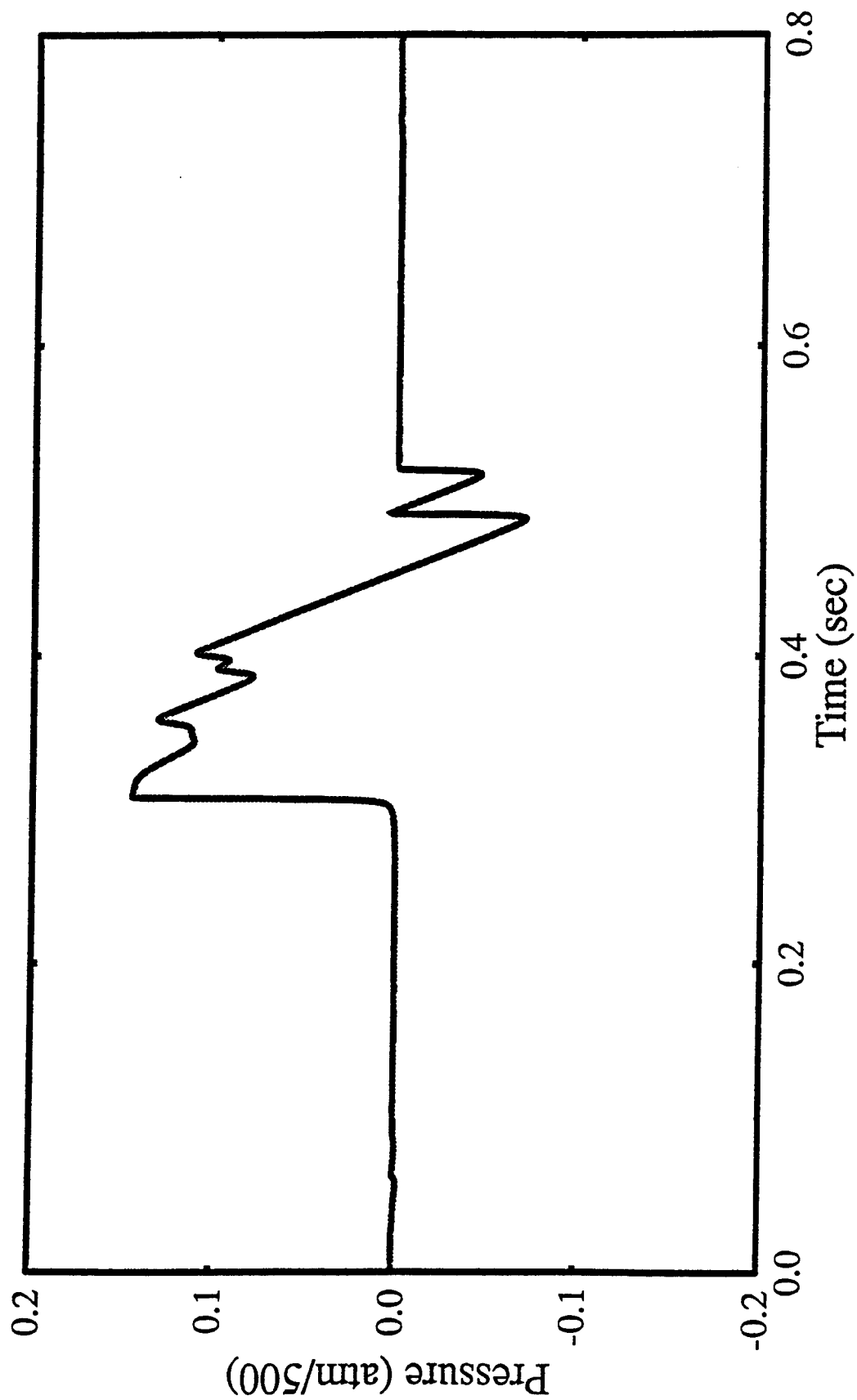


Figure 1b. HSCT waveform at the ground predicted using the enhanced Anderson algorithm.

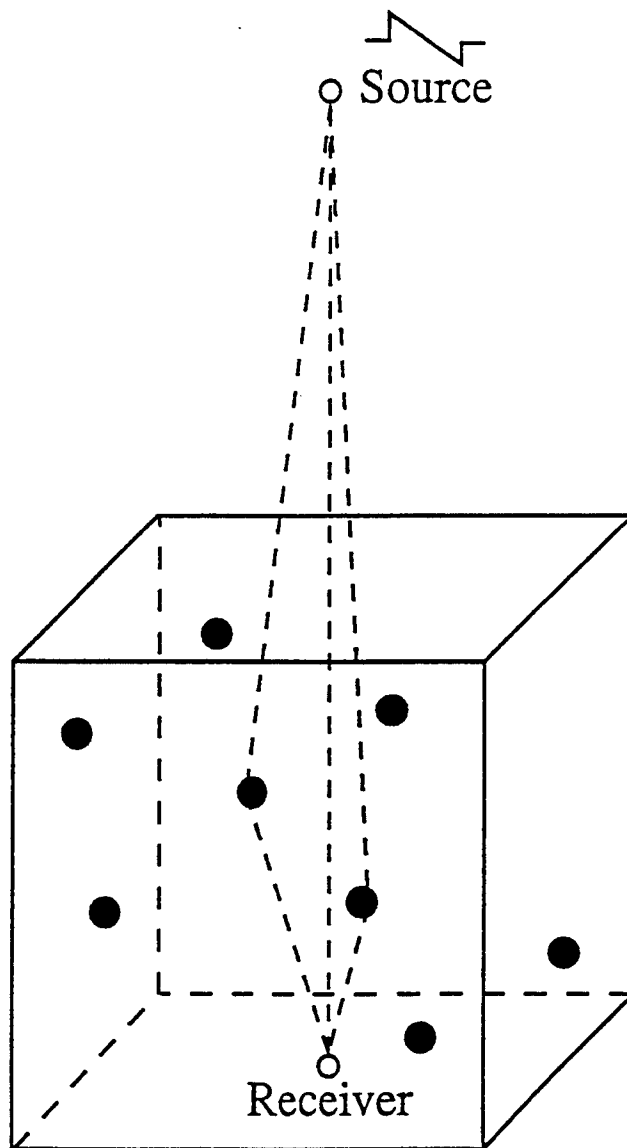


Figure 2. Scattering center calculation for sonic booms.

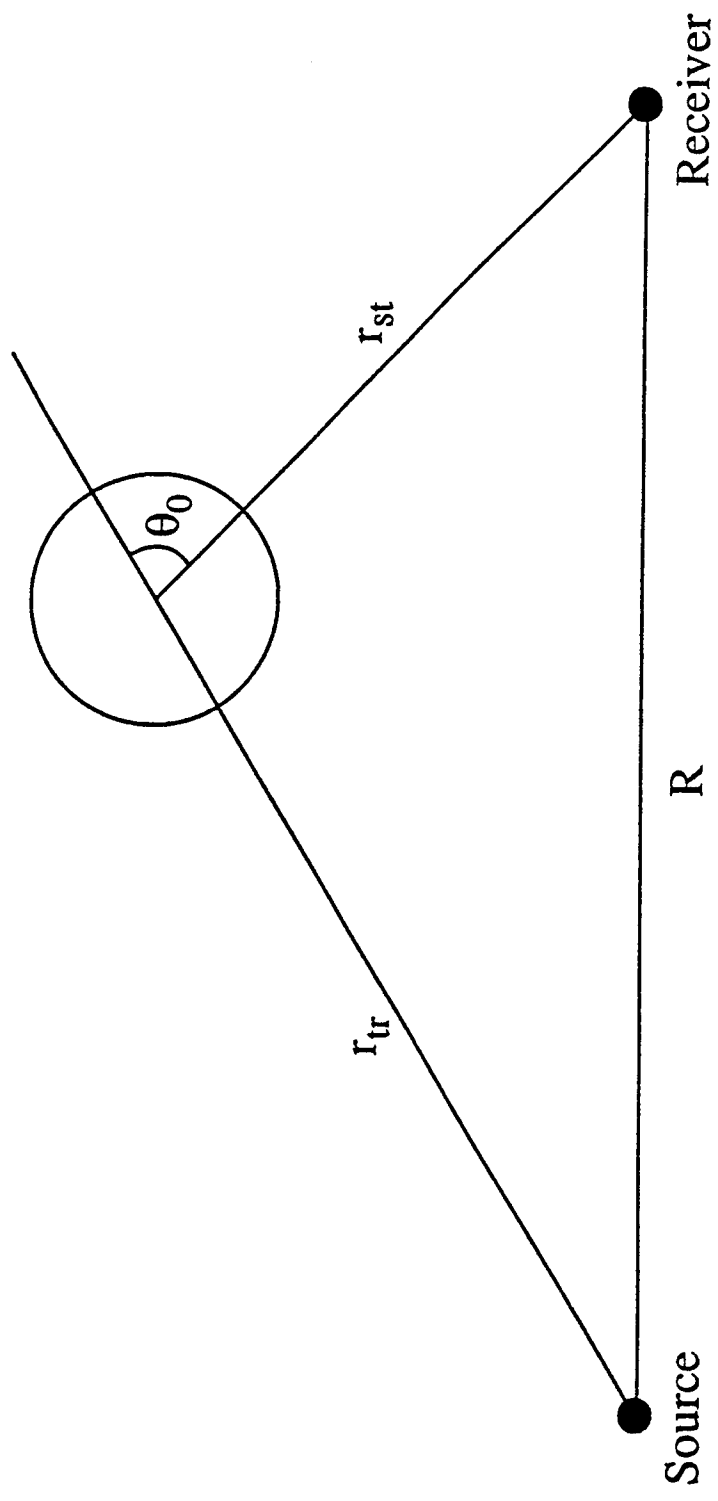


Figure 3. Geometry for the scattering calculation.

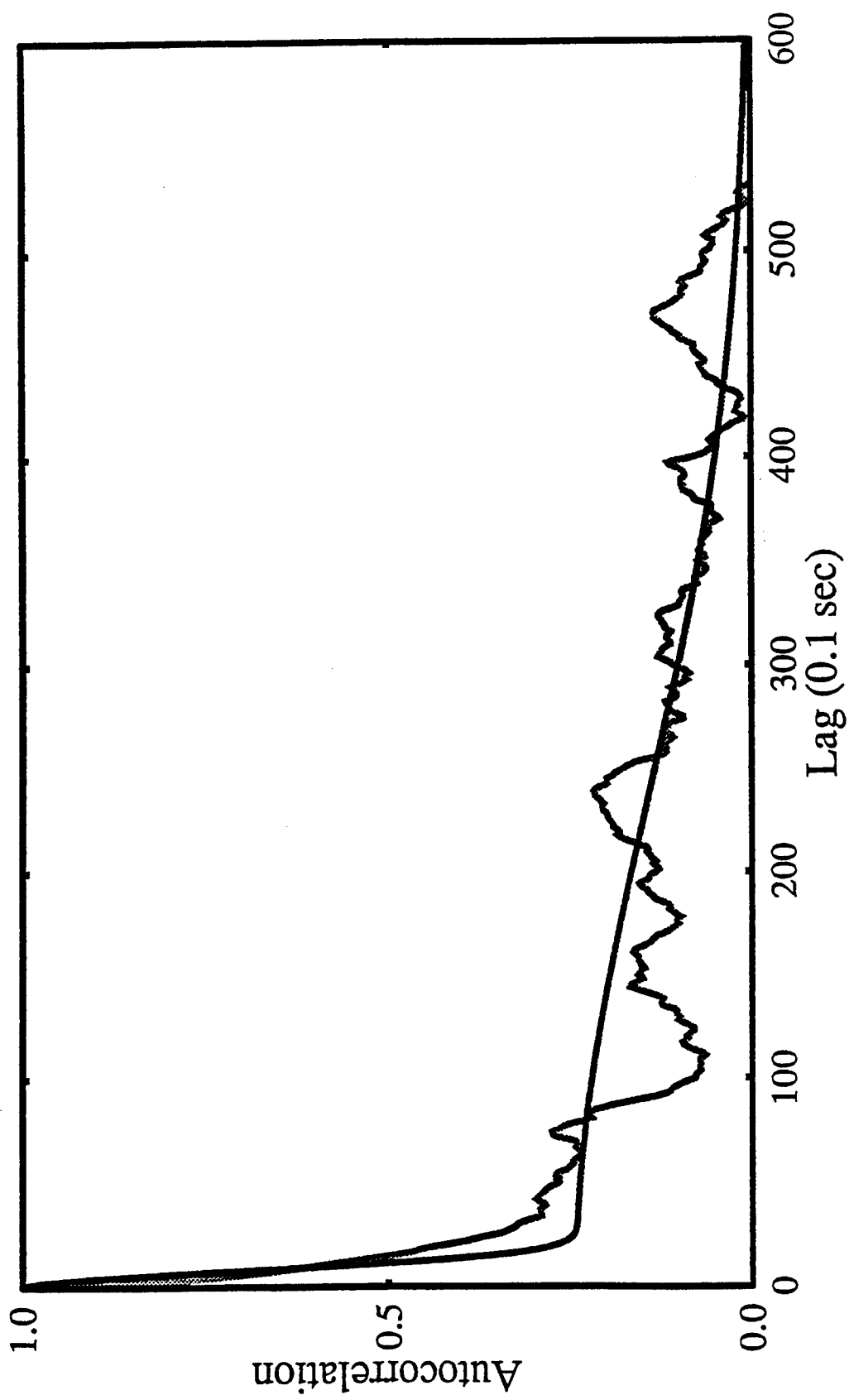


Figure 4. Two scale fit to the autocorrelation of the wind speed signal.

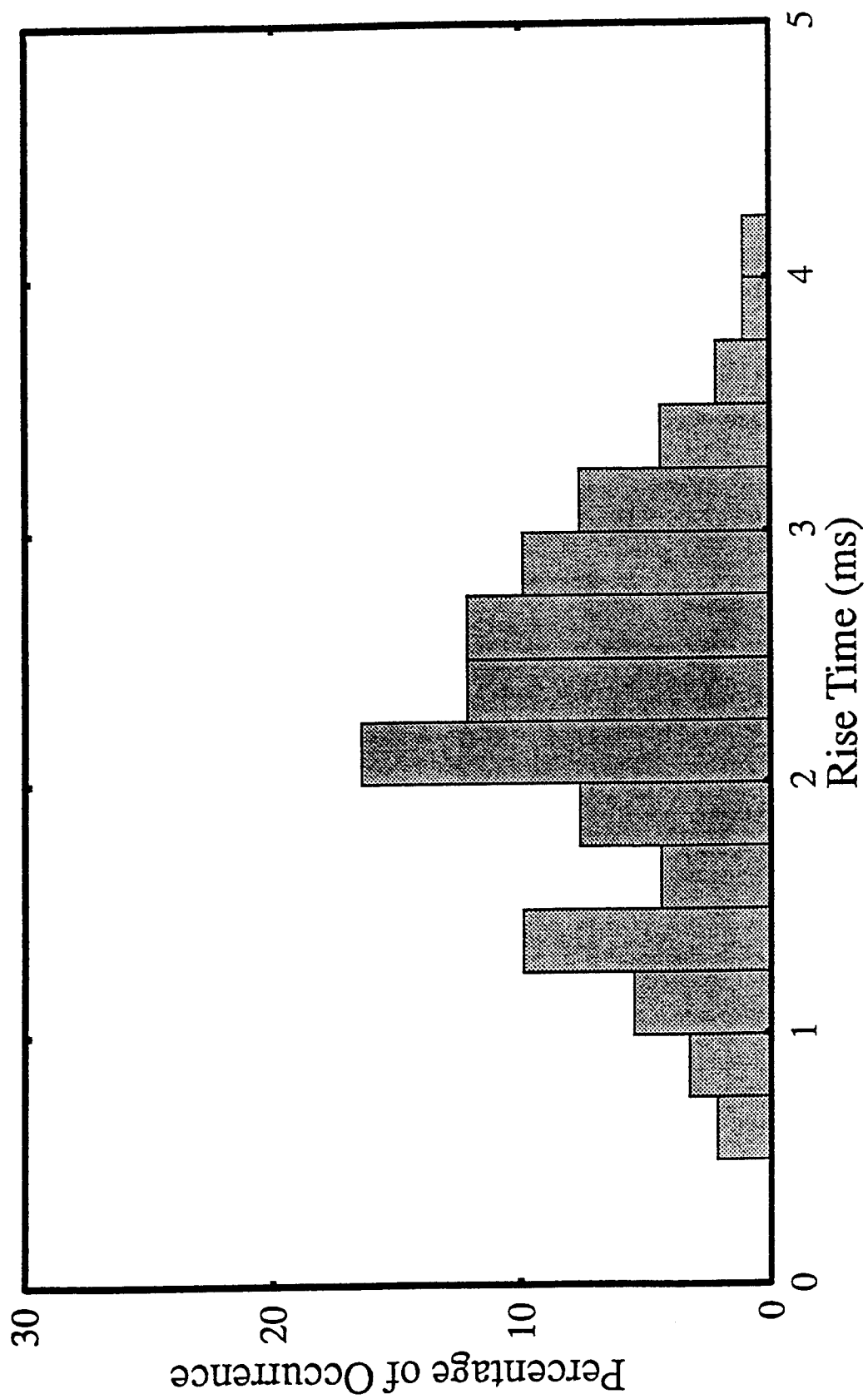


Figure 5a. Measured risetime distribution for the T-38 aircraft.

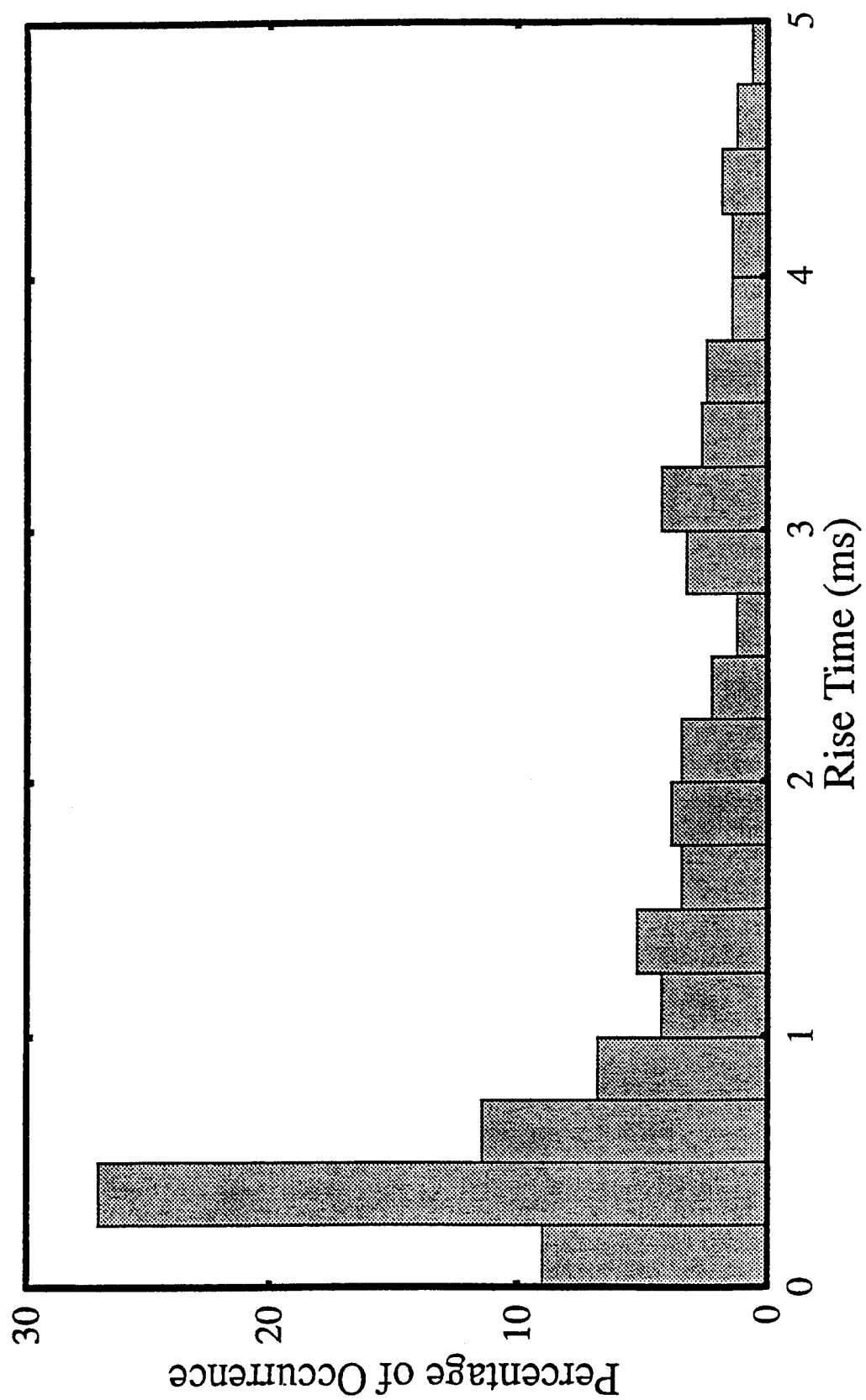


Figure 5b. Predicted distribution using the two scale model.

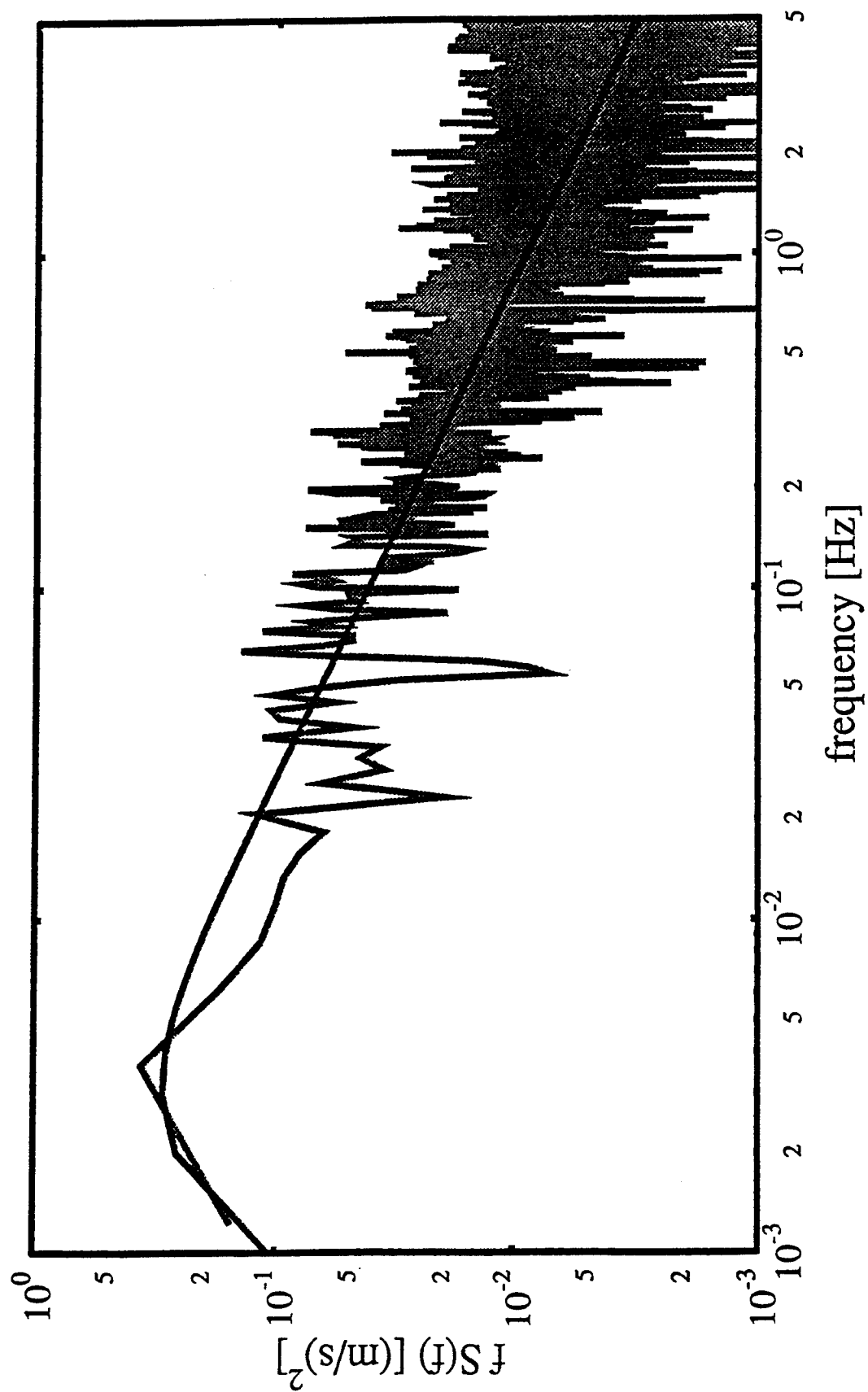


Figure 6. Fit of the von Karman spectrum to a 23 minute sample of wind data.

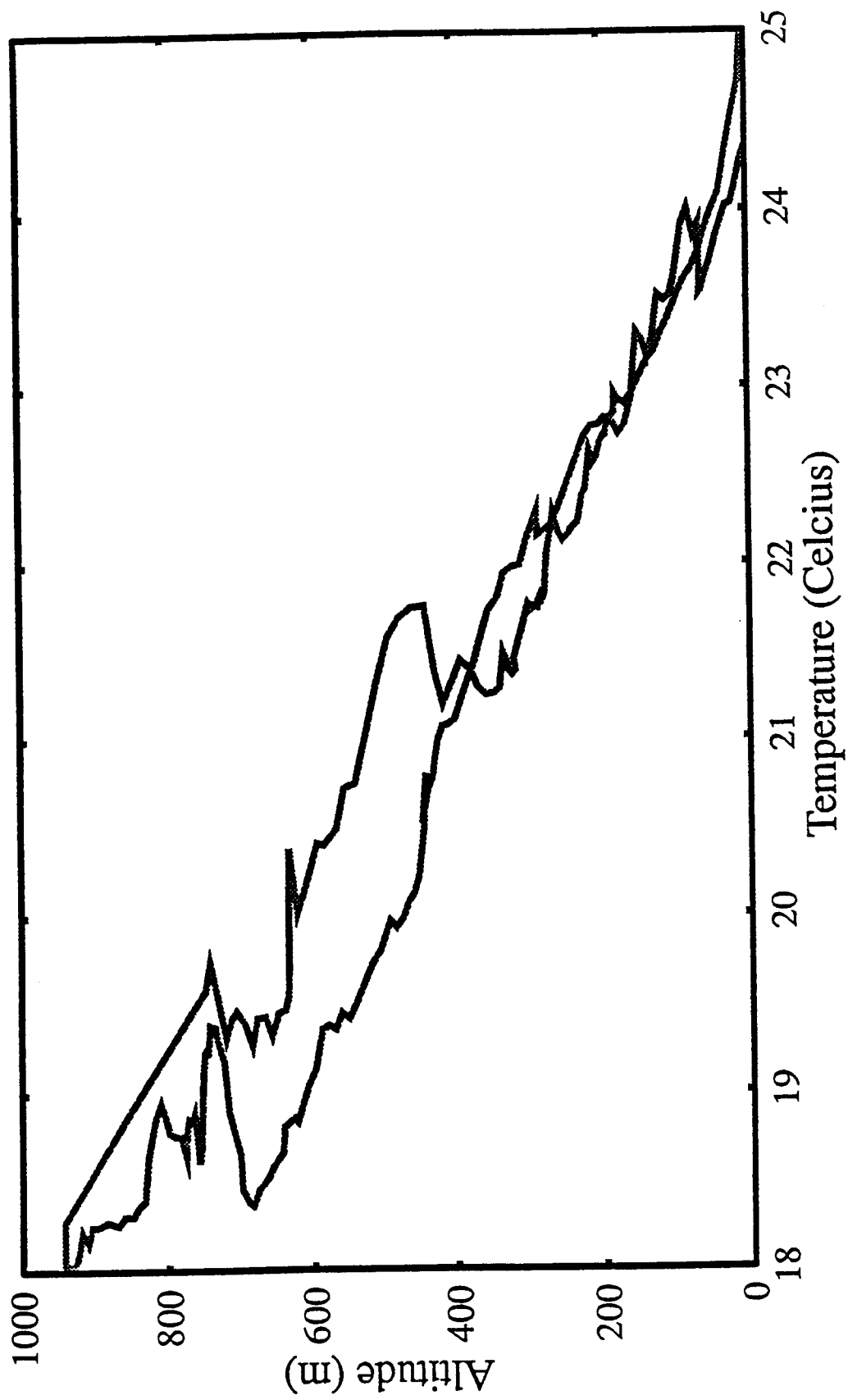


Figure 7. Temperature versus height for one flight at JAPE-2.

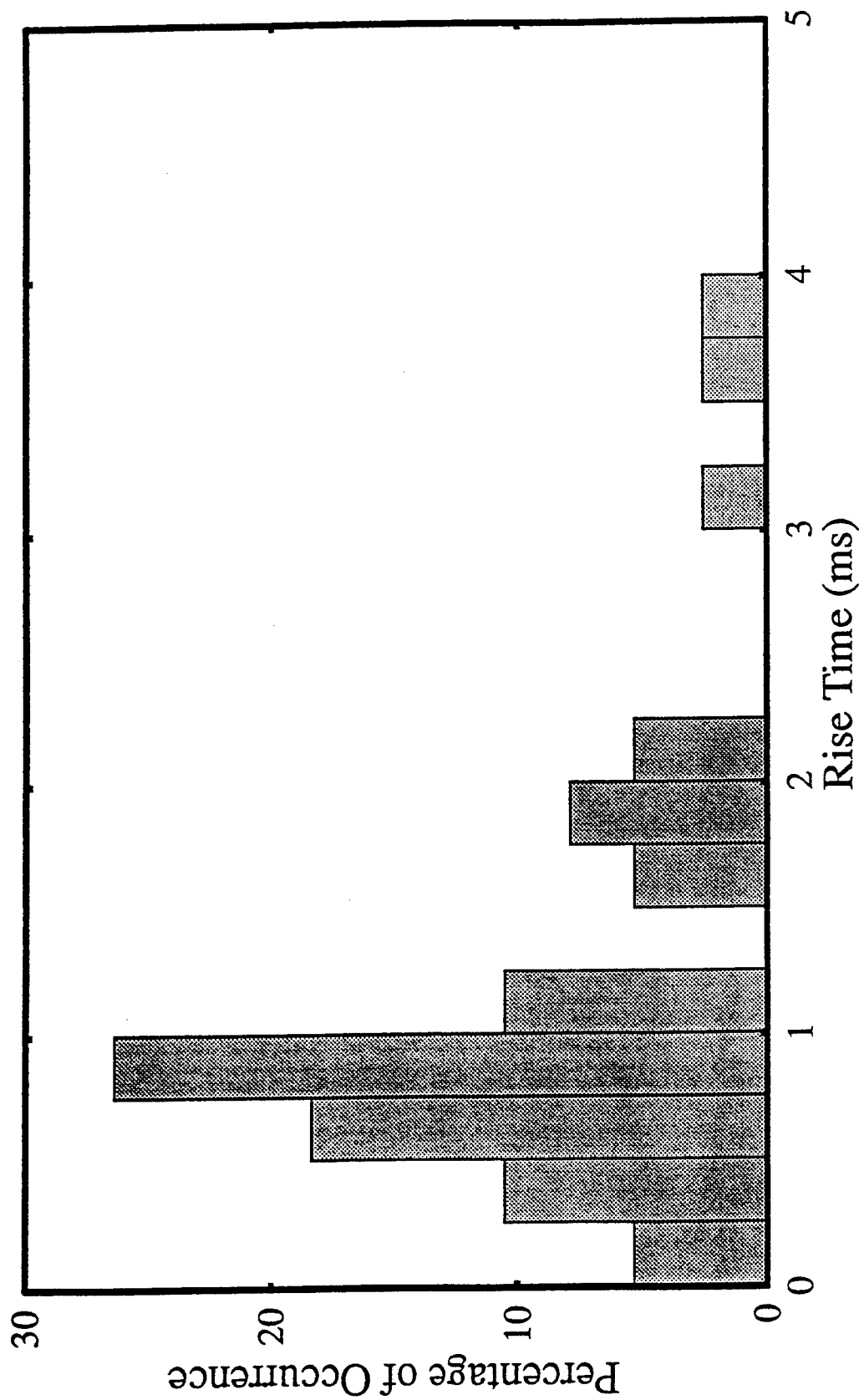


Figure 8. Prediction of risetime distribution using the von Karman spectrum. (20 realizations).

Effect of stratification of the atmosphere on sonic boom propagation.*

Robin O. Cleveland, Mark F. Hamilton and David T. Blackstock

Applied Research Laboratories,

The University of Texas at Austin, Austin, TX 78713-8029,

and

Mechanical Engineering Department,

The University of Texas at Austin, Austin, TX 78712-1063

ABSTRACT

Stratification of the atmosphere means that a sonic boom travels through an inhomogeneous medium. An inhomogeneous medium can slow down the nonlinear distortion of a finite-amplitude wave and in some cases put a limit on the amount of distortion, a phenomenon called waveform freezing. For sonic booms in a real atmosphere nonlinear effects are indeed reduced as the boom approaches the ground but waveform freezing does not occur. A new computer code, based on work by Lee and Hamilton [1], is presented which solves a Burgers-type equation in the time domain. The algorithm includes the effects of nonlinear distortion, thermoviscous absorption, molecular relaxation, and geometrical spreading. The code is used to determine the distance required for a steady-state shock, on encountering an abrupt change in relative humidity, to reach a new steady state based on the new humidity. It is found that step shocks require long propagation distances to reach a new steady state; typically more than 3 km. The effect of spherical and cylindrical spreading on a shock is also considered. We demonstrate that a spreading shock wave can never maintain steady state.

1 Introduction

The United States is considering the development of a new supersonic passenger aircraft. An important concern is the annoyance of the sonic boom that is generated by the aircraft once it is in supersonic flight. The proposed aircraft is currently expected to fly at an altitude of 17 km (about 55,000 ft) at a speed of Mach 2.0 to Mach 2.5.

The problem is interesting in that the boom is intense enough that finite-amplitude effects need to be considered. Moreover, the atmosphere is not homogeneous: the acoustical properties are stratified. Stratification, normally regarded as a deterministic inhomogeneity of the atmosphere, causes large scale refraction or bending of the sound rays. Refraction determines the shape of the primary sonic boom carpet on the ground, produces the sec-

*Work supported by NASA

ondary carpet, and can cause focusing [2]. Stratification also generally weakens the effect of nonlinear distortion on the propagating boom. Indeed so-called “freezing” of the sonic boom signature has been considered possible by some [3]. Waveform freezing refers to the absolute limit on nonlinear waveform distortion imposed by the increase of sound speed and density along the downward ray path, in combination with geometric spreading.

Stratification also affects absorption, particularly because of the strong dependence of absorption on humidity. Atmospheric absorption has both simple and subtle roles in sonic boom propagation. The simple role is to attenuate the boom by frequency dependent dissipation. The more subtle role is to interact with and mitigate the effects of nonlinear distortion. For example, nonlinearity tends to steepen shocks while absorption tends to diffuse them.

Figure 1 illustrates several aspects of sonic boom propagation through the atmosphere. A typical ray path starting at the apex of the sonic cone created by the aircraft is shown. The waveform near the aircraft can be quite complicated, containing many shocks. As the boom propagates downward nonlinear effects simplify the waveform so that it tends towards an N shape. However the turbulent boundary layer near the ground often distorts the signal so that it no longer resembles the classic N wave.

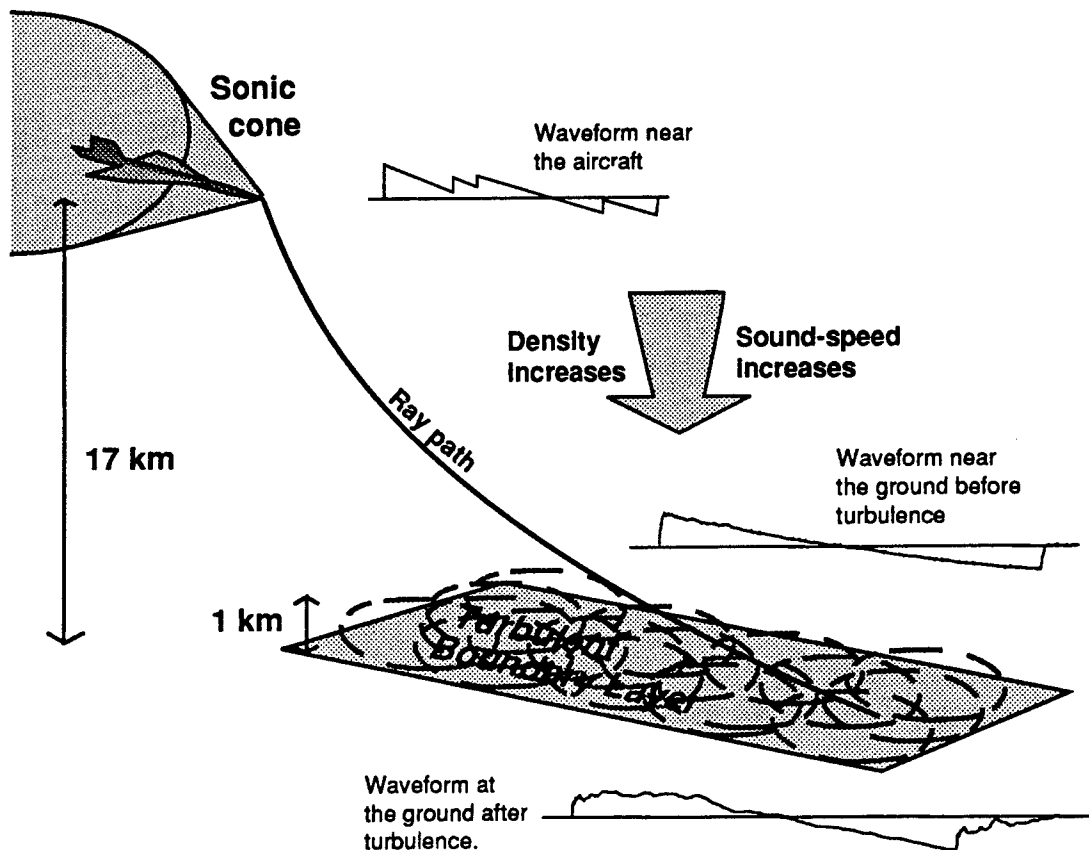


Figure 1: Sonic boom propagation through the atmosphere.

In this paper we examine two aspects of stratification, first, how stratification affects the nonlinear distortion of an N wave in general, and second, how spreading and change

in absorption affect the profile of the shocks in a sonic boom. The effect of the turbulent boundary layer is not addressed.

2 The Burgers Equation

The "classical" Burgers equation [4] is the standard model equation for plane finite-amplitude waves in a thermoviscous medium:

$$\frac{\partial p}{\partial x} - \frac{\beta}{2\rho_0 c_0^3} \frac{\partial p^2}{\partial t'} = \delta_{TV} \frac{\partial^2 p}{\partial t'^2}. \quad (1)$$

Here p is acoustic pressure, t time, $t' = t - x/c_0$ retarded time, x distance, c_0 small-signal sound speed, ρ_0 ambient density, β coefficient of nonlinearity, and δ_{TV} the thermoviscous loss coefficient. Pierce [5] added terms to account for relaxation processes. Each relaxation process ν is characterized by a relaxation time τ_ν and a change in small-signal sound speed $(\Delta c)_\nu$ due to the relaxation. In operator notation Pierce's "augmented Burgers equation" may be written

$$\frac{\partial p}{\partial x} - \frac{\beta}{2\rho_0 c_0^3} \frac{\partial p^2}{\partial t'} = \delta_{TV} \frac{\partial^2 p}{\partial t'^2} + \sum_\nu \frac{(\Delta c)_\nu \tau_\nu}{c_0^2} \frac{\frac{\partial^2}{\partial t'^2}}{1 + \tau_\nu \frac{\partial}{\partial t'}} p. \quad (2)$$

Although very compact this equation is not in useful form for numerical solution. The numerical algorithm described below breaks the equation into separate parts and solves each independently. Note the operator $\frac{1}{1 + \tau_\nu \frac{\partial}{\partial t'}} p$ may be expressed as an integral:

$$\frac{1}{1 + \tau_\nu \frac{\partial}{\partial t'}} p(t') = \frac{e^{-t'/\tau_\nu}}{\tau_\nu} \int_{-\infty}^{t'} e^{\tau/\tau_\nu} p(\tau) d\tau.$$

Equation 2 is valid for plane waves. If geometrical spreading is included, the equation becomes

$$\frac{\partial p}{\partial x} + \frac{a}{x} p - \frac{\beta}{2\rho_0 c_0^3} \frac{\partial p^2}{\partial t'} = \delta_{TV} \frac{\partial^2 p}{\partial t'^2} + \sum_\nu \frac{(\Delta c)_\nu \tau_\nu}{c_0^2} \frac{\frac{\partial^2}{\partial t'^2}}{1 + \tau_\nu \frac{\partial}{\partial t'}} p, \quad (3)$$

where the spreading factor a is 0 for plane waves, $\frac{1}{2}$ for cylindrical waves, and 1 for spherical waves. We have solved this equation numerically to obtain the results reported in the second part of this paper.

Burgers' equation may be further generalized to include effects of stratification. An extra term to account for the change in impedance is required, and geometrical spreading must now be modeled using linear ray theory and ray tube areas. The resulting equation is

$$\frac{\partial p}{\partial s} + \frac{\frac{\partial}{\partial s}(S)}{2S} p + \frac{\frac{\partial}{\partial s}(\rho_0 c_0)}{2\rho_0 c_0} p - \frac{\beta}{2\rho_0 c_0^3} \frac{\partial p^2}{\partial t'} = \delta_{TV} \frac{\partial^2 p}{\partial t'^2} + \sum_\nu \frac{(\Delta c)_\nu \tau_\nu}{c_0^2} \frac{\frac{\partial^2}{\partial t'^2}}{1 + \tau_\nu \frac{\partial}{\partial t'}} p, \quad (4)$$

where s is the distance along the ray tube, the retarded time is now given by $t' = t - \int \frac{ds}{c_0}$, and S is ray tube area. Neglecting the right-hand side (all the loss terms) yields the equation we solve analytically in the first part of this paper. Results from solving Eq. 4 numerically using the time domain code outlined in this paper will be presented at the fall meeting of the Acoustical Society of America [6].

To include diffraction effects, one must use the KZK equation, which is a multi-dimensional form of Burgers' equation. See, for example, Refs. 1 and 7. As a spinoff from the present work, relaxation effects have been included in a computer code that solves the KZK equation, but no formal report of the results has yet been given.

3 Waveform Freezing

The phenomenon of waveform freezing is described mathematically by the following analysis. By assuming ordinary absorption is negligible, we throw away the right hand side of Eq. 4.[†] We start with a variant of the Poisson solution for *plane* waves of finite amplitude in a *homogeneous*, gaseous medium [8]. If the source excitation is $p = f(t)$, that is, $f(t)$ is the pressure waveform at $x = 0$, the waveform after the wave has propagated to position x is given by

$$p(x, t') = f(t' + \frac{\beta x p}{\rho_0 c_0^3}), \quad (5)$$

The argument $t' + \beta x p / \rho_0 c_0^3$ may be thought of as being proportional to the phase of the wave. The second term in the phase factor governs the distortion of the waveform that occurs as the wave propagates (the factor $\beta x / c_0$, which has dimensions of time, is an elementary form of what in Hayes's terminology is called an age variable [9]). In the case of small-signal waves, for example, the second term is negligible, i.e., $p = f(t')$, and the wave propagates without change of shape. For finite-amplitude waves, however, the linear dependence of the second term on x shows that not only does the waveform change with propagation distance, the change continues indefinitely. In other words the waveform never freezes.

Next suppose that the gaseous medium through which the finite-amplitude wave propagates is inhomogeneous. Assume that ray theory holds. Although the wave suffers geometrical spreading and encounters an ever changing impedance as it travels down the ray tube, it turns out to be easy to deal with these complications. Given certain realistic approximations, one may reduce the problem to plane wave form by introducing two transformations. First, a new dependent variable q (a scaled pressure) is defined by

$$q = \sqrt{\frac{\rho_0 \bar{c}_0 S}{\rho_0 c_0 \bar{S}}} p.^\ddagger \quad (6)$$

Because of the inhomogeneity of the medium, ρ_0 and c_0 , as well as S , vary with the distance s along the ray tube. An overbar denotes a value at a reference point close to the source.

[†]Shocks in the waveform may be accommodated by incorporating weak shock theory in the description of the propagation. The presence of shocks does not, however, alter any of the arguments presented or conclusions drawn.

[‡]This transformation may be deduced from the fact that in a ray tube the energy flow, which is proportional to $S p^2 / \rho_0 c_0$, is constant. If the atmosphere has a steady flow, that is, if a wind is present, the Blokhintsev invariant replaces the energy flow as the quantity that is constant in the ray tube. A somewhat different independent variable is then appropriate [9].

Second, a new independent variable \tilde{x} (a scaled distance) is introduced,

$$\tilde{x} = \int_{\bar{s}}^s \sqrt{\frac{\bar{S} \bar{\rho}_0 \bar{c}_0^5}{S \rho_0 c_0^5}} ds' . \quad (7)$$

In terms of the new variables, the solution is

$$q(\tilde{x}, t') = f(t' + \frac{\beta \tilde{x} q}{\rho_0 c_0^3}) . \quad (8)$$

This equation is similar to Eq. 5 except the distance in the phase term is replaced by the scaled distance \tilde{x} . The scaled distance can be considered to be a "distortion distance" in that it is related to the amount of nonlinear distortion the wave has undergone.

Two examples will help fix ideas. First consider a spherically spreading wave in a homogeneous medium. In this case ρ_0 and c_0 are constant (overbars for these quantities are therefore omitted), the rays are straight lines, and the ray tube area is proportional to r^2 (distance s along the ray tube is just the radial distance r in this case, and we denote the reference distance \bar{s} by r_0). Equations 6 and 7 become

$$q = \frac{r}{r_0} p , \quad (9)$$

$$\tilde{x} = r_0 \ln(r/r_0) . \quad (10)$$

The first relation shows that q is the acoustic pressure scaled to compensate for spherical spreading. In general the role of the first transformation, Eq. 6, is to compensate for geometrical spreading and for amplification or diminution due to impedance variation. In other words q describes a "plane-wave-like" function. When the second relation is combined with Eq. 8, the result is

$$q(r, t') = f(t' + \frac{\beta r_0 \ln(r/r_0) q}{\rho_0 c_0^3}) . \quad (11)$$

The presence of the slowly growing factor $r_0 \ln(r/r_0)$ (in place of the factor x that appears in Eq. 5) shows that the distortion develops more gradually for a spherical wave than for a plane wave. Note, however, that although the distortion grows ever more slowly as distance increases, the growth never ceases altogether, i.e., waveform freezing does not occur.

For the second example, consider a plane wave propagating downward through an isothermal atmosphere. Let x be positive downward and let the reference distance \bar{s} be the origin $x = 0$. In an isothermal atmosphere the sound speed does not change with distance (we therefore omit the overbar with c_0), but the density varies as $\rho_0 = \bar{\rho}_0 e^{x/H}$, where H is the scale height of the atmosphere (about 8.5 km). The expressions for q and \tilde{x} are found to be

$$q = e^{x/2H} p , \quad (12)$$

$$\tilde{x} = 2H(1 - e^{-x/2H}) . \quad (13)$$

Of particular interest is Eq. 13, which shows that \tilde{x} does *not* increase indefinitely with propagation distance x but instead only approaches the asymptotic value $\tilde{x} = 2H$. Substitution of Eq. 13 into Eq. 8 yields

$$q(x, t') = f(t' + \frac{\beta 2H(1 - e^{-x/2H}) q}{\bar{\rho}_0 c_0^3}) . \quad (14)$$

In this case the distortion not only slows down as the wave travels, it has an upper bound. In the limit as $x \rightarrow \infty$, we obtain

$$q(x, t') = f(t' + \frac{\beta 2Hq}{\rho_0 c_0^3}) . \quad (15)$$

Like a small-signal wave, the phase term has no explicit dependence on x . Distortion, although present (as indicated by the dependence of the phase on q), no longer changes with distance: the waveform is frozen.

In Fig. 2 the distortion distance “profile” is shown for a plane wave, a spherically spreading wave, and a plane wave in an isothermal atmosphere. For the ordinary plane wave we see that 20 km of propagation yields 20 km of distortion. For a spherically spreading wave 45 km of propagation is needed to produce the same 20 km worth of distortion. For the plane wave in an isothermal atmosphere no more than 13.5 km worth of distortion can occur no matter how far the wave travels.

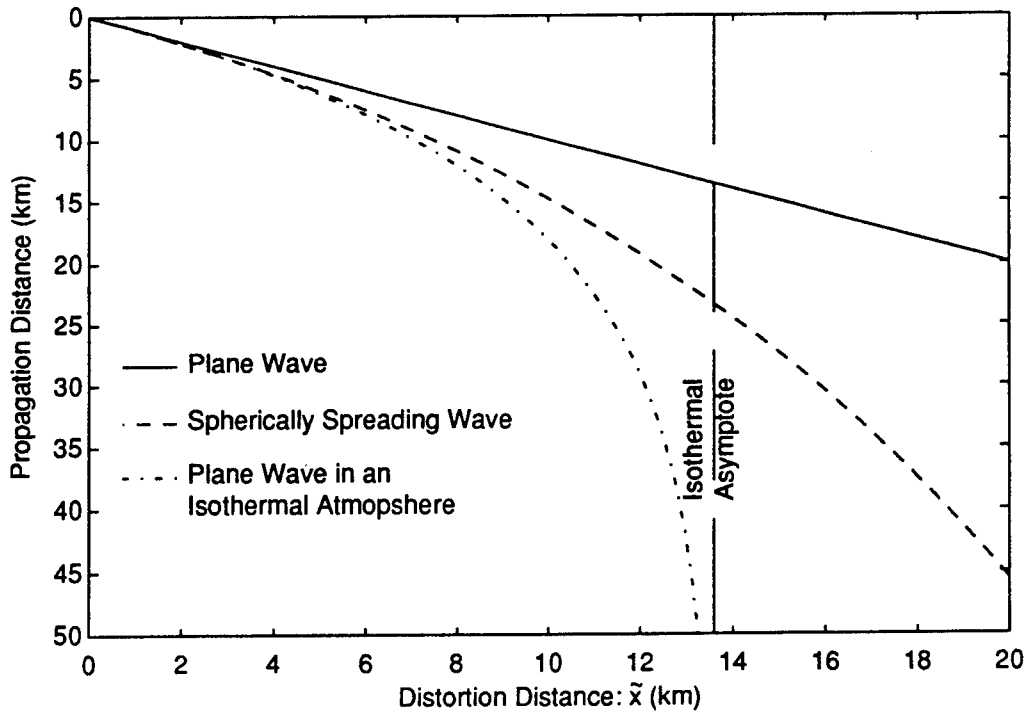


Figure 2: The distortion distance \tilde{x} for a plane wave, a spherically spreading wave ($r_0 = 100$ m) and a plane wave in an isothermal atmosphere ($H = 6.8$ km [¶]).

A physical explanation for freezing is that the coefficient of nonlinearity appears to decrease as the wave propagates. To see this, we inspect the wave equations for which Eqs. 5, 11, and 14 are solutions. For plane waves the equation is

$$\frac{\partial p}{\partial x} - \frac{\beta}{\rho_0 c_0^3} p \frac{\partial p}{\partial t'} = 0 , \quad (16)$$

[¶]The scale height used here is based on the average temperature from the ground to an altitude of 17 km and so is less than the 8.5 km mentioned above.

for spherical waves

$$\frac{\partial q}{\partial r} - \frac{\beta r_0}{\rho_0 c_0^3} q \frac{\partial q}{\partial t'} = 0, \quad (17)$$

and for plane waves in an isothermal atmosphere

$$\frac{\partial q}{\partial x} - \frac{\beta e^{-x/2H}}{\bar{\rho}_0 c_0^3} q \frac{\partial q}{\partial t'} = 0. \quad (18)$$

One sees that propagation of spherical waves is like propagation of plane waves in a medium having an effective nonlinearity coefficient β_{eff} that decreases as $1/r$. Similarly, the isothermal atmosphere resembles a homogeneous medium in which $\beta_{\text{eff}} = \beta e^{-x/2H}$. Since distortion is cumulative, the total amount of distortion at any given point is proportional to the integral $\int \beta_{\text{eff}} ds = \beta \tilde{x}$ (which is proportional to the age variable). In the case of spherical waves, the integral is proportional to $\ln(r/r_0)$, which tells us that distortion, while slowing down as propagation distance increases, never comes to a full stop. For waves traveling downward in an isothermal atmosphere, however, the integral approaches a finite value as $x \rightarrow \infty$. In this case the waveform freezes.

The concept of an effective coefficient of nonlinearity is easily extended to include all changes in cross sectional area and properties of the medium. Equation 7 shows that the general definition of β_{eff} should be

$$\beta_{\text{eff}} = \beta \sqrt{\frac{\bar{S} \bar{\rho}_0 \bar{c}_0^5}{S \rho_0 c_0^5}}. \quad (19)$$

Whether the waveform freezes then depends on whether the infinite integral of β_{eff} is bounded.

It should be noted that, as appropriate for the lower atmosphere, β itself has been treated as a constant in this analysis. For a medium in which β varies, such as the ocean, the variation may be accounted for simply by including the factor $\bar{\beta}/\beta$ in the integrand of Eq. 7, where again the overbar denotes a reference value [10].

3.1 Application to the Atmosphere

The foregoing analysis is now applied to the atmosphere. Since the cruising altitude of the high speed civil transport aircraft is expected to be about 17 km (roughly 55,000 ft), we restrict our attention to the atmosphere below this height. In this region the U. S. Standard Atmosphere may be modeled as having a bilinear temperature profile: no change in temperature T_0 from 17 km down to 11 km, and a linear increase (the rate is $6.5^\circ\text{C}/\text{km}$) from 11 km to the ground, where the temperature is assumed to be 15°C . For simplicity a quiet medium is assumed.

To investigate the question of whether waveform freezing takes place in such an atmosphere the shape of the scaled distance curve \tilde{x} as a function of altitude is used as a criterion. If at ground level the curve seems to be very close to an asymptotic value, freezing is deemed to have occurred. If not, then the waveform is still changing appreciably when the boom reaches the ground. Results were obtained for various Mach numbers and azimuthal angles.

It was found that distortion slowed down the most on the ray path following the shortest possible path to the ground. The distortion distance of this ray is shown for two Mach numbers in Fig. 3. In order to indicate how close the ground value is to an asymptote,

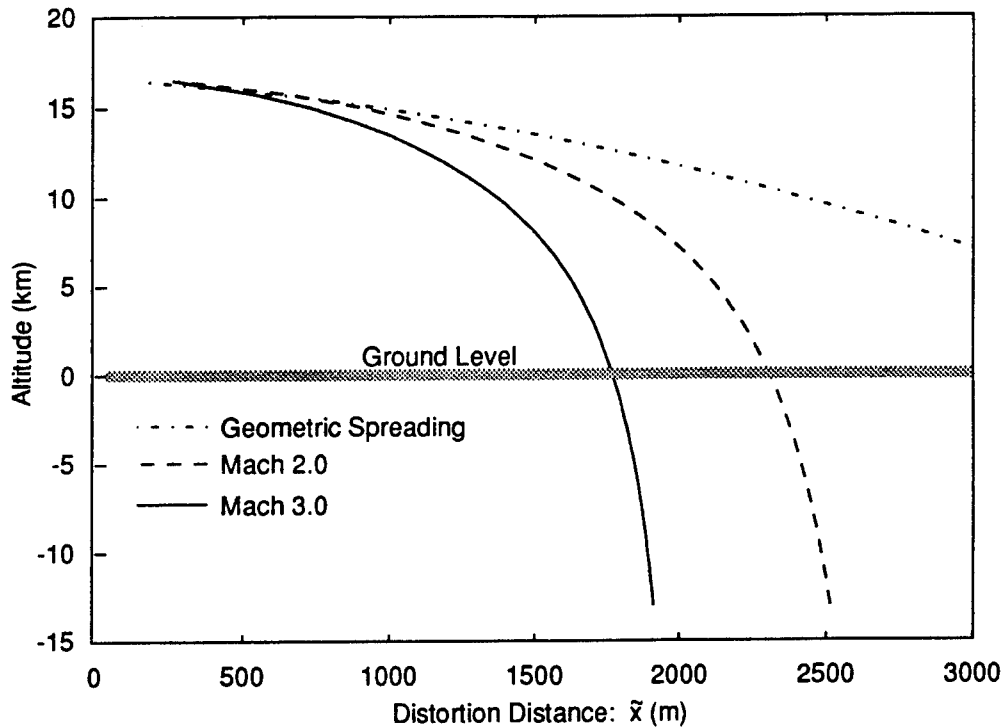


Figure 3: The distortion distance \tilde{x} for a source at altitude 17 km flying at either Mach 2.0 or Mach 3.0.

we have continued the curves beyond ground level (the atmosphere has been assumed to continue with the same properties, i.e., the sonic boom is not reflected). For all the cases considered: Mach numbers in the range 1.2 to 10 and azimuthal angle from 0° to 60° , it was found that the waveform freezing was never obtained at the ground. At best the distortion distance was within 10% of reaching its asymptotic value.

4 Absorption

When shocks are present in a waveform, such as an N wave, weak shock theory may be used to keep the wave single valued as it propagates. However, weak shock theory provides no information about the profile of the shock, only its location and amplitude. To obtain the actual profile of the shock — and subsequently the rise time, which is important in determining the loudness of sonic booms — one must take explicit account of atmospheric absorption. Absorption in air is due mainly to oxygen and nitrogen relaxation but also to thermoviscous effects.

For purposes of predicting shock profile and rise time,^{||} it has commonly been assumed that the shock is in steady state. That is, the competing forces of nonlinearity and absorp-

^{||}In this paper rise time is defined to be the time it takes a shock to go from 10% to 90% of its peak value.

tion are in balance. However, stratification of the atmosphere means that absorption varies with altitude. For example, molecular relaxation, which is a major factor controlling sonic boom rise time, is strongly dependent on relative humidity. Because humidity varies with altitude, rise time varies as the sonic boom propagates downward. In addition the amplitude of the shock, and hence the nonlinear strength, changes because of stratification and geometrical spreading. The question is whether rise time depends only on local conditions or is also affected by the variation of humidity and other properties along the propagation path.

The work of Pierce and Kang [11] motivated our study. They made rise time predictions based on the assumption that the sonic boom shock near the ground is in steady state. Kang [12, Chap. 7.2] argues that shocks respond to change in humidity quickly enough that they are in effect always in steady state. In other words only local conditions are important. Robinson [13, Chap. 5.2] however disagrees with this hypothesis. Raspet *et al.* [14] found that perturbed 100 Pa shocks (step waveform) require propagation distance of order 1 km for the rise time to return to within 10% of its steady shock value.

We suspect that the shock wave at the head of a sonic boom does not respond quickly enough to variation in atmospheric conditions (and to other changes that affect the profile, such as geometrical spreading and even wave shape) to justify the steady-state assumption. If our hypothesis is correct, then to improve on the Pierce-Kang prediction requires that more than local conditions be taken into account. Past history along the propagation path must be significant. Figure 4 shows profiles of temperature, pressure, and relative humidity for the ISO 9613-1 atmosphere [15]. It is seen that conditions can change rapidly, particularly during the lower part of the propagation path.

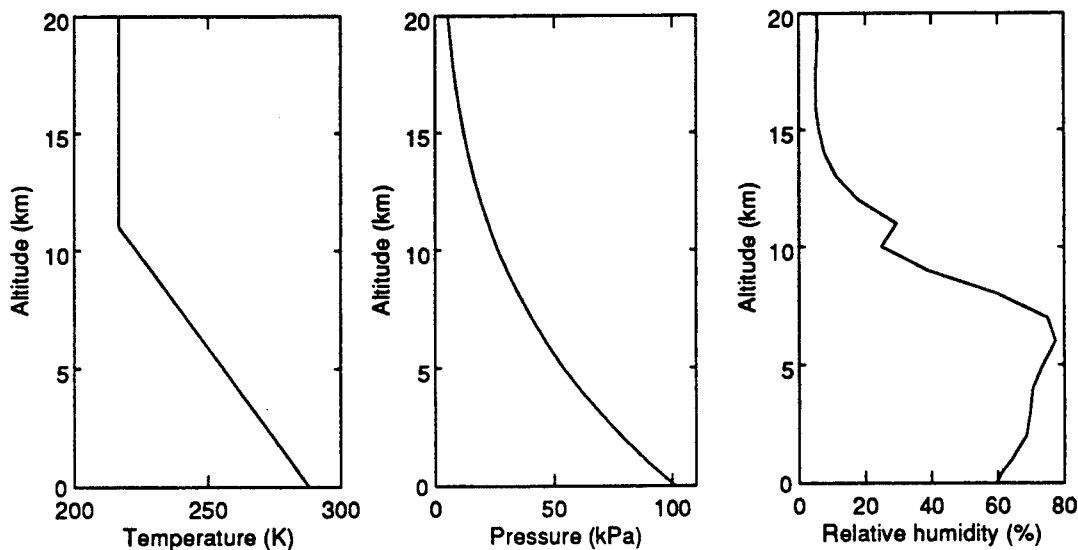


Figure 4: Atmospheric conditions in the ISO 9613-1 atmosphere.

The purpose of this investigation is to determine the effect of unsteadiness (not associated with turbulence) on rise time. The unsteadiness considered here is due to (1) geometrical spreading, and (2) stratification, which includes variation in density, temper-

ature, and relative humidity. The Burgers equation described above, which includes all these effects, is the propagation model for our study. The equation is solved by a new computational algorithm in which all the calculations are done in the time domain.

This part of the paper is a progress report in which some of the factors contributing to unsteadiness are studied, namely geometrical spreading and variation in relative humidity. To determine whether the sonic boom profile can respond quickly to changes of this order, we have calculated the effect on rise time of an abrupt change in atmospheric conditions. We have also examined the effect of geometrical spreading on rise time. For purposes of this paper, temperature and pressure are fixed at their ground level values.

4.1 Time Domain Algorithm

Solutions of the generalized Burgers equation Eq. 4 that are not in steady state involve solving a partial differential equation. Except for a few rare cases the solution can only be obtained numerically and it is common to use some sort of marching scheme. The scheme used in this paper was developed by Lee and Hamilton [1, 7]. A time waveform is digitized with M samples and then small steps are taken in the propagation direction. At each step absorption and nonlinearity are solved in series. It is popular to do the absorption and dispersion effects in the frequency domain as this requires M complex multiplications. However in the frequency domain the nonlinear term involves a convolution — which requires of order M^2 operations. If the nonlinear distortion is applied in the time domain it requires only order M operations. The fast fourier transform requires order $M \log M$ operations. Algorithms like the Pestorius code [16] flip-flop between the time and frequency domain at each step to take advantage of calculating absorption in the frequency domain and nonlinear distortion in the time domain. The penalty incurred is the use of the FFT.

It would be nice to stay in one domain but without having to pay the computational price of a convolution. Lee and Hamilton [1, 7] recently developed an algorithm that combines the calculations for nonlinearity, thermoviscous absorption, and diffraction in the time domain. A method for including the effects of multiple relaxation phenomena was also described [1]. The method involves approximating the differential form of each relaxation equation by finite differences which yield a tridiagonal matrix. As in the solution of the absorption equation, the tridiagonal matrices for the relaxation equations are solved explicitly. Calculations for all four effects (nonlinearity, absorption, diffraction, and relaxation) require order M operations. In the present work, we implemented the procedure for including relaxation, and we replaced the diffraction routine with one which can account for cylindrical or spherical spreading. The individual operations taken at each step are shown in Fig. 5.

Apart from its numerical advantage this algorithm has the nice property that it can propagate pulses. Because the FFT isn't used it is not necessary that the endpoints of the waveform match to make a periodic waveform. Therefore step shocks and N waves are easily dealt with. This is particularly advantageous when a steady-state solution is desired. Raspet *et al.* [14] used a square pulse waveform to find the steady-state behavior of a shock.

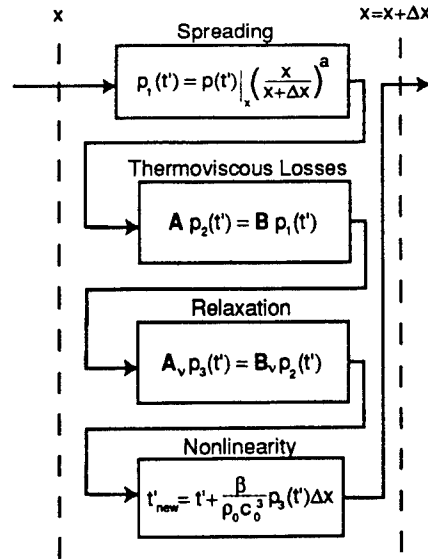


Figure 5: Time domain approach to solving the Burgers equation. **A** and **B** are tridiagonal matrices.

However, a square pulse wave has limited propagation range. It eventually turns into a sawtooth wave, which does not maintain constant amplitude. In the time domain code the distance a true step shock can be propagated is virtually unlimited.

4.2 Verification of time domain algorithm.

A number of cases were run to test the validity of the code. The first was to obtain the steady-state solution of the classical Burgers equation for a thermoviscous fluid. The known analytical solution for the steady shock is the hyperbolic tangent function. Figure 6 shows how a shock front is propagated with the time domain code; σ is the distance variable. The first figure shows the initial profile, selected because it looked interesting. The other figures show how the profile develops. The final figure, at distance $\sigma = 2$, shows that the numerical result agrees very well with the analytical steady-state solution.

The modeling of relaxation was verified by comparing the code with a steady-state solution by Polykova *et al.* [17] for a finite amplitude wave in a medium with one relaxation process but no thermoviscous losses. Their result (denoted PSK in Fig. 7) is

$$\frac{t - t_0}{\tau} = \ln \frac{(1 + p/p_0)^{D-1}}{(1 + p/p_0)^{D+1}},$$

where

$$D = \frac{(\Delta c) \rho_0 c_0}{p_0 \beta}.$$

Figure 7 shows the result from the propagation program in a monorelaxing fluid. For the values chosen relaxation was not enough to stop the waveform from becoming multivalued. In the analytical result Fig. 7(a) weak shock theory was used to ensure a single valued function. Multivaluedness was prevented in the numerical algorithm Fig. 7(b) by including a small amount of thermoviscous attenuation. The comparison Fig. 7(c) shows excellent agreement between the analytical and numerical predictions.

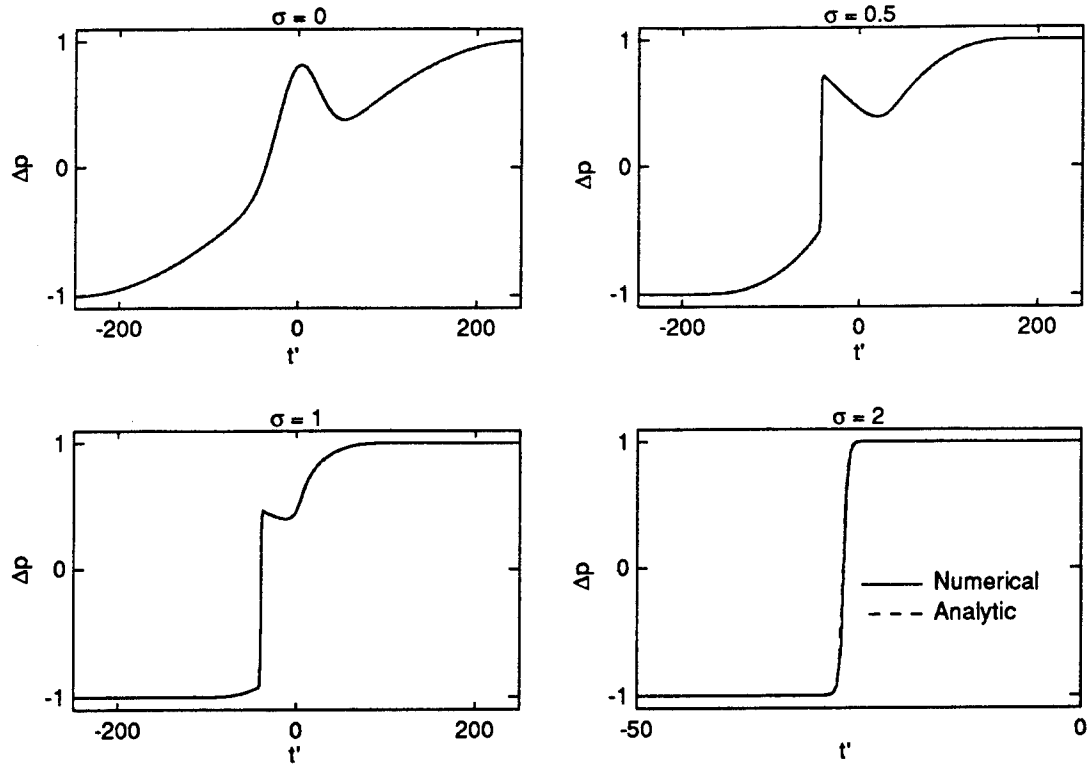


Figure 6: Propagation of a shock in a thermoviscous medium.

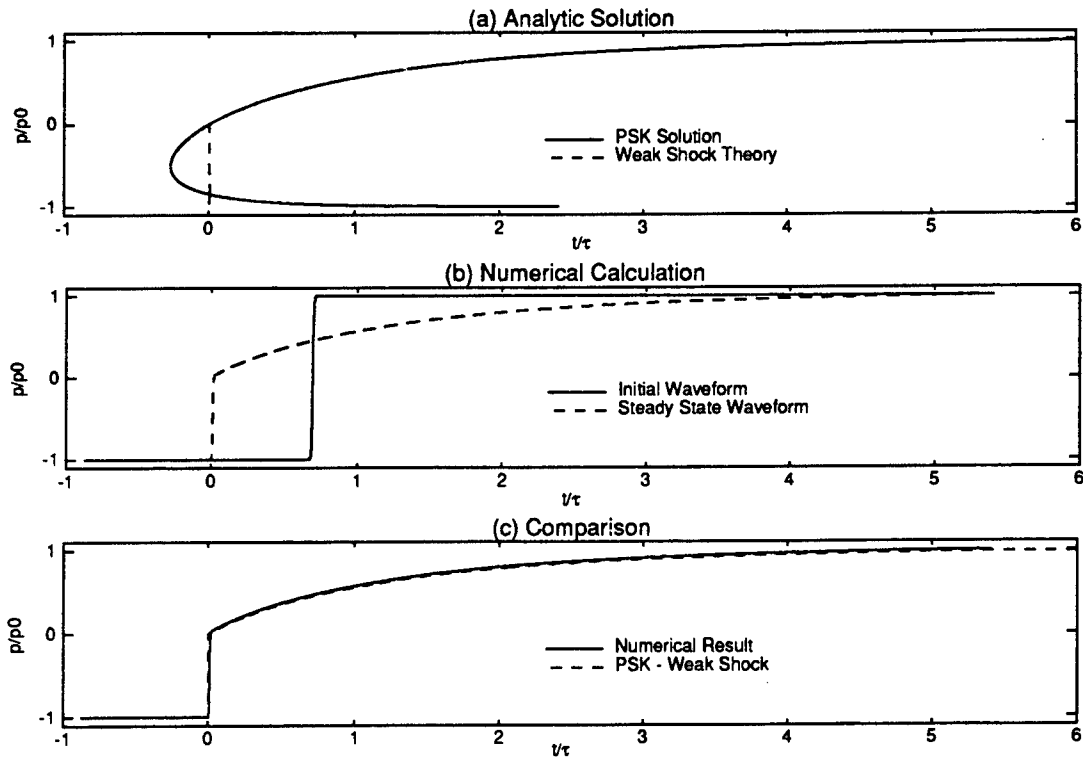


Figure 7: (a) The analytical result for the steady-state solution in a relaxing medium with no thermoviscous effects; $D = 0.5$. (b) The initial and steady-state profiles obtained by the time domain code. (c) Comparison of the analytical and numerical steady-state profiles.

Finally a plane wave shock front was sent into a standard atmosphere with a relative humidity of 10%. In this case absorption is due to thermoviscous effects and two relaxation processes: oxygen and nitrogen. Results can be compared with Kang's numerical steady-state results. In our calculation the shock was started out with a hyperbolic tangent profile and was then propagated until the profile no longer changed. Figure 8 compares the two results. The agreement is excellent.

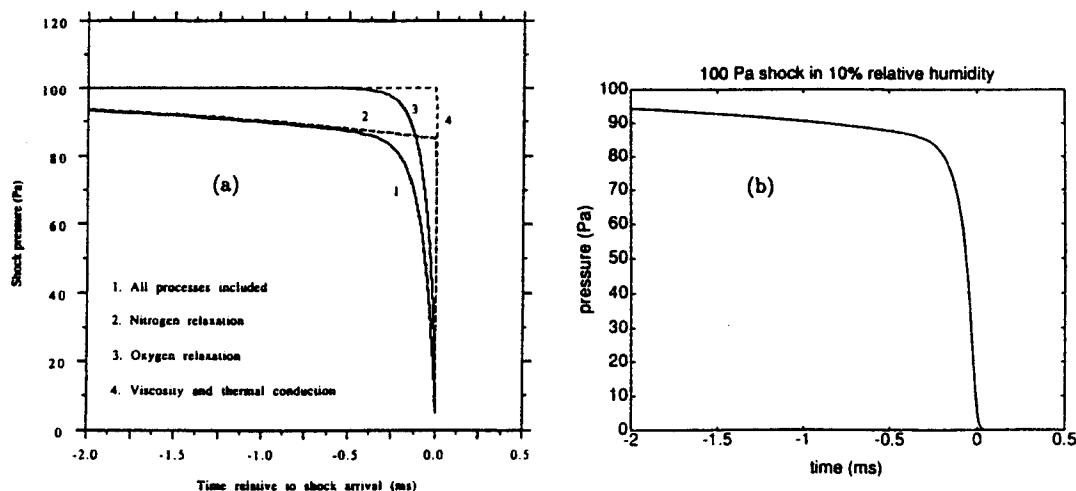


Figure 8: Steady-state solution in air; $T = 20^\circ\text{C}$, $P_0 = 1$ atm, and a relative humidity of 10%. (a) Kang's profile [12, Fig. 5.8]. (b) Profile from the time domain code.

5 Effects on Rise time

We now use the time domain code to investigate the behavior of shock rise time in air. In all calculations the temperature is 20°C , and the pressure is 1 atm.

First, we examine how long it takes a waveform to recover from a small but abrupt change in relative humidity. A plane shock wave is propagated in air of given relative humidity until it reaches steady state. The steady-state waveform is then used as the input waveform for an atmosphere with another relative humidity.

Second, we investigate the effect of spreading on the rise time of a shock front. Shocks that are in steady state are propagated as spreading waves. Geometrical spreading reduces the amplitude of the shock as it propagates. This in turn reduces the nonlinear strength of the shock. The shock should therefore diffuse and its rise time increase. We wish to investigate whether the diffusion of the shock front is rapid enough to keep up with geometrical spreading.

5.1 Transition Distances

We use the term transition distance to describe how far a shock needs to travel to go from one steady-state profile to another. A somewhat similar term, "healing distance," is

commonly used in literature related to turbulence for the distance a perturbed shock needs to return to its original state [14]. In this case we shall look at transition distances due to a change in relative humidity.

Figure 9 shows rise time as a function of propagation distance for a plane step shock of amplitude 70 Pa which starts in a medium of 20% relative humidity. The relative humidity of the second atmosphere is 10%, 20%, or 30%. The results show the transition distance to be at least 5 km. Transition distances of the same order were found for shock amplitudes

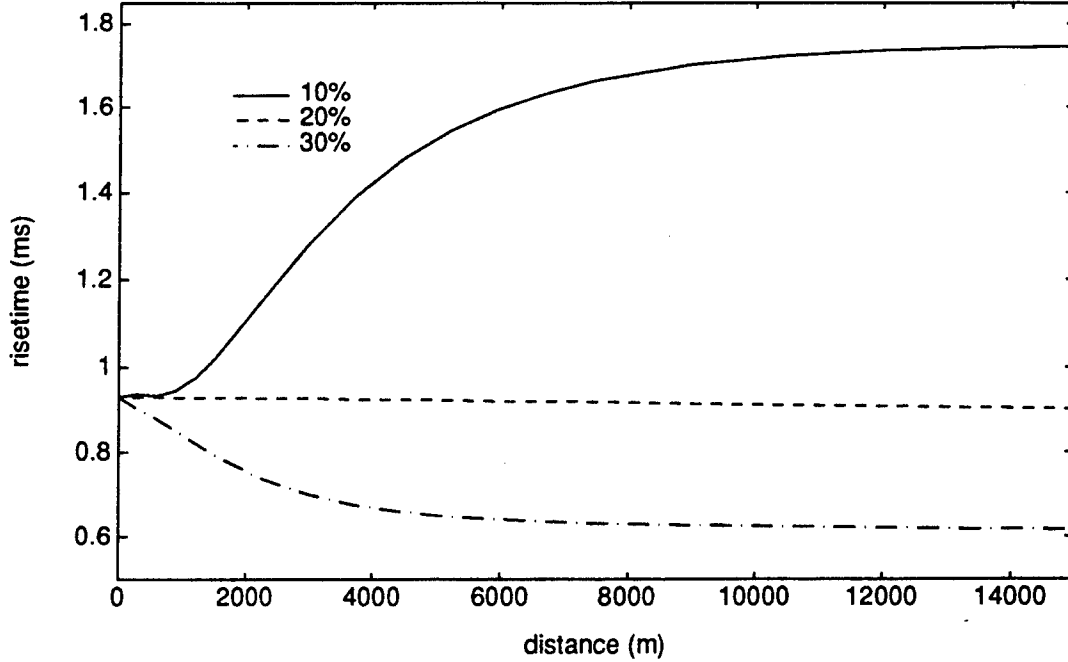


Figure 9: Change in rise time for a waveform leaving a medium of 20% relative humidity.

varying from 50 Pa to 150 Pa and with the relative humidity of the second atmosphere varying from 10% to 90%.

The initial fluctuations in rise time (10% curve in Fig. 9) are due to rather gross changes in the profile. The changes are such that the 10% to 90% definition is not a very suitable measure of rise time. Similar fluctuations were observed by Raspert *et al.* [14].

5.2 Spreading

In an isothermal atmosphere a sonic boom spreads cylindrically. The amplitude of the boom decreases as it propagates away from the aircraft. The effects of both cylindrical and spherical spreading on the rise time of a shock are now examined.

If one applies only the laws of geometrical spreading, the amplitude of a spherically spreading step shock should decrease as

$$\Delta p = \frac{r_0}{r} \Delta p_0, \quad (20)$$

and for cylindrical spreading,

$$\Delta p = \sqrt{\frac{r_0}{r}} \Delta p_0.$$

where Δp_0 is the initial shock pressure jump at a radius r_0 and Δp is the pressure jump at radius r .

The steady state rise time found from the analytical solution of the classical Burgers equation is

$$\Delta\tau = \ln(9) \frac{4\delta_{TV}\rho_0 c_0^3}{\beta\Delta p}. \quad (21)$$

In steady state nonlinear steepening is exactly balanced by thermoviscous absorption. Therefore as the amplitude of a spreading waveform decreases, the rise time increases because nonlinear steepening is weaker. However it is not clear that a spreading waveform will be in steady state. For steady state to be maintained, the shock would have to diffuse immediately in response to the spreading. Naugol'nykh [18] argued that a spreading shock in a thermoviscous medium should have a rise time that is shorter than the steady-state value because the absorption mechanism can not work fast enough.

If a spreading shock were to remain in steady state then, from Eq. 21, the rise time would vary inversely as the pressure jump. Since for spherically spreading waves the pressure varies inversely with distance, Eq. 20, we would expect

$$\Delta\tau \propto r,$$

and for a cylindrically spreading wave

$$\Delta\tau \propto \sqrt{r}.$$

To investigate the validity of these relations we started with the hyperbolic tangent profile appropriate for a plane step shock. The shock was then propagated as a spreading wave, the starting range being $r = r_0$. Figure 10 shows the initial waveform and how the shock diffuses as it loses amplitude. It does not however diffuse quickly enough for the shock to remain in steady state. For example at $r = 20r_0$ the steady-state shock for that amplitude has a rise time that is about 50% longer than the actual shock. Figure 11 compares the steady-state prediction of the rise time to the numerically calculated rise time. In the upper plots we see that for cylindrical spreading, absorption can almost keep up with the spreading but quickly falls behind for spherical spreading. In the lower plots the amplitude is increased by four. In this case absorption is four times weaker and cannot even keep up when the spreading is cylindrical. Note that the steady-state prediction always overestimates the rise time. Absorption cannot act quickly enough to diffuse the profile before more amplitude decrease, due to spreading, occurs. These tests confirm Naugol'nykh's hypothesis.

5.3 Conclusion

For downward propagation, stratification of the atmosphere generally slows down nonlinear effects. The slowing is enhanced by geometrical spreading. In extreme cases the cumulative amount of nonlinear distortion is finite — the phenomenon of waveform freezing. The medium behaves as though it has an effective coefficient of nonlinearity β_{eff} that is range dependent. Waveform freezing occurs when β_{eff} vanishes with propagation distance in

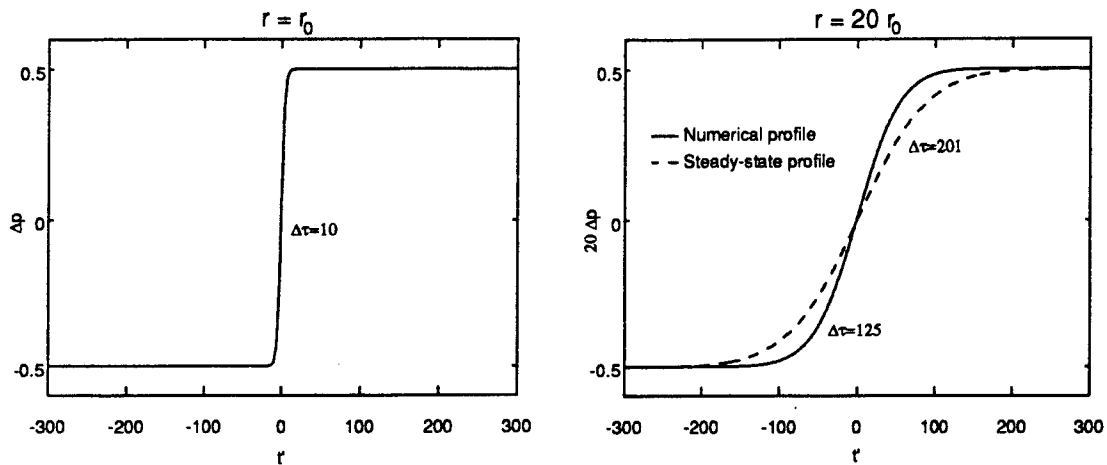


Figure 10: A shock front that starts off in steady state in a thermoviscous medium is propagated as a spherical wave. The left-hand plot shows the initial waveform. The right-hand plot shows the waveform at 20 times the source radius; the steady-state waveform, with its much longer rise time, is also shown.

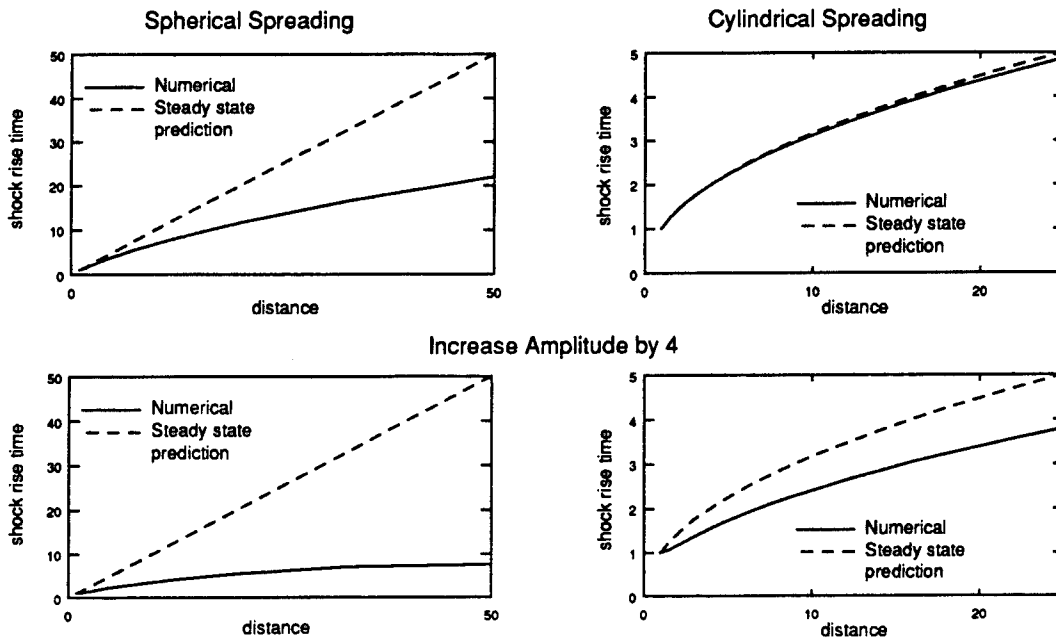


Figure 11: The rise time of a step shock in a thermoviscous medium. The waveform starts off in steady state and is propagated as either a spherically or cylindrically spreading wave. Two different initial amplitudes are used. Rise time is normalized to the initial rise time and distance is normalized to the source radius.

such a way that $\int_0^\infty \beta_{\text{eff}} ds < \infty$. Stratification of the atmosphere can in principal cause waveform freezing to occur. In practice, however, although stratification and spreading lead to a slowing of the distortion, waveform freezing of sonic booms does not occur, when the aircraft flies at or below an altitude of 17 km.

A time domain code has been presented for the propagation of finite-amplitude waves in a medium with thermoviscous absorption and multiple relaxation processes. The code has been used to investigate the effect of a change in relative humidity on the rise time of sonic boom shocks. Results from this code have indicated that the stratified atmosphere changes rapidly enough that absorption and nonlinearity are never in balance at a shock front. Geometrical spreading also prevents the establishment of a steady-state shock. The shocks in a sonic boom waveform are therefore never in steady state. The path history of a sonic boom must be taken into account to make an accurate prediction of rise time.

References

- [1] Y.-S. Lee and M. F. Hamilton, "Time-domain modeling of pulsed finite-amplitude sound beams," submitted to *J. Acoust. Soc. Am.* in March 1994.
- [2] C. M. Darden, C. A. Powell, W. D. Hayes, A. R. George, and A. D. Pierce, "Status of Sonic Boom Methodology and Understanding," NASA CP 3027 (1989).
- [3] W. D. Hayes, "Brief review of basic theory," in *Sonic Boom Research*, A. R. Seebass, ed., NASA SP-147 (1967), pp. 3-7.
- [4] D. T. Blackstock, "Thermoviscous attenuation of plane, periodic, finite-amplitude sound waves," *J. Acoust. Soc. Am.* **36**, 534-542 (1964).
- [5] A. D. Pierce, *Acoustics: An Introduction to Its Physical Principles and Applications* (McGraw-Hill, New York, 1981), pp 587-593.
- [6] R. O. Cleveland and D. T. Blackstock, "Sonic boom rise time," *J. Acoust. Soc. Am.* **96**, Paper 3pPAa2 (1994).
- [7] Y.-S. Lee and M. F. Hamilton, "Nonlinear effects in pulsed sound beams," in *Ultrasonics International 91 Conference Proceedings*, D. E. Gray, ed. (Butterworth-Heinemann, Oxford, 1991), pp 177-180.
- [8] See, for example, D. T. Blackstock, "Nonlinear Acoustics (Theoretical)," in *American Institute of Physics Handbook*, D. E. Gray, ed. (McGraw-Hill, New York, 1972), Chap. 3n, pp. 3-183 to 3-205.
- [9] W. D. Hayes, R. C. Haefeli, and H. E. Kulsrud, "Sonic Boom Propagation in a Stratified Atmosphere, with Computer Program," NASA-CR1299, Aeronautical Research Associates of Princeton, Inc., April 1969.

- [10] C. L. Morfey, "Nonlinear Propagation in a Depth-Dependent Ocean," Tech. Rep. ARL-TR-84-11, Applied Research Laboratories, The University of Texas at Austin (1 May 1984) (AD A145079).
- [11] A. D. Pierce and J. Kang, "Molecular relaxation effects on sonic boom waveforms," in *Frontiers of Nonlinear Acoustics: Proceedings of the 12th ISNA*, M. F. Hamilton and D. T. Blackstock, eds. (Elsevier Applied Science, London, 1990), pp. 165-170.
- [12] J. Kang, "Nonlinear acoustic propagation of shock waves through the atmosphere with molecular relaxation," Ph.D. Thesis, Department of Mechanical Engineering, Pennsylvania State University (1991).
- [13] L. D. Robinson "Sonic boom propagation through an inhomogeneous windy atmosphere," Ph.D. dissertation, Department of Physics, The University of Texas at Austin, (1991).
- [14] R. Raspet, H. Bass, L. Yao and W. Wu, "Steady state risetimes of shock waves in the atmosphere," in NASA CP 3172, High-Speed Research: Sonic Boom, NASA Langley Research Center, Hampton, Virginia, C. M. Darden, ed., Vol. I, pp. 109-116 (1992).
- [15] International Standard ISO9613-1 "Acoustics — Attenuation of sound during propagation outdoors — Part 1: Calculation of the absorption of sound by the atmosphere." International Organization for Standardization, Switzerland. Ref. Num. ISO 9613-1:1993(E)
- [16] F. M. Pestorius, "Propagation of plane acoustic noise of finite amplitude," Technical Report ARL-TR-73-23, Applied Research Laboratories, The University of Texas at Austin (August 1973), AD 778 868.
- [17] A. L. Polyakova, S. I. Soluyan, and R. V. Khokhlov, "Propagation of finite disturbances in a relaxing medium," *Sov. Phys. Acoust.* **8**, 78-82 (1962).
- [18] K. A. Naugol'nykh, "Transition of a shock wave into a sound wave," *Sov. Phys. Acoust.* **18**, 475-477 (1973).

Fast Field Program Compared To Helicopter Field Data

John M. Noble
U.S. Army Research Laboratory
Battlefield Environment Directorate
ATTN: AMSRL-BE-S
White Sands Missile Range, NM 88002

Abstract

A study was conducted to compare the Fast Field Program (FFP) to data from helicopters out to a range of 20 km. The purpose of the study was to observe how the FFP predictions compared to helicopters over ranges out to 20 km and determine if the FFP could reliably be used to predict the propagation conditions for acoustic arrays listening for helicopters. The helicopter data consisted of many passes of a variety of helicopters over a period of several weeks to obtain a large different propagation conditions. Simultaneous acoustic and meteorological data was collected during the experiment. The meteorological data consisted of surface observations of relative humidity and pressure with winds measured from the surface to 2 km and the temperature measured from the surface to 400 m. This provided a good set of meteorological data to use as input to the FFP for the comparisons. For most of the comparisons made, the signal-to-noise ratio for the acoustic data was quite good which contributed to the comparison. For the cases where the signal-to-noise ratio was not good, the FFP provided a good comparison until the signal was buried in the noise. The results of the comparison shows that the FFP predictions agreed very well with the trends in the helicopter data.

Introduction

The Fast Field Program (FFP) is a one-way solution to the acoustic wave equation originally developed for underwater sound propagation predictions.^{1,2} It was adapted to propagation in the atmosphere by Raspet et al.³ and Lee et al.⁴ The FFP incorporates geometrical spreading, molecular absorption, refraction, diffraction, and complex impedance flat earth. The validity of a model is only as good as it's ability to predict measured data under a variety of scenarios. The purpose of this comparison is to evaluate

how well the FFP predicts the acoustic propagation in a refractive atmosphere over a complex impedance surface.

Experiment

The experiment was conducted at SHORAD test site located on McGregor Range near Orogrande, NM which is 50 miles northwest of El Paso, TX, see Fig. 1. The test was composed of several types of helicopters flying in toward the test site along various paths at different speeds. To simplify the comparison, two types of helicopters were used in the comparison flying along the path shown in Fig. 1. This path was chosen because the helicopter flew almost straight at the sensor and the terrain along most of the flight path is fairly flat. The helicopters were tracked with a radar system to know the location of the helicopter at any point in time during the test flight. Data runs consisted of 1 to 4 helicopters flying from 20 km out in range to the sensor location.

The acoustic array consisted of six microphones arranged in a simple box array format with four microphones comprising the corners of the box and two microphones located at the center of the box. The microphones used were B&K 4166 microphones with a low frequency cutoff of 2.6 Hz and a high frequency cutoff of 10 kHz. The microphones were bandpassed through Tektronix AM 502 Differential Amplifiers with a bandpass of 0.1 Hz to 1 kHz. Since the acoustic source was helicopters, most of the acoustic energy is in the region between 10 and 500 Hz. The acoustic data was recorded on a Teac RD-200T PCM data recorder running in 6 channel mode giving a bandwidth of DC to 5 kHz. The data was analyzed using an HP 35660A signal analyzer. The data was averaged over a period of 15 seconds. The position of the helicopter was obtained from correcting the measurement time for the acoustic signal for the propagation time and using the radar track to find the location of each helicopter.

The meteorological data was collected from a number of sensors. A 10 m tower provided temperature, wind speed, wind direction, and humidity at 2 and 10 m and pressure at 2 m. A 924 Mhz wind profiling radar was used to obtain wind speed and wind direction from 100 m to 2 km with a height resolution of 100 m with a 15 minute average every 20 minutes. A Radio Acoustic Sounding System (RASS) provided temperature readings from 100 m to 500 m with a height resolution of 150 m with a 5 minute average every 20 minutes. The averaging intervals for the profilers are such because the wind profiling radar was used to operate the RASS. The temperature data was interpolated or extrapolated to the heights for the wind profiling radar. The two relative humidity readings were averaged and used for all the heights. This gave a meteorological profile from the surface to 2 km for each run of the helicopter(s).

Comparison

Since the flight path of the helicopter was not always constant in direction, the relative sound pressure level with range was calculated along several azimuths. The helicopter path was used to interpolate among the azimuths to determine the relative sound pressure with range along the actual flight path of the helicopter for each pass. The typical flight path used in the comparison is shown in Fig. 2. This flight path was chosen because almost the entire path is over fairly flat earth which is assumed in the propagation model and the aspect angle of the helicopter over the path is the same.

Through the analysis of the acoustic data, the frequencies to run the model was chosen from the main and tail rotor peaks and their respective harmonics. The value for the ground impedance was calculated from Attenborough's Four Parameter Model⁵ using ground parameters measured the year before by Attenborough and Bass. The height of the helicopter was obtained from the radar tracking data. Using this information and the closest meteorological profile in time to the run, the FFP was used to calculate the relative sound pressure level along the flight path. The FFP output was adjusted to the field data by performing a 'best fit' to the field data.

Figure 3 shows the comparison between the FFP and field data for run #1 at a frequency of 21 Hz. It contains the characteristic decrease of the sound level with range. The FFP shows very good agreement with the data out to 14 km where the signal from the helicopter was lost. The sound speed profile is shown in Fig. 4. It shows a characteristic acoustic ducting region within the first 300 m of the atmosphere due to a wind shear at that height. This allows for the good propagation conditions allowing for the propagation out to 14 km. Figure 5 shows the comparison between the FFP and field data for run #1 at a frequency of 124 Hz. The higher frequency still shows good comparison of the FFP to the field data with similar trends in the data and model between 6 and 8 km.

Run #2 was made on the same day as run #1 but run #2 was 1.5 hours later. The sound speed profile, Fig. 6, shows the slope in the lower part of the duct is almost zero. This is due to the increase in the temperature lapse rate near the surface from run #1. However, the ducting region is still present with the vertical extent of the duct to 400 m. Figure 7 shows the comparison between FFP and field data for run #2 at a frequency of 21 Hz. The model performs well when compared to the data out to 17 km. At about 17 km, the data continues to decrease while the model increases. In the discussion of the next data run, an explanation will be provided why this discrepancy is present. Looking at the 124 Hz data, the comparison between the model and data is very good, see Fig. 8.

Run #3 was made on another day from runs #1 and #2. Figure 9 shows the sound speed profile for run #3. The sound speed profile is similar to the other two, but there are some distinct differences between them. The lower region of the ducting area is upward

refracting instead of homogeneous or downward refracting. This initially causes sound propagating from the source to propagate upward, possibly forming a shadow zone region. Looking at the comparison between model and data (Fig. 10), there is a very good fit between the FFP and the field data. However, there are two interesting items not in the comparison, but in the behavior of the data and the model. Examining the previous two runs, the mean slope of the sound levels with range decrease as the source is further from the sensors as would be expected from spreading losses. However, the decrease of the sound levels with range for run #3 is almost zero. This means that beyond a certain distance, the sound wave is not attenuated very much. This characteristic is supported by both the model and the data. The signal-to-noise ratio for this run is well above the noise floor indicating that data is valid for this run out to 20 km. Something very interesting is occurring in this case which is limiting the rate of energy loss with range for the acoustic signal. Looking at the higher frequency comparison (Fig. 11), the low attenuation with range is still present and the model does a good job in predicting this behavior. The helicopter used in this comparison is different from the one used in the previous two comparisons, however, other runs made with this helicopter on other days do not show this type of behavior. So this behavior is not due to using another helicopter. As in run #2, there is a deviation between model and data starting about 17 km in range for the low frequency comparison. After examining several possible reasons, the best reason for the deviation between the model and the data is due to terrain. Examining the map of the testing area, the helicopter runs start over near a range of mountains. The start of the helicopter path is actually in a canyon. The local terrain in the canyon is probably causing a problem with the sound propagating from the helicopter either from its presence or the canyon's effect on the local meteorology. In any case, this is a region where the model should not have worked to begin with.

Conclusions

A comparison was conducted to evaluate the performance of using the FFP for predicting the sounds at ranges up to 20 km for helicopters. The data was collected for a variety of helicopters flying from 20 km toward the sensor under a variety of atmospheric conditions. The FFP was used to calculate the attenuation of the sound along the helicopter's flight path and compared to the measurements. The comparison was restricted to helicopter flight paths over flat earth since the FFP does not have terrain incorporated into it. The FFP results showed very good predictions when compared to the field data for a variety of frequencies where there was good signal-to-noise ratios. The data also showed some interesting behavior in one of the comparisons. At this time, the cause of the behavior is not known.

References

1. F.R. DiNapoli, A fast field program for multilayered media. Naval Underwater Systems Center, Tech. Report 4103, 1971.
2. H.W. Kutschale, The integral solution of the sound field in a multilayered liquid-solid half-space with numerical computations for low-frequency propagation in the Arctic Ocean. Report No. 1(CU1-1-70, ONR Contract N00014-67-A-0108-0016), Lamont-Doherty Geological Observatory, Columbia University, Palisades, New York, 1970.
3. R. Raspet, S.W. Lee, E. Kuester, D.C. Chang, W.F. Richards, R. Gilbert, and N. Bong, "Fast-field program for a layered medium bounded by complex impedance surfaces," J. Acoust. Soc. Am. 77 (1985) 345-352.
4. S.W. Lee, N. Bong, W.F. Richards, and R. Raspet, "Impedance formulation of the fast field program for acoustic wave propagation in the atmosphere," J. Acoust. Soc. Am. 79 (1986) 628-634.
5. K. Attenborough, "Acoustical Impedance Models For Outdoor Surfaces," J. Sound Vib. 99 (1985), 521-544.

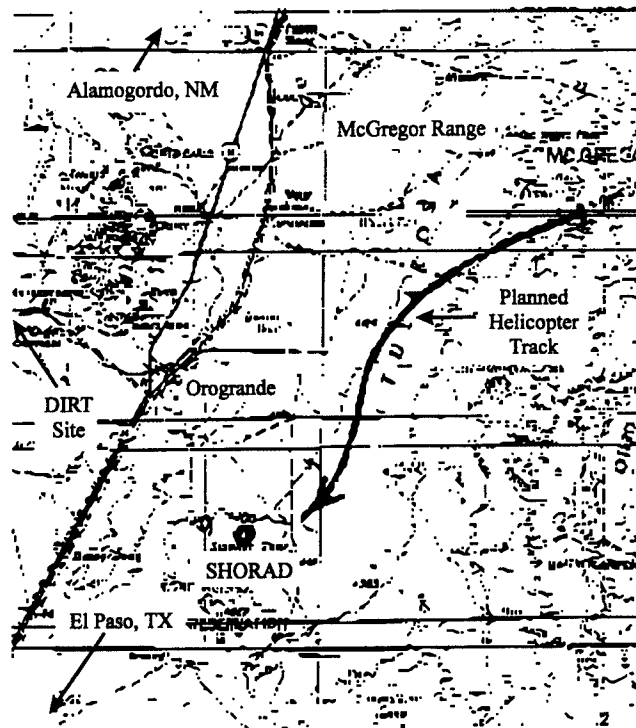


Figure 1. Map of area around SHORAD test site.

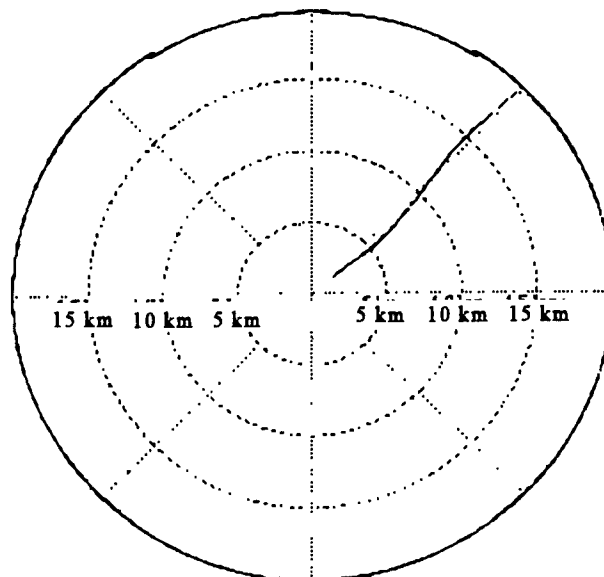


Figure 2. Typical radar track of helicopter used in comparison.

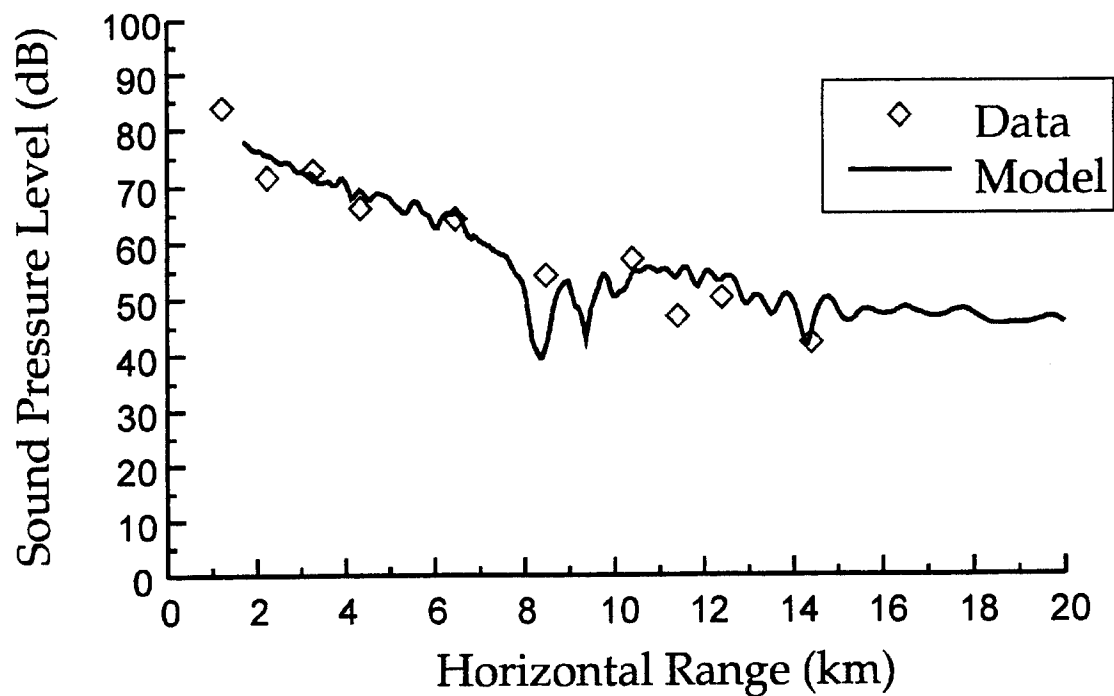


Figure 3. Comparison between FFP and field data at 21 Hz for run #1.

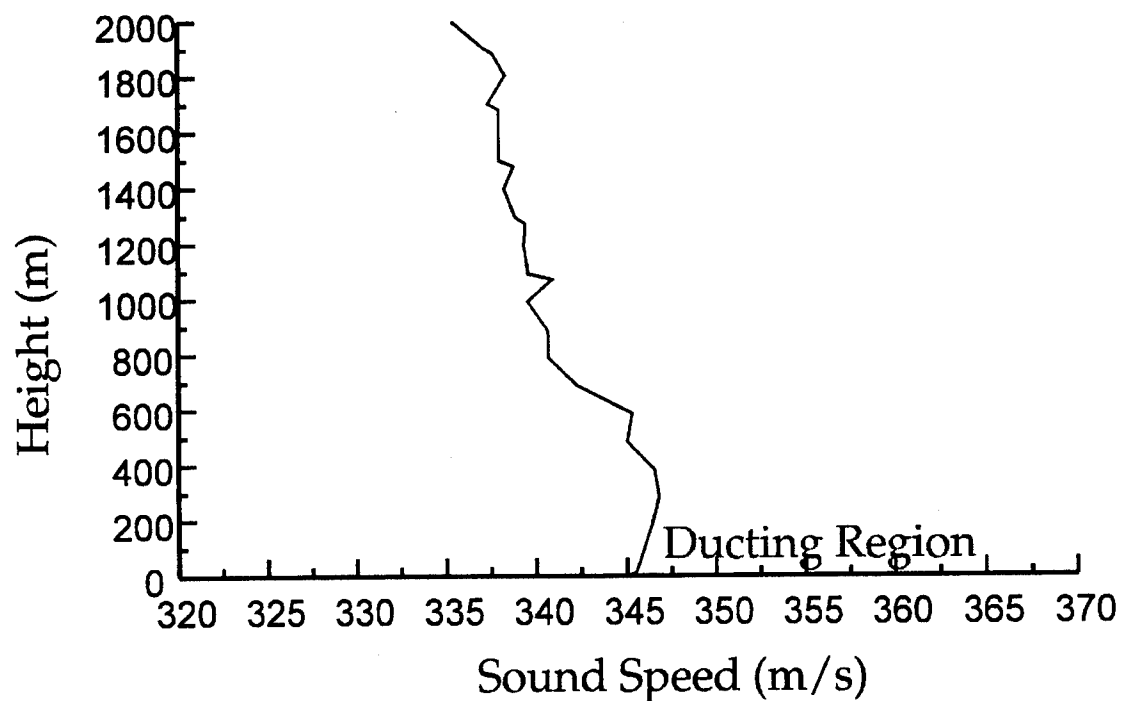


Figure 4. Sound speed profile in the direction of propagation for run #1.

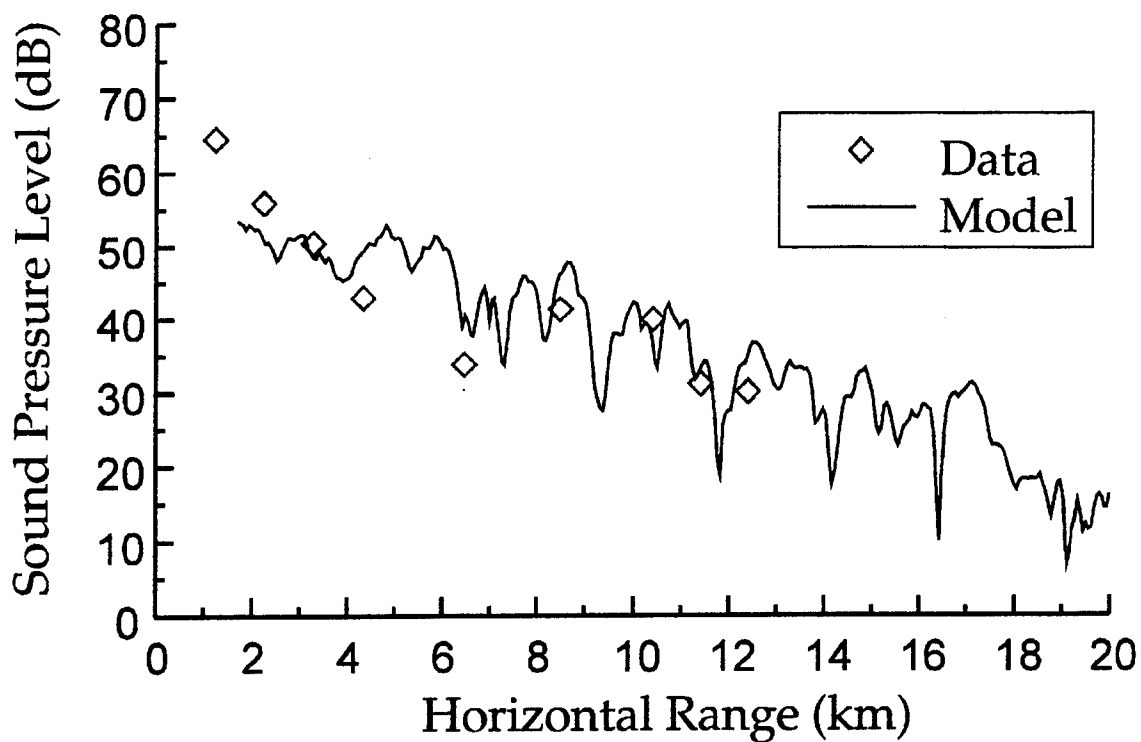


Figure 5. Comparison between FFP and field data at 124 Hz for run #1.

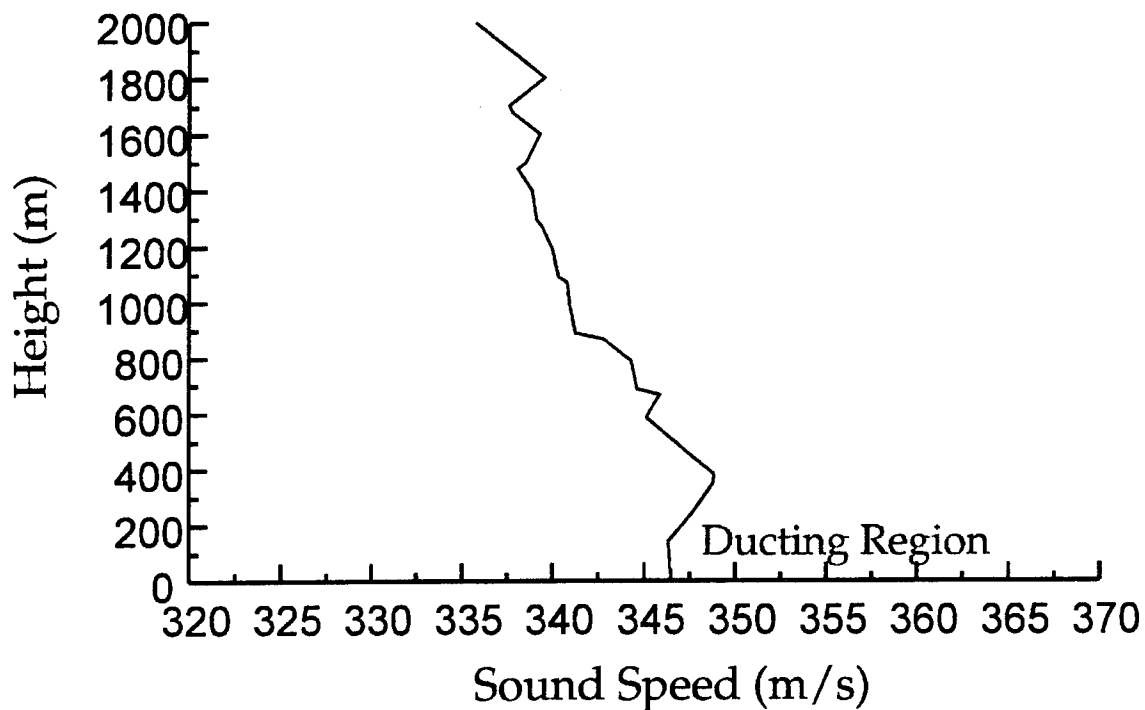


Figure 6. Sound speed profile for run #2.

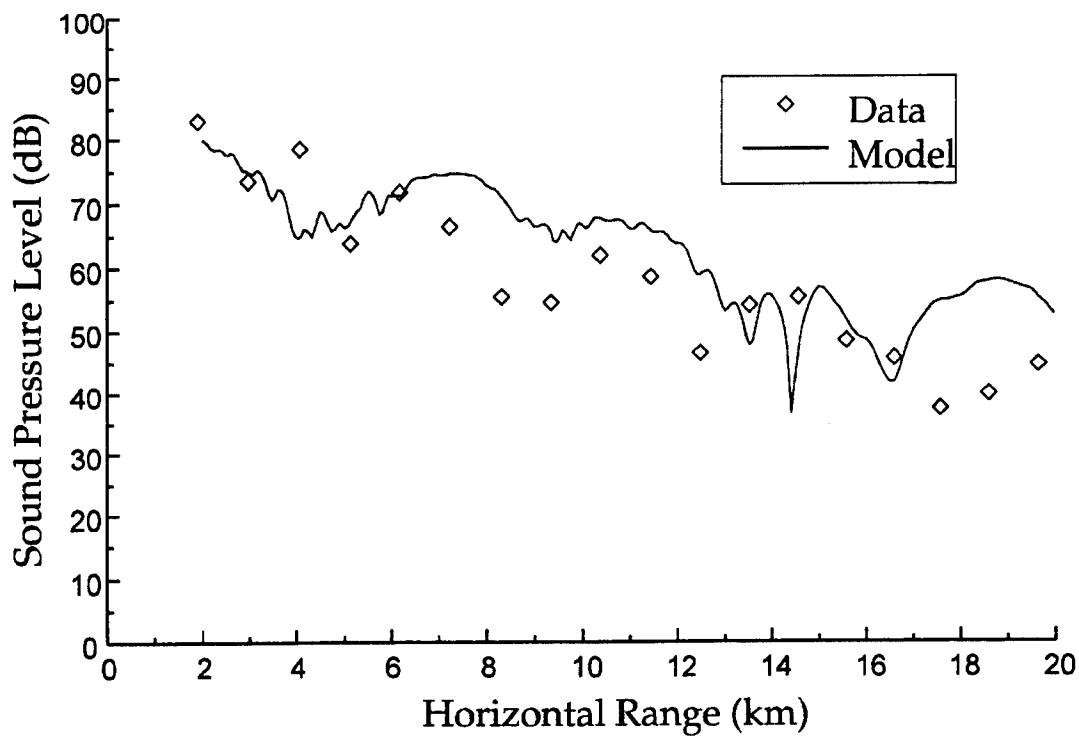


Figure 7. Comparison between FFP and field data at 21 Hz for run #2.

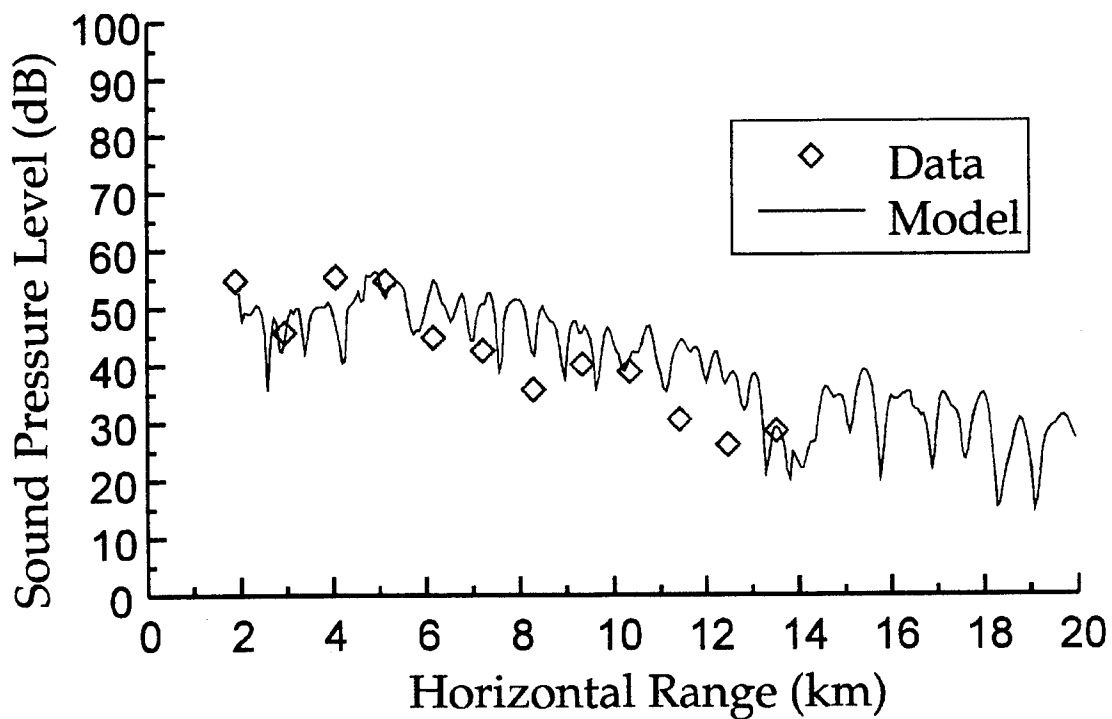


Figure 8. Comparison between FFP and field data at 124 Hz for run #2.

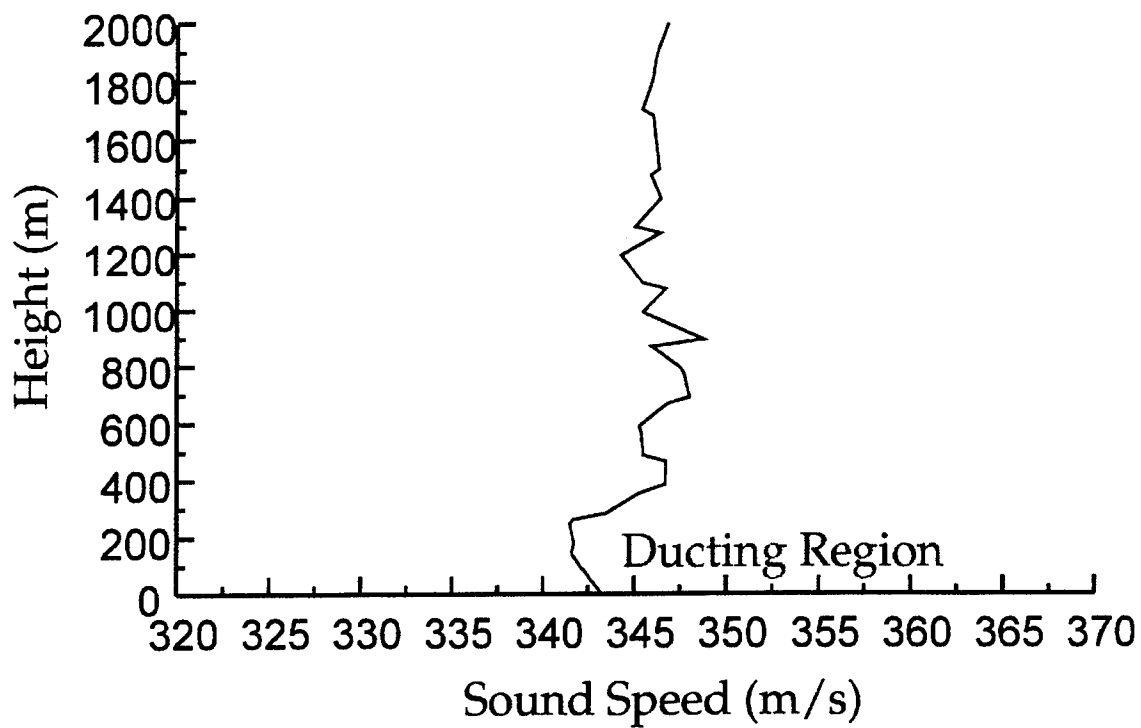


Figure 9. Sound speed profile for run #3.

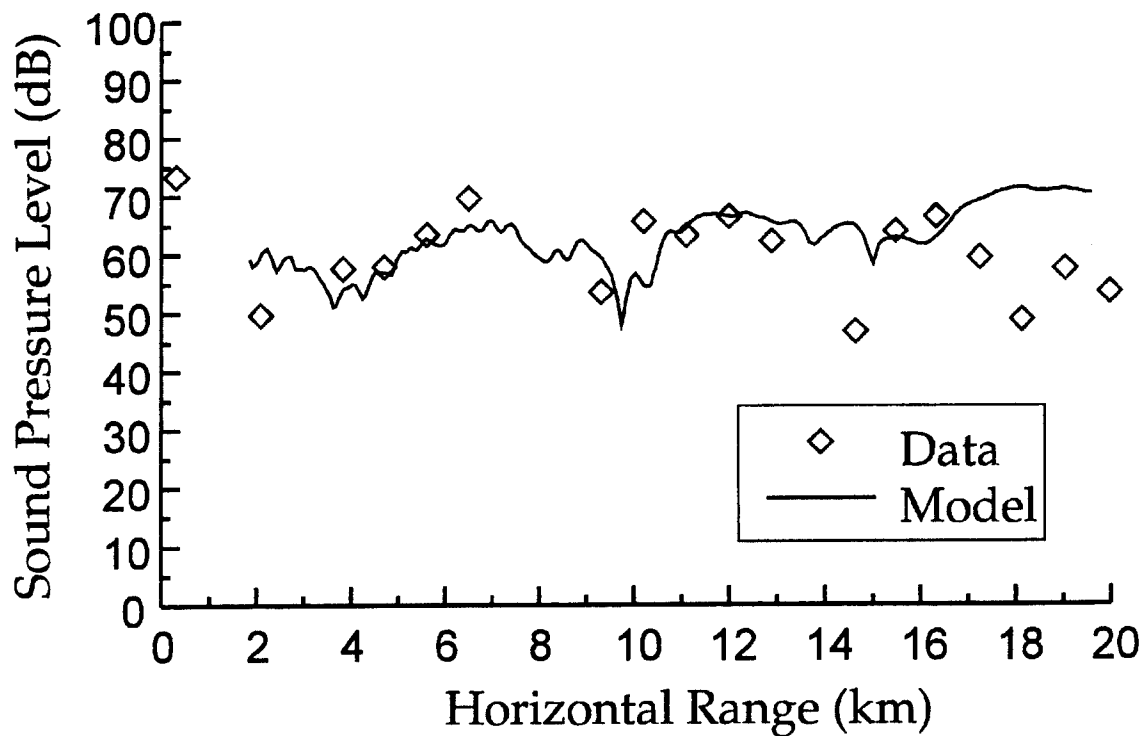


Figure 10. Comparison between FFP and field data at 23 Hz for run #3.

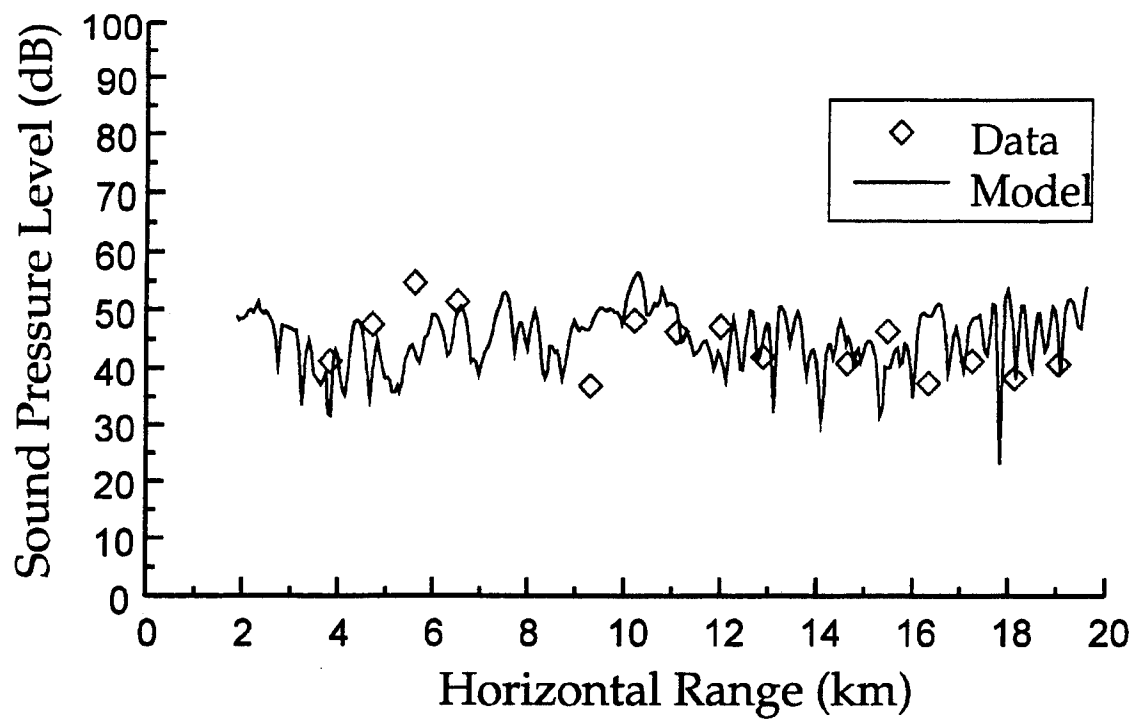


Figure 11. Comparison between FFP and field data at 113 Hz for run #3.

PROPAGATION NEAR THE GROUND FROM A FIXED JET ENGINE SOURCE

Keith Attenborough
Faculty of Technology
The Open University
Milton Keynes MK7 6AA
England

Cyrus Chinoy and Reginald Lambert
ESDU International plc
27 Corsham Street
London N1 6UA
England

ABSTRACT

Spectrum levels have been measured at an array of microphones deployed over grassland out to 1.158 km from a fixed jet engine source. There was simultaneous recording of wind speed and temperature profiles as a function of height. Under low wind speed conditions, tolerable agreement has been achieved between predictions using a two-parameter ground impedance model and allowance for turbulence. This agreement is found to be superior to that obtained using a Delany-Bazley-Chessel prediction model with turbulence.

1. INTRODUCTION

A classical series of measurements of near-grazing propagation from a fixed jet engine over grassland at two airfields were carried out by Parkin and Scholes in the 1960's [1,2]. These data have been used intensively to test theories of propagation over finite impedance boundaries [3] and the influence of meteorological conditions [4].

This paper describes early results from a recent repeat of these classical measurements involving improved meteorological monitoring. Attempts to characterize the acoustical properties of the ground by short-range level difference measurements are detailed. After describing the test layout, evidence that the nearest microphone array at 15 m range was in the near-field is presented. The restricted data sets presented are for low turbulence, low wind speed, and small temperature gradient conditions. Subsequently, it is shown that the level difference spectra, even at the furthest microphone positions (1158 m from source), are predicted well after including turbulence and a two parameter ground model in the classical formula for propagation from a point source in a homogeneous atmosphere.

2. MEASUREMENTS

2.1 Propagation to Long-Range

The jet engine (Rolls Royce Avon 204) was mounted with the centre of the jet nozzle 2.16 m above the end of a disused concrete runway at the Rolls Royce jet engine test facility at Hucknall, in North Nottinghamshire, England, and the nozzle directed at an angle of 37.5° to the runway axis. Eleven vertically separated pairs of microphones were deployed as shown in Fig. 1, five of these microphone pairs being over grassland. The microphones over the concrete runway are shown in their original positions. Subsequently they were discovered to be too near the edge of the runway and moved to the centre. However analysis of the resulting data is not reported here. A meteorological station between microphone positions D and E recorded wind speed and direction and temperature at two heights. In addition, a meteorological balloon observation was made before and after each test. Acoustic data were recorded in thirty-second blocks on each of several days representing distinct meteorological conditions. Twenty thirty-second blocks of low wind speed data on a single day have been recorded over grass as detailed in Table 1. The resulting spectrum levels are shown in Fig. 2, where the evident wide spread is primarily due to turbulence. The turbulence intensity shown in Table 1 is given by $\left\langle \frac{\sigma_v^2}{v^2} \right\rangle$, where σ_v is the standard deviation of the velocity fluctuation measured with a cup anemometer and v is the wind speed. Within these twenty low wind speed data sets, the three with the lowest turbulence intensities have been selected for further analysis at this stage.

2.2 Short-Range

Short-range level difference spectra measurements have been advocated as a method of ground characterization [5,6] and several such measurements have been carried out over the grass at the Hucknall site. Results from two such measurements are shown in Figs. 3 and 4, together with fits using a two parameter ground impedance model [7].

According to the two-parameter model, the normalised acoustic impedance of the ground, Z, is given by

$$Z = (\pi\gamma\rho)^{-1/2} (\sigma / f)^{1/2} (1 + i) + \frac{ic}{4\gamma\pi fd}$$

where γ is the ratio of specific heat capacities of air
 ρ is the equilibrium density of air in kg m^{-3}
 c is the adiabatic sound speed in air in km s^{-1}
 σ is the flow resistivity of ground surface layer in kPa s m^{-2}
 d is the effective thickness of the surface layer in m
 f is frequency in kHz

It is noticeable from these data that the grassland is laterally inhomogeneous to a small extent with $20 < \sigma < 35$ and $0.017 < d < 0.025$.

3. THEORY

Excess attenuation has been calculated for each microphone position using a simplified version of the formulation due to Clifford and Lataitis [8],

$$EA = 10 \log \left| 1 + \left(\frac{r_1^2}{r_2^2} \right) |Q|^2 + 2 \left(\frac{r_1}{r_2} \right) \{ \cos [k(r_2 - r_1)] \text{Re}(Q) - \sin [k(r_2 - r_1)] \text{Im}(Q) \} T \right| \quad (1)$$

where $T = \exp(-\alpha \epsilon^2 (1 - \delta)) \quad (0 \leq \delta \leq 1)$
 $\epsilon^2 = \sqrt{\pi} \langle n^2 \rangle k^2 d L_0$
 $\alpha = 1 \text{ or } 0.5$
 $\langle n^2 \rangle =$ mean square refractive index
 $L_0 =$ outer scale of fluctuations
 $Q = R_p + (1 - R_p)F(w)$
 $F(w) = 1 + i\sqrt{\pi} w e^{-w} \text{erfc}(-iw)$

$$w = (ikr_2/2)(\cos\theta + \beta)^2$$

$\theta =$ angle of specular reflection at the ground

$\beta =$ relative normal admittance = $1/Z$

4. ANALYSIS OF RESULTS

4.1 Reference Microphone Position

To check on whether the reference microphone positions at 15 m from the end of the jet nozzle were in the far-field the following calculations were made:

- (a) The free-field levels for the jet broad band and shock cell noise were calculated from measured and estimated parameters listed in Table 2 using the S.A.E. method (ARP876C) and the Harper-Bourne and Fisher method (AGARD CP-131 1973), respectively.
- (b) The former ESDU ground correction procedure (based on Delany-Bazley-Chessell, $\sigma = 200 \text{ kPa s m}^{-2}$ without turbulence [9]) was used to predict the spectrum levels at the reference (15m range) microphone positions.

An example result is shown in Fig. 5. From this it is clear that there are significant differences between the measured and predicted spectra at such short range. On the other hand, repetition of this procedure for the next microphone range of 152.4 m gives much better agreement with the measured spectrum level (see Fig. 6). The discrepancy between prediction and measurement cannot be attributed only to ground impedance and turbulence. This, coupled with the fact that the effective jet source length would extend for several jet nozzle diameters down stream, suggested that the 15 m reference range was within the near-field. Subsequent data analysis was based upon use of signals from the microphones at 152.4 m range as reference.

4.2 Ground Models and Turbulence

Figure 7 illustrates the improvement obtained by including a non-zero value of T in predictions based on Eq. (1). The "measured" excess attenuation spectra shown in this figure have been obtained by calculation as follows:-

(a) A predicted excess attenuation spectrum due to ground effect and turbulence effect at 152.4 m range has been added to the measured spectrum at 152.4 m to give a measured free-field level.

(b) This has then been used to calculate the "measured" excess attenuation spectrum at the range of interest (1158 m) after correcting for spherical spreading and atmospheric absorption between 152.4 m and 115.8 m (using the ESDU procedure [10]).

The improvements resulting from inclusion of turbulence with $\langle n^2 \rangle = 10^{-7}$, $L_0 = 2$, $\delta = 0$ are apparent.

Figures 8 and 9 illustrate the improvement in the prediction in the frequency range of the leading edge of the ground effect dip resulting from the use of a two parameter model [7] rather than the widely-used one parameter impedance model [9].

However, it should be noted that the best fit impedance model parameters ($\sigma = 30$ kPa s m⁻², $d = 0.05$ m) for the long-range data differ slightly from either of the parameter pairs deduced from short-range measurements.

4.3 Horizontal Level Difference

A stricter comparison between predictions and data is obtained by comparing the difference in levels recorded at the reference microphones and more distant microphones, corrected for spherical spreading and atmospheric absorption, with predictions of these horizontal corrected level differences. An example is shown in Fig. 10, confirming the good agreement following from choice of a two-parameter ground model and inclusion of turbulence.

ACKNOWLEDGEMENTS

The tests reported here were initiated and monitored by ESDU International plc and were carried out with the support of British Airways, British Aerospace, Rolls-Royce, the Department of Trade and Industry, Department of Transport and EPSRC. The source free-field and near-field calculations were carried out by Stephen Perkins of Rolls Royce. The short-range level difference spectra were obtained by Shahram Taherzadah and Brendan Aegenheister of The Open University.

REFERENCES

1. Parkin, P.H. and Scholes, W.E. "The horizontal propagation of sound from a jet engine close to the ground at Radlett" *J.Sound.Vib.* 1 1-13 (1964).
2. Parkin, P.H. and Scholes, W.E. "The horizontal propagation of sound from a jet engine close to the ground at Hatfield" *J.Sound.Vib.* 2 (4) 353-374 (1965).
3. Attenborough, K. "Review of ground effects on outdoor sound propagation from continuous broadband sources" *Applied Acoustics* 24 289-319 (1988).
4. Piercy, J.E., Embleton, T.F.W. and Sutherland, L.C. "Review of noise propagation in the atmosphere" *J.Acoust.Soc.Am.* 61 (6) 1403-1418 (1977).
5. Embleton, T.F.W., Piercy, J.E. and Daigle, G.A. "Effective flow resistivity of ground surfaces determined by acoustical measurements" *J4* (4) 1239-1244 (1983).
6. Hess, H.M., Attenborough, K. and Heap, N.W. "Ground characterization by short-range propagation measurements" *J.Acoust.Soc.Am.* 87 (5) 1975-1986 (1990).
7. Attenborough, K. "Ground parameter information for propagation modeling" *J.Acoust.Soc.Am.* 92 418-427 (1992).
8. Clifford, S.F. and Lataitis, R.T. "Turbulence effects on acoustic wave propagation over a smooth surface" *J.Acoust.Soc.Am.* 73 1545-1550 (1983).
9. ESDU, "The correction of measured noise spectra for the effects of ground reflection" Item Number 80038, ESDU International plc, London, November 1980. (A revised Item including turbulence and a 2 parameter ground model is in preparation, 1994).
10. ESDU, "Evaluation of the attenuation of broad-band sound by a non-uniform still atmosphere", Item No. 78003, ESDU International plc, London, September 1978.

BLOCK	WIND SPEED m/s at stations		WIND DIRECTION deg. compass bearing (Downwind)	TEMPERATURE deg. C at stations		TURBULENCE INTENSITY
	2.5cm	6.4 m		2.5 cm	6.4 m	
1	1.09	1.46	2.4	10.7	9.7	0.1367
2	1.57	1.85	33.7	10.4	9.9	0.0486
3	1.34	1.61	45.1	10.4	9.9	0.0962
4	1.27	1.96	68.0	10.5	9.8	0.0672
5	0.00	1.57	73.8	10.5	9.8	0.0873
6	0.00	1.46	71.0	10.5	9.8	0.1251
7	0.00	1.81	74.2	10.7	9.9	0.2371
8	1.85	2.54	56.1	10.5	9.9	0.1066
9	1.67	2.61	46.0	10.6	9.9	0.0754
10	1.22	2.02	65.7	10.5	9.8	0.0836
11	0.00	1.97	68.9	10.5	9.8	0.0805
12	0.00	1.97	92.2	10.6	9.8	0.0607
13	0.00	1.09	60.1	10.6	9.8	0.0678
14	0.00	0.01	59.3	10.4	9.9	10.1489
15	1.02	1.53	6.4	10.4	9.9	0.0764
16	0.00	1.58	18.5	10.4	10.0	0.0928
17	0.00	0.92	36.1	10.3	9.9	0.1792
18	0.00	1.16	43.0	10.2	9.9	0.0424*
19	0.00	0.00	115.4	10.2	9.8	0.0000*
20	0.00	0.00	180.1	10.2	9.8	0.0000*

* - Selected

Table 1 Meteorological conditions recorded during twenty low wind speed data blocks.

Quantity	Symbol	Value	Unit	Comment
Ambient temperature	TO	10	°C	Measured on test
Ambient pressure	PO	14.8	p.s.i.	Measured on test
Relative humidity	RH	66.5	%	Measured on test
Shaft speed	N	≈7500	RPM	Nominal recorded
Jet pipe temperature	T	562	°C	Measured on test
Final nozzle diameter	D	23	inches	Measured
Jet effective area	Ae	2.597	sq.ft	= 0.9 x (final nozzle area)
Jet effective diameter	De	1.818	ft	2 x sqrt (Ae/π)
Pressure ratio	P/PO	2.05		Estimated
Specific heat	Cp	1148	J/Kg.K	Estimated
Cp/Cv for the jet	γ	1.31		Estimated
Jet Mach number	M	1.093		Calc. from P/PO and γ
Jet sound speed	a	1643	ft/s	Calc. from Cp, γ, M, and T
Jet Velocity	V	1796	ft/s	Calc. from a and M

Table 2 Measured and deduced parameters used for source level calculation for Rolls Royce Avon 204 jet engine.

LIST OF FIGURES AND CAPTIONS

- Figure 1 Original deployment of source and receivers at Hucknall.
- Figure 2 Measured sound level spectra during twenty 30-second long, low wind speed recordings at 1158 m range and 1.2 m height.
- Figure 3 Level difference spectrum between microphones at 0.3 m and 0.05 m height, 1.5 m from a loudspeaker point source at 0.3 m height over short grass at Hucknall. Continuous line is prediction.
- Figure 4 Level difference spectrum as for Figure 3 but over long grass at Hucknall. Continuous line is prediction.
- Figure 5 Measured and predicted sound level spectra at the 1.2 m high microphone at the 15 m range over grass.
- Figure 6 Measured and predicted spectra at the 6.4 m high microphone at 15 m range over grass.
- Figure 7 "Measured" and predicted excess attenuation at 1158 m range and 1.2 m height showing the change in predictions when turbulence is included.
- Figure 8 (a) Best fit to data of Figure 7 using one parameter model
($\sigma = 200 \text{ kPa s m}^{-2}$)
- (b) Best fit to data of Figure 7 using two parameter model
($\sigma = 30 \text{ kPa s m}^{-2}$, $d = 0.05 \text{ m}$)
- Figure 9 Measured (continuous lines) and predicted (broken line) corrected level difference spectra between receivers at 6.4 m height and ranges of 152.7 and 1158 m.

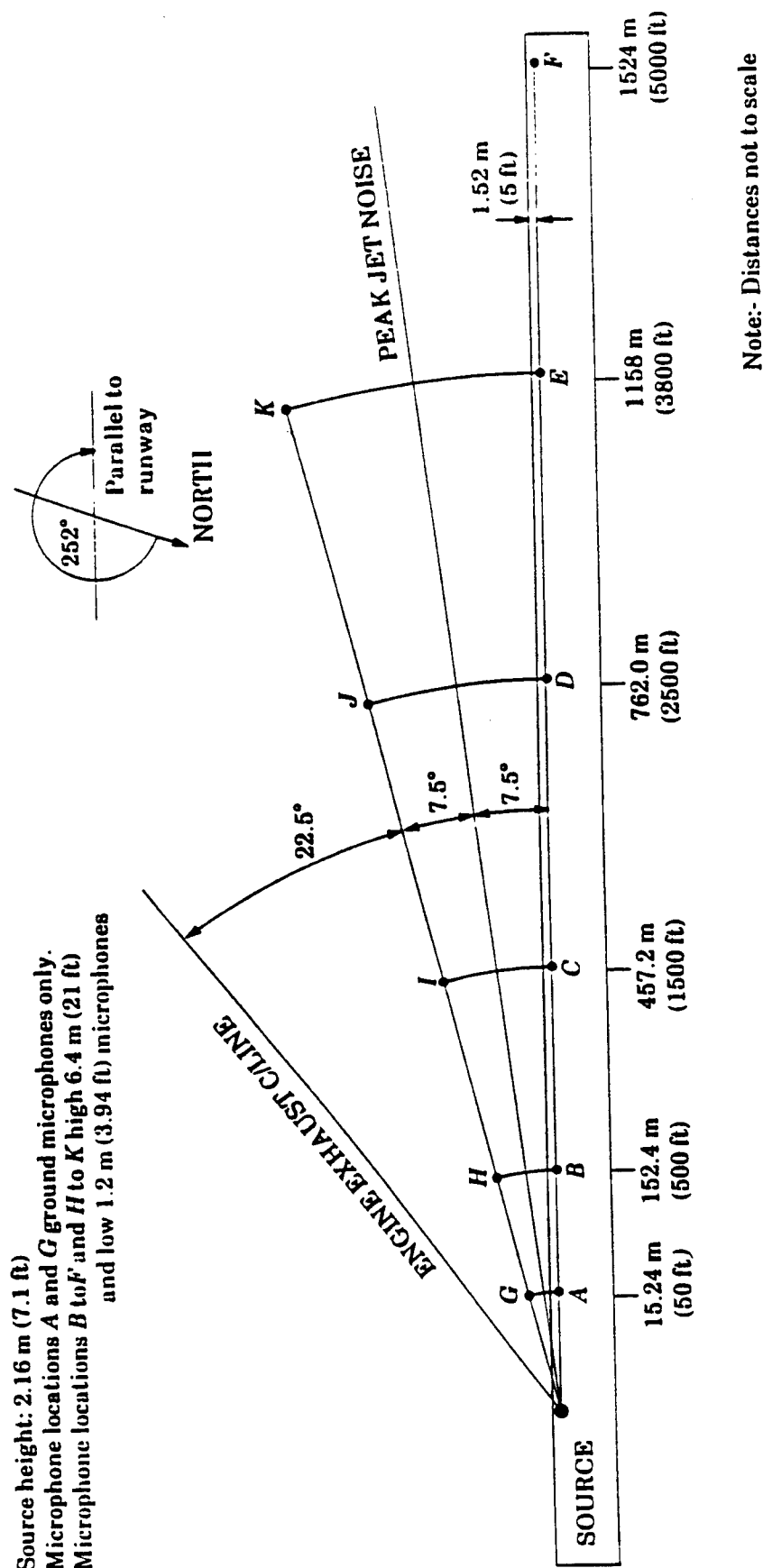


Figure 1. Original source-receiver geometry

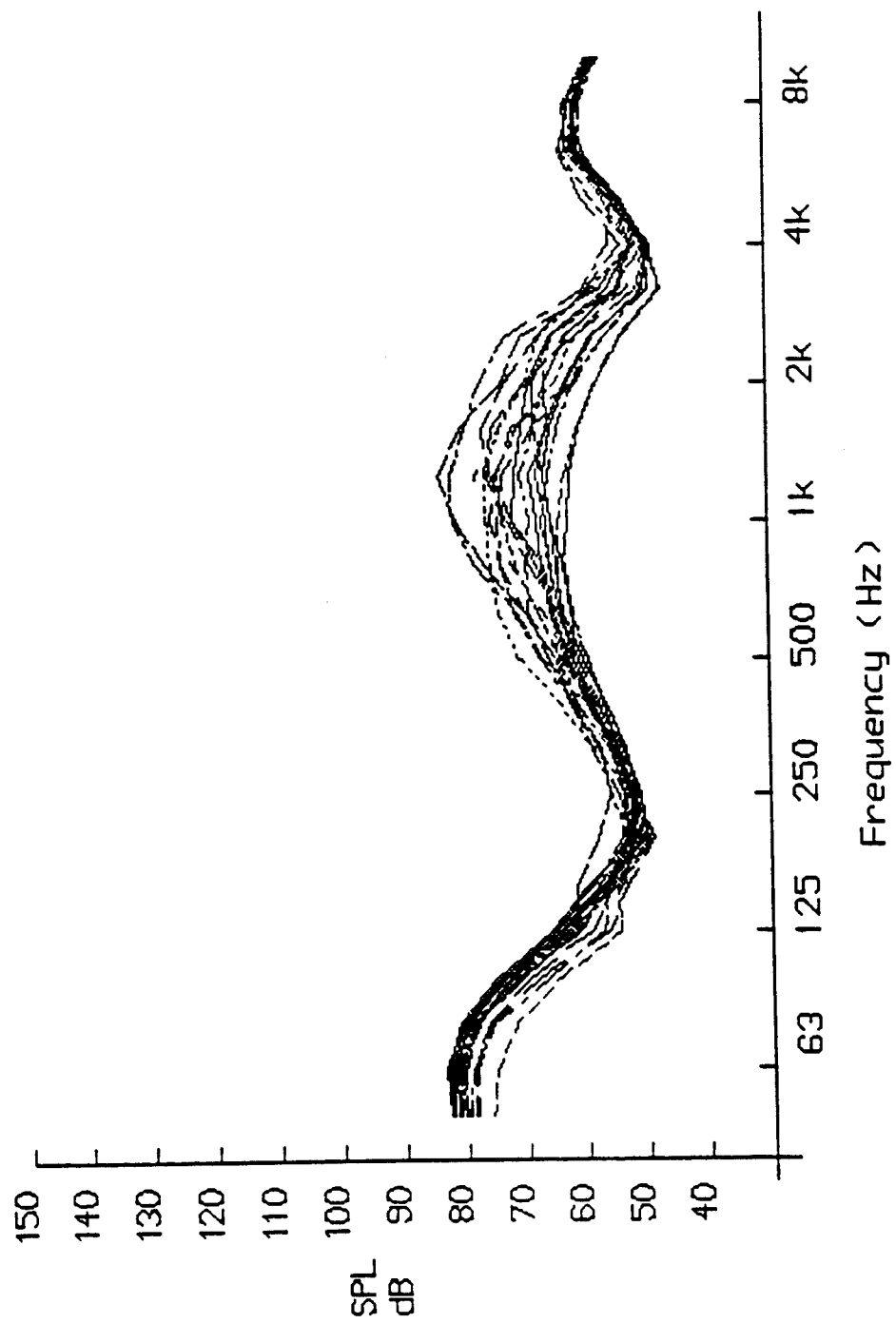
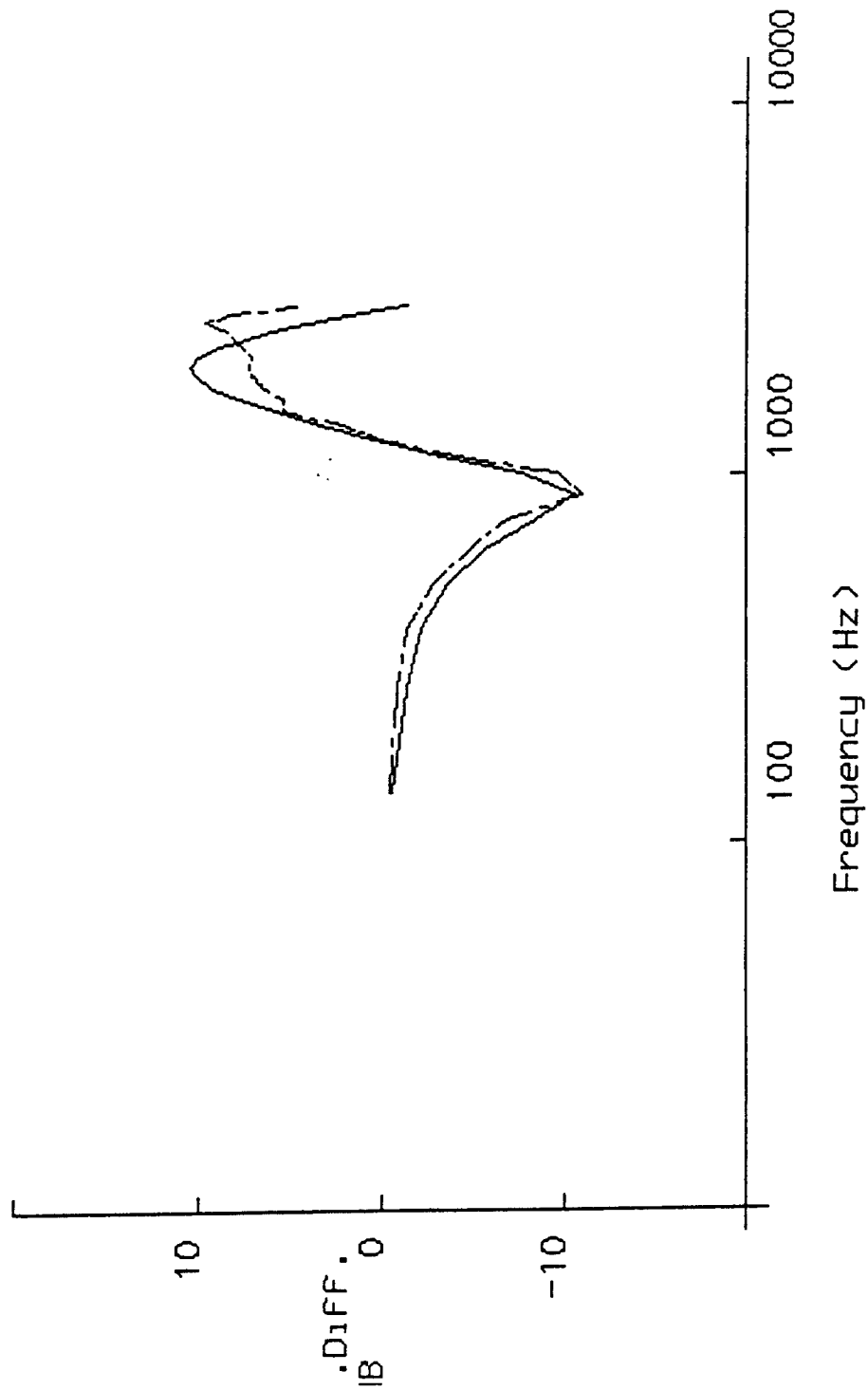


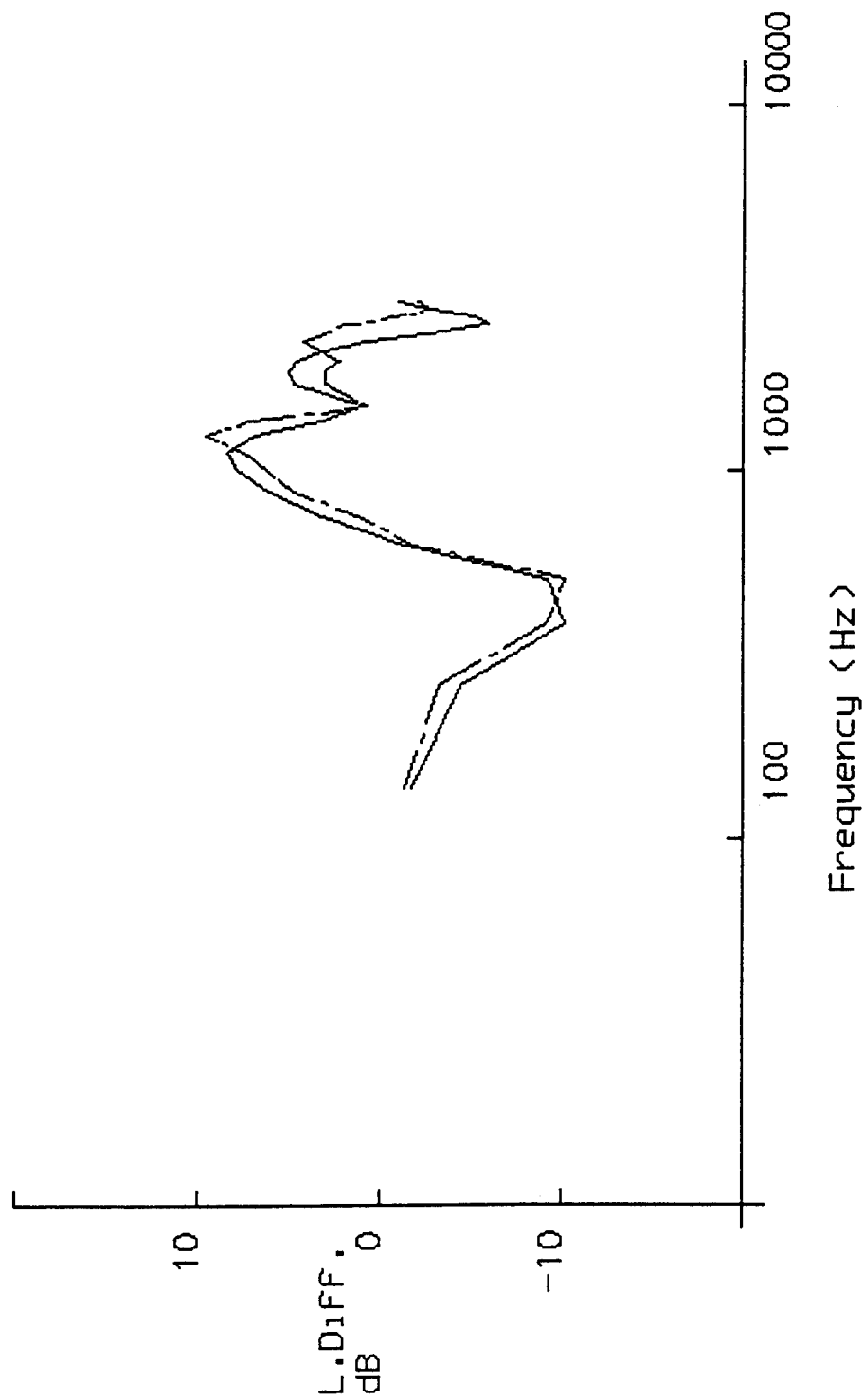
Figure 2 Low microphone at position K

P2
Shoutgill
Day 4



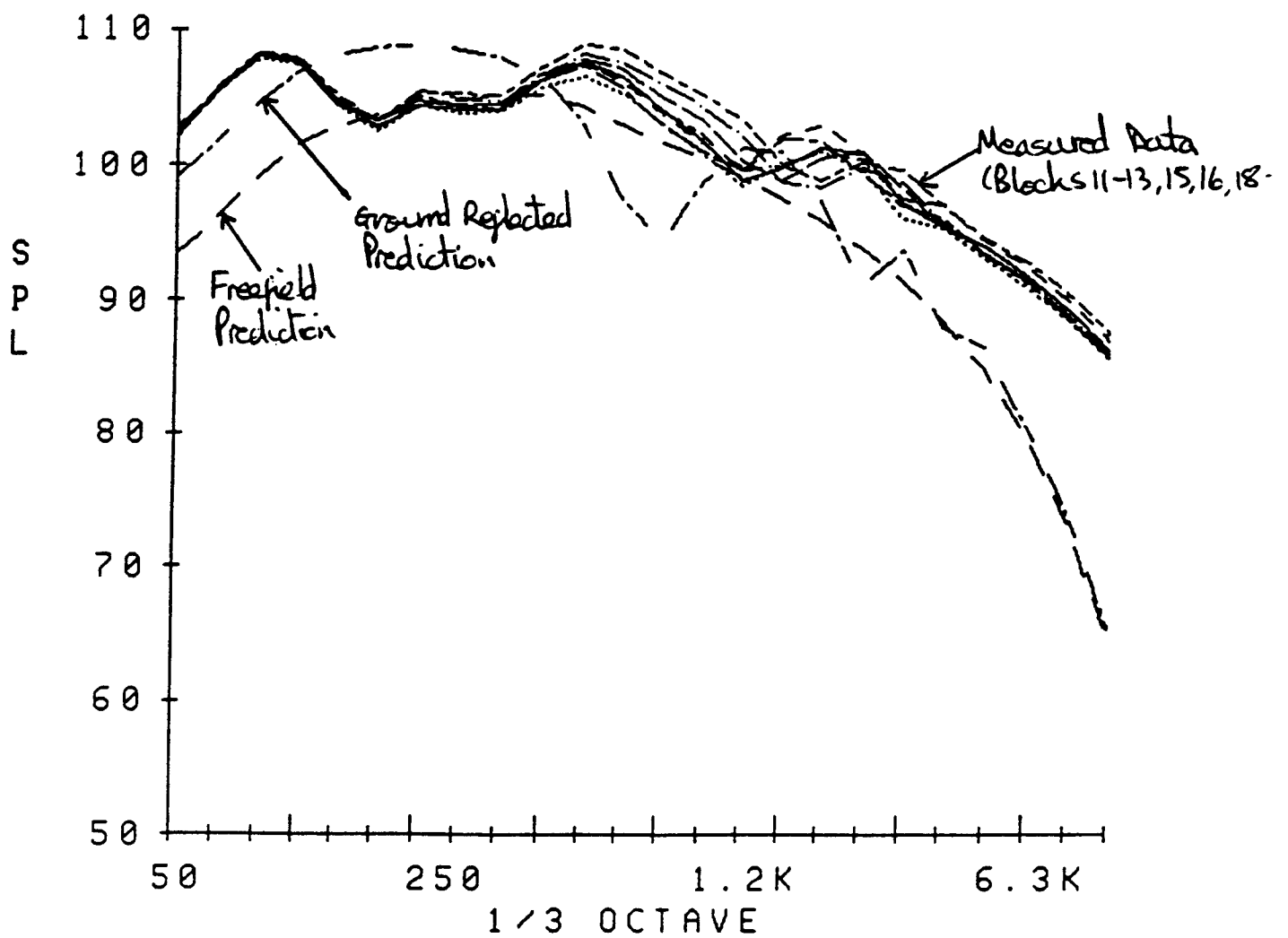
SIGMAe = 35000. ALPHA = 60.
Level differences Run 4125

P4
long grass
Day 4

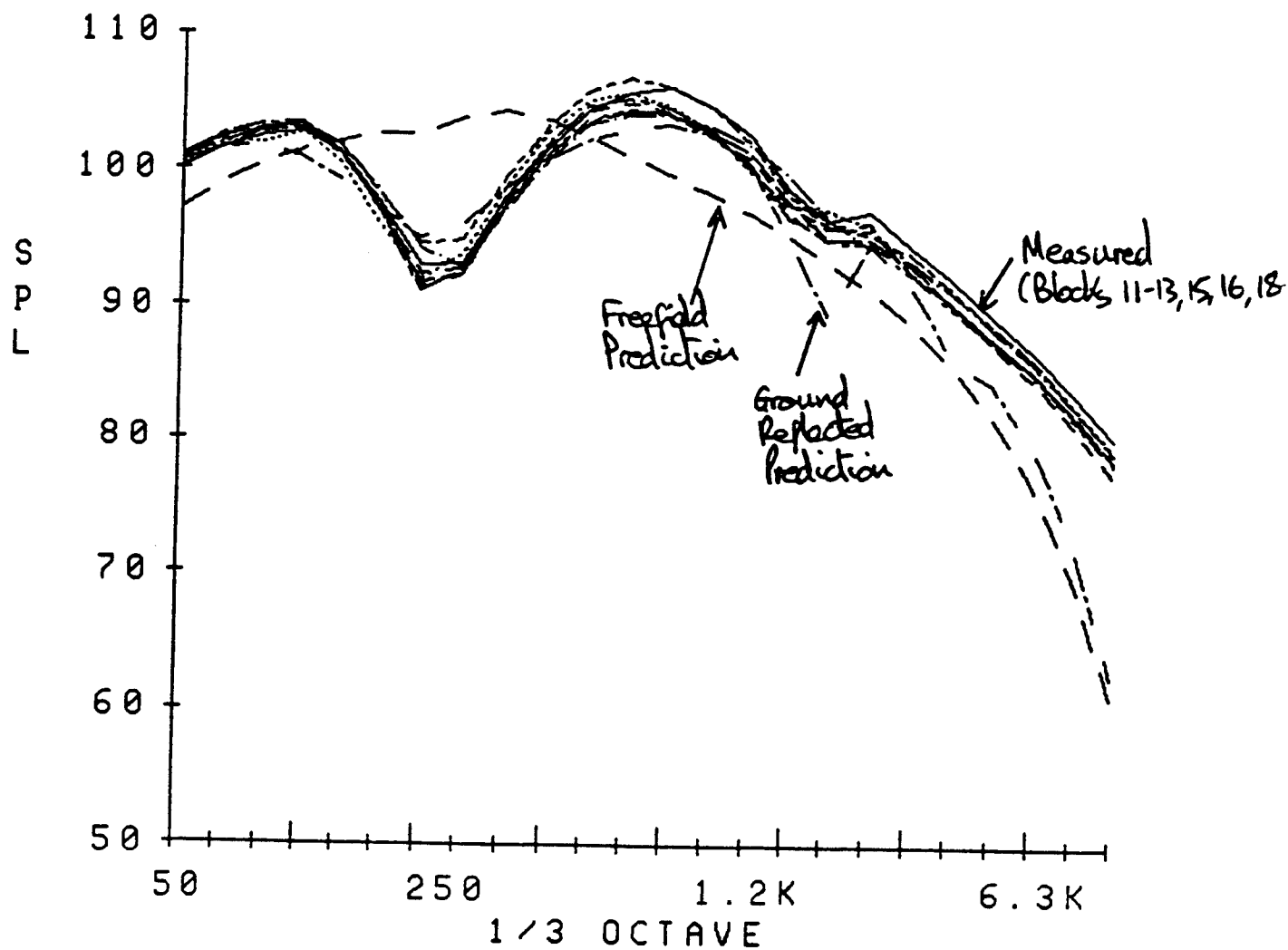


SIGMAe = 20000. ALPHA = 40.
Level differences Run 4117

Location B . High Microphone



Location H. High Microphone



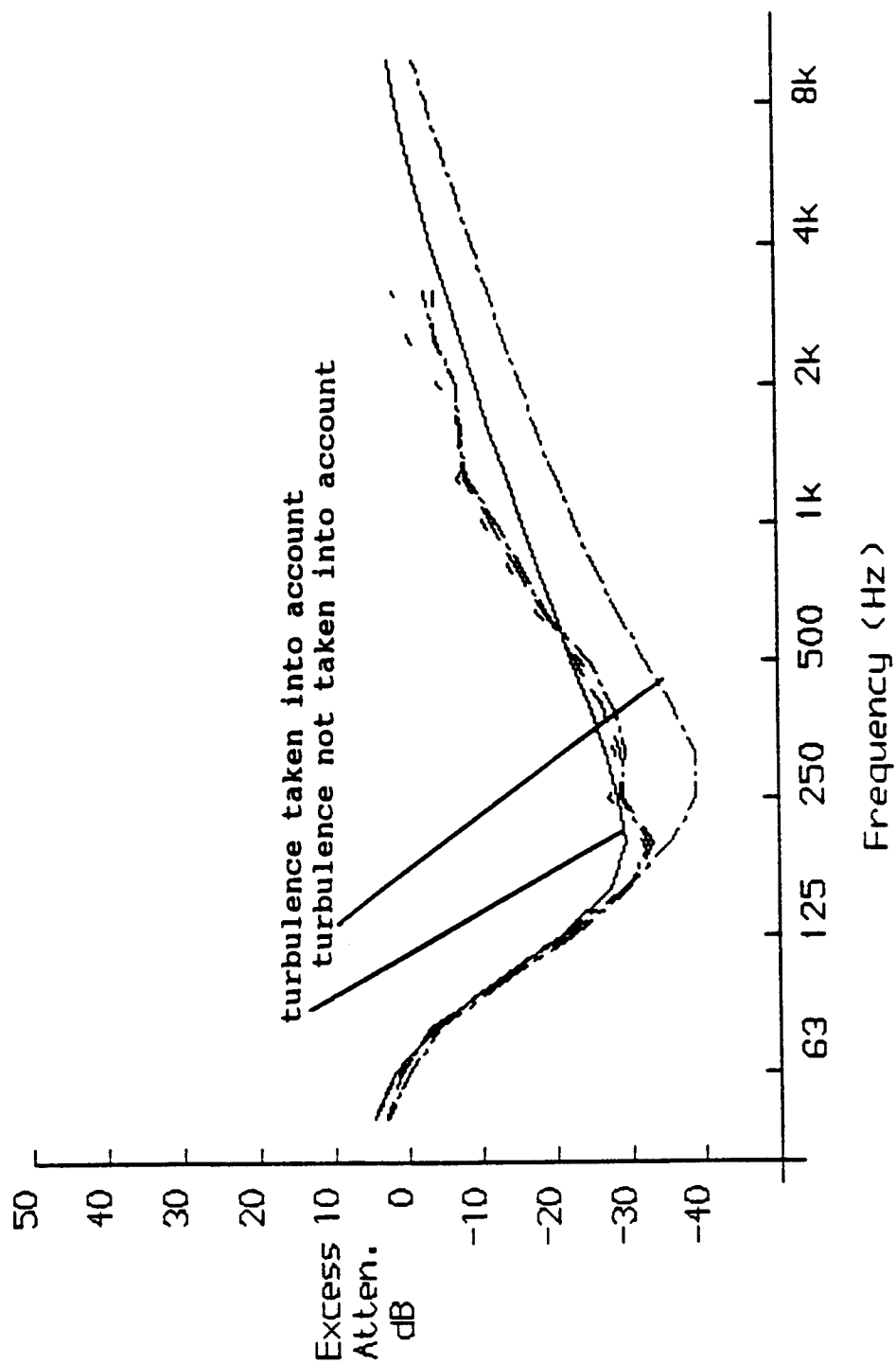
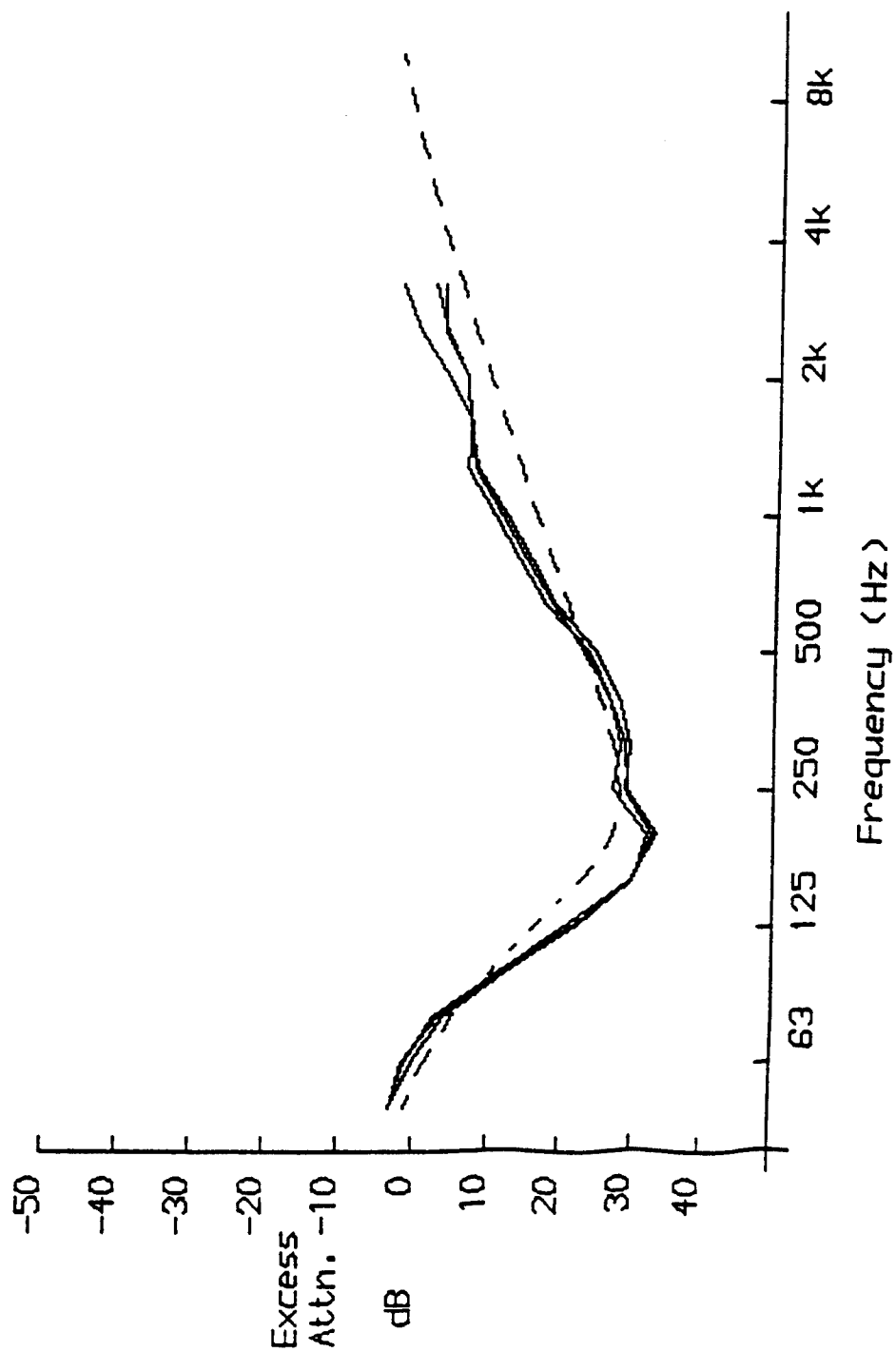
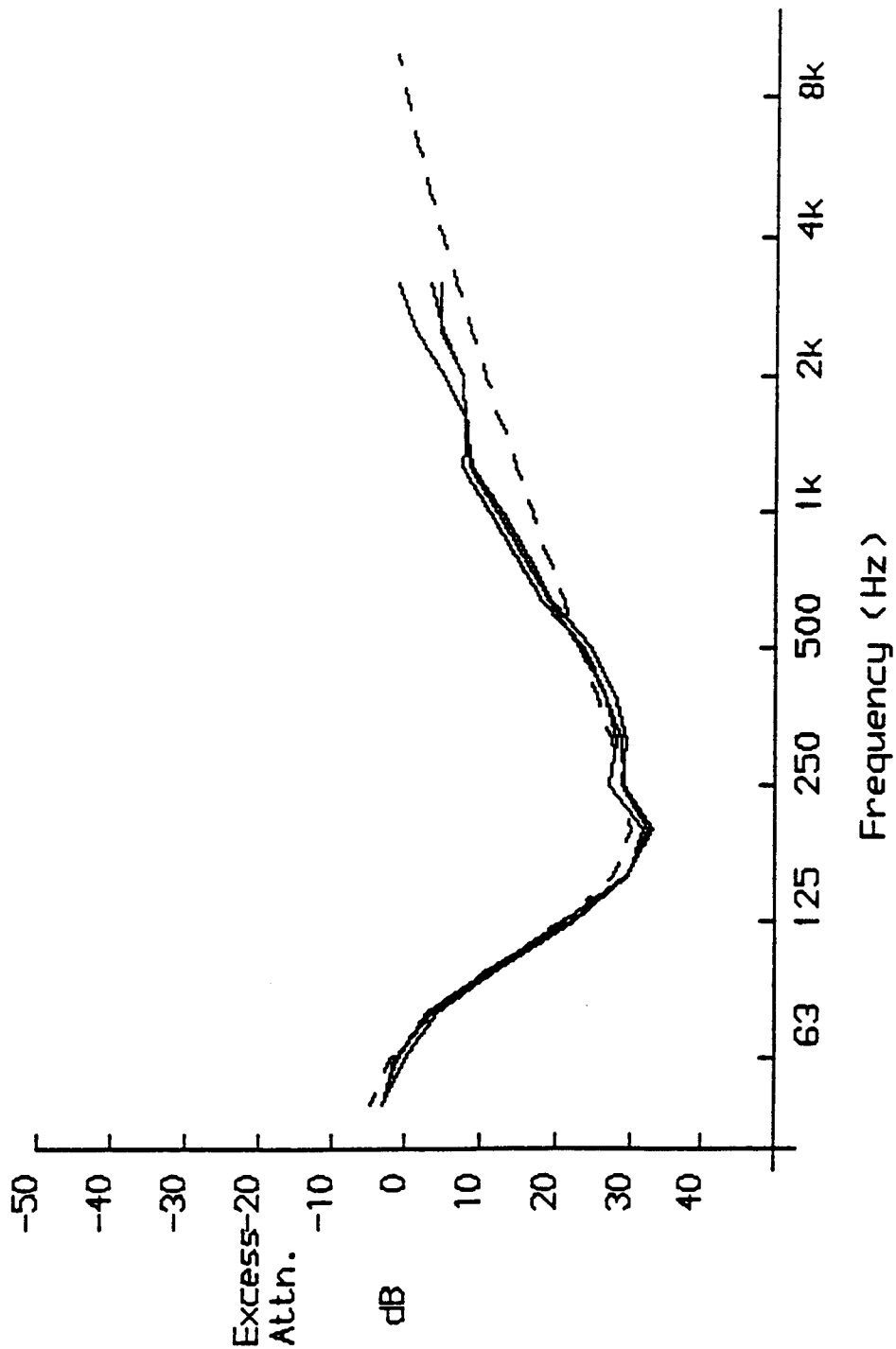


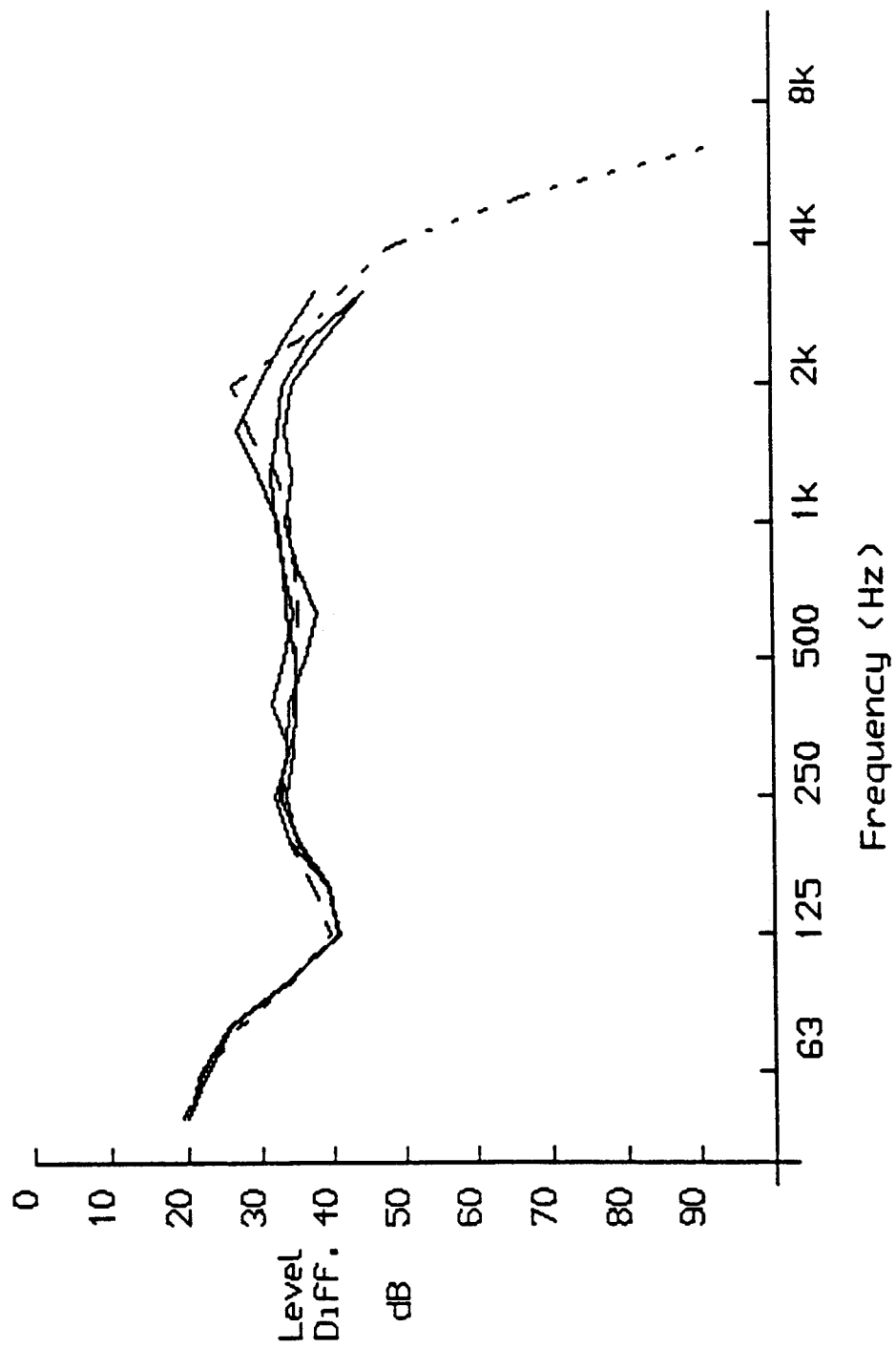
Figure 7 Excess attenuation at position K, low mic



EXCESS ATTENUATION AT POSITION K LOW MIC.
Figure .8(c) One parameter model



EXCESS ATTENUATION AT POSITION K LOW MIC.
 Figure - 8(b) Two parameter model



LEVEL DIFFERENCES AT POSITION KH MIC.
Run 454 Blocks 18-20 μ sq. = 8.5E-8

ACOUSTIC HELICOPTER CLASSIFICATION

Ton van Koersel, Martijn Miedema and Chris Nieuwenhuize,
TNO Physics and Electronics Laboratory,
PO Box 96864, 2509 JG The Hague, The Netherlands.
Email: A.Koersel@fel.tno.nl

Abstract

This presentation describes the results of a research project which has been funded by the Dutch Ministry of Defence, School of Military Intelligence. During the project "acoustic helicopter classification" a number of algorithms to classify helicopters were developed. A number of techniques have been refined, i.e. neural network, harmonic series and template matching. The algorithms are trained and tested on a database of 8 different helicopters (hovering and moving) recorded at distances ranging from 90m up to 8km (Measurement campaign AMI 1 and 2). To investigate the sensitivity to noise; jet, tank and artillery noise has been used as input. For target distances up to 2 km all algorithms perform well. At longer distances the performance decreases. Overall the neural network has the best performance. With a combination of the evaluated techniques the development of an operational system seems possible. Preferably however is the development of a demonstrator, which can be used to optimize the performance for different operational applications.

Future work will be carried out on the deterioration of the classification results under the influence of propagation effects and wind and environment noise. With an automatic measurement station data for a range of meteo parameters will be gathered. At a later stage helicopter data will be distorted by propagation effects and by measured noise, and subsequently fed to the classification algorithms. The results will give insight in the possible detection and classification ranges for an operational system.

1 Background

The research on detection and classification of airborne acoustic sources at TNO dates back to 1927. Under Van Soest a number of so called listening devices were tested for the Royal Dutch army. Most listening devices consist of a mechanical acoustic antenna of some shape. The antenna is linked to the ear of the human receiver by means of an acoustic waveguide, usually a rubber hose. One of the findings of the research was that the transmission of the sound from the receiving antenna through the waveguide seriously degraded the performance regarding the localization of the airborne targets. Therefore a new device was developed, which linked the ear of the receiver directly to the acoustic antenna, see Van Soest [1]. The elimination of the waveguide resulted in an improved localization ability of the Dutch system (named "Luistertoestel Groot") compared to the other systems.

Recently the work on acoustic detection and classification has been resumed, with the intent to develop algorithms to classify different helicopter types automatically.

For the development and the testing of the algorithms data collected during the AMI 1 (Schweinfurt, Germany, 1987) and AMI 2 (Dreux, France, 1988) measurement campaign has been used. From the large amount of data available a set of helicopter data of approximately 250 Mb has been digitized. The digitized data consists of sets with a duration of 32 seconds, from a triangular array of three microphones and three geophones. The digitized dataset contains:

- Single helicopter data of 8 different helicopter types, recorded at a distance of 90 m up to 8 km.
- Multiple helicopter data, at ranges from 1 km to 4 km, in hover positions as well as approaching the recording position.
- Jet aircraft overhead flights.
- Tracked vehicle and simulated artillery noise (propane gun and explosives).
- Simulated white noise.

During the measurements wind and other meteo conditions were recorded as well. An overview of the helicopter measurement points in relation to the recording position is given in figure 1.

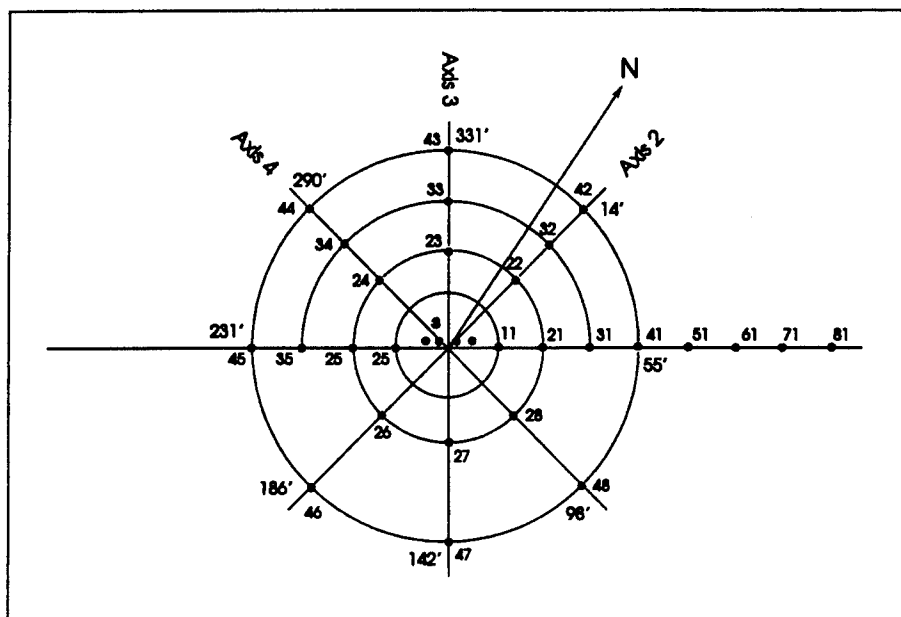


Figure 1 Overview of Dreux helicopter measurement positions. The TNO measurement position is near the centre of the circle.

3

Classification Algorithms

In this section an outline of the three classification techniques is given. The preprocessing of the acoustic signals is described in section 4.

3.1

Artificial Neural Network

A general description of artificial neural networks and a good overview of the present state of affairs is given by Hush and Horne [2]. Since it has been shown by Hornik [3] that a three layer

network is sufficient to perform any segmentation of a dataset, we started using a three layer feed forward network with sigmoid neurons. The network is trained (or: the weights are determined) with the backpropagation procedure using gradient descent, see Rummelhart [4]. Initial research on three helicopter types has shown that the simple three layer feedforward network performs well (although i.e. Cabell et al [5] use a four layer network). The number of nodes in the so called hidden layer determines the performance. In our case we use the (preprocessed) logarithmic power spectrum as input. The number of output nodes is equal to the number of helicopter types in the dataset. Experiments have been carried out with eight types and with three types. The experiments with three types are focussed on training the network with signals containing real and artificial Doppler shift as well as hover signals. To prevent false classifications, the type identification from the output layer of the network is performed using an upper and a lower threshold. If the highest output node is below the upper threshold, the pattern is rejected. If the other output nodes are above the lower threshold, the pattern is rejected as well. Only if the highest output node (i.e. node 1) is above the upper threshold and the other nodes are below the lower threshold, the input pattern is classified as type 1. The procedure using the upper and lower threshold is illustrated in figure 2. Finally, the results are improved by averaging the power spectra and by using a majority vote between several input patterns.

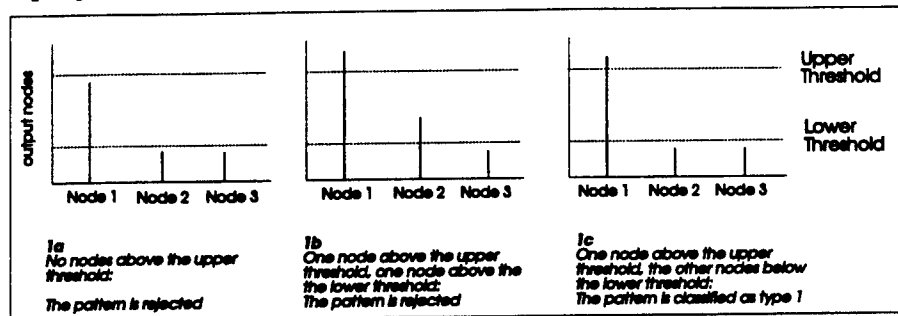


Figure 2 Classification with network output nodes and an upper and a lower threshold. Of three possible situations the value of the output nodes relative to the thresholds are given.

3.2 Harmonic series

The algorithm finds harmonic series in the (preprocessed) logarithmic power spectrum. First an estimation of the noise is made. Next peaks above the noise are identified, from which possible harmonic series are determined. The peaks and harmonic series found are divided into two sets. One set in the region where main rotor frequencies are to be expected, the other set outside that region. This is the start of the identification procedure, using 4 categories.

- 1 One or more series in the main rotor region, and one or more series outside the main rotor region are found. The main/tail rotor ratio is determined for all possible combinations, and compared to a table of known ratios. If one ratio found fits the table, the input is classified as that type. If more ratios fit the table, the one with the highest power in the tail series is classified. If no ratio fits the table, category 2 applies.
- 2 One or more series in the main rotor region, and one or more series outside the main rotor region are found. The main/tail rotor ratio is determined, and no ratio fits the table. For the possible main rotor series a search procedure for a tail rotor peak in specific

harmonic intervals is started. The intervals are based on the main series ground frequency and the table of known ratios. If no classification occurs, the input pattern is rejected.

- 3 Only one harmonic series in the main rotor interval is found, and no series outside this interval. The same procedure as in category 2 is started, leading to classification or rejection of the input pattern.
- 4 No harmonic series in the main rotor region are found. The procedure of category two is started, using single peaks which are identified above the noise in the main rotor region. This leads to either classification or rejection of the input pattern.

3.3 Template Matching

Originally template matching uses a database of known frequencies for each type to be classified. Classification is performed by comparing the power in a window around the known frequencies. For helicopter signals the harmonic properties of the signal are used. The power for type i is determined by:

$$P_i = \left\{ \sum_{n=1}^k W(f - nf_{m,i}) + \sum_{n=1}^k W(f - nf_{t,i}) \right\} \bullet S(f) \quad (1)$$

W is a small symmetric window, and f_m and f_t are the main and tail rotor frequency of the known types in the database. The term between brackets is the template, and the inner product of the template and the spectrum yields the power in the template. The disadvantage of this approach is the inability to cope with Doppler shifted signals.

Therefore a different approach has been chosen. To find harmonic series in the region where the main rotor BPF is expected, a series comb filters is used. For each comb filter the inner product between the filter and the spectrum is determined. The procedure is illustrated in figure 3. In the output of the combfilters maxima are identified. The "exact" frequency of those maxima is determined using an interpolation method according to Parker and Stoneman [6]. Using the frequencies found and the main/tail rotor ratio from a database, templates for possible tailrotor frequencies are determined. For the calculation of the power for each type in the database, formula 1 is applied with the tailrotor contribution only.

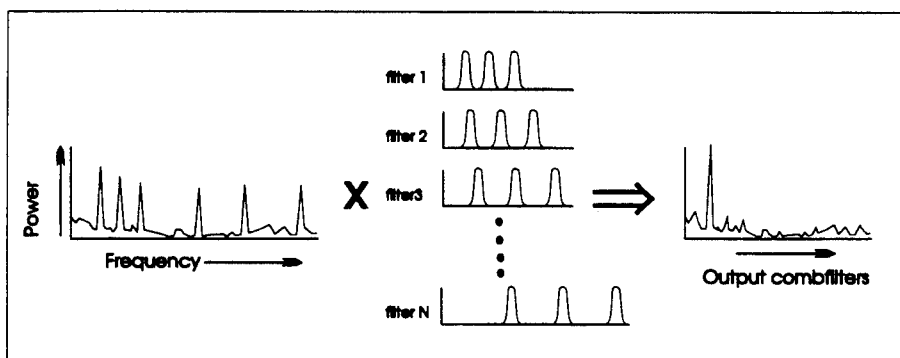


Figure 3 The comb filter procedure

The signal from the microphones and geophones is recorded on an analog multi-channel recorder using a high-pass filter. The signal is played back and sampled, using an anti aliasing filter. The signals are stored on disk in blocks of 32 second segments for six sensors. From the sampled signal the power spectrum is calculated using a Hanning window and a FFT routine. After averaging the power spectrum over a number of seconds the logarithmic spectrum is calculated. The low frequency trend in the log spectrum is removed by applying a high pass FIR filter (Rabiner et al [7]) on the log spectrum. The resulting "whitened" spectrum is used as input for the harmonic series and the template matching algorithm. The preprocessing of the acoustic and seismic signals is illustrated in figure 4.

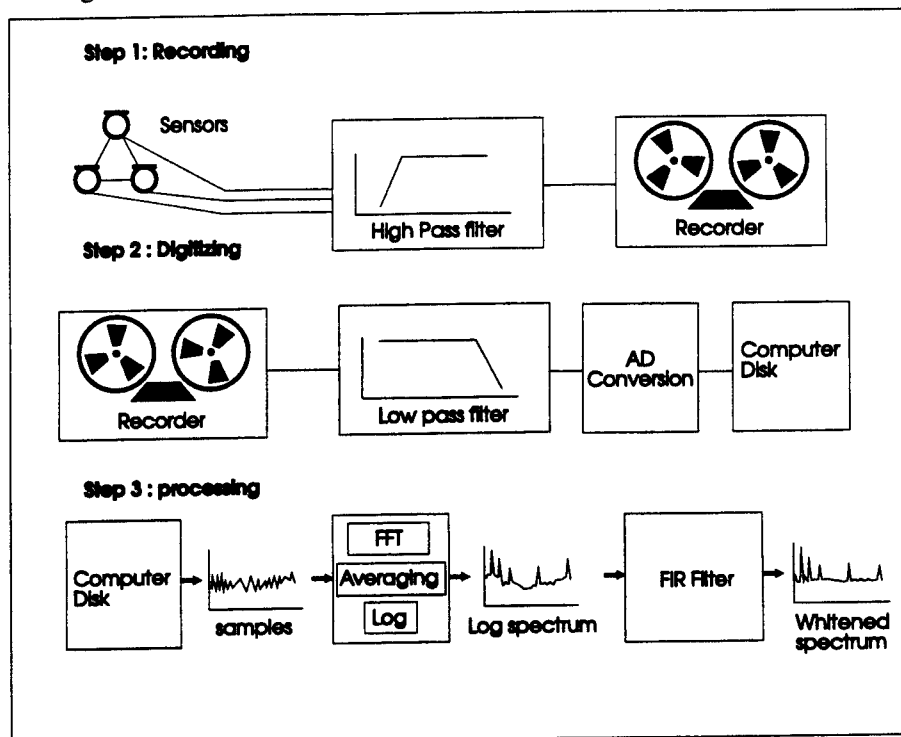


Figure 4 Illustration of the preprocessing of the acoustic data.

Using the dataset described in section 2, experiments to evaluate the developed algorithms have been performed. The initial dataset is divided in learning sets and test sets.

5.1 8 types

A neural network with eight output nodes has been trained with hover data, for different values of the upper and lower threshold. After the training procedure the optimum upper and lower threshold have been chosen to reject noise. The harmonic series and template matching algorithms have been optimized on a small training set. Both algorithms use parameter values that determine the classification procedures (i.e. number of averages, shape of the combfilter,

template width etc.). The performance on a testset of eight types containing hover signals is comparable regarding the number of correct classifications for all three algorithms.

If noise is supplied as input pattern, the neural network has superior performance. The basic difference with the neural network for eight types is that both the harmonic series and template matching algorithms can cope with Doppler shifted signals. The neural network for eight types fails for those signals. Therefore experiments with a learningset with real and artificial Doppler shift have been performed.

5.2 3 types

If classification of Doppler shifted signals is attempted using a neural network, those signals have to be part of the learning set. The network can only "interpolate" or distinguish between patterns that have been part of the learning set. Signals with different Doppler shift were available only for three types. A network with three outputnodes has been trained with data with real Doppler shift, and with data with simulated Doppler shift. After optimization regarding the rejection of noise, a testset with hover and Doppler shifted data has been evaluated. The results were not very good, but still significantly better than random guessing.

6 Future Plans

6.1 Classification

Regarding the classification problem, the neural network seems to have a large potential. The main drawback of the approach in the performed experiments is the rejection of noise. If algorithms are to reject noise correctly, their classification performance decreases. A relatively simple classification algorithm between "possible helicopter" and noise will have a positive impact on the performance. Another possibility is to use a similar approach as Sabourin and Mitchie [8] in the field of character recognition. For helicopter classification this would lead to a classification algorithm comprising:

- an initial network to classify helicopters in groups that have a close main rotor frequency
- smaller networks to determine the type within the chosen group.

Such a network can be combined with the other algorithms, i.e using a weighted majority vote between the classifier outputs.

6.2 Environmental Influence

In the near future we plan to estimate the influence of wind noise, meteo conditions and propagation on the classification results.

For the influence of wind noise we are developing an automatic measurement station to gather acoustic and seismic data for different categories of wind speed and rms deviation of the wind speed. These are the main factors determining the generation of wind noise at the microphone (Morgan and Raspet [9]). Later, the wind noise data will be added to helicopter data recorded at close range to estimate the impact on the classifier performance.

Acknowledgment

The research concerning the helicopter classification has been carried out under the guidance of Lcol. H.H. Slots and Lcol. W.G.F. van Kempen of the Dutch School of Military Intelligence. The work on neural networks has been mainly performed by Chris Nieuwenhuize, the work on harmonic series by Martijn Miedema and Frits Willems. Furthermore, Huub van Hoof has provided valuable input during the various stages of the research project.

References

- [1] J.L. van Soest, *Speurwerk, van luistertoestel tot radar*, Overdruk voordrachten no. 1, 1949, Kivi, NL.
- [2] D.R. Hush and B.G. Horne, Progress in supervised neural networks, *IEEE Signal Processing Magazine*, jan 1993, pp. 8-39.
- [3] K. Hornik, M. Stinchcombe and H. White, Multilayer feedforward networks are universal approximators, *Neural Networks* (2), 1989, pp. 359-366.
- [4] D.E. Rumelhart, G.E. Hinton and R.J. Williams, Learning perceptrons by backpropagating the errors, *Nature* (323), 1986, pp. 533-536.
- [5] R.H. Cabell, C.R. Fuller and W.F O'Brien, Identification of Helicopter Noise Using a Neural Network, *AIAA Journal* 30(3), mrt 1992.
- [6] R. Parker and J.A.T. Stoneman, "on the use of fast fourier transforms when high frequency resolution is required", *J sound vibr.*, (1986) 104(1), pp.75 - 79.
- [7] L.R. Rabiner and C.A. McGonegal, FIR Windowed Filter Design Program WINDOW, In *IEEE Programs for digital signal processing*, John Wiley & sons, New York, 1979.
- [8] M. Sabourin, A. Mitiche, Optical Character Recognition by a Neural Network, *Neural Networks*, Vol. 5 pp. 843-852, 1992
- [9] S. Morgan and R Raspel, Investigation of the mechanisms of low frequency wind noise generation outdoors, *J. Acoust. Soc. Am.* 92 (2), p 1180-1183.

ACOUSTIC CHARACTERIZATION OF RICOCHETS

by Huub van Hoof

TNO Physics and Electronics Laboratory,
PO Box 96864, 2509 JG The Hague, The Netherlands.

1. Abstract

Research carried out by: J. van der Haven, H.A. van Hoof, H.C.A. Romijn, M.G.A. Ruizenaar

This presentation describes the activities which have been carried out within the scope of a task appointed by the Ministry of Defence, Dienst Gebouwen Werken & Terreinen. Projectiles fired at a firing range will sometimes undesirably fly over the present bulletstop after hitting the ground surface. The task was to identify these stray bullets at a specific firing range. First the most suitable method has been determined. A pre-investigation showed that determination of different characteristics, related to the projectile's trajectory, might be feasible by analysis of the acoustic signals. Therefore it was decided to install an array of microphones at the end of the firing range and to record the data during shooting exercises. The data collection campaigns have been carried out on various days. This presentation gives more details about the acoustic model used and examples are shown which compares the model with real data.

2. Background

To keep soldiers well experienced they have to practice in shooting exercises. For this purpose there are a number of firing ranges in the Netherlands. For reasons well understood, these areas are kept as far as possible from the urban areas. One of these ranges is in a part of Holland where it borders on an ecologically sensitive area, the so called Dutch Shallows. These shallows fall dry with the tides and are very rich on food (snails etc). A huge number of birds are foraging here during their migration. Stray bullets which might fall into these shallows, might cause chemical pollution in this area. To prevent this to happen as good as possible, a number of measures was already taken.

In figure 1 (not on scale) the problem has been illustrated. The elevation angle (of the gun) and the angle of incidence are very small so there is a reasonable chance that projectiles will glance off and will follow a new and unpredictable trajectory. Some of these projectiles might pass the bulletstop and the sea dike which is pretty close behind the bullet stop.

Illustration:

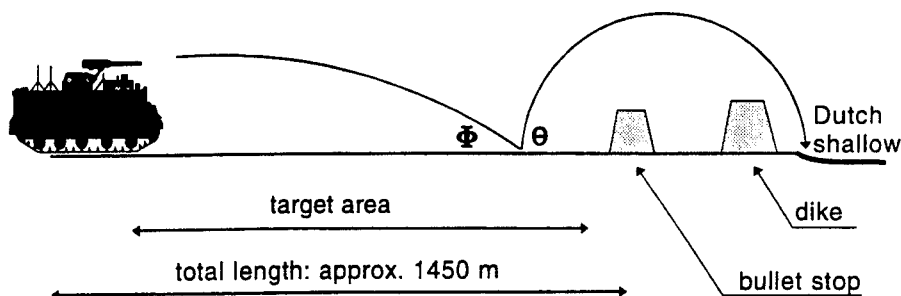


Figure 1 *Illustration of the problem.*

To get a better information about the real number of projectiles falling into the area, the Ministry of Defence, Dienst Gebouwen Werken & Terreinen, asked to develop tools to measure it.

Most currently 25 mm calibre ammunition is being used which has a muzzle velocity of approximately 1300 m/s. If the target is missed and the projectile is not stopped (e.g. by hitting the bullet stop) the velocity at the end of the shooting range is in the order of 500 m/s (after roughly 1.5 sec).

To determine whether or not the projectile is crossing the dike, various options were considered, such as the application of radar, cameras perpendicular to the vertical plane of fire, all having their specific advantages and disadvantages. Finally it was decided to find a way to solve the problem acoustically.

3. The acoustic approach

Close to the dike an array of 10 microphones has been deployed, all microphones separated 200 meter from each other. In figure 2 the sensor-configuration has been shown.

CONFIGURATION & INSTRUMENTATION

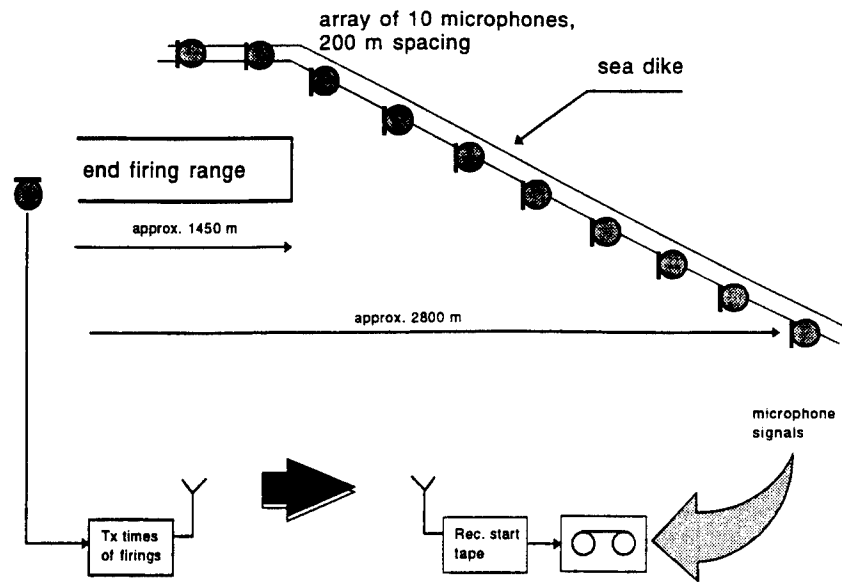


Figure 2 Sensor configuration for acoustic data acquisition.

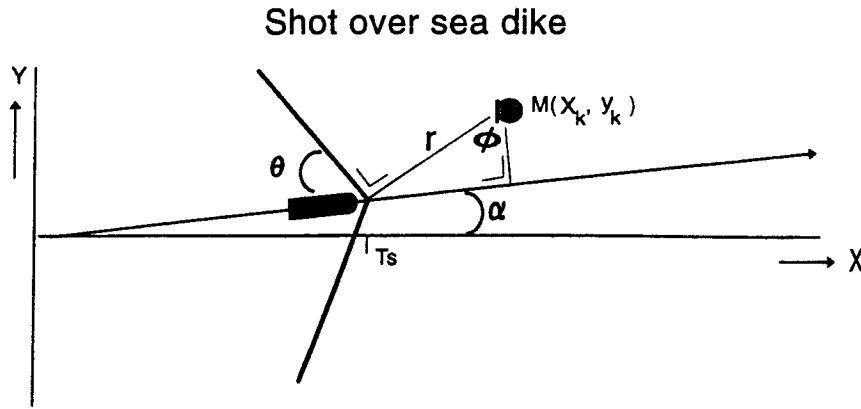
All microphone signals were stored on analog tape. Because during the exercises nobody was allowed to remain in the area, the taperecorder had to be started remotely. This starting was initiated automatically by an impulse derived from the muzzle blast at the moment the gun went off; a trigger signal was then transmitted radiographically to start the tape recorder. As there were 4 guns, there were 4 muzzle blast sensors. In addition information about the shots was logged, such as the target number the gunner is shooting at, etc. (there are targets all over the terrain). The data collected at the firing range were then analysed at the office afterwards.

The main classes of trajectories to be recognized, were those of projectiles which:

- (1): slightly touch the soil and then cross the sea dike (with hardly loss of projectile's speed)
- (2): hit the target or bullet stop and clearly remain at the firing range
- (3): clearly touch the soil and then cross the sea dike (with significant loss of projectile's speed)

4. Acoustic characterization

Let us first assume a projectile slightly touching the ground, glancing off and then crossing the sea dike with only a small loss of its kinetic energy. This kind of a trajectory is almost equivalent with the trajectory the projectile would follow if the shot would have been fired intentionally directly over the sea dike (with no loss of kinetic energy due to the ground touch). As the shockwave propagates perpendicularly to the shockwave front, the shockwave a microphone will receive, comes from a point at the trajectory where the wave front is perpendicular to the microphone direction, or where φ equals θ , see figure 3.



For $M > 1$:

- * shockwave propagates perpendicular to shockwave front
- * microphone receives the shockwave from a source point, attained after T_s sec.
- * T_s can be calculated from the condition: $\theta(T_s) = \phi(T_s)$

$$\tan \theta = 1 / \sqrt{M(t)^2 - 1}$$

$$\tan \phi = [X_k / \cos \alpha + (Y_k - X_k \tan \alpha) \sin \alpha - s(t)] / (Y_k \cos \alpha - X_k \sin \alpha)$$

Figure 3 Geometry for calculations.

This point is called the source point and the projectile has reached that point after T_s seconds. The angle θ is a function of time due to the diminishing speed, the angle ϕ can be expressed as a function of the projectile position $s(t)$, the trajectory azimuth α and the microphone coordinates (X_k, Y_k) .

If the projectile is not stopped by the target or by the bullet stop, it will somewhere get a speed lower than the speed of sound ($M < 1$). In that case Toa is given by "Toa = time the projectile need to reach the point where $M=1$, plus the time the wave needs to hit the microphone with the normal speed of sound".

The times of arrival of the shockwave have been calculated for these type of firings, using a simple model and assuming no loss of kinetic energy due to the ground touch. First the source point was calculated, the times of arrival then simply were obtained by " $Toa = T_s + r/c$ ".

The picture in figure 4 shows the 10 microphone signals, recorded for a shot as discussed in this paragraph. The signal at the end of each trace represents the muzzle blast of the gun. A few small spikes in the signal are due to cross talk components which sometimes occurred if the signal amplitude was very large. To verify the model, the measured times of arrival were compared with the calculated ones.

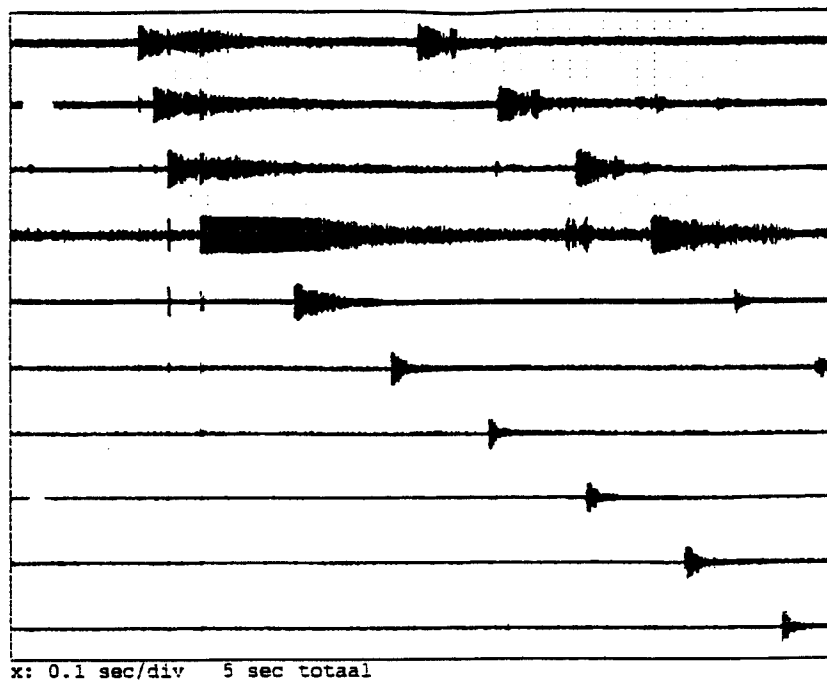


Figure 4 *Example of the acoustic response of a shot.*

In figure 5 the measured times of arrival of figure 4 have been plotted while in addition the calculated times for this shot are shown: the similarity is reasonable.

Choosing small changes in the azimuth angle may give even a better fit.

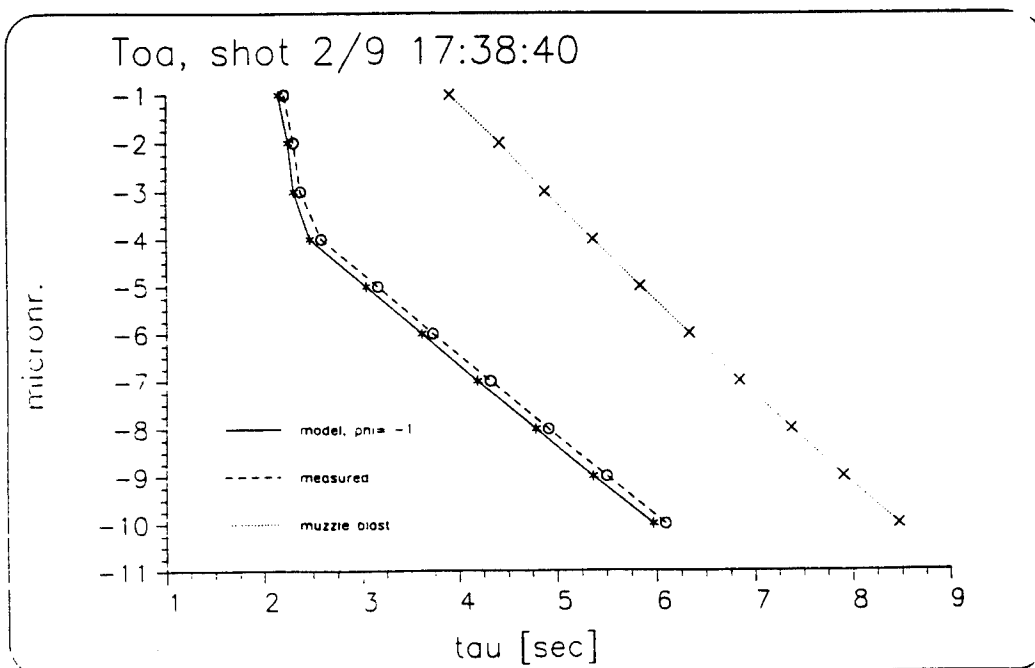


Figure 5 *Measured and calculated times of arrival.*

Figure 6 shows the results for another shot. In most cases a reasonable fit between measured data and the model is very well possible. The steep gradient of the curve up to the first 3 or 4 microphones is a very characteristic feature that all those shots have in common; this feature could be used for the identification of this type of projectile trajectories.

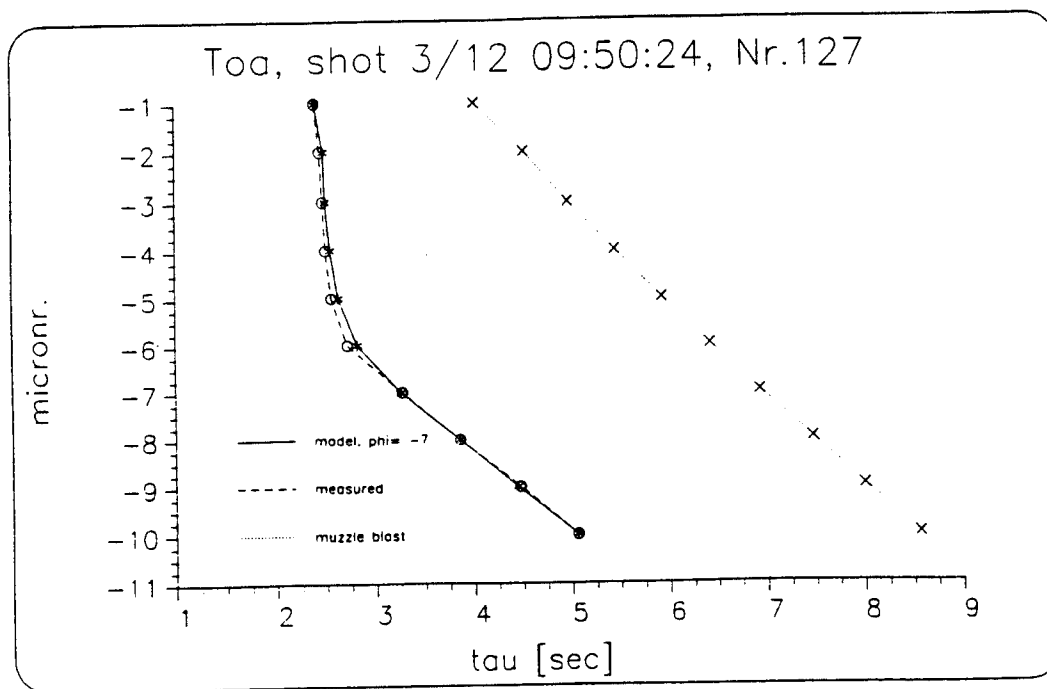
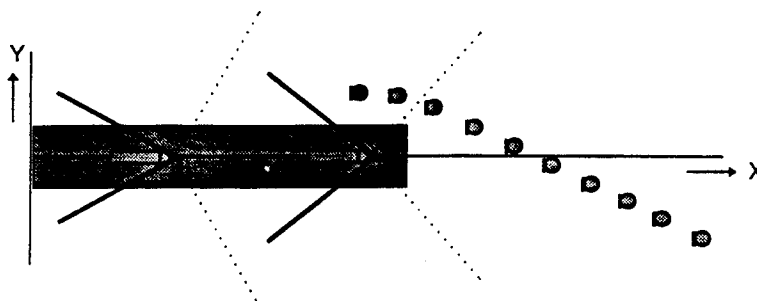


Figure 6 Another example of measured and calculated times of arrival.

Now what happens if the projectile hits the target or ends in the soil or the bullet stop ? In that case it can easily be calculated that only the first 2 or 3 microphones will detect the shockwave because all other microphones will remain out of the Mach area, which is illustrated in figure 7.

MACH AREA



If projectile hits the target or goes right into bulletstop, only the first 2 (3) microphones are in Mach area

Figure 7 Only 2 sensors in the Mach area.

Figure 8 illustrates the signals recorded for such a shot; only the first two channels show a response.

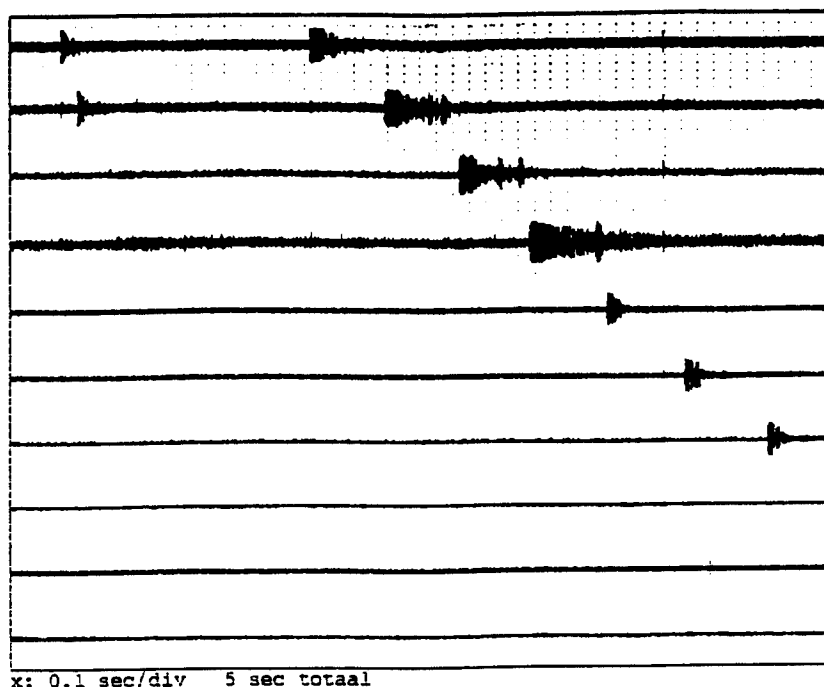


Figure 8 *Acoustic response of a shot where the projectile hits the bullet stop.*

How do the signals look like if the projectile behaves as a ricochet ? Figure 9 shows the signals, of a ricochet.

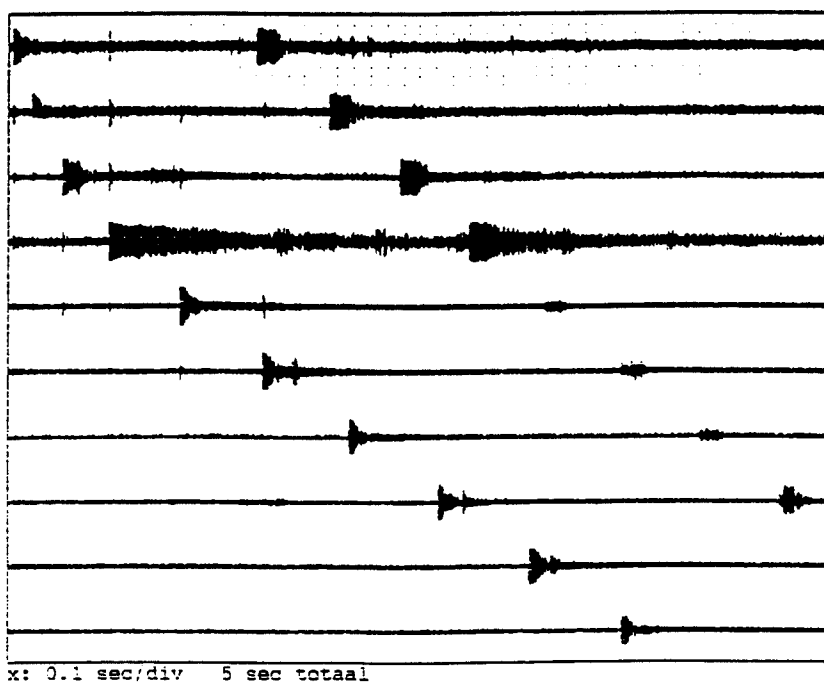


Figure 9 *Acoustic signals of a ricochet.*

Again the times of arrival have been plotted (figure 10).

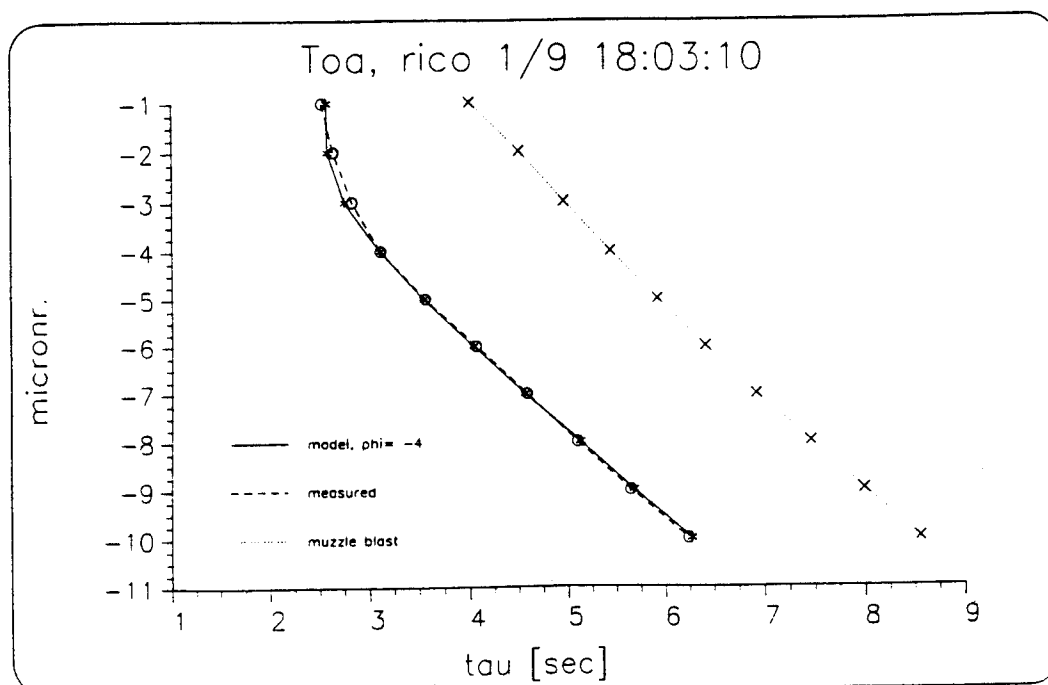


Figure 10 Measured and calculated times of arrival of the.

The plot of figure 10 gives the measured times of arrival of the signals, shown in fig. 9 and the calculated ones. The model, previously described, was changed a little bit for this purpose.

An arbitrary point of time at which the bullet is assumed to hit the ground surface, has been entered in the model. Secondly, a rather arbitrary factor, less than one, has been introduced which simulates the loss of the bullet's velocity from that point of time.

In figure 10, a time of 1.1 seconds was chosen as the moment the projectile touched the ground, and a factor of 0.6 to describe the decrease of velocity.

Also other evident ricochets could be fitted in this way.

5. Conclusions

The characteristic curves of the times of arrival could be used to discriminate between various trajectories of the projectiles. Comparison of the results of simple models with a number of controlled firings (and which could clearly recorded on video) gave the evidence for a reliable discrimination.

References

- [1] A.D. Pierce, Acoustics, An introduction to its Physical principles and Applications, Acoustical Society of America, Woodbury, New York, 1989.

Acoustical Characteristics of the Mother of All Speakers

James M. Sabatier

ABSTRACT

The University of Mississippi designed and built a low frequency, high intensity, portable loudspeaker for the U.S. Army Battlefield Environmental Directorate. The system was modified to accommodate an upward projecting acoustic horn which could be moved at speeds of a few tens of miles per hour. The measured acoustic output as a function of critical system parameters, pneumatic gas pressure, voice-coil current and frequency is described. These results establish optimal performance values for these parameters. Radiation patterns and efficiency of the acoustic horns positioned above a finite ground impedance are theoretically described and compared to measured data.

I. INTRODUCTION

A pneumatic loudspeaker system has been designed¹ which is capable of producing high intensity, low frequency sound. Acoustic levels of 156 dB (re 20 μ Pa, 1m) have been measured. The system consists of five major components: the acoustic horn, air-stream modulator, air-supply and cooling system, system controller, and transportation and operation platform.

Two acoustic horns were constructed. One is a true 10 Hz exponential horn which is 17.1 meters (56 feet) long and has a mouth diameter of 2.3 meters (92 inches). The second is a smaller 25 Hz horn with a 90° bend, 6.6 meters (21.7 feet) long with a 2.1 meters (6.9 feet) mouth diameter.

The air-stream modulator (WAS-3000) is a commercially available pneumatic valve which was modified to provide alternative cooling.² The air-supply and cooling system consists of a rotary lobe blower driven by a 150 horsepower (115 KW) diesel engine and an air-to-air heat exchanger with a cooling capacity of 2000 BTU/hr (.6 KW).

The platform which supports and provides a means for transporting the loudspeaker system is a telescoping semi-trailer. In the transportation mode, the trailer length is 13.7 m (45 ft) long, and 19.8 m (65 ft) in the operational mode. The trailer length in the transportation mode is completely legal on all U.S. highways, bridges, and overpasses, and no permits are required. A previous report describes procedures for positioning and removal of each horn.³

Due to the intense sound levels at the source, a remote radio frequency communication network is used to handle communication between the operator and pneumatic speaker. This system consists of a transceiver, a terminal node controller, and a small personal computer. Acoustic signals can be broadcast from the horn by remotely starting a control program on the computer.

Here we describe the acoustic performance of MOAS. Section II discusses the measurement geometry, receiving microphones, broadcast signals, and recording instrumentation. An important physical limitation of the WAS-3000 voice coil, the full-modulation current, is measured.

Section III reports typical time and frequency domain acoustic signals and discusses optimal gas pressure and voice coil current.

Section IV is the theoretical section which compares the radiation pattern of a piston in a tube above a finite ground impedance to the measured directivity pattern of the 25 Hz horn.

II. EXPERIMENTAL MEASUREMENTS

In this section, we determine the full-modulation voice coil current of the WAS-3000 as well as the experimental set-up, choice of electrical signals, gas pressure, voice coil current and data recording instrumentation to acoustically characterize MOAS.

1. Description of the measurement site

Measurements were calculated at the DIRT Site. The ground surface at this site had been characterized by probe microphone and acoustic level difference measurements.⁴ Measurements of the d.c. flow resistivity, porosity, grain size, compressional and shear wave speeds, density and layer depths have also been documented in Reference 4. The terrain near the sound source was generally flat but covered with desert type grasses and bushes.

2. Microphone location and types

Because of the different orientations of the mouths of the 10 and 25 Hz horns relative to the ground, different measurement geometries were used to characterize their acoustic outputs. The axis of the 10 Hz horn is horizontal. Microphones (B&K 4165) were positioned at 4.6 meters, 76 meters, and 137 meters from the horn mouth. The two distant microphones were 0.5 meters above the ground; the closest microphone was positioned at the horns axis 2.7 meters above the ground. All three microphones were set up along a compacted road that runs the length of the DIRT Site. The 4.6 meter microphone was used in measurements to determine the full modulation current described in Section II.5.

The mouth of the 25 Hz horn points upwards, away from the ground surface. To characterize this horn, two 30 meter towers were erected 75 meters apart. Microphones were positioned on these towers and between them such that microphones were located at 15 degree intervals from the normal of the horn mouth. The microphone directly overhead was 27 meters from the horn mouth. This array was used to determine radiation patterns for the 25 Hz horn discussed in Section IV.3 and shown in Figure IV.4 a,b.

3. Broadcast signal characteristics

We chose to characterize the frequency dependent acoustic output of the horns using tones at standard one-third octave spacings between 12.5 and 500 Hz. Additionally, band limited periodic noise between 10 and 500 Hz was used.

Since the acoustic output of the pneumatic speaker is dependent upon pneumatic gas pressure, this pressure was varied between 20 and 55 kPa (3 and 8 psig). The voice coil current which also effects acoustic output was varied between 3 and 10 Amperes.

4. Microphone signal recording instruments

The acoustic data was recorded on several different instruments. A Hewlett Packard 35662A two-channel spectrum analyzer was used to provide the real-time power spectrum. For each voice coil current, pneumatic gas pressure, and one-third octave tone the Fourier spectrum was stored on disk. Typically, ten averages were recorded. Additionally, a Sony PC204 four-channel DAT recorder was used to provide continuous back-up of all data. When the 25 Hz horn was positioned between the 30 meter towers, a 16 Channel Teac DAT recorder was used to record microphone data. Before and after each run (typically every two hours) microphone calibration tones (94 dB at 1000 Hz) were recorded on each microphone.

5. Full modulation current

It was first desired to determine the electrical current required to fully open or close the modulation slots in the WAS-3000. Maximum acoustic output will occur at maximum modulation of the slots. Electrical current beyond that required for full closure of the slots will not produce any more acoustic energy in the fundamental tone being broadcast. To make this measurement, a tone was broadcast and the Fourier spectrum of the microphone signal monitored as the voice coil current was increased. Table II.1 shows the amplitude of the fundamental tone and the second harmonic as the voice coil current was increased for select frequencies between 12 and 100 Hz. The pneumatic gas pressure was 55 kPa (8 psig) for this measurement.

Table II.1

Amplitudes of first two harmonics for tonal input as a function of voice coil current at 55 kPa (8 psig) for 12, 25, 90, and 100 Hz.

RELATIVE SPL (dB)									
Frequency	Current (A)	3	4	5	6	7	8	9	10
100 Hz	SPL	-3.1	3.3	6.6	8.2	8.3	8.1		
200 Hz	SPL	-19.9	-5.9	1.2	3.8	4.1	4.1		
	Current (A)	3	4	5	6	7	8	9	10
50 Hz	SPL		2.7		5.6	6.7	6.3		
100 Hz	SPL		-13.0		-6.3	-3.5	-1.2		
	Current (A)	3	4	5	6	7	8	9	10
25 Hz	SPL	-4.1		2.4		5.6	6.7	7.5	6.0
50 Hz	SPL	-31.0		-15.6		-7.8	-4.8	-2.7	-6
	Current (A)	3	4	5	6	7	8	9	10
12 Hz	SPL	-10.7		-5.6		-2.6	-1.2	-.07	0.2
24 Hz	SPL	-27.7		-16.5		-9.6	-6.1	-4.8	-2.9

At the lowest frequency, 12 Hz, the amplitude of the fundamental increases from -10.7 dB at 3 Amperes up to the highest current level of 10 Amperes. This is not the case for all other frequencies. In these cases the amplitude generally stops increasing for current levels higher than 7 Amperes and over 6 Amperes for the 100 Hz tone.

The non-linearity in the horn can be observed in the amplitude of the second harmonic. At the lowest current level, 3 Amperes, the second harmonic is 17 to 27 dB below the fundamental for the four frequencies broadcast. At all frequencies, the second harmonic increases much faster than the fundamental with increases in current. At 55 kPa (8 psig), minimum harmonic distribution occurs at current levels of 3 Amperes. To achieve maximum energy in a tone, voice coil current levels of 7 Amperes are adequate. This value is below that needed to fully close the air-slots in the modulator.⁵ Current levels above 7 Amperes only put energy in higher harmonics through non-linearities in the horn.

III. TONAL AND NOISE DATA ANALYSIS

The effort to determine the full modulation current in Section II indicates the non-linearity in MOAS. In this section, time and frequency data are used to indicate efficient operating pressures and currents. Choices of voice coil current and gas pressure affect the temperature of the voice coil, the degree of non-linearity and the acoustic output of MOAS. The frequency response of the horns for broadband noise and one-third octave spaced tones is discussed.

1. Typical time and FFT signals

Time signals were obtained from DAT tapes and displayed on a Hewlett Packard 54504A Digitizing Oscilloscope. Figure III.1a-d shows typical time signals for a 25 Hz tone with current and pressure of 5 Amperes and 34 kPa (5 psig) and 7 Amperes and 48 kPa (7 psig) at distances of 137 and 76 meters from the mouth of the 10 Hz horn.

Figure III.1 a-d

Time domain signals for 25 Hz tone; a,b: 5 Amperes, 34 kPa (8 psig), 137 m and 76 m; c,d: 7 Amperes, 48 kPa (7 psig), 137 m and 76 m.

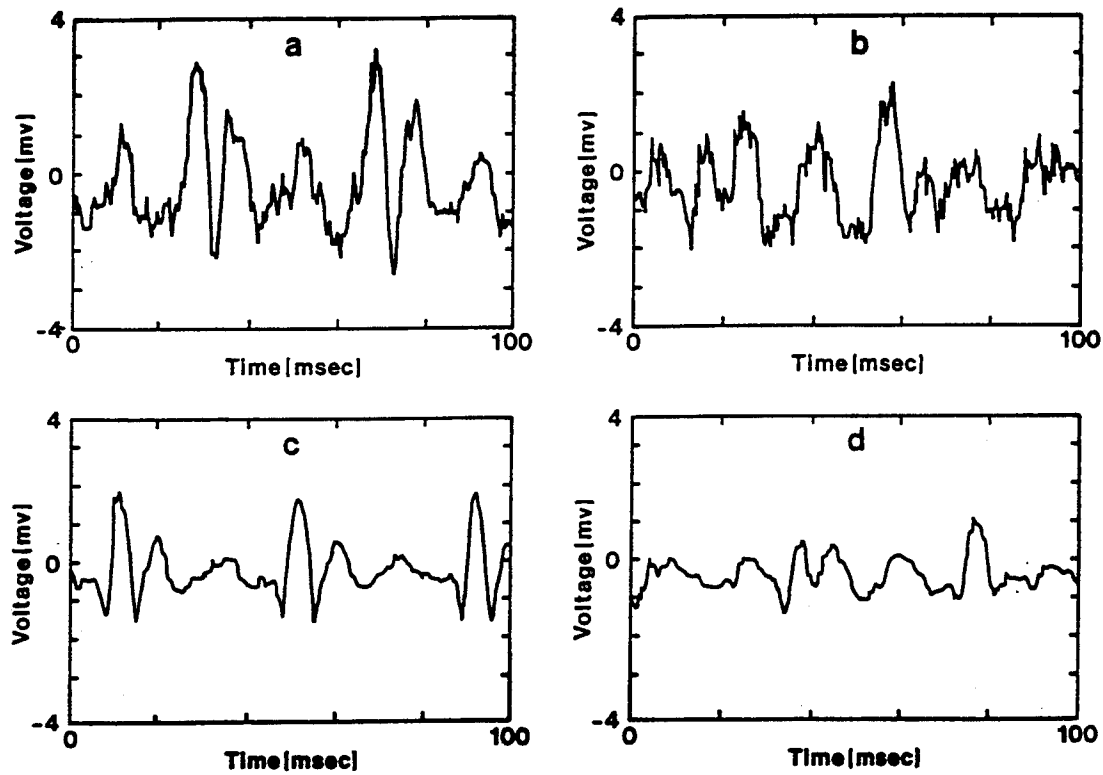


Figure III.2 a-d

Time domain signals for 100 Hz tone; a,b: 5 Amperes, 34 kPa (8 psig), 137 m and 76 m; c,d: 7 Amperes, 48 kPa (7 psig), 137 m and 76 m.

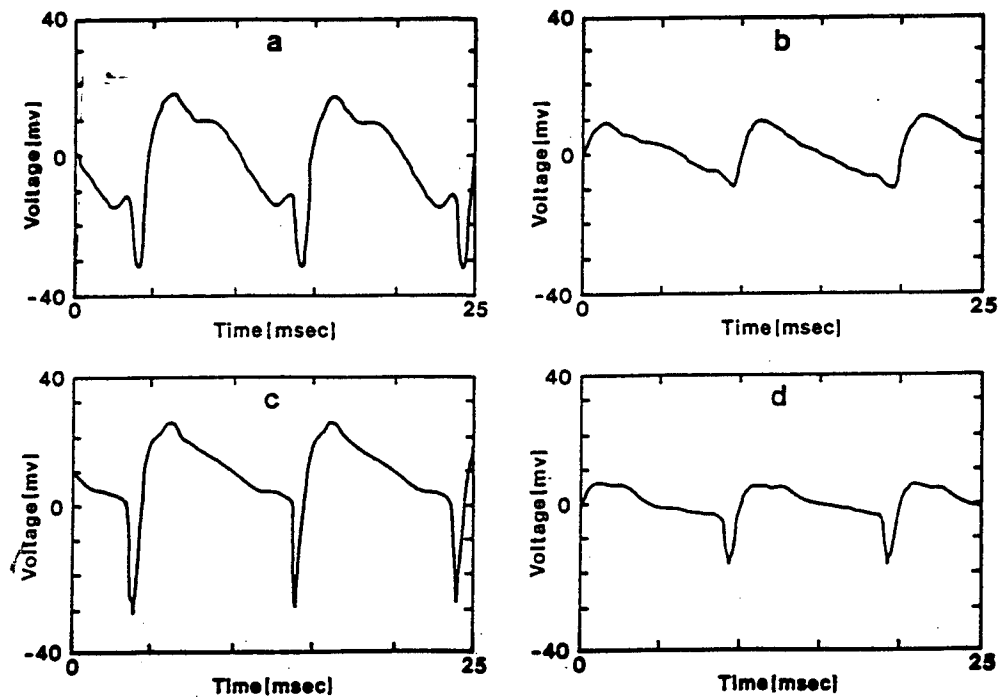


Figure III.2a-d shows typical time signals for a 100 Hz tone under the same conditions. These figures show a significant non-linearity in the time signal. Also note that the microphones are inverting the pressure, as expected.

At close range, 76 meters, the 100 Hz tone shows a rapid decrease and increase in pressure followed by a gradual decrease in pressure for most of the period. This is due to the pressure build-up in the modulator when the slots are at their minimum opening. Each time the slots close and begin to open there is a small explosion or puff of air released. The 25 Hz signal is quite different. Here there is a rapid pressure change as before but followed by a ringing down in the pressure which takes place over the remainder of the cycle period.

At the 137 meter microphone distance, there is considerable attenuation of the high frequency energy resulting in a smoothing of the 100 Hz tone. Similarly, the attenuation shows up in the 25 Hz tone but the fundamental period of the oscillation is reduced by more than half.

Figure III.3a shows the Fourier spectrum for a 25 Hz signal, a current of 5 Amperes and pressure of 34 kPa (5 psig), while Figure III.3b shows the Fourier spectrum for a 100 Hz signal for 5 Amperes and 48 kPa (7 psig). The first peak in these figures represents the fundamental tone being broadcast and is followed by equally spaced harmonics. The voltage level from the Fourier spectrum is not the actual sound pressure level of the horn. A calibration constant is added to the measured voltage level to obtain the actual sound pressure level and this pressure is referenced to 1m, assuming spherical spreading.

Figure III.3 a

Figure III.3 b

Fourier spectrum of 25 and 100 Hz tones.

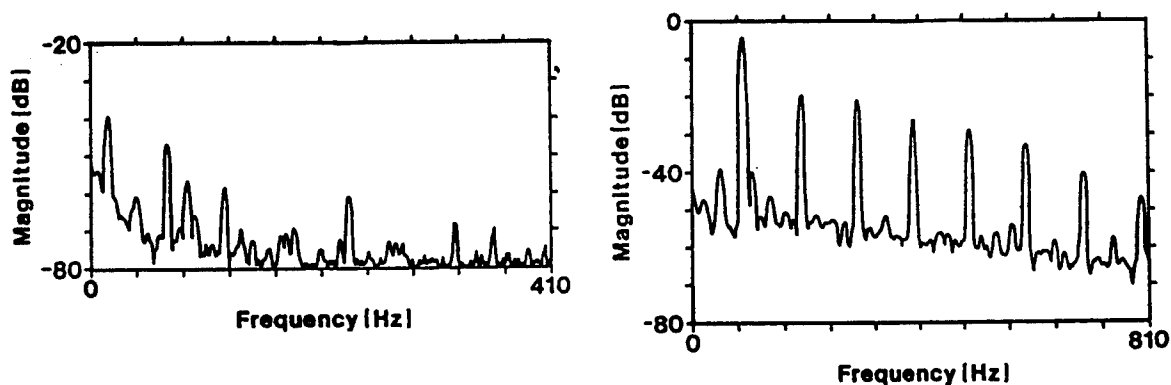
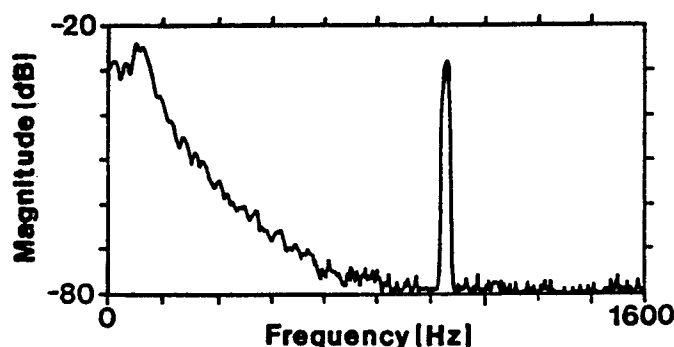


Figure III.4 shows the Fourier spectrum of the calibration tone recorded on the microphone directly over the 25 Hz horn. The 94 dB (re: 20 μ Pa), voltage level calibration tone at 1000 Hz has a voltage level of -27.8 dB. This means that -27.8 voltage

level for this Fourier spectrum is equivalent to 94 dB sound pressure level or a 0 dB voltage level is equivalent to $94 + 27.8 = 121.8$ dB sound pressure level. To reference this sound pressure level to 1 meter, add $\log(r/1m)$ to 121.8, where r is the distance in meters the microphone is away from the horn. This result will be the sound pressure level at 0 dB voltage level for these spectra 1 meter away from the mouth of the horn. The microphone was located 27 meters from the mouth of the 25 Hz horn. Therefore the sound pressure level that represents the value for 0 dB voltage level is $121.8 \text{ dB} + 27.8 \text{ dB} = 150.5 \text{ dB}$. Therefore, the value labeled 0 dB in Figures III.3 can be changed to 150.5 dB and now the spectra are calibrated accordingly. The sound pressure level can now be found for the peaks in the Fourier spectrum and the effects gas pressure and current have on sound pressure level for various frequencies can be evaluated.

Figure III.4
Fourier spectrum of 94 dB calibration tone.

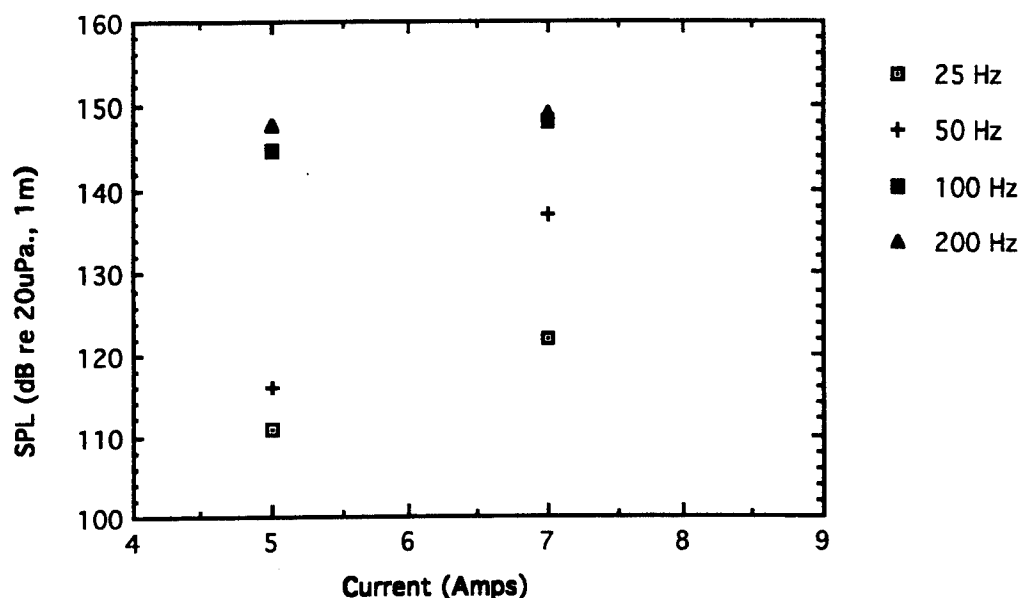


2. Sound pressure level vs. current, pressure and frequency

This section will discuss how the acoustic output for low and high frequencies changes with an increase of pressure or current. At a pressure of 34 kPa (5 psig), Figure III.5a shows there is a significant increase in sound pressure level as the voice coil current increases for low frequencies. For example, at 25 Hz the sound pressure level increases from 111 dB to 121 dB when the current is increased from 5 to 7 Amperes yielding an increase of 10 dB. At 50 Hz the sound pressure level increases from 116 dB to 138 dB yielding an increase of 22 dB for the same current levels. However, at 100Hz and 200Hz there was only an increase of 3 dB and 2 dB respectively when the current was increased from 5 to 7 Amperes.

Figure III.5a

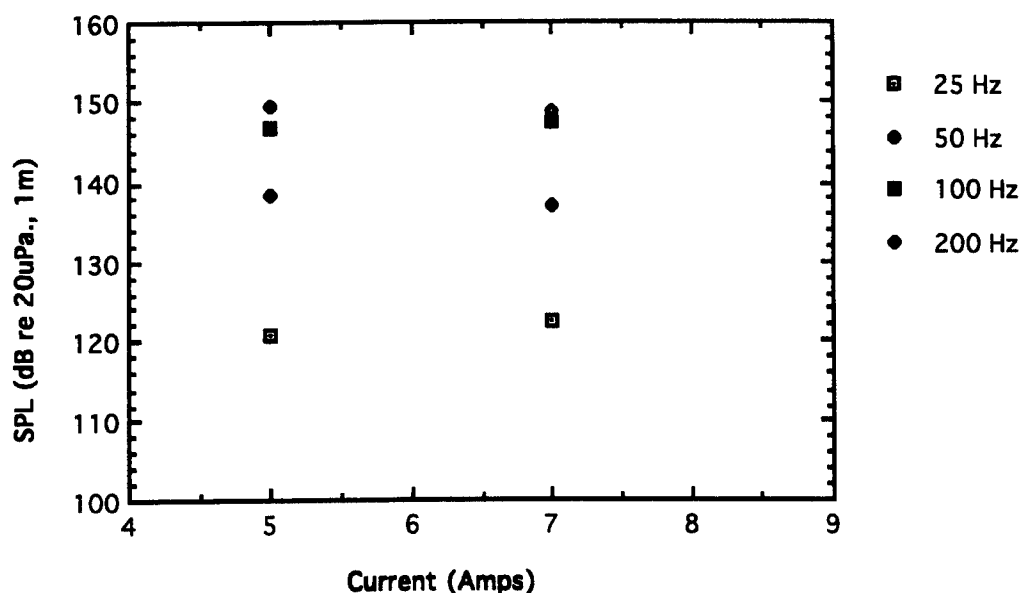
SPL for 25, 50, 100, and 200 Hz tones at 34 kPa (5 psig) vs. voice coil current.



Alternatively, at a pressure of 48 kPa (7 psig), Figure III.5b shows that, by increasing the current, there is no significant increase in sound pressure level at any frequency. The greatest increase in sound pressure level is at 25Hz. At this frequency the sound pressure level increases 1 dB as the current increases from 5 to 7 Amperes.

Figure III.5b

SPL for 25, 50, 100, and 200 Hz tones at 48 kPa (7 psig) vs. voice coil current.

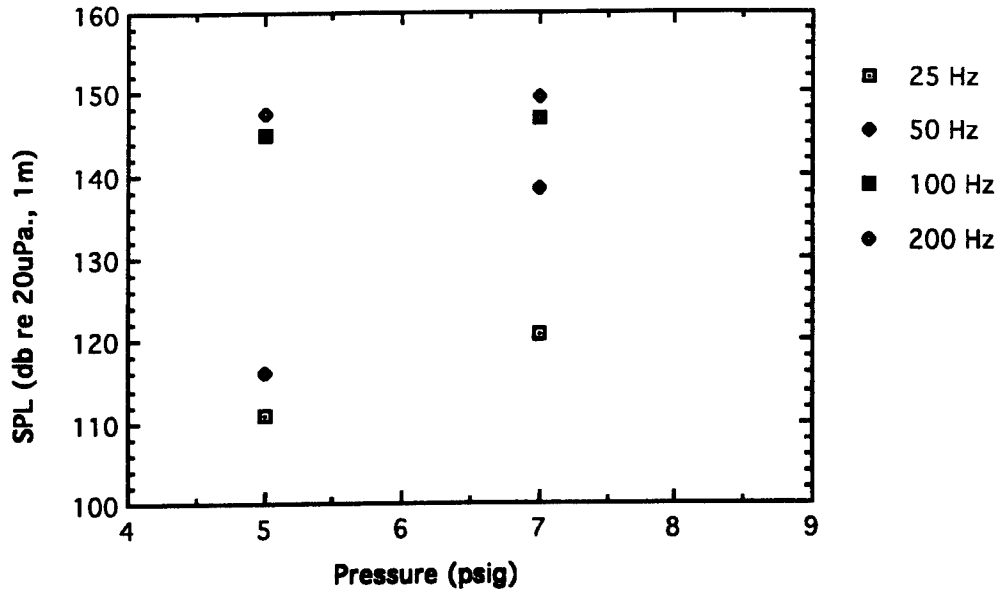


A similar result is observed when the current is held constant and the pressure is changed. At a current of 5 Amperes Figure III.5c shows there is a significant increase in sound pressure level for low frequencies when the pressure is increased. For example,

when the pressure is increased from 34 to 48 kPa (5 to 7 psig) the sound pressure level increases from 111 dB to 122 dB at 25 Hz and from 116 dB to 138 dB at 50 Hz yielding a 11 dB and 22 dB increase respectively. But at frequencies of 100 Hz and 200 Hz the sound pressure level increases only by 1 to 3 dB.

Figure III.5c

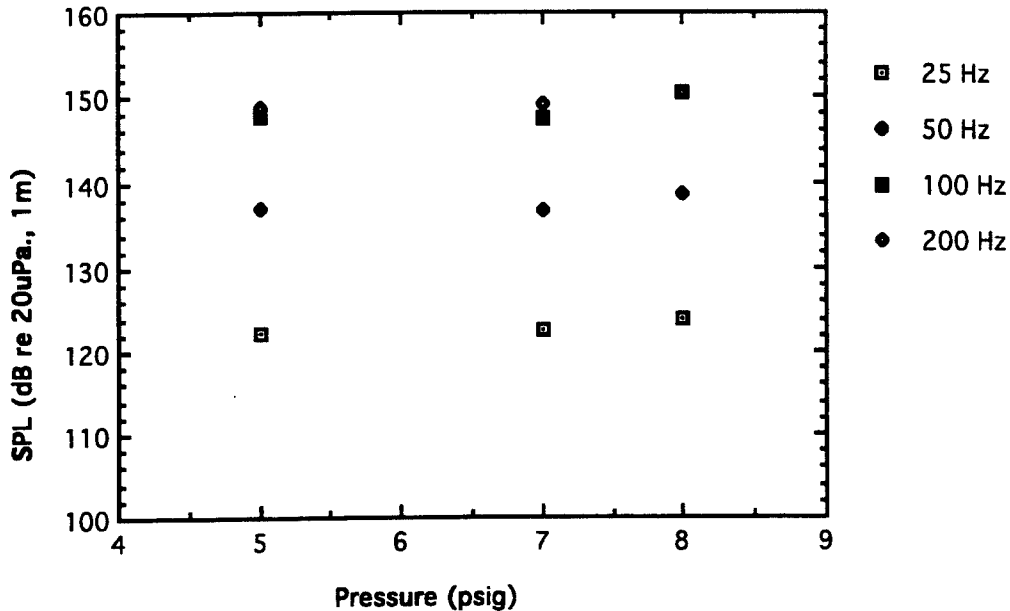
SPL for 25, 50, 100, and 200 Hz tones at 5 Amperes vs. pneumatic gas pressure.



At a current of 7 Amperes Figure III.5d shows that increasing the pressure results in no significant increase in sound pressure level at any frequency. The greatest increase in sound pressure level is 3 dB at 100 Hz when the pressure is changed from 48 to 55 kPa (7 to 8 psig).

Figure III.5d

SPL for 25, 50, 100, and 200 Hz tones at 7 Amperes vs. pneumatic gas pressure.



In conclusion there is only a small advantage operating the horn at both a high current and a high pressure at any frequency. For a low frequency, increasing the pressure when the current is low or increasing the current when the pressure is low yields the same result; a significant increase in sound pressure level. However, increasing the pressure raises the temperature of the gas flowing through the WAS-3000 and horn which may cause damage to the voice coil or other equipment. Therefore, it is preferred to keep the pressure low and increase the current when broadcasting low frequencies.

At high frequencies, the horn should be operated at a low current and pressure because an increase in either the pressure or the current hdoes not increase the sound pressure level.

3. Frequency response

Figure III.6a shows the measured frequency response of the 10 Hz horn for standard one-third octave spaced tones. One can see that the response of the horn above 63 Hz is relatively flat within plus and minus three dB. Below this frequency, however, there is a rapid decrease in sound pressure level as the frequency decreases from 63 to 12 Hz, with a minimum occurring at 16 Hz. Although there is a major decrease in sound pressure level, at 12 Hz the sound pressure level is still 134 dB.

Figure III.6a

Measured frequency response for the 10 Hz horns at one-third octave spaced tones.

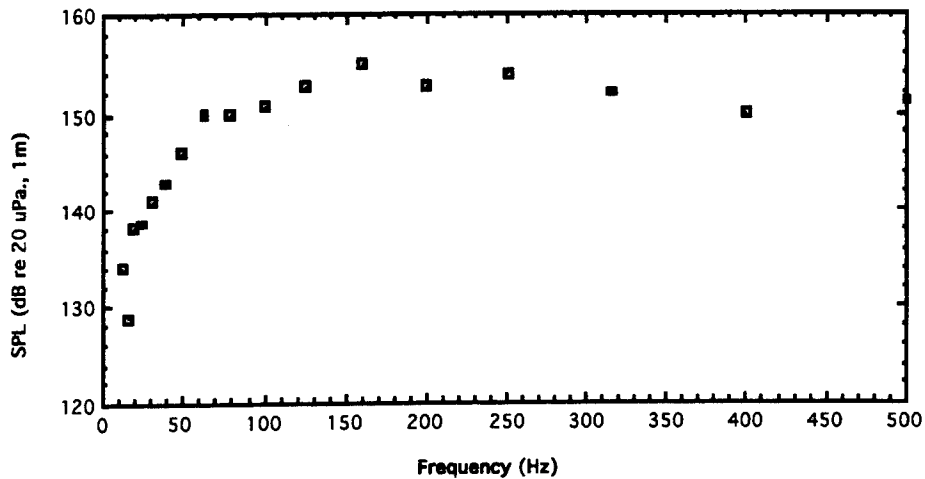


Figure III.6b shows the experimental frequency response of the 25 Hz Horn. This response curve is relatively flat above 100 Hz within plus or minus 3 dB. Below this frequency, the sound pressure level oscillates with fluctuations of about 7 to 10 dB and finally the curve reaches a minimum of 124 dB at 25 Hz.

Figure III.6b

Measured frequency response for the 25 Hz horns at one-third octave spaced tones.

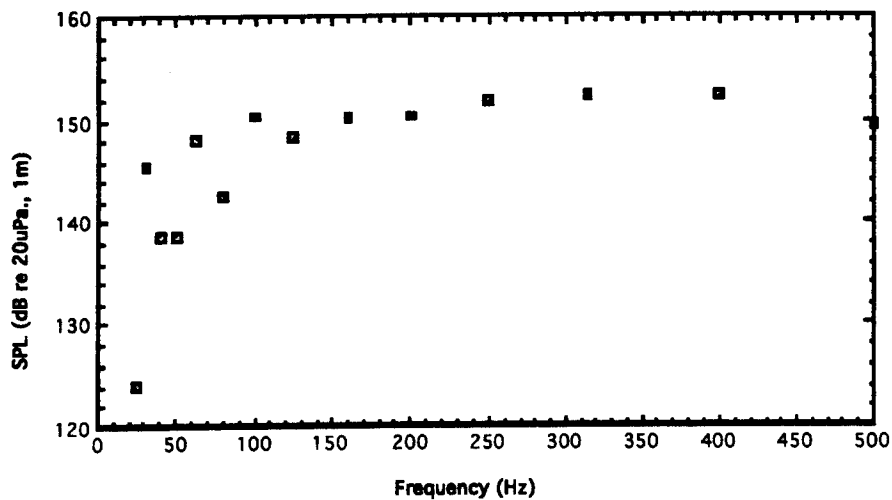
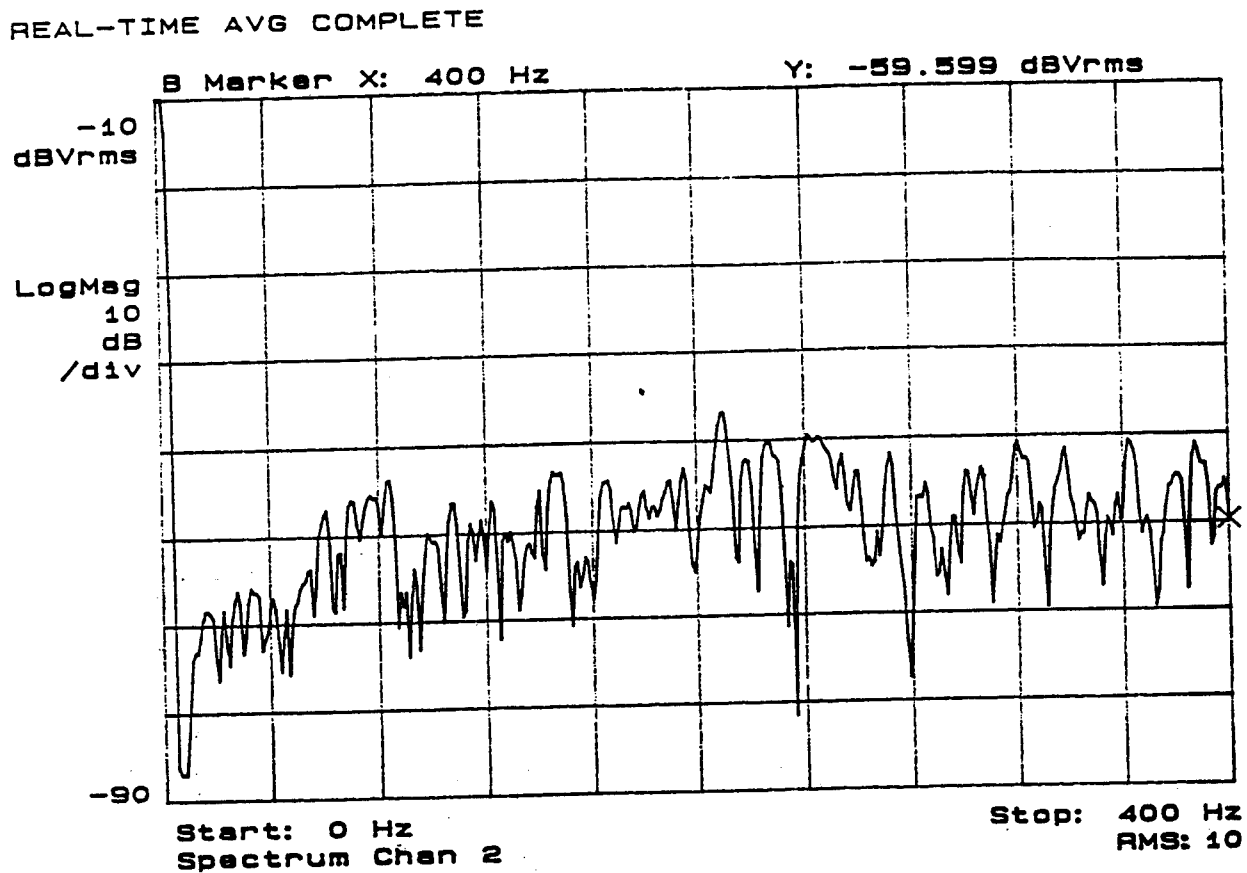


Figure III.7 shows the frequency response of the 10 Hz horn for band limited noise (10 - 500 Hz) measured at the 137 meter microphone when the pressure is 48 kPa (7 psig) and the current is 7 Amperes. The band limited response maximizes at 210 Hz which corresponds to the maximum in the tonal frequency response. At this frequency the sound pressure level is about 143 dB.

Figure III.7

Measured frequency response for band limited noise (10 - 500 Hz).



IV. DIRECTIVITY PATTERNS

In Section III, measurements to determine the directivity of the 25 Hz horn were described. The analyzed measured directivity patterns were provided by PSL and ARL. Here, the theoretical directivity pattern for this horn is approximated and compared to measured data. Although one can find the directivity patterns for various shaped radiators in the literature,⁶ typically such reflecting boundaries as finite impedance grounds are not considered. Ideally, we would like the directivity pattern for a finite length-unflanged exponential horn radiating as a piston, normal to the ground and above a finite impedance ground. To accomplish this, it is assumed that the angular distribution of the far field pressure is the product of an area averaged point source above a finite impedance ground and the angular distribution of the free field emitted radiation from an unflanged circular tube.

1. Radiation from an unflanged, semi-infinite circular tube

The directivity pattern for a horn in free space can be approximated by an unflanged circular pipe in free space. Levine and Schwinger⁷ considered the reciprocal problem of absorption by a circular disc. The angular distribution of the emitted radiation from an unflanged circular pipe was expressed as

$$G(\theta) = \frac{4}{\pi \sin^2 \theta} \frac{J_1(ka \sin \theta)}{\left[(J_1(ka \sin \theta))^2 + (N_1(ka \sin \theta))^2 \right]^{1/2}} \frac{|R|}{1 - |R|^2} \exp \left[\frac{2ka \cos \theta}{\pi} P \right] \cdot \int_0^{ka} \frac{x \tan^{-1}(-J_1(x)/N_1(x)) dx}{\left[x^2 - (ka \sin \theta)^2 \right] \left[x^2 + (ka)^2 \right]^{1/2}}, \quad (\text{IV.1})$$

defined relative to an isotropically radiating point source. The angle θ is measured from the normal to the piston and P is the principal value of the integral. J_1 and N_1 are Bessel function, k is the wave number ($k = 2\pi/\lambda$), a is the pipe radius. $|R|$ is the magnitude of the reflection coefficient for plane waves incident at the piston from within the tube and is given by

$$|R| = \exp \left\{ \frac{-2ka}{\pi} \int_0^{ka} \frac{\tan^{-1}(-J_1(x)/N_1(x))}{x \left[(ka)^2 - x^2 \right]^{1/2}} dx \right\}. \quad (\text{IV.2})$$

Equation IV.2 assumes plane waves and is valid only for the dominant mode propagating in the tube; ka must be less than 3.83. The above equation was solved on Mathematica 2.0 and Figure IV.1 a,b show results for $ka = 0.9$ and 3.5.

Figure IV.1a

Directivity pattern for unflanged piston for $ka = 0.9$ and 3.5.

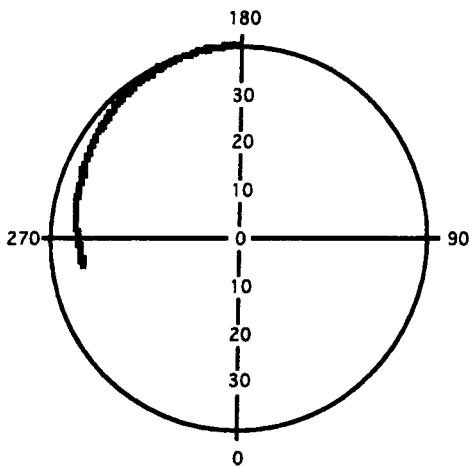
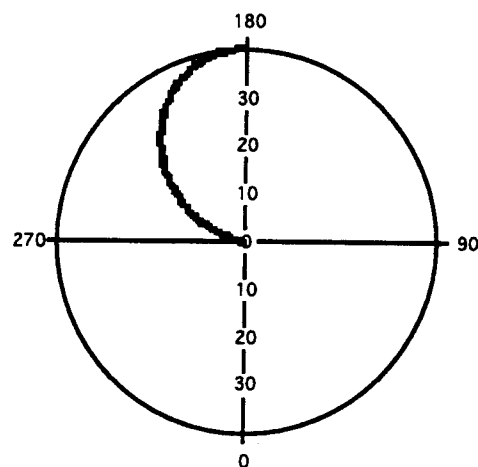


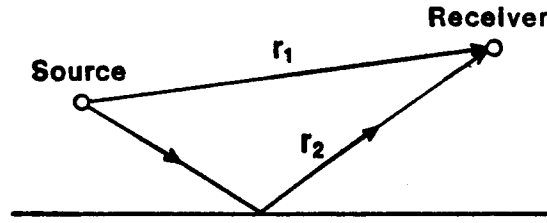
Figure IV.1b



2. Point source above a finite impedance ground

In Figure IV.2, a point source and a receiver are located above a flat porous surface.

Figure IV.2
Geometry for point source and receiver above a flat surface.



The total pressure (p) received at the microphone is composed of a direct (r_1) and a reflected (r_2) sound ray. This may be expressed mathematically as

$$p = \frac{\exp(ik_0 r_1)}{r_1} + Q \frac{\exp(ik_0 r_2)}{r_2} \quad (\text{IV.3})$$

where k_0 is the propagation constant of sound in air. In Equation IV.3 r_1 is the source-to-microphone distance. The reflection coefficient, Q is dependent on the angle of incidence (ψ) of the sound ray to the vertical on the surface, the impedance of the soil (Z) and the frequency (f). The reflection coefficient can be written as

$$Q = R + (1 - R)F(f, \psi, Z) \quad (\text{IV.4})$$

where $F(f, \psi, Z)$ is called the boundary loss factor and is given by

$$F(f, \psi, Z) = 1 + i\sqrt{\pi}\omega \exp(\omega^2) \text{erfc}(i\omega) \quad (\text{IV.5})$$

where

$$\text{erfc}(i\omega) = \frac{2}{\sqrt{\pi}} \int_{i\omega}^{\infty} \exp(-t^2) dt \quad (\text{IV.6})$$

is the complementary error function, and ω^2 can be expressed for the air in the soil pores by

$$\omega^2 = \frac{ik_0 r^2 (\cos \psi + \beta)^2}{2}. \quad (\text{IV.7})$$

In Equation IV.7, $\beta = 1/Z$ where $Z(f)$ is the impedance and is a function of the porous properties of the ground. Equation IV.7 is valid for locally reacting soils in which sound is strongly refracted toward the normal at the air-soil boundary.

The pressure at a distance r from a point source is extended to a finite size radiating piston by assuming each elemental area of the piston acts as a point source and that the total field is the sum of the elemental pressure for all such elements. The total pressure can be expressed as

$$P_{\text{tot}} = \frac{1}{A} \oint p dA \quad (\text{IV.8})$$

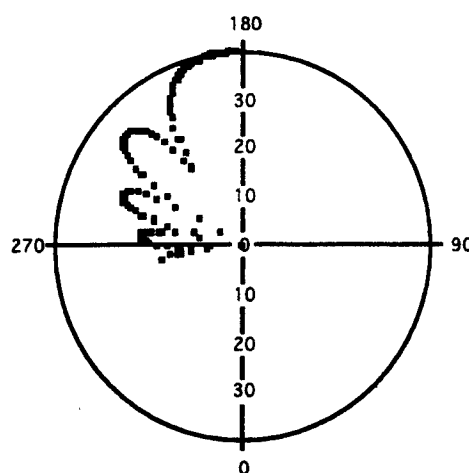
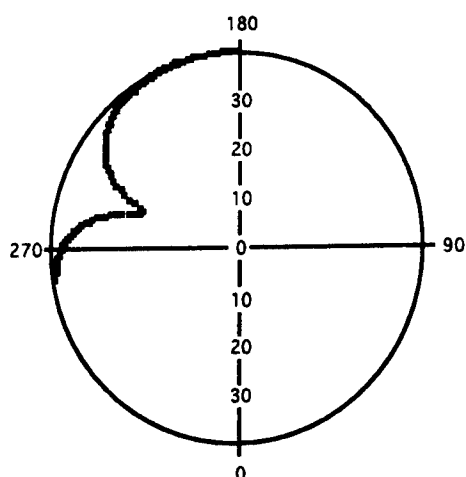
where p can be found from Equation IV.3 for each elemental area. Numerically, the piston surface was divided into a grid of 100 x 100 elements. Figure IV.3 a,b shows the angular pressure field for a circular array of point sources representing the mouth of the

25 Hz horn for 40 Hz and 160 Hz. The geometry used was that of the 25 Hz horn positioned at the center of the tower microphone array. The height of the horn mouth above the ground was 4.3 meters.

Figure IV.3a

Figure IV.3b

Area averaged angular pressure field for a circular array of point sources above a finite ground impedance for 40 and 160 Hz.



The flow resistivity, porosity, and tortuosity used in the impedance calculation are 1.1×10^6 rayls/m, 0.4, and 2.0, respectively. The shape factor ratio was set equal to 0.36.

3. Comparison to measured directivity pattern

The last step in calculating the directivity pattern of the horn is to find the combined effects of the radiation pattern of a tube and the ground effect. The pressure amplitude for each effect is normalized to 0 dB. The product of the two sets of pressure amplitudes gives the directivity pattern of a finite tube above a finite ground impedance. Figures IV.4 a,b show a comparison between this calculated directivity pattern and the measured pattern where the radial scale is 20 log of the pressure amplitude. At 40 Hz, the calculated result for the 25 Hz horn (solid line) falls within 5 dB of the measured data (x and +). At 160 Hz, the results show, at certain angles, a 20 dB difference between the measured and calculated directivity pattern.

This calculation did not take into account two trailers that were in the vicinity of the measurements. The 25 Hz horn was placed on a flat-bed trailer about 15 meters long and positioned directly below the center microphone. This trailer was parked perpendicular to the line of microphones and in the center of the two towers. There was also an instrument trailer parked approximately 75 meters away from one of the towers. In Figure IV.4 a,b, the x, ♦ data points represent data taken from microphone on one side of the flat-bed trailer and the +, ■ data points represent data taken from microphones on the other side of the flat-bed trailer.

Figure IV.4a

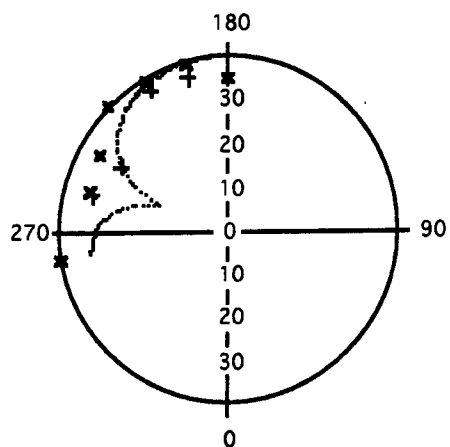
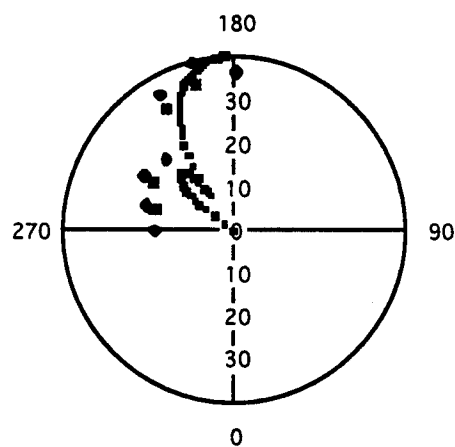


Figure IV.4b



Sound will reflect off these trailers and will interfere with the direct and reflected sound. This interference will tend to wash out the minima that are predicted to occur in the theoretical result.

V. CONCLUSIONS

We have reported the results of the acoustic characterization of MOAS. These include frequency response, directivity, voice coil current and pneumatic gas pressure characteristics of the speaker. The most important result for an operator of MOAS is the high degree of non-linearity in the system. Harmonic disturbances as high as 70% can easily be achieved. MOAS was designed to produce acoustic levels of 140 dB. This goal was reached with levels of at least 140 dB above 30 Hz.

Analysis of the measured acoustic output as a function of voice-coil current and gas pressure suggest the following. The "full modulation" current for the WAS-3000 is 7 Amperes. For higher current values, the sound pressure level change in a fundamental tone changes less than 2 dB. Higher levels of current are possible but dump energy into higher harmonics. For frequencies below 50 Hz, full modulation (7 Amperes) is necessary for maximum acoustic output. However, for frequencies above 100 Hz, current levels of 5 Amperes are adequate for maximum acoustic output in the fundamental.

Changes in the pneumatic gas pressure can dramatically change the acoustic output. For all frequencies, the pressure should be kept below 34 kPa (5 psig), since higher pressure will increase the gas temperature and not the acoustic energy in the fundamental tone. However, higher pressures will dump more energy into harmonics, which could be desirable.

We have also compared measured directivity patterns for the 25 Hz horn to an unflanged piston in a tube above a finite ground impedance. These calculations are approximate and limited to frequencies below 160 Hz. Agreement is, at best, only fair. In measuring the directivity pattern, the data was measured in 15 degree intervals. As a consequence, it was hard to see if any minima occurred in the directivity pattern as the theory predicted. Any further theoretical work should include the exponential horn shape and extend the calculations to higher frequencies.

REFERENCES

1. James M. Sabatier, "Pneumatic Loudspeaker Acoustic Generation System," Technical Report, U. S. Army Construction Engineering Research Laboratory, Contract Number DACA 88-90-D-0047, December 1991.
2. James M. Sabatier, "The Effect of Compressed Gas Injection Cooling on a Voice Coil in a Large Pneumatic Loudspeaker," Technical Report, U.S. Army Construction Engineering Research Laboratory, Contract Number CERENA-0090-0396-T3, March 1993.
3. James M. Sabatier, "Integration of a Large Pneumatic Loudspeaker," Technical Report, U.S. Army Construction Engineering Research Laboratory, Contract Number DACA 88-90-D-0047, March 1993.
4. Joint Acoustic Propagation Experiment, edited by Robert O. Olsen, Beany L. Carnes, and Bruce Kenedy, U.S. Army Research Laboratory, Battle Field Environmental Directorate, April 1993.
5. Operation Manual, Wyle Laboratories WAS 3000 Airstream Modulator (January 1992).
6. Leo L. Beranek, Acoustics, (American Institute of Physics, 1986).
7. H. Levine and J. Schwinger, "On the radiation of sound from an unflanged circular pipe," *Phys. Rev.*, **73**, 383-406 (Feb. 15, 1948).

THE EFFECTS OF DENSITY AND HUMIDITY FLUCTUATIONS ON SOUND PROPAGATION AND SCATTERING IN THE TURBULENT ATMOSPHERE

V. Mellert, V. Ostashev and R. Wandelt*

Carl von Ossietzky Universitat Oldenburg, FB Physik, 26111 Oldenburg, Germany

(* Present address: Physical Science Laboratory, NM State University, Las Cruces, NM 88003-0002)

ABSTRACT

The effects of density and humidity fluctuations on sound propagation and scattering in the turbulent atmosphere are investigated. The equation for the sound scattering cross section in the humid air is derived, and on its basis, new methods for remote sensing of the atmosphere are proposed. The equation for the effective structure parameter of acoustic refractive index fluctuations in the humid air is obtained. Using this equation, the relative contribution to the effective structure parameter from temperature, humidity and temperature-humidity fluctuations is studied for different climate zones.

1 INTRODUCTION

Sound propagation in the turbulent atmosphere is often considered in the approximation of the effective sound speed $c_{\text{eff}} = c + v_r$, where c is the adiabatic sound speed and v_r is the wind velocity component in the direction from the source to the receiver. Moreover, it is usually assumed that sound speed fluctuations depend only on temperature fluctuations.

The aim of the paper is the study of the effects of density and humidity fluctuations on statistical characteristics of a sound wave propagating in the turbulent atmosphere. In Section 2, we explain how density and humidity fluctuations can be incorporated into the theory of sound propagation in the turbulent atmosphere. In Section 3, the equation for the sound scattering cross section in the humid air is considered and new methods for remote sensing of humidity fluctuations in the atmosphere are proposed. In

Section 4, the effects of humidity fluctuations on the effective structure parameter C_{eff}^2 of acoustic refractive index fluctuations are investigated.

2 THE INCORPORATION OF DENSITY AND HUMIDITY FLUCTUATIONS INTO THE THEORY

The starting equation of the theory of sound propagation in the turbulent atmosphere is given by [1,2]

$$\begin{aligned} & [\nabla^2 + k^2 - 2k^2 \frac{\tilde{c}}{c} - (\frac{\nabla \tilde{\rho}}{\rho}) \cdot \nabla - \\ & - \frac{2i}{\omega} \frac{\partial v_1}{\partial x_1} \frac{\partial^2}{\partial x_1 \partial x_1} + \frac{2ik}{c} \vec{v} \cdot \nabla] p(\vec{R}) = 0. \end{aligned} \quad (1)$$

Here p is the sound pressure, $\vec{R} = (x_1, x_2, x_3)$ are the Cartesian coordinates, $\nabla = (\partial/\partial x_1, \partial/\partial x_2, \partial/\partial x_3)$, $k = \omega/c$ is the wave number, ω is the frequency, c and ρ are mean values of the adiabatic sound speed and density, and \tilde{c} , $\tilde{\rho}$ and \vec{v} are fluctuations in the adiabatic sound speed, density and wind velocity vector.

From Eq.(1) it follows that the sound pressure p is not directly affected by fluctuations in the effective sound speed c_{eff} ; it is affected by fluctuations in the sound speed \tilde{c} , density $\tilde{\rho}$ and wind velocity vector \vec{v} . From this equation it also follows that sound speed fluctuations scatter the sound field like monopoles because \tilde{c} enters into this equation without any derivative. On the other hand, density fluctuations scatter the sound field as a combination of monopoles and dipoles because $\tilde{\rho}$ enters into the equation with the first order derivatives. Finally, wind velocity fluctuations scatter the sound field as a combination of monopoles, dipoles and quadrupoles because \vec{v} enters into the equation with derivatives up to the second order.

Although in the starting equation (1) derived from the linearized system of fluid dynamic equations p is affected by sound speed and density fluctuations, in the atmosphere it is more convenient to deal with temperature fluctuations \tilde{T} and specific humidity fluctuations \tilde{q} . Therefore, in Eq.(1) it is reasonable to express \tilde{c} and $\tilde{\rho}$ as the linear

combinations of \tilde{T} and \tilde{q} [3]:

$$\tilde{c} = \frac{c}{2} (\beta_c \tilde{T}/T + \eta_c \tilde{q}), \quad \tilde{\rho} = \rho (\beta_\rho \tilde{T}/T + \eta_\rho \tilde{q}). \quad (2)$$

In Eqs.(2), T is the mean value of the temperature, and the coefficients β_c , η_c , β_ρ and η_ρ are given by

$$\beta_\rho = (T/\rho)(\partial\rho(P,T,q)/\partial T), \quad \eta_\rho = (1/\rho)(\partial\rho(P,T,q)/\partial q), \quad (3)$$

$$\beta_c = (2T/c)(\partial c(P,T,q)/\partial T), \quad \eta_c = (2/c)(\partial c(P,T,q)/\partial q),$$

where P and q are mean values of the atmospheric pressure and specific humidity, $\rho(P,T,q)$ and $c(P,T,q)$ are equations for the density and adiabatic sound speed in the humid air.

The equation for ρ is known in the literature [4]

$$\rho(P,T,q) = \frac{P}{R_a T} (1 - (\mu_a/\mu_w - 1)q) = \frac{P}{R_a T} (1 - 0.608 q). \quad (4)$$

Here R_a is the gas constant for the dry air; μ_a and μ_w are molecular weights of the dry air and water vapor, respectively; hereinafter, we neglect terms of the order of q^2 because in the atmosphere $q < 0.03$.

In the literature, there are different equations for the adiabatic sound speed in the humid air. For example, in [5] c^2 is given by

$$c^2 = \gamma_a R_a T (1 + 0.450 q), \quad (5)$$

and in [6] its value is given by

$$c^2 = \gamma_a R_a T (1 + 0.494 q), \quad (6)$$

where γ_a is the ratio of specific heats for the dry air. Note that Eq.(5) was previously used [7-9] for calculating sound field statistical characteristics in the humid air.

Because Eqs.(5) and (6) are different, we have rederived the equation for c^2 in the humid air:

$$c^2 = \gamma_a R_a T \left[1 + \left(\frac{\mu_a}{\mu_w} \left(1 - \frac{\gamma_a - 1}{\gamma_w - 1} + \frac{1 - \gamma_a^{-1}}{1 - \gamma_w^{-1}} \right) - 1 \right) q \right], \quad (7)$$

where γ_w is the ratio of specific heats for the water vapor. In Eq.(7), the coefficient before q is expressed through the thermodynamical constants that allows us to calculate the value of this coefficient for different meteorological conditions. For $T = 20^\circ\text{C}$, calculating the coefficient before q in Eq.(7) yields

$$c^2 = \gamma_a R_a T (1 + 0.511 q). \quad (8)$$

In this equation the numerical coefficient before q differs from those used previously, see Eqs. (5) and (6). Using Eqs.(3), (4) and (8) and assuming that the mean value of q is 0.008 (this value of q is typical for the midlatitude atmospheres), we calculate the coefficients β_c , η_c , β_ρ and η_ρ :

$$\beta_\rho = -1; \quad \beta_c = 1; \quad \eta_\rho = -0.596; \quad \eta_c = 0.501. \quad (9)$$

Note that in Eqs.(5) and (8), the numerical coefficients before q differ only by 12%. Nevertheless, some sound field statistical characteristics calculated using Eq.(5) may differ dramatically from those calculated using Eq.(8). For example, the sound scattering cross section at 90° is proportional to $(\eta_c + \eta_\rho)^2$. Because η_c is close to η_ρ , see Eqs.(9), even small variations in the coefficient η_c , caused by variations in the coefficient before q in the equation for c^2 , may dramatically change the value of $(\eta_c + \eta_\rho)^2$. Using Eqs.(9), we get $(\eta_c + \eta_\rho)^2 = 0.009$; on the other hand, in [7-9], where Eq.(5) was used, $(\eta_c + \eta_\rho)^2 = 0.026$.

Substituting Eqs.(9) into Eq.(2) yields the equations for sound speed and density fluctuations in the humid air,

$$\tilde{c} = \frac{c}{2} \left(\frac{\tilde{T}}{T} + 0.501 \tilde{q} \right), \quad \tilde{\rho} = -\rho \left(\frac{\tilde{T}}{T} + 0.596 \tilde{q} \right). \quad (10)$$

It should be noted here that according to Eqs.(4) and (7), the effects of mean humidity q on the mean density ρ and sound speed c can be ignored. But \tilde{q} may be of the order of \tilde{T}/T , and in accordance with Eqs.(10), humidity fluctuations may significantly affect sound speed and density fluctuations.

Substituting Eq.(10) into Eq.(1) yields

$$\begin{aligned} & [\nabla^2 + k^2 - k^2 \frac{\tilde{T}}{T} + (\frac{\nabla \tilde{T}}{T}) \cdot \nabla - 0.501 k^2 \tilde{q} + 0.596 (\nabla \tilde{q}) \cdot \nabla - \\ & - \frac{2i}{\omega} \frac{\partial v_i}{\partial x_j} \frac{\partial^2}{\partial x_i \partial x_j} + \frac{2ik}{c_0} \vec{v} \cdot \nabla] p(\vec{R}) = 0. \end{aligned} \quad (11)$$

From this equation it follows, that temperature fluctuations scatter a sound wave as a combination of monopoles and dipoles because \tilde{T} enters into the equation with derivatives up to the first order. The humidity fluctuations also scatter a sound wave as a combination of monopoles and dipoles but with different amplitudes proportional to the numerical coefficients before \tilde{q} and a first derivative of \tilde{q} . Therefore, the radiation patterns due to sound scattering by temperature and humidity fluctuations are different, and they also differ from the radiation pattern due to sound scattering by wind velocity fluctuations.

If $\tilde{q} = 0$, Eq.(11) becomes the classic Monin-Tatarskii's equation [10,11]. Therefore, if $\tilde{q} \neq 0$, Eq.(11) is the generalization of the Monin-Tatarskii's equation, which allows us to take into account sound scattering by humidity fluctuations.

3 SOUND SCATTERING CROSS SECTION IN THE HUMID AIR

Starting from Eq.(11), the equation for the sound scattering cross section in the inertial range of homogeneous and isotropic turbulence is derived

$$\sigma(\theta) = \frac{0.03k^{1/3}}{(\sin \frac{\theta}{2})^{11/3}} \left[\frac{3}{22} \left(\cos^2 \theta \frac{c_T^2}{T^2} + (-0.095 + 0.596 \cos \theta)^2 c_q^2 + \right. \right. \\ \left. \left. \right] \quad (12)$$

$$+2\cos\theta (-0.095 + 0.596\cos\theta)R_{qT}C_q \frac{C_T}{T} \Big) + \cos^2\theta \cos^2 \frac{\theta}{2} \frac{C_v^2}{C^2} \Big].$$

Here θ is the scattering angle, C_T^2 , C_q^2 and C_v^2 are the structure parameters for temperature, humidity and wind velocity fluctuations, R_{qT} is the coefficient for the cross correlation of temperature and humidity fluctuations. From Eq.(12) we really see that the radiation patterns due to sound scattering by temperature, humidity, temperature-humidity and wind velocity fluctuations are different.

The derived equation (12) for the sound scattering cross section in the humid atmosphere allows us to propose new methods for remote sensing of the structure parameter C_q^2 and the coefficient R_{qT} which are of primary importance for the boundary layer meteorology, for electromagnetic wave propagation, etc. We will consider only two of these methods. In the first method, using commercially produced sodar, we propose to measure the sound backscattering cross section $\sigma(180^\circ)$. From Eq.(12) it follows that $\sigma(180^\circ)$ is given by

$$\sigma(180^\circ) = 4.08 \cdot 10^{-3} k^{1/3} \left(\frac{C_T^2}{T^2} + 1.382 R_{qT} C_q \frac{C_T}{T} + 0.477 C_q^2 \right). \quad (13)$$

Using a clear air radar, we can also measure the backscattering cross section for microwaves [12]

$$\sigma_e(180^\circ) = 8.4 \cdot 10^{-7} k^{1/3} \left(0.0029 \frac{C_T^2}{T^2} - 0.107 R_{qT} C_q \frac{C_T}{T} + C_q^2 \right). \quad (14)$$

Finally, using commercially produced sodars and the bistatic scheme of acoustic sounding, we can measure the sound scattering cross sections at two angles θ_1 and θ_2 :

$$\sigma(\theta_1) = A_1 k^{1/3} \left(\frac{C_T^2}{T^2} + \alpha_1 R_{qT} C_q \frac{C_T}{T} + \beta_1 C_q^2 + \gamma_1 \frac{C_v^2}{C^2} \right), \quad (15)$$

$$\sigma(\theta_2) = A_2 k^{1/3} \left(\frac{C_T^2}{T^2} + \alpha_2 R_{qT} C_q \frac{C_T}{T} + \beta_2 C_q^2 + \gamma_2 \frac{C_v^2}{C^2} \right). \quad (16)$$

Here the coefficients A_i , α_i , β_i and γ_i (where $i = 1, 2$) depend on θ_i and may easily be obtained from Eq. (12).

As a result of such measurements, we would have a system of four Eqs. (13)-(16) for four unknown parameters C_T^2 , C_q^2 , C_v^2 and R_{qT} . It can be shown, that this system can be solved with respect to these parameters if the following inequality is valid:

$$C_T^2/T^2 > 2.29|B| C_v^2/C^2. \quad (17)$$

Here B is the Bowen ratio which is widely used in the meteorology. The Bowen ratio is of the order of 0.1 and 0.25 for the tropical atmospheres and midlatitude marine or coastal atmospheres, respectively, [13]. Over land, B varies from 0.1 for rain forests and swamps to 10 for deserts. For example, over mixed forests and agricultural land of central Pennsylvania, and over the Kansas prairie, B is typically of the order of 0.5.

In the second method for remote sensing of humidity fluctuations in the atmosphere, we propose to measure only $\sigma(180^\circ)$ and $\sigma_e(180^\circ)$, and use some theoretical model for the vertical profile of R_{qT} . For example, we can assume that $R_{qT} = 1$ because this equality is approximately valid within a few hundred meters above the ground in the convective boundary layer. If we know R_{qT} , it is a straightforward procedure to retrieve C_T^2 and C_q^2 from Eqs. (13) and (14).

4 THE EFFECTIVE STRUCTURE PARAMETER IN THE HUMID AIR

In atmospheric acoustics, the main statistical characteristics of a sound wave are: the variances of log amplitude and phase fluctuations, $\langle \chi^2 \rangle$ and $\langle \phi^2 \rangle$; the structure functions of log amplitude and phase fluctuations, D_χ and D_ϕ ; the transverse coherence function Γ . Practically all of experiments deal with these sound field statistical characteristics. Using geometric acoustic, Rytov and parabolic equation methods, the equations for $\langle \chi^2 \rangle$, $\langle \phi^2 \rangle$, D_χ , D_ϕ and Γ were obtained in electrodynamics and underwater acous-

tics. For the Kolmogorov spectrum, these equations contain the factor C_T^2/T^2 .

Starting from the derived equation (11) it is shown [3,8], that in atmospheric acoustics the equations for $\langle \chi^2 \rangle$, $\langle \phi^2 \rangle$, D_χ , D_ϕ and Γ are the same as analogous equations in electrodynamics or underwater acoustics if in the latter equations C_T^2/T^2 is replaced by the effective structure parameter C_{eff}^2 given by

$$C_{eff}^2 = \frac{C_T^2}{T^2} + 1.002 R_{qT} C_q \frac{C_T}{T} + 0.251 C_q^2 + \frac{22}{3} \frac{C_v^2}{C^2}. \quad (18)$$

For example, the variance of log amplitude fluctuations of the plane wave, calculated by the Rytov method, is given by

$$\langle \chi^2 \rangle = 0.077 C_{eff}^2 k^{7/6} x^{11/6}. \quad (19)$$

The effects of C_q^2 and R_{qT} on C_{eff}^2 were usually ignored. Using the derived equation (18), let us investigate the relative contribution to C_{eff}^2 from C_T^2 , C_q^2 and R_{qT} . As it was mentioned above, in the convective boundary layer within a few hundred meters above the ground $R_{qT} \sim 1$. Then, the ratio $\frac{C_q}{C_T/T}$ may be expressed [6] through the Bowen ratio B ,

$$\frac{C_q}{C_T/T} = \frac{1}{8.1|B|}. \quad (20)$$

This equation is valid [12] if the ratio $C_q \langle v_z \tilde{T} \rangle / (C_T \langle v_z \tilde{q} \rangle)$ has an absolute value near unity that is usually valid up to 1.2 kilometer in the convective boundary layer. Here v_z is the vertical component of the wind velocity vector.

Using Eq.(20) and presented above data on B , we can conclude that for marine and coastal atmospheres, over the rain forests and swamps the ratio $\frac{C_q}{C_T/T}$ is in the range:

$$0.5 < \frac{C_q}{C_T/T} < 1.2, \quad (21)$$

and over the Kansas prairie, over mixed forests and agricultural land of Central Pennsylvania it is given by

$$\frac{C_q}{C_T/T} \sim 0.25. \quad (22)$$

From derived equation (18) it follows that in all of these climate zones and also many other ones, we must take into account temperature-humidity and humidity fluctuations in Eq. (18) if in this equation we account for temperature fluctuations.

REFERENCES

1. Ostashev V.E., "On sound wave propagation in a three-dimensional inhomogeneous moving medium", *Diffraction and Wave Propagation in Inhomogeneous Media*, pp.42-49, Moscow, 1987.
2. Abdullaev S.S. and Ostashev V.E., "Propagation of sound waves in three-dimensionally inhomogeneous and randomly inhomogeneous moving media", *Izv. Acad. Scienc. USSR. Atmos. Ocean. Phys.* **24**, No 4, pp.417-426, 1988 (Translated into English).
3. Ostashev V.E., "Sound propagation and scattering in media with random inhomogeneities of sound speed, density and medium velocity", *Waves in Random media*, **4**, Sept., 1994.
4. Beers N.R., "Meteorological thermodynamics and atmospheric statistics", *Handbook of meteorology*, ed. by F.A.Berry, E.Bollay, N.R.Beers, pp.314-409, McGraw-Hill, 1973.
5. Kallistratova M.A. and A.I. Kon, *Radioacoustic sounding of the atmosphere*, Nauka, Moscow, 1985.
6. Wesely M.L., "The combined effect of temperature and humidity fluctuations on refractive index", *J. Appl. Meteorol*, **15**, No 1, pp.43-49, 1976.
7. Ostashev V.E., "Scattering of sound in a moving random medium and possibility of the humidity fluctuations remote sensing in the atmosphere", *Izv. Acad. Scienc. USSR. Atmos. Ocean. Phys.* **27**, No 12, pp.1308-1315, 1991 (Translated into English).
8. Ostashev V.E., "Propagation and scattering of sound waves in turbulent media (the atmosphere and ocean)", *Atmospheric*

Optics. 4, No 9, pp.931-937, 1991 (Translated into English).

9.Ostashev V.E., "Remote sensing of humidity fluctuations in the atmosphere", *Atmospheric Propagation and Remote sensing II*, A.Kohnle and W.B.Miller, Eds. Proc. SPIE 1968, pp.504-513, 1993.

10.Monin A.S., "Some features of sound scattering in the turbulent atmosphere", *Sov. Phys. Acoustics*. 7, No 4, p.457, 1961 (Translated into English).

11.Tatarskii V.I., *The effects of the turbulent atmosphere on wave propagation*, Israel, 1971.

12.Burk S.D., "Refractive index structure parameters: time dependent calculations using a numerical boundary-layer model", *J. Appl. Meteorol.* 19, pp.562-575, 1980.

13.Fairall C.W., "The humidity and temperature sensitivity of clear-air radars in the convective boundary layer," *J. Appl. Meteorol.* 30, pp.1064-1074, 1991.

Aspects of Sound Field Fluctuations in a Refractive Shadow

David I. Havelock
Michael R. Stinson
Gilles A. Daigle

National Research Council
Ottawa, ON, Canada K1A 0R6

Abstract

Characteristics of the fluctuations in magnitude and phase of a sound field in a shadow region are presented. In particular, it is shown that the phase fluctuations are related to the signal magnitude, that the magnitude exhibits brief drop-outs, and that distinct phase shifts occur at the drop-outs. These characteristics relate to the random nature of the received signal and to its autocorrelation function which is determined by the dynamics of the turbulent medium. A simulated sound field, generated using an upward refracting atmospheric model with isotropic Gaussian turbulence, exhibits characteristics similar to those of the measured data.

1. Introduction

An acoustic shadow region is generated near the ground in an upward refracting atmosphere, or in the presence of large ground features causing terrain masking. The sound field within a shadow regions is less well understood than is the sound field within line of sight regions. Only recently have propagation codes provided sound pressure level (SPL) predictions in the shadow region which agree well with experimental measurements.

Near the boundary of the shadow region the sound field can be predicted by diffraction theory but deeper within the shadow, where energy scattered from atmospheric turbulence dominates the energy diffracted at the shadow boundary, there is no complete theoretical framework for predicting the sound field. While it is possible to predict the SPL and some long-term statistics, it is more difficult to formulate the characteristics of the sound field fluctuations over time intervals of only a few seconds. The difficulty is due, in part, to the fact that the turbulence structures which are most important are commensurate in size with the signal wavelength and are within the (indeterminate) input regime of the turbulence spectrum. Recently, efforts have been made to gain further understanding of how atmospheric turbulence affects the sound field through examination of the sound field characteristics and the dynamics of the propagation channel (see, for example, [1]–[6]).

In this paper, characteristics of the measured fluctuations in magnitude and phase of the sound field deep within a refractive shadow are presented. Comparisons are made with random data and with simulations based on propagation through a model atmosphere.

2. Experimental Data

The data considered here was collected at a small airport near Ottawa ON, Canada. Propagation was upwind over an acoustically hard asphalt runway. A minor thermal lapse existed and the wind speed was 3–6 m/s. Both the source and receiver were on the ground, separated by 700 m. Signal frequencies of 100 Hz, 500 Hz and 1000 Hz were investigated but, for brevity, only the 500 Hz data is presented.

The raw data is sampled at 8 kHz and then filtered, bandshifted and decimated. The processed data has a bandwidth of about 50 Hz and a sampling rate of 400 Hz. The magnitude and phase data are calculated from the complex timeseries which is obtained by applying the Hilbert transform to the processed data.

3. The Phase and Magnitude

The received signal, expressed as a complex function of time, has the form $Z = Z_0 \exp(A + i(\omega t + \phi))$, where Z_0 is some reference signal level, A is the log-magnitude of the signal, ω is the source signal frequency and ϕ is the phase fluctuation. Both A and ϕ are stochastic whereas Z_0 and ω is constant. The log-magnitude of the received signal over an interval of about 40 seconds is shown in Fig. 1. There are frequent brief drop-outs which may be 30 dB below the mean signal level. (The 0 dB level, which is determined by the value of Z_0 , is arbitrary in this and subsequent figures.) The phase fluctuations (referred to as simply the phase) for the corresponding time interval are shown in Fig. 2.

The real and imaginary parts of the received signal have identical and independent Gaussian distributions. Using the real and imaginary parts as the plot axes, the data is distributed symmetrically about the origin as shown in Fig. 3. This distribution is as expected in the saturated regime[7]. The variance of the signal magnitude is 6 dB and the phase fluctuations span several cycles, which is in agreement with measurement of Daigle et al[8].

4. Phase-Magnitude Relationship

When examined on time intervals of only a few seconds, the phase appears to vary most rapidly when the signal level is near a minimum and to be more steady when the signal level is near a peak. To demonstrate this phase-magnitude relationship, the derivative of the phase is estimated by simple finite difference, the absolute value of this estimate is averaged for 0.25 s, and the negative of the result is compared to with the signal magnitude. The result, scaled and vertically displaced for convenient comparison, is shown in Fig. 4. overlaid with the magnitude data for a 2.5 s time interval. The vertical scale is linear signal magnitude in arbitrary units and the horizontal scale is time in seconds. The two curves are similar, while not in perfect agreement, and the correlation coefficient is 0.7.

The correlation coefficient calculated for each 5 second interval over a period of 200 seconds is plotted in Fig. 5. Similar results are obtained for data at other

frequencies, with the correlation generally being between 0.6 and 0.8, indicating that the phase-magnitude relationship is valid and is persistent.

5. The Complex Logarithm Plot

It is instructive to plot the phase as a function of signal magnitude. The complex logarithm of the (complex) varying signal $Z = \exp(A + i\phi)$ is defined as $A + i\phi$, where both A and ϕ are real. In Fig. 6 the complex log of the signal for a 2.5 second time interval is shown, with the log-magnitude on the horizontal axis and the (unwrapped) phase on the vertical axis. Each dot on the plot is a single data point. The evolution of the signal can be seen by tracing adjacent dots. On the right side of the plot, corresponding to higher signal levels, horizontal levels are evident. On the left side, corresponding to lower signal levels, are smooth arching curves which join up the horizontal levels.

Considering the density of the dots in the plot, the signal remains for some time at a single 'level' in the curve and then rapidly moves to another level. Figure 7 shows a 10 second interval of data plotted in the same format. The horizontal levels and the smooth arches are still very evident, although the plot is much more cluttered.

Another feature of the plot is the similarity between the arches. Although they extend to different low-signal levels, they tend to have similar phase width. In fact, the arches correspond to the signal drop-outs observed in Fig. 1 and they usually span a phase shift of about half a cycle (π radian).

The phase changes quickly near the apex of the arches. Based on the spacing of the sample points in the complex-log plots, the rate of change in phase can be about 125 radians per second, or 20 Hz. This agrees well with the observed bandwidth of the measured data.

6. Statistical Basis for the Phase-Magnitude Relationship

Although the average signal to noise ratio (SNR) for the test data is about 20 dB, it is greatly reduced during the brief signal dropouts. To investigate the possibility that noise is responsible for the apparent characteristic form of the complex logarithm plots, Gaussian noise was added to the signal. In principle, if the added noise is similar to the existing noise in the data, then as the level of added noise is increased, the characteristic form of the complex logarithm plot should evolve in some sort of consistent manner.

The effect of adding Gaussian noise 25 dB less than the RMS signal level is illustrated in Fig. 8. The smooth curves (as in Fig. 6) become jagged, especially at lower signal levels. As the added noise level is increased, the jaggedness increases but the other characteristics of the curve remain essentially unaltered. This suggests that random, uncorrelated noise does not play a significant role in generating the characteristic form of the complex logarithm observed in the received data.

Considering the signal as a point travelling randomly on the complex plane (as in Fig. 3) we have seen that its probability distribution is Gaussian in both the real and imaginary parts; however, the probability distribution alone does not determine the *evolution* of the signal. It is the higher order statistics which determine this evolution and any possible phase-magnitude relationships.

To illustrate this point, consider a complex noise with uncorrelated Gaussian real and imaginary parts (just like the observed data). The plot of the real versus imaginary parts of this noise will look somewhat like Fig. 3 (without the filament character) but the plot of the complex logarithm, shown in Fig. 9, has little resemblance to the observed data (note the different scale on the phase axis).

The uncorrelated Gaussian noise has a unit-impulse autocorrelation function; by altering this autocorrelation, it is possible to generate noise which follows a smoother track, both in the complex plane and in the complex logarithm plots. A synthetic noise signal was generated by applying a random phase to the magnitude spectrum of the measured data, resulting in a Gaussian noise with exactly the same autocorrelation function as the measured data. Figure 10 shows the complex logarithm plot for this synthetic signal and it resembles the corresponding plot for the observed signal. It thus appears that the autocorrelation of the measured data (and not noise) is responsible for the observed characteristics. Since the autocorrelation is determined by the structure and dynamics of the propagation channel, the signal characteristics are evidently due to the properties of the atmospheric turbulence.

7. Time Between Drop-outs

The magnitude data was examined to estimate the time duration between signal drop-outs. For this analysis, a drop-out is defined to be an interval during which the signal is more than 10 dB below the average log-magnitude signal level. Figure 11 shows a histogram of the time between drop-outs for a 3 minute data segment. There are 203 drop-outs and the average time between them is 0.8 seconds.

Similar calculations were done for 100 Hz and 1000 Hz signals, giving average time between drop-outs of 6.1 and 0.3 seconds respectively. This suggests that the duration roughly scales with the wavelength of the signal.

8. Simulated Sound Field

The Fast-PE [9-11] was used to simulate the sound field deep within a refractive shadow. The turbulence was modelled as an isotropic homogenous 2-dimensional Gaussian field with strength $\langle \mu^2 \rangle = 2 \times 10^{-6}$ and correlation length $l = 1.1$ m. A logarithmic velocity profile of the form $1 - (a/c_0) \ln(z/0.0006)$ was used, where $c_0 = 340$ m/s and z is in meters. A moderately strong upward refraction profile was modelled using $a = 2$ m/s. The signal frequency was 500 Hz and the range was 900 m. A single turbulence field was shifted longitudinally from source to receiver in steps of 0.1 m, with the sound field re-calculated at each step. The resulting phase and magnitude plots are shown in Fig. 12. The time scale is based on a drift in the turbulence of 1 m/s.

The phase and magnitude plots resemble those of the measured data (Figs. 1 and 2) except that the time scale appears to be somewhat expanded. (This discrepancy is presumed to reflect deficiencies in the atmospheric model.) Drop-outs are clearly visible in the magnitude plot and the jumps in phase are coincident with the drop-outs.

The complex-log of the simulated data is shown in Fig. 13. The characteristic horizontal levels joined by smooth arches are apparent. Just as in the measured data, the arches span approximately half a cycle in phase.

Qualitative agreement between the experiment and simulation data further validates the ability of the Fast-PE and similar propagation codes to accurately predict properties of the sound field within a refractive shadow [11].

9. Summary

For propagation through a turbulent atmosphere, the sound field in a refractive shadow exhibits frequent brief signal drop-outs and coincident rapid changes in phase. The phase change across signal drop-outs is typically about 180 degrees. The rate of change of phase during signal drop-outs determines the bandwidth of the received signal from a monochromatic source. This bandwidth, as measured for the test signal of 500 Hz, was about 40 Hz (20 Hz on either side of the center frequency). The long-term statistics of the (complex) signal follows a Gaussian

distribution. Random complex Gaussian data, with the same autocorrelation as the measured signal, exhibits similar characteristics. The interval between signal drop-outs was 0.8 s for the 500 Hz signal and varies approximately linearly with signal wavelength. Simulations using the Fast-PE with an isotropic Gaussian turbulence model in an upward refracting atmosphere exhibit phase and magnitude fluctuations similar to the measured data.

10. Acknowledgment

The authors would like to acknowledge the cooperation of the Gatineau Gliding Club and the use of their property for the experiments.

References

- [1] /Bass'91/ H. E. Bass, L. N. Bolen, R. Raspet, W. McBride, and J. Noble, "Acoustic propagation through a turbulent atmosphere: experimental characterization," *J. Acoust. Soc. Am.* **90**, 3307-3313 (1991).
- [2] /Blanc-'92/ Ph. Blanc-Benon, Y. Hugon-Jeannin and D. Juvé, "Reconstruction de fronts d'onde distordus par la turbulence", (in French) *J. de Physique IV*, Colloque C1, supp. au *J. de Physique III*, Vol. 2, C1-545, April 1992.
- [3] /Havel'92/ D. I. Havelock, M. R. Stinson, and G. A. Daigle, "Investigation of sound field coherence in a refractive shadow," *Proc. 5th International Symposium on Long Range Sound Propagation*, Milton Keynes, England, 24-26 May 1992 (The Open University, Milton Keynes, England, 1992), pp. 239-248.
- [4] /Juve'92/ D. Juvé, Ph. Blanc-Benon and P. Chevret, "Numerical simulations of sound propagation through a turbulent atmosphere," *Proc. 5th International Symposium on Long Range Sound Propagation*, Milton Keynes, England, 24-26 May 1992 (The Open University, Milton Keynes, England, 1992), pp. 282-296.
- [5] /Noble'92/ J. M. Noble, "The effect of large-scale atmospheric inhomogeneities on acoustic propagation," *J. Acoust. Soc. Am.* **92**, 1040-1046 (1992).

- [6] /Wilson'93/ D. Keith Wilson, "Acoustic tomographic monitoring of the atmospheric surface layer," Proc. 5th International Symposium on Long Range Sound Propagation, Milton Keynes, England, 24-26 May 1992 (The Open University, Milton Keynes, England, 1992), pp. 249-262.
- [7] /Dashen'79/ R. Dashen, "Path integrals for waves in random media," J. Math. Phys **20**, 894-921 (1979).
- [8] /Daigle'86/ G. A. Daigle, T. F. W. Embleton, and J. E. Piercy, "Propagation of sound in the presence of gradients and turbulence near the ground," J. Acoust. Soc. Am. **79**, 613-627 (1986).
- [9] /Gilbert'93/ K. E. Gilbert and X. Di, "A fast Green's function method for one-way sound propagation in the atmosphere," J. Acoust. Soc. Am. **94**, 2343-2352 (1993).
- [10] /Di'92/ X. Di and K. E. Gilbert, "Application of a fast Green's function method to long range sound propagation in the atmosphere," Proc. 5th International Symposium on Long Range Sound Propagation, Milton Keynes, England, 24-26 May 1992 (The Open University, Milton Keynes, England, 1992), pp. 128-146.
- [11] /Havel'94a/ D. I. Havelock and X. Di, "Comparison of the spatial coherence in a refractive shadow as calculated using measurement and simulation data," Presented at 127th meeting of the Acoust. Soc. Am., Boston MA, 6-10 June, 1994.

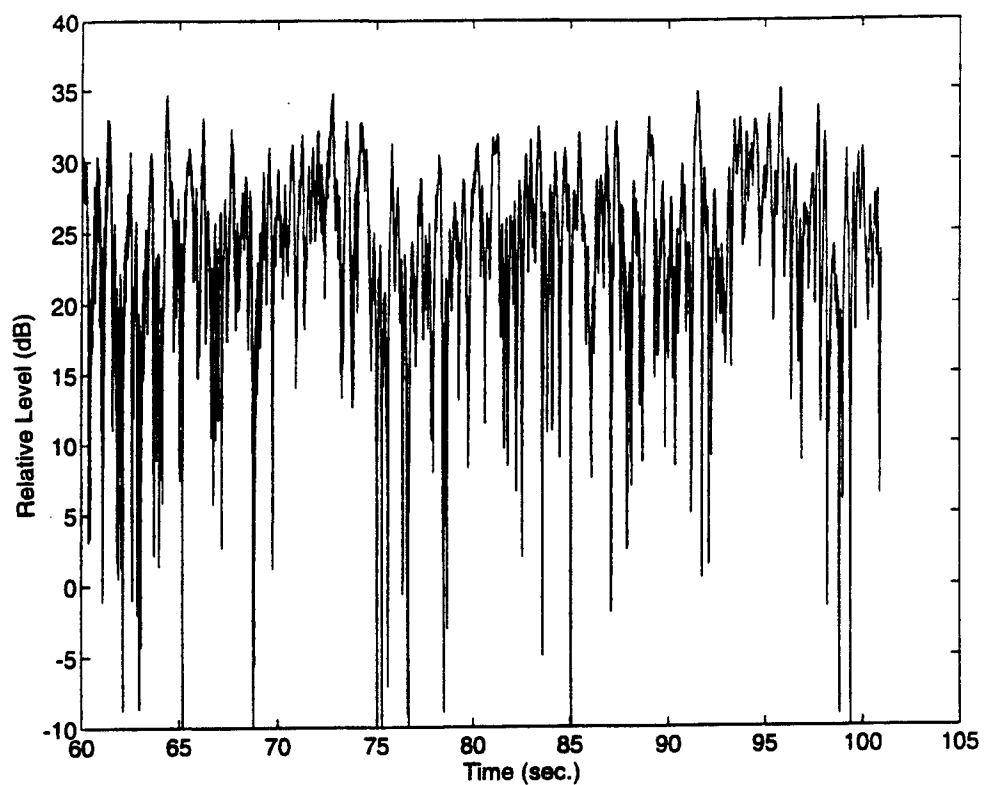


Figure 1
Log-magnitude of the received signal. The test signal is 500 Hz and the range is 700 m. (The 0 dB level is arbitrary.)

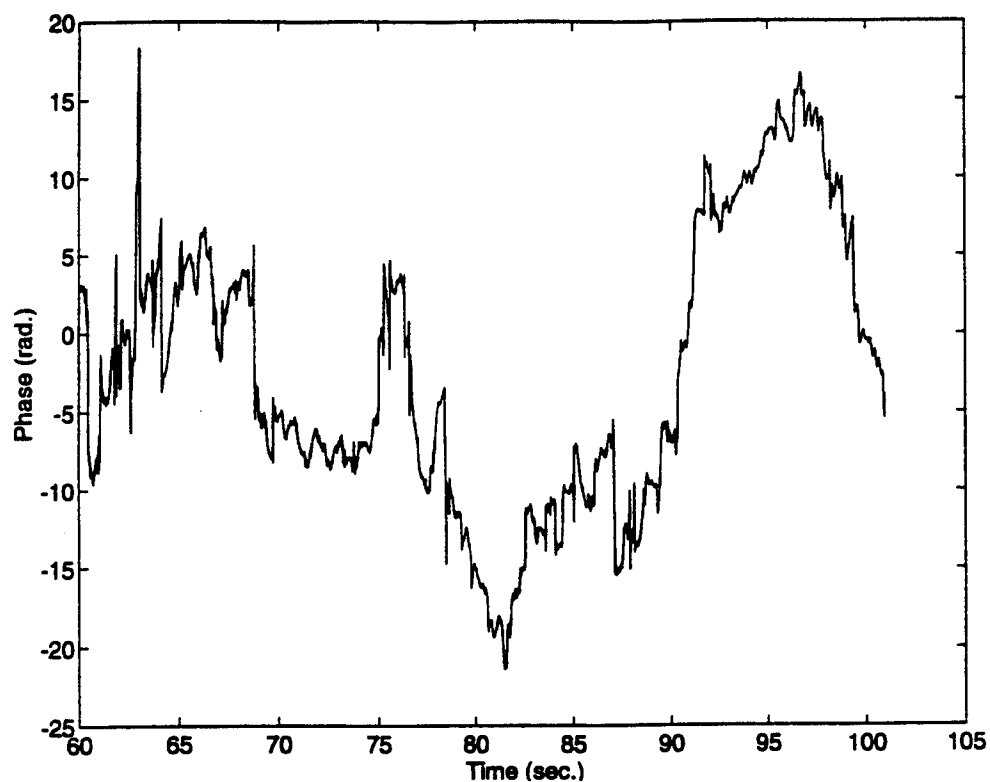


Figure 2
Phase variations in the received signal. The test signal is 500 Hz and the range is 700 m.

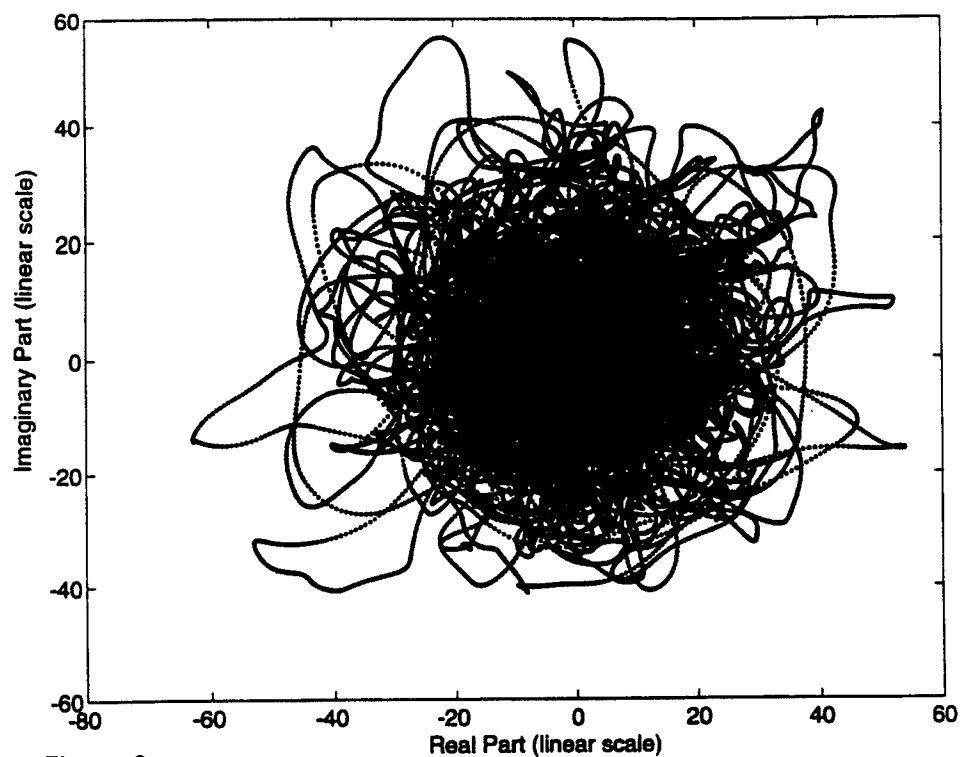


Figure 3
Distribution of data on complex plane. Real and imaginary parts have identical Gaussian distributions. (The units are arbitrary.)

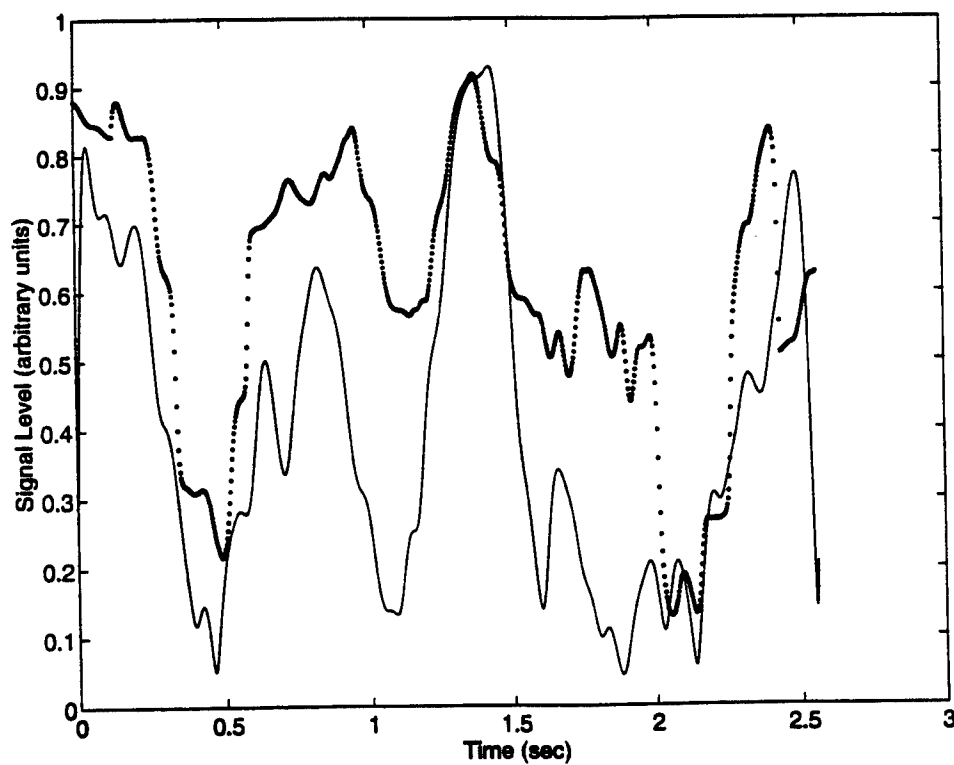


Figure 4
Magnitude and phase relationship. The smoothed, negated, absolute value of the gradient of the phase (dotted curve) is scaled and overlaid on the magnitude (solid curve).

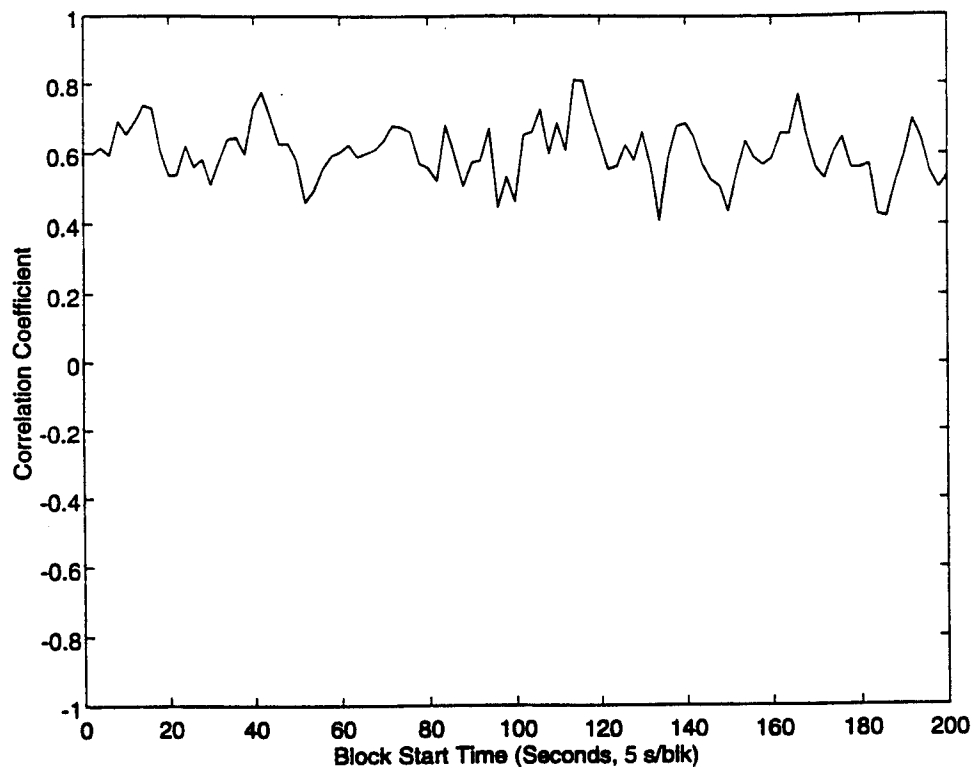


Figure 5

Correlation coefficient for the magnitude and phase relationship. Using the relationship demonstrated in Fig. 4, the correlation is calculated for each 5 seconds of a 200 second time interval.

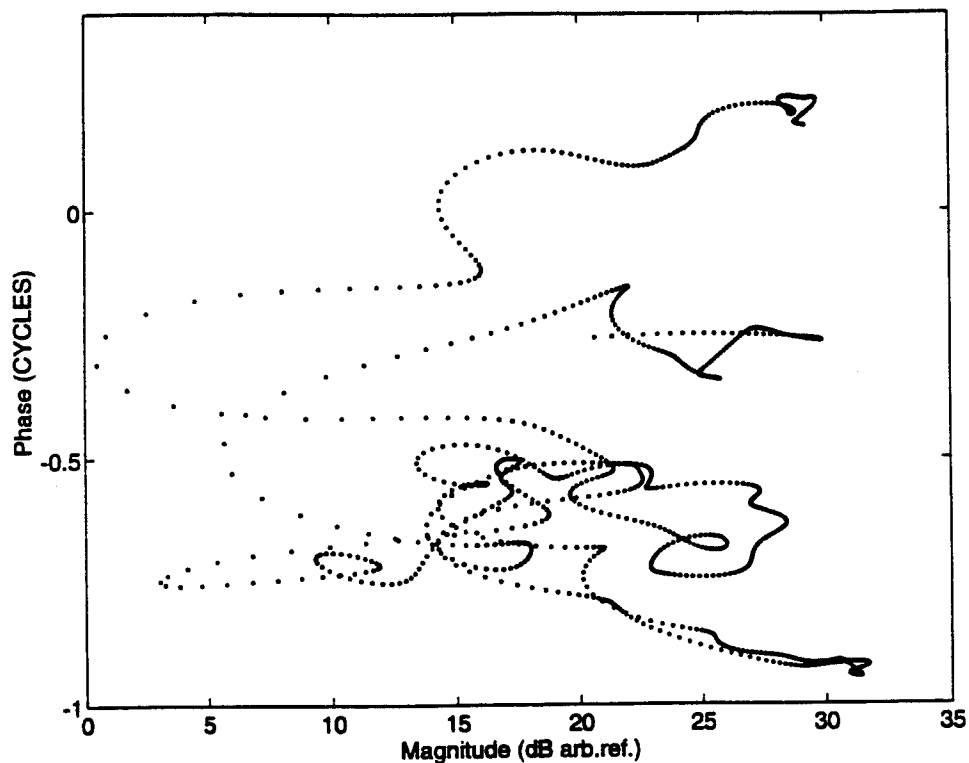


Figure 6

Complex logarithm for 2.5 seconds of data. The (unwrapped) phase is plotted as a function of the log-magnitude. The characteristic horizontal structure and the smooth arching curves are evident. Each dot is a sample point and the sampling rate is 400 samples/second. The signal frequency is 500 Hz.

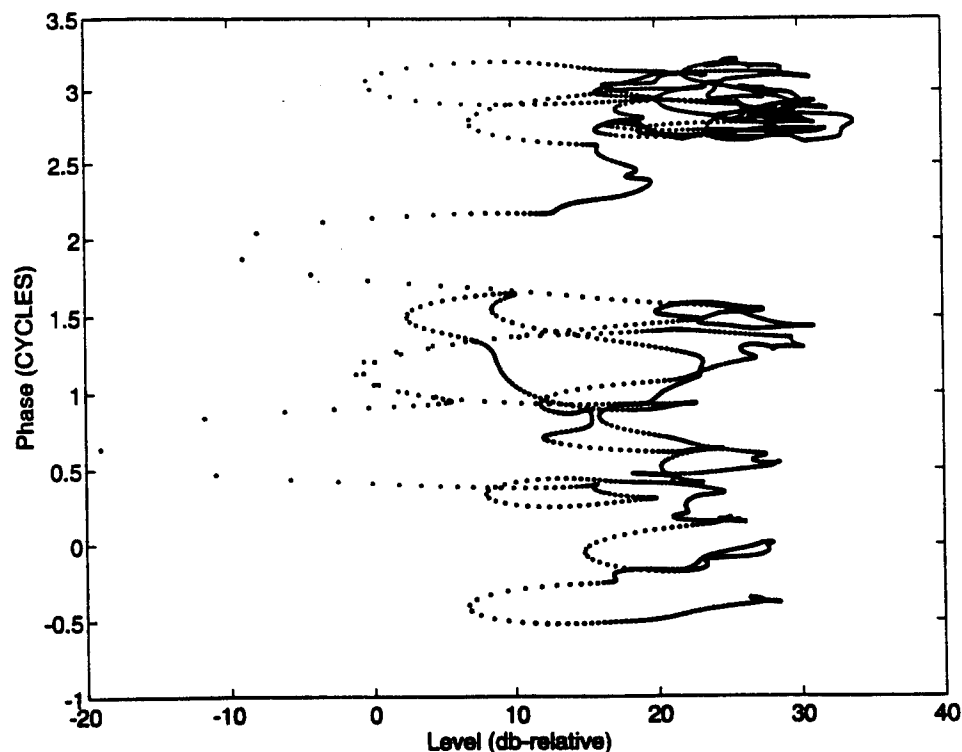


Figure 7

Complex logarithm for 10 seconds of data. As for Fig. 6, horizontal levels and smooth arches are evident. Many arches have a similar width — about half a cycle. Phase variations between drop-outs (arches) are small.

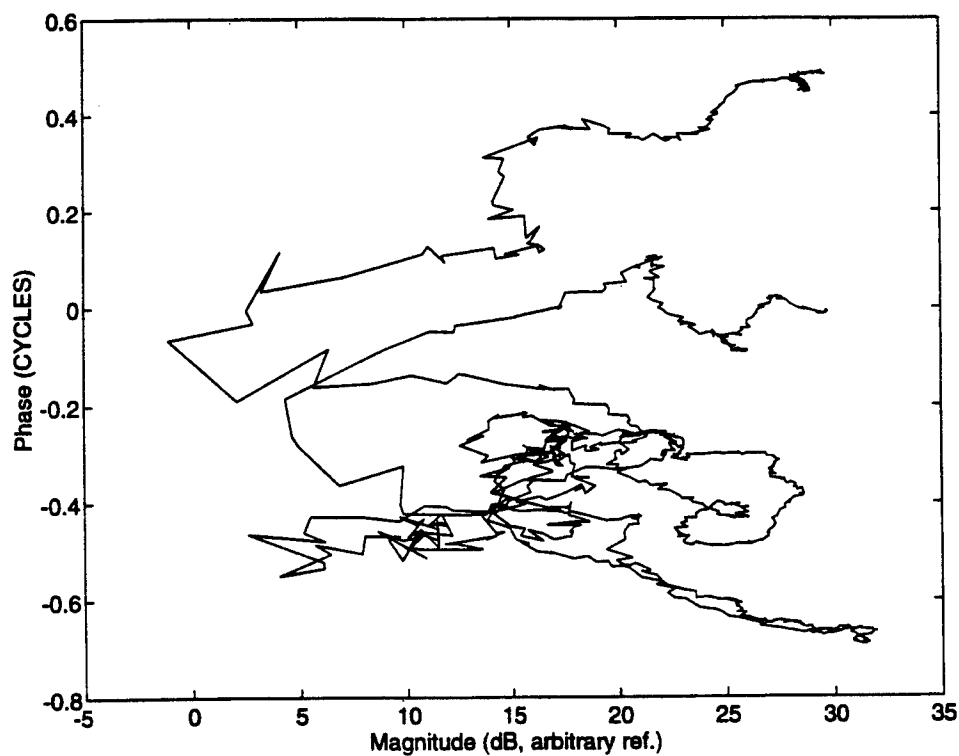


Figure 8

A small amount of Gaussian noise is added to the received signal. The noise is 25 dB below the RMS signal. It causes the data to form a jagged curve. (Compare with Fig. 6.)

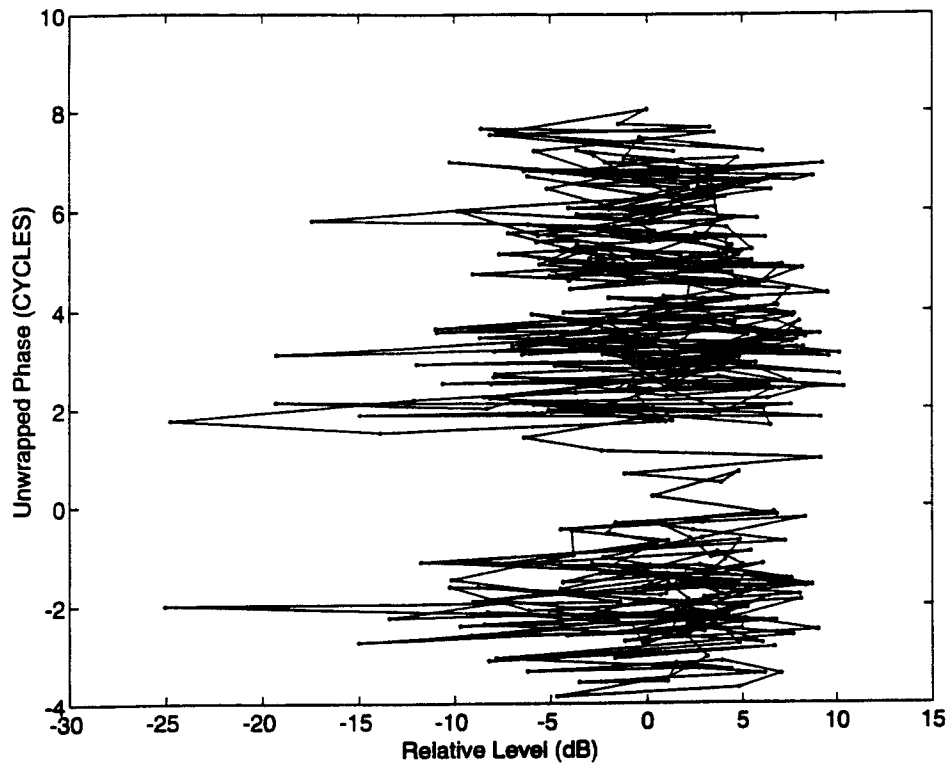


Figure 9

Uncorrelated (complex) Gaussian data bears little resemblance to the received signal. The probability distribution does not determine the characteristics of the signal. Higher order statistics must be considered.

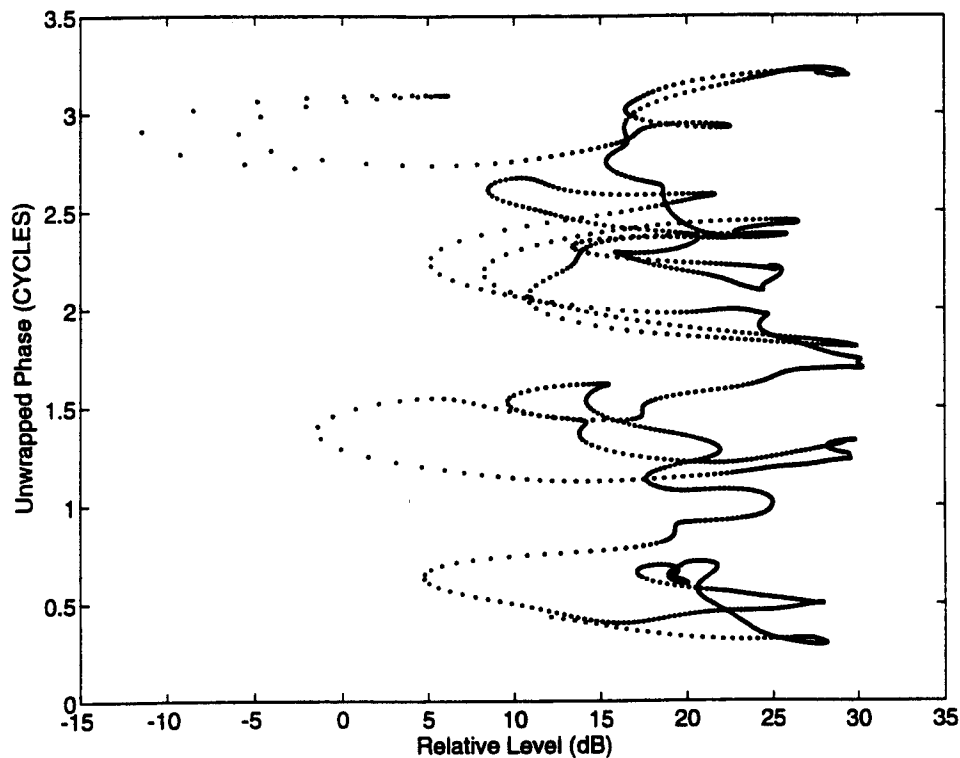


Figure 10

Complex logarithm of a synthesized signal based on the autocorrelation (or power spectrum) of the received signal. By matching all first and second order statistics, the characteristics of the signal can be synthesized.

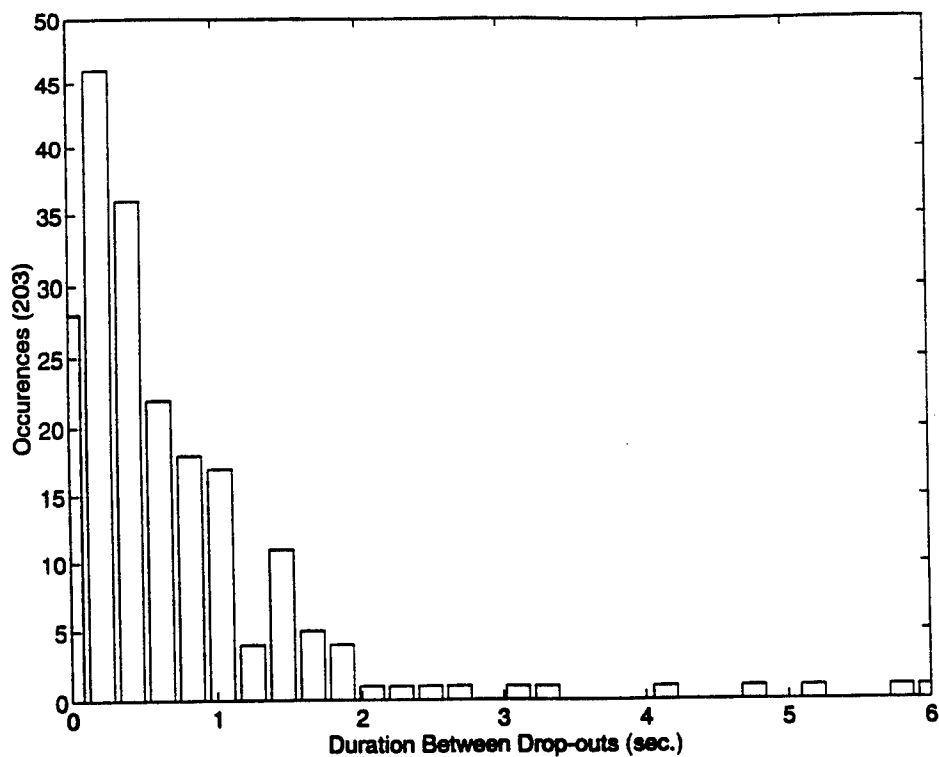


Figure 11
Histogram of time duration between signal drop-outs. Based on a 180 second time interval with 203 drop-outs, the average time between drop-outs is 0.8 seconds for the 500 Hz test signal.

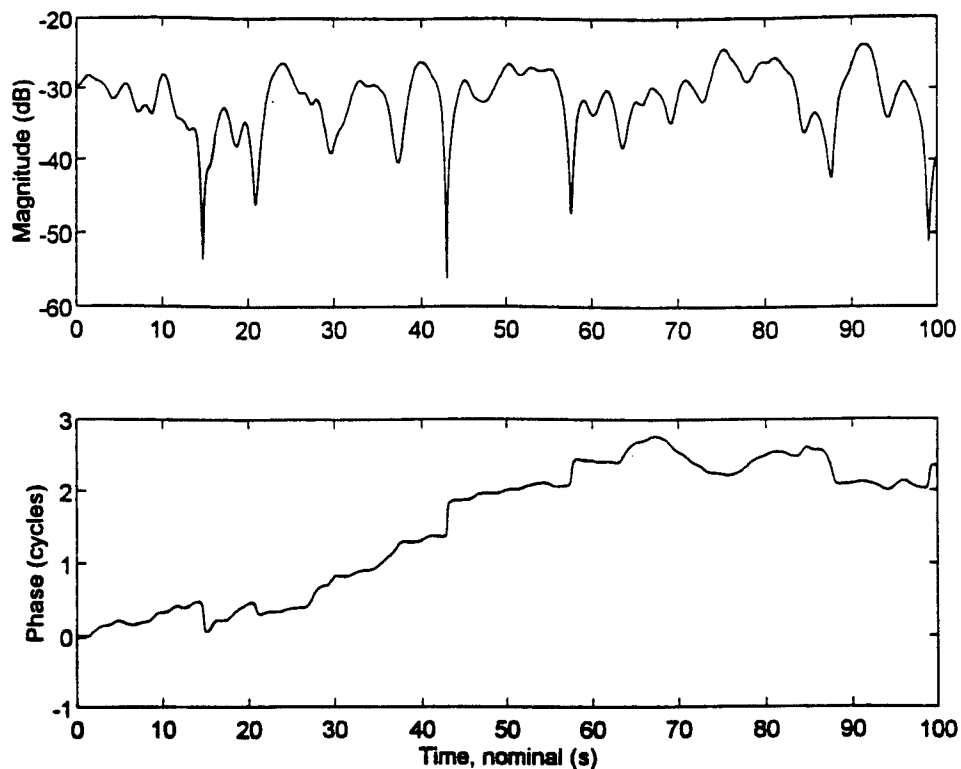


Figure 12
Simulated sound field phase and magnitude. The steps in phase correspond to the drop-outs in the magnitude. The drop-outs occur less frequently and are more gradual than for the measured data.

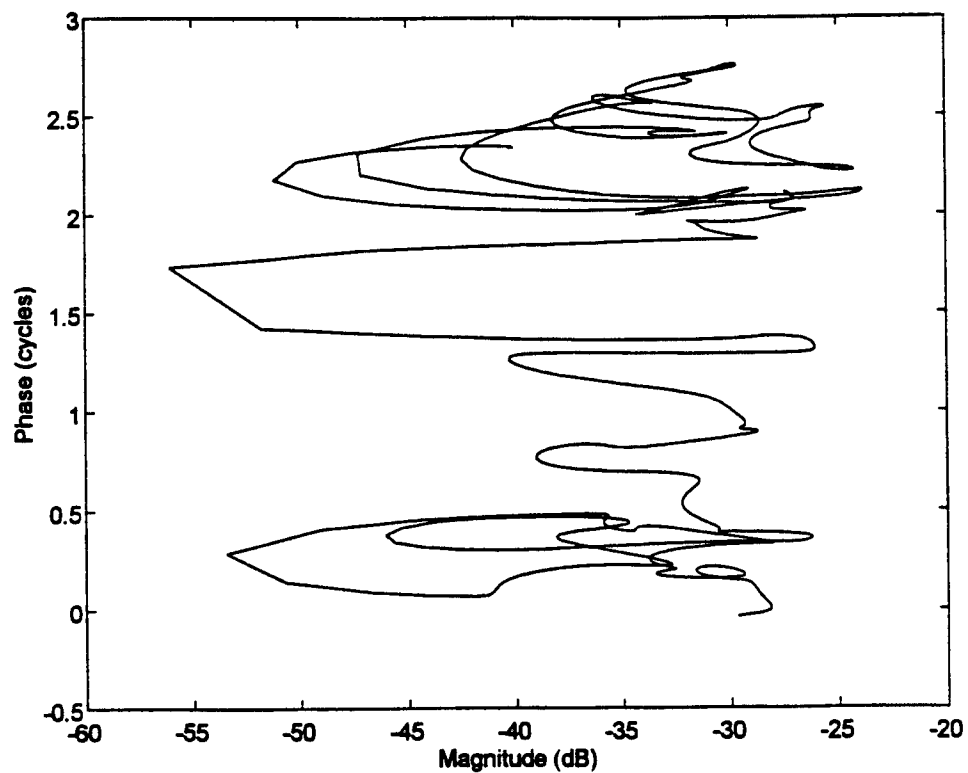


Figure 13
Complex logarithm of the simulated sound field. The characteristics of the curves are similar to those of the received data.

Abstract

PROPAGATION OF LOW FREQUENCIES IN THE PRESENCE OF A SOUND SPEED GRADIENT

A.J. Cramond and C.G. Don

Department of Physics

Monash University

Victory, Australia.

Impulse propagation measurements have been used to investigate the formation of a shadow zone due to the presence of a sound speed gradient. Creeping wave theory grossly underpredicts the experimental levels obtained outdoors deep within the shadow zone. The linear gradient assumption in the creeping wave theory and/or turbulent scattering into the shadow zone have been suggested as the explanation of the discrepancy. Experimental results taken using two sources of different pulse amplitude and duration have been obtained for both upwind and downwind propagation. These have been analysed in terms of the relative attenuation with distance of the individual frequency components. After comparison with both creeping wave and neutral atmosphere theory, a relatively simple model is proposed which allows both pulse shape and amplitude to be correctly predicted at distances beyond 100m from the source.

A new approach in predicting sound propagation outdoors

K M Li, S Taherzadeh and K Attenborough

Engineering Mechanics Discipline

Faculty of Technology

The Open University

Milton Keynes

United Kingdom

(I) Abstract

A new method is presented in this paper that allows an accurate calculation of the sound propagation in a moving stratified atmosphere. With the use of the method of Fourier transformation, we generalize from the case of a homogeneous medium to a moving stratified medium. The sound field can be represented by a two-fold Fourier integral that can be estimated by the method of stationary phase. It is found that the acoustical path length is identical to the classical ray-tracing procedure. However, Fermat's principle of least time is not required in our method but it is implied by the asymptotic evaluation of the integral. The present approach also leads to a modified Snell Law in a moving stratified medium that is particularly useful in tracing the ray trajectory.

In this paper, we develop an analytic expression for the direct sound field in a moving stratified atmosphere and show that how the present theory and the classical ray-tracing procedure can result in the same expression. Finally, we outline a new numerical scheme for the prediction of sound propagation outdoors.

(II) Formulation of the problem

Let a monopole source of strength V_s be situated at $(0,0,z_s)$ in a horizontally stratified medium such that the field properties (*e.g.* velocity and density, *etc.*) only depend on the vertical distance, z . The angular frequency of the source is ω_s . Further, we ignore the effect of gravity and assume that the wavelength of acoustic disturbances are much smaller than the characteristic length scale and the characteristic time scale for the medium. Use of the continuity and momentum equations, we can express the governing wave equation as¹

$$\frac{1}{\rho} \nabla \cdot (\rho \nabla \phi) - \frac{D}{Dt} \left(\frac{1}{c^2} \frac{D\phi}{Dt} \right) = V_s \delta(x) \delta(y) \delta(z - z_s) e^{-i\omega_s t} \quad (1)$$

where $\frac{D}{Dt}$ and ∇ are the total and spatial derivatives given by

$$\frac{D}{Dt} = \frac{\partial}{\partial t} + \mathbf{u} \cdot \nabla$$

$$\nabla = \left(\frac{\partial}{\partial x}, \frac{\partial}{\partial y}, \frac{\partial}{\partial z} \right) .$$

We note that, in Eq. (1), x , y , z , and t are the independent variables, ρ is the mean density of air, c is the speed of sound, and the velocity potential ϕ is the dependent wave field amplitude to which the acoustics pressure is related by

$$p = -\rho \frac{D\phi}{Dt} \quad (2)$$

We use $\mathbf{u} = (u_r, u_z)$ to designate the mean velocity field through which the disturbances propagate. The horizontal velocity u_r can further be resolved into two components (u_x, u_y) along the x - and y -axes. The subscripts r and z denote the horizontal and vertical components respectively. In order to simplify the analysis, we ignore the vertical flow velocity, *i.e.* $u_z = 0$, as it is small in comparison with the horizontal component.

Equation (1) may be solved by the method of Fourier transformation. Introduce the Fourier transform pair for the acoustic pressure in the horizontal plane,

$$p = \frac{1}{(2\pi)^3} \int_{-\infty}^{\infty} \int_{-\infty}^{\infty} \int_{-\infty}^{\infty} \hat{p} e^{-i(\omega t - k_x x - k_y y)} dk_x dk_y d\omega \quad (3)$$

where

$$\hat{p} = \int_{-\infty}^{\infty} \int_{-\infty}^{\infty} \int_{-\infty}^{\infty} p e^{i(\omega t - k_x x - k_y y)} dx dy dt \quad (4)$$

and a similar transform for the velocity potential from ϕ to $\hat{\phi}$. Then Eqs. (1) and (2) become

$$\frac{1}{\rho} \frac{d}{dz} \left(\rho \frac{d\hat{\phi}}{dz} \right) + [(\omega_m/c)^2 - k_x^2 - k_y^2] \hat{\phi} = 2\pi V_s \delta(z - z_s) \delta(\omega - \omega_s) \quad (5)$$

$$\hat{p} = i\rho\omega_m \hat{\phi}, \quad (6)$$

where

$$\omega_m = \omega - k_x u_x - k_y u_y. \quad (7)$$

The variable ω_m may be interpreted as the 'convected' angular frequency as opposed to the 'stationary' angular frequency, ω_s . For convenience, we introduce a variable P such that

$$P = i\sqrt{\rho} \hat{\phi}. \quad (8)$$

Substitution of Eq. (8) into Eq. (5) leads to

$$\frac{d^2 P}{dz^2} + k_0^2 Q^2 P = 2\pi i \sqrt{\rho} V_s \delta(z - z_s) \delta(\omega - \omega_s), \quad (9)$$

where

$$Q = \sqrt{\frac{(\omega_m/c)^2 - k_x^2 - k_y^2 + [-(\rho''/2\rho) + (\rho'/2\rho)^2]}{k_0}} \quad (10)$$

It is important to note that the sign of Q is chosen so that it is either positive real or negative imaginary in order to ensure a finite and bounded solution for Eq. (9) and, in turn, for the acoustic pressure. The expression given in Eq. (9) is not new but a similar result has been reported by Nijs and Wapenaar.²

We also remark that the form of Q given in Eq. (10) appears to be different from the result given by Li.³ A close examination reveals that both expressions are equivalent. Basically, in Ref. 3, Eq. (6) was used to replace $\hat{\phi}$ with \hat{p} . By rewriting P in terms of \hat{p} , ρ and ω_m :

$$P = \hat{p} / \sqrt{\rho} \omega_m , \quad (11)$$

we can then arrive at the same second order differential equation, *cf.* Eq. (9), with Q given by

$$Q = \sqrt{\frac{(\omega_m / c)^2 - k_x^2 - k_y^2 + [\vartheta_1 - \vartheta_2]}{k_0}} \quad (12)$$

where $\vartheta_1 = \frac{f''}{2f} - \frac{3}{4} \left(\frac{f'}{f} \right)^2 , \quad (13)$

$$\vartheta_2 = \frac{(\sqrt{\rho f})''}{\sqrt{\rho f}} - \frac{f'}{f} \frac{(\sqrt{\rho f})'}{\sqrt{\rho f}} , \quad (14)$$

$$f = \rho \omega_m^2 . \quad (15)$$

However, if we expand Eqs. (13) and (14) and express ϑ_1 and ϑ_2 in terms of ρ , then we can show that

$$\vartheta_1 - \vartheta_2 = -(\rho''/2\rho) + (\rho'/2\rho)^2 . \quad (16)$$

Thus Eqs. (10) and (12) are identical but the form for Q given in Eq. (10) is more revealing because of its relatively simple form. In view of the density variation in atmosphere is usually small, we can ignore the terms involving ρ'' and ρ'^2 in Eq. (10).

Hence, Q can be approximated by

$$Q \approx \sqrt{\frac{(\omega_m / c)^2 - k_x^2 - k_y^2}{k_0}} \quad (17)$$

There is a considerable problem for solving Eq. (9) to give an exact analytical expression for P . Rather we resort to an approximate scheme that will lead to a simplified solution yet sufficient to yield an accurate expression for the total sound field. The WKB method seems to be more appropriate among other approximate schemes because we are primarily interested in the high frequency analysis. By imposing the boundary condition of the ground surface, we can derive an expression for sound propagation outdoors in the presence of an impedance plane. However, the derivation of this formula has been described elsewhere³ and will not be repeated here. We restrict our attention to the direct wave because the reflected wave has exactly the same form but they are only different by a multiplicative factor, a spherical wave reflection coefficient. It suffices just to 'trace' the direct wave in this paper. Consequently we concentrate on the problem where there are no boundary surfaces in the vicinity of the source and receiver and the sound field is outgoing as $z \rightarrow \pm\infty$ (the so-called Sommerfeld radiation condition).

The WKB solution for Eq. (9) is well-known⁴ and is given in the form of

$$\hat{p} = \frac{\pi \delta(\omega - \omega_s)}{k_0 \sqrt{Q Q_s}} \left(\frac{f}{f_s} \right)^{1/2} e^{ik_0(L_s - L_r)}, \quad (18)$$

where
$$L_{s,r} = \int_0^{z_s, z_r} Q(Z) dZ \quad (19)$$

$$z_> = \max(z, z_s) \quad (20)$$

$$z_< = \min(z, z_s) \quad , \quad (21)$$

f is given by Eq. (15) and the subscript s denotes the ambient variables evaluated at $z = z_s$. We note that the source strength, V_s , [see Eq. (9)] is assumed to be $-i/\rho_s \omega_s$ so that the sound pressure in a homogeneous medium can be reduced to

$$p = \exp[-i(\omega_s t - kR)] / 4\pi R \quad ,$$

where R is the separation between the source and receiver. In addition, the term $\exp[ik_0(L_> - L_<)]$ corresponds to the outgoing wave, whilst the incoming wave term $\exp[-ik_0(L_> - L_<)]$ is suppressed in Eq. (18) because of the Sommerfeld radiation condition.

Substitution of Eq. (18) into Eq. (3) and the evaluation of the outer integral with respect to ω leads to

$$p = \frac{i}{4\pi^2} \int_{-\infty}^{\infty} \int_{-\infty}^{\infty} \frac{e^{i[k_0(L_> - L_<) + k_x x + k_y y]}}{2k_0 \sqrt{Q Q_s}} \left(\frac{f}{f_s} \right)^{1/2} dk_x dk_y \quad (22)$$

The above integral may be estimated by the method of stationary phase.⁵ The analysis can be simplified considerably if we use a spherical polar co-ordinate system such that each wave front normal has a constant azimuthal angle, ϵ , but its elevation angle, μ , varies as a function of the vertical height, z . We point out that the elevation angle is measured from the vertical z axis and the azimuthal angle from the x axis. With the new co-ordinate system, we can write the horizontal wave number, k_x , and k_y , as^{4,6}

$$k_x = k_0 \sin \mu_0 \cos \epsilon \quad ; \quad k_y = k_0 \sin \mu_0 \sin \epsilon \quad (23)$$

and $dk_x dk_y = k_0^2 \cos \mu_0 \sin \mu_0 d\mu_0 d\varepsilon$, (24)

where the subscript 0 denotes the field variables at $z = 0$. We choose $z = 0$ as our reference plane in Eq. (22). Without loss of generality, we assume the receiver is situated on the x -axis with the co-ordinate of $(r, 0, z)$.

The convected angular frequency, ω_m is related to the stationary angular frequency, ω by⁵

$$\omega_m = \frac{\omega}{1 + M \cos(\varepsilon - \psi_w) \sin \mu} , \quad (25)$$

where M is the Mach number of the flow given by

$$M = u / c$$

with the horizontal velocity (u_x, u_y) expressed in its corresponding polar co-ordinate form as (u, ψ_w) . Thus one may rewrite Q as,

$$Q = \sqrt{m^2 - \sin^2 \mu_0} \quad (26)$$

where $m = \frac{n}{1 + M \cos(\varepsilon - \psi_w) \sin \mu}$, (27)

$$n = \frac{k}{k_0} . \quad (28)$$

Additionally, the direction of propagation for the wavefront varies as a function of z according to⁷

$$\sin \mu_0 = m \sin \mu = \text{constant} . \quad (29)$$

Here, in Eqs (26) and (29), m may be identified as the index of refraction in a moving stratified medium and n as that in a stationary medium. This definition agrees with the analysis that is based on the dispersion law.⁸ The index of refraction, m , is modified by a Doppler factor,

$$D = (1 + M \cos(\epsilon - \psi_w) \sin \mu)^{-1} \quad (30)$$

in a moving medium and m is reduced to n provided that the mean velocity of the medium is zero. Furthermore, we may express f [see Eq. (15)] as

$$f = \frac{\rho \omega^2}{[1 + M \cos(\epsilon - \psi_w) \sin \mu]^2} \quad (31)$$

We may now express the Fourier integral in the spherical polar co-ordinate^{4,6} as,

$$p = \frac{ik_o}{4\pi^2} \int_{-\pi/2+i\infty}^{\pi/2-i\infty} \cos \mu_0 \sin \mu_0 d\mu_0 \int_{-\pi/2}^{\pi/2} g(\mu, \epsilon) e^{ik_o R_L(\mu, \epsilon)} d\epsilon, \quad (32)$$

where
$$g(\mu, \epsilon) = \frac{\sqrt{f/f_s}}{2\sqrt{m \cos \mu} \sqrt{m_s \cos \mu_s}}, \quad (33)$$

and
$$R_L(\mu, \epsilon) = (L_s - L_c) + r \sin \mu_0 \cos \epsilon. \quad (34)$$

The variable, R_L , may be regarded as the acoustical path length and it has units of length.

By expanding the integrand at the saddle point and integrating term by term,³ we can evaluate the integral in Eq. (32) asymptotically. The saddle point is determined by setting, simultaneously, $\partial R_L / \partial \epsilon$ and $\partial R_L / \partial \mu_0$ to zero. Before we proceed to determine the saddle point, it is useful to obtain the following identities,

$$\frac{\partial \mu}{\partial \epsilon} = -\frac{M \sin^2 \mu \sin(\epsilon - \psi_w)}{\cos \mu} \quad (35)$$

$$\text{and} \quad \frac{\partial \mu}{\partial \mu_0} = \frac{\cos \mu_0}{n \cos \mu} \times [1 + M \cos(\epsilon - \psi_w)]^2, \quad (36)$$

that can be derived by differentiating Eq. (29) with respect to ϵ and μ_0 . It is then straightforward to show that the stationary point for the acoustical path length can be determined by

$$r \cos \psi = \int_{z_c}^{z_s} \frac{\sin \theta + M \cos(\psi - \psi_w)}{\cos \theta} dZ \quad (37)$$

$$\text{and} \quad r \sin \psi = \int_{z_c}^{z_s} \frac{M \sin(\psi - \psi_w)}{\cos \theta} dZ, \quad (38)$$

where θ and ψ are, respectively, the required polar angle and the azimuthal angle of the wave front normal. As pointed out by Ostashev,⁷ the angles of wave front normal (θ and ψ) do not correspond to the trajectory of the sound ray connecting the source and receiver. This fact is evinced by considering Eqs. (37) and (38). Obviously, the wave front normal and the ray trajectory of the sound ray do not coincide in a moving medium. Noting the receiver position at $(r, 0, z)$, one may use the traditional ray trace approach as described by, for example, Ostashev⁷ or Thompson⁸, to obtain

$$r = \int_{z_c}^{z_s} \frac{\sin \theta \cos \psi + M \cos \psi_w}{\cos \theta} dZ \quad (39)$$

$$\text{and} \quad 0 = \int_{z_c}^{z_s} \frac{\sin \theta \sin \psi + M \sin \psi_w}{\cos \theta} dZ \quad (40)$$

With the use of Eq. (40), we can show that Eq. (39) can be converted to either Eq. (37) or Eq. (38). It is reassuring to start from the present approach and to result in the same expressions as the traditional ray trace. It is sometimes more convenient to use the

polar angle, α of the ray trajectory rather than that of the wave front normal, θ . Equations (37) and (38) can be transformed, in favour of α , to

$$r \cos \psi = \int_{z_0}^{z_1} \cos \xi \tan \alpha dZ \quad (41)$$

and
$$r \sin \psi = \int_{z_0}^{z_1} \sin \xi \tan \alpha dZ \quad , \quad (42)$$

where ξ is the azimuthal angle of the ray trajectory measured from the wave front normal, *i.e.* measured from ψ . We can then verify that the angles ξ and α must satisfy

$$\cos \xi = \left[1 + \frac{M^2 \sin^2(\psi - \psi_w)}{[\sin \theta + M \cos(\psi - \psi_w)]^2} \right]^{-1/2} \quad (43)$$

and
$$\cos \alpha = \frac{\cos \theta}{\sqrt{1 + 2M \cos(\psi - \psi_w) \sin \theta + M^2}} \quad . \quad (44)$$

The angles, ξ and α , agree with that derived by Ostashev.⁷ We can also eliminate ψ from the left hand side of Eqs. (41) and (42) to give

$$r = \int_{z_0}^{z_1} \cos(\xi - \psi) \tan \alpha dZ \quad . \quad (45)$$

If the angles of the wave front, θ and ψ , have been determined, then the acoustical path length at the stationary point, R'_1 , is given by

$$R'_1 = R_l(\theta, \psi) \quad . \quad (46)$$

Use of Eqs. (27), (29), (34), (43) and (44), we can show that

$$R'_1 = \int_{R_0}^{R_1} m \hat{a}_n \cdot \hat{a}_t dR_n \quad (47)$$

where R_n is the arc length of the ray with R_0 and R_1 denoting the initial and final points along the ray path. In addition, \hat{a}_n and \hat{a}_t are, respectively, the unit vector of the wavefront normal and the trajectory of the ray where

$$\hat{a}_n \cdot \hat{a}_s = \cos \alpha \cos \theta + \cos \xi \sin \alpha \sin \theta \quad (48)$$

The acoustical path length given in Eq. (47) is identical to the result derived from the Eikonal method.⁹ It is obvious that R'_1 is stationary with respect to infinitesimal variations in the acoustical path length as required by the method of stationary phase. This is consistent with Fermat's principle of least time.^{7,9} We remark that there are two typographical errors in Ref. 3 [his Eqs. (55) and (58)] which have been corrected as shown in Eqs (45) and (47) respectively.

With the above evaluation at the stationary point, we may now derive the asymptotic expression for the direct sound field. The details of the derivation are described in Ref. 3 and the asymptotic solution for the acoustic pressure is

$$p = \frac{S_d e^{ik_0 R'_1}}{4\pi\sqrt{|J_d|}} \quad (49)$$

where the stratification factor, S_d , and the Jacobian factor, J_d , are given by

$$S_d = \frac{D}{D_s} \sqrt{\frac{\rho}{\rho_s}} \sqrt{\frac{\cos \theta_0}{m \cos \theta}} \sqrt{\frac{\cos \theta_0}{m_s \cos \theta_s}} \quad (50)$$

$$J_d = \left(\frac{1}{\sin \mu_0} \right)^2 \left\{ \frac{\partial^2 R_L}{\partial \mu_0^2} \frac{\partial^2 R_L}{\partial \epsilon^2} - \left[\frac{\partial^2 R_L}{\partial \mu_0 \partial \epsilon} \right]^2 \right\} \bigg|_{\mu=\theta, \epsilon=\psi} \quad (51)$$

with

$$\frac{\partial^2 R_L}{\partial \theta^2} = -\cos^2 \theta_0 \left[\int_0^{z_s} - \int_0^{z_i} \right] \left(\frac{n^2}{m^3 \cos^3 \theta} \right) dZ \quad ,$$

$$\frac{\partial^2 R_L}{\partial \psi^2} = -\sin^2 \theta_0 \left[\int_0^{z_s} - \int_0^{z_i} \right] \left(\frac{1}{m \cos \theta} + \frac{M^2 \sin^2(\psi - \psi_w) \sin^2 \theta_0}{m^3 \cos^3 \theta} \right) dZ \quad ,$$

$$\frac{\partial^2 R_L}{\partial \theta \partial \psi} = \cos \theta_0 \sin \theta_0 \left[\int_0^{z_s} - \int_0^{z_i} \right] \left(\frac{nM \sin(\psi - \psi_w) \sin \theta_0}{m^3 \cos^3 \theta} \right) dZ \quad .$$

The Doppler factors, D and D_s , are evaluated at the receiver and source respectively [c.f. Eq. (30)]. We remark that the Jacobian factor is different from that derived by Ostashev by a factor of $k_0^2 \cos^2 \theta_0$ as a result of different definitions for the Jacobian factor. However the direct sound field given in Eq. (49) is identical to that given by Ostashev.⁷

(III) Concluding remarks

The principal objective of this investigation was to develop a rigorous method for the calculation of the sound propagation in a moving stratified atmosphere. It was demonstrated that the sound field can be expressed as a Fourier integral. The total sound field was estimated by the method of stationary phase which resulted in a closed form analytic solution. Such an analytical approximation has clear advantages in computational requirements and physical understanding for routine application in predicting sound propagation outdoors.

Nevertheless, we emphasize that Eqs. (41), (42) and (45) may be used to trace the ray path. The polar angles of the wave front normal at different heights are given by Eq. (29). The polar angle at a reference point, θ_0 say, is used to relate the corresponding angle at different heights. Consequently, θ_0 and ψ are the only variables in Eqs. (41) and (42) and these angles can be solved simultaneously by standard numerical methods. We can then use Eq. (29) and the known values for θ_0 and ψ to give the polar angle at different heights. One may then use Eq. (47) to evaluate the phase angle and Eqs. (50) and (51) to give the amplitude of the sound wave, *i.e.* the sound field for the direct wave. Using a similar approach and the details in Ref. 3, we can also calculate the sound field due to the reflected wave with the inclusion of the ground wave term. However, the

present contribution is limited to production of the new formula. Future publications will be concerned with numerical comparisons.

Acknowledgments

The work reported in this paper is supported by the EPSRC, UK. ST and KA acknowledge receipt of travel grant from NRC, Canada for attending the Sixth International Symposium of Long Range Sound Propagation.

References

1. A D Pierce, "Wave equation for sound in fluids with unsteady inhomogeneous flow," J. Acoust. Soc. Am. **87**, 2292-2299 (1990).
2. L Nijs and C P A Wapenaar, "The influence of wind and temperature gradients on sound propagation, calculated with the two-way wave equation," J. Acoust. Soc. Am. **87**, 1987-1998 (1990).
3. K M Li, "A high-frequency approximation of sound propagation in a stratified moving atmosphere above a porous ground surface," J. Acoust. Soc. Am. **95**, 1840-1852, (1994).
4. L M Brekhovskikh, Waves in Layered Media, (Academic Press, New York, 1980).
5. M J Lighthill, Waves in fluids, (Cambridge University Press, Cambridge, 1978).
6. K M Li, "On the validity of the heuristic ray-trace-based modification to the Weyl-Van-der Pol formula," J. Acoust. Soc. Am. **93**, 1727-1735 (1993).
7. V E Ostashev, "Theory of sound propagation in an inhomogeneous moving medium," Izv. Atmos. Oceanic Phys. **21** (4), 274-285 (1985).
8. R J Thompson, "Ray-acoustic intensity in a moving medium," J. Acoust. Soc. Am. **55**, 729-732, (1974).
9. P Uginčius, "Ray acoustics and Fermat's principle in a moving inhomogeneous medium," J. Acoust. Soc. Am. **51**, 1759-1763, (1972)

Abstract

ESTIMATION OF LINEAR SOUND SPEED GRADIENTS ASSOCIATED TO GENERAL METEOROLOGICAL CONDITIONS

A. L'Espérance

Groupe d'Acoustique de l'Université de Sherbrooke
Département de génie mécanique
Université de Sherbrooke, Sherbrooke (Quebec) J1K 2R1

G.A. Daigle

Institute for Microstructural Sciences
National Research Council
Ottawa ON K1A 0R6

Y. Gabillet

Centre Scientifique et Technique du Bâtiment
24 rue Joseph Fourier
38400 Saint-Martin d'Hères, France

In a recent paper, an heuristic acoustical model for outdoor sound propagation has been presented (L'Espérance et al., Appl. Acoust. 37 (1992) 111-139). This model however assumes a linear sound speed profile. The aim of this paper is to present a method to estimate this linear sound speed profile according to general meteorological conditions. This evaluation is done in two steps. First the sound speed profile (SSP) and fluctuating index of refraction ($\langle \mu^2 \rangle$) are estimated according to the general meteorological conditions. In a second step, the linear sound speed profile is evaluated based on the fact that the zone of the space concerned with the propagation process is mostly defined by the first Fresnel ellipsoid. To verify the validity and limitation of this approach, various acoustical and meteorological measurements of the noise emitted by strong and steady sources of an industrial plant have been done during the summer 93. Three results obtained show the accuracy, usefulness and limitations of the model. Comparison and analysis with other experimental results also show that the weakness of the whole model is the prediction of the effective sound speed profile from the general meteorological conditions rather than the linearisation of the profile.

ESTIMATION OF LINEAR SOUND SPEED GRADIENTS ASSOCIATED WITH GENERAL METEOROLOGICAL CONDITIONS

INTRODUCTION

- 1 - SOUND SPEED PROFILES UNDER GENERAL
METEOROLOGICAL CONDITIONS**
- 2 - EQUIVALENT LINEAR SOUND SPEED GRADIENTS**
- 3 - PRESENTATION OF SOME EXPERIMENTAL RESULTS**
- 4 - CONSIDERATIONS ABOUT THE EFFECT OF THE
TURBULENCE**

CONCLUSION

by A.L'Espérance, G. Daigle and Y. Gabillet

**6th INTERNATIONAL SYMPOSIUM ON
LONG RANGE SOUND PROPAGATION
Ottawa June 12-14, 1994**

TO GET A PRACTICAL AND COMPLETE ACOUSTICAL MODEL FOR ENGINEERING PURPOSES, AN HEURISTIC MODEL HAS BEEN DEVELOPED.(1)

THIS HEURISTIC MODEL:

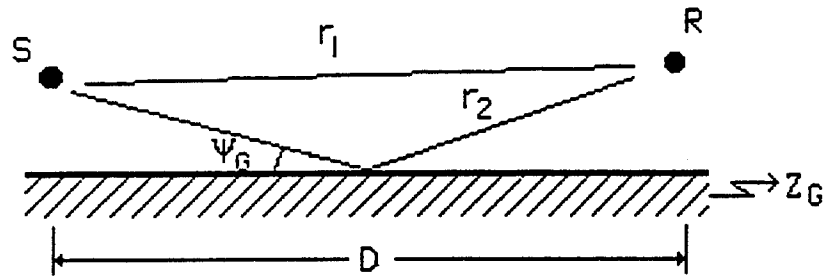
- 1- Based on the the geometrical ray theory**
- 2- Includes the ground effect and the effect of meteorological conditions**
- 3- Fast computation time**
- 4- Supposed a linear sound speed profile.**

(1) L'Espérance et al."Heuristic model for outdoor sound propagation based on an extension of the geometrical ray theory in the case of a linear sound speed profile" Appl. Acoust. 37 p. 111-139 (1992)

Review:

HEURISTIC GEOMETRICAL RAY MODEL(1)

CASE WITHOUT REFRACTION:



$$P(R) = \frac{e^{jkR_1}}{R_1} AT(R_1) + Q \frac{e^{jkR_2}}{R_2} AT(R_2)$$

where $1/R_i \Rightarrow$ geometrical spreading

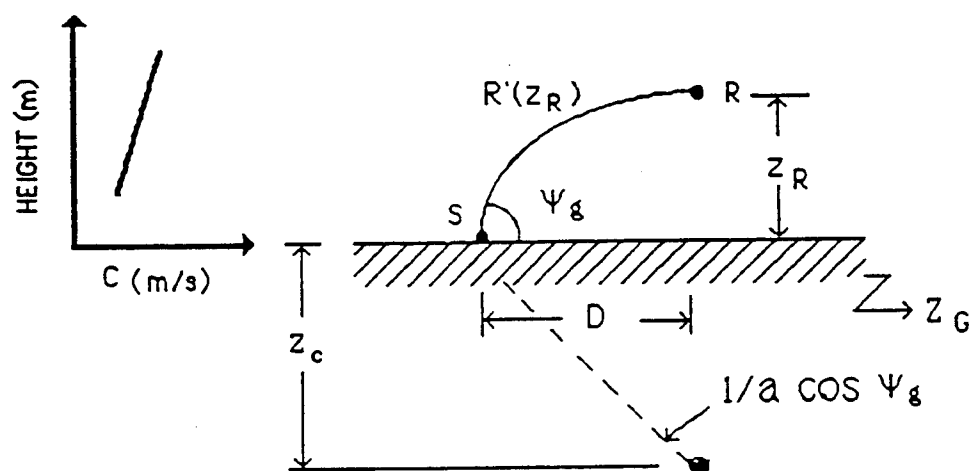
$Q \Rightarrow$ spherical reflection coefficient
 $\Rightarrow R_p + (1 + R_p) * f(w)$

and $AT(R_i) \Rightarrow$ atmospheric absorption (ANSI S1-26)

CONSIDERING A LINEAR SOUND SPEED PROFILE:

$$C(Z) = C_0 * (1 + a Z)$$

THE RAY PATHS ARE CIRCULAR

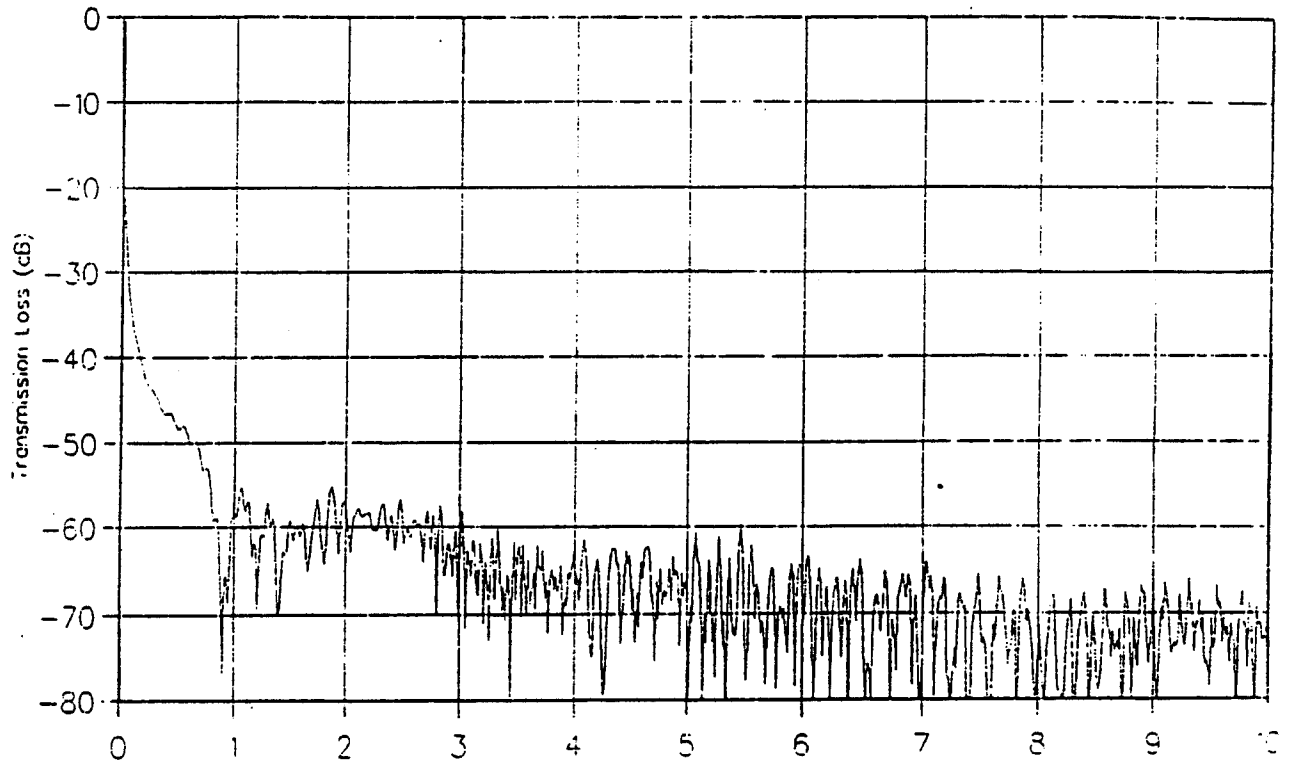


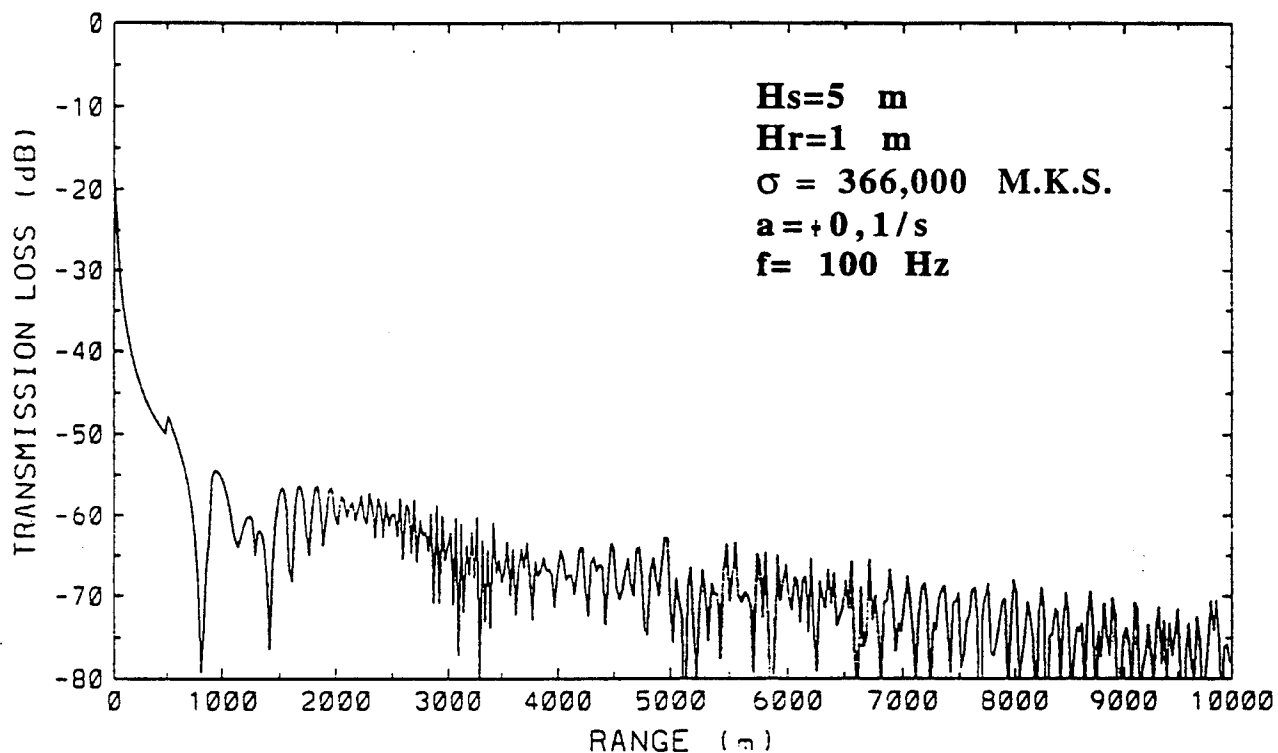
$$\operatorname{tg} \psi_g = \frac{a D}{2} + \frac{z_R(2 + a z_R)}{2 D}$$

$$R(z_R) = \frac{1}{a \cos \psi_g} \left[\sin^{-1} ((1 + a z_R) \cos \psi_g) - \frac{\pi}{2} + \psi_g \right]$$

Brekhovskikh, L.M. " Waves in layered media " Academic Press (1960)

FFP





- (2) K. Attenborough,...A.L'Espérance and others,
"Benchmark Cases for Outdoor Sound Propagation
Models ", accepted for publication in J.A.S.A.

1.0 PREDICTION OF THE SOUND SPEED PROFILES (SSP)

$$c(z) = u(z) \cos(\alpha_w - \alpha_{sr}) + c_o \sqrt{1 + T(z)/273},$$

- WIND PROFILE(1):

$$u(z) = \frac{u_*}{k_a} \left[\ln \frac{z}{z_o} - \psi_m \left(\frac{z}{L} \right) \right]$$

- TEMPERATURE PROFILE:

$$T(z) = T_o + \frac{T_*}{k_a} \left[\ln \frac{z}{z_o} - \psi_h \left(\frac{z}{L} \right) \right]$$

where ψ_m and ψ_h are functions of the Monin-Obukhov length L .

2) PANOFSKI, H.A., DUTTON, J.A. *Atmospheric Turbulence, Models and Methods for Engineering Applications*, John Wiley & Sons inc., 397 p. (1984)

- For $L < 0$ (unstable conditions, day):

$$\psi_h = 2 \ln \left[\frac{1}{2} \left(1 + \sqrt{1 - 16 \frac{z}{L}} \right) \right]$$

and
$$\psi_m = \ln \left[\left(\frac{1 + x^2}{2} \right) \left(\frac{1 + x}{2} \right)^2 \right] - 2 \arctan x + \frac{\pi}{2}$$

where
$$x = (1 - 16 z/L)^{1/4}.$$

- For $L > 0$ (stable conditions, night):

$$\psi_m = \psi_h = -5 \frac{z}{L}$$

The Monin-Obukhov length L corresponds to :

$$L = - \frac{u_*^3 T_0}{k_a g Q}$$

Estimation of L using general meteorological informations:

- 1^o Determination of the Net Radiation Index,
- 2^o Determination of the Turner Classes, and
- 3^o Determination of L based on the relation between the Turner Classes, z_0 and L .

1^o Determination of the Net Radiation Index, N.R.I(3):

- a) Insolation class:
- | | |
|---|-------------------------------|
| 1 | ($60^\circ < a < 90^\circ$) |
| 2 | ($35^\circ < a < 60^\circ$) |
| 3 | ($15^\circ < a < 35^\circ$) |
| 4 | ($0 < a < 15^\circ$) |
- b) Cloud cover:
- | | |
|---|------------------------|
| 1 | ($c < 25\%$) |
| 2 | ($25\% < c < 50\%$) |
| 3 | ($50\% < c < 75\%$) |
| 4 | ($75\% < c < 100\%$) |
- c) Cloud height: (1-low, 2-medium, 3-high)

- 3) PANOFSKI, H.A., DUTTON, J.A. *Atmospheric Turbulence, Models and Methods for Engineering Applications*, John Wiley & Sons inc., 397 p. (1984)

20 Determination of the Turner Classes using:

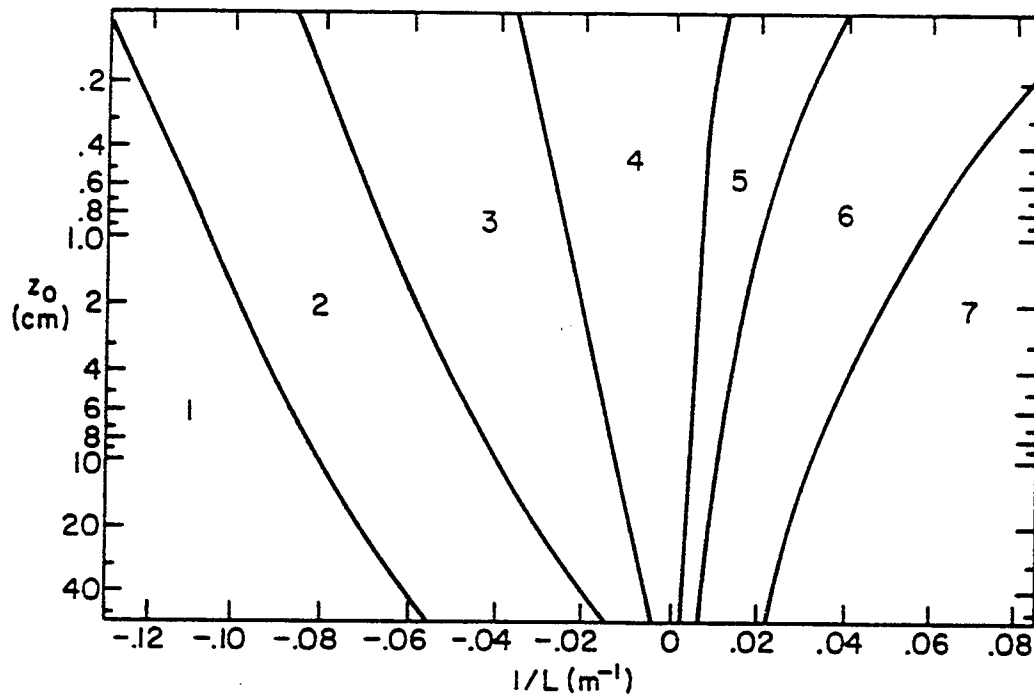
a) N.R.I.

b) Wind velocity

TABLE DEFINITIONS OF TURNER CLASSES

Wind Speed (knots)	Net Radiation Index						
	4	3	2	1	0	-1	-2
0-1	1	1	2	3	4	6	7
2-3	1	2	2	3	4	6	7
4-5	1	2	3	4	4	5	5
6	2	2	3	4	4	5	6
7	2	2	3	4	4	4	5
8-9	2	3	3	4	4	4	5
10	3	3	4	4	4	4	5
11	3	3	4	4	4	4	4
≥ 12	3	4	4	4	4	4	4

3^o Determination of L based on the relation observed by Golder⁽⁴⁾ between the Turner Classes, z_0 and L .

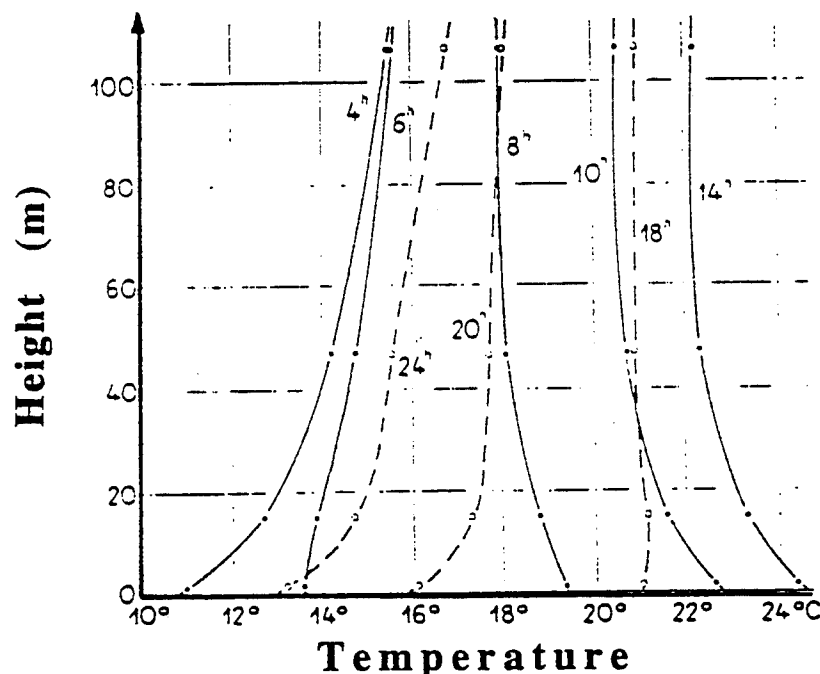


RELATIONS AMONG STABILITY PARAMETERS AND ESTIMATION OF L

- (4) Golder D. (1972) *Relations Among Stability Parameters in the Surface Layer*, *Boundary Layer Meteorol.*, vol. 20, p. 242-249.

DETERMINATION OF THE SCALE TEMPERATURE, T_*

From the experimental results of C. Best(5) about the temperature profiles above the ground:



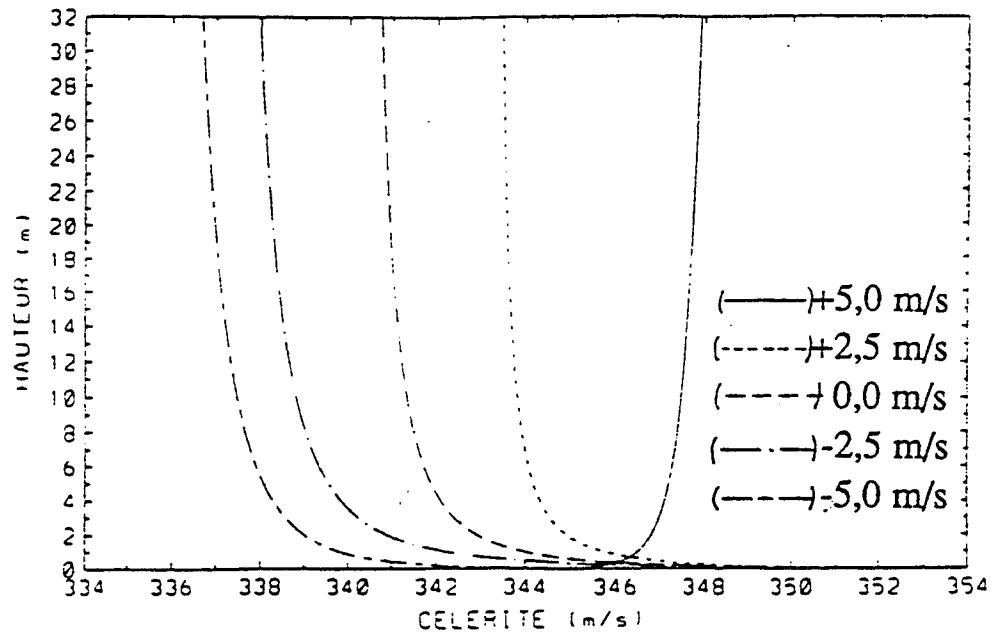
We proposed to estimate the temperature at a giving height from the temperature at 2 m with:

$$T(z) = T(2) + 15(1/L + .006) * \text{Log}(z/2)$$

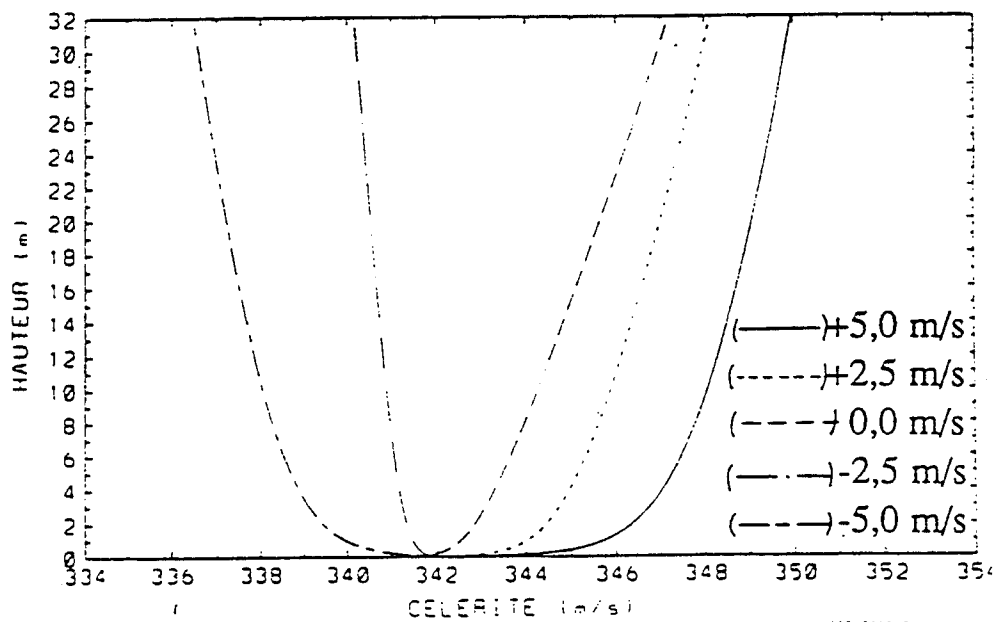
Using this temperature at a second height, it is than possible to estimate the Temperature Scale(5).

(5) L'Espérance, et al. "Sound propagation in the atmospheric surface layer: Comparison of experiment with FFP predictions", Applied. Acoustics 40 p. 325-346 (1993)

CLEAR DAY

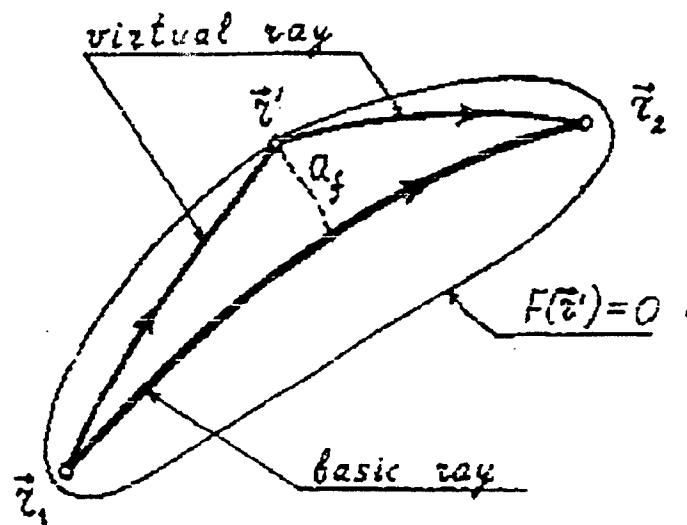


CLEAR NIGHT

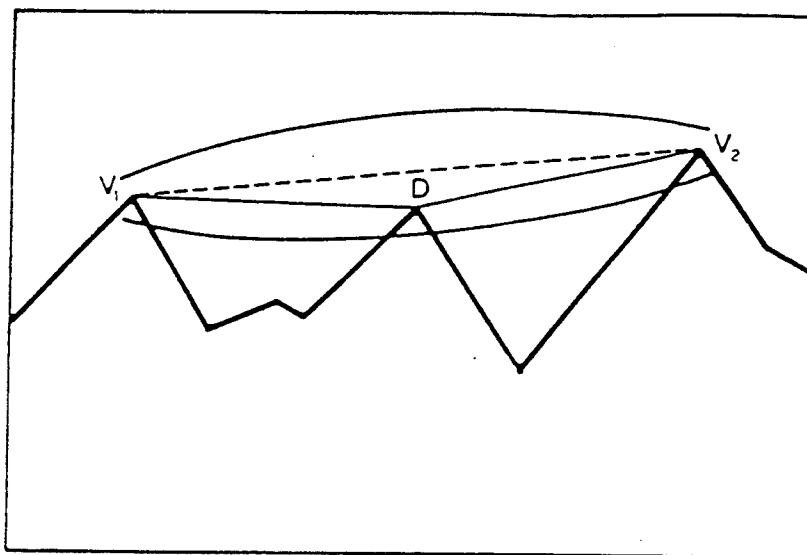


2.0 ESTIMATION OF THE EQUIVALENT LINEAR SSP

From Kravtsov⁽⁶⁾ the characteristics of a wave (amplitude and phase) should vary just slightly over the cross section of the Fresnel volume.

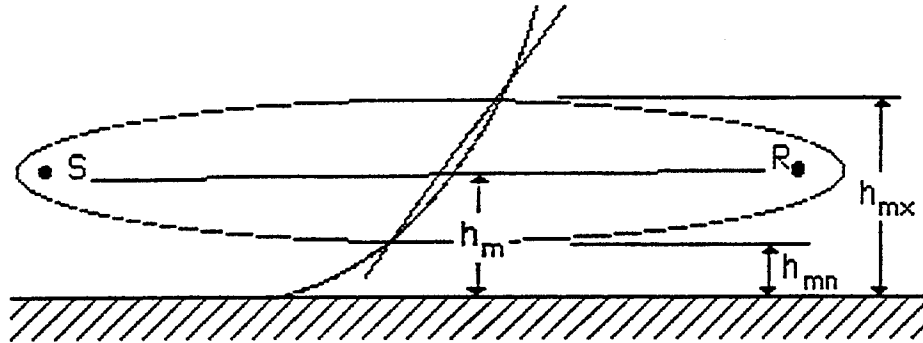


This principle was used by Bisceglia⁽⁷⁾ in electromagnetic wave propagation.



- 6) Kravtsov et al. *Boundaries of geometrical optical Applicability and related problems*, URSI General Assembly, Munich (DBR), (1980)
- 7) Bisceglia, et al. *Symbolic Code Approach to GTD Ray-Tracing*, *IEEE Trans. Antennas and propagation*, vol. 36 n° 36, p.1492,1495 (1988)

Mean linear SSP is estimated by the mean profile in the First Fresnel zone.



$$\frac{\lambda}{2} = r_1 + r_2 - r$$

$$h_F = \sqrt{\frac{\lambda}{4} \left(r + \frac{\lambda}{4} \right)}$$

$$a = \frac{c(h_{mx}) - c(h_{mn})}{c(0)(h_{mx} - h_{mn})}$$

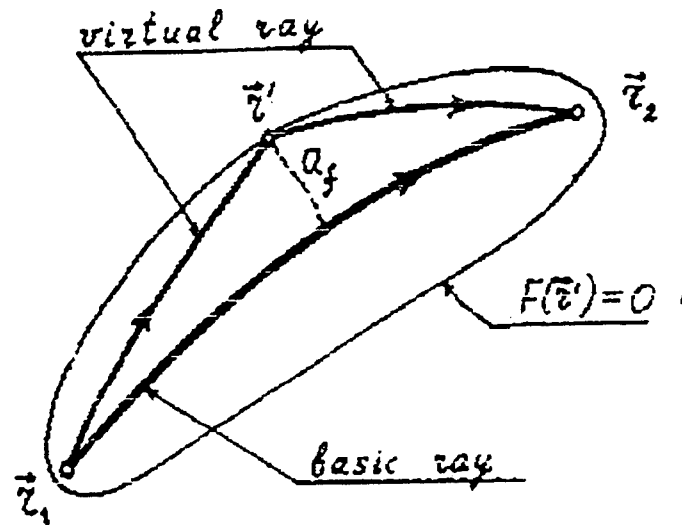
with

$$h_{mn} = h_m - h_F$$

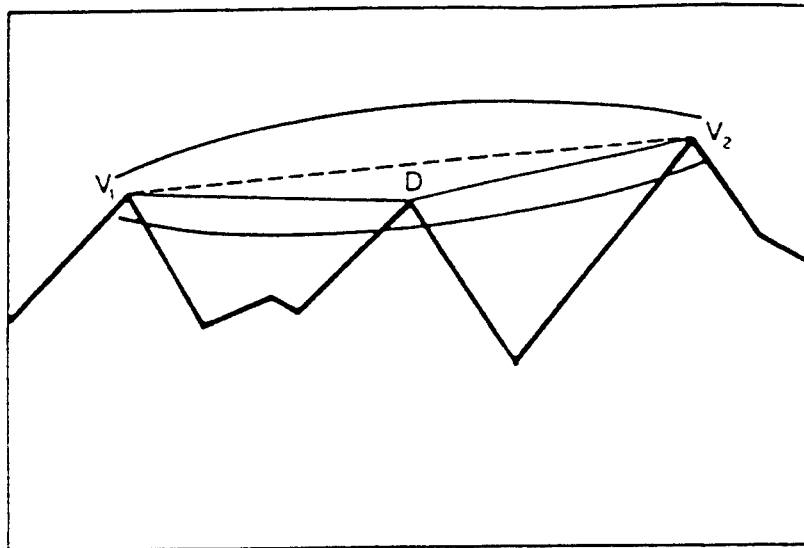
$$h_{mx} = h_m + h_F$$

2.0 ESTIMATION OF THE EQUIVALENT LINEAR SSP

From Kravtsov⁽⁶⁾ the characteristics of a wave (amplitude and phase) should vary just slightly over the cross section of the Fresnel volume.



This principle was used by Bisceglia⁽⁷⁾ in electromagnetic wave propagation.

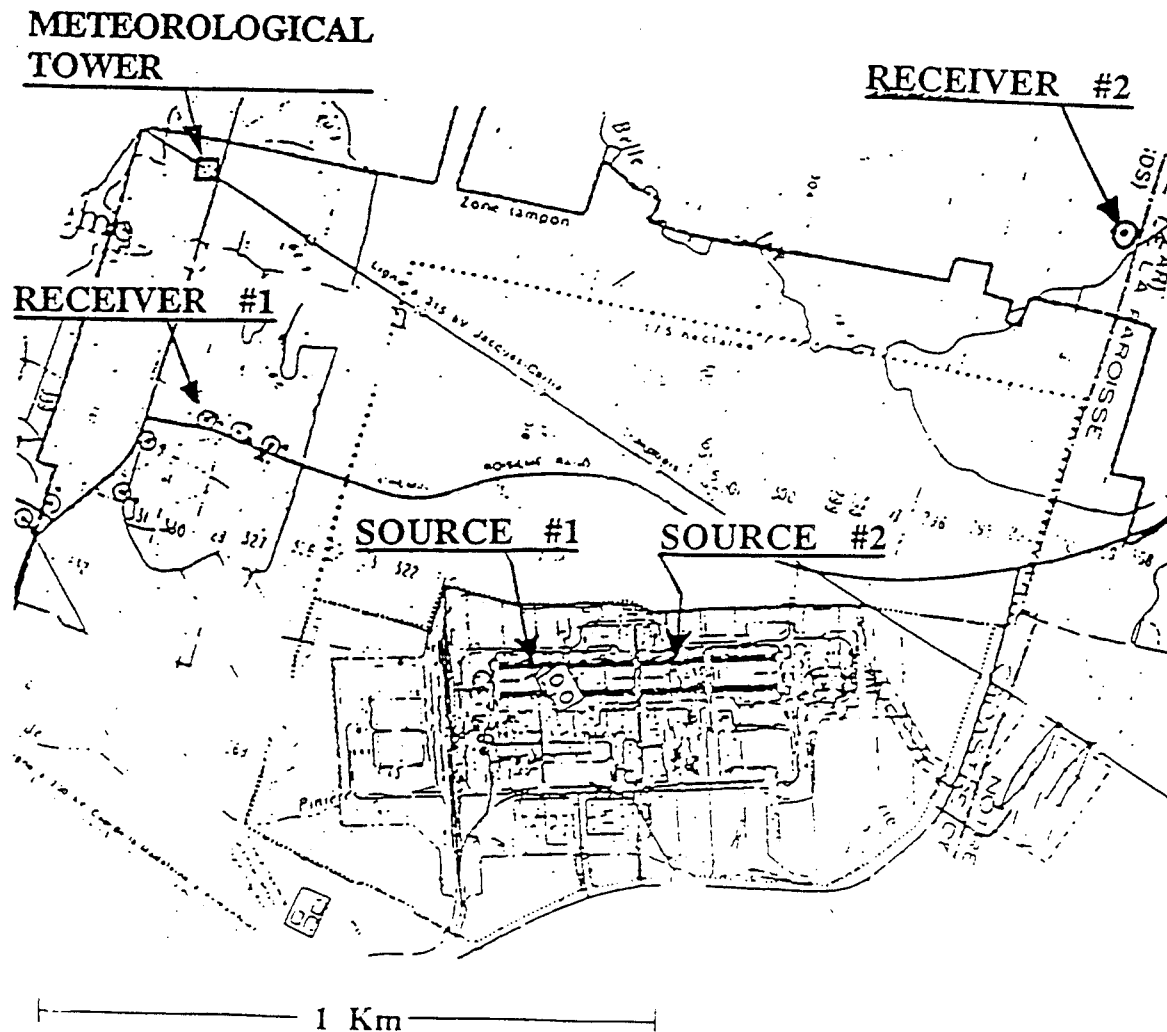


- 6) Kravtsov et al. *Boundaries of geometrical optical Applicability and related problems*, URSI General Assembly, Munich (DBR), (1980)
- 7) Bisceglia, et al. *Symbolic Code Approach to GTD Ray-Tracing*, *IEEE Trans. Antennas and propagation*, vol. 36 n° 36, p.1492,1495 (1988)

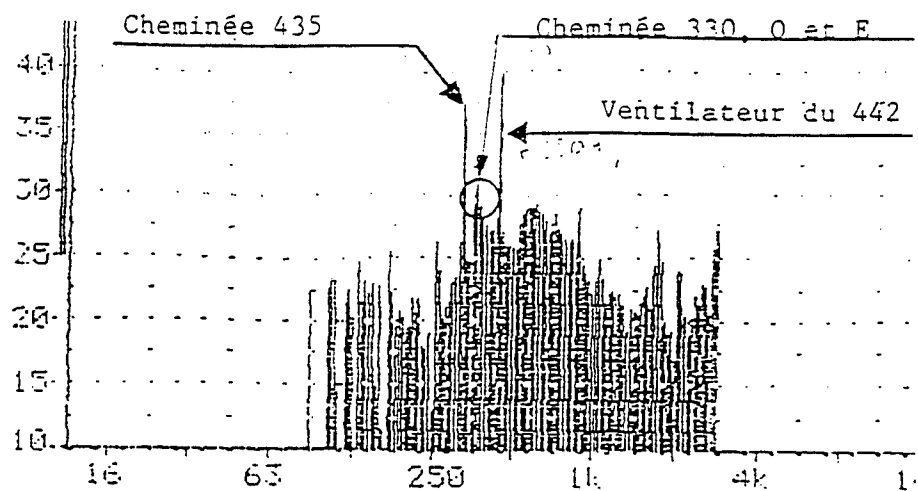
3.0 COMPARISON WITH EXPERIMENTAL RESULTS

b) PRACTICAL CASE:

- Noise generated by sources of an industrial plan
 - SPL measured during different periods of the day and different days.
 - Meteorological wind speed and direction evaluated using a nearby meteorological tower
 - Noise sources height's: 30 m and 40 m



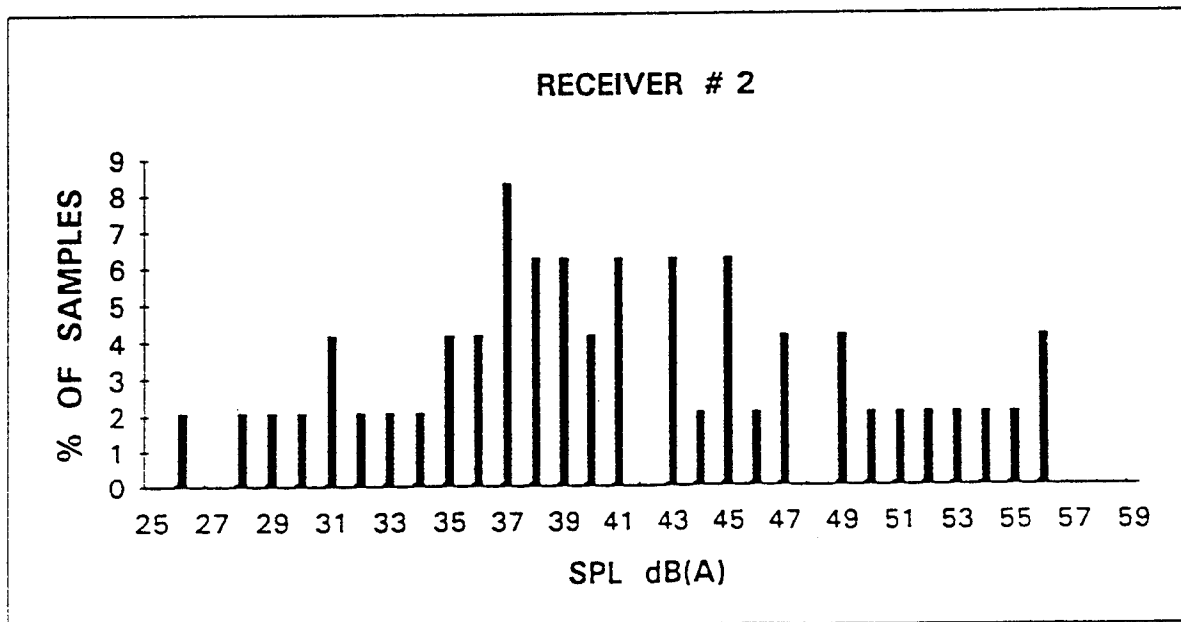
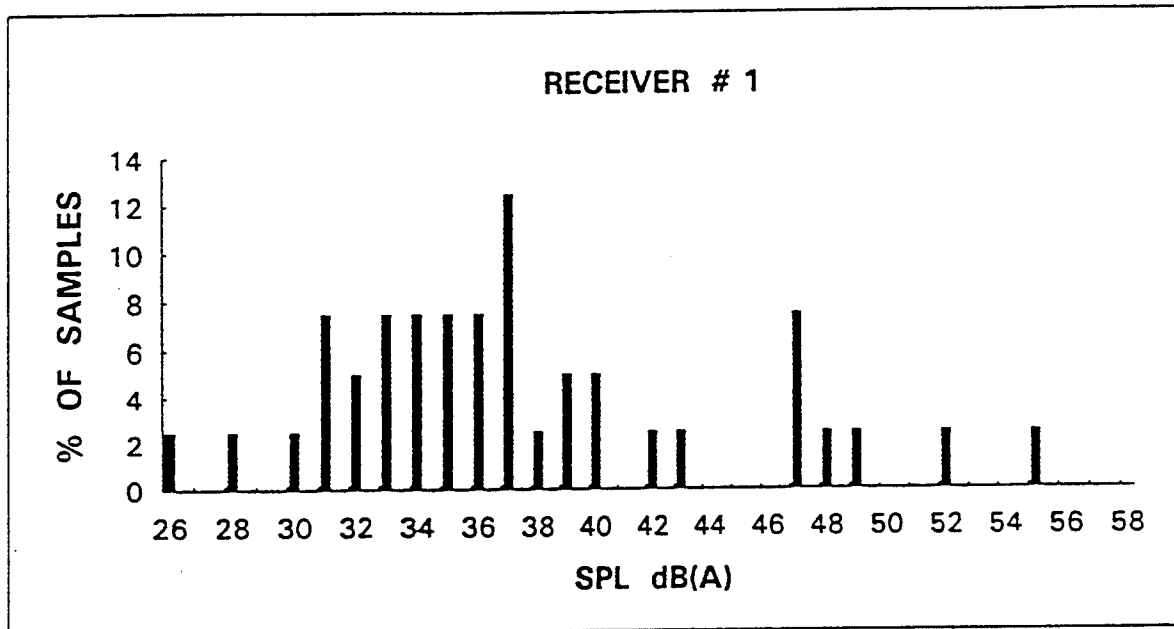
TYPICAL ACOUSTICAL DATA



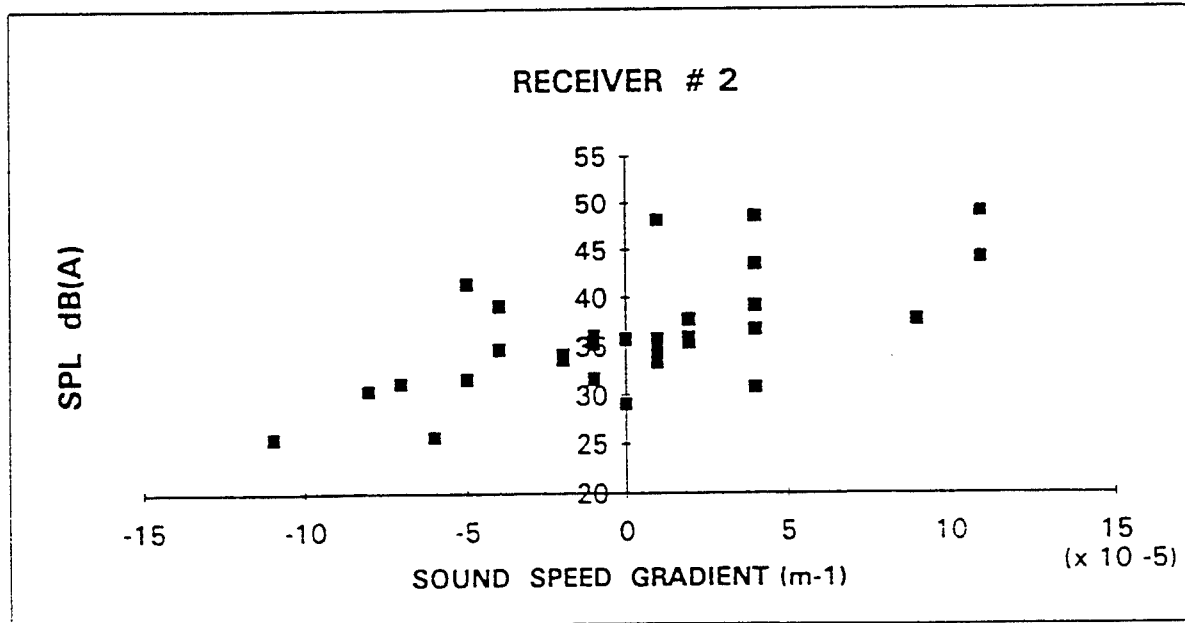
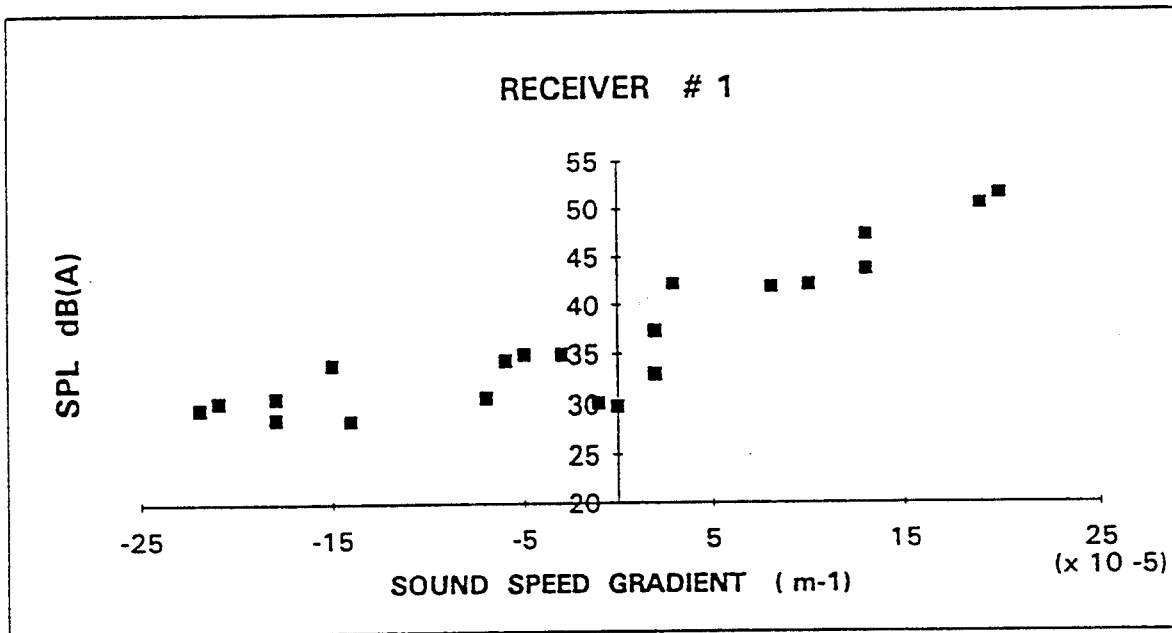
TYPICAL METEOROLOGICAL DATA

Date	JUNE 16	JUNE 16	JUNE 16	JUNE 17	JUNE 17	JUNE 25	JUNE 25
Normal time	9h00	19h00	22h00	9h00	13h00	10h00	14h00
Temperature	15.0	16.8	14.9	18.7	22.2	19.2	27.0
Wind speed	9.7	9.7	6.1	10.4	13.7	5.8	9.0
Wind direction	292	315	315	248	270	112	190
Solar altitude	45	15	0	60	90	45	90
Cloud cover	0.50	0.00	0.25	0.00	0.00	0.00	0.75
Sound Speed Gradient (10^{-5})	-14	-7	-3	-18	-22	2	-7

DISTRIBUTION OF THE EXPERIMENTAL SPL



SPL VS LINEAR SOUND SPEED GRADIENT



4.0 CONSIDERATIONS ABOUT THE ATMOSPHERIC TURBULENCE

From Wilson⁽⁸⁾:

$$\langle \mu^2 \rangle = \frac{\sigma_w^2}{C_0^2} + \left(\frac{\sigma_T}{2 T_0} \right)^2$$

where σ_w^2 is the standard deviation of wind in the axis of propagation.

$$\sigma_w^2(z) = (\sigma_U(z) \cos(\alpha_w - \alpha_{sr}))^2 + (\sigma_V(z) \sin(\alpha_w - \alpha_{sr}))^2$$

- For $L > 0$ (stable conditions, night)⁽¹⁾:

$$\sigma_u(z) = 2.4 u_*$$

$$\sigma_v(z) = 1.9 u_*$$

$$\sigma_T(z) = 1.5 T_*$$

- For $L < 0$ (unstable conditions, day):

$$\frac{\sigma_u(z)}{u_*} = \left(12 - 0.5 \frac{z}{L} \right)^{1/3}$$

$$\frac{\sigma_v(z)}{u_*} = 0.8 \left(12 - 0.5 \frac{z}{L} \right)^{1/3}$$

$$\frac{\sigma_T(z)}{T_*} = 2 \left(1 - 18 \frac{z}{L} \right)^{-1/2},$$

8 WILSON, D.K., THOMSON, D.W. (1991) *Propagation in Atmospheric convective Boundary-Layer Turbulence*, 121st Meeting of the A.S.A., 89, p. 1952.

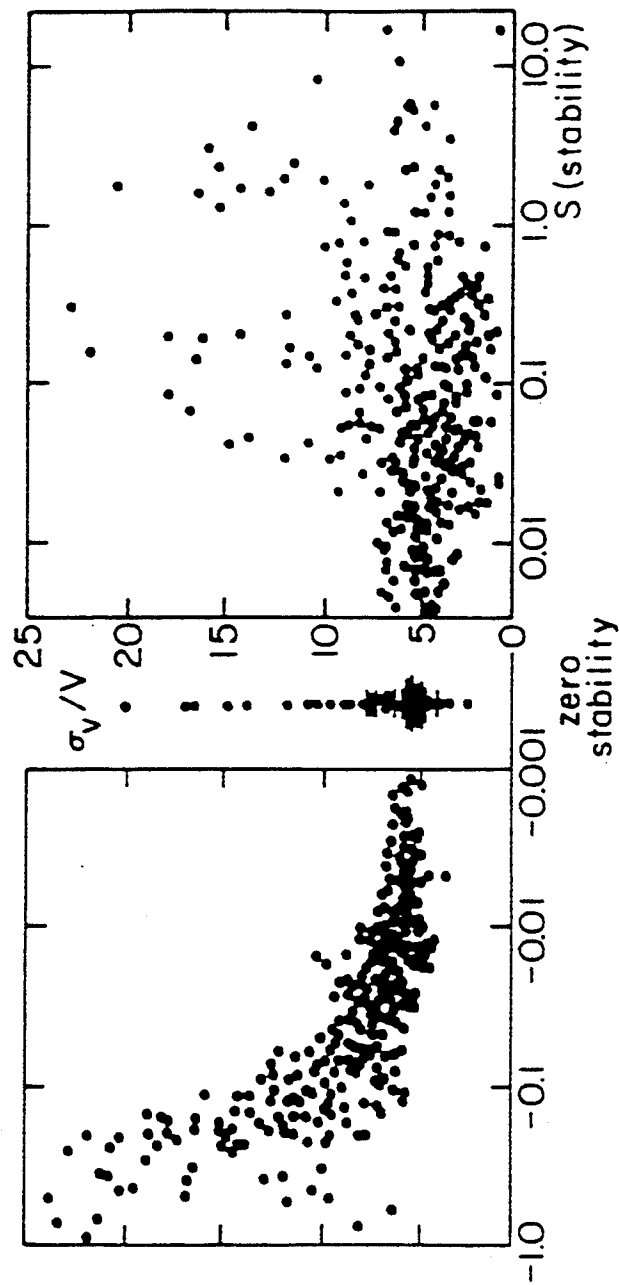
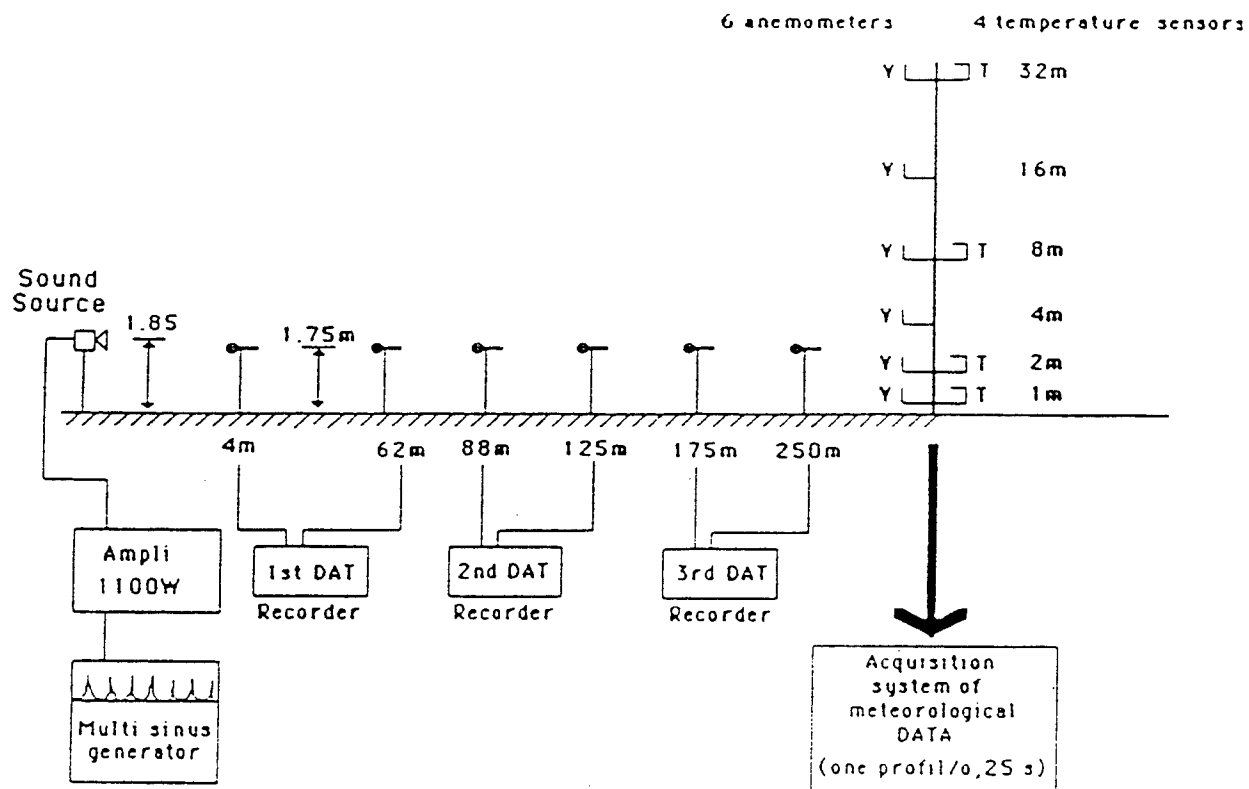


FIGURE 7.7. σ_v/V at 16 m as a function of a stability index proportional to Ri (after Smith and Abbott, 1961). Published with permission, *Quarterly Journal*, Royal Meteorological Society.

COMPARISON WITH EXPERIMENTAL MEASUREMENTS OF BOUIN EXPERIMENTS⁽⁹⁾:



- (9) A. L'Espérance et al. *Outdoor Sound Propagation: Experimental study of atmospheric turbulence and simulation with FFP*, Proceeding Inter-Noise 92, p.139-142 (1992)

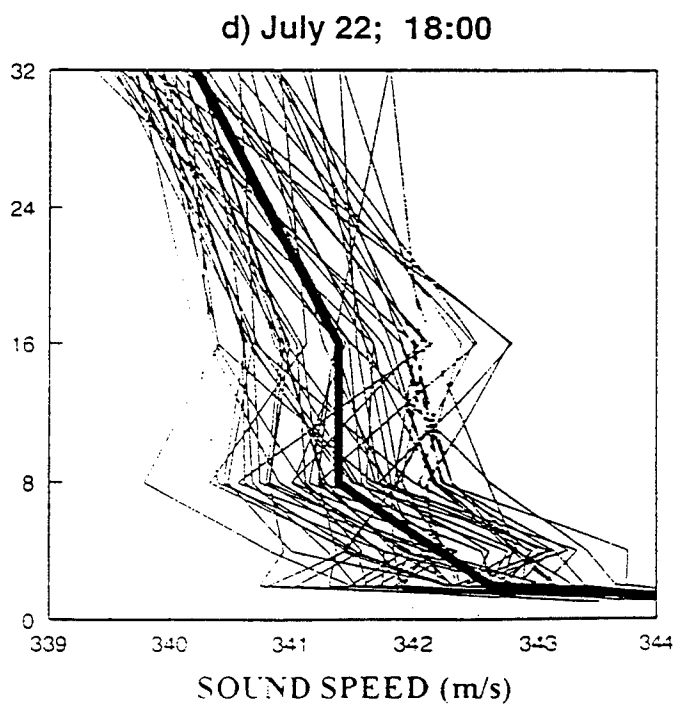
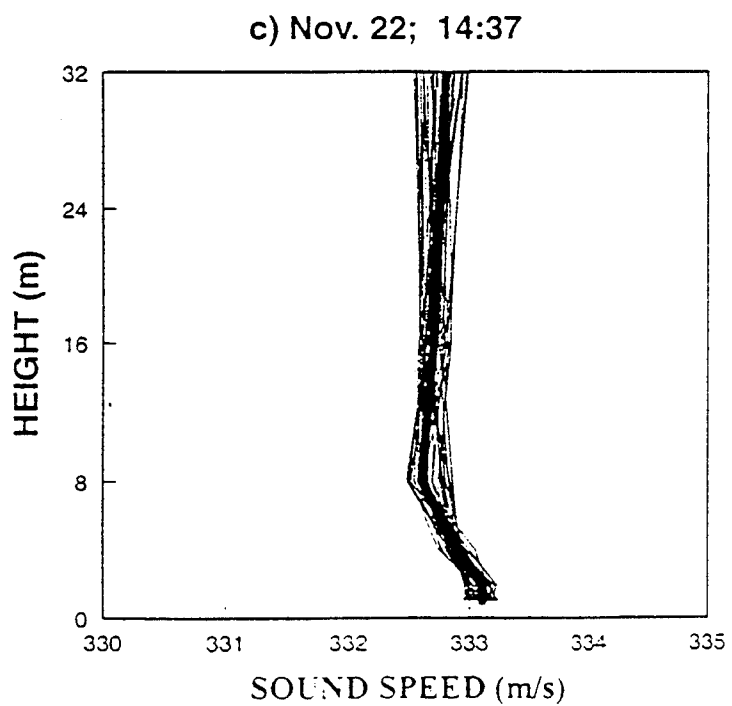
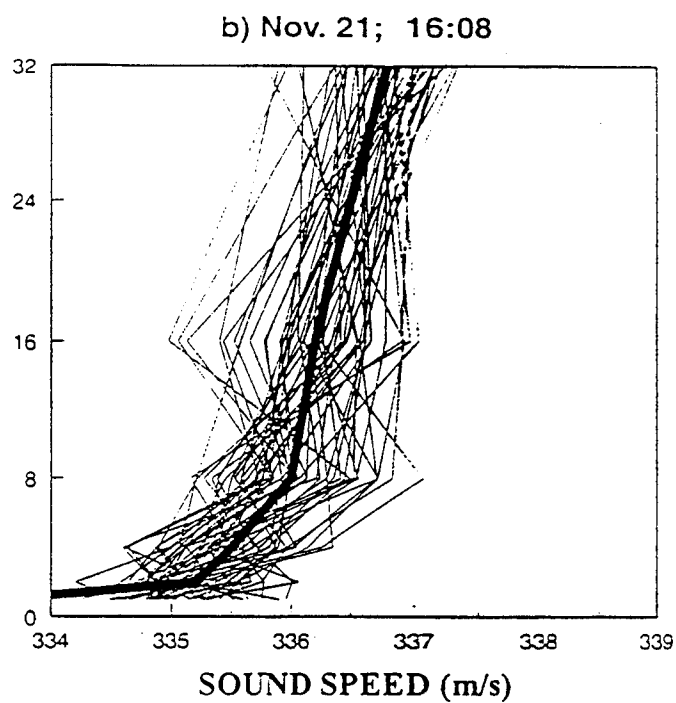
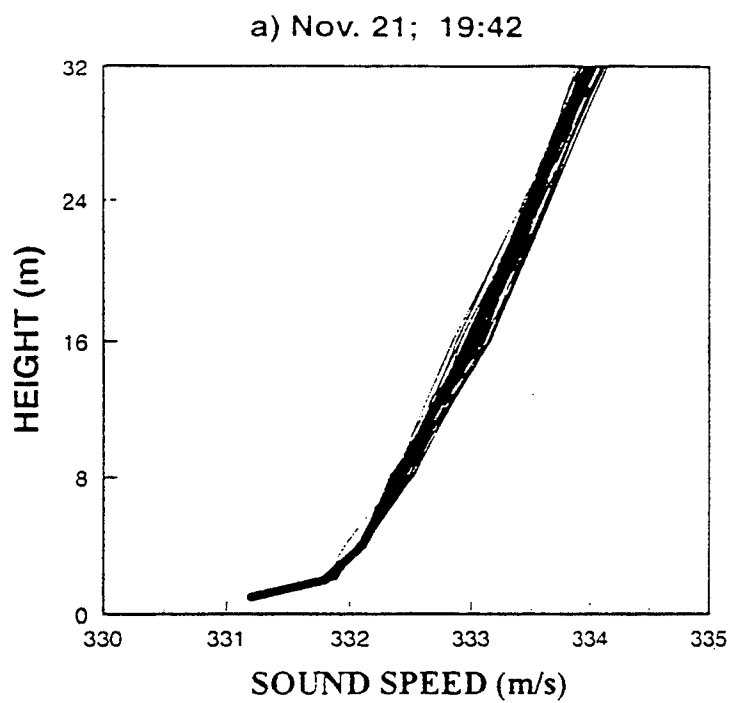
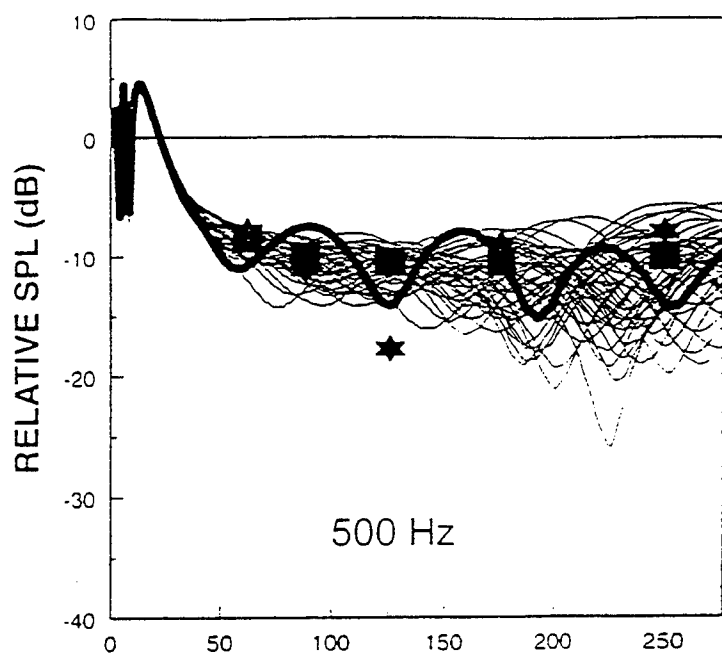
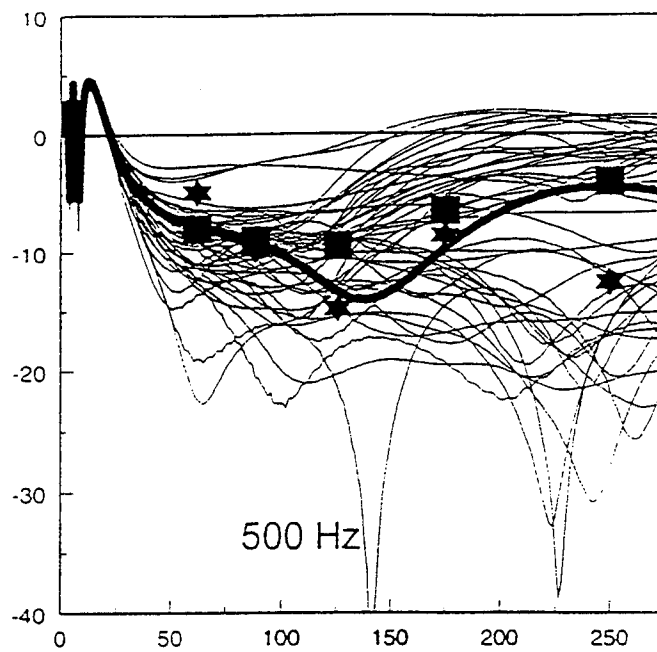


Fig.2

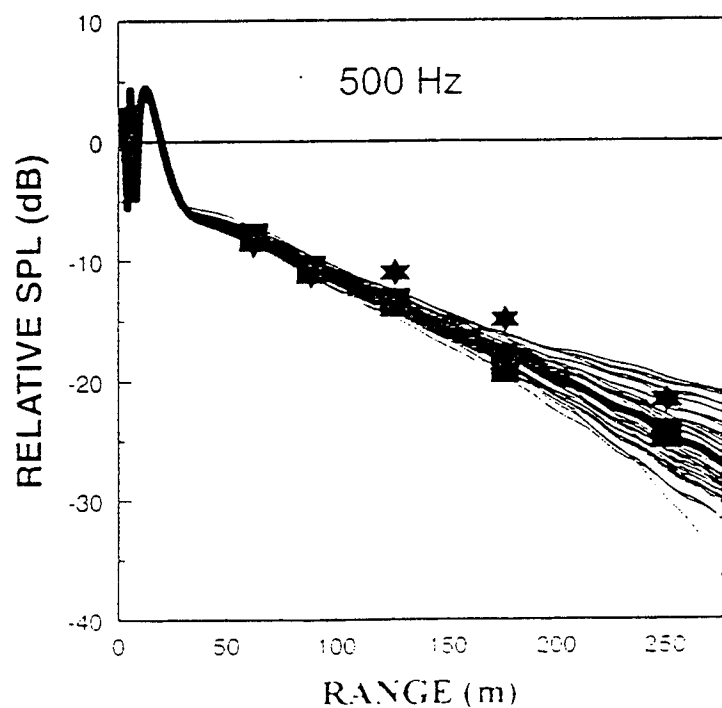
a) Nov. 21; 19:42



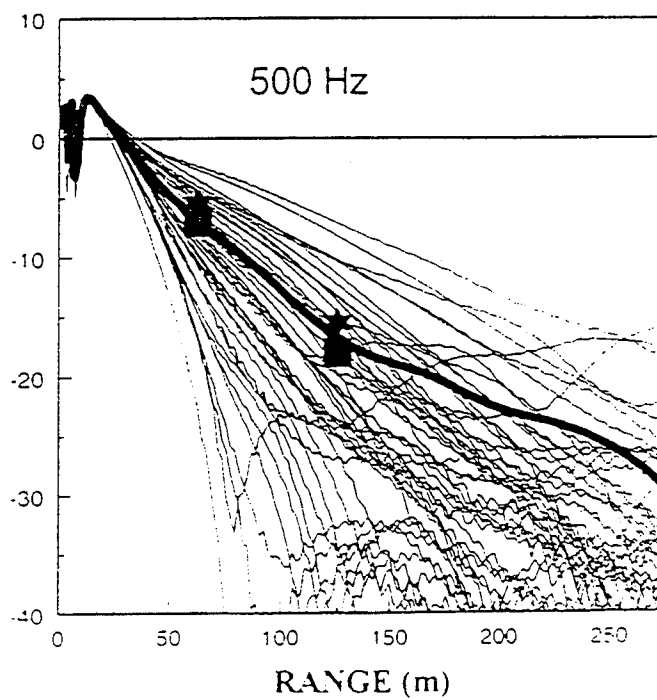
b) Nov. 21; 16:08

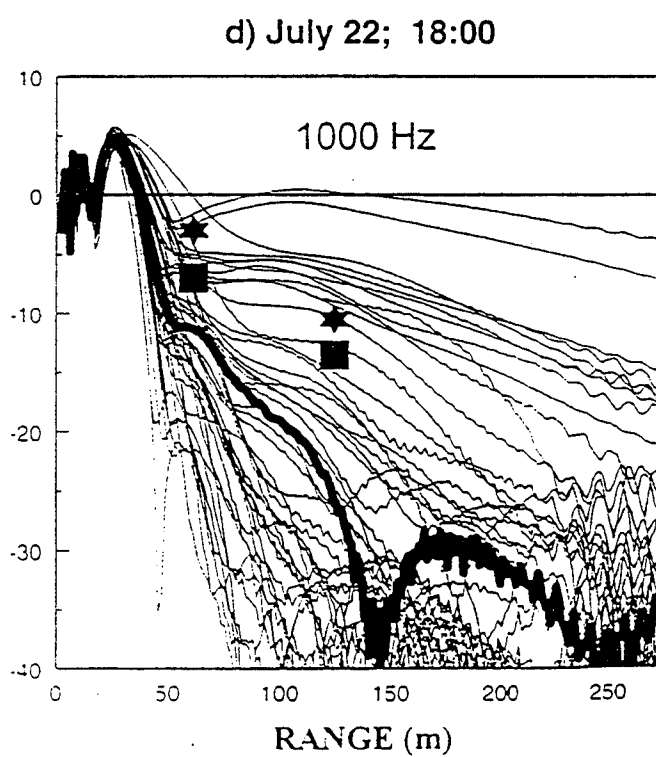
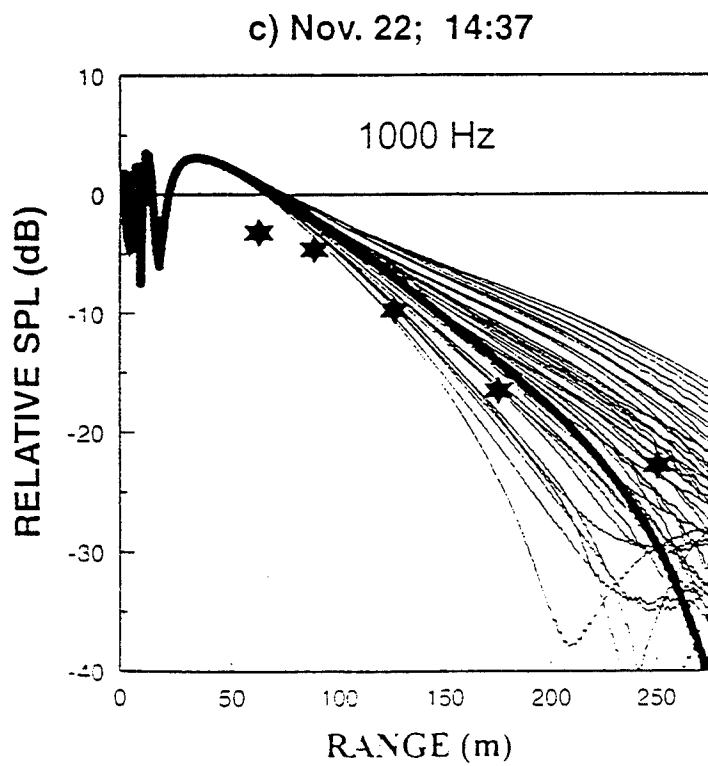
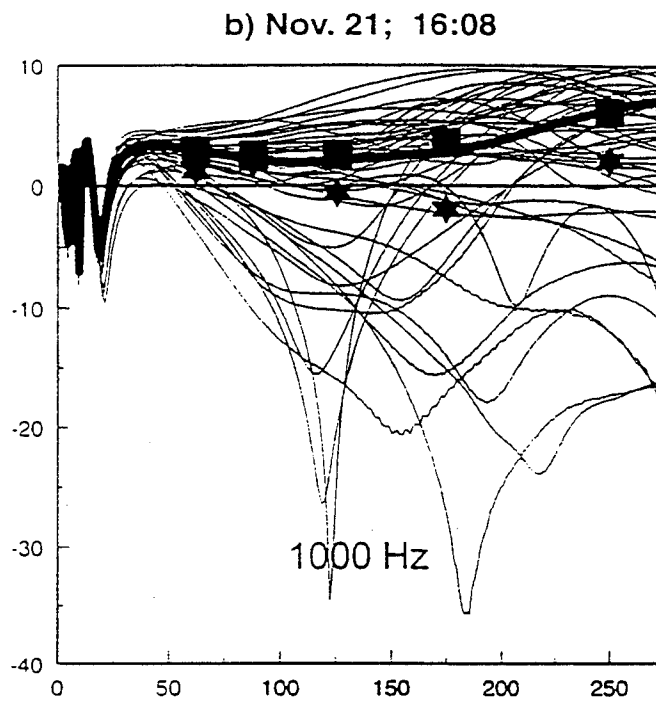
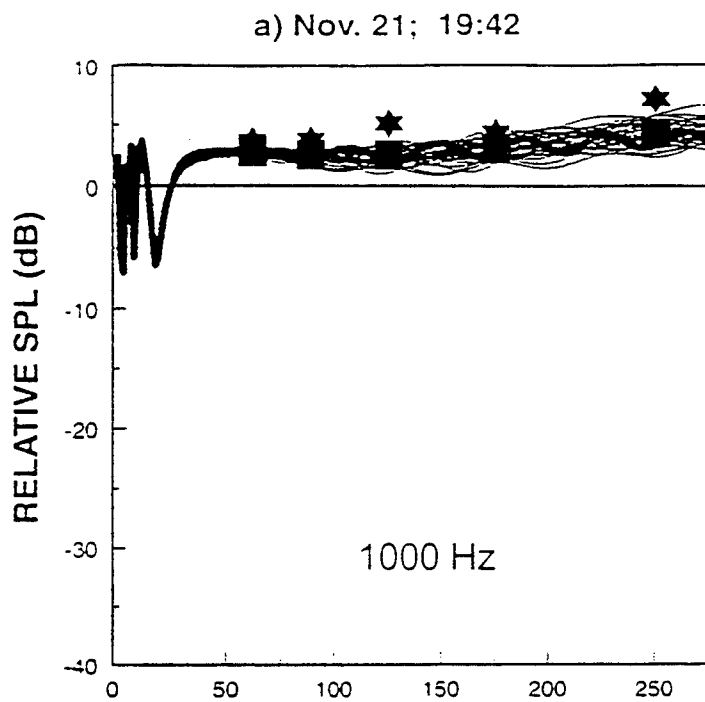


c) Nov. 22; 14:37



d) July 22; 18:00





CONCLUSION:

- Based on the classical knowledge of meteorologists on the structure of the atmosphere in the surface layer, a practical method to predict SSP's and $\langle \mu^2 \rangle$ from general meteorological informations has been investigated.
- A method to obtain an equivalent linear sound speed gradient has been proposed.
- Comparisons with experimental meteorological results have shown that the general tendencies of the SSP are well respected, but particular details could not be reproduced.
- It seems that the estimation of the effective SSP from general meteorological conditions and the effect of the turbulence may be the weak part of the acoustical prediction model.

Long-term average sound transfer through the atmosphere: predictions based on meteorological statistics and numerical computations of sound propagation

Erik M. Salomons, Frank H.A. van den Berg and Hans E.A. Brackenhoff

TNO Institute of Applied Physics, P.O. Box 155, 2600AD Delft, The Netherlands

A practical model is described for predicting long-term average transfer functions for atmospheric sound propagation. The transfer functions are determined as weighted averages of transfer functions computed with the PE method for a representative set of sound-speed profiles. The profiles are calculated with a Businger-Dyer model, using the Pasquill classification for atmospheric stability. Examples are presented of average transfer functions up to distances of 15 kilometers, for different seasons, for the day and the night, and for different directions of sound propagation.

1. Introduction

As meteorological variations cause large variations of atmospheric sound propagation, the usual approach in outdoor noise control is to work with long-term average sound levels, i.e., levels averaged over a long period (a month, or a year). Therefore, there is a need for reliable methods for predicting long-term average transfer functions.

A reliable model for predicting long-term average transfer functions, should combine meteorological statistics and computations of sound propagation. Computations of sound propagation in an inhomogeneous atmosphere can be performed with a numerical method for solving the wave equation, such as the parabolic-equation method (PE method). Meteorological statistics should provide the description of the atmosphere used in the computations, in terms of the parameters relevant for sound propagation. These parameters are the temperature, the wind speed and the wind direction.

This paper describes such a model, for sound propagation near the ground over distances up to 15 kilometers. The model combines meteorological statistics with PE solutions. The model is developed specifically for our country, The Netherlands, as the meteorological statistics of our country are used.

2. Statistical model for long-term average transfer function

To model the effect of the atmosphere on sound propagation, i.e., atmospheric refraction, we make use of the effective sound speed. The effective sound speed is the sum of the thermal sound speed and the vector wind, and is a function of the height z above the ground:

$$c(z) = 20.064\sqrt{T(z)} + u(z)\cos(\phi-\beta) \quad (1)$$

where T is the temperature, u the horizontal wind speed, ϕ the wind direction, and β the direction of sound propagation (ϕ and β are expressed as angles with respect to the north). In the following, the function $c(z)$ is referred to as the sound-speed profile.

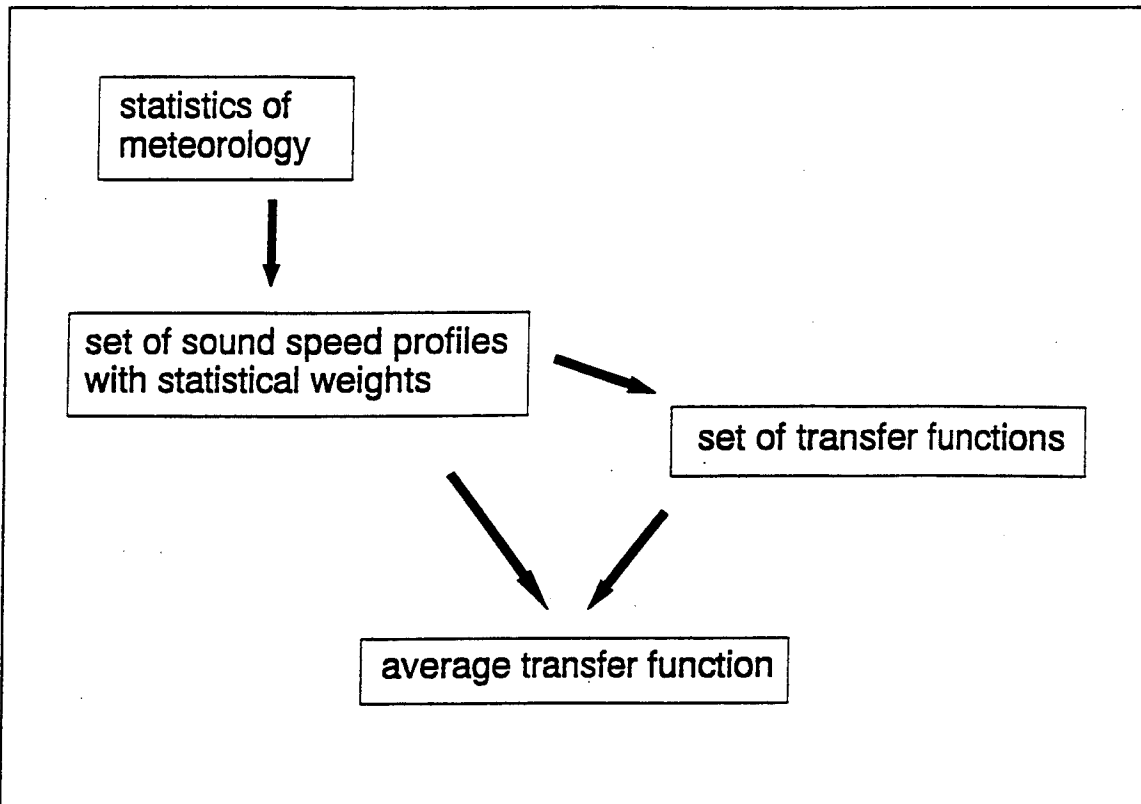


FIG 1. Scheme of the computation of the long-term average transfer function.

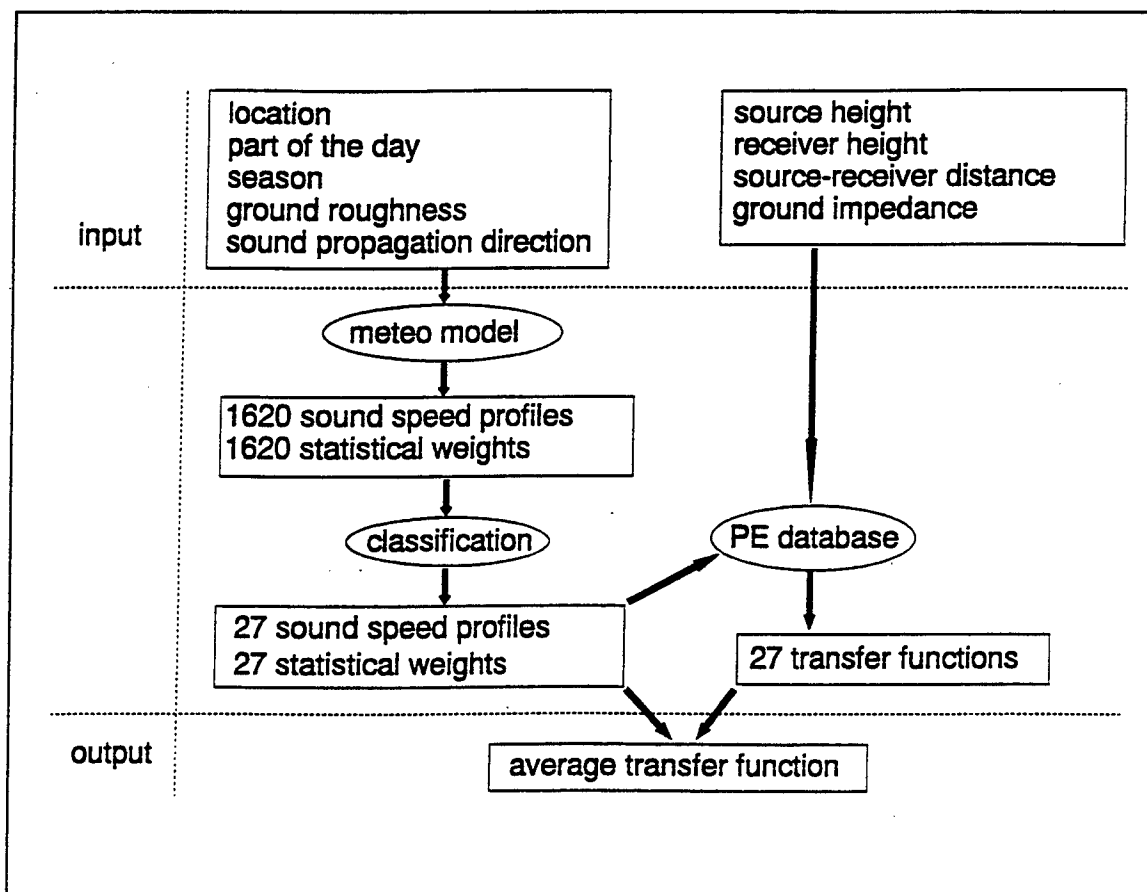


FIG 2. Detailed scheme of the computation of the long-term average transfer function.

The sound-speed profile varies with the time (time of the year, time of the day), as a consequence of variations of the profiles of temperature and wind. To compute long-term average transfer functions, these variations have to be taken into account. Therefore, we make use of a probability distribution of the sound-speed profile: this is a representative set of sound-speed profiles with given statistical weights. For all profiles of the set we compute the transfer function. The long-term average transfer function is computed as the energetical average of all transfer functions, weighted with the statistical weights of the profiles. This statistical scheme is represented in Fig. 1.

For the computation of the transfer functions we use the PE method for atmospheric sound propagation [1]. The PE method yields the transfer function as a function of distance, at a single frequency. By averaging over ten frequencies per octave band, we obtain the octave-band average transfer function as a function of distance (see Sec. 2.3).

Figure 2 shows a more detailed scheme of the statistical model. At the top of the scheme the input parameters are given, divided into two groups. One group determines the sound-speed profiles, the other group contains geometrical parameters and the acoustical ground impedance.

We first compute a set of 1620 sound-speed profiles with 1620 statistical weights, using a meteorological model (this is described in Sec. 2.1). It would take too much computer time to compute transfer functions for all 1620 profiles. Therefore we replace the set of 1620 profiles by a smaller set of 27 profiles (this is described in Sec. 2.2). For all 27 profiles the transfer function is computed.

We obtain a major reduction in computing time by choosing a *fixed set* for the set of 27 profiles, independent of the input parameters of the meteorological model. Now the 27 transfer functions have to be computed only once, for a given source height and ground impedance. In other words, we first generate a PE database, and then we study different situations using this database. Different situations correspond with different statistical weights of the 27 profiles.

2.1 Statistical meteorological model

In this section we describe a meteorological model for the computation of the probability distribution of the sound speed profile. The probability distribution consists of a set of 1620 sound-speed profiles with 1620 statistical weights.

The model is schematically represented in Fig. 3. There are five input parameters: the location in The Netherlands, the part of the day (day or night), the season, the ground roughness, and the direction of sound propagation. The direction of sound propagation is expressed by the angle with respect to the north, measured anti-clockwise (90° corresponds to propagation from east to west).

The model makes use of three statistical variables:

- the wind speed u_{10} at a height of ten meters
- the wind direction ϕ
- the cloud cover N .

The cloud cover is a parameter that determines the amount of sunshine that reaches the earth surface during the day, and the amount of radiation emitted by the earth during the night. Therefore, the cloud cover affects the thermal state of the atmosphere.

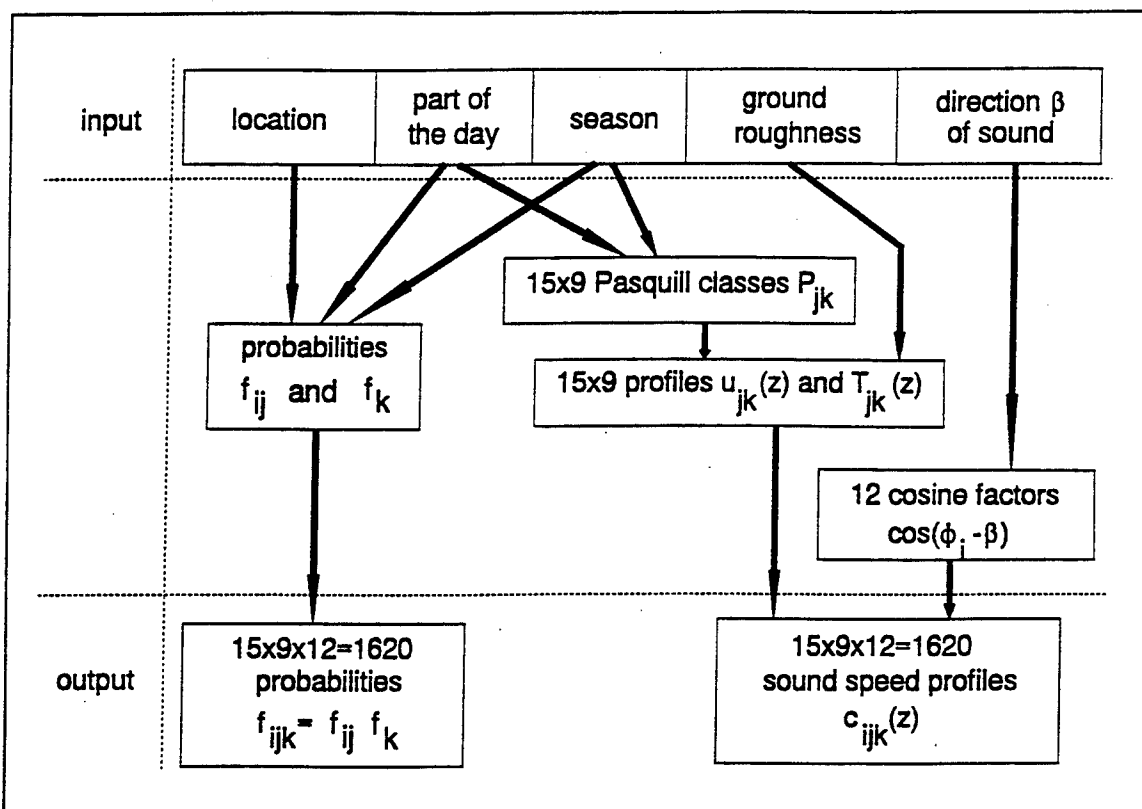


FIG 3. Scheme of the meteorological model in Fig. 2.

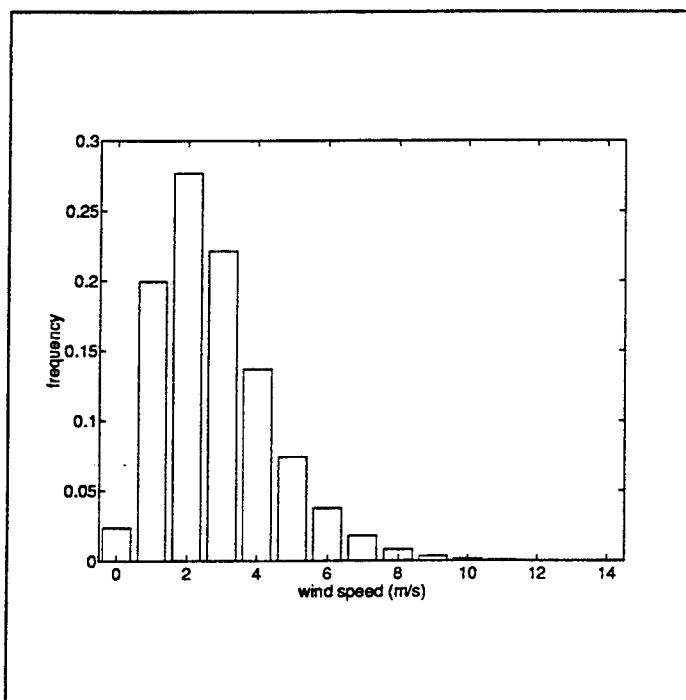


FIG 4. Example of frequency distribution of the wind speed, with fifteen classes.

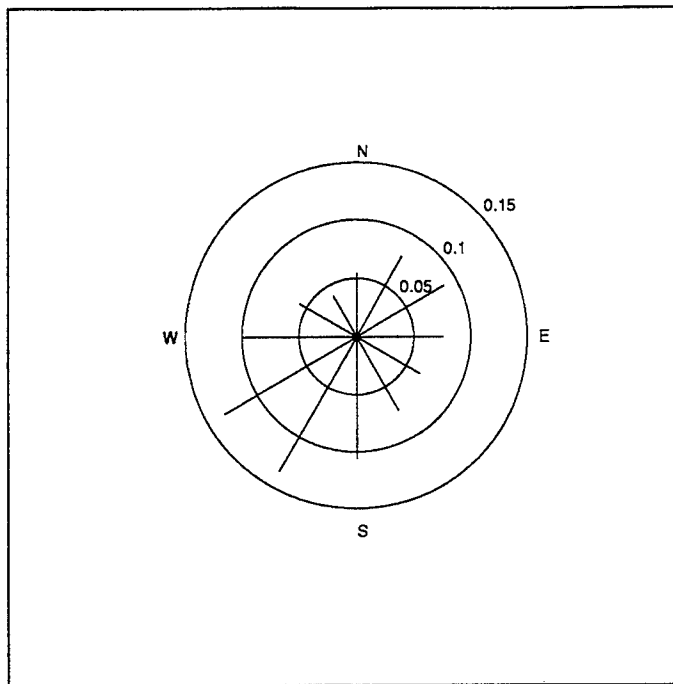


FIG. 5. Example of frequency distribution of the wind direction, displayed as a wind rose with twelve directions.

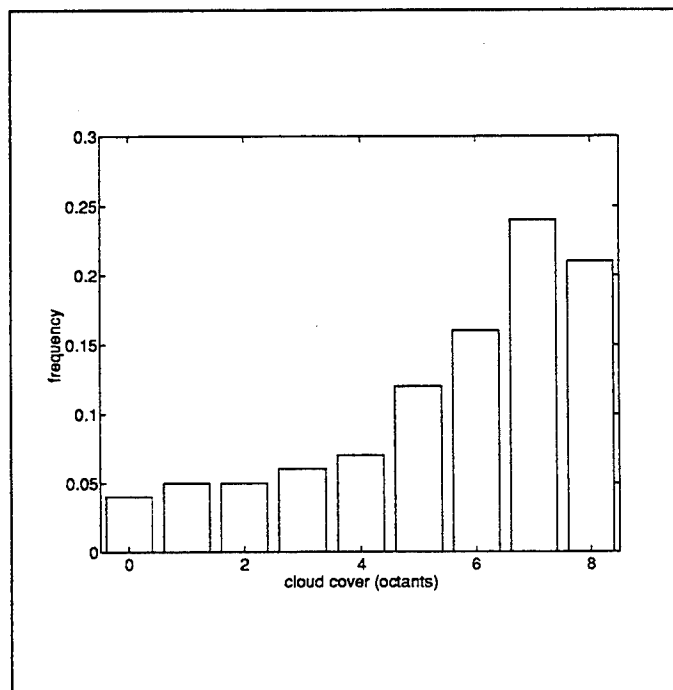


FIG 6. Frequency distribution of the cloud cover, with nine classes.

To come to a practical model, we discretize the three variables:

- $u_{10,j} = 0, 1, \dots, 14 \text{ m/s}$ with $j=1, \dots, 15$
- $\phi_i = 0^\circ, 30^\circ, \dots, 330^\circ$ with $i=1, \dots, 12$
- $N_k = 0, 1, \dots, 8$ octants with $k=1, \dots, 9$.

Each discrete value represents a class. For example, the value $u_{10,2}=1 \text{ m/s}$ represents the class $[0.5-1.5 \text{ m/s}]$. The statistical probability, or statistical frequency, of a class is denoted as f_j , f_i or f_k , respectively. The frequency distribution of the wind direction is usually represented as a wind rose, for the other two variables we use a histogram. Figures 4, 5 and 6 show examples of the distributions.

Each combination (i,j,k) corresponds with a sound-speed profile. There are $12 \times 15 \times 9 = 1620$ combinations. In the following two sections we describe how the sound-speed profiles and the statistical weights are determined.

2.1.1 Sound-speed profiles

Equation (1) shows that the sound-speed profile depends on the temperature profile, the wind-speed profile, and the wind direction. For the profiles of the temperature and the wind speed we use a Businger-Dyer model. Appendix A describes the computation of Businger-Dyer profiles based on the following three parameters: the wind speed at a height of ten meters, the cloud cover, and the ground roughness.

The ground roughness is represented by a roughness length. The roughness length of a terrain can be estimated visually, using the Davenport classification [2]. Grass-covered ground has a roughness length of the order of a few centimeters.

An important parameter of the Businger-Dyer profiles is the Obukhov length. The Obukhov length is a measure of atmospheric stability. A more practical measure of atmospheric stability is the Pasquill class. There are six Pasquill classes: A, B, C, D, E, and F. Class A represents a very unstable atmosphere (i.e., an atmosphere with strong vertical transport), class F represents a very stable atmosphere, and class D represents a neutral atmosphere. A neutral atmosphere has a logarithmic wind-speed profile, and a potential temperature independent of height. In a stable atmosphere, the potential temperature increases with height, and wind-speed gradients are usually larger than in a neutral atmosphere (at night, the atmosphere is usually stable). In an unstable atmosphere, the potential temperature decreases with height, and wind-speed gradients are usually smaller than in a neutral atmosphere (by day, the atmosphere is usually unstable).

We use empirical relations to determine the Obukhov length from the Pasquill class and the ground roughness (see Appendix B). Further, we use empirical tables for the Pasquill class as a function of cloud cover and wind speed at a height of ten meters (see Appendix C).

2.1.2 Statistical weights

For the statistics of the wind speed and the wind direction we make use of a meteorological model for wind in The Netherlands [2,3] (see Appendix D).

The parameters of this model have been fitted to wind data of a large number of meteorological stations in The Netherlands, collected over a period of fifteen years. The model yields the statistics of the wind speed and the wind direction, depending on three parameters: part of the day, season, and location in The Netherlands.

The wind speed and the wind direction are not independent of each other, as the wind-speed distribution f_j is not equal for all wind directions i . The statistical weight of a combination (i,j) is denoted as f_{ij} ($f_{ij} \neq f_i f_j$).

For the cloud cover we use a fixed probability distribution f_k , independent of the part of the day, the season, and the location. We have determined the distribution from a limited set of data [4]. The distribution is given in Fig. 6.

The statistical weight of a combination (i,j,k) is approximated by $f_{ijk}=f_{ij}f_k$. We assume here that the probabilities f_{ij} and f_k are approximately independent of each other.

2.2 Classification of sound-speed profiles

In this section we describe a method to reduce the set of 1620 sound-speed profiles to a set of 27 profiles.

Figure 7 shows an example of a set of 1620 sound-speed profiles. For almost all profiles the sound speed either increases monotonically with height, or decreases monotonically with height. For simplicity, profiles with a positive sound-speed gradient will be called downwind profiles, profiles with a negative sound-speed gradient will be called upwind profiles.

The average transfer function is equal to the weighted average of the transfer functions for the 1620 sound-speed profiles. The average is dominated by the contribution of the downwind profiles. The contribution of the upwind profiles is usually negligibly small, except at small distances from the source.

To reduce computing time, we replace the set of 1620 profiles by a set of 27 profiles. Each profile from the set of 1620 is attributed to one profile from the set of 27. Each profile from the set of 27 is given a statistical weight equal to the sum of the weights of the attributed profiles.

The transfer function averaged over the 27 profiles should be a good approximation of the transfer function averaged over the 1620 profiles. It is therefore important that in particular the downwind profiles are well represented by the set of 27 profiles.

We have constructed the set of 27 profiles shown in Fig. 8. The plots on the left side have a logarithmic height axis, the plots on the right side have a linear height axis. The set consists of three groups of profiles, and the profiles are labeled with index $n=1,...,27$:

$$\text{group 1} \quad n=1,...,7 \quad c_n(z) = c_0 + b_n [(10z+1)^{-0.3}-1] \quad (2)$$

$$\text{group 2} \quad n=8,...,18 \quad c_n(z) = c_0 + b_n \ln(10z+1) \quad (3)$$

$$\text{group 3} \quad n=19,...,27 \quad c_n(z) = c_0 + b_n [(10z+1)^{0.3}-1] \quad (4)$$

with z the height in meters. The values of the parameters b_n are given in Table 1. For all profiles the sound speed at zero height is equal to c_0 . The exact value of the constant c_0 is unimportant, and we set $c_0=343$ m/s.

The difference between the three groups clearly emerges from the plots in Fig. 8 with a logarithmic height axis. The profiles of group 2 are straight lines, the profiles of group 1 are upward curving lines, the profiles of group 3 are downward curving lines.

We use the following method to attribute a profile from the set of 1620 to a profile from the set of 27. First, we determine in which of the three groups the profile fits best. We compute a shape parameter α :

$$\alpha = \lg \left(\frac{|\alpha(99.9) - \alpha(9.9)|}{|\alpha(9.9) - \alpha(0.9)|} \right) \quad (5)$$

If $\alpha < -0.15$ then we choose group 1, if $-0.15 \leq \alpha \leq 0.15$ then we choose group 2, and if $\alpha > 0.15$ then we choose group 3. The reason for these choices is that group 1 corresponds to $\alpha = -0.3$, group 2 corresponds to $\alpha = 0$, and group 3 corresponds to $\alpha = 0.3$ (these values are obtained by substitution of Eqs. (2) to (4) into Eq. (5)). In other words, we choose the group for which the absolute difference in shape parameter α is a minimum.

After the group has been chosen, we compute a parameter β :

$$\beta = \frac{\alpha(99.9) - \alpha(0.9)}{100^{-0.3} - 10^{-0.3}} \quad \text{for group 1} \quad (6)$$

$$\beta = \frac{\alpha(99.9) - \alpha(0.9)}{\ln(100)} \quad \text{for group 2} \quad (7)$$

$$\beta = \frac{\alpha(99.9) - \alpha(0.9)}{100^{0.3} - 10^{0.3}} \quad \text{for group 3} \quad (8)$$

From the chosen group we now choose the profile for which the absolute difference $|\beta - b_n|$ is a minimum.

From the above description it follows that the classification makes use of the atmospheric layer between one meter and a hundred meter above the ground (more precisely, 0.9 meter and 99.9 meter). Of course, this does not mean that the profiles cannot be used above a hundred meter or below one meter.

Table 1 Values of the parameters b_n (in m/s) of Eqs. (2), (3) and (4).

$b_1=10$	$b_2=3$	$b_3=1$	$b_4=-1$	$b_5=-3$	$b_6=-6$	$b_7=-10$
$b_8=-1$	$b_9=-0.4$	$b_{10}=-0.2$	$b_{11}=0$	$b_{12}=0.2$	$b_{13}=0.4$	$b_{14}=0.7$
$b_{15}=1.1$	$b_{16}=1.5$	$b_{17}=2$	$b_{18}=2.5$	$b_{19}=-1$	$b_{20}=-0.5$	$b_{21}=-0.2$
$b_{22}=0.2$	$b_{23}=0.4$	$b_{24}=0.65$	$b_{25}=1$	$b_{26}=1.4$	$b_{27}=2$	

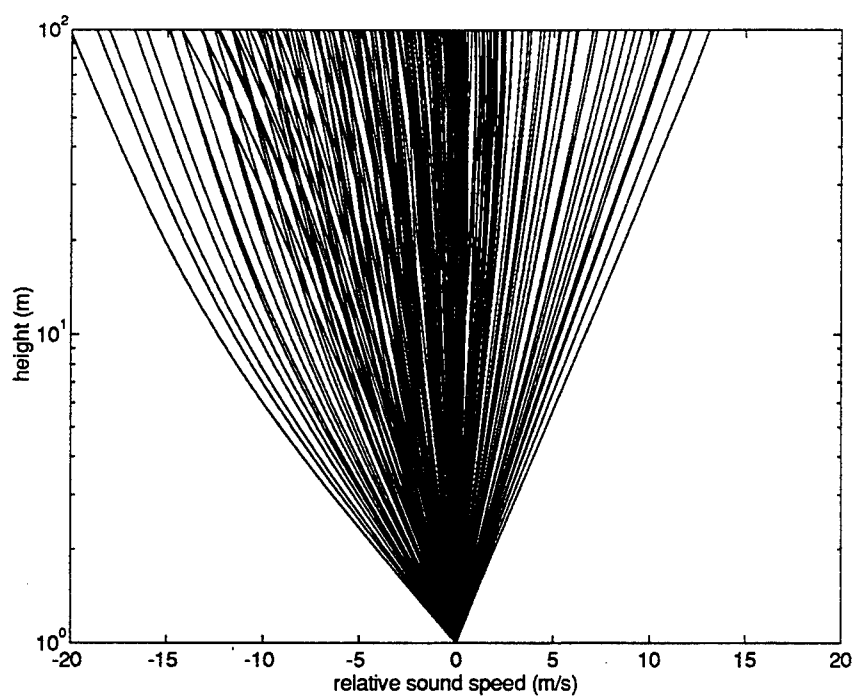


FIG 7. Example of set of 1620 sound-speed profiles (for a summer day, a ground with $z_0=0.1\text{m}$, and $\beta=90^\circ$).

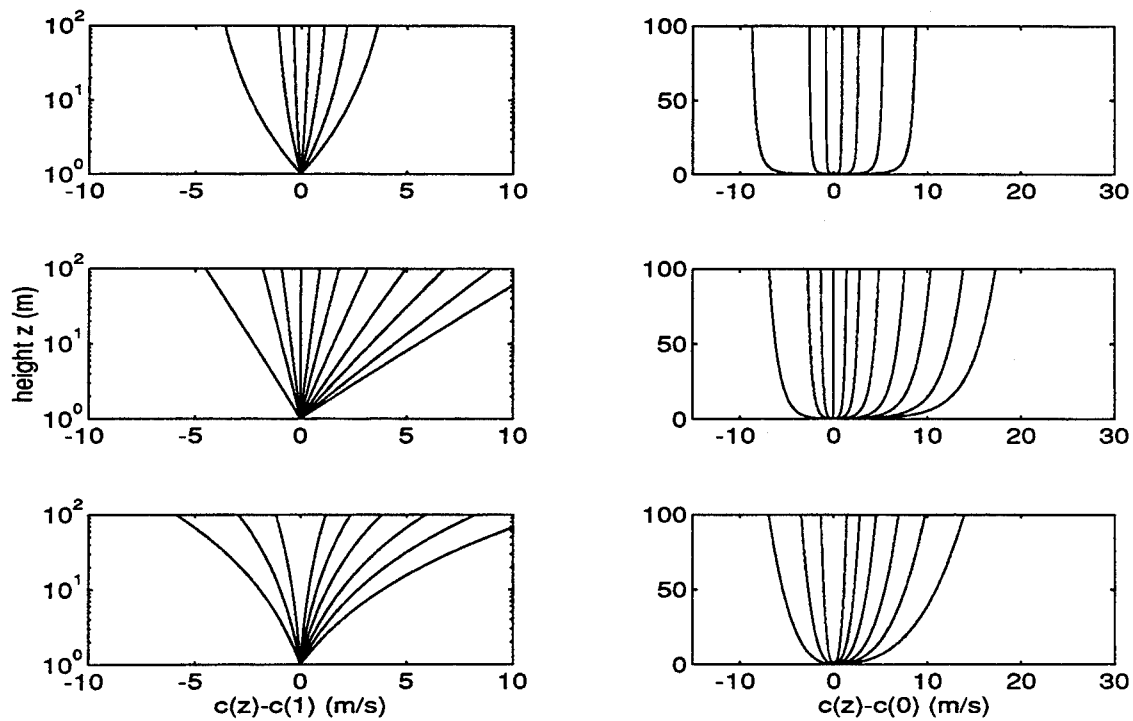


FIG 8. Set of 27 sound-speed profiles for classification, with logarithmic (left) and linear (right) height axis. From top to bottom: group 1, 2 and 3

2.3 PE computations

In this section we describe the generation of the PE database, i.e., the set of transfer functions for the 27 profiles in Fig. 8.

For the computations we use the wide-angle PE method [1], as described by West et al. [5]. We use a numerical grid with a spacing of about one tenth of a wavelength. The system contains a number of vertical grid points varying between 4000 and 8000 depending on the frequency, and an absorbing layer at the top with a thickness of at least 50 wavelengths and an imaginary part of the wave number that increases quadratically with height. The starting function is the sum of two Gaussians, one centered at the source height and another one centered at the image source height [6]. We have developed a code in FORTRAN, that runs on a DEC α computer.

The transfer function is expressed relative to the free field. Geometrical spreading and atmospheric absorption are not included in the transfer function.

We compute octave-band averages, by averaging over ten frequencies per band. The lowest octave band is the 16 Hz band, the highest band is the 4000 Hz band. The PE database consists of octave-band averages as a function of the distance to the source. We use a source height of 2 meters, and five receiver heights: 0.5, 1.5, 5, 10 and 50 meters. For the bands 16 Hz to 250 Hz the transfer function is computed up to a distance of 15 kilometers. For higher bands we use a smaller maximum distance, as molecular absorption in the atmosphere increases with frequency (see Table 2).

We have performed computations both for an absorbing ground and for a reflecting ground. For the absorbing ground we use the impedance model of Attenborough [7], with the following parameters: flow resistivity $\sigma = 3 \cdot 10^5 \text{ Nsm}^{-4}$, pore shape factor 0.75, grain shape factor 0.5, and porosity 0.3. These parameters can be considered as representative of grass-covered ground.

The octave-band averaged transfer function is found to show oscillations as a function of distance. The oscillations have an amplitude of a few decibels at most, and are largest for strong downwind profiles and at large distance from the source. An example is shown in Fig. 9.

The oscillations can be explained as interference effects of sound rays: with increasing distance an increasing number of sound rays arrive at the receiver. The oscillations also depend on the finite number of frequencies per octave band.

In this work we are not interested in the oscillations. Therefore, we eliminate them by 'logarithmic smoothing', i.e., by averaging the transfer function over a spatial window with a width that increases linearly with distance. An example of a smoothed transfer function is also shown in Fig. 9.

The transfer function shown in Fig. 9 is for profile 16. This is a downwind profile. Transfer functions for other downwind profiles are similar, gradually decreasing with distance. The transfer functions for upwind profiles are quite different, decreasing below -30 dB beyond a certain distance. This is a consequence of the shadow region in upwind propagation.

Sound propagation in a shadow region is strongly affected by atmospheric turbulence. Atmospheric turbulence can be taken into account in the PE method [8], but we have not done this here, as the low levels in the shadow region have a negligible contribution to the average transfer function.

Table 2 Maximum distance used in PE computations. Also given is the molecular atmospheric absorption at a relative humidity of 80% and a temperature of 20°C [9], for different octave bands.

octave band center-frequency (Hz)	≤250	500	1000	2000	4000
maximum distance (km)	15	10	5	2.5	1
molecular absorption (dB/km)	≤1	2	3.6	8.8	29

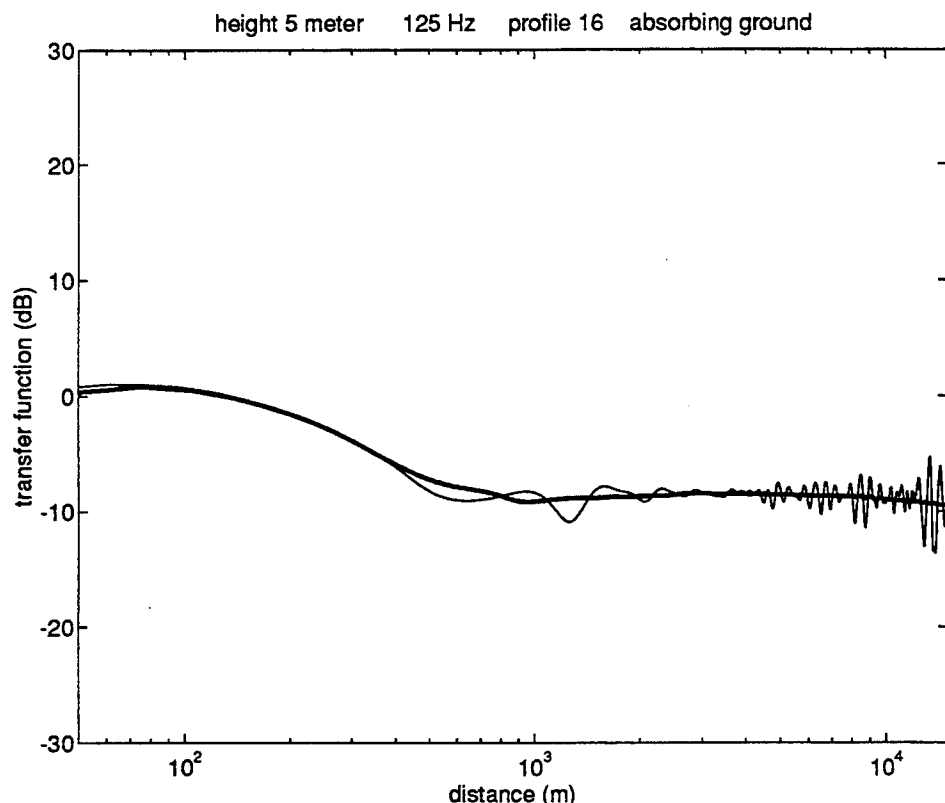


FIG 9. Example of smoothing of PE results, to eliminate oscillations.

3 Influence of various parameters on the long-term average transfer function

In this section we study the influence of various parameters on the long-term average transfer function. Results are shown for three octave bands: 31.5 Hz, 125 Hz and 1000 Hz. The source height is 2 meters, the receiver height is 5 meters (the system is reciprocal, so that the results also apply to a system with a source at a height of 5 meters and a receiver at a height of 2 meters). All results are for specific location in The Netherlands (De Bilt), but the variation with the location in The Netherlands is small.

First we study the difference in average sound transfer between summer and winter, and the difference between day and night. Figure 10 shows the transfer function for a summer day (solid line), a winter day (dashed line), and a night (dash-dotted line; the variation with season is negligibly small for the night), for propagation over an absorbing ground. We used a roughness length of 0.1 m, and a direction of sound propagation of

$\beta=10^\circ$.

The differences are largest in the 125 Hz band, with a maximum of about 8 dB.

The figure shows that sound propagation is better at night than by day. This can be explained as follows.

The ground is heated by sunshine during the day, and therefore the ground is warmer by day than at night. The temperature profile above the ground is also affected by sunshine and emission of radiation by the earth: by day the temperature usually decreases with height, at night the temperature usually increases with height. Hence, sound-speed gradients are more positive at night, and sound propagation is better.

The difference between a winter day and a summer day can be explained in the same way. On a summer day, sunshine is stronger than on a winter day. As a consequence, the average temperature gradient is more negative on a summer day than on a winter day.

The transfer functions in Fig. 10 decrease gradually with distance. This behaviour is found in all cases for propagation over the absorbing ground. We will consider this behaviour in some detail for the transfer function at 125 Hz, for a summer day.

At a distance of 15 km, the long-term average transfer function is -20.5 dB (see Fig. 10). There are only five profiles from the set of 27 that contribute significantly to this average, the contributions of the other profiles are negligible (either because the transfer function is low, or because the statistical weight is small). The transfer functions for the five profiles are given in Table 3, together with the statistical weights of the profiles. It can be verified that the weighted energetical average of the transfer functions is equal to -20.5 dB.

At a distance of 100 meters, the long-term average transfer function is 2 dB (see Fig. 10). In this case, almost all 27 profiles contribute to the average, as the transfer function at 100 meters varies between -1 dB and +2 dB for the different profiles from the set of 27. The weighted energetical average of the transfer functions is equal to 2 dB.

Next, we study the variation of average sound transfer with the propagation direction. Figure 11 shows the variation of the transfer function with the direction of sound propagation, for a summer day and an absorbing ground with a roughness length of 0.1 m. The variation is small, with a maximum of about 5 dB at 125 Hz. The transfer function is highest for propagation in eastern direction ($\beta=270^\circ$), and lowest for propagation in western direction ($\beta=90^\circ$). The explanation is that west wind occurs more often than east wind (see Fig. 5), so that downwind conditions prevail more often for eastward propagation than for westward propagation.

Finally, we study the influence of the ground. The model contains two ground parameters: the roughness length and the acoustical impedance. These parameters are not independent of each other. In general, a ground with a larger roughness length is acoustically softer, i.e., more absorbing. Grass-covered ground is acoustically soft and has a roughness length of about 10 cm, water is acoustically hard and has a roughness length of about 0.02 cm.

Figure 12 shows the transfer function for propagation over water, i.e., for a reflecting ground with a roughness length of 0.02 cm, again for the four directions of propagation. Comparison with Fig. 11 shows that the ground has a large effect on sound propagation.

Table 3 Most important contributions to the long-term average transfer function at a distance of 15 km, for the 125 Hz octave band (for a summer day, an absorbing ground with a roughness length of 0.1 m, and direction $\beta=10^\circ$).

profile number	4	5	6	14	15	weighted average transfer function
transfer function (dB)	-22	-14	-15,5	-11	-10	
statistical weight (%)	6	5	4	3	1	-20,5 dB

Acknowledgements. This work was financially supported by the Dutch Ministry of Defence.

References

- [1] K.E. Gilbert and M.J. White, "Application of the parabolic equation to sound propagation in a refracting atmosphere", J. Acoust. Soc. Am. **85**, 630-637 (1989)
- [2] J. Wieringa en P.J. Rijkoort (KNMI), "Windklimaat van Nederland" (Staatsuitgeverij, Den Haag 1983)
- [3] P.J. Rijkoort, "A compund Weibull model for the description of surface wind velocity distributions", Wetenschappelijk rapport KNMI, WR 83-13, De Bilt 1983
- [4] "Klimatologische gegevens van Nederlandse stations", nr. 3 to 7, for De Bilt, Den Helder, Eelde, Beek and Vlissingen, KNMI, Staatsdrukkerij.
- [5] M. West, K. Gilbert and R.A. Sack, "A tutorial on the parabolic equation (PE) model used for long range sound propagation in the atmosphere", Appl. Acoustics **37**, 31-49 (1992)
- [6] E.M. Salomons, "Diffraction by a screen in downwind sound propagation: a parabolic-equation approach", J. Acoust. Soc. Am. **95**, june (1994)
- [7] K. Attenborough, "Acoustical impedance models for outdoor ground surfaces", J. Sound Vib. **99**, 521-544 (1985)
- [8] K.E. Gilbert, R. Raspet, and X. Di, "Calculation of turbulence effects in an upward-refracting atmosphere", J. Acoust. Soc. Am. **87**, 2428-2437 (1990)
- [9] ISO/DP 9613-1 for acoustics, "Attenuation of sound during propagation"
- [10] C.A. Paulson, "The mathematical representation of wind speed and temperature profiles in the unstable atmospheric surface layer", J. Appl. Meteor. **9** (1970) 857-861
- [11] J.A. Businger, "Turbulent transfer in the atmospheric surface layer", in: "Workshop on Micrometeorology", ed. D.A. Haugen (Am. Meteor. Soc., Boston, 1973)
- [12] A.A.M. Holtslag, "Estimates of diabatic wind speed profiles from near surface weather observations", Boundary-Layer Meteorology **29** (1984) 225-250
- [13] E.M Salomons, J.D. van der Toorn, and F.H.A. van den Berg, report for the Dutch Ministry of Defence, TPD-HAG-RPT-93-0217 (1994)
- [14] D. Golder, "Relations among stability parameters in the surface layer", Boundary-Layer Meteorology **3** (1972) 47-58
- [15] Royal Dutch Meteorological Institute (KNMI De Bilt), "Luchtverontreiniging en weer", (Staatsuitgeverij, Den Haag 1979)

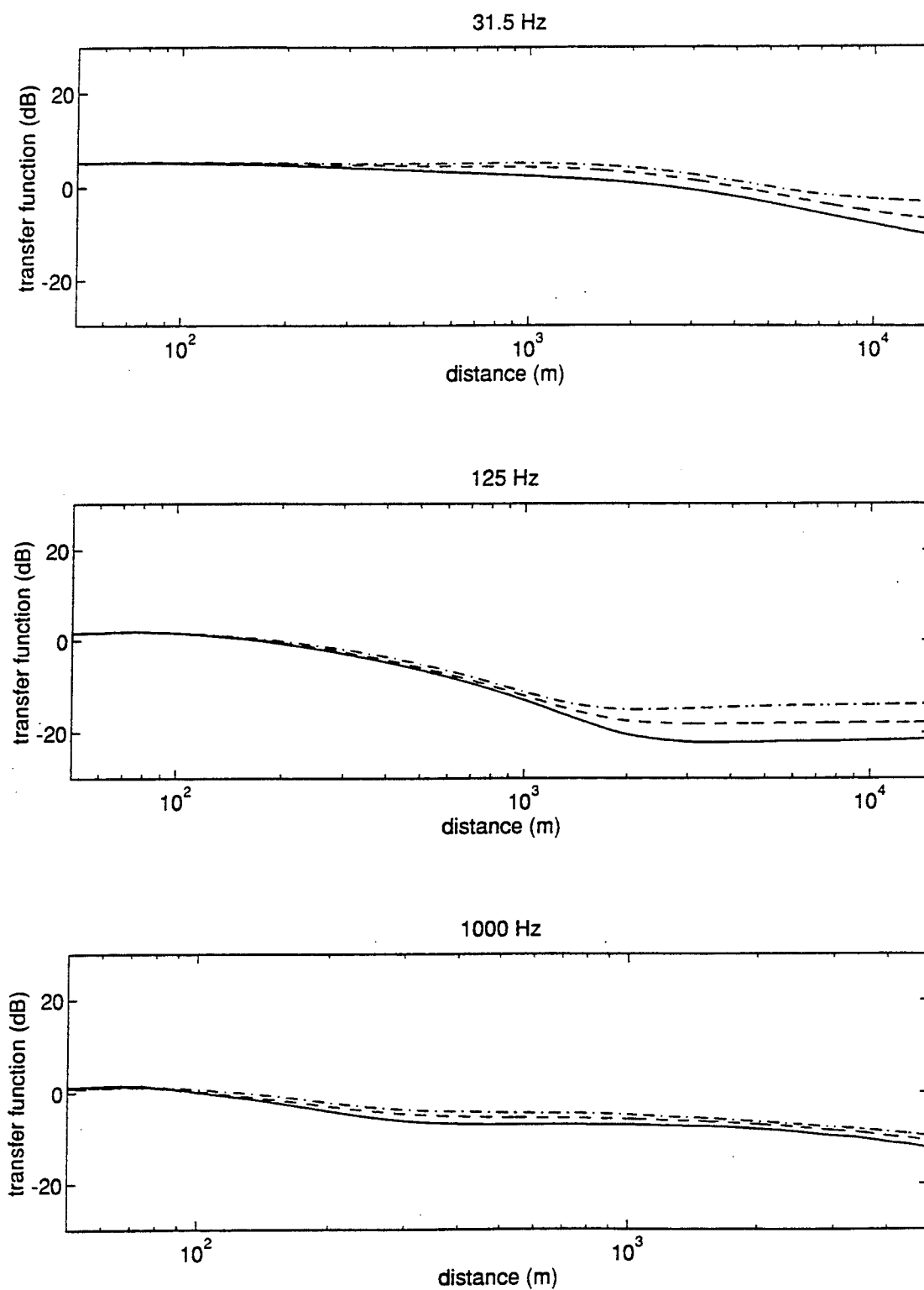


FIG. 10. Long-term average transfer function for three octave bands, as a function of the distance to the source. The solid line is for a summer day, the dashed line is for a winter day, and the dash-dotted line is for the night. Other parameters are given in the text.

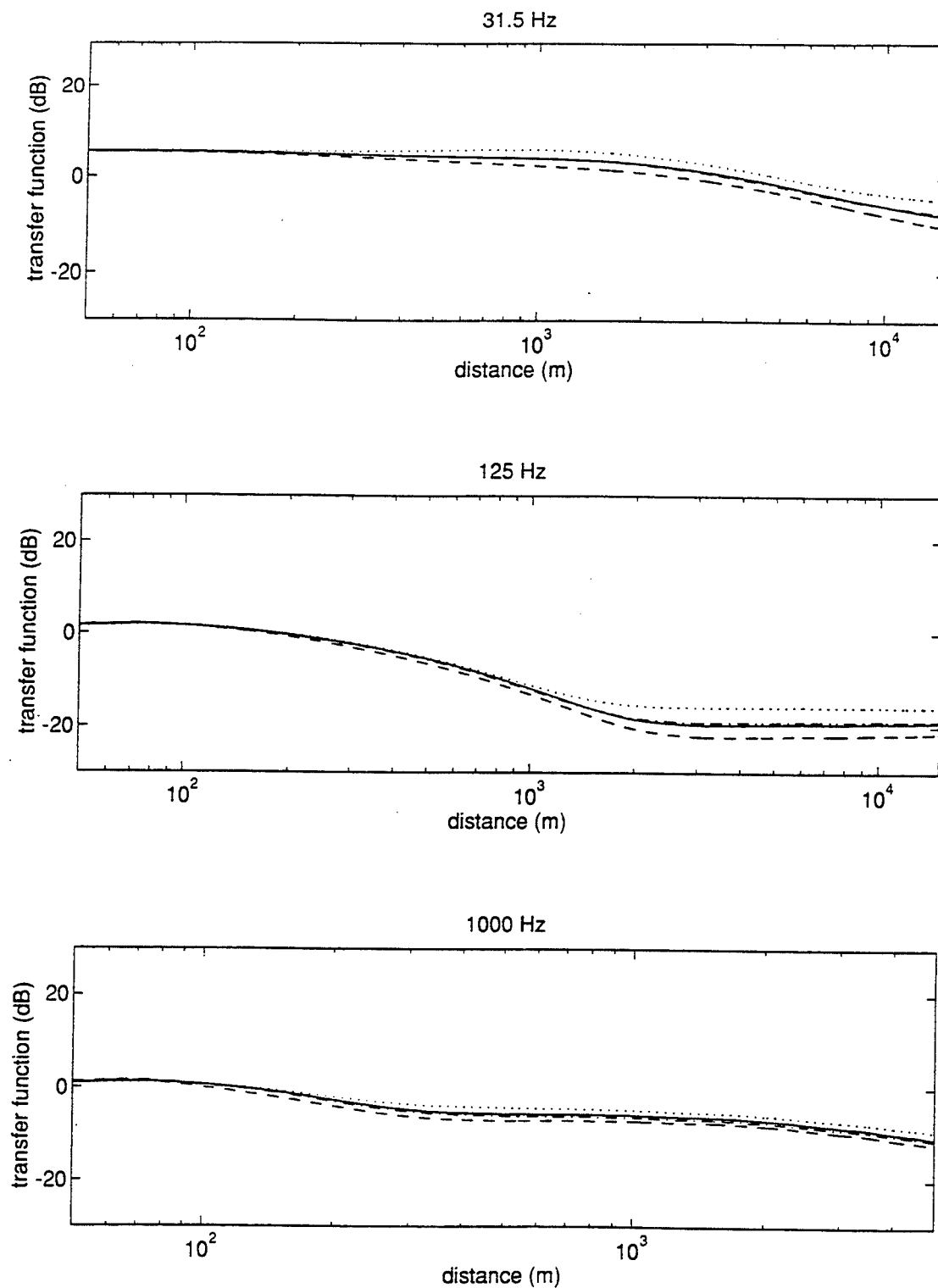


FIG. 11. Long-term average transfer function for three octave bands, as a function of the distance to the source. The solid line is for propagation direction $\beta=0^\circ$, the dashed line is for $\beta=90^\circ$, the dash-dotted line is for $\beta=180^\circ$, and the dotted line is for $\beta=270^\circ$. Other parameters are given in the text.

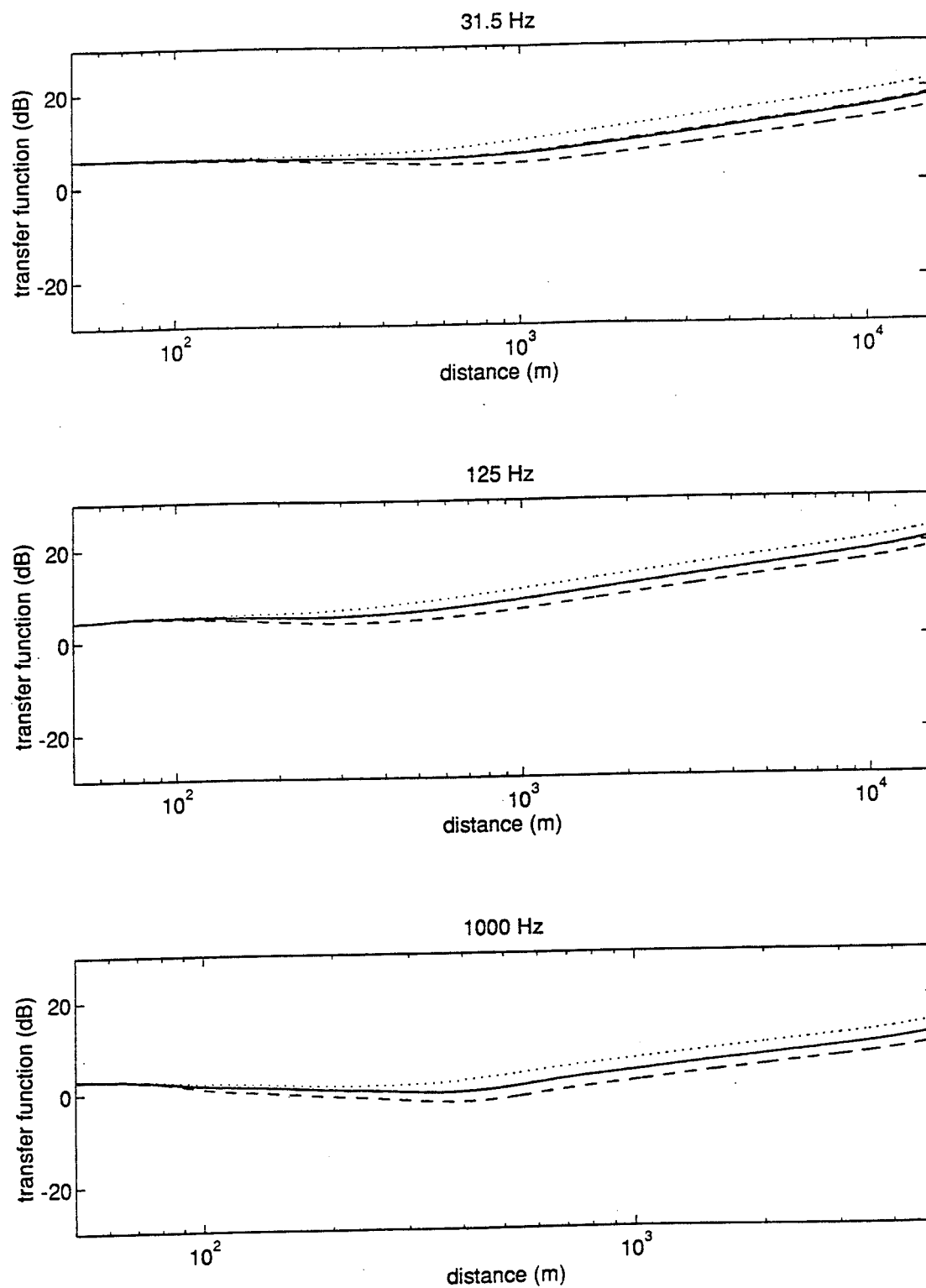


FIG. 12. As FIG. 11, but now for a reflecting ground surface with a roughness length of 0.02 cm.

Appendix A: Businger-Dyer-profiles

For the profiles of the wind speed $u(z)$ and the potential temperature $\theta(z)$ we use empirical relations known as Businger-Dyer profiles [10,11]:

$$u(z) = \frac{u_*}{\kappa} \left[\ln\left(\frac{z}{z_0} + 1\right) - \psi_M\left(\frac{z}{L}\right) \right] \quad (\text{A1})$$

and

$$\theta(z) - \theta_0 = \frac{\theta_*}{\kappa} \left[\ln\left(\frac{z}{z_0} + 1\right) - \psi_H\left(\frac{z}{L}\right) \right] \quad (\text{A2})$$

Here u_* , θ_* , θ_0 , z_0 and L are parameters, and κ is a constant. The parameter z_0 is the roughness length of the ground, L is the Obukhov length, and $\kappa=0.41$ is the Von Karman-constant. The functions ψ_M and ψ_H contain a number of constants, and in different publications slightly different values are used for these constants. We use the following functions.

For an unstable atmosphere ($z/L < 0$) we use:

$$\psi_M\left(\frac{z}{L}\right) = 2 \ln\left(\frac{1+x}{2}\right) + \ln\left(\frac{1+x^2}{2}\right) - 2 \arctan(x) + \frac{\pi}{2} \quad (\text{A3})$$

and

$$\psi_H\left(\frac{z}{L}\right) = 2 \ln\left(\frac{1+x^2}{2}\right) \quad (\text{A4})$$

with $x = (1 - 16z/L)^{1/4}$.

For a stable atmosphere ($z/L > 0$) we use [12]:

$$\psi_M\left(\frac{z}{L}\right) = \psi_H\left(\frac{z}{L}\right) = \begin{cases} -\frac{5z}{L} & \text{for } z \leq 0.5L \\ -7 \ln\left(\frac{z}{L}\right) - \frac{4.25}{(z/L)} + \frac{0.5}{(z/L)^2} - 0.852 & \text{for } z > 0.5L \end{cases} \quad (\text{A5})$$

The profiles yield good agreement with experimental profiles, up to a height of at least about 100 meters [13].

The argument of the logarithms in the profiles is usually (z/z_0) , instead of $(z/z_0 + 1)$. This makes a negligible numerical difference, as the roughness length is small. The advantage of our choice is a zero wind speed at zero height (strictly, the Businger-Dyer relations are not valid down to zero height).

The Businger-Dyer profiles contain five parameters: u_* , θ_* , θ_0 , z_0 and L .

We suppose that the roughness length z_0 is known. This parameter can be estimated with the Davenport classification [2]. The parameter θ_0 , the potential temperature at zero height, is irrelevant for sound propagation, and we set $\theta_0 = 288$ K.

There are three parameters left: u_* , θ_* and L . We will describe a method to determine these parameters, based on two meteorological parameters: the wind speed u_{10} at a height of ten meters, and the cloud cover N .

First we determine the Pasquill class corresponding to N and u_{10} , using the tables from Appendix C. Next, the relations given in Appendix B are used to compute the value of the Obukhov length L . The sign of L determines the stability, and with the Businger-Dyer

profile (A1) the value of u_* is computed from u_{10} .

Finally, the value of θ_* is determined from the following relation:

$$L = \frac{T u_*^2}{\kappa g \theta_*} \quad (\text{A6})$$

where g is the gravitational acceleration and T the temperature. This relation is in fact the definition of the Obukhov length L .

The final step is the transformation of the potential temperature to the absolute temperature, using the relation:

$$T(z) = \theta(z) - 0.01z \quad (\text{A7})$$

This relation assumes that the atmosphere consists of dry air. Moist influences the term $-0.01z$. However, the difference between the potential temperature and the absolute temperature is small, and we neglect the influence of moist.

Appendix B: Obukhov length and Pasquill classification

Based on a paper of Golder [14], we have determined relations between the Obukhov length L and the roughness length z_0 , for the six Pasquill classes:

$$\frac{1}{L} = B_1 \lg(z_0) + B_2 \quad (\text{B1})$$

The values of the constants B_1 and B_2 are given in Table B1 for the six Pasquill classes. The maximum value of z_0 for which these relations are valid is $z_0=0.5$ m, extrapolation to larger values is not possible.

Table B1. Values of the constants B_1 and B_2 in Eq. (B1), for the six Pasquill classes A to F.

Pasquill class	A	B	C	D	E	F
B_1	0.04	0.03	0.02	0	-0.02	-0.05
B_2	-0.08	-0.035	0	0	0	0.025

Statistics of Pasquill classes

Below we give statistical tables for the Pasquill class as a function of cloud cover N (in octants: $N=0$ for a clear sky, $N=8$ for a completely overcast sky) and wind speed u at a height of ten meters, for The Netherlands [15]. For the day a distinction is made between the four seasons, for the night the variation with season is negligible.

DAY WINTER

8	D	D	D	D	D	D	D
7	D	D	D	D	D	D	D
6	B	B	C	C	C	D	D
5	B	B	C	C	C	C	D
4	B	B	B	C	C	C	D
3	B	B	B	C	C	C	C
2	B	B	B	B	C	C	C
1	A	A	B	B	B	B	C
0	A	A	B	B	B	B	C

DAY SPRING

8	D	D	D	D	D	D	D
7	D	D	D	D	D	D	D
6	B	B	C	C	C	C	D
5	B	B	B	C	C	C	D
4	B	B	B	B	C	C	C
3	A	A	B	B	B	C	C
2	A	A	A	B	B	B	C
1	A	A	A	B	B	B	C
0	A	A	A	B	B	B	C

DAY SUMMER

8	D	D	D	D	D	D	D
7	D	D	D	D	D	D	D
6	B	B	B	B	C	C	D
5	B	B	B	B	B	C	C
4	A	A	B	B	B	C	C
3	A	A	A	B	B	B	C
2	A	A	A	B	B	B	C
1	A	A	A	A	B	B	C
0	A	A	A	A	B	B	C

DAY AUTUMN

8	D	D	D	D	D	D	D
7	D	D	D	D	D	D	D
6	B	B	C	C	C	D	D
5	B	B	C	C	C	C	D
4	B	B	B	B	C	C	D
3	A	B	B	B	C	C	C
2	A	A	B	B	B	C	C
1	A	A	B	B	B	B	C
0	A	A	B	B	B	B	C

NIGHT YEAR

8	D	D	D	D	D	D	D
7	D	D	D	D	D	D	D
6	F	F	E	D	D	D	D
5	F	F	E	D	D	D	D
4	F	F	F	E	D	D	D
3	F	F	F	E	D	D	D
2	F	F	F	F	E	D	D
1	F	F	F	F	E	E	D
0	F	F	F	F	E	E	D

→ u (m/s)

Appendix D: Statistics of wind in The Netherlands

We use an empirical statistical model for wind in The Netherlands, developed by Rijkoort [2,3]. The parameters of this model have been fitted to wind data, collected over the period 1962-1976 at various meteorological stations in The Netherlands.

The model makes use of the cumulative frequency distribution $F(u)$ of the wind speed. The function $F(u)$ is defined as the probability that the wind speed is smaller than the value u . The function $F(u)$ increases monotonically from zero at $u=0$ to one at $u=\infty$. The derivative of $F(u)$ is the frequency distribution of the wind speed: $f(u)=dF(u)/du$. Thus, $f(u)du$ is the probability that the wind speed is between u and $u+du$. The function $f(u)$ has a maximum near the average wind speed.

For the day, the cumulative distribution is well described by the Weibull function:

$$F(u) = 1 - \exp\left(-\left(\frac{u}{a}\right)^k\right) \quad (D1)$$

with two parameters: a and k .

For the night, the cumulative distribution is well described by a slightly different function:

$$F(u) = 1 - \exp\left(-\left[\frac{u}{a}(1+\gamma \exp(-u/5))\right]^k\right) \quad (D2)$$

with three parameters: a , k and γ . The values of a and k are equal for the day and the night. The parameter γ is positive, as average wind speeds are smaller at night than by day.

The model uses twelve wind directions (twelve sectors of 30°) and six periods of the year (january-february, march-april,..., november-december). The parameters a , k and γ depend on the wind direction and the period of the year. This dependence is indicated by two indices i and j ($i=1,\dots,12$; $j=1,\dots,6$). There are $12 \times 6 = 72$ different parameters a_{ij} , 72 different parameters k_{ij} , and 72 different parameters γ_{ij} . Moreover, these parameters vary with the location in The Netherlands. In addition, two more sets of 72 parameters are required: d_{ij} and n_{ij} . These parameters represent the season-dependent numbers of hours of wind direction i , for the day and the night, respectively.

In total, there are $5 \times 72 = 360$ parameters, for each location in The Netherlands. Rijkoort shows that the number of independent parameters is considerably smaller. He has fitted the independent parameters to wind data collected over the period 1962-1976 at various meteorological stations in The Netherlands. As a result, Rijkoort gives the values of the independent parameters, for a large number of locations in The Netherlands. We use these values to compute wind speed distributions and wind roses.

THE METEOROLOGICAL INFLUENCE ON THE ATMOSPHERIC ABSORPTION FOR HORIZONTAL AND VERTICAL SOUND PROPAGATION

Conny Larsson
Department of Meteorology
Uppsala University
Box 516, S-751 20 Uppsala
Sweden

ABSTRACT

The atmospheric absorption are important for long range sound propagation. A method for computing the atmospheric absorption for both horizontal and vertical sound propagation have been deduced. The distribution of the atmospheric absorption for horizontal sound propagation from two stations in Sweden have been computed. The vertical absorption for a number of different meteorological situations have also been carried out.

INTRODUCTION

The understanding of sound propagation outdoors has increased during the past decades ^{1,2}. Today there exist different types of prediction schemes and propagation models for planning purposes. They are often restricted to certain meteorological conditions, e.g. 'moderate downwind', and do not take the local climate into consideration. How common these conditions are for an actual site is

not taken into consideration. The predicted quantity is often a single value, e.g. the long-term average sound level, and gives no information about the highest noise levels and how often they occur.

The cumulative distribution ought to be a more useful tool for users. It contains more information needed for decision-making, e.g. the fraction of time a certain noise level is exceeded, or what noise level is exceeded, e.g. the worst 5 % of the time. The mean or the median sound level gives no information about the upper and lower tail of the distribution. Two distributions with different highest levels can have the same mean value.

The only way to obtain the distribution, without expensive long-time sound level measurements, is to include the effects of the weather and the climate for an area.

Since 1976, investigations concerning meteorological effects on sound propagation have been carried out at the Department of Meteorology at the Uppsala University. A number of experimental and theoretical studies ³⁻¹² have been performed. It was found that the meteorological effects were noticeable at a distance of 25 m from the source and increased with decreasing receiver height.

METEOROLOGICAL EFFECTS ON SOUND PROPAGATION

The three most significant meteorological effects on sound propagation are: *refraction*, *scattering by turbulence* and *atmospheric absorption*. This paper will focus on the last effect. The other effects will only be discussed briefly.

Refraction of sound rays occurs if the sound velocity and/or the wind speed change along the ray path, i.e. there are gradients of wind and temperature. The wind and temperature fields are horizontally homogeneous in reasonably flat terrain. Thus wind speed and temperature depend on elevation only. They are dependent on each other through the governing hydrodynamic equations. The refraction influences the sound level. The angle of incidence at the ground is changed, which results in varying ground attenuation. In downwind conditions and/or temperature inversion the sound rays are bent downwards, and in upwind conditions and/or lapse they are bent upwards. Upwind conditions and/or lapse create areas which no direct sound ray can reach, known as sound shadow zones. The refractive effects of the gradients of the temperature and the component of the wind in the direction of propagation are additive. As the refractive conditions change, the various path lengths between the waves intersecting at the

receiver change. Thus, depending on the phase relationships between these waves, some frequencies will be amplified and other decreased.

Turbulence has a two-fold effect on sound propagation. First, the temperature fluctuations lead to fluctuations in the velocity of sound. Secondly, turbulence velocity fluctuations produce additional random distortions of the sound wavefront. Turbulence scatters sound into sound shadow zones and causes fluctuations of the phase and the amplitude of the sound waves, thus destroying the interference between different rays reaching the receiver. This gives higher sound levels than expected for frequencies where the ground effect has its maximum. The effect of turbulence can be disregarded for low frequencies and distances up to a few hundred meters. Integration over many turbulence cycles will minimize the effect of turbulence on the sound level. Mean values over 5-10 minutes gives more reproduceable results than just an instantaneous measurement.

The atmospheric absorption depends on frequency, relative humidity, temperature and atmospheric pressure. The sound attenuation due to the absorption can be calculated.^{13,14} The atmospheric absorption increases with distance and becomes more important the longer sound propagation is under study. Figure 1 shows the atmospheric absorption for different frequencies and relative humidity at 15 °C and figure 2 for 0 °C.

The proposed standard in ISO 3891¹⁵, using 15 °C and 70 % rel. humidity, are given in the box at the top of fig. 1. Great deviations from this values can be found for many situations. For low values of relative humidity, i.e. over deserts in daytime, very little attenuation can be found.

Annual and diurnal variations of relative humidity and temperature introduce large variations of atmospheric absorption. Relative humidity reaches its maximum close after sunrise and it's minimum in the afternoon when temperature is highest. The diurnal variations are greatest during the summer.

A computer program was made to calculate the atmospheric absorption.¹⁴ Long term measurements of temperature and humidity close to the ground at two stations in Sweden has been used in order to get the distribution for **horizontal sound propagation**. Figure 3 gives the cumulative distribution for Arlanda (60 °N), in the southern part of Sweden and in fig. 5 for Abisko (68 °N), in the northern part of Sweden. The cumulative distribution for temperature and relative humidity for the two stations are given in figs. 4 and 6.

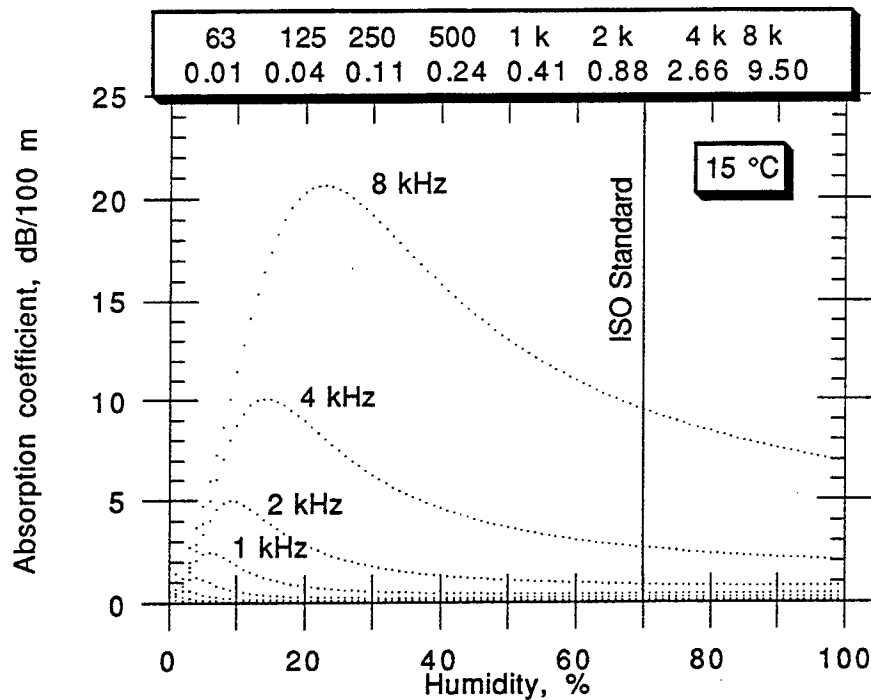


Figure 1. Atmospheric absorption 14 (dB/100 m) for various relative humidity (%) at 15 °C and normal air pressure (1013.25 hPa). Values from ISO 3891¹⁵ are given in the top of the figure.

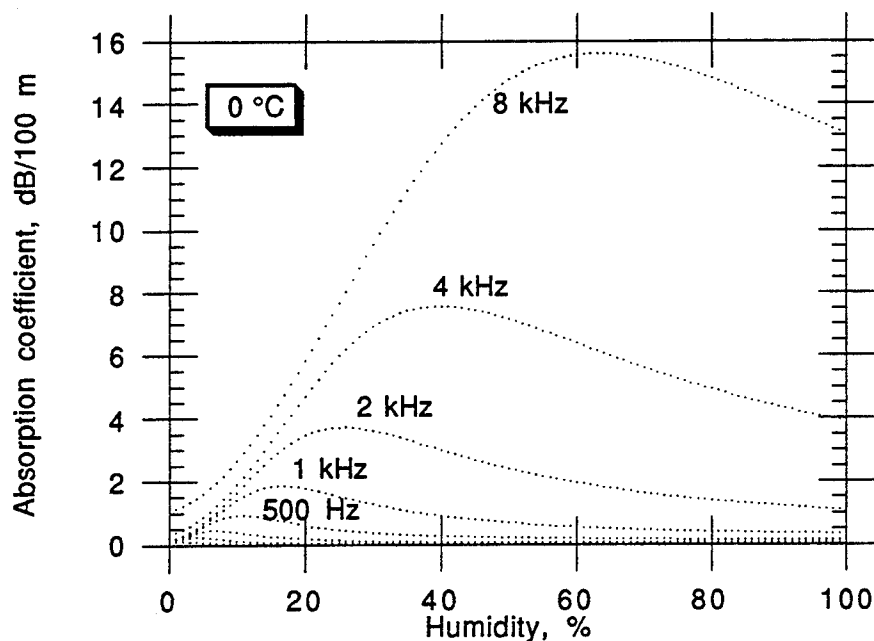


Figure 2. Atmospheric absorption 14 (dB/100 m) for various relative humidity (%) at 0 °C and normal air pressure (1013.25 hPa).

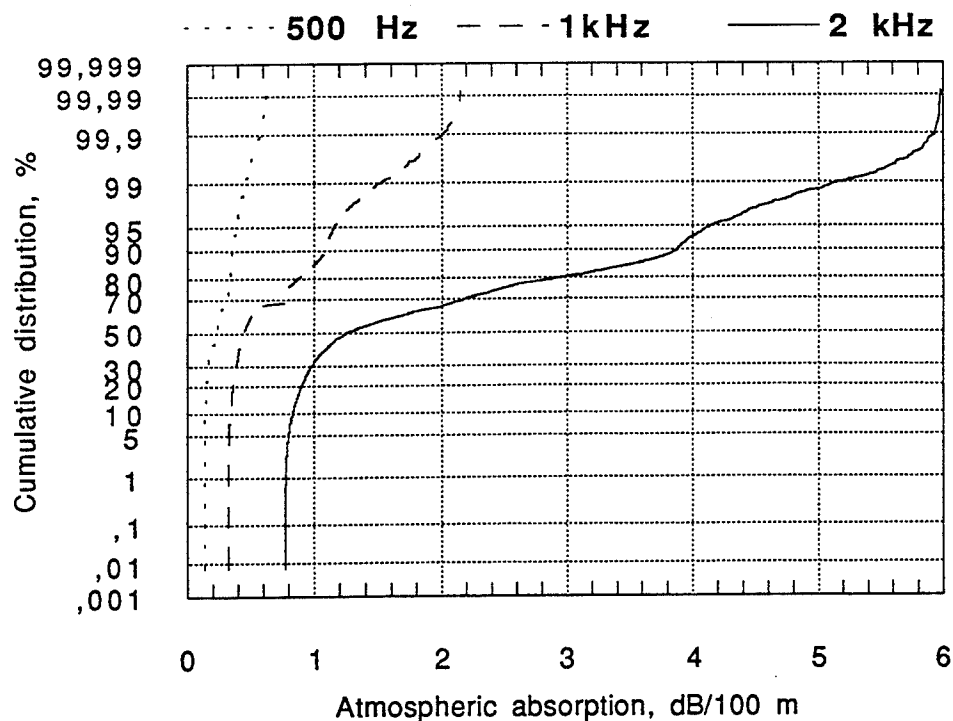


Figure 3. Cumulative distribution of atmospheric absorption ¹⁴ for a place close to the Stockholm-Arlanda airport 1990-1991.

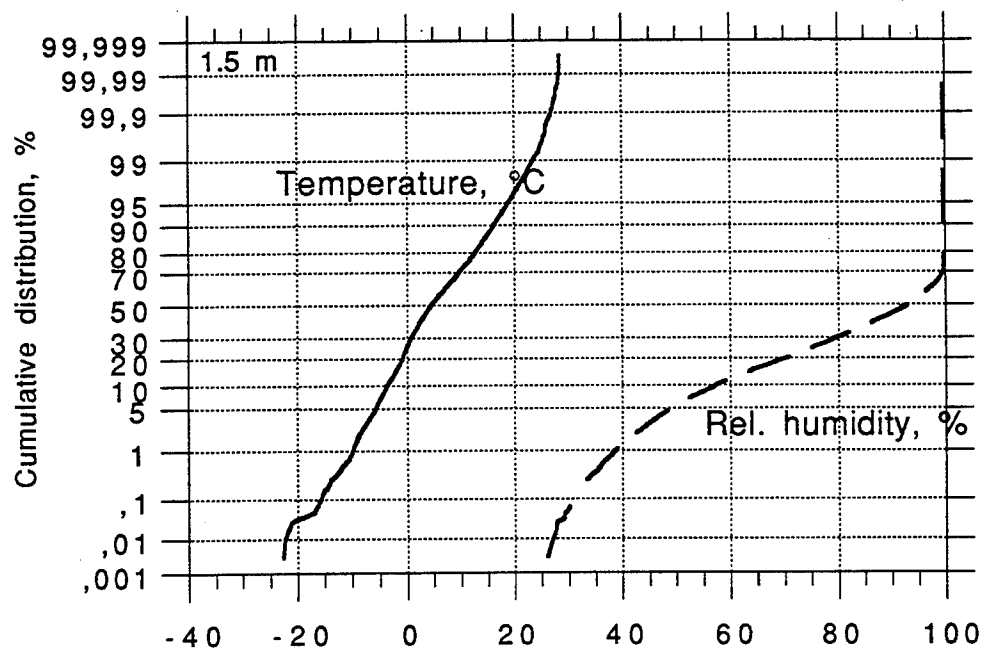


Figure 4. Cumulative distribution of temperature and relative humidity close to the Stockholm-Arlanda airport.

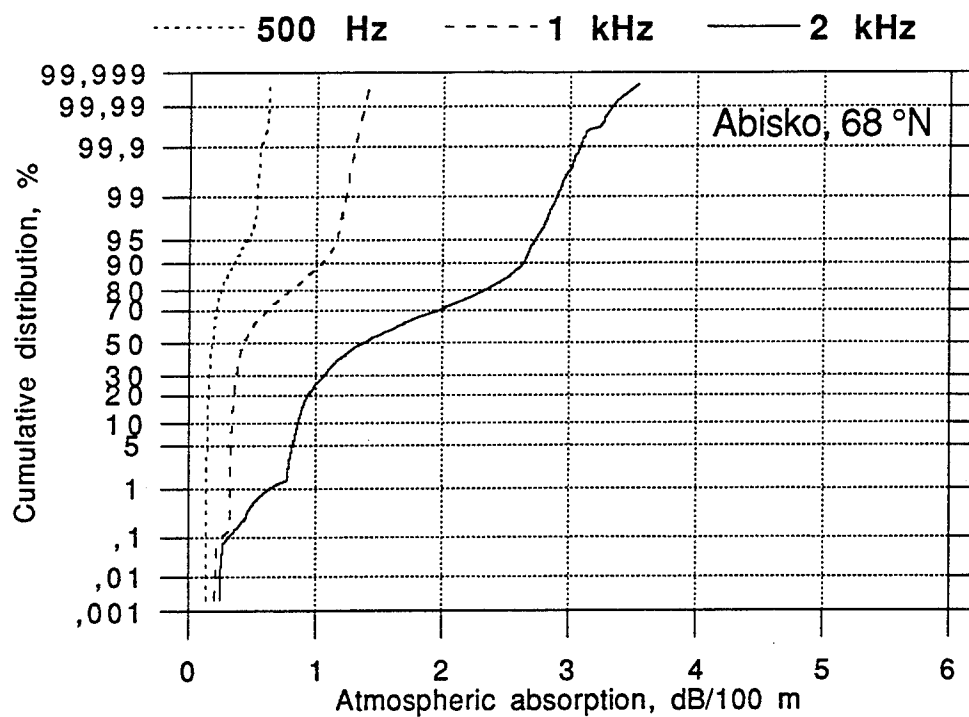


Figure 5. Cumulative distribution of atmospheric absorption ¹⁴ for different frequencies for Abisko (68 °N) 1987-1989.

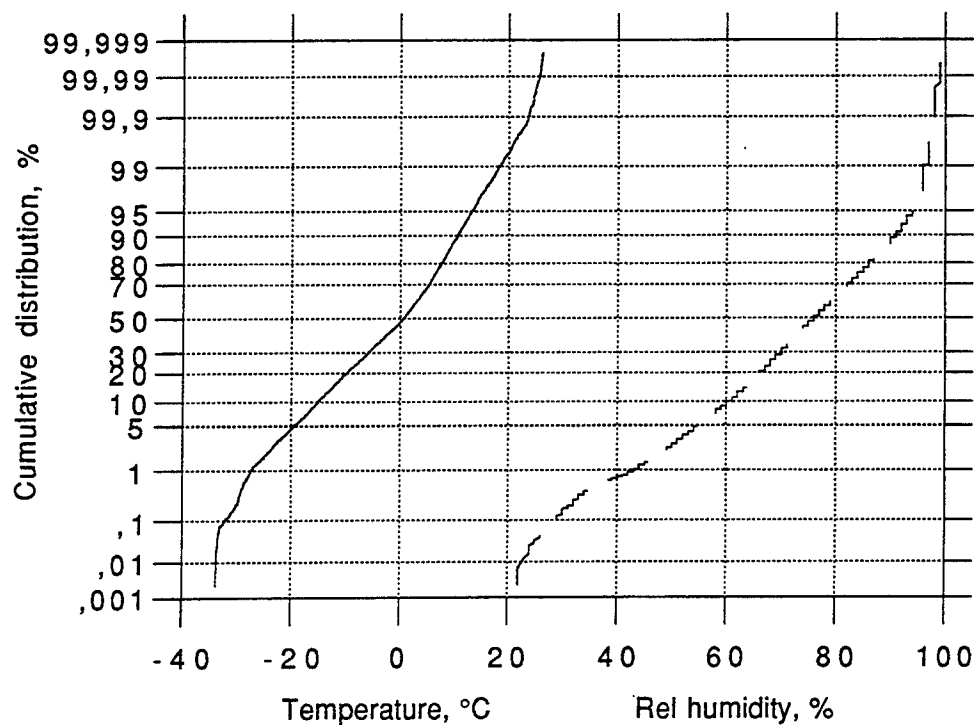


Figure 6. Cumulative distribution of temperature and relative humidity at 1.5 m height for for Abisko 1987-1989.

Large deviations are found between these two locations. Comparison with the proposed standard, see figs. 1, 3 and 5, indicate an overestimation of the absorption values between 1 and 60 % of the time for these sites. Good estimates of long range sound propagation need correct information of the temperature and humidity. Dataset from local weather stations should be included in the calculation of long distance sound propagation.

Temperature and humidity profiles from radiosonds are used for calculation of the atmospheric absorption for **vertical sound propagation**. The air pressure is also included in the calculations. Figure 7 gives the result for an atmosphere with a ground temperature of 15 °C and a dry adiabatic lapse rate (≈ 1 °C/100 m). The relative humidity is 70 % at all levels. The atmospheric absorption for 1 kHz from an aircraft at 1000 m is 4 dB if the atmosphere looks like the one assumed in fig. 7. If however the atmosphere is like the one in fig. 8 the atmospheric absorption will be 7 dB for the same height and frequency. There is very little extra absorption above 4000 m as the rel. humidity is very low.

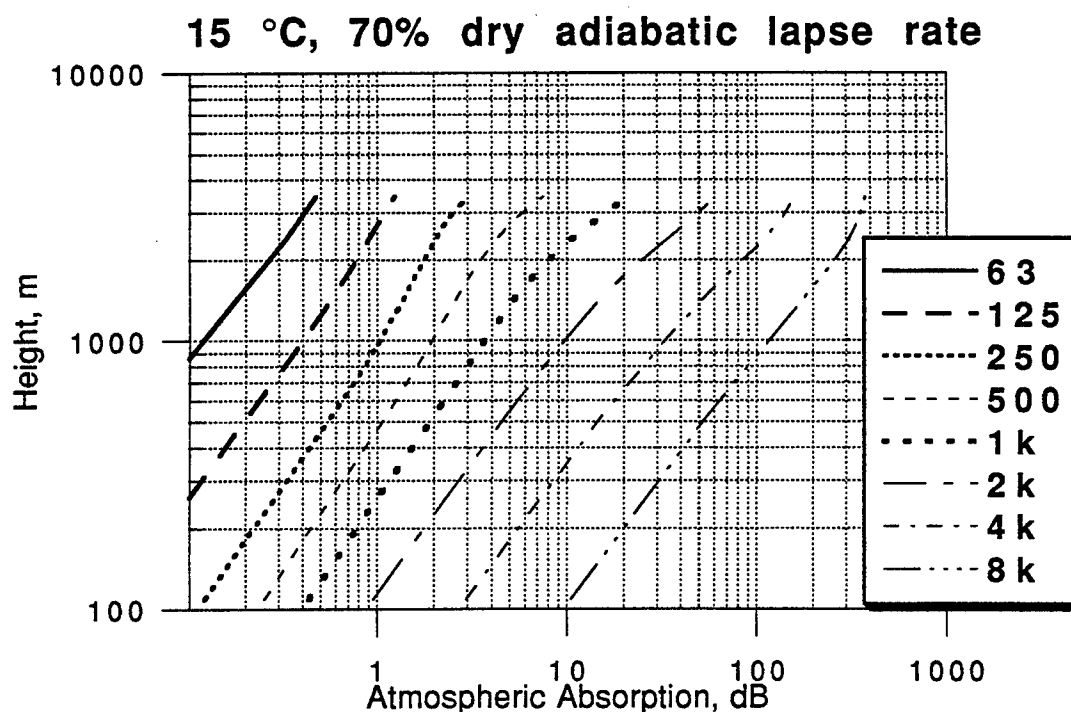


Figure 7. Atmospheric absorption for vertical sound propagation.

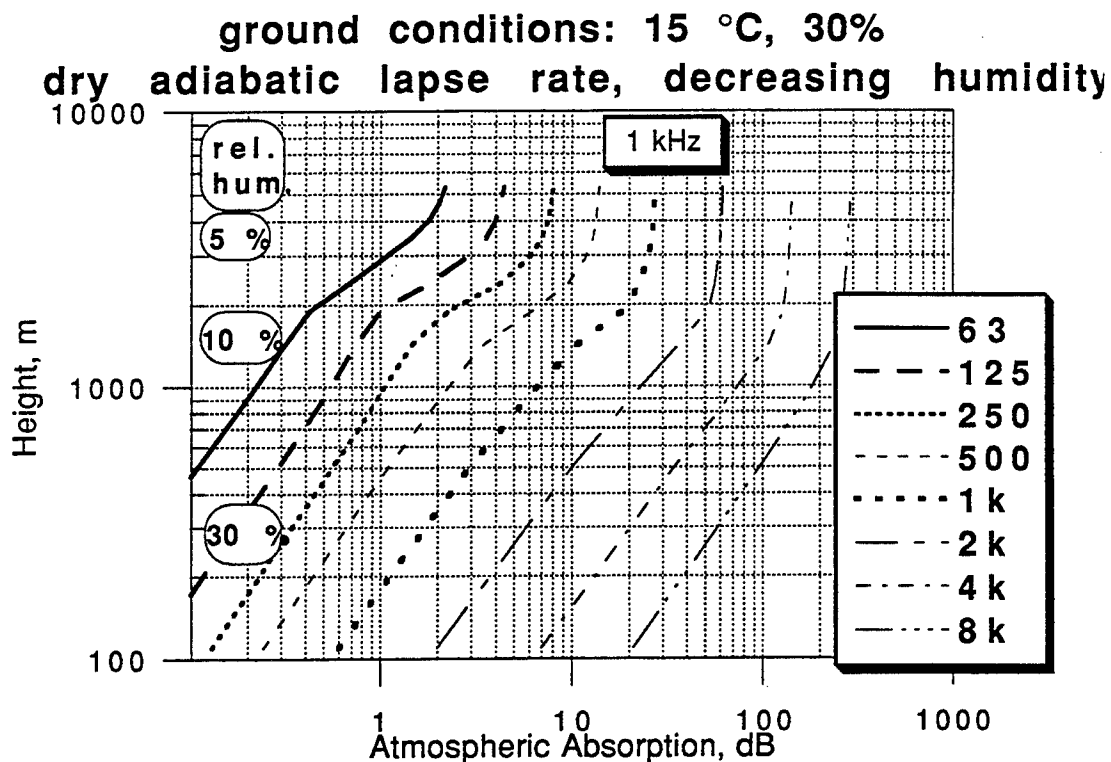


Figure 8. Atmospheric absorption for vertical sound propagation.

Calculations of the atmospheric absorption for vertical sound propagation have been carried out for a number of real temperature and humidity profiles taken from the radiosond station at the Stockholm-Bromma airport. The sondings at noon on November 3, 1992 and January 5, 1993 are used for the calculations. Figure 9 and 10 display the absorption values. Temperature profiles and humidity profiles are given in figs. 11 and 12.

The absorption values for the January case in fig. 10 are higher than those for the November case in fig. 9. Relative humidity are mostly high close to the ground. The humidity decrease faster for the case in January than for the one in November, see fig. 12. Decreasing humidity at higher altitudes will give increasing absorption when the maximum are reached, see the curves in fig. 1 and 2. Very little absorption are found for very low humidity, e.g. the almost vertical curves above 2-4 km in Figs. 9 and 10. Such conditions are common at altitudes above 2-4 km during high pressure weather situations.

The relationship between temperature, humidity, air pressure and atmospheric absorption are rather complex. Rough estimates from standard atmosphere could introduce large errors and can be avoided by use of data from radiosond stations.

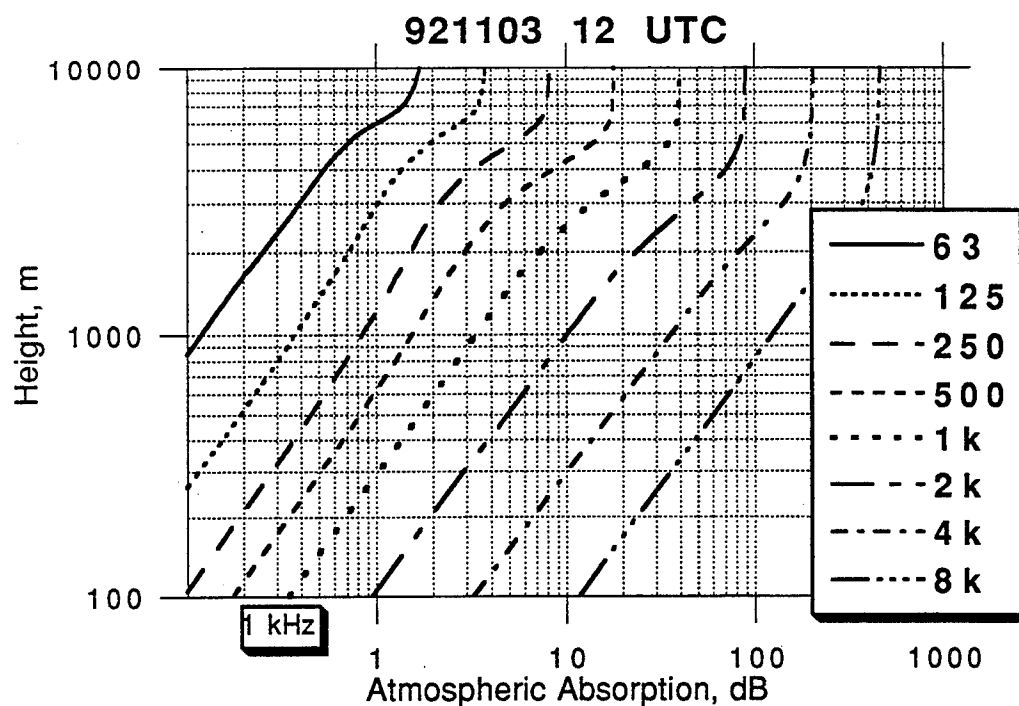


Fig 9. Vertical atmospheric absorption (November 3, 1992 at 12 UTC. Stockholm, Sweden).

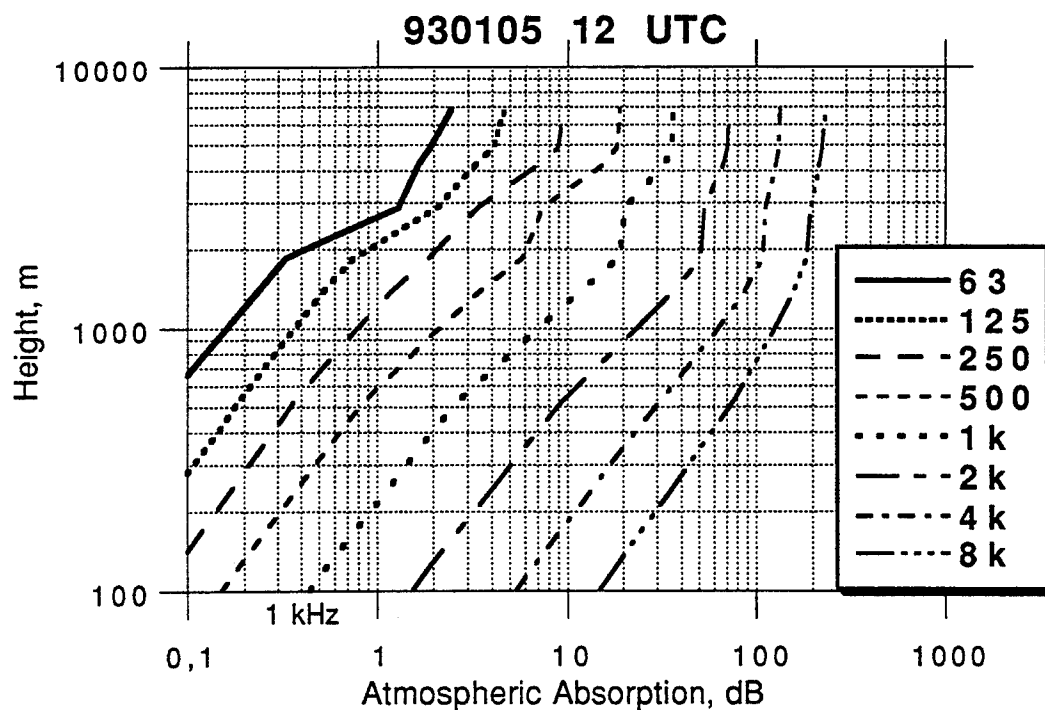


Fig 10. Vertical atmospheric absorption (January 5, 1993 at 12 UTC. Stockholm, Sweden).

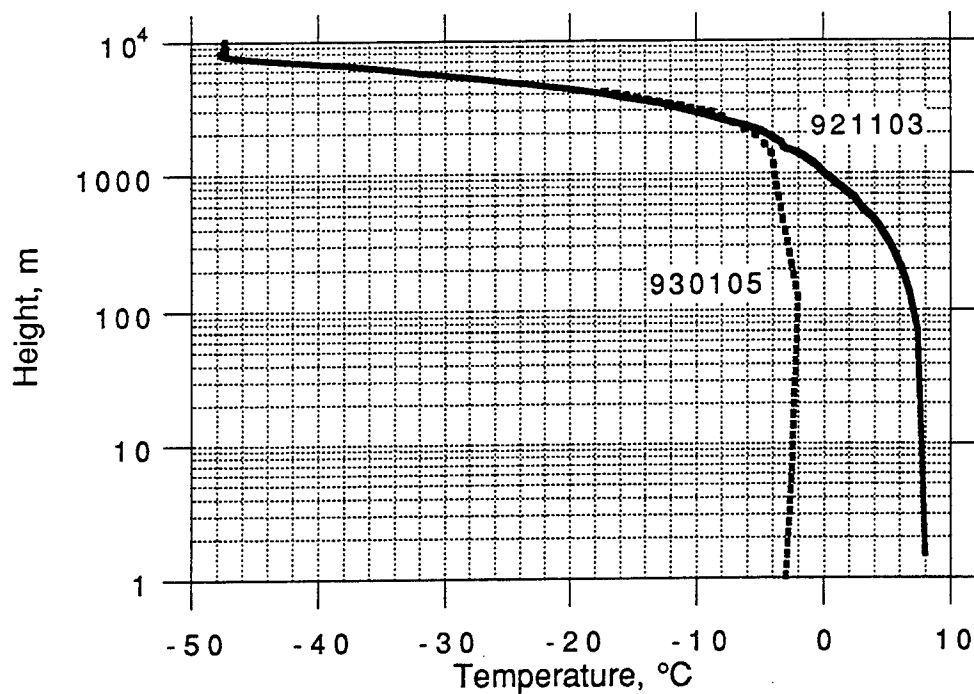


Figure 11. Vertical temperature profiles (November 3, 1992 and January 5, 1993 at 12 UTC, Stockholm, Sweden).

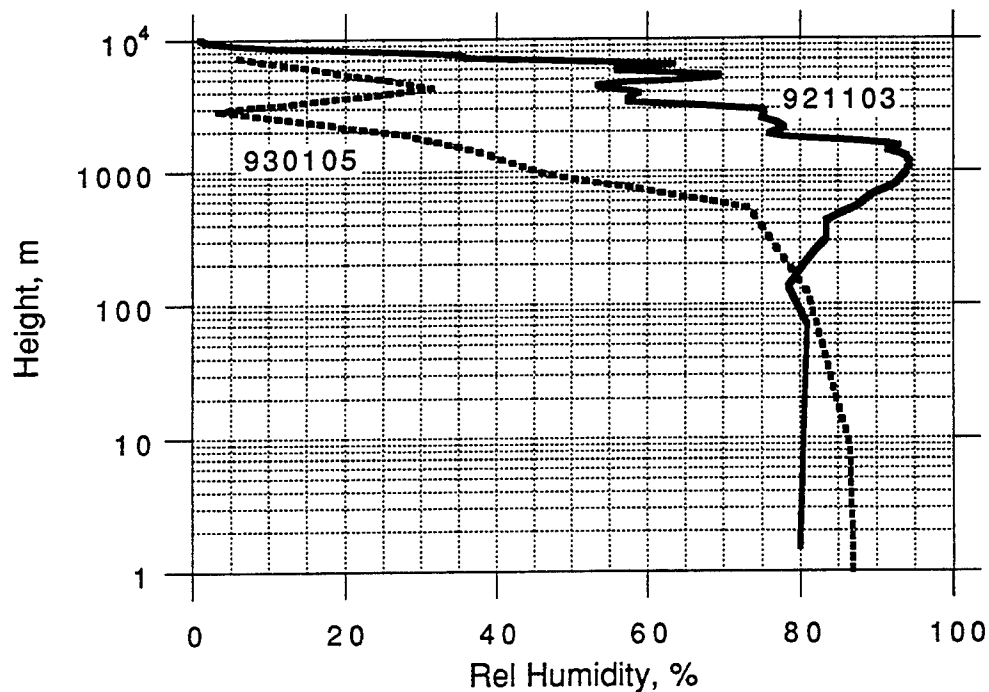


Fig 12. Figure 9. Vertical humidity profiles (November 3, 1992 and January 5, 1993 at 12 UTC, Stockholm, Sweden).

CONCLUSIONS

The atmospheric absorption are important for long range sound propagation. Great deviations from the proposed standard in ISO 3891 can be found for many situations. For low values of relative humidity, i.e. close to the ground over desserts in daytime or at altitudes around 2-4 km during high pressure situations, very little attenuation are be found.

Correct estimates of long range sound propagation need correct information of temperature and humidity. Datasets from local weather stations should be included in the calculation of long distance sound propagation.

The relationship between temperature, humidity, air pressure and atmospheric absorption are rather complex. Rough estimates from standard atmosphere can introduce large errors, which can be avoided by use of data from radiosond stations.

The time has come for using data from local meteorological stations.

ACKNOWLEDGEMENTS

This study was financially supported by the Swedish Environmental Protection Agency.

REFERENCES

- 1 Delany, M. E., Sound propagation in the atmosphere: a historical review. *Acustica*, 38 (1977), pp. 201-23.
- 2 Piercy, J. E., Embleton, T. F. W. & Sutherland, L. C., Review of noise propagation in the atmosphere. *J. Acoust. Soc. Am.*, 61(6) (1977), pp. 1403-18.
- 3 Larsson, C. and Israelsson, S.: The influence of the meteorological parameters on the sound propagation from a traffic road. *Inter-Noise 79*, Warszawa, Poland (1979), pp. 513-516.
- 4 Larsson, C. and Israelsson, S.: The effects of meteorological parameters on sound propagation from a point source. Report No. 67, Dept. of Meteorology, Uppsala (1982).
- 5 Hallberg, B., Larsson, C. and Israelsson, S.: Measurements of meteorological effects on long-range sound propagation using m-sequence correlation. *J. Acoust. Soc. Am.* 78(3) (1985), pp. 1038-1044.
- 6 Larsson, C. and Hallberg, B.: Sound propagation over ground with a barrier - some meteorological effects. *Inter-Noise 83*,

- Edinburgh, Great Britain (1983), pp. 271-274.
- 7 Larsson, C., Hallberg, B. and Israelsson, S.: Long-term audible noise and radio noise performance from an operating 400-kV transmission line. IEEE. Transactions on Power Delivery, Vol. 3, No 4 (1988), pp. 1842-1846.
 - 8 Larsson, C. and Israelsson, S.: Effects of meteorological conditions and source height on sound propagation near the ground. Applied Acoustics 33, pp 109-121 (1991).
 - 9 Larsson, C., Hallberg, B. and Israelsson, S.: A method to estimate meteorological effects on sound propagation near the ground. Applied Acoustics 25, pp. 17-31 (1988).
 - 10 Larsson, C: Weather effects on sound propagation near the ground. Second International Congress on recent developments in air & structure-borne sound and vibration, Auburn, Alabama, U.S.A. (1992).
 - 11 Hallberg, B., Larsson, C. och Israelsson, S.: A numerical ray tracing model for sound propagation. Department of Meteorology, Uppsala (1988) (in Swedish).
 - 12 Hallberg, B., Larsson, C. och Israelsson, S.: Numerical ray tracing in the atmospheric surface layer. J. Acoust. Soc. Am. 83(6) (1988), pp. 2059-2068.
 - 13 ASA, ANSI, Method for the calculation of the absorption of sound by the atmosphere. ANSI S1.26 (ASA 23-1978), (1978).
 - 14 International Standard Organization/Draft Proposal 9613.2 (1989): Attenuation of sound during propagation outdoors. Part 1: Calculation of the absorption of sound by the atmosphere.
 - 15 International Standard Organization 3891: (1978): Acoustics - Procedure for describing aircraft noise heard on the ground.

Sound propagation in a spatially inhomogeneous medium

K M Li

Faculty of Technology, The Open University,
Milton Keynes MK7 6AA, United Kingdom

Abstract

This paper examines the propagation of sound in a spatially inhomogeneous medium. The high-frequency sound field due to a monopole source in a range-dependent environment has been derived. The governing wave equation is simplified by applying the method of Liouville-Green transformation that is extended to three dimensions. The method of Fourier transformation is then used to express the solution in terms of a Fourier integral. This integral can be estimated asymptotically by the method of stationary phase. The sound field can be expressed in a convenient form for numerical implementation. The present approach contrasts sharply with the classical ray method where the form of the asymptotic solution is assumed. Nevertheless, it is found that the amplitude and the phase function of the propagated sound agree with that determined by the ray method. This is perhaps not surprising because both methods exploit the asymptotic behaviour of the solution.

Theory

To derive an approximate equation for the propagation of acoustic disturbances in a spatially inhomogeneous medium, we begin with the Helmholtz equation

$$\nabla^2 p + k_0^2 n(\mathbf{r}) = -\delta(\mathbf{r}) \quad (1)$$

where the time-harmonic factor $e^{-i\omega t}$ is suppressed. Here, p is the acoustics disturbances, k_0 is a reference wavenumber and n is the index of refraction, which is assumed to vary as

a function of the three-dimensional space. Without loss of generality, we assume that the source is located at the origin and the receiver at (x_1, x_2, x_3) . In the present studies, we restrict our attention only to the problem where there is no boundary plane in the vicinity of the source. A monopole source of unit strength is introduced at the right side of Eq. (1).

As in our previous studies^{1,2} we shall base our analysis on the use of the method of Fourier transformation. However we can not apply the method directly because the governing wave equation, cf. Eq. (1), is non-separable as it stands. Certain approximations are required that can remove the analytical difficulties pertaining to the direct treatment. Our first step aims to seek such approximations.

In order to present the problem in an amenable form to solution by the method Fourier transformation it is convenient to introduce a new set of co-ordinates, (z_1, z_2, z_3) . The choice of the new co-ordinates are solely on the basis of obtaining a simplified and separable Helmholtz equation. We note here that the new independent variables, z_1, z_2 and z_3 , are functions of the original spatial variables, x_1, x_2 and x_3 , respectively. With the new independent variables, Eq. (1) becomes

$$\left[\delta_{ij} \frac{\partial z_k}{\partial x_i} \frac{\partial z_l}{\partial x_j} \right] \frac{\partial^2 p}{\partial z_k \partial z_l} + \delta_{ij} \frac{\partial^2 z_k}{\partial x_i \partial x_j} \frac{\partial p}{\partial z_k} + k_0^2 n^2 p = -\delta(r) \quad (2)$$

where δ_{ij} is Kronecker Delta function defined by

$$\begin{aligned} \delta_{ij} &= 1 \text{ if } i = j; \\ \delta_{ij} &= 0 \text{ if } i \neq j. \end{aligned}$$

Here, tensor notation is used in Eq. (2) throughout where the summation over repeated indices is from 1 to 3. Obviously, it is difficult, if not impossible, to obtain a solution for the acoustic disturbances from Eq. (2). Further approximations are needed in order to simplify the situation. If we are interested in a high frequency sound field where the wave

length of the acoustic disturbances is much smaller than the scale of inhomogeneity, then the analysis can be simplified considerably. In other words, we are primarily interested in a slowly varying medium such that the spatial derivatives of the refractive index, n , is of the order of ϵ where $1 \gg \epsilon$, i.e.

$$\frac{\partial n}{\partial x_i} = O(\epsilon).$$

With these assumptions, we can choose

$$z_i = \int n dx_i \quad (3)$$

where $i = 1, 2, 3$. It follows directly from Eq. (3) that

$$\begin{aligned} \frac{\partial z_i}{\partial x_j} &= n = O(1) \text{ if } i = j; \\ \frac{\partial z_i}{\partial x_j} &= \int \frac{\partial n}{\partial x_j} = O(\epsilon) \text{ if } i \neq j. \end{aligned}$$

Hence, ignoring those terms of the order of ϵ in Eq. (2), we can simplify the governing equation to

$$\begin{aligned} &\left(\frac{\partial z_1}{\partial x_1}\right)^2 \frac{\partial^2 p}{\partial z_1^2} + \left(\frac{\partial z_2}{\partial x_2}\right)^2 \frac{\partial^2 p}{\partial z_2^2} + \left(\frac{\partial z_3}{\partial x_3}\right)^2 \frac{\partial^2 p}{\partial z_3^2} + \\ &\frac{\partial^2 z_1}{\partial x_1^2} \frac{\partial p}{\partial z_1} + \frac{\partial^2 z_2}{\partial x_2^2} \frac{\partial p}{\partial z_2} + \frac{\partial^2 z_3}{\partial x_3^2} \frac{\partial p}{\partial z_3} + k_0^2 n^2 p = -\delta(r) \end{aligned} \quad (4)$$

The first spatial derivatives of p in Eq. (4) can be removed by transformation. This is achieved by introducing a new term, \bar{p} where

$$\bar{p} = \frac{p}{g(z_1, z_2, z_3)}. \quad (5)$$

The function, g , is included for the elimination of the term involving first derivative in Eq. (4). Substitution of Eq. (5) into Eq. (4) leads to

$$\frac{\partial^2 \bar{p}}{\partial \bar{z}_i \partial \bar{z}_i} + (1 + \phi) \bar{p} = \frac{-\delta(x_1) \delta(x_2) \delta(x_3)}{(k_0 n)^{3/2}} \quad (6)$$

where

$$\phi = \frac{1}{\sqrt{k_0 n}} \frac{\partial^2}{\partial z_i \partial z_i} (\sqrt{k_0 n}) \quad (7a)$$

with g is determined by

$$g = (k_0 n)^{-1/2} \quad (7b)$$

If the index, i is restricted to 1 for the one-dimensional case, then Eqs. (6) and (7a) can be reduced to the result given by the standard method of Liouville-Green transformation.³

We remark that our procedure generalizes the method of Liouville-Green transformation to the three-dimension space. In view of the requirement of a slowly varying medium, the term ϕ is small in comparison with 1. Hence it will be ignored in our subsequent analysis.

Our next step is to seek an approximate analytical solution for Eq. (6) which, in turn, gives an approximate solution for the acoustic pressure, p , through the use of Eq. (5). In Eq. (6), we note that the magnitude of the source term is modified to $(k_0 n)^{-3/2}$ and the source position is still expressed in its original space, (x_1, x_2, x_3) for convenience. It follows that an extra factor is required in the final solution for the acoustic pressure to reflect the difference in the source strength between Eqs. (1) and (6).

We now introduce a two-fold Fourier transform where the transformed variable, \bar{p}_s is related to \bar{p} by

$$\bar{p}_s = \int_{-\infty}^{\infty} \int_{-\infty}^{\infty} \bar{p} \exp[i(\bar{k}_1 z_1 + k_2 z_2)] dz_1 dz_2, \quad (8)$$

and

$$\bar{p} = \frac{1}{4\pi^2} \int_{-\infty}^{\infty} \int_{-\infty}^{\infty} \bar{p}_s \exp[-i(\bar{k}_1 z_1 + k_2 z_2)] dz_1 dz_2. \quad (9)$$

Using Eq. (8), we can reduce Eq. (6) to a second order ordinary differential equation as follows,

$$\frac{d^2 \bar{p}_s}{dz_3^2} + \bar{N}^2 \bar{p}_s = -(k_0)^{-3/2} \int_{-\infty}^{\infty} \int_{-\infty}^{\infty} \frac{\delta(x_1)\delta(x_2)\delta(x_3)}{n^{3/2}} dz_1 dz_2, \quad (10)$$

where $\bar{N} = \sqrt{1 - \bar{k}_1^2 - \bar{k}_2^2}$. (11)

In order to ensure a finite and bounded solution for the acoustic pressure, the root for \bar{N} is taken as either positive real or negative imaginary.

The integration at the right side of Eq. (10) can be evaluated straightforwardly⁴ to yield,

$$\frac{d^2 \bar{p}_s}{dz_3^2} + \bar{N}^2 \bar{p}_s = -\sqrt{k_0 n_s} \delta(x_3) \quad (12)$$

where $n_s = n(0, 0, x_3)$. Introducing an analogue transform pair for \bar{x}_3 , we may express the transformed variable, \bar{p}_s , in an integral form as

$$\bar{p}_s = \frac{(k_0 n_0)^{3/2}}{2\pi} \int_{-\infty}^{\infty} \frac{\exp[i\bar{k}_3 \bar{z}_3]}{\bar{N}^2 - \bar{k}_3^2} d\bar{k}_3, \quad (13)$$

where the subscript 0 denotes the variables evaluated at the origin. Before we proceed, it is worth pointing out that the three-dimensional space, $\bar{\mathbf{x}}$, is independent of the $\bar{\mathbf{k}}$ -space. We can simply replace $\bar{k}_3 \bar{x}_3$ with $\int_0^{\bar{x}_3} \bar{k}_3 d\bar{y}_3$ and, similarly, for the other pairs of variables.

We can now evaluate the integral in Eq. (13) asymptotically⁵ to give

$$\bar{p}_s = \frac{i(k_0 n_0)^{3/2} \exp\left\{i \int_0^{\bar{x}_3} \bar{N} d\bar{y}_3\right\}}{2\bar{N}} + O[\exp(-\bar{k}_3 \bar{x}_3)], \quad (14)$$

with \bar{k}_3 lying on the surface Γ^+ which satisfies the following conditions,

$$1 = \bar{k}_1^2 + \bar{k}_2^2 + \bar{k}_3^2 \quad \text{and} \quad \bar{k}_3 > 0. \quad (15)$$

We note that the solution given in Eq. (14) comprises of outgoing waves only. It is of interest to point out that an extra term should be included in Eq. (14) but this extra

term is cancelled out later in the analysis.⁶ Consequently, the extra term will not be treated in our analysis for simplicity and the omission will not affect the final form of the approximate solution. With the use of Eqs. (9) and (14), we can express the transformed pressure, \bar{p} , as

$$\bar{p} = \frac{i(k_0 n_0)^{3/2}}{4\pi^2} \iint_{\Gamma^+} \frac{\exp\left\{i\left[\int_0^{x_1} \bar{k}_1 d\bar{y}_1 + \int_0^{x_2} \bar{k}_2 d\bar{y}_2 + \int_0^{x_3} \bar{N} d\bar{y}_3\right]\right\}}{2\bar{N}} d\bar{k}_1 d\bar{k}_2, \quad (16)$$

where the approximate solution is accurate to the order of $O[\exp(-\bar{k}_3 \bar{x}_3)]$. Equation (16) gives the solution for the transformed pressure in the \bar{r} -space. However, it is more convenient to express the solution in the original space for the ease of interpretation.

Substitution of Eqs. (5) and (7b) into Eq. (16) and some algebraic manipulations lead to

$$p(x_1, x_2, x_3) = \frac{i}{4\pi^2} \iint_{\Gamma^+} \frac{\exp[ik_0 S(k_1, k_2)]}{2k_0 \sqrt{N_0 N_x}} dk_1 dk_2, \quad (17)$$

where

$$S(k_1, k_2) = \int_0^{x_1} \frac{k_1}{k_0} dy_1 + \int_0^{x_2} \frac{k_2}{k_0} dy_2 + \int_0^{x_3} N dy_3, \quad (18)$$

$$N = n\bar{N} = \sqrt{n^2 - (k_1/k_0)^2 - (k_2/k_0)^2}, \quad (19)$$

$$k_1 = k_0 n \bar{k}_1 \quad \text{and} \quad k_2 = k_0 n \bar{k}_2. \quad (20)$$

The subscript x in Eq. (17) denotes the variable evaluated at the point of reception and $S(k_1, k_2)$ may be regarded as the phase function of the acoustic pressure. Further, the conditions [see Eq. (15)] for the surface, Γ^+ , can be written in terms of the original space as

$$k_0^2 n^2 = k_1^2 + k_2^2 + k_3^2 \quad \text{and} \quad k_3 > 0. \quad (21)$$

Up to this point we have shown that the formidable governing equation, *cf.* Eq. (1), may be approximately reduced to a one-dimensional Helmholtz equation. We may approximate the solution by evaluating a double Fourier integral given in Eq. (17). To obtain a closed form analytic solution for Eq. (17), the exact evaluation of the integral poses a considerable problem. However, the integral is amenable in the high frequency analysis provided that we are prepared to accept a lower order of approximation. This may be achieved by the method of stationary phase.⁵

We start by writing the phase function, $S(k_1, k_2)$, in terms of the arc length, R , of the ray path. The direction cosines of the ray path is simply given by $(dx_1/dR, dx_2/dR, dx_3/dR)$. It follows directly from Eq. (18) that we may recast $S(k_1, k_2)$ as

$$S(k_1, k_2) = \int_0^{R_z} \left\{ \frac{k_1}{k_0} \frac{dx_1}{dR} + \frac{k_2}{k_0} \frac{dx_2}{dR} + \sqrt{n^2 - \left(\frac{k_1}{k_0}\right)^2 - \left(\frac{k_2}{k_0}\right)^2} \frac{dx_3}{dR} \right\} dR . \quad (22)$$

Differentiation of $S(k_1, k_2)$ with respect to k_1 and k_2 leads to

$$\frac{\partial S}{\partial k_1} = \frac{x_1}{k_0} - \int_0^{R_z} \frac{(k_1/k_0^2) dy_3}{\sqrt{n^2 - (k_1/k_0)^2 - (k_2/k_0)^2}} , \quad (23)$$

$$\frac{\partial S}{\partial k_2} = \frac{x_2}{k_0} - \int_0^{R_z} \frac{(k_2/k_0^2) dy_3}{\sqrt{n^2 - (k_1/k_0)^2 - (k_2/k_0)^2}} . \quad (24)$$

The stationary point (\hat{k}_1, \hat{k}_2) can then be determined by setting

$$\frac{\partial S}{\partial k_1} = \frac{\partial S}{\partial k_2} = 0 .$$

Hence, we can fix the values for \hat{k}_1 and \hat{k}_2 by solving the above simultaneous equations to get

$$\hat{k}_1 = k_0 n \frac{dx_1}{dR} \quad \text{and} \quad \hat{k}_2 = k_0 n \frac{dx_2}{dR} , \quad (25)$$

for all points lying on the ray trajectory. The stationary value of the phase function can then be determined by substituting Eq. (25) into Eq. (18) to yield

$$\hat{S}(\hat{k}_1, \hat{k}_2) = \int_0^{R_x} n dR . \quad (26)$$

We can then expand the phase function about the stationary point by means of Taylor's theorem as follows,

$$S(k_1, k_2) = \hat{S}(\hat{k}_1, \hat{k}_2) + \frac{1}{2}(k_q - \hat{k}_q)(k_r - \hat{k}_r)(\partial^2 \hat{S} / \partial k_q \partial k_r) , \quad (27)$$

where the summation indices for q and r are from 1 to 2 only, the symbol $\hat{}$ on S or on its second derivative indicates the values evaluated at the stationary point, (\hat{k}_1, \hat{k}_2) . We note that any functions higher than the order of $|k_r - \hat{k}_r|^3$ are ignored in Eq. (27).

Replacing N_0 and N_x with their corresponding values at the stationary points and using Eq. (27), we can approximate the integral in Eq. (17) by

$$p(x_1, x_2, x_3) = \frac{i}{4\pi^2} \iint_{\Gamma} \frac{\exp[ik_0 \hat{S} + \frac{1}{2}ik_0(k_q - \hat{k}_q)(k_r - \hat{k}_r)(\partial^2 \hat{S} / \partial k_q \partial k_r)]}{2k_0 \sqrt{\hat{N}_0 \hat{N}_x}} dk_1 dk_2 . \quad (28)$$

Our next step is to evaluate the integral in Eq. (28) that will give the total sound field due to a point monopole source in a spatially inhomogeneous medium. There is a standard method to evaluate a double integral asymptotically by the method of stationary phase. The method is described elsewhere.⁷ In essence, the product terms of the second derivative in the integral of Eq. (28) is removed by a linear transformation with two new variables, ξ and η where

$$\xi = (k_1 - \hat{k}_1) + \frac{(\partial^2 S / \partial k_1 \partial k_2)}{(\partial^2 S / \partial k_1^2)}(k_2 - \hat{k}_2) \quad (29)$$

$$\text{and} \quad \eta = k_2 - \hat{k}_2 . \quad (30)$$

Hence Eq. (28) can be transformed to

$$p(x_1, x_2, x_3) \approx \frac{i}{4\pi^2} \frac{\exp[ik_0 \hat{S}]}{2k_0 \sqrt{\hat{N}_0 \hat{N}_x}} \int_{-\infty}^{\infty} \int_{-\infty}^{\infty} \exp\left[\frac{1}{2}ik_0(\lambda \xi^2 + J\eta^2/\lambda)\right] d\xi d\eta, \quad (31)$$

$$\text{where} \quad \lambda = \frac{\partial S}{\partial k_1}, \quad (32)$$

$$\text{and} \quad J = \frac{\partial(\partial S/\partial k_1, \partial S/\partial k_2)}{\partial(k_1, k_2)}. \quad (33)$$

The integral in Eq. (32) can now be evaluated straightforwardly to give the asymptotic solution of the total sound field,

$$p(x_1, x_2, x_3) = \frac{1}{4\pi \sqrt{k_0 \hat{N}_0} \sqrt{k_0 \hat{N}_x}} \cdot \frac{\exp[ik_0 \hat{S}]}{\sqrt{|J|}}. \quad (34)$$

We conclude this section by noting that the variable J appears in Eqs. (31) and (34) may be interpreted as the Jacobian of the transformation. We have established a more rigorous method in applying the rules of geometrical acoustics for sound propagation in a spatially inhomogeneous medium with no boundary surfaces in the close proximity of the source and receiver.

Conclusions

A new method has been developed to evaluate the propagation of sound in a spatially inhomogeneous medium. Although the results derived here have perhaps been known for some time. Our purpose is to show that our new approach is very versatile and general, and that these (and other) results may be derived in a systematic way. The present work is concentrated on the derivation of a new formula without boundary surfaces. Future works include extending the present work to include a ground surface in the close

proximity to the source and receiver. We would emphasize that use of the conventional ray tracing approach would only allow for the inclusion of the direct and reflected wave terms.⁸ However, the present approach should be able to include the surface or ground wave term as well as the creeping wave term in the solution. The new method may also be used to shed light in the development of numerical schemes in handling the problems of spatially inhomogeneity. Finally, we also plan to compare the current theoretical prediction with experimental measurements in future.

Acknowledgment

The author acknowledges the US Army Research Office for support in his trip to attend the 6th International Symposium on Long Range Sound Propagation.

References

1. K M Li, "On the validity of the heuristic ray-trace-based modification to the Weyl-Vander Pol formula," J. Acoust. Soc. Am **93**, 1727-35, (1993).
2. K M Li, "A high-frequency approximation of sound propagation in a stratified moving atmosphere above a porous ground surface," J. Acoust. Soc. Am. **95**, 1840-52, (1994)
3. F W J Olver, "Asymptotics and special functions," Academic Press, (1974).
4. D S Jones, "Generalised functions," McGraw-Hill, (1966).
5. M J Lighthill, "Waves in fluids," Cambridge University Press, (1978).
6. M J Lighthill, "Emendation to a proof in the general three-dimensional theory of oscillating sources of waves," Proc. R. Soc. Lond. A **427**, 31-42, (1992).
7. R Wong, "Asymptotic approximations of integrals," Academic Press, (1989).
8. J S Lamancusa and P A Daroux, "Ray tracing in a moving medium with two-dimensional sound-speed variation and application to sound propagation over terrain discontinuities," J. Acoust. Soc. Am. **93**, 1716-26, (1993).

**SIXTH INTERNATIONAL SYMPOSIUM ON LONG RANGE SOUND
PROPAGATION**

12 - 14 JUNE 1994

OTTAWA , CANADA

**A QUALITATIVE APPROACH OF ATMOSPHERICAL EFFECTS
ON LONG RANGE SOUND PROPAGATION**

V. ZOUBOFF *, Y. BRUNET **, M. BERENGIER *, E. SECHET***

* Laboratoire Régional des Ponts et Chaussées, 23 Avenue de l'Amiral Chauvin,
43130 Les Ponts de Cé, France;

** Institut National de la Recherche Agronomique, Station de Bioclimatologie, 71
Avenue E. Bourleaux, BP 81, 33883 Villenave d'Ornon Cedex, France.

*** Laboratoire Central des Ponts et Chaussées, Centre de Nantes, BP 19
44340 Bouguenais, France.

SUMMARY

It is well known that propagation of noise in the lower atmosphere can be strongly affected by the meteorological conditions, and it is of primary importance for acousticians to be able to evaluate these effects, when dealing with field measurements of noise levels.

We present here an experimental study and especially the results of an outdoor experiment using a constant high level point source, performed in a large open area, combining acoustic and meteorological measurements.

A statistical study is carried out on the data, using multiple correspondence analysis, hierarchical classification and discriminant analysis. It allows us in a first step, to highlight the experimental links between the climatic factors and the measured noise levels, in a second step, to demonstrate the major effect of wind vector and air temperature gradients and in a third step to show the random effect of meteorological conditions on the noise level.

Finally, we propose a simple method to help the acoustician in the qualitative estimation at least, of the effects of meteorological conditions on long range sound propagation. This method is based on a double-entry grid that only requires simple meteorological observations. Then, we compare the qualitative estimations given by the grid to the results of experiments outdoors. Human evaluation of climatic conditions is shown to be satisfactory for a qualitative estimation of their effects on noise measurements.

1. Introduction

Noise levels at some distance from a source in open air depend primarily on the spatial variations of the speed of sound, which are mainly influenced by the mean wind speed, the wind direction and the air temperature. More precisely, any spatial variation in air temperature or wind speed induces a refraction of the acoustic rays leading to changes in their trajectories.

This problem is well known from the theoretical point of view, and has been studied by a number of authors. For instance, Chessell¹ described a method for three-dimensional acoustic-ray tracing in an inhomogeneous anisotropic atmosphere, with a method derived from geometrical optics; Raspet et al.² studied sound propagation in a layered atmosphere bounded by a ground. This model is formulated in terms of a Green's function integral in the spectral domain. Thompson³ and Kornhauser⁴ have developed a ray theory for a moving medium. This problem has also been studied by Attenborough⁵, who developed an impedance model of the ground.

In addition to these, various models of outdoor sound propagation, taking into account the influence of meteorological effects, have been carried out: for instance, Daigle et al.^{6,7} have performed several studies on the propagation of sound in the presence of gradients and turbulence. Bérangier and Daigle⁸ studied the same problem above a surface with an impedance discontinuity. Rasmussen⁹ has also developed a calculation method to account for the influence of wind and temperature gradients.

A second approach of the influence of meteorology on long range sound propagation is based essentially on experimental studies. The first important study was performed by Scholes and Parkin¹⁰, who described the results of measurements of noise propagation from a jet engine placed between 1 and 5 meters above the ground. This experiment clearly showed the influence of wind and temperature gradients as well as ground effects on the noise level at distances up to 1200 m from the source. In France, O.N.E.R.A.¹¹ has studied the excess attenuation caused by some meteorological conditions.

Another way of accounting for meteorological effects consists of performing a classification of the atmospheric conditions, which is very interesting for engineers engaged in practical problems and measurement procedures. Such a classification was developed by Pasquill¹² to define atmospheric stability and predict the propagation of smoke in the atmosphere. Marsh¹³ used this classification to determine meteorological categories for sound classification. Turner¹⁴ also suggested a classification based on atmospheric conditions.

In this paper we first present an experimental study combining meteorological data and noise levels at distances up to 640 meters. A statistical analysis of the results then allows us to build a simple method of classification. Finally, the classes thereby defined enable one to compare qualitatively a noise measurement in the presence of meteorological effects with noise levels in the absence of such effects.

2. Experimental procedures

2.1. Experimental set up

An experiment on outdoor sound propagation was performed over several weeks in the Crau plain (South-East France) from autumn 1986, to winter 1988. The Crau plain is a large, flat, homogeneous area covered with pebbles and sparse gramineous. Ground impedance was measured, and can be considered as constant throughout the year.

A point source, consisting of a loudspeaker fed by a broadband noise having maximum energy in 500 and 1000Hz octaves, was installed 6m above the ground. Microphones were set up at two heights ($z=1.5$ and 6m), at various distances up to $x=640$ m (Fig. 1). A control microphone was installed near the loudspeaker for monitoring purposes and for making sure that the sound level remained constant with time.

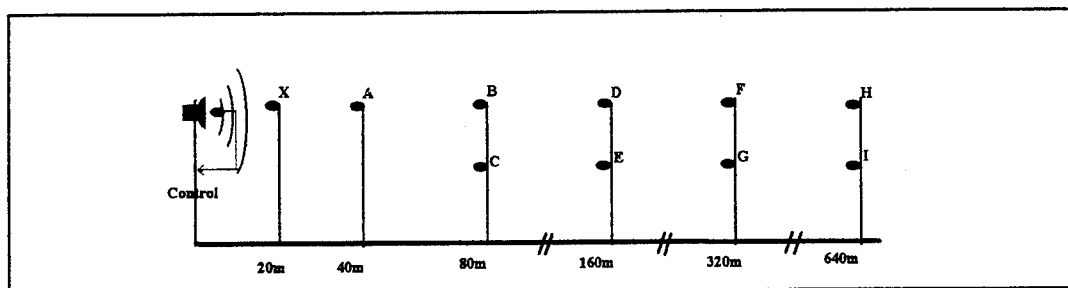


Figure 1. Schematic illustration of the experimental setup. The sound source and the receivers X, A, B, D, F, H were set 6 meters above the ground. Receivers C, E, G and I were at $z = 1.5$ m.

A 22m high tower was erected approximately in the middle of the measurement line in order to collect meteorological parameters. Mean air temperature and horizontal wind speed were measured at $z=2, 5, 10$ and 20 m. Wind direction, solar radiation and hygrometry were also measured. Solar elevation was calculated from astronomical functions and cloud cover was continuously estimated. Meteorological data and sound levels at the receivers were recorded simultaneously.

2.2. Raw results and discussion

We obtained 195 samples of 10 minutes each, with all meteorological data and sound levels, expressed in terms of mean energy value L_{Aeq} . The raw statistical results are shown in Table 1. The acoustic data have first been normalized to 100 dB(A) at receiver X, 20m away from the source (Fig. 1).

Table 1 - Raw results

NAME	x (m)	z (m)	SAMPLES	MEAN VALUE dB(A)	STANDARD DEVIATION dB(A)	MIN VALUE dB(A)	MAX VALUE dB(A)	RANGE dB(A)
A	40	6	125	94,7	0,9	92,1	97,1	5
B	80	6	125	88,6	0,8	86,4	90,7	4,3
D	160	6	195	83,5	1,4	77,7	88,5	10,8
F	320	6	195	74,2	5,6	52,1	81,8	29,7
H	640	6	195	63,4	9,4	37	75,2	38,2
C	80	1,5	125	89,4	1,3	86,2	92,1	5,9
E	160	1,5	195	79,8	4,4	67,2	85,8	18,6
G	320	1,5	195	68,4	8,4	52,8	79,6	26,8
I	640	1,5	195	59,7	11,2	36,2	74	37,8

First of all, Table 1 shows that the standard deviation, which can be principally attributed to meteorological effects, increases with distance and for a constant distance of propagation it appears bigger near the ground than at $z=6\text{m}$.

Secondly, the range of the acoustic results also increases with distance (Fig. 2). For instance, we can observe a difference of 38 dB(A) between two L_{Aeq} levels measured at 640m, with a constant sound source.

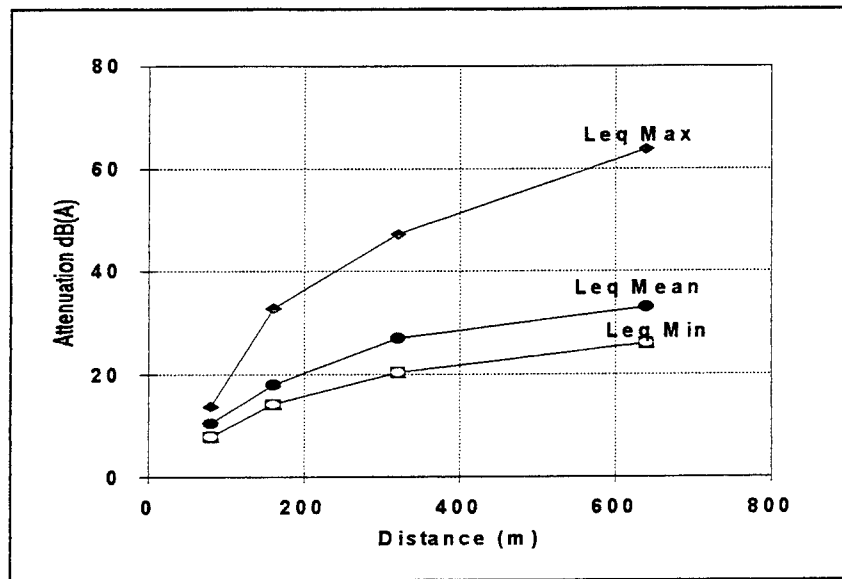


Figure 2. Experimental attenuations at the various receivers ($z=1.5\text{ m}$), the reference being at $x = 20\text{ m}$. The upper curve represents the maximum value of the attenuations in terms of L_{Aeq} . The middle one shows the mean attenuations and the lower the minimum attenuations.

These results were obtained for an integration time of 10 minutes. Generally, such differences cannot be observed over a day for example, because meteorological parameters are always fluctuating. However, we recorded a difference of 17 dB(A) at 320m and 23 dB(A) at 640m over a period of 2 hours. Also, a comparison between days differing in wind direction and cloud cover shows that the mean difference in energy over about 8 hours was about 8 dB(A) at 320m and 19 dB(A) at 640m.

So, even over long integration times, a difference in mean meteorological conditions can induce significant differences in sound levels at a fixed distance from a constant source. This is an important problem for the measurer when he is called for an expert evaluation. Indeed the question we are concerned with is how widely the results obtained under specific conditions can be applied to other meteorological situations.

3. Multivariate analysis

In order to highlight possible links between the factors involved and the sound levels, various factorial analyses were performed on discrete variables. We will firstly present a multiple correspondence analysis (MCA), then a hierarchical classification on MCA factors.

3.1. The discrete variables

Most of the discrete variables are obtained by splitting the initial continuous variables into several classes, defined as follows :

-a- Meteorological variables (active)

* Couple "wind gradient - temperature gradient" (combination of wind vector gradient **vv** and temperature gradient **gt**).

tv1 : $vv < 0$ and $gt < 0$

tv2 : $vv < 0$ and $gt > 0$

tv3 : $vv > 0$ and $gt < 0$

tv4 : $vv > 0$ and $gt > 0$

(note that $vv = gv \cdot \cos(wd, prop)$, where gv is the wind speed gradient and $(wd, prop)$ the angle between the wind direction and the propagation axis).

* Solar radiation (W/m^2)

so1 : $0 W/m^2$

so2 : from 0 to $50 W/m^2$

so3 : from 50 to $250 W/m^2$

so4 : over $250 W/m^2$

* Solar elevation (degree)

hs1 : less than 10°

hs2 : from 10 to 20°

hs3 : from 20° to 25°

hs4 : over 25°

* Cloud cover (octas)

cn1 : 0 or 1
cn2 : 2 3 or 4
cn3 : 5 or 6
cn4 : 7 or 8

* Wind speed (m/s)

vi1 : less than 2.5 m/s
vi2 : from 2.5 to 4 m/s
vi3 : from 4 to 6.5 m/s
vi4 : over 6.5 m/s

* Angle between the wind direction and the propagation axis (degree)

dv1 : from 0 to 20° (downwind propagation : wind blowing from the source to the receiver)
dv2 : from 20 to 50°
dv3 : from 50 to 90°
dv4 : over 90° (upwind propagation : wind blowing from the receiver to the source)

-b- Acoustic variables (illustrative)

* Acoustic attenuation between 20 and 640m, at $z=6m$ (dBA)

axh1 : less than 31 dBA
axh2 : from 31 to 38 dBA
axh3 : from 38 to 43 dBA
axh4 : from 43 to 49 dBA
axh5 : over 49 dBA

* Acoustic attenuation between 20 and 320m, at $z=6m$ (dBA)

axf1 : less than 20 dBA
axf2 : from 20 to 26 dBA
axf3 : from 26 to 32 dBA
axf4 : from 32 to 38 dBA
axf5 : over 38 dBA

* Difference between L_{Aeq} 6m and L_{Aeq} 1.5m at $x=640m$ (dBA)

dhi1 : less than 3 dBA
dhi2 : from 3 to 6 dBA
dhi3 : from 6 to 9 dBA
dhi4 : over 9 dBA

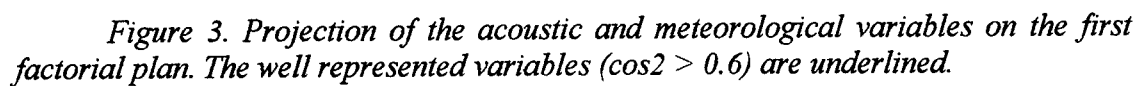
* Difference between L_{Aeq} 6m and L_{Aeq} 1.5m at $x=320m$ (dBA)

dfg1 : less than 0 dBA
dfg2 : from 0 to 5 dBA
dfg3 : from 5 to 10 dBA
dfg4 : over 10 dBA

rede : downwards
rect : linear
remo : upwards

The meteorological variables are considered as active variables and the acoustic variables as illustrative ones¹⁶. All these variables are projected on the first factorial plan (Fig. 3). The variables which are underlined in the plan are well represented ($\cos^2 > 0.6$); however, it can be noticed that the poorly represented variables are often logically located in the plan.

However, from this analysis we found that only 30 % of the total variance of the data can be explained in this plan.



A further analysis will be performed on all four quadrants.

- Quadrant C

Quadrant C is principally characterized by a high sun (hs4) and upwind propagation (dv4). We can find other characteristics which are logically related to these observations: high solar radiation (so4) is linked with hs4 because we had very few clouds during the experiment; this results in negative temperature gradients (tv1 and tv3) on the second axis. This meteorological situation corresponds to upwards acoustic rays (remo) caused by the conjunction of negative wind and temperature gradients. Acoustic attenuation is then quite significant (axf4, axh4), due to the presence of a shadow region. Note that in this case, there is also a large, positive vertical gradient of sound levels at position H (640m away from the source).

- Quadrant A

On the contrary, quadrant A is characterized by a low sun (hs1), low solar radiation (so1) and positive gradients of wind speed and temperature (tv4). Overcast skies (cn4) are not well represented in this first plan but are logically located in quadrant A. This situation corresponds to downward rays (rede) leading to small vertical acoustic gradients (dfg2, dh11).

- Quadrant B

Quadrant B is characterized by positive wind gradients and negative temperature gradients (tv3), leading to partial or full compensation effects on the acoustic rays. However, no conclusion can be drawn on the acoustic variables since they are not represented in this quadrant.

- Quadrant D

There are no well-represented variables. However, the presence of tv2 allows one to think that this quadrant represents the cases when the gradients are opposite to those of quadrant B (negative wind gradients and positive temperature gradients).

All four quadrants correspond to one particular combination of wind vector and temperature gradients. There is an important diagonal axis from quadrant A to quadrant C, which opposes two characteristic meteorological situations: downwind propagation and positive temperature gradient on the one hand, upwind propagation and negative temperature gradient on the other. Accordingly, this axis also opposes downward and upward propagating rays. Meteorological and acoustic results are therefore quite consistent. In order to get a more detailed picture, we performed a sample projection on the first factorial plan, providing a chronological interpretation (Fig. 4).

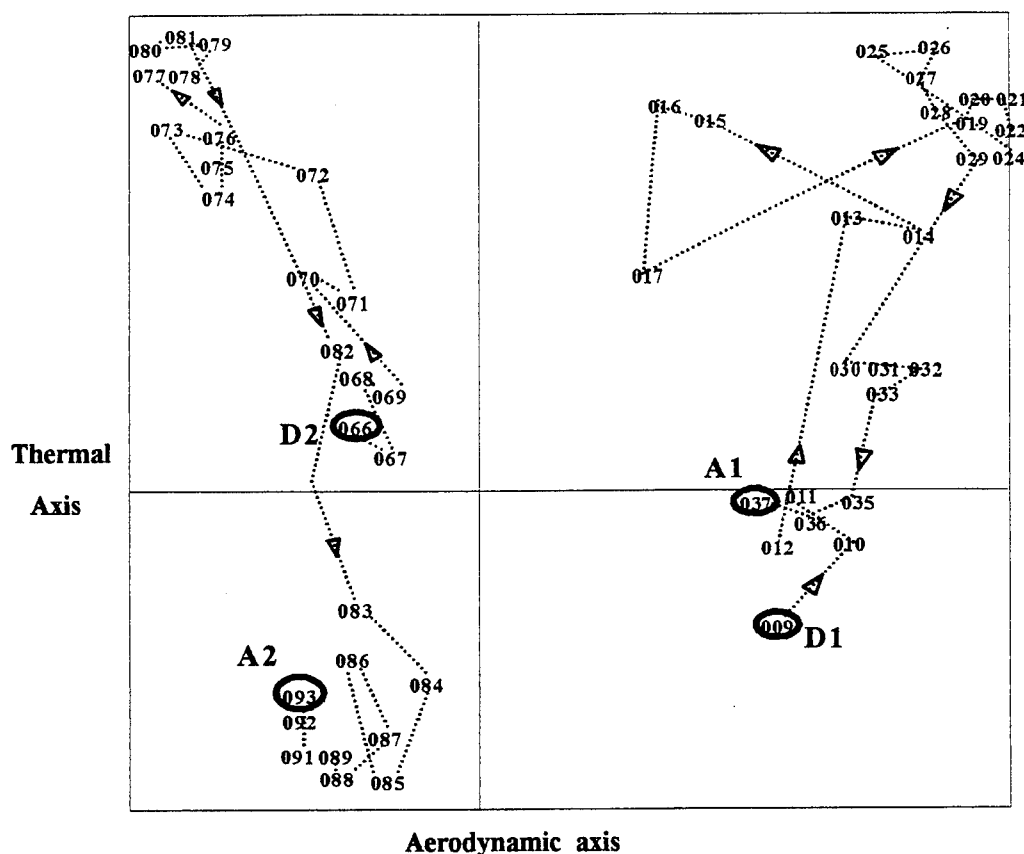


Figure 4. Projection of the two sets of samples on the first factorial plan.

The first projection D1-A1 corresponds to samples 9 to 37 and represents an entire day with upwind propagation. It started at 5:31 (U.T.) on September 2 (sunrise) and stopped on the same day at 18:12 (sunset). The second one (D2-A2) is constituted by samples 66 to 93 and represents another entire day with downwind propagation. It started at 8:45 on December 17, some time after sunrise and stopped at 17:31, one hour after sunset.

Path 1 (upwind) remains in the two right quadrants (D and C) and path 2 (downwind) on the two left quadrants (B and A); they correspond to negative (tv1, tv2) and positive (tv3, tv4) wind vector gradients, respectively. In the early morning the starting points are projected in quadrant D for D1 and quadrant B for D2 (note that the downwind series D2-A2 started later than D1). On the contrary the end A2 of the downwind series is lower than A1 on the second axis, because of its later time (one hour after sunset). The evolution of the sample projection on the first plan shows that the propagation conditions change significantly, in relation to the thermal conditions.

It has to be pointed out that the vertical extent of the paths would be reduced on cloudy days, which exhibit a narrower range of thermal conditions.

In conclusion, it is therefore possible to represent on one plan the influence of the meteorological conditions on sound pressure level outdoors.

3.3. Hierarchical classification

In the course of this study several hierarchical classifications were performed, based on different sets of variables. In all cases it was found that the thermal and aerodynamic variables are those which define characteristic classes best. This leads us to propose the following classification.

Class 1 : (statistically stable class)

Nighttime samples with strong, positive temperature gradients, with strong wind, direct downwind propagation, and a clear sky. The acoustic rays curve downwards.

Class 2 : (statistically very stable class)

Around noon, when the sun is around zenith in a clear sky. Solar radiation is strong and there is a light wind, with direct upwind propagation. The acoustic rays curve slightly upwards.

Class 3 : (statistically unstable class)

Daytime situation with little radiation and a rather clear sky. The temperature gradients are small, slightly positive or negative. The wind is light and most often opposed to the direction of propagation. Compensation effects produce linear or slightly ascending rays.

Class 4 : (statistically very stable class)

Daytime situation with more radiation than class 3 and only slightly negative temperature gradients. However, the wind is usually strong, with direct downwind propagation. The acoustic rays are always downwards.

Class 5 : (statistically very stable class)

The sun is around zenith but the sky is overcast, leading to low radiation levels. Temperature gradients are slightly negative. As in class 4, the wind is rather strong with direct upwind propagation. Consequently, the acoustic rays curve upwards.

Class 6 : (statistically very unstable class)

Samples around dawn or twilight with overcast sky and very low radiation. Temperature gradients are always slightly positive. All types of wind can be found here. Consequently, the sound propagation is not very stable: acoustic rays propagate sometimes upwards, sometimes downwards. Globally, propagation is close to linear. Note that very few samples correspond to this modality (rect).

Class 7 : (statistically unstable class)

Late morning or early afternoon, with clear sky and strong radiation. Temperature gradients are negative or strongly negative. The winds, light and causing rather downwind propagation, lead to compensation effects and the propagation is often linear.

In order to characterize each class from an acoustic point of view, we have calculated a so-called "excess attenuation", defined as the part of the experimental attenuation due solely to the meteorological effects and the combined effects of meteorology and ground surface. This excess attenuation was computed as the difference between the total (experimental) attenuation and the other attenuation terms (due to geometrical scattering, absorption in the air and soil effects), each evaluated separately

Table 2 displays the mean excess attenuation for all seven classes, estimated at 640m away from the source.

Table 2 - Mean excess attenuation for the 7 classes

Class	1	4	6	7	3	2	5
Excess attenuation (dBA)	-4,0	-2,0	0,0	+1,5	+5,5	+9,5	+15,0

The seven classes turn out to be rather well characterized, from +15dBA for class 5, which corresponds to upward rays, to -4 dBA (negative attenuation) for class 1, which only contains downward rays. The effects of wind gradients (class 5) are more significant than those of temperature gradients (class 2). At a distance of 320m from the source the range of attenuation values is smaller but all seven classes can still be distinguished. At 160m only two classes are visible, encompassing classes 3 and 5 on one hand, and 1,2,4,6,7 on the other.

3.4. Discriminant analysis

The previous analysis shows that the meteorological data, and more specifically the wind and temperature gradients, are very influent on noise propagation. However, in order to know them, an instrumented mast is required, which in practice will rarely be available. The aim now is therefore to find a way of estimating the experimental L_{Aeq} from as few meteorological variables as possible.

Using multiple regressions did not provide satisfactory results for this. However, a discriminant analysis on different groups of variables gave interesting information¹⁸. As an illustration, we present here the results of a discriminant analysis undertaken on three variables only (wind direction, temperature and wind speed at only one level), against the variable " L_{Aeq} at 640m" discretized into 5 classes (Table 3).

Table 3 - Results of the discriminant analysis

Exp. Group	samples	Predicted groups				
		1	2	3	4	5
37< L_{Aeq} <50 1	16	<u>15</u>	1			
50< L_{Aeq} <60 2	23	5	<u>16</u>	2		
60< L_{Aeq} <68 3	19		2	<u>12</u>	4	1
68< L_{Aeq} <71 4	40				<u>34</u>	6
71< L_{Aeq} 5	25			4	4	<u>17</u>

From wind direction, wind speed and temperature, one can predict 76% of the cases on average. Furthermore, the poorly predicted groups are generally adjacent to the

good ones. The fact that the results from the discriminant analysis were better than those from the regression analysis may be due to the presence of non-linearities in the acoustic and meteorological phenomena.

All analysis which were performed here show the difficulties to establish a deterministic relation between atmospherical conditions and noise level. This is mainly due to the fact that meteorological conditions vary during the time and in the space between the source and the receivers : Far from the source, the sound level must be considered as a random value.

Consequently, the exact knowledge of wind and temperature gradient on a single point for a given period of time cannot represent the entire behaviour of the sound energy between the source and the receiver, and cannot explain all the variations of the sound level at this receiver.

So, in a first time, the knowledge of an approximative state of the atmosphere is sufficient to estimate the influence of the meteorological factors on the noise level. That is the main reason of the carrying out of our qualitative method.

4. Meteorological conditions and noise propagation: a qualitative prediction method

Before going into the details of the qualitative method, it is necessary to recall a few facets of the structure of the atmospheric surface boundary layer.

4.1. Wind and temperature gradients in the atmospheric surface layer

For the sake of simplicity, we will focus in this study on the atmospheric turbulent flow over a flat, homogeneous, semi-infinite area that may be a bare soil or a surface covered with short vegetation. We will limit ourselves to the lower part of the overall boundary layer (the so-called surface layer), where turbulent fluxes and stress vary by less than 10% of their magnitude. In daytime conditions the surface layer extends typically over 50-100 m, and is usually thinner at night. With the above assumptions the flow can be considered to be in equilibrium with the underlying surface, which implies that all streamwise and crosstream variations in the flow variables are negligible compared with their vertical variations.

The precise form of the vertical gradients of mean wind speed U and air temperature T is given by the well-known Monin-Obukhov similarity theory. A detailed presentation, beyond the scope of this study, can be found in standard textbooks ¹⁵.

We will consider first purely dynamical flows (i.e., without thermal stratification). Mean wind speed increases logarithmically with height, at a rate proportional to the surface stress, or vertical flux of horizontal momentum extracted by the surface. In an equilibrium boundary layer, the magnitude of surface stress is an increasing function of two external parameters: the geostrophic wind and the surface roughness. The wind speed gradient itself is inversely proportional to height z above the surface and proportional to surface stress. This "neutral" case is characterized by the absence of a

vertical temperature gradient and occurs principally under strong winds or important cloud cover limiting surface heating by solar radiation.

In most common daytime situations, the net radiative energy at the surface is partly converted into sensible heat which warms up the atmosphere, thereby producing negative temperature gradients. These gradients are all the larger (in absolute value) as the radiation is stronger (high sun, little cloud cover), the soil drier (if the surface is wet, most of the radiative energy is converted into latent heat) and the surface stress smaller (low wind speed). They are largest near the surface. In these "unstable" conditions the wind speed profile is affected by the temperature gradient and exhibits slightly lesser variation with height than in the neutral case.

On the contrary, "stable" conditions prevail at night. The radiative losses of the surface generate positive temperature gradients, which are largest under clear sky with low wind speed. At a given height the wind speed gradient is a little larger in this case than in neutral conditions.

wind gradient

t e m p. g r a d.		0	>0	>>0
	<<0			
	<0			
	0			
	>0			
	>>0			

Figure 5. Schematic presentation of the combined cases of wind speed and air temperature gradients. The definitions of the classes are given in the text. The degree of shading refers to the probability of occurrence of the various cases. Heavy shading: very rare or impossible cases; light shading: occasional cases; no shading: most frequent cases.

It has to be pointed out that the gradients of wind speed and air temperature are not independent from each other since they are linked by the equations of fluid motion and energy conservation, forced by the boundary conditions (surface energy budget and surface parameters). For instance, very large temperature and wind speed gradients cannot coexist because strong turbulence does not allow the development of a marked thermal stratification. This can be seen in Figure 5, where we feature a rough estimate of the probability of occurrence of the various cases. For this, we have distinguished three categories of wind speed gradient (≈ 0 , >0 and $>>0$, corresponding roughly to no wind, moderate wind and strong wind, respectively) and five categories of temperature gradients (from strongly negative to strongly positive).

These wind speed classes are defined from a purely micrometeorological point of view. In fact, wind direction is of great importance for noise propagation, so that the variable to be taken into account is the vertical gradient of the mean wind velocity component in the line of the source and the receiving point. We will therefore refer to negative and positive wind speed gradients, according to the sign of the projected component (by convention, the sign is positive when the component is oriented towards the receiving point).

It has been shown that the vertical gradients of mean wind speed and air temperature exert a major influence on the propagation of noise, through their combined effects on the trajectory of acoustic rays. Direct measurement or calculation of these gradients throughout the relevant layer of atmosphere would provide firsthand information on the level of noise attenuation at remote distances from the source. As mentioned above, in practice the data required for this are usually not available : it is not possible to obtain the entire state of the atmosphere at each moment and at each point between the source and the receiver. Consequently, we propose a practical qualitative method based on simply observable meteorological criteria.

As a first step the wind speed gradient categories must be redefined as we have to consider the projection of the wind vector on the direction of propagation. With this simple qualitative approach it is not necessary to account for the influence of surface roughness and atmospheric stability on the gradients, which are primarily determined by the mean wind speed itself and the angle between the mean wind direction and the source/receiver line. Consequently, the new classes are as follows:

- U1 Strong wind (from the acoustical point of view, i.e. $\approx 3-5 \text{ ms}^{-1}$) from the receiver to the source.
- U2 Moderate wind ($\approx 1-3 \text{ ms}^{-1}$) from the receiver to the source or strong wind shifted by about 45° from this direction.
- U3 No wind or any wind perpendicular to the source/receiver direction.
- U4 Moderate wind ($\approx 1-3 \text{ ms}^{-1}$) from the source to the receiver or strong wind shifted by about 45° from this direction.
- U5 Strong wind ($\approx 3-5 \text{ ms}^{-1}$) from the source to the receiver.

We also distinguish five classes of temperature gradient T1 to T5, corresponding to the classes of section 2.1 (from $<<0$ to $>>0$, respectively), and defined as follows:

- T1 Daytime with strong radiation (high sun, little cloud cover), dry surface and little wind.
- T2 Same as T1, with at least one condition missing.
- T3 - Early morning or late afternoon (e.g., one hour after sunrise or before sunset).
- Daytime with overcast sky (or partial cloud cover with low sun), moist surface and substantial wind.
- T4 Nighttime with overcast sky or substantial wind.
- T5 Nighttime with clear sky and no (or little) wind.

This approach is similar to using Pasquill's well-known stability categories, the range T1-T5 covering roughly his classes A-G. Our choice is dictated by two main reasons: (i) the classes T1-T5 are defined so that they can be determined from very simple observations, and (ii) the moisture status of the surface must be taken into account.

The 5 x 5 categories thus defined provide the grid entries in Figure 6. The results obtained in this study allow a qualitative estimate of the noise level to be attributed to each grid cell. Here also, five classes are defined:

- Z Noise level equivalent to that obtained with zero meteorological influence (still neutral air).
- + Noise level slightly higher than Z.
- ++ Noise level higher than Z.
- Noise level lower than Z.
- Noise level much lower than Z.

	U1	U2	U3	U4	U5
T1		-	-0.5	-1.5	
T2	-1.5	-	-	Z	+2
T3	-	-5.5	Z	+	+
T4	-	Z	+	+	++
T5		+	+	++	

Figure 6. The effect of meteorological conditions on noise levels. The definitions of the classes of wind speed gradient (U1 to U5), temperature gradient (T1 to T5) and noise level (- to ++) are given in the text. The figures correspond to minus the mean attenuations (dB) corresponding to the seven classes provided by the statistical analysis. The four corner cells correspond to impossible combinations of wind vector and temperature gradients.

The dissymmetry in the definitions of positive and negative categories is due to the existence of a similar dissymmetry in the relevant physical phenomenon: the increases in noise level are in absolute value smaller than the attenuations. The latter are indeed often due to the presence of a shadow region, which is very effective at decreasing the noise level.

Figure 6 shows that the whole range of possible conditions is displayed along the first diagonal, going from strong attenuation (opposed wind in a highly unstable atmosphere) to marked increase in noise levels (wind blowing towards the receiving point in highly stable situations). On the contrary, the Z cases are aligned along the second diagonal of the grid. This is due to the opposite role of wind and temperature gradients in the refraction of acoustic rays, leading to compensating effects.

We also display in Figure 6 the mean levels of attenuation corresponding to the seven classes provided by the statistical analysis described before (with a minus sign, since the grid gives noise levels instead of attenuation levels). As can be seen, there is very good agreement between these quantitative results and the qualitative information displayed by the grid.

5 - Validation of the grid

The previous values have been obtained on an experimental open site in Southern France and were validated on another site in Eastern France where the mean meteorological states are proportionally quite different

The figure 7 gives a first example. On this new part of the grid, are displayed the chronology of the 10 minutes samples. We observe a lower sound pressure level for negative conditions (T2 U2) corresponding to a refractive zone with respect to the Z condition where the sound speed gradient is about zero.

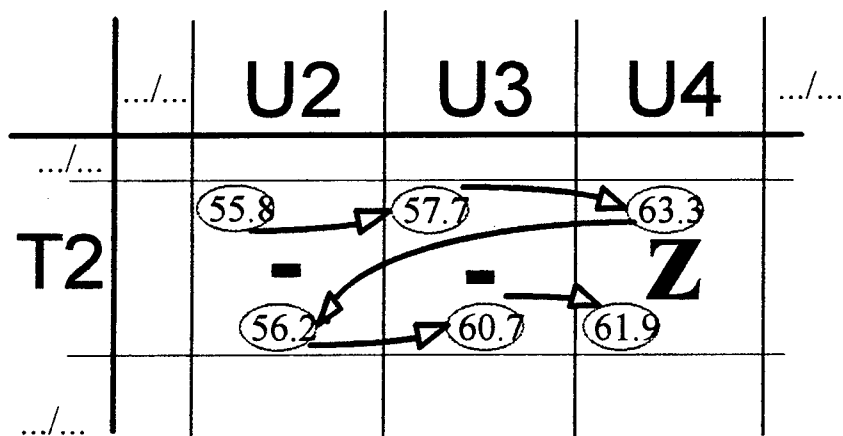


Fig 7. Chronology of 10 minutes samples obtained in Eastern France.

On figure 8, same observations can be done for long term samples between 40 minutes and 3 hours. Moreover, we can see an interesting result concerning the more or less large variation of the acoustic levels. For example in a shadow zone (T2U2) the dispersion of the results is more important than in the "+" area where the levels are higher (T5U3)

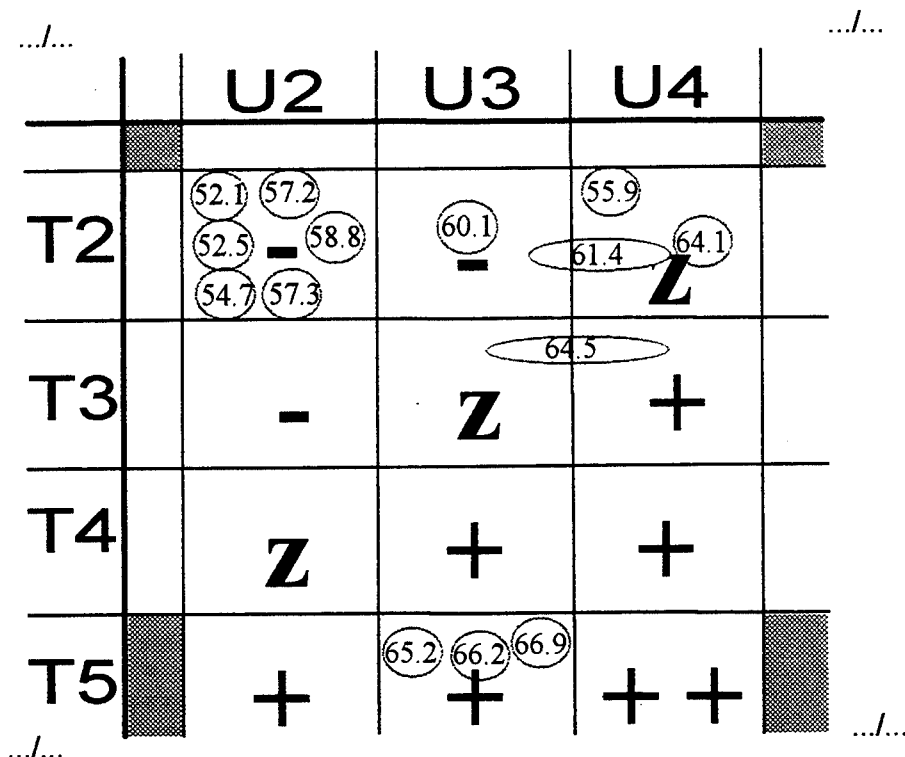


Fig 8 . Validation of the grid on long term equivalent sound level.

5. Conclusions and prospects.

The study presented in this article shows that it is possible to determine the qualitative influence of meteorological conditions on sound levels measured at remote distances from a source with a very simple estimation of the meteorological variables.

Indeed, the exact knowledge of wind and temperature gradients between the source and the receiver is not possible ; furthermore, all these factors are time dependant. Therefore, the knowledge of general meteorological factors is sufficient.

The proposed method does not require much additional equipment, since it is based on simply observable meteorological parameters. By combining systematically the coordinates (U_i , T_i) of the grid in Fig. 6 with each noise measurement, we can get useful information on the sign of the errors caused by the influence of the meteorological conditions, as well as a qualitative appraisal of their importance.

For the field engineer confronted with the practical problems of noise measurements, the method can be very useful for judging the validity of the measurements, especially in the following cases: (i) comparison between two measurements performed under different climatic conditions; (ii) comparison of one particular noise measurement with a legally set threshold.

Furthermore, this grid defines the range of meteorological conditions for which it is better to carry out measurements over long distances: in particular, it is not advisable to perform measurements in the areas "--" or "-" of the grid.

One further goal of the current research is to account for the random effect of the influence of the meteorological conditions. Indeed, the random fluctuations in the time and in the space of meteorological conditions induce random fluctuations in sound level: the latter must be considered as a random variable, and each measurement performed over a certain duration must be associated with a given probability. Thus, when dealing with measurements over a long time period, one should rather assign a set of coordinates (U_i, T_i) , each one of them bearing a given probability, than a unique couple.

This study is to be pursued by a multidisciplinary team, associating specialists in acoustics, micrometeorology and statistics.

REFERENCES

1. C.I. Chessell, Three-dimensional acoustic-ray tracing in an inhomogeneous anisotropic atmosphere using Hamilton's equations. *J.A.S.A.*, 53, (1), 1973, p. 83 - 87.
2. R. Raspet, S.W. Lee, E. Kuester, D.C. Chang, W.F. Richard, R. Gilbert, N. Bong., A fast-field program for sound propagation in a layered atmosphere above an impedance ground., *J.A.S.A.*, 77 (2), 1985, p. 345- 352.
3. R.J. Thompson, Ray theory for an inhomogeneous moving medium. *J.A.S.A.*, 51 (5), 1972, p. 1675-1682.
4. E.T. Kornhauser, Ray theory for moving fluids, *J.A.S.A.*, 25 (5), 1953, p. 945.
5. K. Attenborough, N.W. Heap, K.M. Lee, Source height determination by ground effect inversion in the presence of a sound velocity gradient, *J.S.V.*, 145, 1991, p. 1117.
6. G.A. Daigle, T. Embleton, J.E. Piercy, Line-of-sight propagation through atmospheric turbulence near the ground, *J.A.S.A.*, 74 (2), 1983.
7. G.A. Daigle, T. Embleton, J.E. Piercy, Effects of atmospheric turbulence on the interference of sound waves near a hard boundary, *J. A.S.A.*, 64(2), 1978.
8. M. Bérengier and G.A. Daigle, Diffraction of sound above a curved surface having an impedance discontinuity, *J.A.S.A.*, 84 (3), 1988.
9. K.B. Rasmussen, Outdoor sound propagation under the influence of wind and temperature gradients, *J.S.V.*, 104 (2), 1986, p. 321- 335.
10. W.E. Scholes and P.H. Parkin, The effect of small changes in sound height on the propagation of sound over grassland, *J.S.V.*, 6 (3), 1967, p. 424 - 442.

11. S. Canard-Caruana, S. Levy, J. Vermorel, G. Parmentier, Long range sound propagation near the ground, Noise Ctrl Eng. J., 34 (3), 1990, p.111 - 119.
12. F. Pasquill, Atmospheric diffusion, J. Wiley, London, 1976.
13. K.J. Marsh, The CONCAWE model for calculating the propagation of noise from open-air industrial plants. Applied Acoustics, 15 (1982), p.411.
14. D.B. Turner, Relationships between 24 hours mean air quality measurements and meteorological factors in Nashville, J. of air Pollut. Control Assoc. 11, 1961, p. 483 - 489.
15. R.B. Stull, An introduction to boundary layer meteorology, Kluwer Academic Publishers, Dordrecht, 1988.
16. V. Zouboff, Propagation des bruits à grande distance; première série d'analyses, 1988, (internal report).
17. J. Bertrand et V. Zouboff, Etude bruit/météorologie; deuxième série d'analyses 1991 (Internal report).
18. N. Grolleau et E. Séchet, Influence des conditions météorologiques sur la propagation des ondes sonores à longue distance, 1992, I.M.A, Rapport D.E.S.S., Université Catholique de l'Ouest, Angers.

SOUND PROPAGATION THROUGH A TURBULENT ATMOSPHERE: INFLUENCE OF THE TURBULENCE MODEL

D. Juvé, Ph. Blanc-Benon and P. Chevret

Laboratoire de Mécanique des Fluides et Acoustique,

URA CNRS 263

Ecole Centrale de Lyon,

BP 163

69131 ECULLY Cedex FRANCE

Abstract

Incorporating random aspects in the numerical simulation of atmospheric sound propagation has led to a much better agreement between measurements and predictions but some discrepancies persist. In all of these studies the fluctuations of the refractive index have been considered as scalar and characterized by a single length scale (Gaussian spectrum). It is the aim of this paper to investigate the consequence of these two oversimplifications. For this we first consider the more realistic case of a multi-scale scalar medium (von Karman spectrum with a significant inertial range), and in a second part the different role of velocity fluctuations is emphasized. Illustrations of the importance of the choice of the turbulence model are given for an upward refracting atmosphere, when a deep deterministic shadow zone is present.

1 Introduction

In recent years several authors have taken into account the effect of turbulence on long range sound propagation through numerical simulations (Gilbert et al. [1], Juvé et al. [2], McBride et al. [3]). The common feature of all these studies is that the turbulence is represented as a set of realizations of a random field with prescribed statistical properties; in each realization the "instantaneous" value of the pressure is obtained by solving a deterministic wave equation; ensemble averaging is then performed to obtain relevant statistical values for the mean sound pressure level and for the p.d.f. of intensity fluctuations.

The integration of random effects in the numerical codes has led to a far better agreement between experimental results and numerical ones when upward refracting conditions induce a deep shadow zone. In some circumstances, however, a significant deviation still exists; this may be due to uncertainty in the experimental parameters (intensity of turbulence, correlation length) but also to the use of an oversimplified model of the random field in the numerical simulations. In this paper we describe two possible ways of improving the simulations: by choosing a better spectral representation of the turbulence (von Karman instead of Gaussian form); by taking correctly into account the vectorial nature of wind fluctuations.

2 Acoustic modeling

We start with the farfield approximation of the Helmholtz equation in an environment with azimuthal symmetry:

$$\left(\frac{\partial^2}{\partial r^2} + \frac{\partial^2}{\partial z^2} + k_0^2 n^2\right)p(r, z) = 0 \quad (1)$$

where the index of refraction n is composed of a deterministic and a random part:

$$n = n_d + \mu_t \quad (2)$$

n_d is function only of height z , while μ_t is function both of height z and range r . We use the usual factorization of the Helmholtz equation given by :

$$\left(\frac{\partial}{\partial r} + ik_0 Q\right)\left(\frac{\partial}{\partial r} - ik_0 Q\right)p(r, z) = 0 \quad (3)$$

$$Q^2 = n^2 + \frac{1}{k_0^2} \frac{\partial^2}{\partial z^2} = 1 + \mathcal{L} ; \mathcal{L} = (n^2 - 1) + \frac{1}{k_0^2} \frac{\partial^2}{\partial z^2} = \epsilon_1 + \epsilon_2$$

This is a good approximation as the backscattering by turbulent fluctuations is very weak. From (3) one obtains an equation describing the forward propagation of waves:

$$\frac{\partial p}{\partial r} = ik_0 Q p(r, z) \quad (4)$$

For numerical purposes it is useful to introduce the envelope transformation $p(r, z) = \psi(r, z) \exp(ik_0 r)$; ψ is solution of the equation:

$$\frac{\partial \psi}{\partial r} = ik_0 (Q - 1) \psi(r, z) \quad (5)$$

We solve this parabolic equation using the method first described by Saad and Lee [4]. The fundamental idea is to integrate (5) with respect to range:

$$\psi(r + \Delta r, z) \simeq \exp[ik_0 (Q - 1) \Delta r] \psi(r, z) \quad (6)$$

and to use a Padé (2,2) approximant to the exponential operator. The resulting equation is then discretized by a finite difference technique adapted to the case of an impedance ground. A Gaussian starter is used to simulate point source radiation; reflexions at the top of the numerical grid are controlled by introducing a small artificial absorption in the upper part of the computation domain (typically one third of the total height). More details are given in [5].

3 Turbulence modeling

Our technique to represent the atmospheric turbulence is based on a discretization of the Fourier integral representation of a random scalar field, the fluctuation in temperature $T'(\vec{x})$ to be specific:

$$T'(\vec{x}) = \sum_{i=1}^N T(K^i) \cos(\vec{K}^i \cdot \vec{x} + \varphi^i) \quad (7)$$

For each Fourier mode we must choose four parameters: the modulus K^i and orientation θ^i of the wave-vector, the phase angle φ^i and the amplitude T of the mode (Figure 1). To obtain a statistically homogeneous and isotropic field, θ^i and φ^i must be independent random variables with uniform distributions over $[0, 2\pi]$. The amplitude of each mode is picked from a prescribed energy spectrum $G(K)$ which is sampled uniformly by N values of K between a minimum K_{min} and a maximum K_{max} . The spectrum is chosen so that the energetics of the field is well represented.

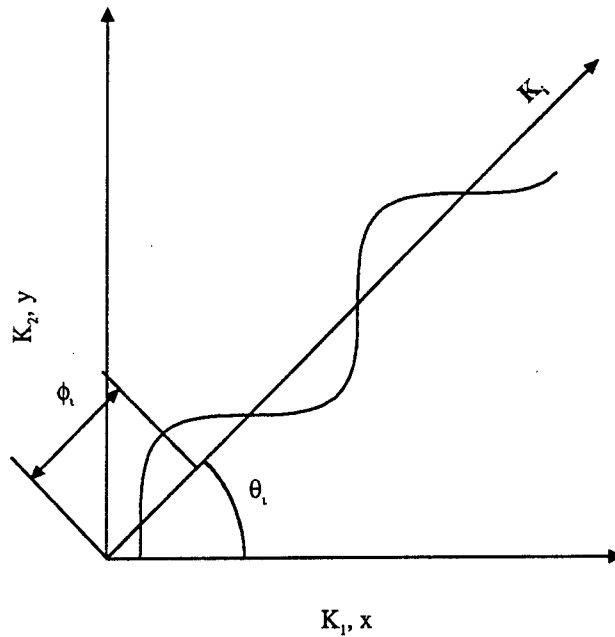


Figure 1: Sketch of one random Fourier mode

In all the recent numerical simulations of atmospheric propagation a Gaussian spectrum has been used. This form is very convenient for both theoretical analyses and numerical studies; it also corresponds to a Gaussian correlation function which seems to fit reasonably well experimental data (Daigle et al. [6]). The correlation function $B_n(r)$ and the spectrum $\Phi_n(K)$ of the index of refraction are respectively given by:

$$B_n(r) = \langle \mu^2 \rangle \exp\left(-\frac{r^2}{L^2}\right) \quad (8)$$

$$\Phi_n(K) = \langle \mu^2 \rangle \frac{L^2}{4\pi} \exp\left(-\frac{K^2 L^2}{4}\right) \quad (9)$$

These functions are completely determined by the variance $\langle \mu^2 \rangle$ of the fluctuations and by a single length scale L proportional to the correlation length. The energy spectrum $G(K)$ and the spectrum $\Phi_n(K)$ are related by : $G(K) = 2\pi K \Phi_n(K)$.

4 Some results obtained with a Gaussian spectrum

One of the most remarkable features of atmospheric turbulence is that it fixes the sound pressure level in the deep shadow zones due to upward refracting conditions

(Figure 2). Deterministic computations dramatically underestimate the measured values; turbulence scatters sound from the illuminated region into the shadow zone.

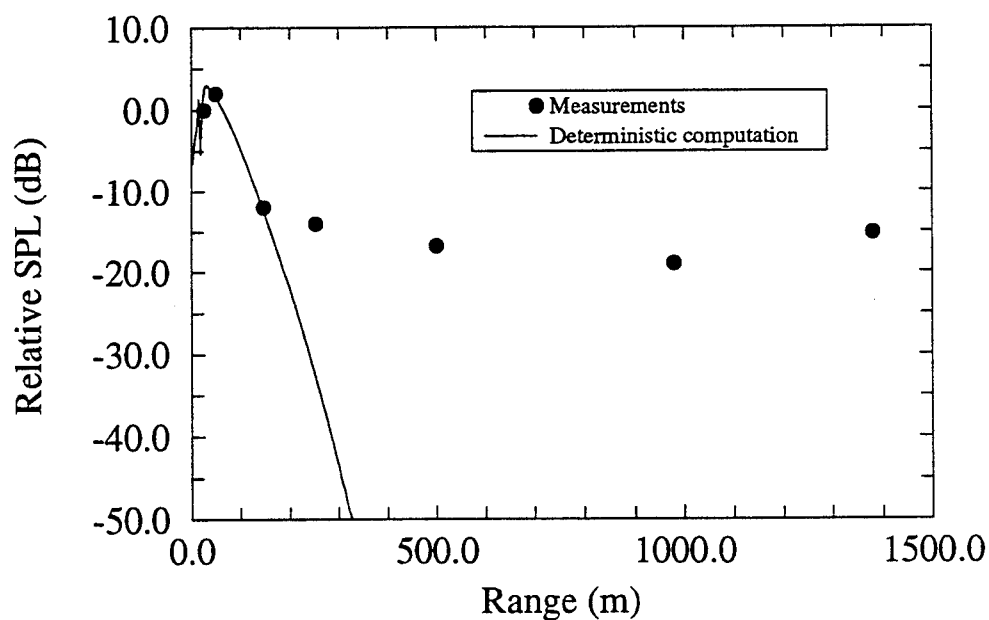
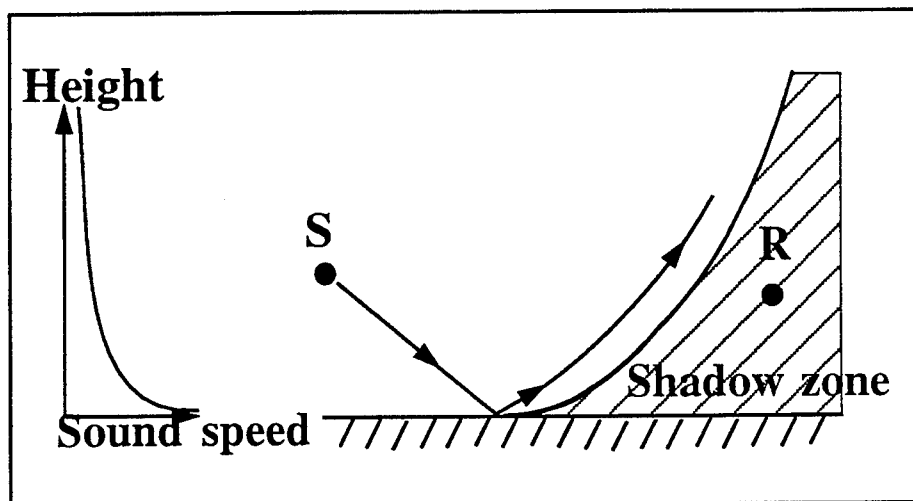


Figure 2: Propagation in a shadow zone. Comparison of experimental data with a deterministic computation.

As a result the relative sound pressure level is approximately independent of range. This is illustrated in Figure 3 where two gray scale maps of the sound pressure level are shown in the deterministic case, and for one particular realization of the turbulence field. The deterministic sound speed gradient and the statistical characteristics of the random field are those chosen by Gilbert et al. [1] to simulate the Wiener and Keast [7] experimental conditions:

$$c(z) = \begin{cases} c_0 + a \ln(z/d) & z \geq z_0 \\ c_0 + a \ln(z_0/d) & z < z_0 \end{cases} \quad (10)$$

where $c_0 = 340 \text{ m/s}$, $z_0 = 0.01 \text{ m}$, $d = 6.10^{-3}$ and $a = -0.5 \text{ m/s}$. The turbulence is characterized by a length scale $L = 1.1 \text{ m}$ and a variance $\langle \mu^2 \rangle = 2.10^{-6}$. The impedance of the ground is obtained from the Delany and Bazley model [8] with an effective flow resistivity $\sigma = 3.10^5 \text{ Nm}^{-4} \text{ s}^{-1}$.

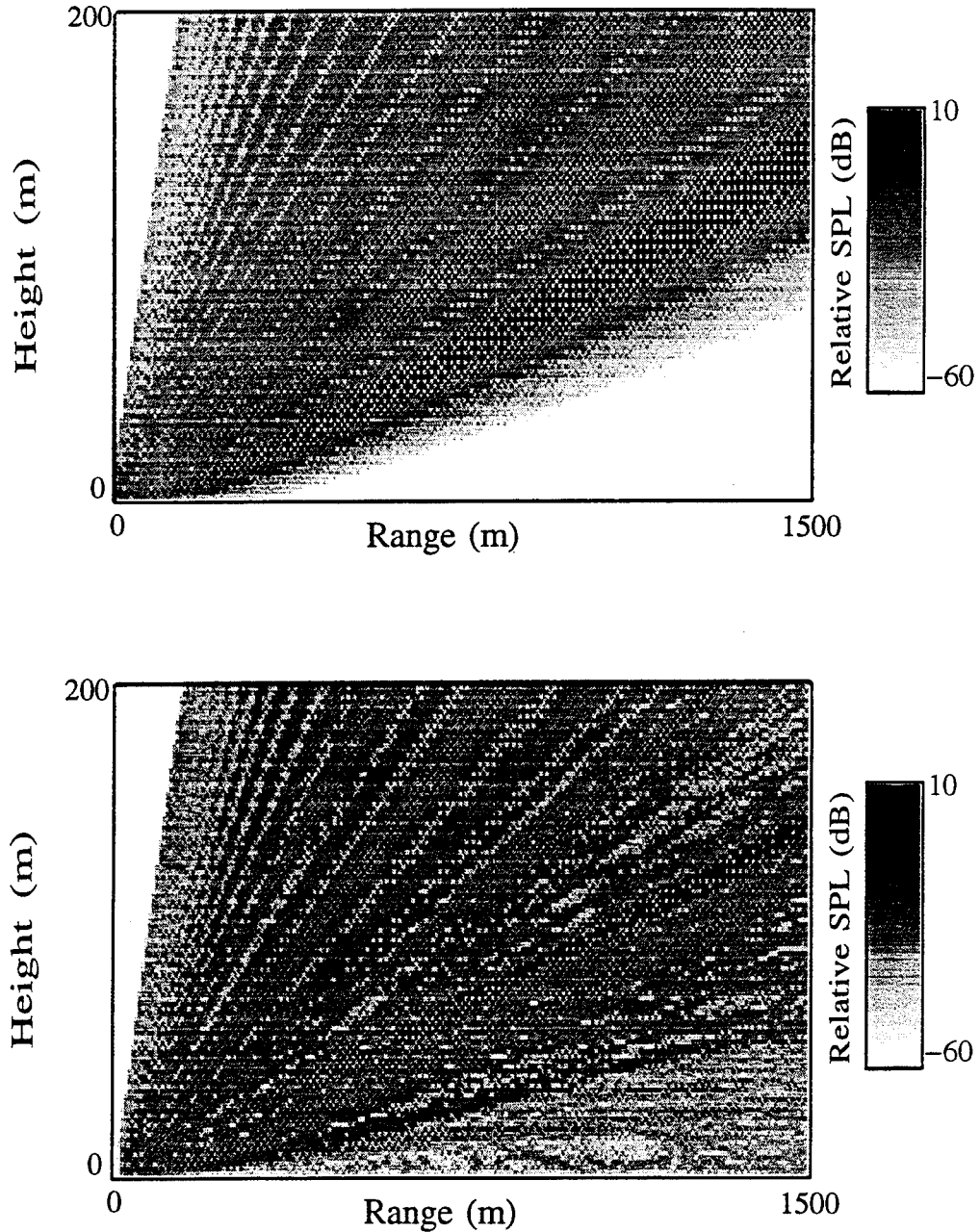


Figure 3: Scattering of sound into a shadow zone. Comparison between the deterministic field and the "instantaneous" sound pressure level (weak upward refraction; $f = 848 \text{ Hz}$; $\langle \mu^2 \rangle = 2.10^{-6}$; $L = 1.1 \text{ m}$; Gaussian spectrum).

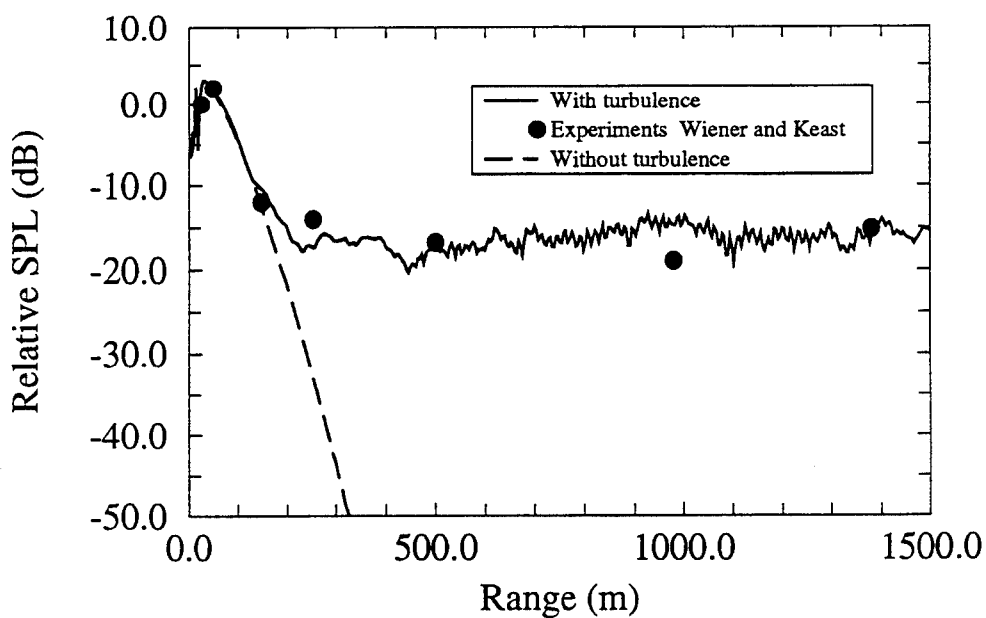


Figure 4: Mean sound pressure level in a turbulent atmosphere: comparison of experimental data with numerical simulations (weak upward refraction; "Gaussian turbulence").

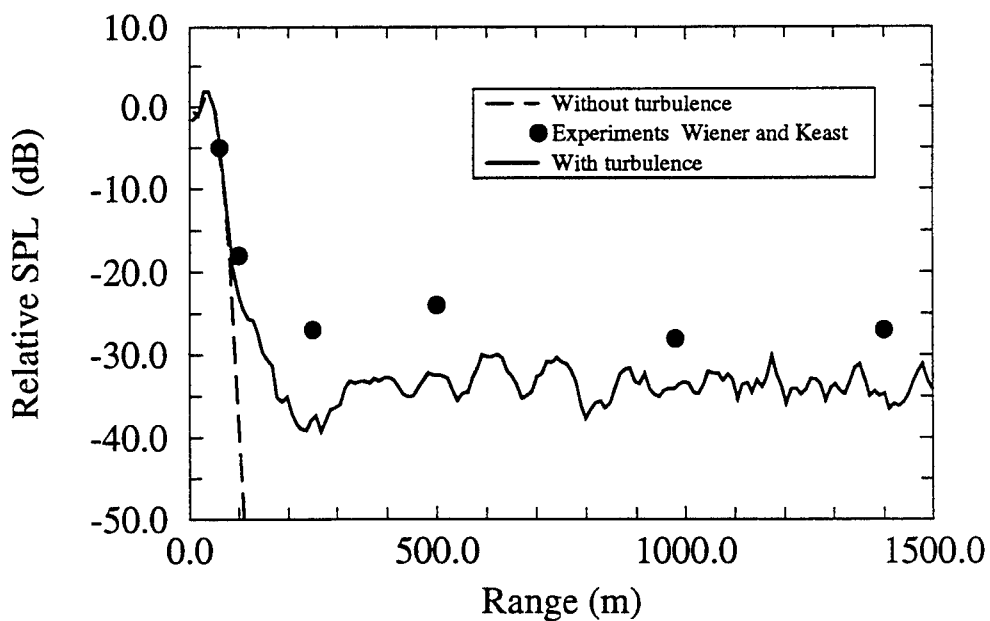


Figure 5: Mean sound pressure level in a turbulent atmosphere: comparison of experimental data with numerical simulations (strong upward refraction; "Gaussian turbulence").

In figure 4 we give the mean sound pressure level obtained with an average over 50 realizations. The agreement with the experimental results is excellent. In some circumstances, this agreement can deteriorate. Figure 5 gives an example of a computation done with the same turbulence characteristics but with a stronger sound speed gradient ($a = -2 \text{ m/s}$).

The global trend is correct, but the measured levels are underestimated by 5 to 10 dB. Many reasons can explain this (slight) discrepancy; for example the turbulence parameters were not measured during the experiments, so that the values used in the simulations can be erroneous. But it is also important to note that the modeling of the turbulent field is not free from approximations.

5 Improving the turbulence model

5.1 Spectral shape

The first idea to improve the model of turbulence is to change the shape of the spectrum of the index fluctuations (Juvé et al. [9]). It is clear that if the Gaussian form is a very convenient one, it is not realistic; this spectrum has a very sharp cut-off for high wavenumbers (small scales) which is not observed in practice; usually spectra have a significant inertial range (Kolmogorov -11/3 law); energy is not concentrated in structures of size roughly equal to L , but on the contrary spread over both larger and smaller turbulent structures in-between an inner and an outer scale (l_0, L_0). Changing the shape of the spectrum presents no special difficulty in our technique; the number of Fourier modes has only to be increased to represent correctly all the range of energetic wavenumbers. In practice we used a von Karman form for the index spectrum, a classical fit to experimental data:

$$\Phi_n(K) = \frac{5}{6\pi} \langle \mu^2 \rangle L_0^{-\frac{5}{3}} \left(K^2 + \frac{1}{L_0^2} \right)^{-\frac{11}{6}} \exp \left(-\frac{K^2}{K_m^2} \right) \quad (11)$$

$$K_m = \frac{5.92}{l_0} \quad (12)$$

In figure 6 we show the result of the two different choices for the spectrum on the behaviour of "instantaneous" index fluctuations in physical space. With a Gaussian spectrum blobs of size roughly equal to L are clearly shown with smooth transition between hot and cold regions. In the case of the von Karman spectrum the behaviour is completely different: the map shows both large (of size greater than L) and small structures; the boundaries between hot and cold zones are highly twisted and are reminiscent of fractal curves. The influence of the spectrum shape on the acoustic pressure field is demonstrated in figure 7.

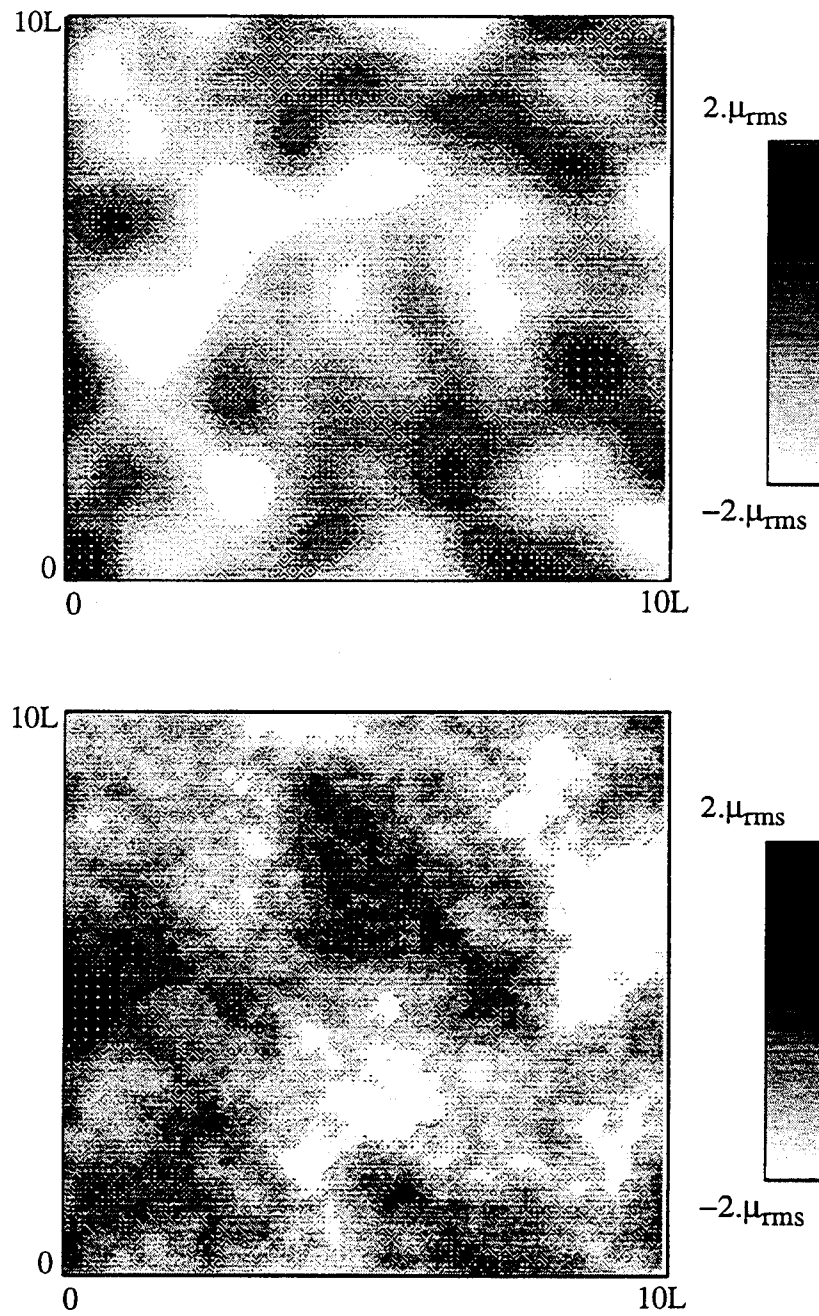


Figure 6: Spatial variation of the index fluctuations for turbulence described by a Gaussian spectrum (top; $L = 1.1m$) and a von Karman spectrum (bottom; $l_0 = 0.05m$; $L_0 = 1.1m$).

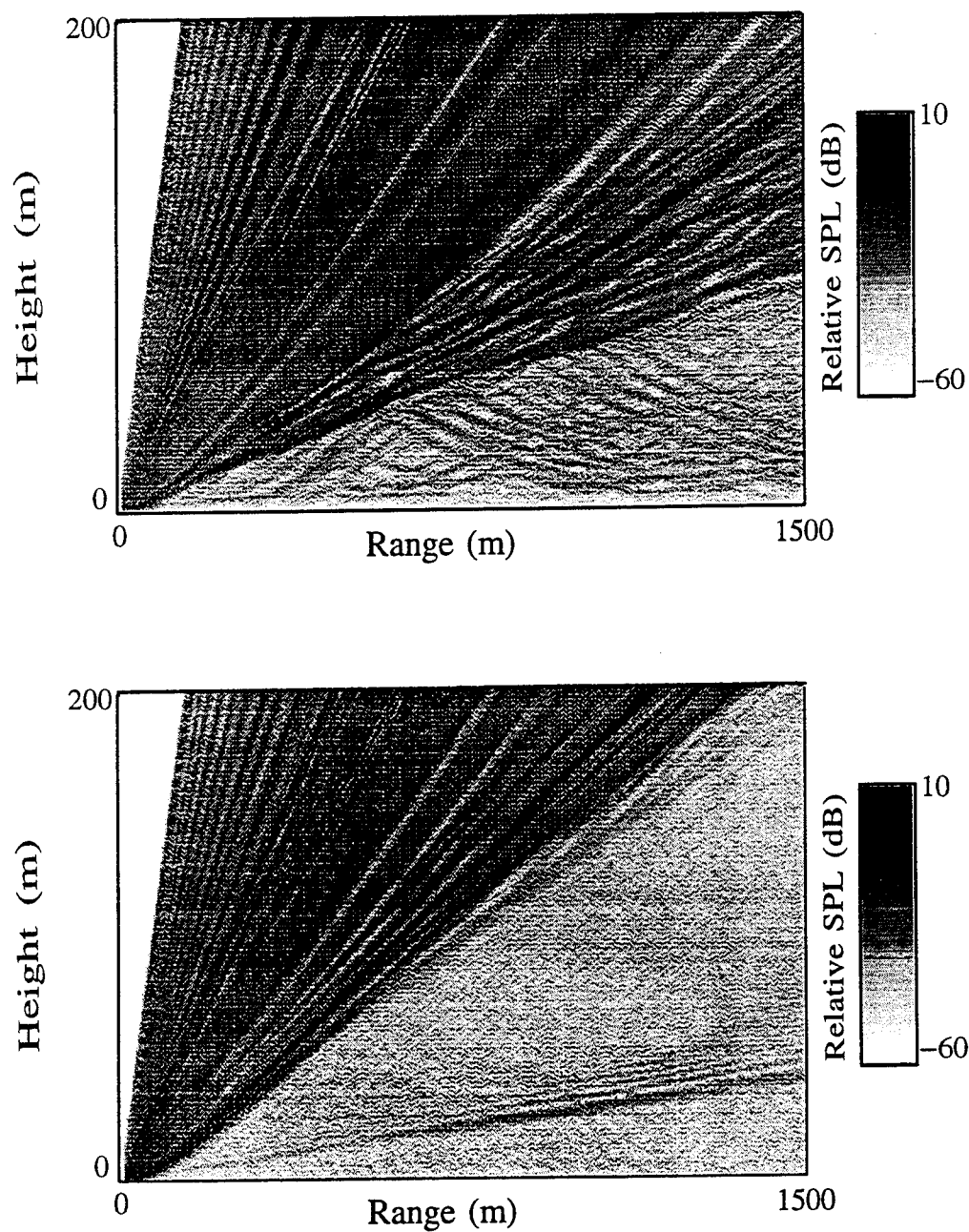


Figure 7: Instantaneous pressure field in a turbulent atmosphere described by: a Gaussian spectrum (top); a von Karman spectrum (bottom) (Strong upward refraction; $f = 848\text{Hz}$; $\langle \mu^2 \rangle = 2.10^{-6}$; $L = 1.1\text{m}$; $l_0 = 0.05\text{m}$; $L_0 = 1.1\text{m}$).

A complete comparison is not possible, as the realizations are not the same (different number of Fourier modes, sampling in $K \dots$), but the trends are nevertheless very clear. In the Gaussian case, scattering occurs for preferential directions with respect to the boundary of the shadow zone, the scattering angle being related directly to λ/L (λ wavelength of sound). For the von Karman case the scattering is more uniform, turbulent energy being spread over a large range of eddies. When an ensemble average is performed the sound pressure level computed near the ground is greater with the von Karman spectrum than with the Gaussian spectrum, and is in close agreement with experimental data (figure 8).

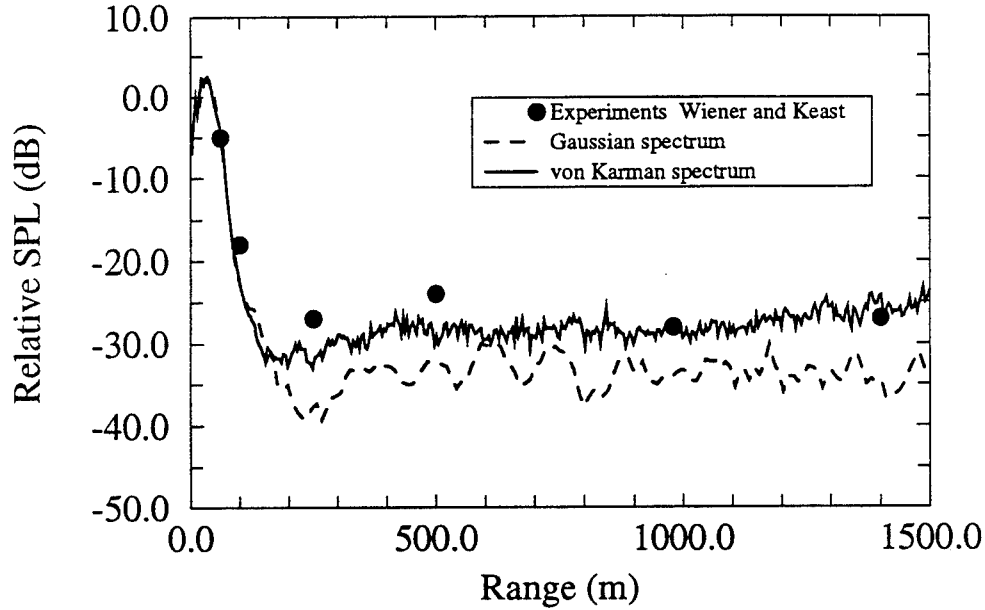


Figure 8: Influence of the spectrum of turbulence on the mean sound pressure level. Comparison between experimental data and numerical simulations with a Gaussian and a von Karman spectrum (Strong upward refraction; $f = 848\text{Hz}$; $\langle \mu^2 \rangle = 2.10^{-6}$; $L = 1.1\text{m}$; $l_0 = 0.05\text{m}$; $L_0 = 1.1\text{m}$).

5.2 Vectorial versus scalar fluctuations

The second idea we want to put forward is the following: in most cases the fluctuations in the refraction index result both from temperature and from wind speed variations. The random part of μ_t is approximated by:

$$\mu_t = -\frac{T'}{2T_0} - \frac{v'_1}{c_0} \quad (13)$$

where v'_1 is the horizontal component of the wind fluctuation. Usually one considers μ_t as an equivalent scalar index, but this approach can be misleading. For an isotropic scalar field the correlation depends only on the distance r between two points through one scalar function $m(r)$:

$$\langle \mu_t(\vec{x}) \mu_t(\vec{x} + \vec{r}) \rangle = \langle \mu^2 \rangle m(r) \quad (14)$$

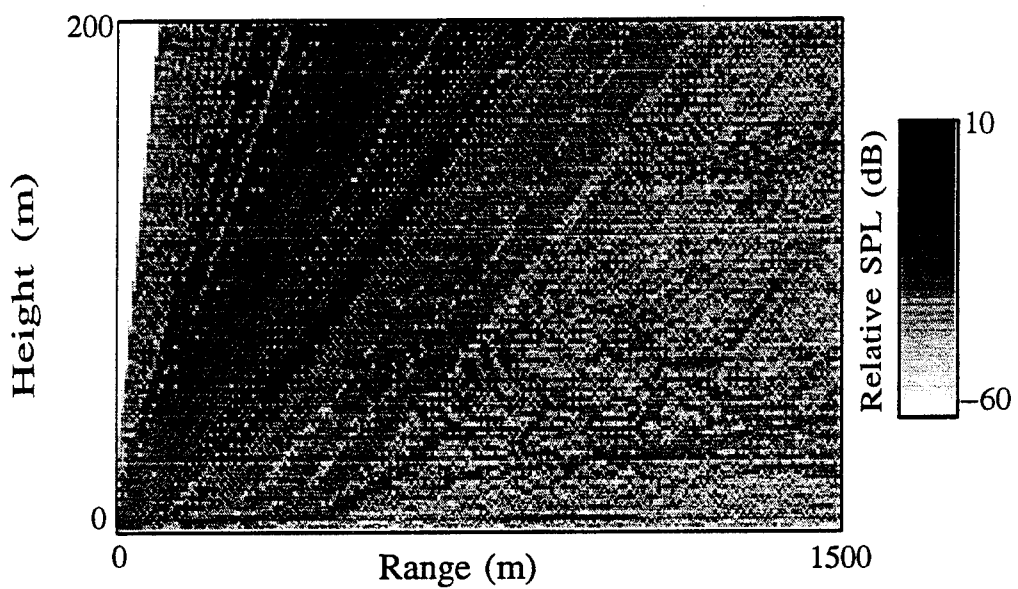
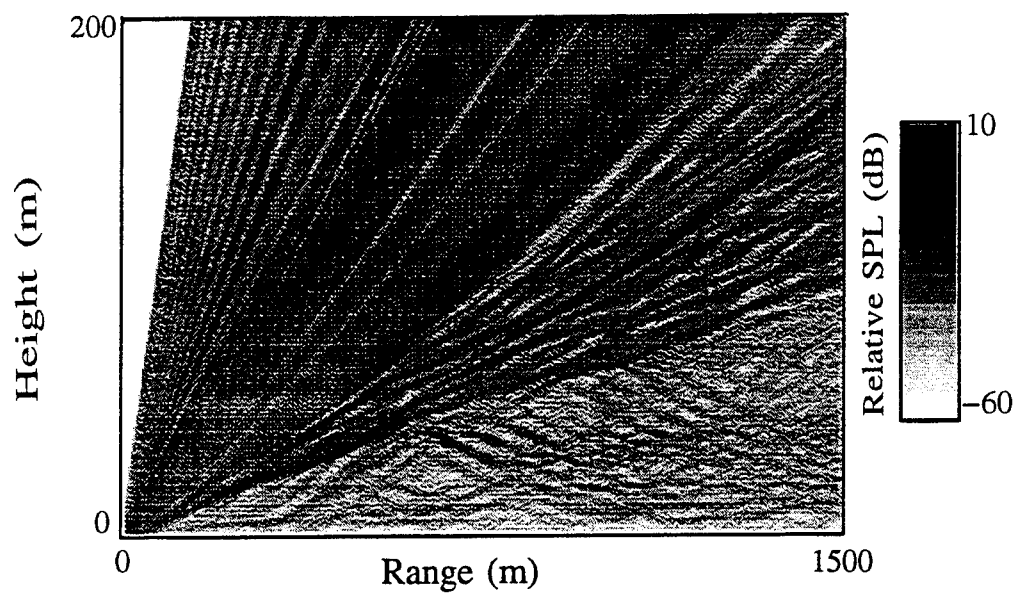


Figure 9: Instantaneous pressure field in a turbulent atmosphere. Comparison between scalar (top) and vectorial (bottom) fluctuations (Strong upward refraction; $f = 848\text{Hz}$; $\langle \mu^2 \rangle = 2.10^{-6}$; $L = 1.1\text{m}$; Gaussian spectrum).

But for an isotropic *vectorial* field the correlation depends of two functions $f(r)$ and $g(r)$:

$$\langle v'_1(\vec{x}) v'_1(\vec{x} + \vec{r}) \rangle = \langle v_1^2 \rangle \left((f(r) - g(r)) \frac{r_1^2}{r^2} + g(r) \right) \quad (15)$$

(f and g are related through the incompressibility constraint). It is clear that the correlation is different for longitudinal ($\vec{r} = (r_1, 0)$), and transverse ($\vec{r} = (0, r_2)$) separations. As a consequence the focusing properties of a vectorial random medium are different from those of a scalar one (Blanc-Benon et al. [10], Ostashev [11]).

Our technique for generating random fields is immediately applicable to vectorial fluctuations; one simply writes:

$$\vec{V}'(\vec{x}) = \sum_{i=1}^N \vec{V}(\vec{K}^i) \cos(\vec{K}^i \cdot \vec{x} + \varphi^i) \quad (16)$$

where $\vec{V}(\vec{K}^i)$ has to be orthogonal to \vec{K}^i to enforce incompressibility (Karweit et al. [12]).

In figure 9 we compare two snapshots of the pressure field for a scalar and a vectorial situation with the same variance of the fluctuations and the same integral scale ($m(r)$ and $f(r)$ being Gaussian). As before a detailed comparison is not allowed, but it can be seen that in the vectorial case, scattering is more intense (this is due to the smaller "lateral scales" involved) and more diffuse. When an average over 50 realizations is performed, one can see (figure 10) that the mean level in the shadow zone is greatly increased with respect to the scalar case (up to 10-12 dB).

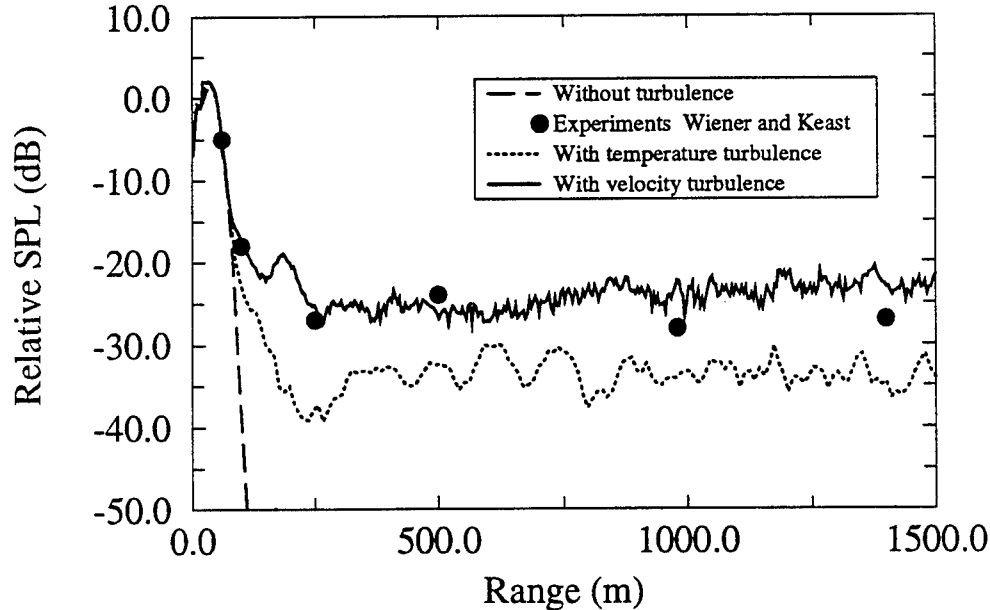


Figure 10: Influence of the type of turbulence on the mean sound pressure level. Comparison between experimental data and numerical simulations with scalar (temperature) and vectorial (velocity) fluctuations (Strong upward refraction; $f = 848\text{Hz}$; $\langle \mu^2 \rangle = 2.10^{-6}$; $L = 1.1m$).

Incidentally the result of the simulation is very close to the experimental data; of course this is only a coincidence as the experimental turbulence was certainly a mixing of temperature and velocity fluctuations, not a pure kinematic turbulence.

6 Conclusion

In this paper we have demonstrated that the choice of the turbulence model can have significant effects on the mean sound pressure level computed in (deterministic) shadow zones. One of the problems encountered when comparing numerical simulations and experimental results is that one often has to estimate the relevant turbulent parameters. It is strongly suggested that in the future experiments, spectra of fluctuations be measured as well as the relative contribution to index fluctuations of temperature and wind velocity.

7 References

- [1] Gilbert, K.E., Raszpet, R. and Di, X. (1990) *Calculation of the turbulence effects in an upward-refracting atmosphere*. J. Acous. Soc. Amer., **87**, 2428-2437.
- [2] Juvé, D., Blanc-Benon, Ph. and Chevret, P. (1992) *Numerical simulation of sound propagation through a turbulent atmosphere*. Pages 282-296 of: Fifth International Symposium on Long Range Sound Propagation, The Open University, England.
- [3] McBride, W.E., Bass, H.E., Raszpet, R. and Gilbert, K.E. (1991) *Scattering of sound by atmospheric turbulence: a numerical simulation above a complex impedance boundary*. J. Acous. Soc. Amer., **90**, 3314-3325.
- [4] Saad, Y. and Lee, D. (1988) *A new algorithm for solving the wide angle wave equation*. Pages 119-132 of: Computational Acoustics, Vol. 2, Elsevier, New-York.
- [5] Chevret, P. (1994) *Simulation numérique des effets de la turbulence sur la propagation du son dans l'atmosphère*. Doctoral Thesis N 94-18, Ecole Centrale de Lyon, France.
- [6] Daigle, G.A., Embleton, T.F. and Piercy, J.E. (1986) *Propagation of sound in the presence of gradients and temperature near the ground*. J. Acous. Soc. Amer., **79**, 613-627.
- [7] Wiener, F.M. and Keast, D.N. (1959) *Experimental study of the propagation of sound over ground*. J. Acous. Soc. Amer., **31**, 724-733.
- [8] Delany, M.E. and Bazley, E.N. (1970) *Acoustical properties of fibrous absorbent materials*. Applied Acoustics, **3**, 105-116.
- [9] Juvé, D., Blanc-Benon, Ph. and Chevret, P. (1993) *A numerical study of sound propagation through a turbulent atmosphere*. J. Acous. Soc. Amer., **93**, 2407.
- [10] Blanc-Benon, Ph., Juvé, D. and Comte-Bellot, G. (1991) *Occurrence of caustics for high-frequency acoustic waves propagating through turbulent fields*. Theor. and Comp. Fluid Dyn., **2**, 271-278.
- [11] Ostashev, V.E. (1994) *Sound propagation and scattering in media with random inhomogeneities of sound speed, density and medium velocity*. Waves in Random Media (To appear)
- [12] Karweit, M., Blanc-Benon, Ph., Juvé, D. and Comte-Bellot, G. (1991) *Simulation of the propagation of an acoustic wave through a turbulent velocity field: a study of phase variance*. J. Acous. Soc. Amer., **89**, 52-62.

SIMULATION OF SCATTERING BY TURBULENCE INTO A SHADOW REGION USING THE GF-PE METHOD

Michael R. Stinson, David I. Havelock and Gilles A. Daigle

Institute for Microstructural Sciences, National Research Council, Ottawa, Ontario K1A 0R6, Canada

Abstract

A Green's function formulation for the parabolic equation (GF-PE) is used to compute the sound field above an impedance plane in the presence of both an upwardly-refractive sound speed profile and turbulence. The scattered field at a receiver in the acoustic shadow is dominated by contributions from a relatively small region midway between source and receiver at the height of the "skywave". Turbulent length scales of 2 to 5 m are found to be the most effective for scattering.

I. Introduction

The detection of acoustic sources at long range depends very much on the propagation conditions. A particular challenge is presented by upward-refracting conditions (e.g., upwind propagation or thermal lapse) for which the sound field within the refractive shadow is determined largely by scattering from atmospheric turbulence. A computational tool, to predict sound fields under these conditions, is a useful companion to experimental measurements.

A Green's Function formulation for the parabolic equation (GF-PE), as described by Di and Gilbert (1992), will be used here to predict acoustic propagation through a refractive, turbulent atmosphere. This implementation (sometimes referred to as the Fast-PE method) follows several stages of development. The initial application of the parabolic equation to treat refraction (Gilbert and White, 1989) and the introduction of a Green's function method to improve computational speed (Gilbert and Di, 1993) have led to a fast and robust tool for sound field calculation in the absence of turbulence

(Daigle, Bass and Raspet, 1992). The effects due to atmospheric turbulence were incorporated into the earlier propagation model by Gilbert, Raspet and Di (1990) and the turbulent scattering of sound into an acoustic shadow demonstrated. More recently, the Green's function method has been extended to include turbulence, through the introduction of phase screens (Di and Gilbert, 1992, 1994). Calculations can now proceed at relatively high speed on a personal computer platform.

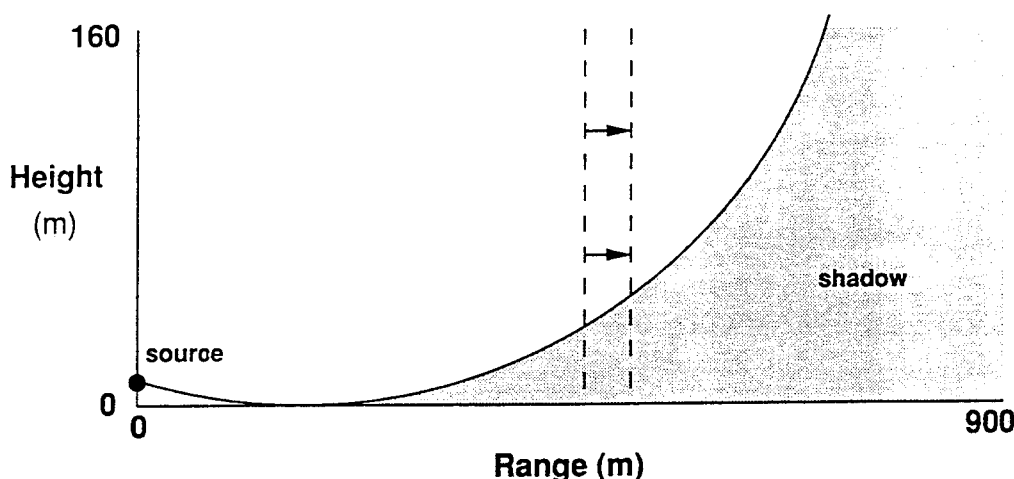


FIG. 1. Geometry used for GF-PE calculations.

The geometry that will be considered for the propagation simulations is shown in Fig. 1. Ranges up to 900 m and heights up to 160 m will be considered. The source is located 3.7 m above a flat ground of normalized specific impedance (7.19, 8.2) at 500 Hz, the only frequency considered. An upward refraction condition is obtained by assuming a logarithmic sound speed profile for the simulations,

$$c(z) = c_o - a \ln(z/d) , \quad (1)$$

for height z , using parameters $c_o=340$ m/s, $a=2$ m/s, and $d=0.006$ m. This profile leads to a region of reduced sound pressure levels, i.e., the acoustic shadow, indicated in Fig. 1 by the shaded area. In the GF-PE approach, the pressure field along one vertical plane is used to compute the pressure along the plane at the next range step, indicated schematically by the dashed vertical lines, and the solution marched outward.

To include turbulence in the simulations, a model for the turbulence is required. Following Gilbert *et al.* (1990) and Juvé *et al.* (1992), a two-dimensional Fourier

representation of the random turbulence field is assumed. For a spatially-varying component $\mu(r,z)$ of the index of refraction, over a region r_{max} by z_{max} ,

$$\mu(r,z) = \sum_m \sum_n T_{mn} e^{-ik_r r} e^{-ik_z z}, \quad (2)$$

where $k_r = 2\pi m/r_{max}$ and $k_z = 2\pi n/z_{max}$. For a Gaussian spectrum of turbulence,

$$|T_{mn}|^2 = \frac{\langle \mu^2 \rangle \pi L^2}{r_{max} z_{max}} \exp[-(k_r^2 + k_z^2)L^2/4]. \quad (3)$$

The phase of each component T_{mn} is selected randomly. The power spectral density $|T_{mn}|^2$ corresponding to a correlation length of $L=1.1$ m and variance of $\langle \mu^2 \rangle = 2 \times 10^{-6}$ in the index of refraction is shown in Fig. 2.

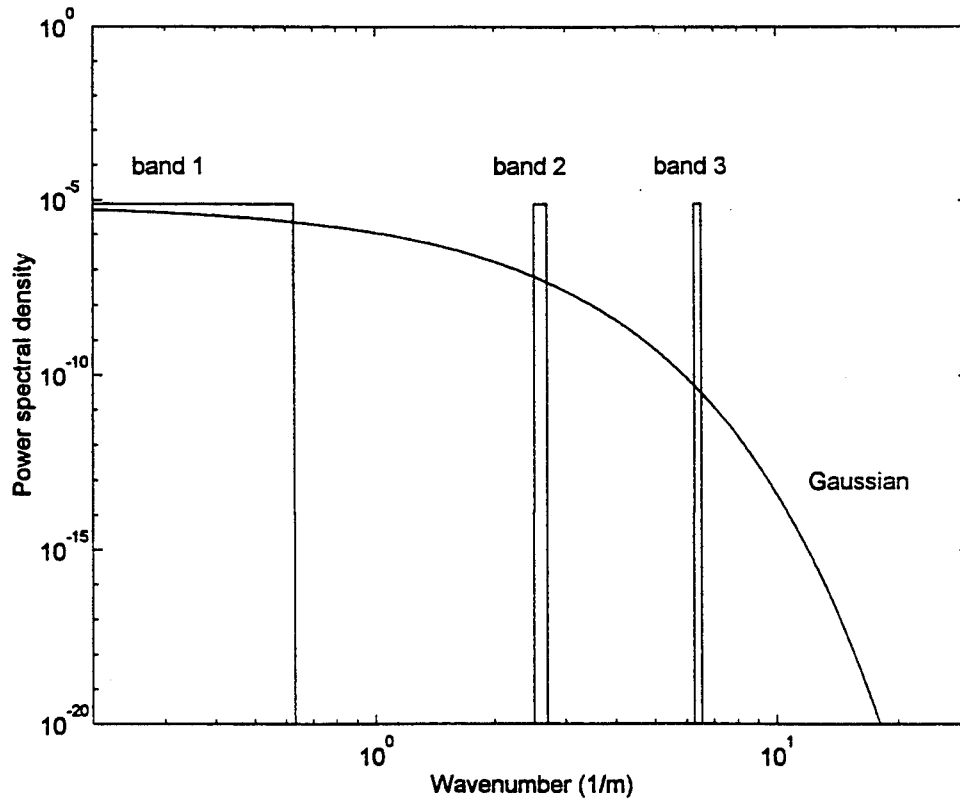


FIG. 2. The spectra used to describe turbulence. The Gaussian spectrum assumes $L=1.1$ m and $\langle \mu^2 \rangle = 2 \times 10^{-6}$. The three flat bands are used in Sec. III.

A simulation based on this spectrum is shown in Fig. 3. A gray-scale with 6 dB steps has been adopted to show the variations in sound pressure level. The limiting

caustic and the acoustic shadow are apparent in this simulation as is the scattering of acoustic energy into the shadow region. Similar pictures have been generated previously by Gilbert *et al.* (1990) and by Juvé *et al.* (1992).

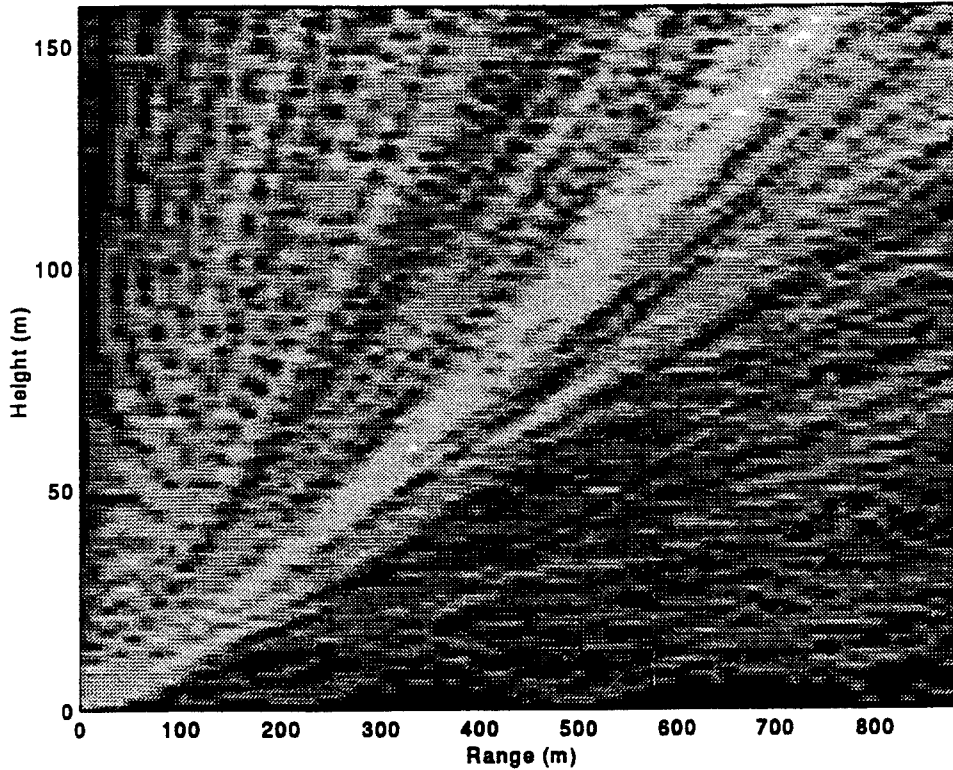


FIG. 3. Gray-scale plots of the relative sound pressure level for sound propagating in an upward-refracting atmosphere with a Gaussian spectrum of turbulence.

II. Comparison of the GF-PE with an approach based on Tatarskii

The GF-PE approach, with no turbulence present, has been tested against other computational techniques (e.g., ray tracing, the Gaussian beam method, and the Fast Field Program) and found to work very well (Daigle *et al.*, 1992). When there is turbulence present in the simulation, the GF-PE is a functioning, but essentially untested, tool. An alternate approach, based on a formulation by Tatarskii, is developed here in an attempt to provide something to which the GF-PE may be compared.

On p. 158 of his book, Tatarskii (1971) gives an expression for the scattered sound field due to a scattering volume δV ($\sim L^3$) having spatially-varying temperature $T(\rho)$ and velocity $u(\rho)$, at a position ρ . For simplicity, only thermal variations will be considered.

The sound pressure at a receiver a distance r' and direction \mathbf{n} away from the scattering region is

$$\delta p = -p_o \frac{\mathbf{k} \cdot \mathbf{n}}{4\pi r'} \exp(ikr') \int_{\delta V} \exp(i\mathbf{K} \cdot \boldsymbol{\rho}) \frac{T'(\boldsymbol{\rho})}{T_o} d^3\rho, \quad (4)$$

where the insonifying field has pressure p_o and wavevector \mathbf{k} (magnitude k), $T(\boldsymbol{\rho}) = T_o + T'(\boldsymbol{\rho})$ where T_o is the mean temperature, and the scattering vector is $\mathbf{K} = \mathbf{k} - k\mathbf{n}$.

The characteristic size L of the scattering volume must be sufficiently small that $L \ll r'$ and $L^2 \ll \lambda r'$, yet should be sufficiently large that a surface integral, dropped from the derivation, be negligible.

Now, for a large volume of space (as indicated in Fig. 1) and for a turbulent atmosphere with significant variations of T' over small fractions of a meter, any calculation based on Eq. (4) would take prohibitively long. A useful calculation can be performed, though, if we restrict the spatial extent of the turbulence. We suppose that the atmosphere is as indicated in Fig. 4. The sound speed is constant through all of the

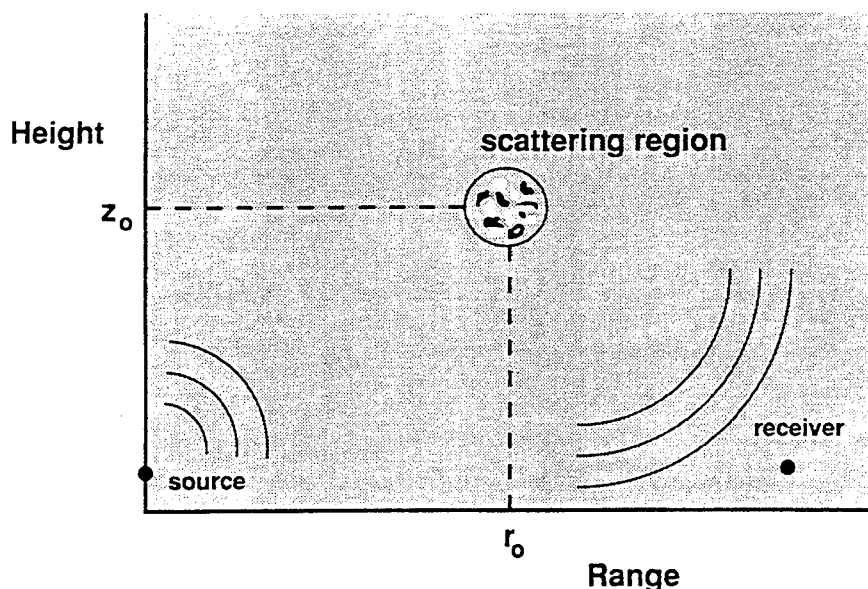


FIG. 4. Turbulent structure assumed for model calculation. The index of refraction is constant except within a small scattering region.

range-height plane, except for a small circular region indicated at range r_o and height z_o . Within this region, the index of refraction has a spatially varying component given by

$\mu(r,z) = -T'(r,z)/(2T_o)$. A turbulent atmosphere $\mu_o(r,z)$ was generated, as described in the previous section, and windowed spatially using a Gaussian envelope. Hence,

$$\mu(r,z) = \mu_o(r,z) \exp \left\{ -[(r-r_o)^2 + (z-z_o)^2]/a^2 \right\} . \quad (5)$$

This turbulence structure can be handled by the current implementation of the GF-PE. It must be noted, though, that this is strictly speaking a two-dimensional description of the turbulent field. Axial symmetry about a vertical axis through the source has been assumed implicitly. The actual three-dimensional situation being assumed by the GF-PE, here and in previous work (e.g., Gilbert *et al.*, 1990), is as indicated in Fig. 5: The circular turbulent structure of Fig. 4 is rotated about the vertical axis resulting in a scattering "torus".

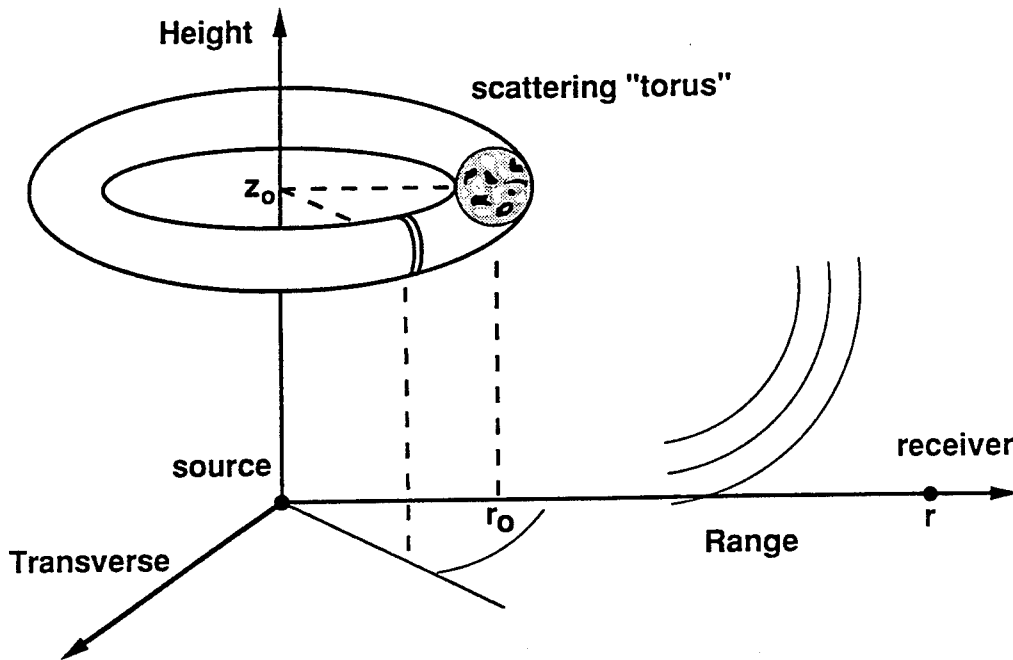


FIG. 5. The effective three-dimensional structure being assumed by most implementations of the GF-PE.

To enable a comparison between the GF-PE and an approach based on Tatarskii, we must ensure that both approaches describe the same physical situation. Hence, Eq. (4) must be applied to the toroidal system of Fig. 5. The torus can be broken into a large number of segments at different azimuthal positions ϕ . The contributions of all segments

are added (coherently) to obtain the total scattered field at the receiver position, giving

$$\frac{p}{p_{ff}} = \frac{k^2 r_o r \exp[ik(\sqrt{r_o^2 + z_o^2} - r)]}{\pi \sqrt{r_o^2 + z_o^2}} \int_0^\pi F(\phi) d\phi, \quad (6)$$

where p_{ff} is the reference free field pressure, r is the distance between source and receiver (both on the ground). At each azimuthal position, the function $F(\phi)$ is obtained from an integral over the cross section $A(\phi)$ of the torus, according to

$$F(\phi) = \frac{(1+R_p) k \cdot \hat{n} \exp(ikr')}{r'} \int_{A(\phi)} \mu(s,z) \exp[i(K_s s + K_z z)] ds dz; \quad (7)$$

R_p is the plane wave reflection coefficient corresponding to the scattering element at ϕ .

Sound pressure levels calculated using the two techniques, Tatarskii and the GF-PE, are shown in Fig. 6. For both, the scattering region was at a range of 409.6 m and height of 20 m and had a diameter $a=10$ m. Two realizations of the turbulence $\mu_o(r,z)$

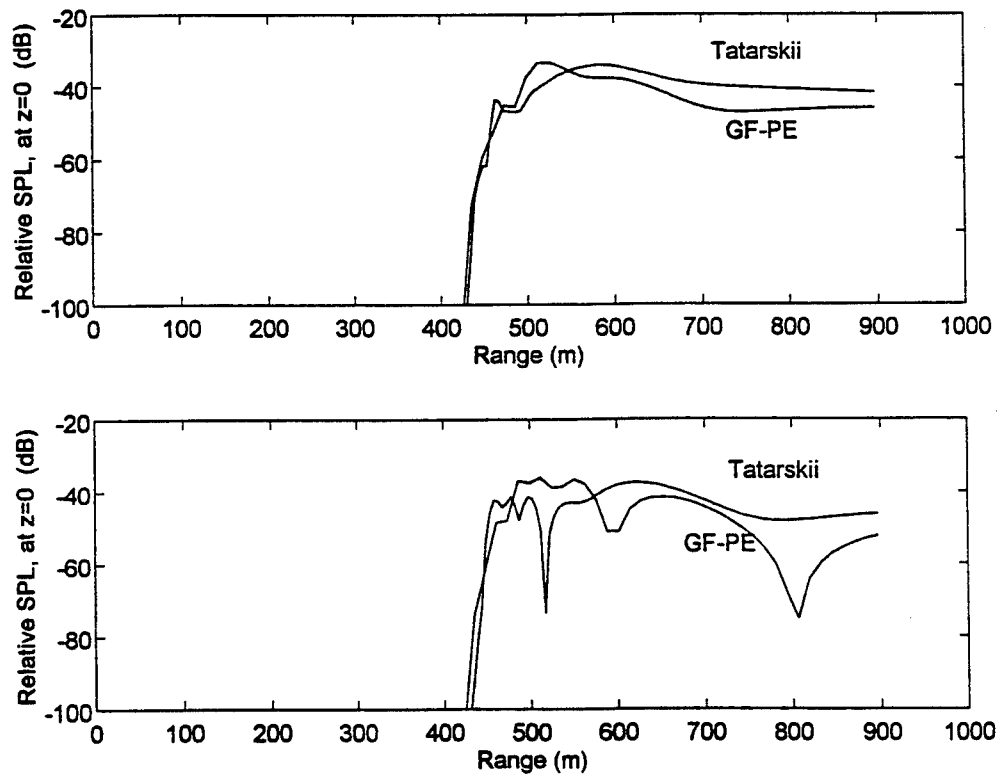


FIG. 6. Predictions of sound pressure level on the ground at various ranges, using the GF-PE and Tatarskii approaches. The scattering region is at a range of 409.6 m and a height of 20 m with a diameter of 10 m, for both realizations.

were used, leading to the two panels. Qualitatively, there is a close relationship between the two computational approaches. We take this to provide support for the general application of the GF-PE approach with turbulence present. There are significant differences between the approaches, though. It is not clear at this time what the explanations for the discrepancies are.

It might be noted in passing that the contributions to the integral in Eq. (6) are dominated by the contributions from azimuthal positions near $\phi=0$. Most of the toroidal scattering structure shown in Fig. 5 can be ignored, so the two-dimensional representation of the turbulence is not entirely inappropriate.

III. Dominant Length Scales for Scattering

The turbulent structure in the atmosphere contains a spectrum of components corresponding to different length scales. Some components might be expected to contribute more to the scattered sound field in the shadow. Simulations using the GF-PE can be used to explore the dependence on scatterer length scale.

Figure 2 shows some alternate spectra to be used as input into the simulations. Three bands of frequency components are shown, with constant power spectral density in each. The first band contains wavenumbers between 0 and 0.628 m^{-1} , corresponding to length scales greater than 10 m. Band 2 contains wavenumbers between 2.513 and 2.591 m^{-1} , corresponding to length scales of about 2.5 m. Band 3 contains wavenumbers between 6.283 and 6.315 m^{-1} , corresponding to length scales of about 1 m. The widths of these bands have been chosen so that each band contains the same number of wavevectors (320) and, equivalently, the resultant $\langle \mu^2 \rangle$ is the same for each (having a value of about 2.5×10^{-7}).

The sound fields obtained with the GF-PE simulations using these three bands of spatial frequencies are shown in Fig. 7 (note that the aspect ratio of height to range has been changed from that in Fig. 3). It is clear that large-scale structures (over 10 m) contribute very little to the scattered energy field: The picture obtained for Band 1 is virtually identical to what is obtained when there is no turbulence assumed at all. For Band 3, with 1 m structures, there is some scattering observed. However, the Band 2 calculations, with 2.5 m structures present, shows the most scattering. Other, similar

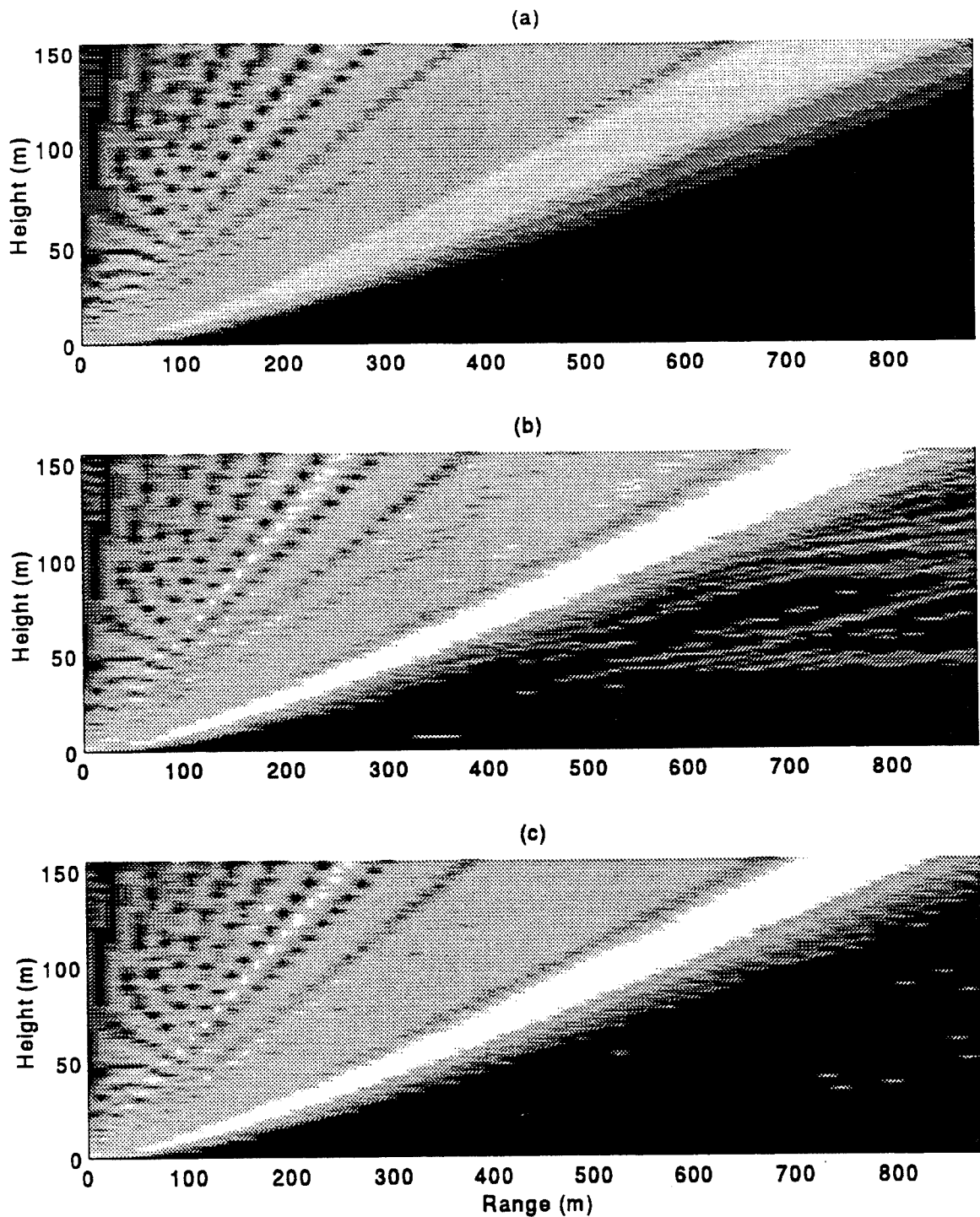


FIG. 7. Gray-scale plots of the relative sound pressure level for three different turbulence spectra. Each corresponds to a different band of spatial frequencies, shown in Fig. 2, and all have $\langle \mu^2 \rangle = 2 \times 10^{-6}$. (a) Only length scales > 10 m included; (b) length scales of about 2.5 m; (c) length scales of about 1 m.

calculations show that structures having length scales between 2 and 5 m are the most important structures for scattering into the shadow, for the geometry being assumed here.

The qualitative results presented in Fig. 7 may be understood in terms of the Bragg reflection condition, formulated originally to describe X-ray diffraction by crystal structures but shown to apply in acoustic scattering by Tatarskii (1971). For a sound wave being scattered through an angle θ , as indicated in Fig. 8, the important scattering structures have a spatial periodicity D , satisfying

$$\lambda = 2D \sin(\theta/2) \quad (8)$$

For a sound frequency of 500 Hz and a scattering angle of 10° , a size of $D=4$ m is predicted, consistent with the observations of Fig. 7.

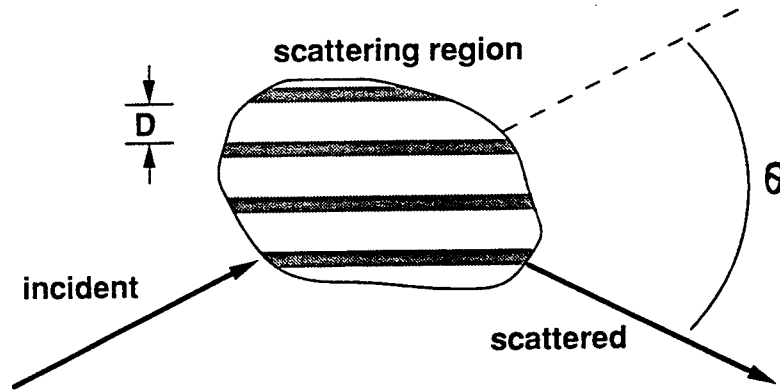


FIG. 8. Bragg reflection condition, for acoustical scattering.

IV. Dominant Location of Scatterers

The relative importance of scattering from different locations can be assessed through simulations. For a given realization of a turbulent atmosphere, the scattered sound field at a receiver within the acoustic shadow will be a sum of contributions from all scattering locations. If a single-scattering approach is adopted, then each contribution can be determined independently. Suppose a realization $\mu_o(r,z)$ of a turbulent atmosphere has been obtained according to the procedure described in the Introduction. A spatial window, e.g., Eq. (5), applied to this structure forces turbulence to be zero everywhere (i.e., $\mu=0$) except within a small region centered at the specified range and height, as sketched in Fig. 4. The scattered acoustic field calculated at a receiver position is due

solely to this region. The process can be repeated with the spatial window shifted to a number of different locations, mapping out the scattered signal from each. Hence, the relative contributions from each location in the range-height plane can be determined for the realization $\mu_o(r,z)$.

Figure 9 displays the output of such a calculation. The two panels display the results for two different realizations of a turbulent atmosphere. The position on the graph corresponds to the location of the scattering region. The strength of the scattered field at the receiver position (on the ground at a range of 896 m) is indicated by the darkness of the plotted point. Nine different shades of gray were used, corresponding to 3 dB changes in SPL. For these calculations, a Gaussian spectrum for the turbulence and a logarithmic refractive profile have been assumed, as for Fig. 3.

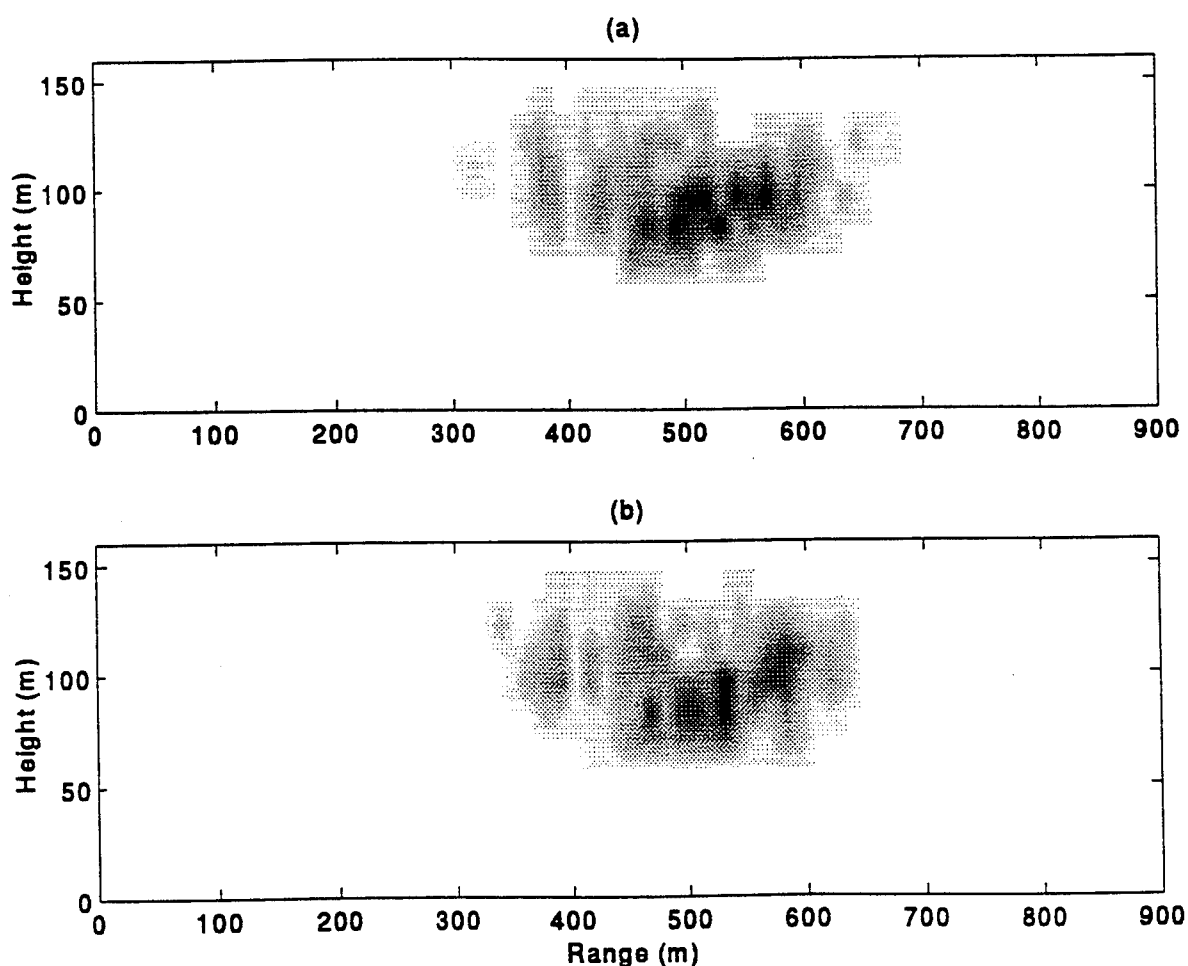


FIG. 9. Relative strength of different scattering positions, for a receiver position on the ground at a range of 896 m. Darker areas are stronger scatterers. The two panels correspond to two different realizations (Gaussian spectrum of turbulence).

The two realizations shown in Fig. 9 are different in detail but show the same general characteristics. The scattering is dominated by a region located between 60 and 120 m in height and between 400 and 600 m in range. The turbulent structure outside of this region can be ignored. Within the region, "hot spots" are evident, corresponding to relatively small structures (of the order of 10 m), which tend to dominate the scattering.

V. Conclusions

Simulations of atmospheric propagation through turbulent, refractive atmospheres are possible using the Green's function formulation for the parabolic equation (GF-PE).

The results in the preceding sections lead to a qualitative picture of the scattering process, summarized in Fig. 10. For a logarithmic profile, at least, there tend to be higher SPL's near the limiting caustic, as indicated by the slanted shading, and a shadow region underneath. Scattered energy will also follow curved ray paths. The dominant scattering regions can be located by following a limiting caustic backwards from the receiver position (Gilbert, 1992). The intersection of this caustic with the forward caustic gives the approximate location. Within this dominant region, "hot spots" are found. These observations suggest that a simple phenomenological model, with a finite number of explicit scattering objects, might be useful for interpreting experimental results

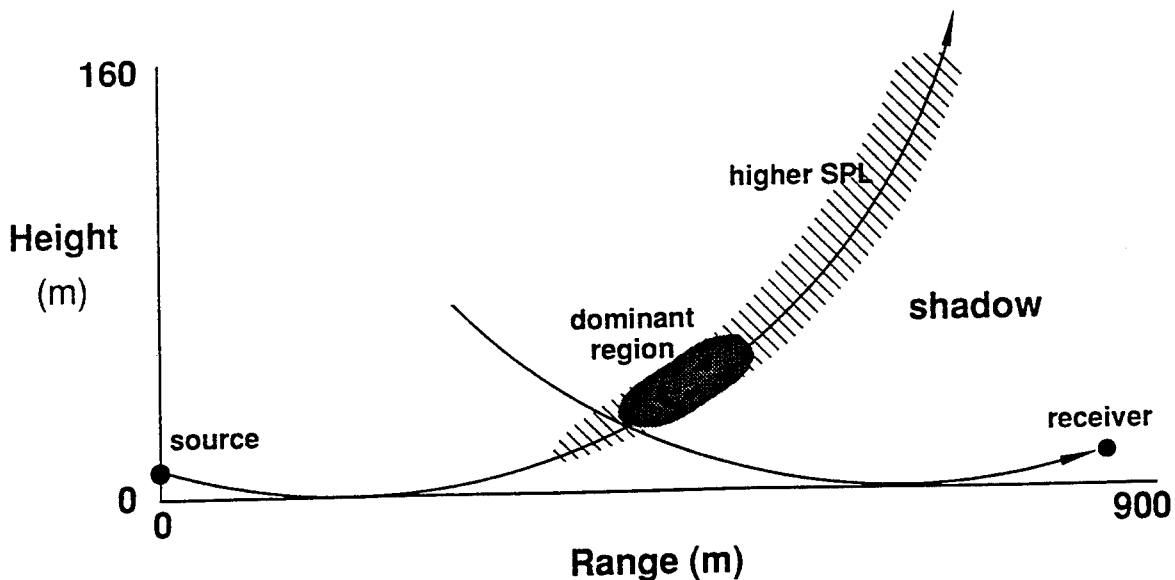


FIG. 10. The dominant region scattering into an acoustic shadow.

References

- Daigle, G.A., Bass, H.E., and Raspet, R. (1992). "Status of numerical methods and the experimental database", *J. Acoust. Soc. Am.* **92**, 2404(A).
- Di, X. and Gilbert, K.E. (1992). "A phase screen approach to sound propagation through small-scale turbulence", *J. Acoust. Soc. Am.* **92**, 2405(A).
- Di, X. and Gilbert, K.E. (1994). "The effect of turbulence and irregular terrain", in *Proceedings of the Sixth International Symposium on Long Range Sound Propagation*, edited by Gilles A. Daigle, David I. Havelock and Michael R. Stinson; Ottawa, Canada.
- Gilbert, K.E. (1992). Private communication.
- Gilbert, K.E. and Di, X. (1993). "A fast Green's function method for one-way sound propagation in the atmosphere", *J. Acoust. Soc. Am.* **94**, 2343-2352.
- Gilbert, K.E., Raspet, R., and Di, X. (1990). "Calculation of turbulence effects in an upward-refracting atmosphere", *J. Acoust. Soc. Am.* **87**, 2428-2437.
- Gilbert, K.E. and White, M.J. (1989). "Application of the parabolic equation to sound propagation in a refracting atmosphere", *J. Acoust. Soc. Am.* **85**, 630-637.
- Juvé, D., Blanc-Benon, Ph., and Chevret, P. (1992). "Numerical simulations of sound propagation through a turbulent atmosphere", in *Proceedings of the Fifth International Symposium on Long Range Sound Propagation*, edited by Keith Attenborough, Kai M. Li and Henry E. Bass; Milton Keynes, England.
- Tatarskii, V.I. (1971), *The effects of the turbulent atmosphere on wave propagation*, (Keter Press, Jerusalem), Chapter 2.B., Section 35.

Acknowledgment

The authors would like to thank Xiao Di for his advice on the implementation and the running of the GF-PE code on their computers.

Calculation of Average Turbulence Effects on Sound
Propagation Based on the Fast Field Program Formulation

by

Richard Raspet and Wenliang Wu
Physical Acoustics Research Group
University of Mississippi
University, MS 38677

ABSTRACT

Daigle has published a series of papers in which he has applied the turbulent scattering theories of Chernov and Karavainikov to sound propagation over hard and finite impedance grounds. In these papers, Daigle has introduced the decorrelation in phase and amplitude due to turbulence along the direct and reflected path into the spherical wave reflection analysis for a non-refracting atmosphere. We have incorporated the phase and amplitude decorrelation terms into the evaluation of the spectral integral of a fast field program for propagation in a refracting atmosphere. Although the calculation involves two significant approximations it reproduces Daigle's results for homogenous atmospheres and compares well with the upward refraction measurement of Parkin and Scholes and with measurements taken under a variety of refractive conditions at Bondville, Illinois by the U.S. Army Construction Engineering Research Laboratory.

PACS NUMBERS: 43.28.F, 43.20.F

INTRODUCTION

The fast field program is an efficient technique for predicting the propagation of sound in a refracting atmosphere above a complex impedance ground surface in a non-turbulent atmosphere.^{1,2} The fast field program does not produce accurate prediction deep in refractive shadow zones where the scattered field is significant.^{1,2} Daigle developed a ray based technique for calculating turbulence effects in a non-refracting turbulence atmosphere above hard³ and finite impedance boundaries.⁴ Clifford and Lataitis⁵ derived results similar to Daigle's using a mathematically rigorous calculation. In brief, Daigle introduced factors into a calculation of the average sound pressure level which account for the phase and amplitude decorrelation between direct and ground reflected rays.

The fast field program uses a Hankel transform to express the horizontal variation of a pressure field as a function of range in a cylindrically symmetrical space as the Fast Fourier Transform (FFT) of a complex function of horizontal wave number. The magnitude of the kernel for each horizontal wave number represents the contribution to the total pressure level for a given propagation angle at the source height. The complete solution requires diffracted terms with complex propagation angles. The fast field program uses a single integration (a single transform) to calculate the sound pressure level versus range.

We have calculated the average sound pressure level in a turbulent atmosphere from the kernel of the fast field program using Daigle's expression for the interference between two ray paths separated by a maximum distance h . In order to perform this calculation we have developed an approximate formula for the separation as a function of horizontal wave number.

Section I describes Daigle's theory and applies this theory to the calculation of average turbulence levels using the kernel of the fast field program. Section IIA compares the results of this calculation with Daigle's theory⁴ and Parkin and Scholes' measurements⁶ and discusses differences observed between the two theories. Section IIB compares the results of the calculation to data by Wiener and Keast⁷ which has been analyzed previously using the parabolic equation.⁸ Section IIC compares the results of the calculation for upward and downward propagation to measurements made by the U.S. Army Construction Engineering Laboratory at Bondville, IL.⁹ Section III demonstrates the effect of turbulence on modal interference for downward refraction and discusses the implications and limitations of coherent calculations.

I. THEORY

This paper is based on Clifford and Lataitis' expression for the turbulence effects on sound propagation above a complex impedance surface assuming a Gaussian turbulence spectrum.⁵ For a spherically symmetric source having unit pressure at one meter the mean squared received pressure is given by:

$$\langle \overline{p^2} \rangle = \frac{1}{r_d^2} + \frac{|Q|^2}{r_r^2} + \frac{2|Q|}{r_r r_d} \cos [k (r_r - r_d) + \theta] T, \quad (1)$$

where $T = \exp[-\sigma^2(1 - \rho)]$. r_d is the distance from source to receiver along the direct path, r_r is the distance from source to receiver along the reflected path, $Q = |Q|e^{i\theta}$ is the complex spherical wave reflection factor, σ^2 is the variance of the phase fluctuation along a path and ρ is the phase covariance between paths. The factor σ^2 is given by

$$\sigma^2 = \frac{\sqrt{\pi}}{2} \langle \mu^2 \rangle k^2 L L_0, \quad \text{for } L > k L_0^2, \quad (2)$$

where $\langle \mu^2 \rangle$ is the variance of the index of refraction, k is the wave number, L is the horizontal path length and L_0 is the Gaussian turbulence scale.

The phase covariance between paths is given by

$$\rho = \sqrt{\pi} \frac{L_0}{2h} \operatorname{erf}\left(\frac{h}{L_0}\right), \quad (3)$$

where h is the maximum path separation.¹⁰ As $\langle \mu^2 \rangle$ goes to zero or as $L_0 \rightarrow \infty$, $T \rightarrow 1$ and the equation describes coherent interference between the direct and ground reflected ray above a complex impedance ground surface. $T < 1$ accounts for the reduced coherence between the direct and reflected waves in a turbulent atmosphere.

We note that Eq. (1), as derived in Ref. 5, only applies to equal source and receiver heights. The term T , which describes the reduction in coherence between different paths due to turbulence, is identical to that used in Ref. 3, with h interpreted as the maximum path separation between the two ray paths. We will apply Eq. (1) to propagation with unequal source and receiver heights using definition of Daigle et al. for h as the maximum path separation.

The fast field program is based on the Hankel transform of the Helmholtz equation in a cylindrically symmetric coordinate system. The separated vertical dependence $\hat{p}(K, z)$ is solved for a vertically layered atmosphere for N discrete horizontal wave numbers K from 0 to K_{\max} . The fast field program we are using is described in Ref. 2. The details of the calculation of $\hat{p}(K, z)$ are not necessary for the description of the turbulence calculation. An example of the magnitude of a kernel is shown in Fig. 1.

In integral form, the pressure as a function of range can be recovered from

$$p(r) = \frac{(1+i)}{\sqrt{2\pi r}} \int_0^\infty \hat{p}(K) \exp(-iKr) \sqrt{K} dK. \quad (4)$$

For numerical calculations using an N point FFT we introduce $\Delta K = \frac{K_{\max}}{(N-1)}$, $K_n = n\Delta K$, $r_m = m\Delta r$ and $\Delta r = \frac{2\pi}{n\Delta K}$. Equation (4) becomes

$$p(r_m) = \frac{(1+i)}{\sqrt{2\pi r_m}} \Delta K \sum_{n=0}^{N-1} \hat{p}(K_n) \sqrt{K_n} \exp\left(\frac{-i2\pi mn}{N}\right) \quad (5)$$

This expression is in the form of an FFT which can rapidly compute $p(r_m)$ for all m .

In a turbulent atmosphere, the complex sound pressure fluctuates in amplitude and phase. This time dependence is introduced into Eq. (4) and the time average pressure squared evaluated using

$$\left\langle \overline{p^2(r,t)} \right\rangle = \frac{1}{2} \text{Real} (p(r,t) p^*(r,t)). \quad (6)$$

The average effect on the interference between different wave number contributions is described by the factor T from Eq. (1):

$$\left\langle \overline{p^2(r,t)} \right\rangle = \frac{1}{2} \text{Real} \left[\frac{1}{\pi r} \int_0^\infty \int_0^\infty \hat{p}(K) \hat{p}^*(K') e^{-i(K-K')r} T(K, K') \sqrt{K} \sqrt{K'} dK dK' \right] \quad (7)$$

The function $T(K, K')$ is the average effect of the decorrelation in phase and amplitude on the interference of the horizontal wave number components K and K' .

The evaluation of the effect of phase and amplitude fluctuation along the propagation paths for an arbitrary refracting atmosphere is a formidable task. We have not attempted such a calculation. Instead, it is assumed that Clifford and Latatis' expression for T for a non-refracting atmosphere is approximately correct for refractive atmospheres, and that the maximum separation between wave numbers can be estimated from the corresponding propagation angles. It is emphasized that these are constructions to estimate h , the maximum path separation between wave number components, and are not related to ray paths between the source and receiver. The constructions are, however, based on familiarity with ray paths for downward refraction and the principle energy transfer paths for scattering under upward refracting conditions.⁸

A. Curved Formulation

The curved formulation calculates the separation between two circular arcs. The arcs leave either the source or the receiver (whichever has the lowest speed of sound) and intersect at the same height at the range D .

The propagation angle corresponding to a given wave number K_n is given by

$$\cos \theta_n = \frac{K_n}{K_c}, \quad (8)$$

where $K_c = \frac{\omega}{c(z')}$ and $c(z')$ is MIN ($c(z_s)$, $c(z_r)$). If n' is the integer value corresponding to K_c (see definitions used in Eq. (5)), the separation is given by

$$h = \frac{D}{2} \left| \left[\frac{1 - \frac{m}{n'}}{1 + \frac{m}{n'}} \right]^{\frac{1}{2}} - \left[\frac{1 - \frac{n}{n'}}{1 + \frac{n}{n'}} \right]^{\frac{1}{2}} \right|. \quad (9)$$

B. Straight Line Formulation

With the same assumptions the straight line formulation can be easily derived. This formulation results in wider separation between contributions and greater decorrelation between wave number components.

$$h = \frac{D}{2} \left| \frac{\left[1 - \left(\frac{m}{n'} \right)^2 \right]^{\frac{1}{2}}}{\frac{m}{n'}} - \frac{\left[1 - \frac{n}{n'} \right]^{\frac{1}{2}}}{\frac{m}{n'}} \right|. \quad (10)$$

The results presented here will mainly employ the curved formulation as it is more realistic in limiting the separation of the wave number contributions. The kernel of the integral contains wave numbers corresponding to propagation at less than the lowest physical speed of sound. These diffracted waves are necessary to obtain convergence of the integral. The phase relationship between these components leads to small or negligible contributions to the integral. If these are truncated too rapidly in the numerical integration however, the rapid phase change caused by the truncation results in significant

error contributions.¹ We note also that diffracted wave number terms cannot be incorporated into the calculation for h , since Eq. (8) results in complex propagation angles. For these contributions we let $T = e^{-\sigma^2}$. In practice we omit these zero terms by summing to n' , not to n_{\max} . We will discuss the selection of n' below.

We take advantage of the form of the function $T(K_n, K_m)$ in the discrete evaluation of Eq. (7). We note that $T \rightarrow e^{-\sigma^2}$ as $|n - m|$ becomes large and separate the integral into a coherent and an incoherent contribution.

$$\begin{aligned} \langle \overline{p^2(r,t)} \rangle = & \frac{1}{2} \text{Re} \left[e^{-\sigma^2} \frac{1}{\pi r} \int_0^\infty \int_0^\infty \hat{p}(K) \hat{p}^*(K') e^{-i(K-K')r} \sqrt{K} \sqrt{K'} dK dK' \right] \\ & + \frac{1}{2} \text{Re} \left[\frac{1}{\pi r} \int_0^\infty \int_0^\infty \hat{p}(K) \hat{p}^*(K') (T - e^{-\sigma^2}) e^{-i(K-K')r} \sqrt{K} \sqrt{K'} dK dK' \right] \quad (11) \end{aligned}$$

The first term is $e^{-\sigma^2}$ times the unperturbed mean pressure squared. The unperturbed pressure amplitude can be calculated quickly using the fast field program. This represents the coherent field reduced by the scattered energy. The second term is scattered energy from K into K' . Note that $(T - e^{-\sigma^2})$ is only large for $K \approx K'$. We have not exploited this feature to decrease the computation time but it should lead to a significant improvement in the future. Figure 3 is a cross section of $\frac{(T - e^{-\sigma^2})}{e^{-\sigma^2}}$ as $n - m$ is varied around $n = 2000$.

The calculation procedure is straightforward. The first term is calculated directly from the coherent fast field program result. The second term is performed as an $n' \times n'$ double summation, where n' corresponds to the largest propagating horizontal wave number;

$$K_{n'} < K_c < K_{n'+1} \quad (12)$$

In practice, we have used $K_{n'+1}$ as our upper limit to assure we do not omit any significant terms. Test cases were insensitive for up to ten additional points.

The next section compares the results of this calculation to Daigle's results for a non-refracting atmosphere and to data for upward and downward refracting atmospheres.

II. RESULTS

The results of turbulent FFP will be compared to three sets of data. The first is Parkin and Scholes' data⁶ for a non-refracting atmosphere with microphones and sources close to the ground. Daigle's⁴ predictions are also shown. Next, the calculation is compared to the data of Wiener and Keast⁷ for a weak upward refracting atmosphere and a strong upward refracting atmosphere. The final data comparison will be with data taken at Bondville, Illinois from a 30.5 m high tower under upward refraction conditions, homogeneous conditions and downward refracting conditions.⁹

All results are presented in terms of the sound pressure level relative to 0.0 dB and 1.0 m. These plots display the variation of sound pressure level with the effects of geometrical spreading and atmospheric attenuation removed. In free space with no refractive effects this level would remain at 0.0 dB for all ranges.

A. Comparison to Parkin and Scholes' Data and Daigle's Predictions.

Figure 4 compares the results of the turbulent FFP calculation using Daigle's estimated values of turbulence strength ($\langle \mu^2 \rangle = 2.0 \times 10^{-6}$) and scale ($L_0 = 1.1\text{m}$) to Parkin and Scholes' data⁶ and Daigle's calculations.⁴ There is good agreement between the data and the turbulent FFP calculations except in the transition region where the coherent and incoherent results begin to diverge. The turbulent FFP calculations use the curved formulation described above. Slightly better agreement is obtained if the straight line method is used. For example, the predicted results for 500 Hz at 350, 600 and 1100 m using the straight line formulation are about 1.0 dB higher than the curved formulation. Since the difference in the two formulations is small, and we believe the curved formulation will give more realistic results in most cases, all other results below use the curved formulation.

Daigle's calculation has employed an empirical adjustment in that half the actual maximum separation is used in the ray based results. This implies that the ray based theory overestimates the effect of scattering in reducing the coherent wave and increasing the incoherent scattered wave. The method described in this paper underestimates the amount of scattering occurring in the transition region. A portion of this error occurs since upward propagating waves and downward propagating waves with the same

horizontal wave number are treated as a single contribution in the turbulent FFP method. Better agreement can be obtained for the turbulent FFP by arbitrarily increasing the path separation by a factor of 2.

B. Comparison with Wiener and Keast

The data of Wiener and Keast⁷ have been compared to the results of the parabolic equation for different realizations of turbulence with $\langle \mu^2 \rangle = 2.0 \times 10^{-6}$ and scale $L_0 = 1.1$ m.⁸ We repeat this comparison using the turbulent FFP with the same atmospheric parameters used in Ref. 8. The source and receiver heights are 3.7 m and 1.5 m respectively. Octave bands of random noise were broadcast. The turbulent FFP calculations are performed for the mid-band frequency, $\sqrt{f_1 f_2}$, where f_1 and f_2 are the lowest and highest frequencies in the octave bands considered, 300–600 Hz and 600–1200 Hz.

The logarithmic sound speed gradients are given by

$$c(z) = c_0 + a \ln \frac{z}{d} \quad z \geq z_0$$

$$c_0 + a \ln \frac{z_0}{d} \quad z \geq z_0 \quad (13)$$

z_0 is the roughness length for mown grass ($z_0 = 0.01$ m), and d is the displacement length ($d = 6 \times 10^{-3}$ m).

The refraction parameter a is -0.5 m/s for weak upward refraction and -2.0 m/s for strong upward refraction. We have used two values for $\langle \mu^2 \rangle$, 2.0×10^{-6} and 8.0×10^{-6} . The first value was used by Gilbert, Raspet and Di⁸ in the parabolic equation study of propagation through turbulence and was based on Daigle's measurements. The second value is estimated based on measurements of wind speed fluctuations in the atmosphere.¹¹ Wind speed measurements display RMS fluctuations on the order of 5 to 15% of the mean wind speed. The wind speed given in Wiener and Keast for the two cases is 15 and 17 mph. If we use 15% for the RMS fluctuation, we calculate $\langle \mu^2 \rangle$ of approximately 8.0×10^{-6} .

Figure 5 displays the measured values as well as the level calculated using the coherent FFP and the levels calculated using the turbulent FFP for the two index of refraction fluctuations. Both turbulent FFP calculations show qualitative agreement with

Wiener and Keast's data. The weak and strongly upward refracting data at 848 Hz and the strong upward refracting data at 424 Hz agree best with $\langle \mu^2 \rangle = 8.0 \times 10^{-6}$. The weak upward refraction data displays lower levels than the turbulent calculation for either of the two index of refraction values. We note that the parabolic equation results in Ref. 8 for $\langle \mu^2 \rangle = 2.0 \times 10^{-6}$ show a similar trend to the calculations in Fig. 5. In fact, the results of Ref. 8 agree well with the turbulent FFP calculations.

C. Comparison of Data from Bondville, Illinois

The U.S. Army Construction Engineering Research Laboratory performed simultaneous meteorological and sound propagation measurements at Bondville Field Station during the period Jan. 1983 to Sept. 1984. Four single frequency sources were used on a tower 30.5 m high. The microphones were 1.2 meters above ground level.

Figure 6 presents average results for days with similar logarithmic sound velocity profiles as defined by Eq (13). The data and the coherent parabolic equation predictions are from Ref. 10. The coherent fast field program results agree in detail with the coherent parabolic equation results presented in this figure. Early analysis¹ of this data displayed the need to include turbulence in prediction of sound propagation in upward refracting conditions. M.A. Johnson et al., performed a study of turbulence parameters at Bondville and developed methods for estimating their values from weather observations.¹²

The strong upward refracting conditions are most affected by the turbulence and these conditions are due to moderate to strong winds. For analysis of the average data in Fig. 6, we have used a turbulent scale of 2.2 m and a value of $\langle \mu^2 \rangle = 10 \times 10^{-6}$. The single scale choice is somewhat arbitrary. For a non-refracting atmosphere, detailed calculation in Ref. 12 showed that the scale near the ground determines the effective average scale. That is, there is little difference between a fixed scale of 1.0 m and a varying scale from 1.0 m at the ground to 7.0 m at 30 m altitude. Such an analysis has not been performed for a refracting atmosphere. Figure 6 displays the results for 630 Hz. The other frequencies in the study show similar agreement. The results are quite good. The turbulent FFP calculation does not differ from the coherent parabolic equation calculation or the data for the non-refracting and downward refracting cases since turbulence effects are greatest at interference minima.⁴

Another interesting point about this calculation should be mentioned. The coherent fast field program cannot correctly predict the coherent levels deep in the shadow. In the coherent fast field program the phase of the various large contributions of order 10 must be very precisely specified to form a superposition of order 10^{-6} . The "noise floor" of the FFP used on the Cray XMP is on the order of -120 dB sound pressure level. The shadow zone kernel will produce an accurate prediction in the turbulent FFP, since the phase relationship between wave number contribution is not critical. The addition of turbulence extends the useful range of the FFP method in the shadow zone.

III. EFFECT OF TURBULENCE ON MODAL STRUCTURE

Calculations of the sound pressure level for downward refracting conditions often result in complicated interference patterns due to the interaction of modes having different horizontal velocities.¹³ There has been some debate over whether these modal structures can be experimentally observed or if turbulence will remove the structure leaving a smooth average level.

Figure 7 presents the predictions of the coherent FFP and the turbulent FFP for a configuration which results in modal structure. The source is at 1.00 m, the receiver at 1.05 m and the frequency is 500 Hz. The sound speed gradient is linear with a slope of 0.1 s^{-1} up to 50 m altitude. The ground is characterized by the Delany-Bazely-Chessell¹⁴ model with a flow resistivity of 300,000 mks rays/m. The turbulence strength is $\langle \mu^2 \rangle = 10 \times 10^{-6}$ and the turbulence scale is 1.1 m. This represents a moderately strong turbulent downwind condition. The incoherent field does not destroy the modal interference pattern. Significant coherence remains between the modes. The amplitude of the interference structure is reduced from about 6 dB to about 3 dB. The minima are effected more by the turbulence as expected from Ref. 4 and from the theory. Interference minima are more sensitive to phase perturbations than are maxima.

IV. CONCLUSION

The effects of decorrelation in amplitude and phase of sound due to turbulent scattering have been incorporated into the spectral calculation of sound pressure levels in a refracting atmosphere above a complex impedance plane. The results of the turbulent FFP agree well with other predictions and measurements of sound propagation and

measurements of sound propagation in a turbulent atmosphere. These results of the calculation are relatively insensitive to the method used to estimate h , the maximum path separation.

The turbulent FFP has been used to demonstrate that moderately high levels of turbulence will not completely remove modal interference structure predicted for downward refraction.

The turbulent FFP can be improved by reducing the integration regime as suggested by Fig. 3. Another facet of the calculation which can be improved is the estimation of the average separation of different wave number contribution for different types of refracting atmospheres.

REFERENCES

- 1) S.W. Lee, W.F. Richards, N. Bong and Richard Raspet, "Impedance formulation of the fast field program for acoustic wave propagation in a layered medium," *J. Acoust. Soc. Am.* **79**, 628-634 (1986).
- 2) S.J. Franke and G.W. Swenson, Jr., "A brief tutorial on the fast field program (FFP) as applied to sound propagation in the air," *Applied Acoustics* **27**, 203-215 (1989).
- 3) G.A. Daigle, J.E. Piercy and T.F.W. Embleton, "Effects of atmospheric turbulence on the interference of sound waves near a hard boundary," *J. Acoust. Soc. Am.* **64**, 622-630 (1978).
- 4) G.A. Daigle, "Effects of atmospheric turbulence on the interference of sound waves above a finite impedance boundary," *J. Acoust. Soc. Am.* **65**, 45-49 (1979).
- 5) S.F. Clifford and R.J. Lataitis, "Turbulence effects on acoustic wave propagation over a smooth surface," *J. Acoust. Soc. Am.* **73**, 1545-1550 (1983).
- 6) P.H. Parkin and W.F. Scholes, "The horizontal propagation of sound from a jet engine close to the ground at Hatfield," *J. Sound Vib.* **2**, 353-374 (1965).
- 7) F.M. Wiener and D.N. Keast, "Experimental study of the propagation of sound over ground," *J. Acoust. Soc. Am.* **31**, 724-733 (1959).
- 8) K.E. Gilbert, R. Raspet and X. Di, "Calculation of turbulence effects in an upward-refracting atmosphere," *J. Acoust. Soc. Am.* **87**, 2428-2437 (1990).
- 9) M.J. White and K.E. Gilbert, "Application of the parabolic equation to the outdoor propagation of sound," *Applied Acoustics* **27**, 227-238 (1989).
- 10) V.R. Karavainikov, "Fluctuations of amplitude and phase in a spherical wave," *Akust. Zk.* **3**, 175-186 (1957).

- 11) S. Morgan and R. Raspet, "Investigation of the mechanism of low frequency wind noise generation outdoors," J. Acoust. Soc. Am. **92**, 1180-1183 (1992).
- 12) M.A. Johnson, R. Raspet and M.T. Bobak, "A turbulence model for sound propagation from an elevated source above level ground," J. Acoust. Soc. Am. **81**, 638-646 (1987).
- 13) R. Raspet, G. Baird and W. Wu, "Normal mode solution for low-frequency sound propagation above a complex impedance plane," J. Acoust. Soc. Am. **91**, 1341-1352 (1992).
- 14) C.I. Chessell, "Propagation of noise along a finite impedance boundary," J. Acoust. Soc. Am. **62**, 825-834 (1977).

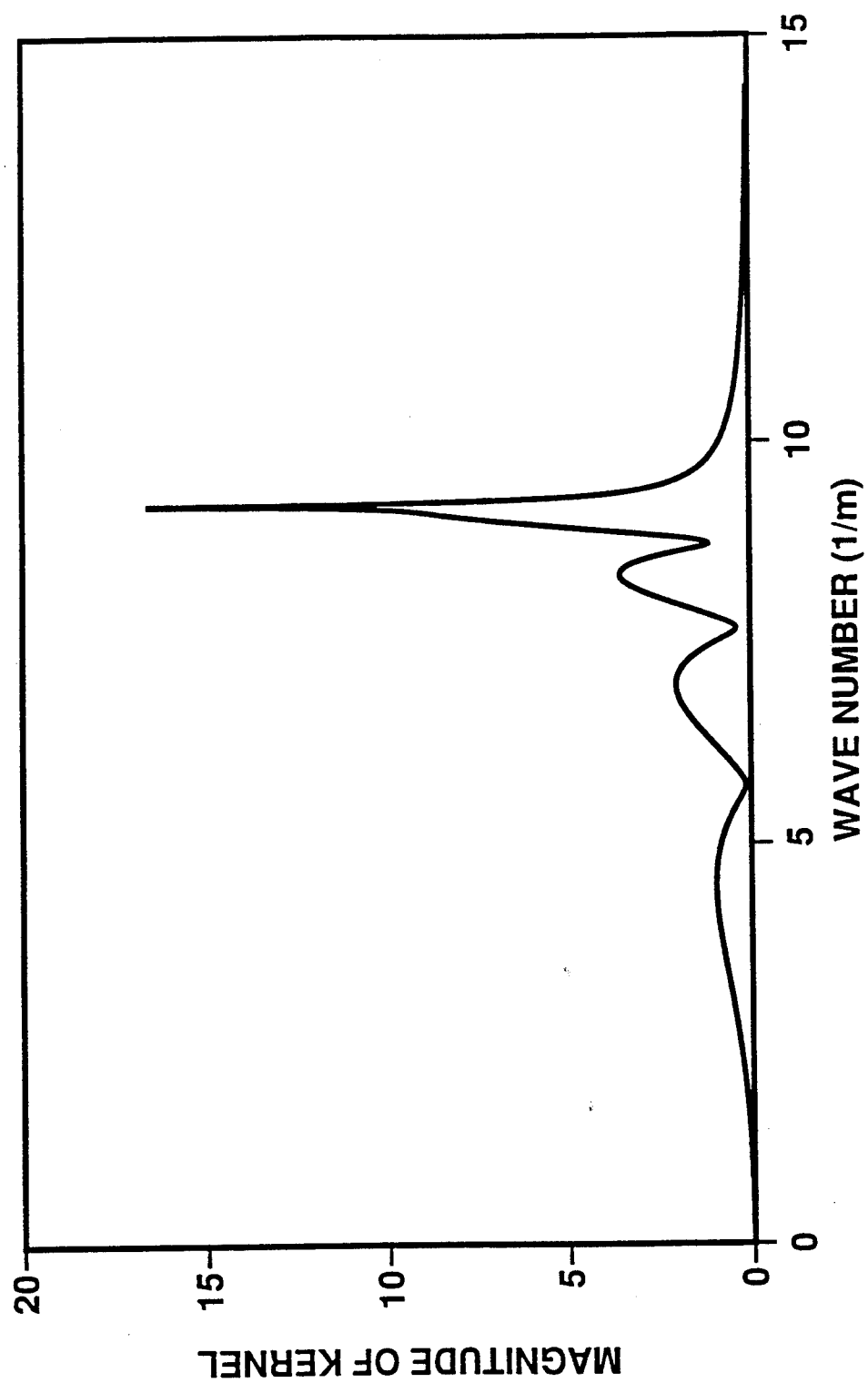
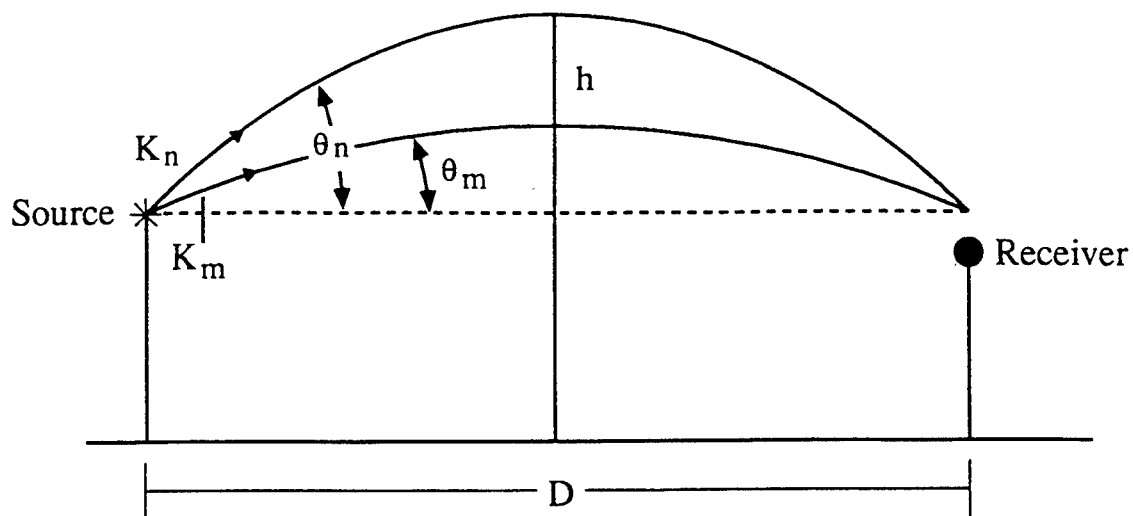
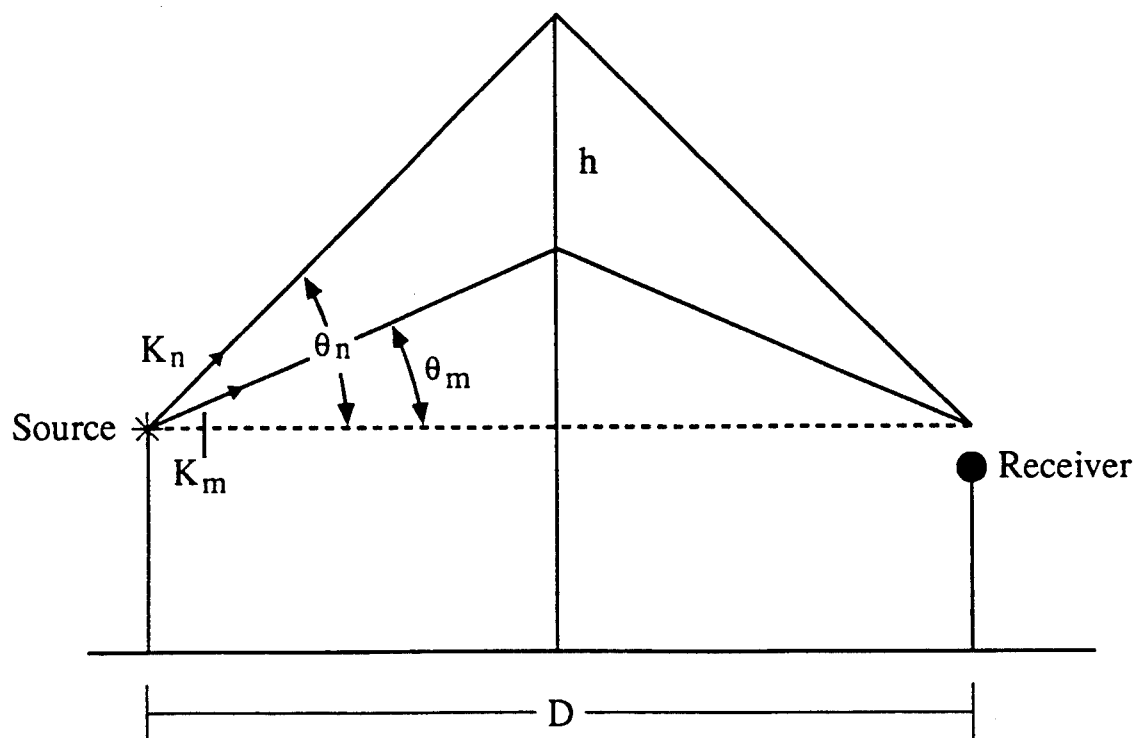


Figure 1. The magnitude of the kernel $\hat{p}(K)$ as a function of horizontal wave number K .



(a) Curved Formulation



(b) Straight Ray Formulation

Figure 2. Construction used to calculate the maximum spatial separation h for two different wave numbers. a) the curved ray formulation. b) the straight ray formulation.

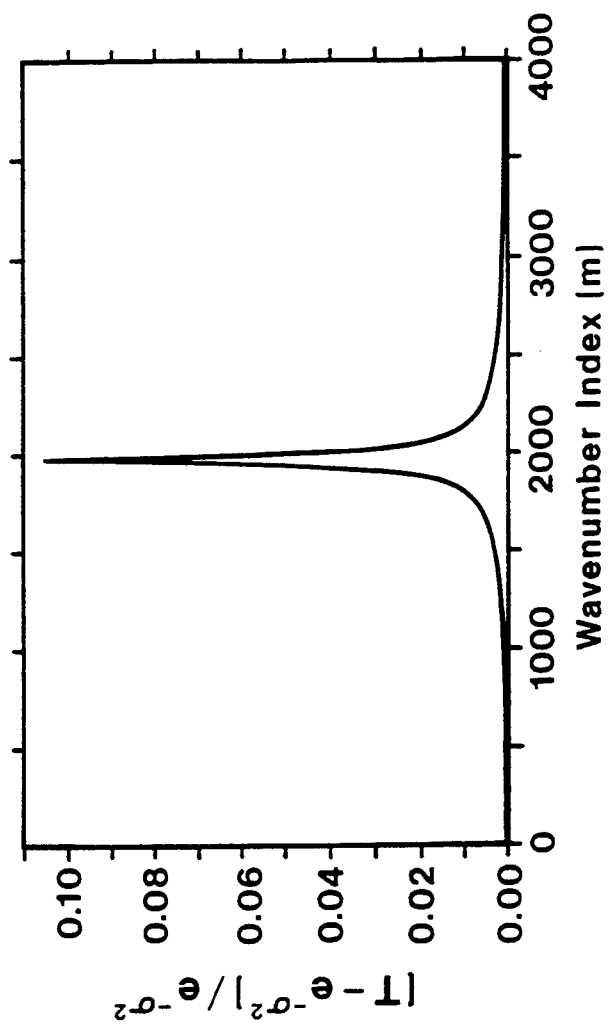


Figure 3. The behavior of $\frac{(T - e^{-\sigma^2})}{e^{-\sigma^2}}$ as m is varied around $n = 2000$.

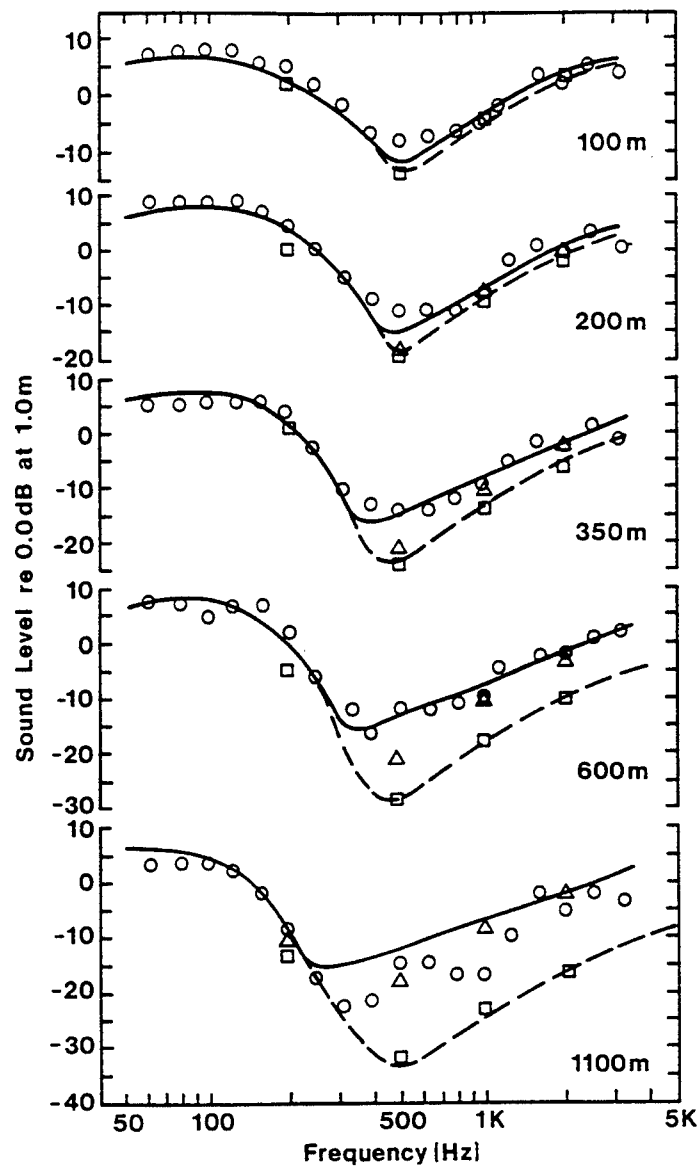


Figure 4. Comparison of Parkin and Scholes' and Daigle's calculation with the results of the turbulent FFP. O data from Ref. 6, □ coherent FFP prediction, Δ turbulent FFP prediction, — Daigle's turbulent prediction, and - - - Daigle's coherent prediction. The distance in each plot is the range from source to receiver.

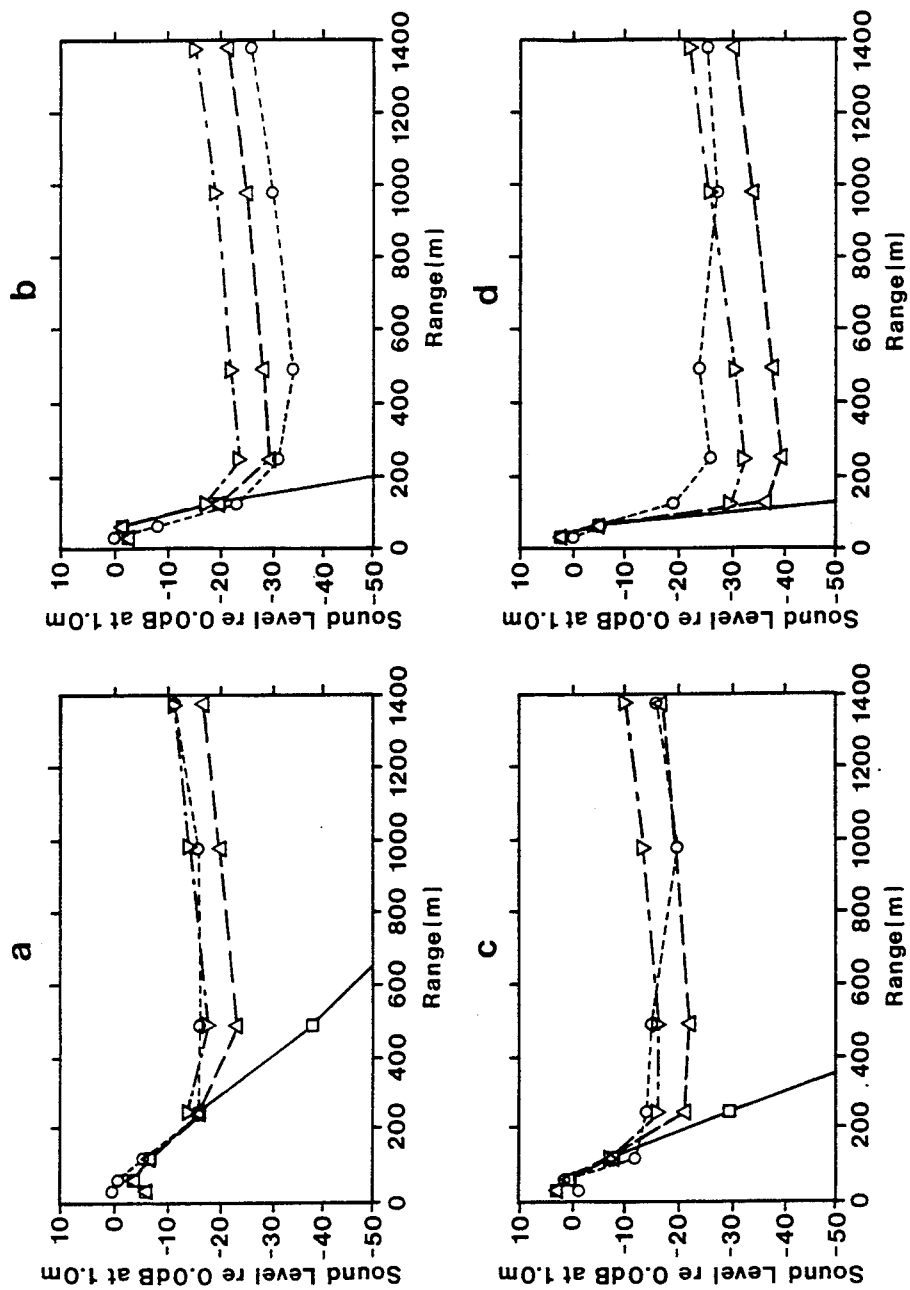


Figure 5. Comparison of the turbulent FFP prediction with data from Wiener and Keast
a) 424 Hz, weak upward refraction, b) 424 Hz, strong upward refraction, c) 848 Hz weak
upward refraction, d) 848 Hz strong upward refraction, \circ - data from Ref. 7.; \square -
coherent FFP calculation; Δ - turbulent FFP calculation with $\langle \mu^2 \rangle = 2.0 \times 10^{-6}$; ∇ -
turbulent FFP calculation with $\langle \mu^2 \rangle = 8.0 \times 10^{-6}$.

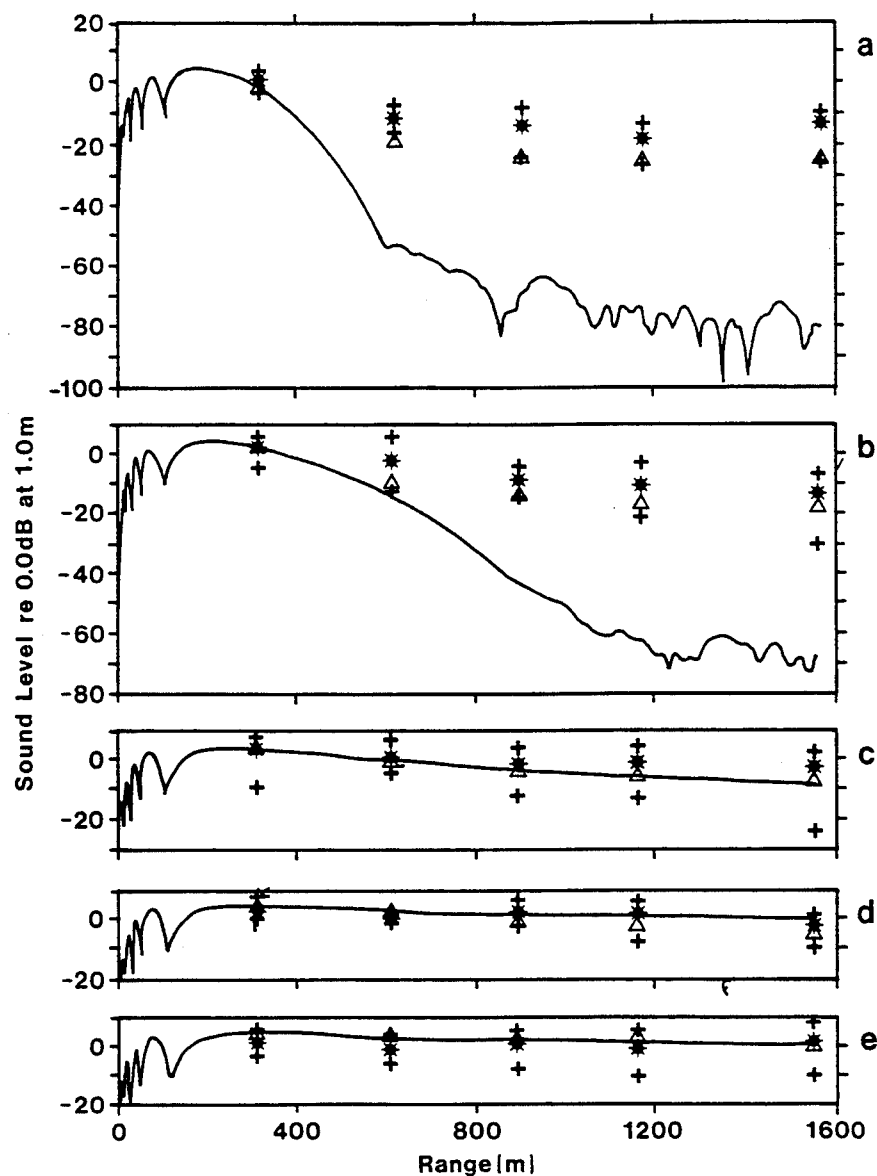


Figure 6. Comparison of the data for Bondville, IL with coherent parabolic equation predictions and with the turbulent FFP calculation. $f = 630$ Hz. (a) $a = -0.8$ m/s, (b) $a = -0.4$ m/s, (c) $a = 0$ m/s, (d) $a = 0.4$ m/s, (e) $a = 0.8$ m/s. \pm are data points with error limits; Δ - turbulent FFP calculation. The continuous line is the coherent parabolic equation calculation.

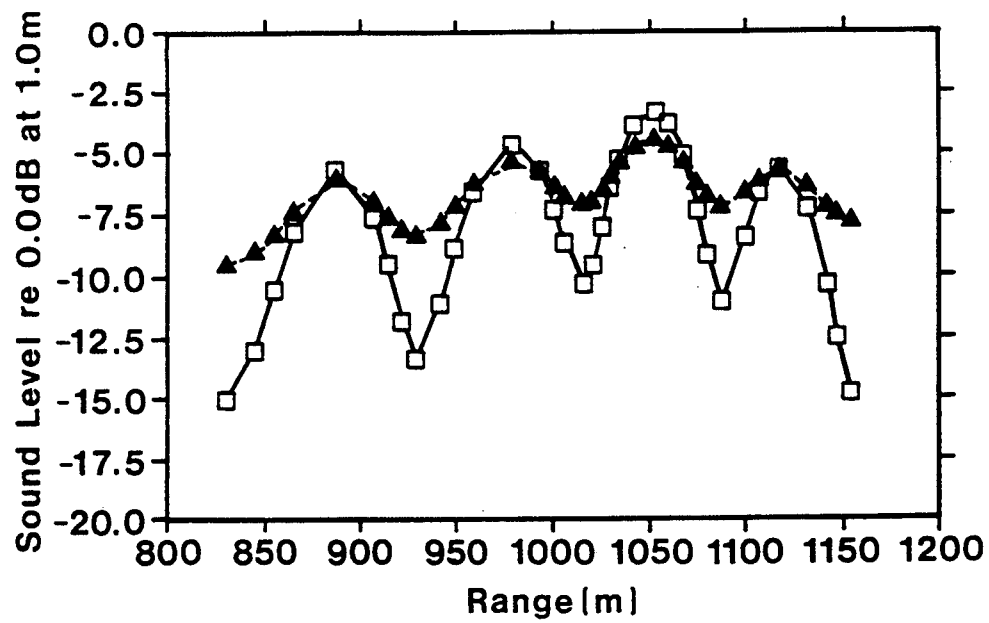


Figure 7. Comparison of coherent FFP and turbulent FFP calculations for modal interference. \square – coherent FFP calculation; \blacktriangle – turbulent FFP calculations.

THE EFFECT OF TURBULENCE AND IRREGULAR TERRAIN ON OUTDOOR SOUND PROPAGATION

Xiao Di and Kenneth E. Gilbert

Applied Research Laboratory and the Graduate Program in Acoustics
Pennsylvania State University, P.O. Box 30, State College, PA 16804

ABSTRACT

A recently developed Green's function parabolic equation method (GF-PE) is applied to sound propagation in a turbulent atmosphere over both flat and irregular terrain. It is shown that small-scale turbulence can be accurately and efficiently treated in the GF-PE calculations by means of a phase screen method and that irregular terrain can be handled using a cascaded conformal mapping method. The GF-PE calculations are compared with existing analytic models, with a different parabolic equation model, and with experimental data. The comparison with experimental data is preliminary. The main purpose of the present study is to illustrate the effects of atmospheric turbulence and irregular terrain on outdoor sound propagation and to demonstrate accurate and efficient approaches for taking the effects into account in numerical calculations.

I. INTRODUCTION

Outdoor sound propagation is complicated by a number of environmental factors. Of the various factors involved, refraction, atmospheric turbulence, and irregular terrain are among the most important. In an upward refracting atmosphere, for example, a shadow region generally exists where, for frequencies above a few hundred Hertz, the sound field is due almost entirely to acoustic scattering from small-scale atmospheric turbulence. Similarly, in the acoustic shadow of a hill, scattering from turbulence can dominate at higher frequencies.

In this paper, we first consider the effects of turbulence and irregular terrain separately. We then combine the two effects to investigate scattering of sound by turbulence into the geometric shadow behind a hill.

To investigate the effects of small-scale atmospheric turbulence on sound propagation in an upward-refracting atmosphere, Gilbert et. al. [1] incorporated turbulence effects into a parabolic

equation method that was based on a Crank-Nicolson range step (CN- PE) [2]. With the Crank-Nicolson method, the spatial oscillations of the acoustic field must be numerically tracked so that a range step of a fraction of a wavelength is required. For the frequencies involved (> 424 Hz) and turbulence scales involved (< 1.5 m), the range steps in the CN-PE were, by default, short enough to numerically track the small-scale turbulence structure at the same time as the acoustic oscillations were tracked. Hence, with a short enough range step, the effects of turbulence can be put into the calculation with little additional computational effort. In situations where a lower frequency or a different propagation algorithm would otherwise permit a longer range step, the range step is nevertheless limited by the need to numerically track the small-scale structure of the turbulence. The GF-PE algorithm, discussed below, is an example of the second situation. The development of the phase screen approach discussed in this paper was motivated by the need to take range steps much longer than the size of the small-scale turbulence.

The GF-PE method discussed in Refs. 3 and 4 was developed to efficiently calculate long-range atmospheric sound propagation. Instead of taking a range step that is a fraction of wavelength as the CN-PE does, the GF-PE takes a range step of 40-100 wavelengths and, as a result, is approximately two orders of magnitude faster. To overcome the problem of small-scale turbulence structure mentioned above and thus take advantage of the longer GF-PE range step, we have developed a phase-screen approach similar to that used in optics for propagation of light [5]. In essence, the method integrates the effect of a continuous turbulence distribution into a series of discrete, uncorrelated phase-screens which can be widely separated relative to the size of small turbulence structure. As a result, the effect of small-scale turbulence can be put into GF-PE calculations without reducing the range step thereby taking advantage of the speed of the GF-PE algorithm.

To take into account the effect of irregular terrain (hills) we use a cascaded conformal mapping method that effectively "flattens" the hills and introduces an effective sound speed in boundary-fitted coordinate system where the air-ground interface is flat. For example, propagation over a concave surface becomes equivalent to downward refraction and over a convex surface becomes equivalent to upward refraction. Within the context of this analogy, the backside of a hill has a terrain-generated shadow that is equivalent to upward refraction. To investigate scattering of acoustic energy into the shadow region created by the hill, we use conformal mapping together with the phase screen method discussed above.

In the sections that follow, we first outline the theory for the GF-PE. Then we discuss in some detail the phase screen approach for turbulence and the conformal mapping method. In the last section we combine the phase screen and conformal mapping methods to investigate turbulent scattering of acoustic energy into a terrain-generated shadow zone.

II. THE GF-PE METHOD FOR THE PARABOLIC EQUATION

The GF-PE method is a marching solver for the one-way wave equation (i.e., the parabolic equation). A unique aspect of the GF-PE is its long range step (40 to 100 wavelengths) relative to more conventional algorithms like the Crank-Nicolson method (CN-PE) which typically are limited to range steps much less than a wavelength. Because the GF-PE program uses a much longer range step, the GF-PE is approximately two orders of magnitude faster than a conventional CN-PE algorithm. In addition, the GF-PE method allows a physical interpretation in terms of a direct wave, a reflected wave, and a surface wave. A detailed development of the GF-PE method can be found in Refs.3-4. The following is a brief description of the GF-PE formulation and its treatment of sound speed profiles and the air-ground interface.

In its present form, the GF-PE algorithm assumes azimuthal symmetry (ϕ -independence) about a vertical axis with r as the horizontal source-receiver separation and z is the height of the receiver. Consequently, a two dimensional propagation model in (r,z) coordinates is used. The two-way far-field equation then has the following form

$$\frac{\partial^2 \Psi}{\partial r^2} + \frac{\partial^2 \Psi}{\partial z^2} + k_0^2 \Psi = 0 \quad (2.1)$$

where $\psi = \sqrt{r} P$, P is the sound pressure, and $k_0 = \omega/c_0$ is the wavenumber. Assuming for the moment that k_0 depends only on z and not on r , Eq. (2.1) can be written as

$$\left[\frac{\partial}{\partial r} + i\sqrt{Q} \right] \left[\frac{\partial}{\partial r} - i\sqrt{Q} \right] \Psi = 0, \quad (2.2)$$

where the operator Q is defined as $\partial^2/\partial z^2 + k_0^2$. One-way propagation is governed by

$$\frac{\partial \Psi}{\partial r} = \pm i\sqrt{Q} \Psi, \quad (2.3)$$

where the (+) sign applies to the forward-going waves and the (-) sign applies to the backward-going waves. Formally integrating Eq. (2.3) we have

$$\Psi(r+\Delta r) = \exp(i\Delta r\sqrt{Q}) \Psi(r) \quad (2.4)$$

where Δr is the range step. By using a spectral representation for the operator Q (See Ref.6, for example) an explicit form for Eq. (2.4) can be obtained. For the case of a constant sound speed the result is given by

$$\begin{aligned}\Psi(r+\Delta r) = & \frac{1}{2\pi} \int_{-\infty}^{\infty} \exp[i\Delta r(k_0^2 - k^2)^{1/2}] e^{ikz} dk \int_0^{\infty} e^{-ikz'} \Psi(r, z') dz' \\ & + \frac{1}{2\pi} \int_{-\infty}^{\infty} R(k) \exp[i\Delta r(k_0^2 - k^2)^{1/2}] e^{ikz} dk \int_0^{\infty} e^{ikz'} \Psi(r, z') dz' \\ & + 2i\beta e^{-i\beta z} \exp[i\Delta r(k_0^2 - \beta^2)^{1/2}] \int_0^{\infty} e^{-i\beta z'} \Psi(r, z') dz'.\end{aligned}\quad (2.5)$$

where

$$R(k_v) = \frac{k_v Z_g - k_0}{k_v Z_g + k_0} \quad (2.6)$$

is the reflection coefficient, Z_g is the normalized ground impedance and $\beta = k_0/Z_g$. Although the present GF-PE formulation is limited to a locally reacting surface, for this case the ground effect is treated exactly.

Note that in Eq.(2.5) one can identify the first term as the direct incident wave, the second term as the specular reflected wave, and the third term as the surface wave contribution. Thus the GF-PE algorithm provides a transparent interpretation of the propagation in terms of distinct physical processes.

For a non-constant sound-speed profile with variation in both the r and z directions, we approximate the profile with a series of vertical slices in which the variation takes place only in the z direction. Within each slice we use the split-step approximation [7, 8] to generalize the result in Eq.(2.5). The wavenumber $k_0(z)$, now a function of z only, is represented in terms of a reference wavenumber k_r and a small variation $\delta k(z)$ as

$$k_0^2(z) = k_r^2 + \delta k^2(z), \quad (2.7)$$

where the variation δk^2 can be either positive or negative but is always small compared with k_r . Accordingly, the operator Q takes the form

$$Q = \frac{\partial^2}{\partial z^2} + k_0^2(z) = \frac{\partial^2}{\partial z^2} + k_r^2 + \delta k^2(z). \quad (2.8)$$

To apply the split-step approximation, the square root of the operator Q is written as

$$\sqrt{Q} = \left[\frac{\partial^2}{\partial z^2} + k_r^2 + \delta k^2(z) \right]^{1/2} \approx \sqrt{\frac{\partial^2}{\partial z^2} + k_r^2} + \frac{\delta k^2}{2k_r} \equiv \sqrt{Q'} + \frac{\delta k^2}{2k_r} \quad (2.9)$$

which is a reasonable approximation for outdoor sound propagation where the sound speed variation relative to the mean value is generally quite small. Substituting Eq. (2.9) into (2.4) and assuming $\delta k^2(z)$ commutes with $\partial^2/\partial z^2$, one obtains

$$\Psi(r+\Delta r) \approx \exp\left[\frac{i\Delta r\delta k^2}{2k_r}\right] \exp[i\Delta r \sqrt{Q'}] \Psi(r), \quad (2.10)$$

which has the same form as Eq. (2.4) except for the presence of a phase factor $\exp(i\Delta r\delta k^2/2k_r)$ and the replacement of wavenumber k_0 with reference wavenumber k_r . Correspondingly, the final formula for the non-constant sound speed profile can be written as the product of the result in Eq. (2.5) and the phase factor $\exp(i\Delta r\delta k^2/2k_r)$. (See Refs. 3 and 4 for the explicit expressions).

As it stands, the formulation in Eq. (2.10) can accurately and efficiently handle a locally reacting ground surface and sound speed profile with large-scale variations. The inclusion of small-scale atmospheric turbulence and terrain effects are discussed in the next two sections.

III. SOUND PROPAGATION IN A TURBULENT ATMOSPHERE

Gilbert et. al. [1] have treated small-scale turbulence effects in CN-PE calculations by multiplying the acoustic field $\Psi(n\Delta r, z)$ at each range step n by a complex factor $\exp[i\phi(n, z)]$ where $\phi(n, z)$ is a random phase. In this paper a similar approach is taken except the phase factor is integrated over range so that small-scale fluctuations in the index of refraction do not have to be tracked numerically. The resulting complex factor, which integrates the continuous random phase change and puts all the phase change at a discrete range, is called a "phase screen" [5].

According to the turbulence model of Daigle [9], the spectrum of small-scale fluctuations in the index of refraction due to near-ground turbulence can be represented, at least approximately, by a Gaussian. The auto-correlation function thus has the form

$$C(s) = \langle \mu(\mathbf{R}+s)\mu(\mathbf{R}) \rangle = \mu_0^2 e^{-s^2/L^2}, \quad (3.1)$$

where the μ_0^2 is the turbulence strength and L is the correlation length of the turbulence. Typical values for μ_0^2 and L are, respectively, 2×10^{-6} to 10×10^{-6} and 1 m to 1.5 m. Since the turbulence correlation length of this model is considerably longer than the range step used in the CN-PE calculations [1], the turbulence effect is simply added at each range update. In contrast, the range

step for the GF-PE program, even for rather high frequencies, is much longer than the correlation length for small-scale turbulence. To maintain the speed of the GF-PE program, which is due to its long range step, a phase screen method is adopted.

To implement a phase screen approach we write the wavenumber as the sum of a deterministic part and a stochastic part,

$$k_0(r,z) = k_r [n_d(z) + \mu(r,z)] = k_d(z) + k_r \mu(r,z). \quad (3.2)$$

In Eq.(3.2), k_r is the same reference wavenumber as in Eq. (2.7), $n_d(z)$ is the deterministic part of the index of refraction and $\mu(r,z)$ is the fluctuation in the index of refraction due to turbulence. Hence $k_d(z)$ and $k_r \mu(r,z)$ are, respectively, the deterministic and stochastic parts of the wavenumber. With the above definitions, the approximation to the square root of the operator Q in Eq. (2.9) can be written as

$$\begin{aligned} \sqrt{Q} &= \left[\frac{\partial^2}{\partial z^2} + k_0(r,z)^2 \right]^{1/2} \approx \sqrt{\frac{\partial^2}{\partial z^2} + k_r^2} + \frac{\delta k^2}{2k_r} + k_r \mu(r,z) \\ &\equiv \sqrt{Q'} + \frac{\delta k^2}{2k_r} + k_r \mu(r,z) \end{aligned} \quad (3.3)$$

The second term in Eq. (3.3) is incorporated in the solution as a phase factor $\exp(i\Delta r \delta k^2 / 2k_r)$ as was done earlier in the non-turbulent case. Because the range step of the GF-PE is much longer than the correlation length, the third term, $k_r \mu(r,z)$, which accounts for the effect of turbulence, undergoes significant fluctuations within each range step Δr . To take the stochastic phase fluctuations into the account, we use a complex factor of the form $\exp[i\Phi(z)]$ where $\Phi(z)$ is a phase screen defined as

$$\Phi(z) = k_r \int_r^{r+\Delta r} \mu(r,z) dr, \quad (3.4)$$

Hence, with a phase screen, we simply integrate the phase fluctuations over the entire range step so that the accumulated effect of the continuous phase change over one range step is inserted at the end of the step. With the phase screen approach, the final form for the GF-PE algorithm is

$$\Psi(r+\Delta r) \approx \exp[i\Phi(z)] \exp\left[\frac{i\Delta r \delta k^2}{2k_r}\right] \exp[i\Delta r \sqrt{Q'}] \Psi(r). \quad (3.5)$$

For calculations involving small-scale turbulence, we have used the phase screen of Eq. (3.4) together with long GF-PE range steps and have obtained the same results as with calculations without the turbulence integration and small range steps. As a result of many calculations we have arrived at an empirical rule. As long as Δr satisfies the condition

$$k_r \mu_0 \Delta r < \pi/8, \quad (3.6a)$$

or, equivalently,

$$\Delta r < \lambda/16\mu_0 \quad (3.6b)$$

satisfactory results are obtained. Since μ_0 is approximately 10^{-3} , Δr must be less than about 50 wavelengths, a distance that is comparable with the usual GF-PE range step without turbulence. Hence in most cases the phase screen allows the inclusion of small-scale turbulence with no reduction in the range step. Finally, we note that if only statistical results are of interest, and not detailed agreement, the $\pi/8$ criteria in Eq. (3.6a) can be relaxed to $\pi/4$.

Figure 1 shows a comparison of the GF-PE and CN-PE for a single realization of Daigle's turbulence model (i.e., a Gaussian spectrum) in a neutral atmosphere. The turbulence parameters are $\mu_0 = 1.42 \times 10^{-3}$ and $L = 1.1$ m. The frequency is 500 Hz, the ground impedance is $Z_g = (7.19, 8.20)$, and source and receiver heights are 1.8 m and 1.5 m, respectively. For accurate results, the range step of .1 m was needed for the CN-PE. Although for the same calculation, the GF-PE can take a range step of over 25 m, to compare the detailed oscillations in the sound level, the GF-PE range step was reduced to 3.2 m. The results in Fig. 1 demonstrate that for a specific realization, the two algorithms give essentially identical results, and thus reinforce one's confidence in both methods.

Figure 2 shows statistical results from the GF-PE obtained from 300 realizations of the turbulence model used in Fig. 1. The same inputs are used as in Fig. 1, except the GF-PE range step was 25.6 m. The thick solid line is the mean level and the dashed lines show the standard deviation. The circles and thin solid line are, respectively, experimental data [10-11] and an analytic theory due to Daigle [9]. The agreement with the data is only fair, but the agreement between Daigle's analytic theory and the GF-PE mean level is quite good.

For a test of the GF-PE predictions in a upward refracting atmosphere, the data of Weiner and Keast [12] is revisited in Fig. 3. The average sound speed profile used in the GF-PE calculations is that inferred from the Weiner and Keast data by Gilbert et al. [1]:

$$c(z) = 340 - 0.5 \log(z / 0.006) \text{ m/s.} \quad (3.7)$$

The turbulence model is same as in the neutral atmosphere case in Figs. 1 and 2. The frequency is 484 Hz, the ground impedance is $Z_g=(8.00,9.24)$, and source and receiver heights are 3.7 and 1.5 m, respectively. The average level (thick solid line) and standard deviation (dashed line) for 300 turbulence realizations are shown in Fig. 3 along with the data of Weiner and Keast (circles). The thin solid line is the GF-PE prediction without turbulence. Considering the simple turbulence model adopted, the GF-PE result gives surprisingly good agreement with the data. In particular, the characteristic "step" function evident in the data is also obtained for the theoretically predicted average sound level. Note also that the standard deviation initially increases linearly and then becomes saturated in the shadow zone .

IV. SOUND PROPAGATION OVER IRREGULAR TERRAIN

To treat outdoor sound propagation over irregular terrain (hills), a cascaded analytic conformal mapping scheme [13-14], has been developed in which the ground topography is approximated by a series of cylindrical surfaces. As indicated schematically in Figs. 4(a) and 4(b) and derived mathematically in Eqs. (4.3) - (4.12) below, irregular terrain fitted in this way can be effectively flattened by means of a cascaded analytic conformal mapping. In the transformed domain where the ground is always flat, the effect of the topography is accounted for by an effective sound speed, which for a cylindrical surface is exponentially increasing or decreasing with height, depending on whether the cylindrical surface is convex or concave.

Conformal mappings are attractive for outdoor sound propagation calculations because of the simple way in which the wave equation transforms under such transformations and the ease of enforcing the air-ground boundary conditions in the transformed domain. In Cartesian coordinates, for example, the wave equation for the acoustic pressure p has the familiar simple form

$$\frac{\partial^2 p}{\partial x^2} + \frac{\partial^2 p}{\partial y^2} + k^2 p = 0 , \quad (4.1)$$

where $k = \omega/c_0$ is the wavenumber, and solving the wave equation is straightforward. However, in Cartesian coordinates, accurately treating the air-ground boundary condition on non-flat topography is problematic.

With boundary-fitted coordinates and a conformal mapping $[x,y] \rightarrow [u(x,y),v(x,y)]$, the wave equation in the transformed domain retains the same simple form as in Cartesian coordinates,

$$\frac{\partial^2 p}{\partial u^2} + \frac{\partial^2 p}{\partial v^2} + J k^2 p = 0 , \quad (4.2)$$

where $J(u,v)$ is the Jacobean of the transformation. Hence, in the transformed domain, the effective wavenumber is $J^{1/2}k$ and the effective sound speed is $c_0/J^{1/2}$. Moreover, since the air-ground interface is flat, the boundary condition there can be accurately treated. Thus, once a conformal mapping is obtained, one can proceed to solve the wave equation with the proper boundary conditions in essentially the same way as with Cartesian coordinates and flat ground.

It should be noted that the analytic cascaded mapping scheme discussed above and represented in Figs. 4(a) and 4(b) is valid only for heights less than the radii of curvature of the cylindrical surfaces R_1 and R_3 in Fig. 4. In other words, the scheme works for the hills that are "gentle" enough that the radii of curvature are large compared with the source and receiver heights.

To arrive at a mathematical representation for the conformal mapping, we consider the single cylindrically curved surface shown in Fig. 5(a). The curved surface has a radius R_0 and has a point source (indicated by a solid dot) located a distance h above the surface. A Cartesian coordinate system (x,y) , referred to as the physical coordinate system, is imposed with the origin located at the circle's center. A new coordinate system (r,z) is introduced in figure 5(b), with the transform relations between the two coordinates given by

$$x = R_0 \exp(z/R_0) \cos(r/R_0 + \phi_0) \quad (4.3)$$

$$y = R_0 \exp(z/R_0) \sin(r/R_0 + \phi_0) \quad (4.4)$$

where ϕ_0 is a constant angle specified in figure 5(b). The transformed equations above are, in essence, a customized logarithmic mapping which can be found in a standard text book, for example [15]. The Jacobean of the transformation is given by

$$J = \exp(2z/R_0), \quad (4.5)$$

so that, after mapping, Eq. (4.1) becomes

$$\frac{\partial^2 p}{\partial r^2} + \frac{\partial^2 p}{\partial z^2} + J k^2 p = 0 \quad (4.6)$$

in the transformed domain shown in Fig. 5(c). As discussed above, an exact analogy can be made between a cylindrically curved surface with a constant sound speed profile and a flat surface with an upward refracting sound speed profile. For a convex surface, for example, the effective sound-speed profile is given by

$$c = c_0 \exp(-z/R_0) \quad (4.7)$$

The inverse transform of Eqs. (4.3) and (4.4) gives

$$r = R_0 [\tan^{-1}(y/x) - \phi_0] \quad (4.8)$$

and

$$z = R_0 \log\left(\frac{R}{R_0}\right) \quad (4.9)$$

where $R = \sqrt{x^2 + y^2}$. One also can write R in the form

$$R = R_0 + h, \quad (4.10)$$

with h being the perpendicular distance from the curved surface. Thus Eq. (4.9) can be written as

$$z = R_0 \log\left(\frac{R_0 + h}{R_0}\right). \quad (4.11)$$

If a source distribution is associated with Eq. (4.6), the source strength should also be multiplied by the Jacobean J . For the source located near the ground, however, the Jacobean is approximately equal to unity so that modification of the source strength is not necessary.

A similar derivation for the concave surface of radius R_0 will result in a downward refracting sound speed profile:

$$c = c_0 \exp(+z/R_0). \quad (4.12)$$

Since a standard closed form solution (residue theory) exists for a point source in a linear sound speed profile, a good deal of attention has been given to an approximate transformation for a cylindrical surface that leads to a linear profile rather than an exponential profile [16,17]. In contrast to the somewhat involved derivations in Refs. 16 and 17, with the conformal mapping method discussed here, the linear profile can be derived directly from the exact exponential profile by a simple one-step algebraic approximation. For example, for a convex surface where R_0 is much larger than z , the exponential profile in Eq.(4.7) reduces to a linear upward refracting profile,

$$c = c_0(1 - z/R_0) \quad (4.13)$$

Similarly, for a concave surface, the same approximation gives a downward refracting linear profile. The simple relation between the exact exponential and approximate linear profile is a useful, physically motivated way to derive the linear approximation and clearly shows its limits of applicability.

We have used the mapping given in Eqs.(4.3) and (4.4) in cascade, together with the GF-PE, to treat sound propagation over irregular terrain. As shown in Fig. 4, a single hill can be modeled by five cascaded regions (However, the first and last regions obviously do not require mapping). The GF-PE calculation is then done in the transformed domains.

The numerical accuracy of the GF-PE using a cascaded conformal mapping has been tested in several ways for the case of a non-turbulent atmosphere. First, the GF-PE and CN-PE were compared using identical cascaded conformal mappings for both calculations. Second, the GF-PE results were compared with calculations made by C. You who used a modified version of the CN-PE (Polar-PE) that treats hills using non-conformal boundary fitted coordinates [14], [18-19]. Finally, a comparison was made with the residue method for a geometry where the exponential and linear profiles are equivalent. In all three cases, the results agreed closely with the GF-PE, indicating the the GF-PE with a cascaded conformal mapping provides accurate numerical results.

V. SOUND PROPAGATION THROUGH A TURBULENT ATMOSPHERE OVER IRREGULAR TERRAIN

To investigate sound propagation over irregular terrain in the presence of atmospheric turbulence, we combine the the phase screen method of Section III with the conformal mapping method of Section IV. Combining the two effects requires only that, in the transformed domain, both the deterministic part and the stochastic part of the wavenumber be multiplied by the Jacobean of the coordinate transformation. The motivation for considering the two effects simultaneously is to investigate scattering due to turbulence into the geometric shadow of a hill.

We first consider propagation over a 30 m hill similar to that in Fig. 4(a). Figures 6(a) and 6(b) show GF-PE calculations of transmission loss at 50 Hz and 500 Hz, respectively, for 50 realizations of Daigle's Gaussian turbulence model. The thick solid line is the mean transmission loss and the dashed lines are the standard deviation. A thin solid line (not visible in the first figure) shows the result without turbulence. The average sound speed is taken to be constant. For the 50 Hz result in Fig. 6(a), the normalized ground impedance is (18.3, 17.5), the turbulence parameters are $\mu_0 = 3.3 \times 10^{-3}$ and $L = 1.5$ m, and the source and receiver heights are both 5 m. In Fig. 6(a), the transmission loss without turbulence overlays the mean transmission loss with turbulence and hence is not visible. Consequently, at 50 Hz, it appears that the effect of small-scale turbulence is negligible for the size of hill considered here.

For the 500 Hz calculation in Fig. 6(b), the normalized ground impedance is (7.2, 8.2), the turbulence parameters are $\mu_0 = 2 \times 10^{-3}$ and $L = 1.5$ m, and the source and receiver heights are 5 m and .5 m, respectively. It is apparent from Fig. 6(b) that, at 500 Hz, the geometric shadow behind the hill is significantly filled in by scattering from small-scale turbulence. In addition, the fluctuation in the level is substantial relative to the mean level. Even though a small-scale turbulence model is questionable for turbulent flow over a 30 m hill, it is nevertheless clear that, at higher frequencies, a calculation without turbulence would grossly underestimate the levels in the geometric shadow of the hill.

The assertion that turbulence has little effect on low-frequency sound propagation over a 30 m hill is supported by Fig. 7 which compares data from the Joint Acoustic Propagation Experiment (JAPE) with a non-turbulent GF-PE calculation at 50 Hz. The calculation shown in Fig. 7 is the same as the non-turbulent calculation for Fig. 6(a) except the hill is 38 m high instead of 30 m and the source and receiver heights are 10 m and .5 m, respectively. The first data point (at 319 m) is at the top of the hill and is chosen as a reference level for the calculation since the JAPE source was uncalibrated. The good agreement between the GF-PE prediction without turbulence and the measured transmission loss is similar to that obtained by C.You et al. in a more extensive comparison with JAPE data [18-20] and shows that, at low enough frequencies, small-scale turbulence effects can be safely neglected.

VI. SUMMARY AND CONCLUSIONS

We have shown that, with a phase screen treatment of small-scale turbulence, the long range step of the GF-PE can be maintained with no loss of accuracy. The GF-PE results for propagation through a turbulent atmosphere over flat ground are in good agreement with a different parabolic equation method, with an analytic result, and with experiment.

A cascaded analytic conformal mapping method was presented that is easily implemented in the GF-PE and effectively flattens the ground so that the boundary condition at the air-ground interface can be treated accurately. The mapping method was combined with the phase screen method to investigate scattering of sound by turbulence into a terrain-generated shadow zone. At 50 Hz both theory and experiment indicate that the effects of turbulence are negligible for the size of hill considered. At 500 Hz, GF-PE calculations indicate that the shadow zone should be filled in considerably by scattering due to turbulence.

In this paper, only preliminary comparisons with data are attempted. More extensive comparisons with data for sound propagation through atmospheric turbulence, with and without irregular terrain, are presently underway and will be reported in future publications.

ACKNOWLEDGMENT

The research reported here was supported by the U.S. Army Research Laboratory.

REFERENCES

1. K.E. Gilbert, R. Raspet, and X. Di, "Calculation of turbulence effects in an upward refracting atmosphere," J. Acoust. Soc. Am. **87**, 2428-2437, 1990.
2. K. E. Gilbert and M. J. White, "Application of the parabolic equation to sound propagation in a refracting atmosphere," J. Acoust. Soc. Amer., **85**, 630-637, 1989.
3. X. Di and K.E. Gilbert, "Application of a fast Green's function method to long range sound propagation in the atmosphere," Fifth International Symposium on Long-Range Sound Propagation Proceedings, pp. 128-146, Milton Keynes, England, May 1992.
4. K. E. Gilbert and X. Di, "A fast Green's function method for one-way sound propagation in the atmosphere," J. Acoust. Soc. Am. **94**, 2343-2352, 1993.
5. B.J. West, "Sensing scaled scintillations," J. Opt.Soc. Am. A, Vol. 7, No. 6, June 1990.
6. E.R. Lorch, *Spectral Theory*, Oxford University Press, New York, pp. 102-103 (1962)
7. F.D. Tappert, "The parabolic approximation method," in Wave Propagation and Underwater Acoustics, edited by J.B. Keller and J.S. Papadakis (Springer, New York, 1977), Chap. V, pp. 224-287.
8. D.J. Thomson and N.R. Chapman, "A wide-angle split-step algorithm for the parabolic equation," J. Acoust. Soc. Am. **74**, 1499-1510 (1983-1853)
9. G.A. Daigle, "Effects of atmospheric turbulence on the interference of sound waves above a finite impedance boundary," J. Acoust. Soc. Am. **65**, 45-49, 1979.
10. P.H. Parkin and W.E. Scholes, "Horizontal propagation of sound from a jet engine close to the ground, at Radlett," J. Sound. Vib. **1** (4), 1-13 (1964).
11. P.H. Parkin and W.E. Scholes, "Horizontal propagation of sound from a jet engine close to the ground, at Hatfield," J. Sound. Vib. **2** (4), 353-374 (1965).
12. F.M. Weiner and D.N. Keast, "Experimental study of the propagation of sound over ground," J. Acoust. Soc. Am. **31**, 724-733 (1959).
13. X. Di, "Application of an analytic conformal mapping for sound propagation over terrain," NCPA Report # XD 1-10-93, National Center for Physical Acoustics, University of Mississippi, Jan. 1993.
14. X. Di, K.E. Gilbert, and C. You, "Application of numerical grid generation to sound propagation over irregular terrain", an invited paper presented at the 124th Meeting of Acoust.Soc. Am., New Orleans, LA, Oct. 1992.

15. M.L. Boas, *Mathematical Methods in the Physical Sciences*, Published by John Wiley & Sons, Inc., (1983), pp. 623
16. A.D. Pierce, *Acoustics*, Published by the Acoustic Society of America, (Woodbury, New York, 1989), pp. 469-478.
17. A. Berry and G.A. Daigle, "Controlled experiments of the diffraction of sound by a curved surface," J. Acoust. Soc. Am. 83(6), June 1988, pp. 2047-2058.
18. C. You, "Non-Line of Sight Sound Propagation Outdoors" , Ph.D Dissertation, University of Mississippi, University, MS. 1993.
19. C. You, K.E. Gilbert, and X. Di, "Non-line of sight sound propagation outdoors," submitted to the Journal of the Acoustical Society of America.
20. C. You, H.E. Bass, and K.E. Gilbert, " Comparisons of experimental measurements of sound propagation over a hill to predictions from the polar parabolic equation method," submitted to the Journal of the Acoustical Society of America.

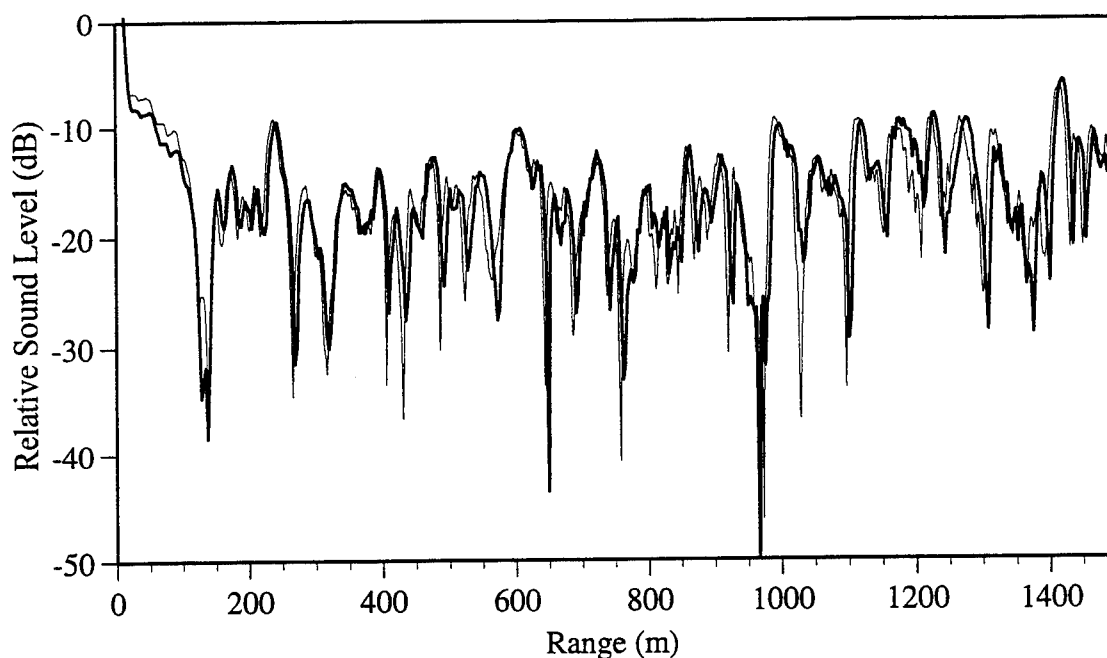


Figure 1. Comparison of the GF-PE and CN-PE for a single realization of Daigle's turbulence model (i.e., a Gaussian spectrum) in a neutral atmosphere. The turbulence parameters are $\mu_0 = 1.42 \times 10^{-3}$ and $L = 1.1$ m. The frequency is 500 Hz, the ground impedance is $Z_g = (7.19, 8.20)$, and source and receiver heights are 1.8 m and 1.5 m, respectively.

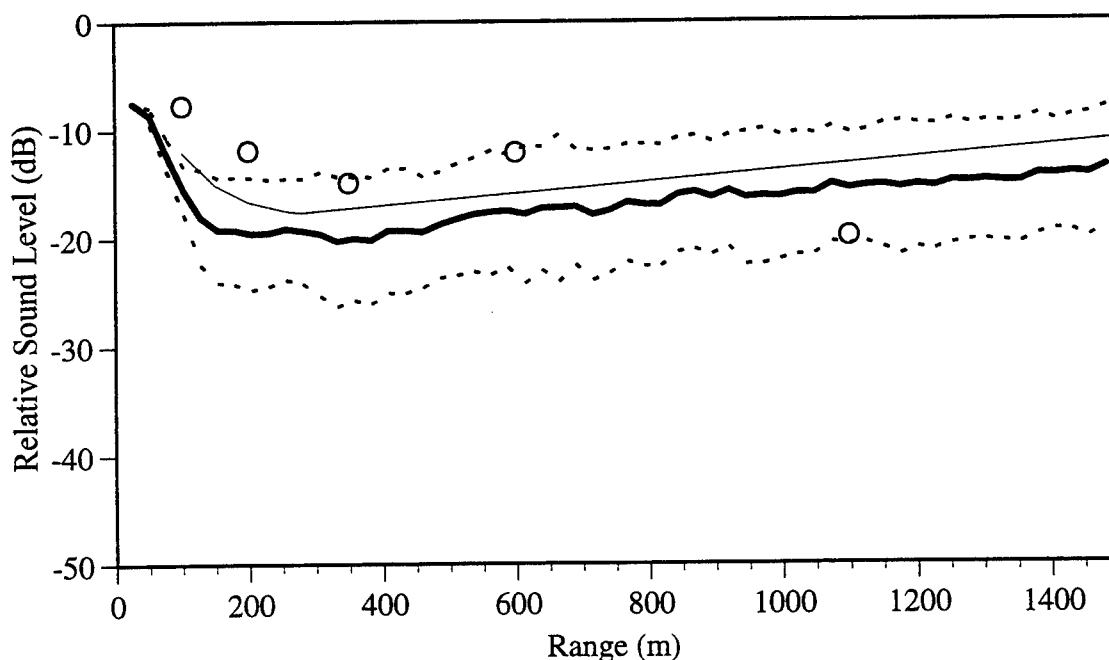


Figure 2. Statistical results from the GF-PE obtained for 300 realizations of the turbulence model used in Fig. 1. On each realization, the same inputs are used as in Fig. 1, except the GF-PE range step was 25.6 m. The thick solid line is the mean level and the dashed lines show the standard deviation. The circles and thin solid line are, respectively, the experimental data of Parkin and Scholes and an analytic theory due to Daigle.

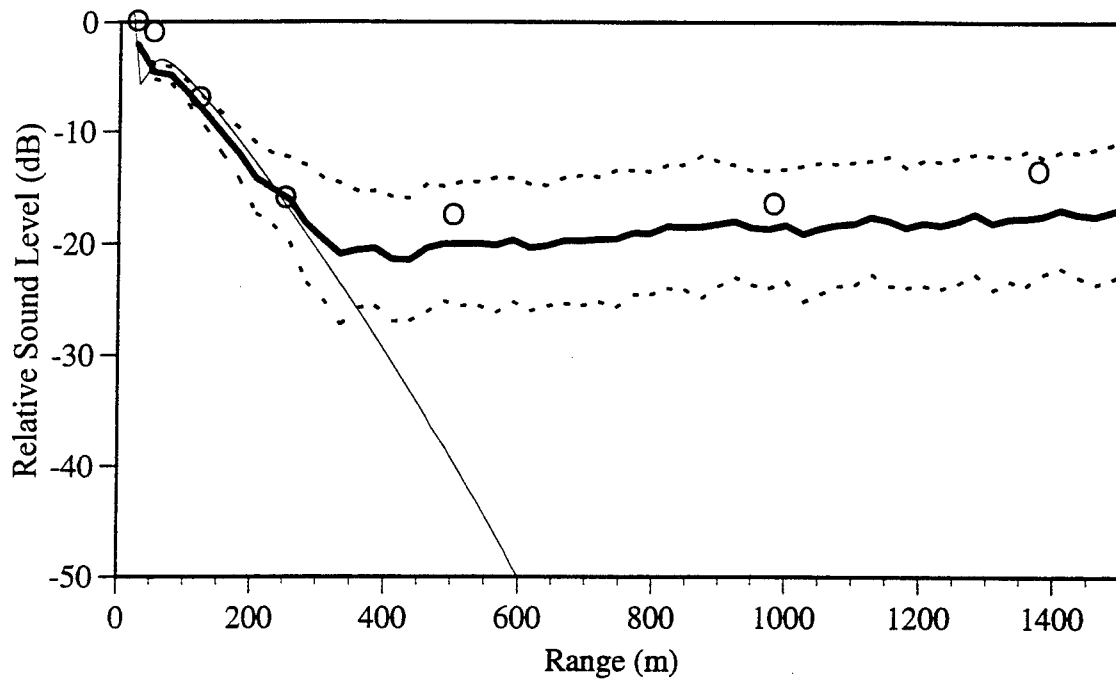


Figure 3. GF-PE calculation (300 realizations) of mean relative sound level (thick solid line) and standard deviation (dotted lines) for a turbulent atmosphere with an average sound-speed that decreases with height (upward refracting). The circles are the experimental data of Weiner and Keast and the thin line is the GF-PE calculation without turbulence.

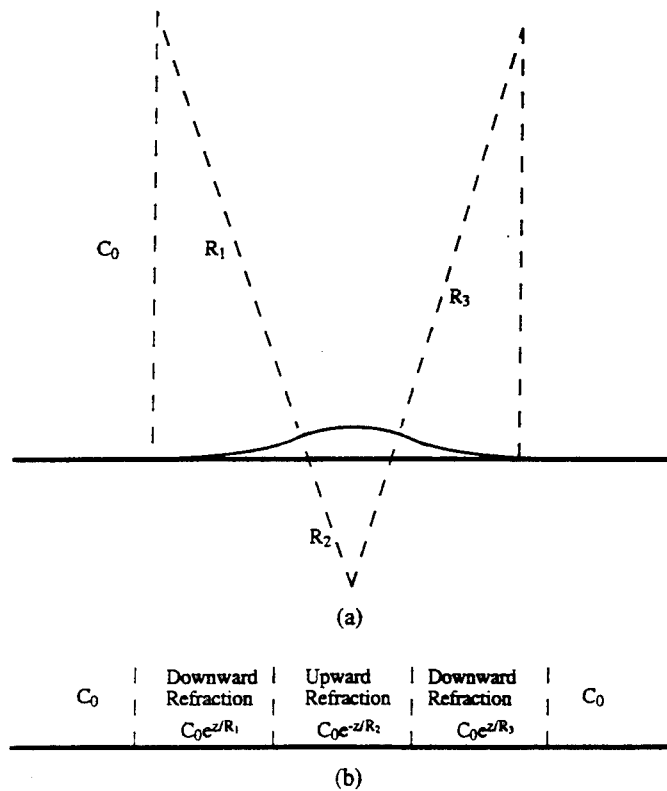


Figure 4. A cascaded conformal mapping scheme. (a) a hill in its physical domain, where the surface has been divided into 5 parts. (b) the five cascaded transformed domains which correspond to the five physical domains in (a).

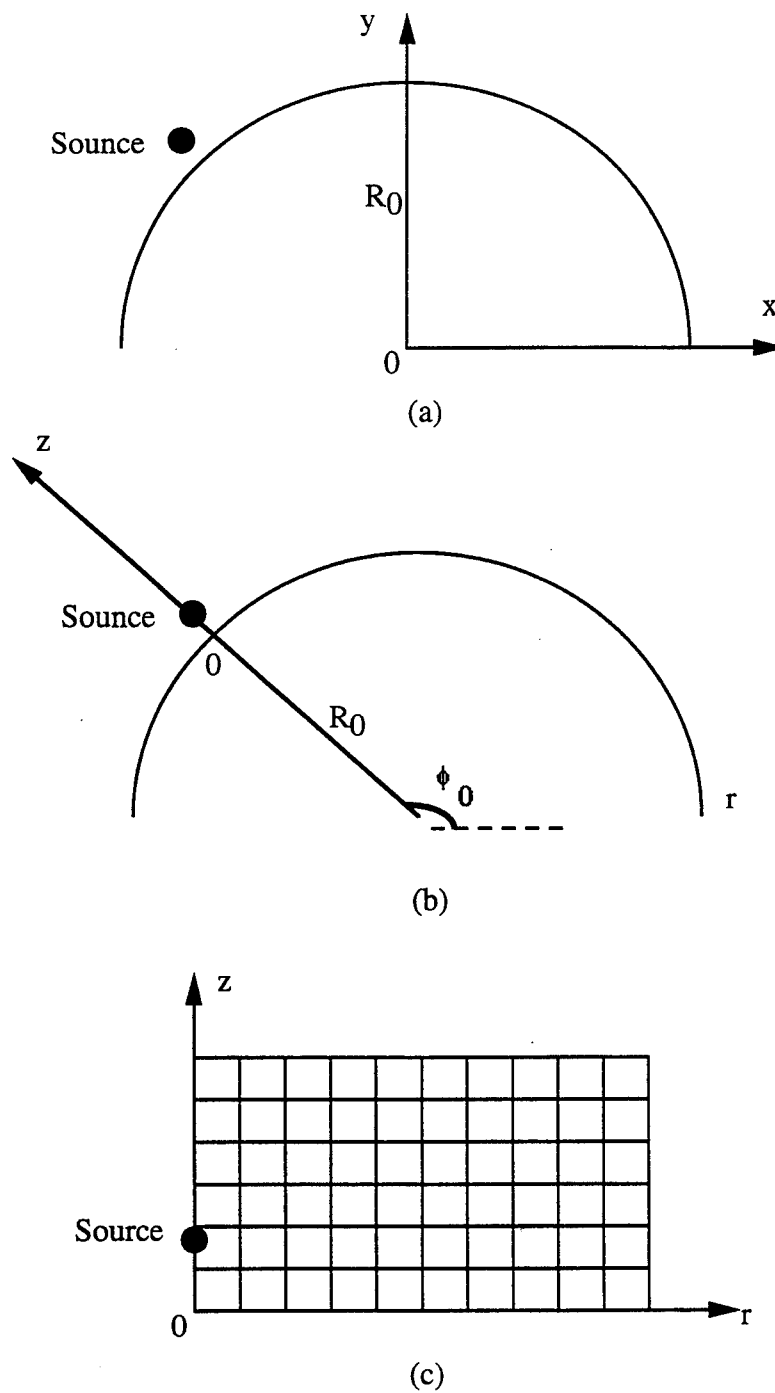


Figure 5. Illustration of conformal mapping for a single convex surface. (a) physical coordinate system (x, y) . (b) transformed coordinate system (r, z) in the physical domain. (c) transformed coordinate system in the transformed domain.

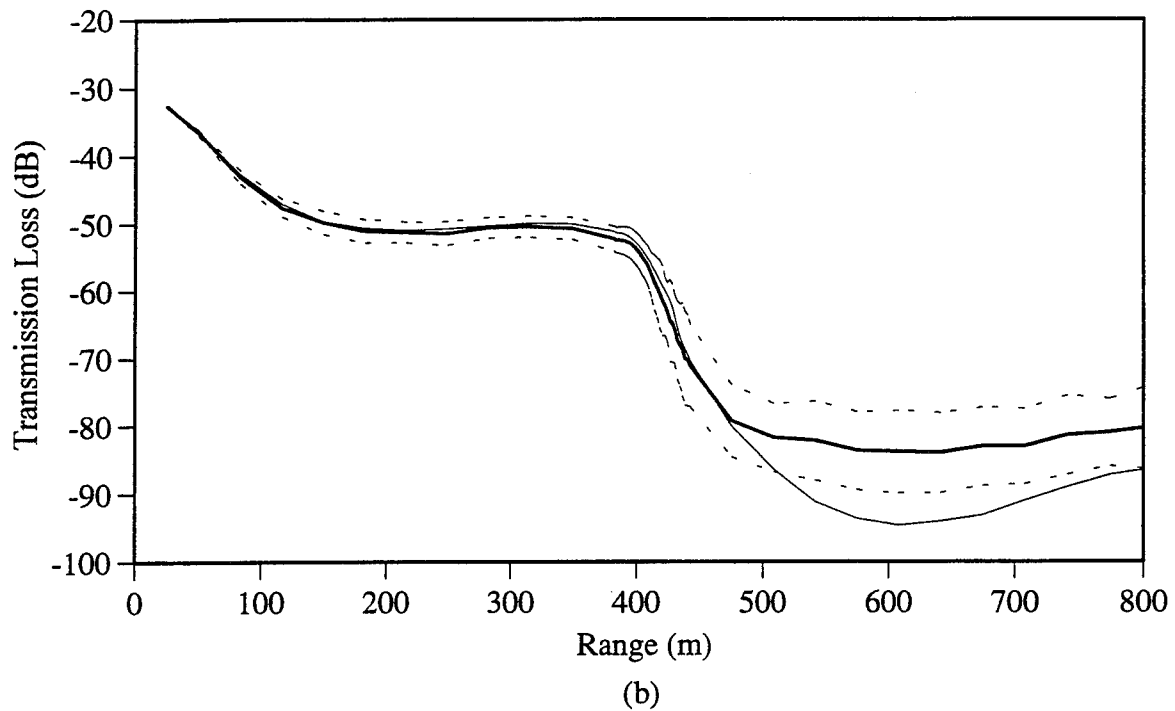
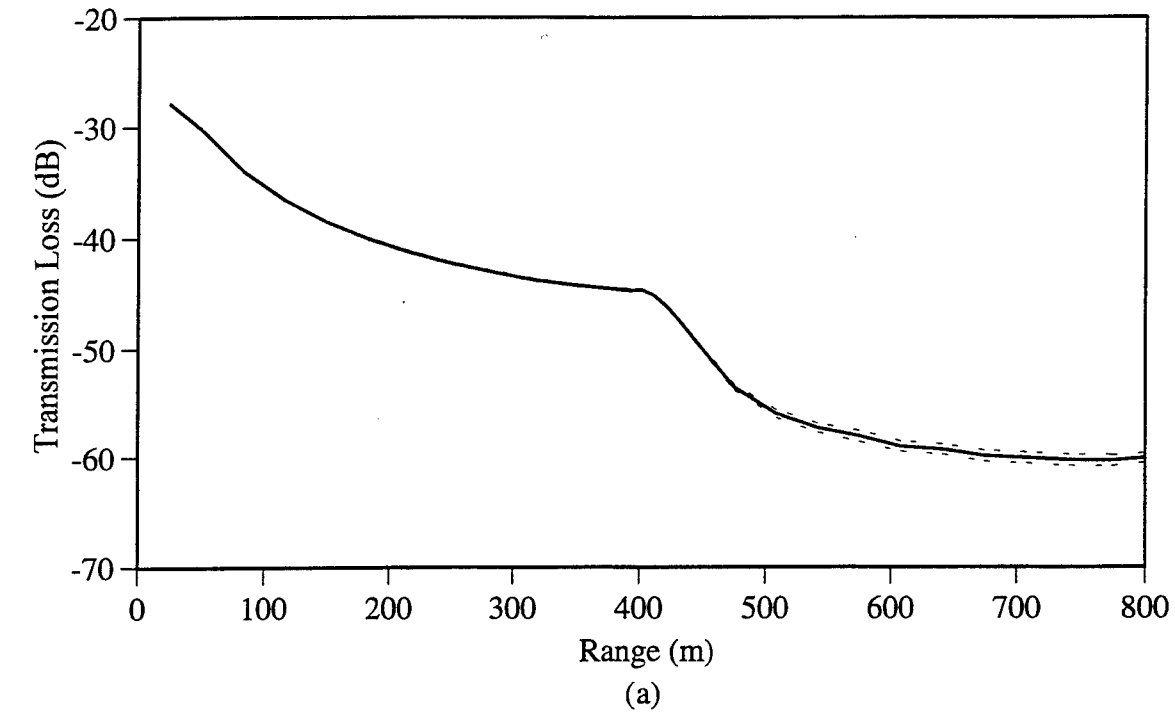


Figure 6. GF-PE calculations with 50 realizations for mean transmission loss (thick solid line) and standard deviation (dotted lines) over a 30 m hill in the presence of atmospheric turbulence. The thin solid line is the calculation without turbulence. The average sound speed is taken to be constant. (a) The frequency is 50 Hz, the normalized ground impedance is (18.3, 17.5) and the source and receiver are both 5 m above the air-ground interface. The turbulence parameters are $\mu_o = 3.3 \times 10^{-3}$ and $L = 1.5$ m. The calculation without turbulence (not shown) is indistinguishable from the mean. (b) The frequency is 500 Hz, the normalized ground impedance is (7.2, 8.2) and the source and receiver are respectively, 5 m and 0.5 m. The turbulence parameters are $\mu_o = 2.0 \times 10^{-3}$ and $L = 1.5$ m.

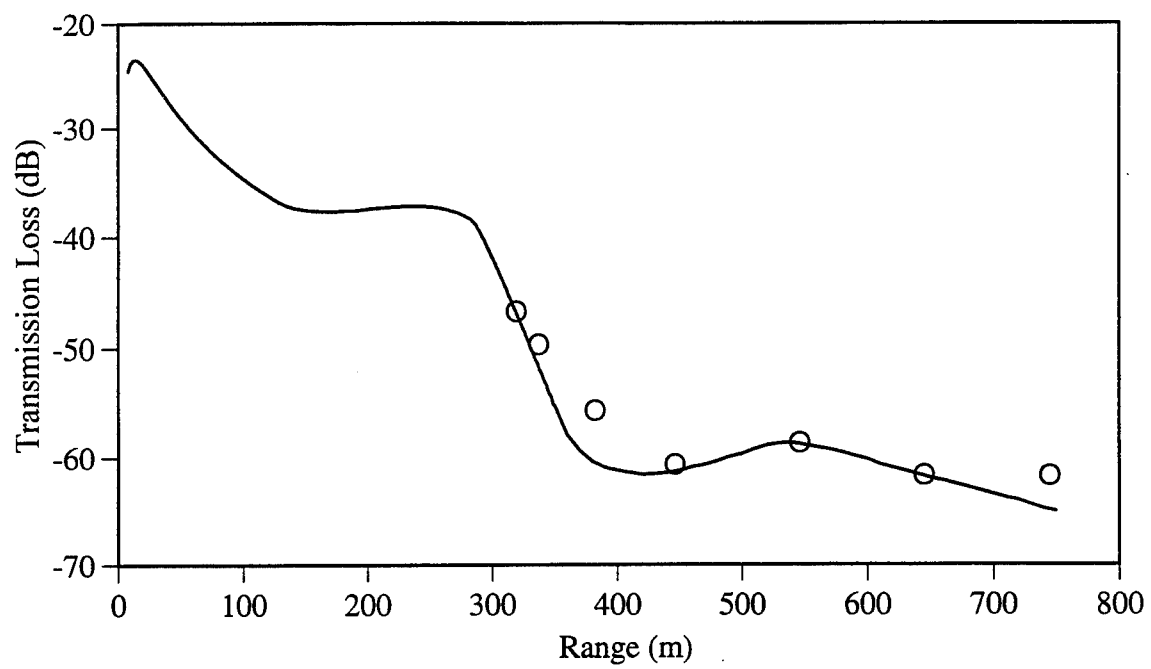


Figure 7. Comparison of GF-PE calculations (without turbulence) for propagation over a hill. The calculation is the same as the non-turbulent calculation in Fig. 6(a) except the hill is 38 m high and the source and receiver are at 10 m and 0.5m, respectively.

SOUND SCATTERING BY SCALAR AND VECTOR RANDOM FIELDS

V. Mellert, V. Ostashev*, R. Wandelt

Carl von Ossietzky Universität Oldenburg, FB Physik, 26111 Oldenburg, Germany

*present address: Physical Science Laboratory, New Mexico State University, NM 88003-0002, USA

1 Introduction

Sound propagation in the turbulent atmosphere is affected by quantities with different tensorial character. Temperature and water vapor concentration are scalars and wind velocity is a vector random field. In the theoretical description these functions are often assumed to be statistically homogeneous and isotropic. While homogeneity does not lead to any problem concerning the tensorial character of the variable, isotropy is a more involved concept for vector random fields. It turns out that the statistically isotropic wind vector cannot be described by isotropic (i.e. direction independent) correlation functions for all velocity components.

Recalling the concept for statistical isotropy, the next section shows the different expressions for the correlation functions of temperature and wind velocity. The main purpose of this paper is to compare results obtained from wave propagation theory by assuming isotropic temperature and isotropic velocity fluctuations. This is done in section 3. To investigate the difference, Gaussian correlation functions are used. It is shown that this difference depends on the quantity calculated. This means that every result obtained for a scalar random field cannot be simply transferred by the use of an effective sound speed but must be recalculated.

2 Statistical isotropic turbulence

To reduce complexity in the theory of wave propagation in random media assumptions on the statistical nature of the atmospheric variables are made. The turbulence is assumed to be homogeneous and isotropic. Homogeneous turbulence is defined by spatially constant statistical moments. Statistical isotropy means invariance of statistical moments under rotations. This definition leads to different mathematical expressions for the correlation functions of scalar and vector random fields.

2.1 Temperature fluctuations

Temperature is a typical scalar variable the wave speed depends on. The corresponding statistical quantity entering moment equations for the sound field is the autocorrelation function:

$$B_T(\vec{r}_1, \vec{r}_2) = \langle T(\vec{r}_1)T(\vec{r}_2) \rangle \quad (1)$$

T is the deviation of Temperature from its mean value T_0 and $\langle \rangle$ means ensemble averaging. In the case of homogeneous turbulence, B only depends on the difference vector $\vec{r}_2 - \vec{r}_1$:

$$B_T(\vec{r}) = \langle T(\vec{r}_1 + \vec{r})T(\vec{r}_1) \rangle \quad . \quad (2)$$

For statistical isotropic turbulence B does not depend on the direction of \vec{r} , but on the distance $r = \sqrt{\vec{r} \cdot \vec{r}}$ only:

$$B_T(r) = \langle T(\vec{r}_1 + \vec{r})T(\vec{r}_1) \rangle \quad . \quad (3)$$

In this paper the correlation function is assumed to be Gaussian:

$$B_T(r) = \sigma_T^2 e^{-r^2/l^2} \quad , \quad (4)$$

where σ_T^2 is the variance of temperature fluctuations and l is the correlation length. The autocorrelation function is often represented by its Fourier transform, the spectral density Φ :

$$\Phi(\vec{\kappa}) = \frac{1}{(2\pi)^3} \int d^3\vec{r} e^{i\vec{\kappa} \cdot \vec{r}} B(\vec{r}) \quad . \quad (5)$$

For a Gaussian correlation function the spectral density is also Gaussian:

$$\Phi_T(\kappa) = \frac{\sigma_T^2 l^3}{8\pi^{3/2}} e^{-\kappa^2 l^2/4} \quad . \quad (6)$$

2.2 Wind velocity fluctuations

To describe correlations in a vector random field a correlation matrix is used. For wind velocity $\vec{v} = (v_1, v_2, v_3)$ it is a 3×3 -matrix whose elements are the correlation functions of the components:

$$B_{ik}(\vec{r}) = \langle v_i(\vec{r}_1 + \vec{r})v_k(\vec{r}_1) \rangle \quad , \quad i, k \in \{1, 2, 3\} \quad . \quad (7)$$

Statistics are assumed to be homogeneous again. For a statistical isotropic vector random field the whole matrix must be invariant under rotations. This is different from assuming all matrix elements to be independent of the direction of \vec{r} .

Because of symmetry the correlation matrix has 6 independent elements. Isotropy reduces the number of independent correlation functions to 2. That means that B_{ik} may be expressed by the correlation function of the radial velocity component $B_{rr}(r) = \langle v_r(\vec{r}_1 + \vec{r})v_r(\vec{r}_1) \rangle$ and the one of the transversal velocity component $B_{tt}(r) = \langle v_t(\vec{r}_1 + \vec{r})v_t(\vec{r}_1) \rangle$, where \vec{t} has a direction perpendicular to \vec{r} . Applying the definition of isotropy the matrix elements are given by [1]:

$$B_{ik}(\vec{r}) = B_{rr}(r) n_i n_k + B_{tt}(r) (\delta_{ik} - n_i n_k) \quad . \quad (8)$$

δ_{ik} is the Kronecker symbol and \vec{n} is the unit vector in the direction of \vec{r} . From equation (8) it can be seen that despite of isotropy the matrix elements do depend on the direction of \vec{r} . Another simplification can be achieved by assuming the air to be incompressible with respect to the turbulent motion: $\vec{\nabla} \cdot \vec{v} = 0$. For sound propagation in the turbulent atmosphere this is not an additional restriction because it is used in deriving the wave equation [1], [2]. Applying $\vec{\nabla} \cdot \vec{v} = 0$ to equation (8) leads to a relation between the radial and the transversal correlation function [1]:

$$B_{tt}(r) = \frac{1}{2r} \frac{d}{dr} (r^2 B_{rr}(r)) \quad . \quad (9)$$

Isotropy and incompressibility allows to describe the correlations of the wind velocity vector by only one correlation function B_{rr} . Following [2] B_{rr} is assumed to be Gaussian with the same correlation length l as for the temperature field but with a different variance σ_v^2 :

$$B_{rr}(r) = \sigma_v^2 e^{-r^2/l^2} \quad . \quad (10)$$

Using equations (8), (9) and (10) all correlation matrix elements can be calculated. To obtain the spectral density matrix each correlation matrix element has to be transformed by equation (5). Because of isotropy and incompressibility the spectral density of wind velocity can be expressed by one function $F(\kappa)$ [1]:

$$\Phi_{ik}(\vec{\kappa}) = (\delta_{ik} - \frac{\kappa_i \kappa_k}{\kappa^2}) F(\kappa) \quad . \quad (11)$$

Calculating Φ_{ik} for the Gaussian form of B_{rr} and comparing the result with equation (11) leads to:

$$F(\kappa) = \frac{\sigma_v^2 l^5}{32\pi^{3/2}} \kappa^2 e^{-\kappa^2 l^2/4} \quad . \quad (12)$$

In the theory of wave propagation through statistically isotropic random media temperature enters by equation (6) while wind velocity enters by equation (12). This leads to significantly different results shown in the next section.

3 Wave propagation theory results

Results obtained from the theory of wave propagation through random media are usually based on two approximations. At first, the medium fluctuations are assumed to be small. At second, the wave length is assumed to be much smaller than the correlation length of the medium. Different methods use these approximations in different ways.

To derive the sound scattering cross section the smallness of medium fluctuations is used to justify the Born approximation (first order perturbation theory). Furthermore the Fraunhofer approximation (far field) is invoked. Based on both approximations Tatarskii calculated the scattered intensity of the sound wave which is closely related to the sound scattering cross section [1] (section 3.1).

The Rytov method described in section 3.2 starts with a parabolic wave equation

which is based on the small wave length assumption. Using the weak medium fluctuation assumption, the logarithm of the wave function is expanded into a perturbation series. Regarding only first order terms, phase and amplitude fluctuations of the sound wave can be calculated. The Rytov method is restricted to short propagation distances.

The parabolic equation method (section 3.3) is based on the parabolic equation, too. Using both above mentioned assumptions again, scattering is regarded as a Markovian random process. The resulting equations for the statistical moments of the sound wave contain perturbation terms of any order. Hence, the parabolic equation method results are valid for larger propagation distances.

The diagram method (section 3.4) does not use the small wave length approximation and is therefore the most general method. Only the assumption of weak medium fluctuations is invoked to derive closed moment equations.

For more details about all those theoretical methods see for instance references [1] and [3]. In the following some results are shown to compare the different effects of the scalar temperature and the vector wind velocity in the different methods.

3.1 Sound scattering cross section

From his wave equation Tatarskii derived the following expression for the sound scattering cross section $\sigma(\theta)$ using Born approximation and Fraunhofer approximation ([1], page 160):

$$\sigma(\theta) = \frac{\pi k^4}{2} \cos^2 \theta \left(\frac{\Phi_T(\kappa)}{T_0^2} + \frac{4 F(\kappa)}{c_0^2} \cos^2 \frac{\theta}{2} \right) \quad (13)$$

Here c_0 is the mean value of the adiabatic sound speed and the wave number κ is a function of the scattering angle θ :

$$\kappa = 2 k \sin \frac{\theta}{2} \quad (14)$$

Inserting (6) for Φ_T and (12) for F leads to:

$$\sigma(\theta) = \frac{k^4 l^3}{16\sqrt{\pi}} \cos^2 \theta e^{-k^2 l^2 \sin^2 \frac{\theta}{2}} \left(\frac{\sigma_T^2}{T_0^2} + \frac{\sigma_v^2}{c_0^2} k^2 l^2 \sin^2 \theta \right) \quad (15)$$

Even for the same contribution from temperature and wind velocity fluctuations to the refractive index, i.e. $\sigma_T^2/T_0^2 = 4\sigma_v^2/c_0^2$, the scattering patterns are different. They are shown in figure 1. Because of $\sin(0) = \sin(\pi) = 0$ sound is scattered forward and back by temperature fluctuations only. It is remarkable that the scattering pattern depends significantly on the spectral density. Tatarskii gave a similar expression for a Kolmogorov spectrum which shows that sound is scattered forward by velocity fluctuations contrary to the Gaussian result presented here ([1], page 161).

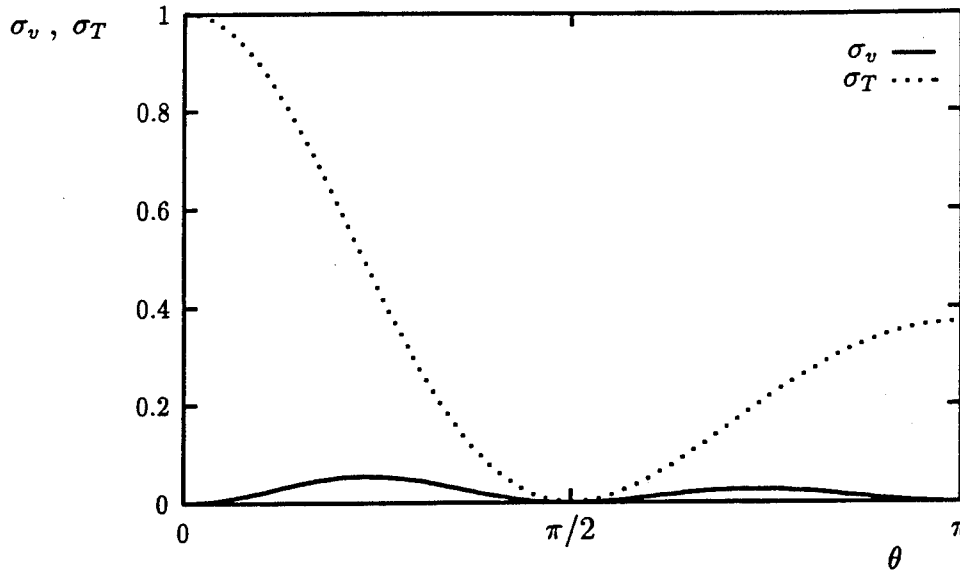


Figure 1: Sound scattering cross section σ_T and σ_v due to scattering at temperature inhomogeneities and wind velocity inhomogeneities, respectively. The ratio of σ_T and σ_v depends on kl as well. This figure is drawn for $kl = 1$.

3.2 Rytov method

The Rytov method or method of smooth perturbations starts with the following parabolic wave equation [2]:

$$\left(2ik \frac{\partial}{\partial x} + \Delta_{\perp} + k^2 \epsilon_{eff}(x, \vec{\rho}) \right) \varphi(x, \vec{\rho}) = 0 \quad . \quad (16)$$

The complex amplitude φ is obtained by separating the phase factor e^{ikx} from the complex sound pressure p . The wave is assumed to propagate mainly in the x -direction here. $\vec{\rho} = (y, z)$ is the vector perpendicular to this direction, Δ_{\perp} is the Laplace operator differentiating with respect to ρ , and ϵ_{eff} represents the fluctuating part of the refractive index in a moving medium:

$$\epsilon_{eff} = \frac{T}{T_0} + 2 \frac{v_x}{c_0} \quad . \quad (17)$$

Because of the small wave length the wave propagates mainly in one direction and the scattering angles are small. Hence, the wave is affected by one velocity component v_x only. Recognizing ϵ_{eff} as a scalar quantity one could be lead to argue as follows. There is no fundamental difference between the parabolic equation for moving and for movingless media. Only $\epsilon = T/T_0$ is replaced by ϵ_{eff} . Hence, all the results obtained for movingless media can be rewritten for moving media replacing only the temperature correlation function by an effective one:

$$B_{eff}(\vec{r}) = \langle \epsilon_{eff}(\vec{r}_1 + \vec{r}) \epsilon_{eff}(\vec{r}_1) \rangle \quad . \quad (18)$$

Now statistical isotropy is assumed. In this case there is no correlation between temperature and any of the wind vector components [1]. Inserting equation (14) into (15) leads to:

$$B_{eff}(\vec{r}) = \frac{B_T(r)}{T_0^2} + \frac{4 B_{11}(\vec{r})}{c_0^2} \quad (19)$$

Arguing this way is quite reasonable up to here. A mistake could be made by looking at B_{eff} as a correlation function of a scalar quantity and interpreting statistical isotropy just as independence of the direction of the vector \vec{r} . It must be realized that B_{11} is a component of a correlation matrix and has therefore to be calculated by equation (8). For a Gaussian B_{rr} the result is:

$$B_{eff}(\vec{r}) = \left(\frac{\sigma_T^2}{T_0^2} + \frac{4 \sigma_v^2}{c_0^2} (1 - \rho^2/l^2) \right) e^{-r^2/l^2} \quad (20)$$

Following the Rytov method, $\Phi_{eff}(0, \vec{\kappa}_\perp)$ must be calculated ([1], [2]) with $\vec{\kappa}_\perp$ as the Fourier variable belonging to $\vec{\rho}$. It follows from equation (11) that $\Phi_{11}(0, \vec{\kappa}_\perp) = F(\kappa_\perp)$. Hence:

$$\Phi_{eff}(0, \vec{\kappa}_\perp) = \frac{\Phi_T(0, \vec{\kappa}_\perp)}{T_0^2} + \frac{4 F(\kappa_\perp)}{c_0^2} \quad (21)$$

Inserting the Gaussian correlation functions from equations (4) and (6) yields:

$$\Phi_{eff}(0, \vec{\kappa}_\perp) = \left(\frac{\sigma_T^2}{T_0^2} + \frac{\sigma_v^2}{c_0^2} \kappa_\perp^2 l^2 \right) \frac{l^3}{8 \pi^{3/2}} e^{-\kappa_\perp^2 l^2/4} \quad (22)$$

Using this function instead of a pure Gaussian function leads to the results for log amplitude and phase fluctuations of plane and spherical waves reported below.

3.2.1 Plane wave

The variances of the log amplitude χ and the phase fluctuations ϕ , calculated by the Rytov method for an incident plane wave are given by [2]:

$$\langle \chi^2 \rangle = \frac{\sqrt{\pi} k^2 l x}{8} \left\{ \frac{\sigma_T^2}{T_0^2} \left(1 - \frac{\arctan D}{D} \right) + \frac{4 \sigma_v^2}{c_0^2} \left(1 - \frac{1}{1 + D^2} \right) \right\}, \quad (23)$$

$$\langle \phi^2 \rangle = \frac{\sqrt{\pi} k^2 l x}{8} \left\{ \frac{\sigma_T^2}{T_0^2} \left(1 + \frac{\arctan D}{D} \right) + \frac{4 \sigma_v^2}{c_0^2} \left(1 + \frac{1}{1 + D^2} \right) \right\}. \quad (24)$$

$D = 4x/kl^2$ is the wave parameter. While the arctan-term related with temperature fluctuations is well known [1], the $1/(1 + D^2)$ -term accounts for the wind being a vector random field. To see what the difference is like, we plotted the ratio of both terms in figure 2. It shows that the effect of velocity fluctuation is three times bigger for small wave parameters, while it is the same for large D .

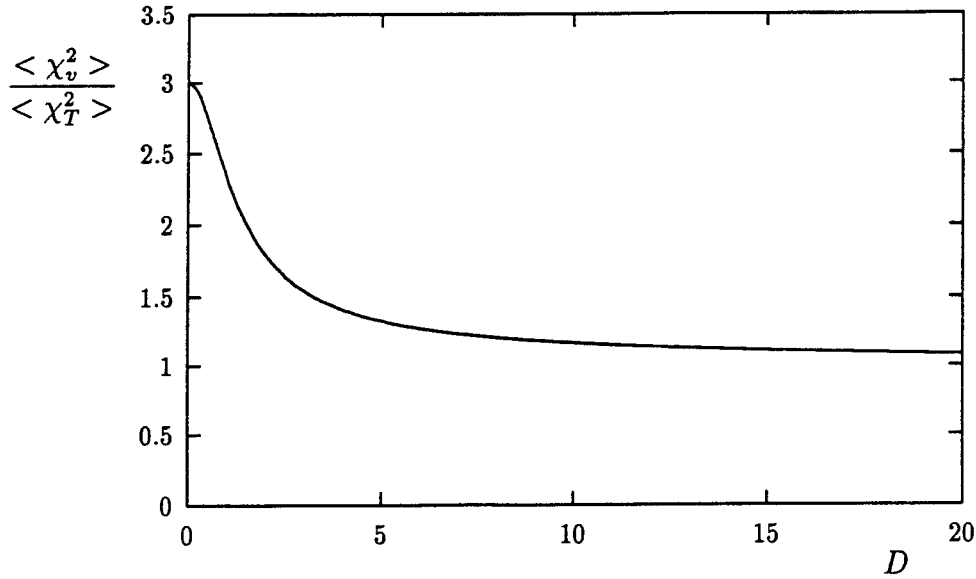


Figure 2: Ratio of log amplitude variances for plane waves. $\langle \chi_T^2 \rangle$ is obtained from equation (23) for $\sigma_v^2 = 0$ and $\langle \chi_v^2 \rangle$ for $\sigma_T^2 = 0$, respectively. Furthermore, the contribution to refractive index variance from temperature and wind velocity are assumed to be the same: $\sigma_T^2/T_0^2 = 4\sigma_v^2/c_0^2$.

3.2.2 Spherical wave

The corresponding result for a spherical wave propagating through a scalar random field was calculated by Daigle [4]:

$$\langle \chi_T^2 \rangle = \frac{\sqrt{\pi} k^2 l x}{8} \frac{\sigma_T^2}{T_0^2} \left(1 - \frac{\arctan \sqrt{\frac{2}{\Omega}} + \frac{\Omega \Delta}{2} \ln \frac{1+\Delta\sqrt{2\Omega}}{1-\Delta\sqrt{2\Omega}}}{\Delta^2(\Omega+1)\sqrt{8\Omega}} \right). \quad (25)$$

$\Delta = x/k l^2 = D/4$ is proportional to the wave parameter D and Ω is defined by $\Omega = \sqrt{1 + \Delta^{-2}} - 1$. Using F from equation (12) instead of Φ from equation (6) the amplitude fluctuation resulting from a wind field can be calculated (see Appendix):

$$\begin{aligned} \langle \chi_v^2 \rangle = & \frac{\sqrt{\pi} k^2 l x}{8} \frac{4\sigma_v^2}{c_0^2} \left\{ 1 - \frac{\Omega(\Omega+2)}{2(\Omega+1)^2} \right. \\ & \cdot \left. \left(1 + \frac{\sqrt{2\Omega}(\Omega+3) \arctan \sqrt{\frac{2}{\Omega}}}{4(\Omega+1)} + \frac{\Delta\sqrt{2\Omega}(\Omega-1)(\Omega+2) \ln \frac{1+\Delta\sqrt{2\Omega}}{1-\Delta\sqrt{2\Omega}}}{8(\Omega+1)} \right) \right\}. \quad (26) \end{aligned}$$

The amplitude fluctuations caused by an atmosphere with temperature and wind velocity fluctuations are just the sum of $\langle \chi_T^2 \rangle$ and $\langle \chi_v^2 \rangle$. Phase fluctuations can be calculated in a similar way. The result only differs in the first sign appearing in the equations, it turns from $-$ to $+$. Figure 3 shows the ratio $\langle \chi_T^2 \rangle / \langle \chi_v^2 \rangle$ for the spherical wave. It is nearly but not exactly the same as for plane waves. Comparing figure 2 and figure 3 it must be kept in mind that $D = 4\Delta$.

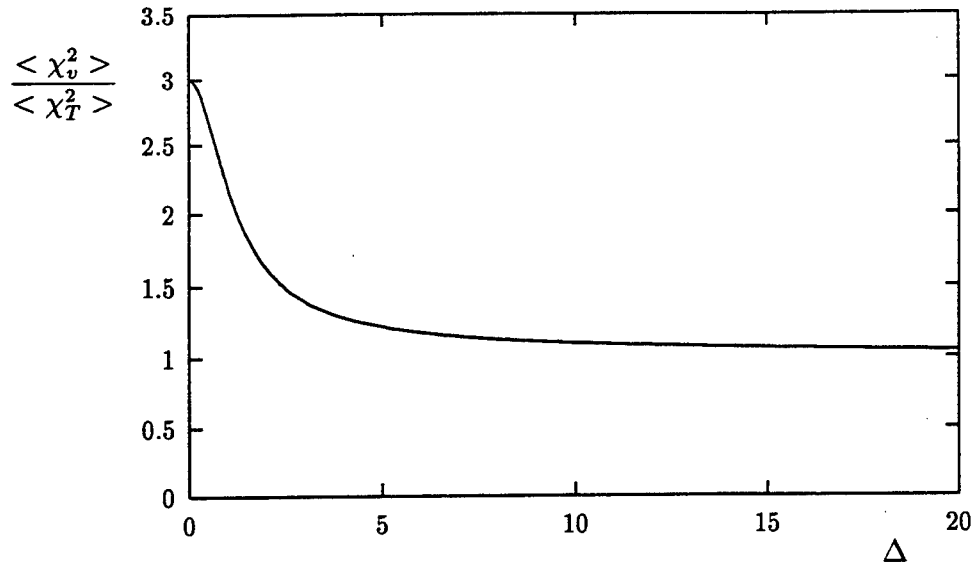


Figure 3: Ratio of log amplitude variances for spherical waves obtained from equations (25) and (26) for $\sigma_T^2/T_0^2 = 4\sigma_v^2/c_0^2$.

3.3 Parabolic equation method

The parabolic equation method starts with the parabolic wave equation (16). In order to derive closed equations for the statistical moments of φ subsequent scattering events are assumed to be uncorrelated. This means that the medium fluctuations are small enough to change statistical properties of the wave only within distances large compared with the correlation length of the medium. Mathematically, the correlation function is a δ -function in the main propagation direction of the wave (Markov approximation):

$$B_{eff}(x, \vec{\rho}) = \delta(x) A_{eff}(\vec{\rho}) \quad , \quad (27)$$

$$A_{eff}(\vec{\rho}) = \int_{-\infty}^{\infty} dx B_{eff}(x, \vec{\rho}) \quad . \quad (28)$$

Inserting equation (17) for B_{eff} yields:

$$A_{eff}(\vec{\rho}) = \sqrt{\pi} l \left(\frac{\sigma_T^2}{T_0^2} + \frac{4\sigma_v^2}{c_0^2} \left(1 - \rho^2/l^2 \right) \right) e^{-\rho^2/l^2} \quad . \quad (29)$$

A_{eff} enters all results calculated by the parabolic equation method. We give two examples here. The mean value of the complex amplitude is given by [3]:

$$\langle \varphi(x, \vec{\rho}) \rangle = \varphi_0(x, \vec{\rho}) e^{-\frac{k^2}{8} A_{eff}(0) x} \quad , \quad (30)$$

where φ_0 is the incident wave. From equation (29) it follows:

$$A_{eff}(0) = \sqrt{\pi} l \left(\frac{\sigma_T^2}{T_0^2} + \frac{4\sigma_v^2}{c_0^2} \right) \quad . \quad (31)$$

Calculating $A_{eff}(0)$ with a Gaussian function for B_{11} would have given the same result. This means that there is no difference between a scalar random field and a vector random field in this case. The reason for that is that the mean value of φ is only affected by the correlation of the refractive index in the x -direction: $B_{11}(x)$ equals $B_{rr}(x)$. The coherence function is a second statistical moment defined by $\Gamma(x, \vec{\rho}, \vec{\rho}') = \langle \varphi(x, \vec{\rho}) \varphi^*(x, \vec{\rho}') \rangle$. For a plane incident wave $\sqrt{\Gamma_0} \exp\{ikx\}$ the coherence function is given by:

$$\langle \Gamma(x, \vec{\rho}, \vec{\rho}') \rangle = \Gamma_0 e^{-\frac{k^2}{4} (A_{eff}(0) - A_{eff}(\vec{\rho} - \vec{\rho}')) x} \quad (32)$$

The coherence of the wave depends on the transverse correlation function of the medium. Hence, there is a difference between an isotropic scalar and an isotropic vector random field. For the plane wave this difference is plotted in Figure 4. It shows that a sound wave scattered by wind velocity fluctuations loses its coherence faster than a wave scattered by temperature fluctuations of the same size.

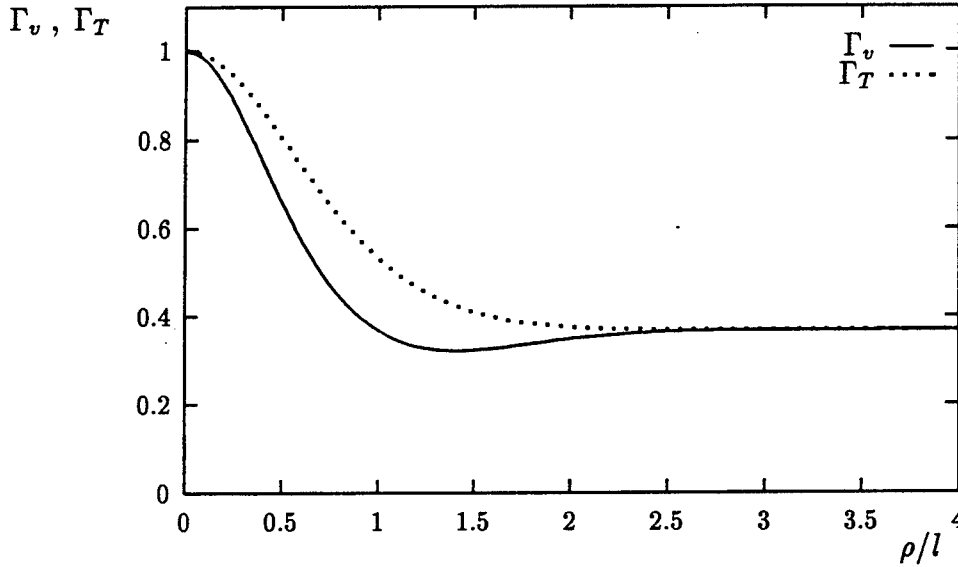


Figure 4: Coherence functions Γ_T and Γ_v for a plane wave are calculated from equations (32) and (29) for $\sigma_v^2 = 0$ and $\sigma_T^2 = 0$, respectively. The propagation distance is chosen so that the coherence is lost by a factor $1/e$.

3.4 Diagram method

The diagram method is based on the full wave equation derived by linearizing the basic equations of fluid dynamics [2]. It does not use the small wave length assumption and is therefore more general than the parabolic equation method. Only weak statistical coupling of the scattering events is assumed to derive closed equations for the mean value and the coherence function [3]. This assumption is physically equivalent to the Markov approximation of the parabolic equation method and is called Bourret approximation here. The integro-differential equation for the mean value of the complex sound pressure can be solved. The solution shows an exponential decay with an extinction coefficient γ . For a statistically isotropic temperature und

wind velocity field $\gamma = \gamma_T + \gamma_v$ is given by [2]:

$$\gamma = \frac{\pi^2 k^2}{2} \int_0^{2k} d\kappa \kappa \left(1 - \frac{\kappa^2}{2k^2}\right) \left\{ \frac{\Phi_T(\kappa)}{T_0^2} + \frac{4F(\kappa)}{c_0^2} \left(1 - \frac{\kappa^2}{2k^2}\right) \left(1 - \frac{\kappa^2}{4k^2}\right) \right\}. \quad (33)$$

Using again the Gaussian function for Φ_T (equation (6)) and equation (12) for F the integration can be performed yielding:

$$\gamma_T = \frac{\sqrt{\pi} k^2 l}{8} \frac{\sigma_T^2}{T_0^2} \left\{ \left(1 - \frac{2}{k^2 l^2}\right) + \left(1 + \frac{2}{k^2 l^2}\right) e^{-k^2 l^2} \right\}, \quad (34)$$

$$\begin{aligned} \gamma_v = \frac{\sqrt{\pi} k^2 l}{8} \frac{4\sigma_v^2}{c_0^2} & \left\{ \left(1 - \frac{10}{k^2 l^2} + \frac{48}{k^4 l^4} - \frac{96}{k^6 l^6}\right) + \right. \\ & \left. + \left(1 + \frac{10}{k^2 l^2} + \frac{48}{k^4 l^4} + \frac{96}{k^6 l^6}\right) e^{-k^2 l^2} \right\}. \quad (35) \end{aligned}$$

Figure 5 shows the ratio γ_v/γ_T to illustrate again the difference between the scalar and the vector random field. There is no difference for large values of kl as expected from the parabolic result (see equations (30), (31)). For small kl , however, the effect of a vector random field is smaller by a factor 5.

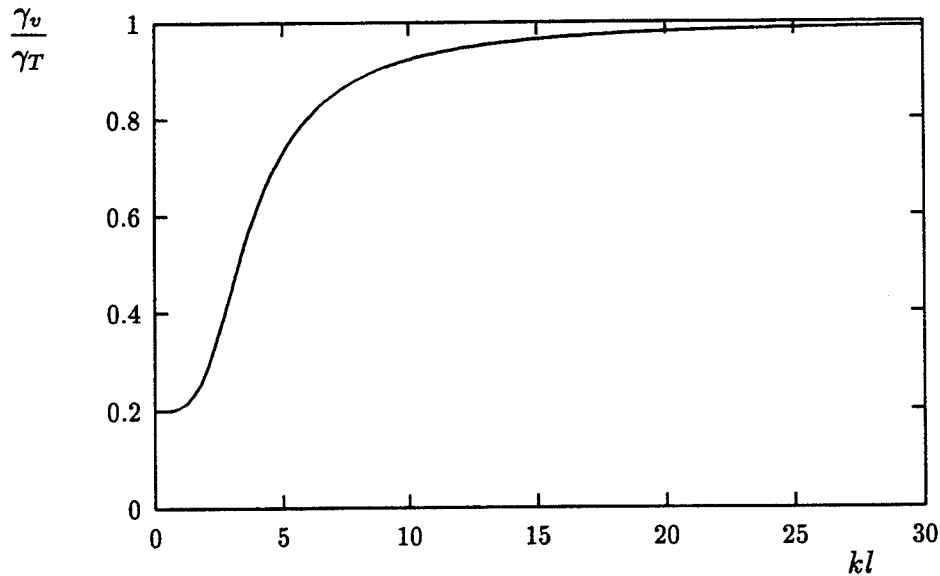


Figure 5: Ratio of extinction coefficients γ_v and γ_T calculated from equations (35) and (34) for $\sigma_T^2/T_0^2 = 4\sigma_v^2/c_0^2$.

4 Conclusions

Statistical isotropic scalar and vector random fields have different effects on the sound wave's statistical characteristics. We gave a number of examples for what the difference is like. It is quite astonishing how this difference varies with the theoretical method used and quantity calculated. The sound scattering cross section has different angular dependence for temperature and wind velocity fluctuations. There is no backscattering by wind, but relatively much backscattering by temperature. Calculating the log-amplitude fluctuations using Rytov method shows that for small wave parameters scattering by wind velocity fluctuations is three times stronger than scattering by temperature fluctuations. For large wave parameters it is the same. This result is true for plane and spherical waves, although the difference has a slightly different wave parameter dependence.

The extinction coefficient calculated by parabolic equation method shows no difference between a scalar and a vector random field. Deriving the coherence function of the sound wave by the same method, however, leads to different expressions. Wind fluctuations cause a faster decorrelation of the sound wave than temperature fluctuations. This result corresponds to the stronger scattering calculated by Rytov method.

Using the diagram method to derive the extinction coefficient leads to different results for scalar and vector random fields. The difference depends on the wave length to correlation length ratio. For short wavelength the difference vanishes in agreement with the corresponding result obtained by the parabolic equation method. For large wave length, however, decorrelation caused by velocity fluctuations is smaller by a factor five.

It is generally not possible to transfer results calculated for a scalar random medium by only replacing the refractive index by an effective one, which contains one component of the wind vector.

Appendix: $\langle \chi_v^2 \rangle$ for spherical waves

The variance of the logarithmic amplitude of a spherical wave will be derived here from the following equation given by Tatarskii ([1], chapter 49, page 247):

$$\langle \chi^2 \rangle = \frac{1}{2} (\langle \Phi_1(x) \Phi_1^*(x) \rangle + \text{Re} \langle \Phi_1^2(x) \rangle) \quad , \quad (36)$$

with ([1], chapter 49, equations (14) and (19)):

$$\langle \Phi_1 \Phi_1^* \rangle = \frac{\pi k^2 x}{2} \int_{-\infty}^{+\infty} d^2 \vec{\kappa}_\perp \Phi_{eff}(0, \vec{\kappa}_\perp) \quad , \quad (37)$$

$$\langle \Phi_1^2 \rangle = -\frac{\pi k^2}{2} \int_{-\infty}^{+\infty} d^2 \vec{\kappa}_\perp \Phi_{eff}(0, \vec{\kappa}_\perp) \int_0^x dt e^{-\frac{i \kappa_\perp^2 (x-t)}{kx}} \quad . \quad (38)$$

Φ_{eff} is given by equation (22) of this paper. Daigle already calculated $\langle \chi_T^2 \rangle$ which is a particular result for temperature fluctuations only ($\sigma_v^2 = 0$, see equation (25)). We therefore only have to calculate $\langle \chi_v^2 \rangle$. Inserting the spectral density from equation (22) with $\sigma_T^2 = 0$ into equation (37) and integrating the Gaussian function leads to:

$$\langle \Phi_1 \Phi_1^* \rangle = \sqrt{\pi} k^2 l x \frac{\sigma_v^2}{c_0^2} \quad (39)$$

Inserting the spectral density into equation (38) and changing the order of integrations yields:

$$\langle \Phi_1^2 \rangle = -\frac{k^2 l^5 \sigma_v^2}{16 \sqrt{\pi} c_0^2} \int_0^x dt \int_{-\infty}^{+\infty} d^2 \vec{\kappa}_\perp \kappa_\perp^2 e^{-\left(\frac{l^2}{4} - \frac{it(t-x)}{kx}\right) \kappa_\perp^2} \quad (40)$$

The κ -integral can be performed now, resulting in:

$$\langle \Phi_1^2 \rangle = -\frac{\sqrt{\pi} k^2 l^5 \sigma_v^2}{16 c_0^2} \int_0^x dt \frac{1}{\left(\frac{l^2}{4} - \frac{it(t-x)}{kx}\right)^2} \quad (41)$$

Using the abbreviation:

$$\varepsilon = \frac{k l^2 x}{4} \quad (42)$$

and regarding the real part of $\langle \Phi_1^2 \rangle$ gives:

$$Re \langle \Phi_1^2 \rangle = -\frac{\sqrt{\pi} k^2 l^5 \sigma_v^2 x^2}{16 c_0^2} \int_0^x dt \frac{\varepsilon^2 - t^2(x-t)^2}{\left(\varepsilon^2 + t^2(x-t)^2\right)^2} \quad (43)$$

The remaining integral can be simplified:

$$\begin{aligned} I &= \int_0^x dt \frac{\varepsilon^2 - t^2(x-t)^2}{\left(\varepsilon^2 + t^2(x-t)^2\right)^2} = \\ &= \int_0^x dt \frac{2\varepsilon^2}{\left(\varepsilon^2 + t^2(x-t)^2\right)^2} - \int_0^x dt \frac{1}{\varepsilon^2 + t^2(x-t)^2} \quad (44) \end{aligned}$$

Both integrals must be evaluated by integrating by parts. After lengthy but straightforward calculations the first integral yields:

$$2\varepsilon^2 \int_0^x dt \frac{1}{(\varepsilon^2 + t^2(x-t)^2)^2} = \frac{8}{x^3(\Omega+1)^2} + \frac{4(\Omega+2)(3\Omega+1)}{x^3\sqrt{2\Omega}(\Omega+1)^3} \arctan \sqrt{\frac{2}{\Omega}} + \frac{2\Delta\Omega^2(3\Omega+5)}{x^3\sqrt{2\Omega}(\Omega+1)^3} \ln \frac{1+\Delta\sqrt{2\Omega}}{1-\Delta\sqrt{2\Omega}}. \quad (45)$$

Δ and Ω are defined for abbreviation by:

$$\Delta = \frac{x}{kl^2} \quad \Omega = \sqrt{1 + \frac{1}{\Delta^2}} - 1. \quad (46)$$

Calculations of the same kind lead to the following expression for the second integral:

$$\int_0^x dt \frac{1}{\varepsilon^2 + t^2(x-t)^2} = \frac{8}{x^3(\Omega+1)\sqrt{2\Omega}} \left(\arctan \sqrt{\frac{2}{\Omega}} + \frac{\Delta\Omega}{2} \ln \frac{1+\Delta\sqrt{2\Omega}}{1-\Delta\sqrt{2\Omega}} \right). \quad (47)$$

Inserting (45) and (47) into (44) the integral I reads:

$$I = \frac{8}{x^3(\Omega+1)^2} + \frac{4\Omega(\Omega+3)}{x^3\sqrt{2\Omega}(\Omega+1)^3} \arctan \sqrt{\frac{2}{\Omega}} + \frac{2\Delta\Omega(\Omega^2+\Omega-2)}{x^3\sqrt{2\Omega}(\Omega+1)^3} \ln \frac{1+\Delta\sqrt{2\Omega}}{1-\Delta\sqrt{2\Omega}}. \quad (48)$$

Inserting I into equation (43) and combining (39) and (43) using equation (36) leads to the final result:

$$\langle \chi_v^2 \rangle = \frac{\sqrt{\pi} k^2 l x}{8} \frac{4\sigma_v^2}{c_0^2} \left\{ 1 - \frac{\Omega(\Omega+2)}{2(\Omega+1)^2} \cdot \left(1 + \frac{\sqrt{2\Omega}(\Omega+3) \arctan \sqrt{\frac{2}{\Omega}}}{4(\Omega+1)} + \frac{\Delta\sqrt{2\Omega}(\Omega-1)(\Omega+2) \ln \frac{1+\Delta\sqrt{2\Omega}}{1-\Delta\sqrt{2\Omega}}}{8(\Omega+1)} \right) \right\}. \quad (49)$$

The variance of the phase can be obtained in a similar way by:

$$\langle \phi^2 \rangle = \frac{1}{2} (\langle \Phi_1(x) \Phi_1^*(x) \rangle - \text{Re} \langle \Phi_1^2(x) \rangle). \quad (50)$$

References

- [1] V.I.Tatarskii
The effects of the turbulent atmosphere on wave propagation
Israel 1971
- [2] V.E.Ostashev
Sound propagation and scattering in media with random inhomogeneities of sound speed, density and medium velocity
WAVES IN RANDOM MEDIA 4, September 1994
- [3] S.M.Rytov, Y.A.Kravtsov, V.I.Tatarskii
Principles of statistical radio physics
Part 4: *Wave propagation through random media*
Berlin, 1989
- [4] G.A.Daigle
Correlation of the phase and amplitude fluctuations between direct and ground-reflected sound
J.Acoust.Soc.Am. 68 (1), 1980

Index-of-Refractive and Profile-Curvature Statistics Derived from Large-Eddy Simulations

D. Keith Wilson
Department of Meteorology
503 Walker Building
Penn State University
University Park, Pennsylvania 16802

Abstract

This paper considers the effect of atmospheric turbulence structure, as derived from large-eddy simulations, on acoustic phase and amplitude variability. The simplest possible model for acoustic propagation is used: line-of-sight in the geometric acoustics limit. Nonetheless, important effects due to the multi-scaled, anisotropic nature of the effective sound speed field are observed. It is found that the acoustic phase variance responds most strongly to large-scale turbulence, whereas the log-amplitude variance responds most strongly to small-scale turbulence. It is also found that both the length scales and the variance of the index of refraction tend to be larger when the direction of acoustic propagation is upwind or downwind than when it is crosswind.

Introduction

Variability of acoustic signals propagated through the atmosphere is a challenging subject. Some of the important complications are partially coherent multipaths (such as ground reflections), scattering in the presence of refraction from mean vertical gradients, and the complex structure of the turbulence itself. In a recent paper [1], D. W. Thomson and I attempted to address this last issue by developing models for the effects of inhomogeneous, anisotropic atmospheric turbulence structure on acoustic propagation. This short paper reinforces and elaborates on some of the points raised in Ref. [1], by computing index-of-refraction and profile-curvature statistics from large-eddy computer simulations of atmospheric turbulence.

I. Large-Eddy Simulations

Much remains to be learned about the structure of atmospheric turbulence. Even from the standpoint of acoustic propagation modeling, where simplified models for the turbulence may be permissible, many significant issues remain unresolved [1]. The primary reason for this shortcoming is the expense of deploying large arrays of wind and temperature sensors outdoors. However, computer simulations of turbulence offer an attractive alternative to experimental data. The advantage of computer simulations is that they can provide simultaneous data at a large number ($\sim 10^6$) of points in space.

In large-eddy simulation (LES) of turbulence, only the most energetic eddies in the flow are simulated. The effects of the smaller eddies which are not resolved by the simulation must be parameterized in some fashion. For the foreseeable future, all simulations of turbulence in the atmospheric boundary layer must be of the large-eddy type. This is because atmospheric flows contain such a broad range of eddy sizes, ranging from about 1 mm to 2 km, and the memory available on today's largest supercomputers is still many orders of magnitude too small to resolve all the eddy scales.

C.-H. Moeng and P. P. Sullivan of the National Center for Atmospheric Research have kindly made available results from their own LES of the atmospheric boundary layer [2, 3]. The simulations cover a range of wind speeds and surface heat fluxes. Three simulations, characterized by the turbulence parameters listed in Table 1, are considered in this paper. Two of the simulations, UGNB and UGFC, are nearly neutral (i.e., the ground is nearly the same temperature as the overlying air), while the third simulation, UGMC, is highly convective (i.e., appreciable heat is transferred from the ground to the overlying air, as typically occurs on a sunny day). All of the simulations were performed on $96 \times 96 \times 96$ point numerical grids. The physical size of UGNB and UGFC was 3 km on a side in the horizontal, and 1 km in the vertical. UGMC was 5 km in the horizontal, and 2 km in the vertical. In all three cases, a temperature inversion was placed at one-half the vertical domain height, in order to confine the eddies to the computational domain. The wind speed outside the boundary layer (i.e., the geostrophic wind speed) was 15 m/s for UGNB and UGFC, and 10 m/s for UGMC.

II. Phase Statistics

Assuming geometric acoustics is valid, and considering only line-of-sight propagation, the variance of the acoustic phase fluctuations is given by [4, 1]

$$\langle \phi^2 \rangle = k_0^2 \langle \mu^2 \rangle R^2, \quad (1)$$

case	u_* (m/s)	w_* (m/s)	Q (Km/s)	L (m)	domain size (km)
UGNB	0.56	0.79	0.03	-480	$3 \times 3 \times 1$
UGFC	0.59	0.94	0.05	-270	$3 \times 3 \times 1$
UGMC	0.56	2.0	0.24	-56	$5 \times 5 \times 2$

Table 1: Parameters of the large-eddy simulations considered in this paper. u_* is the friction velocity, w_* is the convective velocity scale, Q is the surface (ground to air) heat (temperature) flux, and L is the Monin-Obukhov length.

for $R \ll L_\mu$, and

$$\langle \phi^2 \rangle = 2k_0^2 \langle \mu^2 \rangle R L_\mu, \quad (2)$$

for $R \gg L_\mu$, where $k_0 = \omega/c_0$ is the wavenumber, $\mu \approx (u' \cos \alpha + v' \sin \alpha + c')/c_0$ is the index-of-refraction fluctuation, R is the length of the path, L_μ the integral length scale, and α the angle between the propagation path and the mean wind. The angle brackets indicate ensemble average, the primes indicate the fluctuating part (e.g., $u = \langle u \rangle + u'$). The propagation path is assumed to be straight.

Note that the properties of the turbulence enter into Eq. 1 through two parameters, L_μ and $\langle \mu^2 \rangle$. Furthermore, each of these parameters is a function of the structure of both the wind and temperature fields, and is anisotropic.

Figures 1–3 (upper) show the integral length scale and variance of the index of refraction for the three cases. The computations extend from the ground to one-half the boundary layer depth, and are shown for directions upwind, cross wind, and downwind. The computations were performed by calculating 96 96-point 1-D FFT's of the index of refraction field at each horizontal level, squaring and averaging to find the 1-D power spectra, Fourier transforming to obtain the correlation function, and then integrating to obtain the length scale. [In this numerical study, *spatial* averaging over many large eddies was used to approximate the ensemble average. However, it is worth noting that most experimental studies use *temporal* averages. A proper experimental study of the effects of large-scale turbulence on acoustic phase must use averaging periods equal to many large-eddy turnover times $\tau = z_i/w_*$, where z_i is the inversion height and w_* is the convection velocity, as indicated in Table 1. For example, for the conditions of simulation UGFC, $\tau = (500 \text{ m})/(0.94 \text{ m/s}) = 530 \text{ s}$.]

For all three cases, the length scales are much longer in the upwind and downwind directions than cross wind. The upwind and downwind length scales generally decrease with increasing surface heat flux, being longest for case UGNB. Horizontal cross sections of the fields (not shown) show the formation of large, longitudinal roll structures in case UGNB; these rolls probably cause the comparatively longer length scales. The cross wind length scales are about 100 m, regardless of the surface heat flux.

The index-of-refraction variance (Figs. 1–3, lower) increases with increasing surface heat flux, particularly in the cross-wind direction. There is also a strong height dependence: for all three cases, the variance initially increases with height, and then gradually decreases. The initial increase is almost certainly an artifact of the finite resolution of the LES: the small eddies, which carry most of the variance near the surface, are not being resolved. Hence it is probably the case that the variance decreases monotonically with height, beginning at the surface.

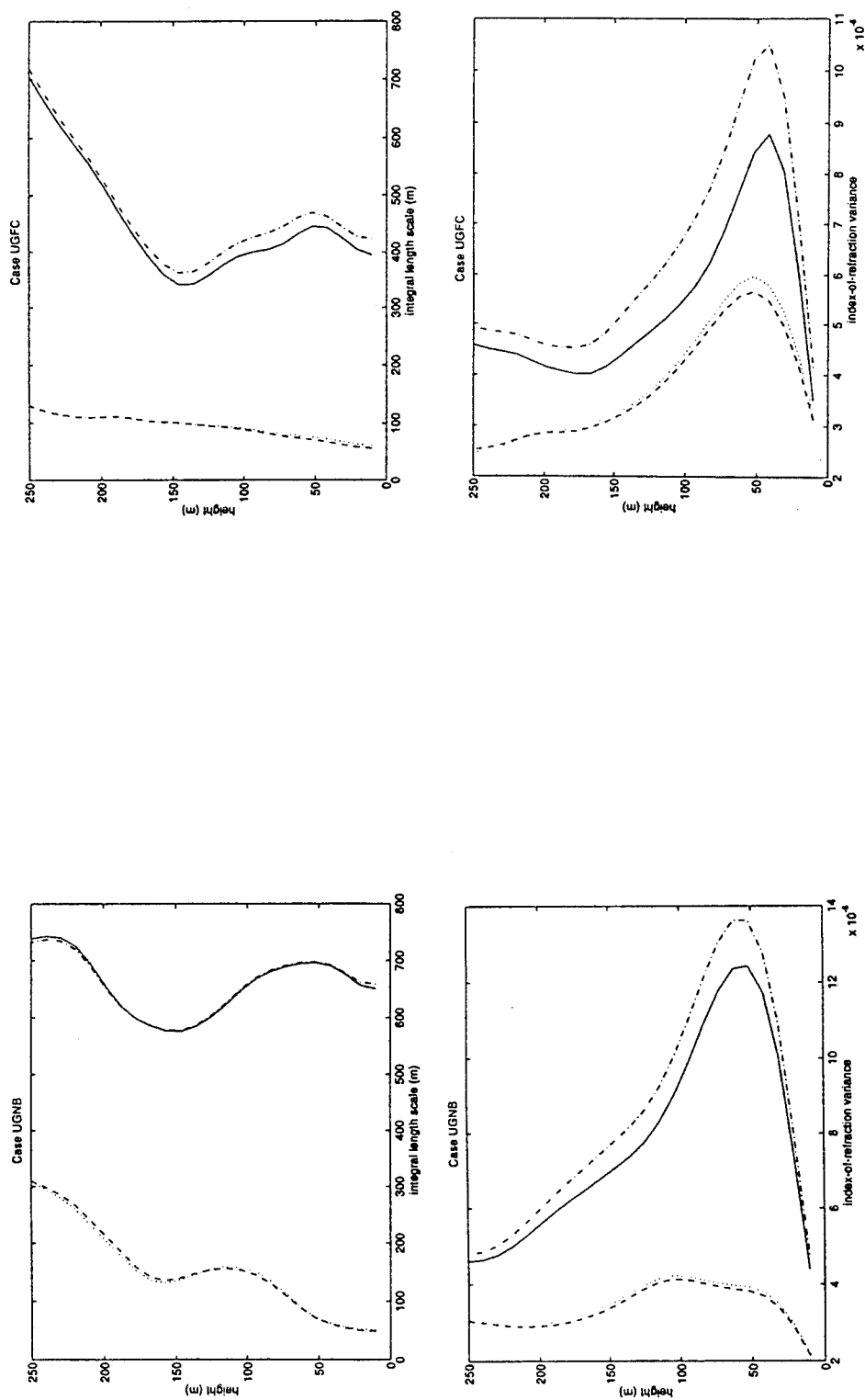


Figure 1: Index of refraction parameters for Case UGNB. (upper) Integral length scale. (lower) Variance. Solid line: Downwind. Dash-dot line: Upwind. Dotted and dashed lines: Cross wind.

Figure 2: Index of refraction parameters for Case UGFC. (upper) Integral length scale. (lower) Variance. Line types same as Fig. 1.

III. Log-Amplitude Statistics

Let us write the normalized, complex acoustic pressure $p/\langle p \rangle = \exp(\chi + i\phi)$. The phase and log-amplitude fluctuations are, respectively, ϕ and χ . In the framework of geometric acoustics, log-amplitude fluctuations are effected by the second derivatives (the curvature) of the effective sound speed in the two directions normal to the propagation. Concave curvature causes focusing of the sound energy, and hence usually increases sound levels. Convex curvature causes defocusing and decreased sound levels. For approximately horizontal propagation near the ground, the vertical curvature of the effective sound speed probably plays the most significant role in driving log-amplitude fluctuations.

In Ref. [1], the following approximate model for the variance of the log-amplitude fluctuations was derived:

$$\langle \chi^2 \rangle = \langle g'^2 \rangle R^4 / 8 \quad (3)$$

for $R \ll L_g$, and

$$\langle \chi^2 \rangle = \sqrt{2\pi} \langle g'^2 \rangle R^3 L_g / 24 \quad (4)$$

for $R \gg L_g$. In the above, g is the effective sound speed profile curvature, given by

$$g = \frac{1}{c_0} \frac{\partial^2 c_{eff}}{\partial z^2} \approx \cos \alpha \frac{\partial^2 u}{\partial z^2} + \sin \alpha \frac{\partial^2 v}{\partial z^2} + \frac{c_0}{2T_0} \frac{\partial^2 T}{\partial z^2}. \quad (5)$$

The challenge lies in determining the profile curvature variance, $\langle g'^2 \rangle$, and its integral length scale, L_g . Since $\partial^2 / \partial z^2$ becomes $-k_z^2$ in the wavenumber domain, we see that the profile curvature is dominated by large wavenumbers, or small-scale turbulence. Hence the finite resolution of LES becomes even more of a problem when examining profile curvature statistics than index-of-refraction statistics, and LES appears to be a more useful tool for calculating the effects of atmospheric turbulence on acoustic phase fluctuations than on log-amplitude fluctuations. This would also explain why Wilson [5] calculated unrealistically weak sound level fluctuations when LES data was used as input to a three-dimensional acoustic propagation model.

Despite these shortcomings in using LES data to calculate profile curvature statistics, the results for $\langle g'^2 \rangle$ and L_g are shown in Figs. 4–6. The profile curvatures were calculated by fitting each effective sound speed profile with a cubic spline, and then taking the second derivative of the spline.

The calculated integral length scales (Figs. 4–6, upper) are all comparable to the horizontal resolution of the simulations (about 10 m for UGNB and UGFC, and 20 m for UGMC), and are therefore unreliable. UGNB and UGFC, the nearly neutral cases, show an increase in the length scale near the ground. This suggests the possibility that large eddies can drive strong variations in the profile curvature near the ground, although it could also be an artifact of the finite resolution of the simulations.

The variance calculations (Figs. 4–6, lower) exhibit two important trends: the profile curvature variance tends to decrease with height, and tends to be less in the crosswind than in the upwind or downwind directions. These trends also emerge from the model developed in Ref. [1].

IV. Discussion

The results of this study reinforce many of the conclusions made in Ref. [1]. In particular, they illustrate the inaccuracies that can arise from using a single-scaled Gaussian correlation function for the effective sound speed. Atmospheric turbulence spans a broad range of

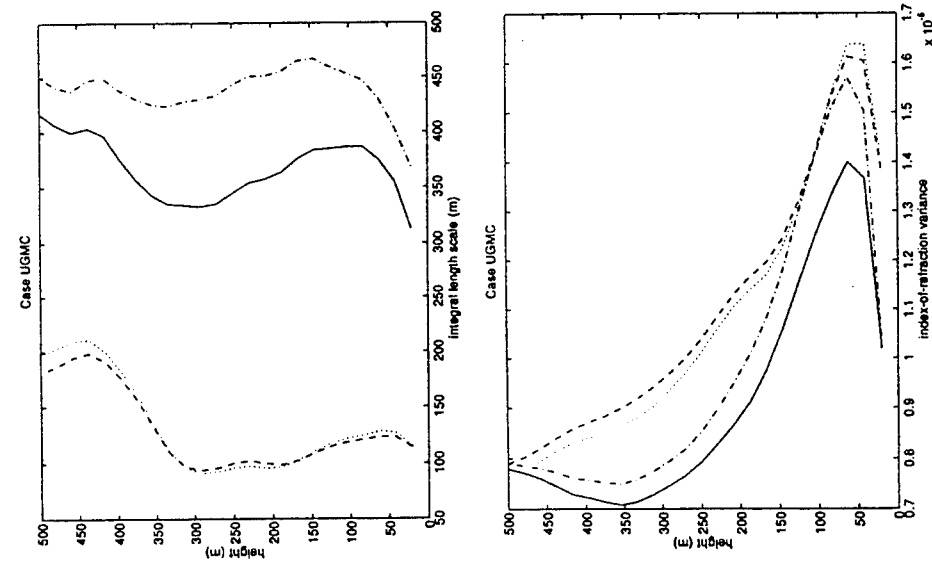


Figure 3: Index of refraction parameters for Case UGMC. (upper) Integral length scale. (lower) Variance. Line types same as Fig. 1.

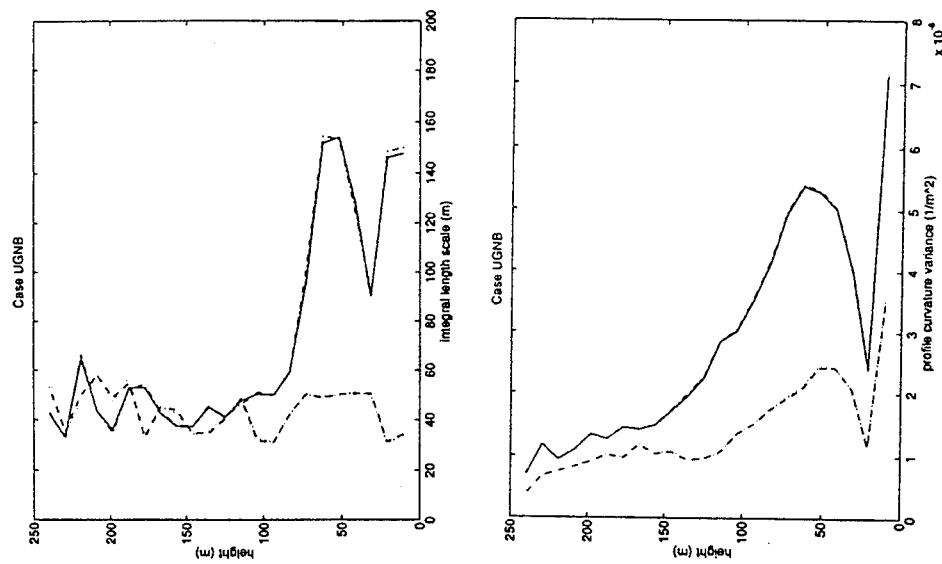


Figure 4: Profile curvature parameters for Case UGNB. (upper) Integral length scale. (lower) Variance. Solid line: Downwind. Dash-dot line: Upwind. Dotted and dashed lines: Cross wind.

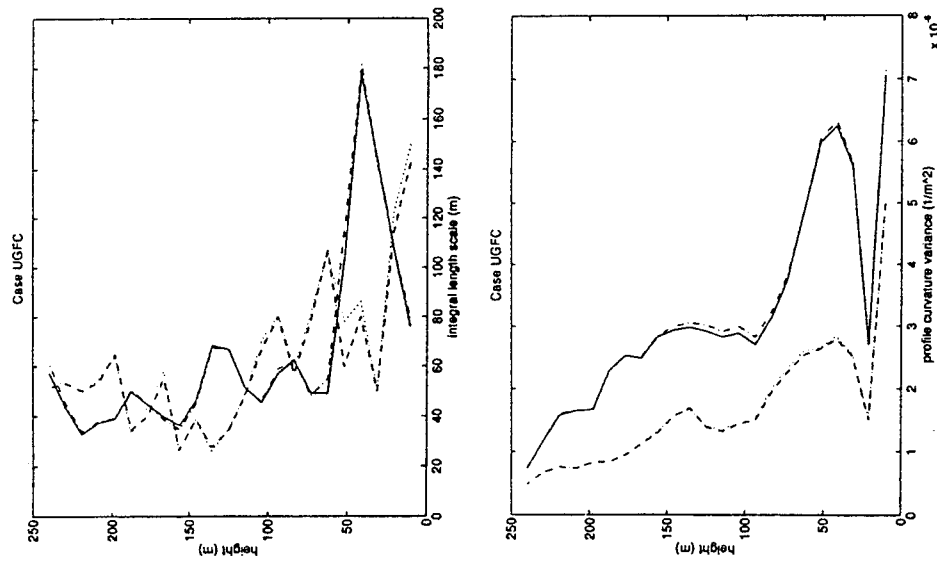


Figure 5: Profile curvature parameters for Case UGFC. (upper) Integral length scale. (lower) Variance. Line types same as Fig. 1.

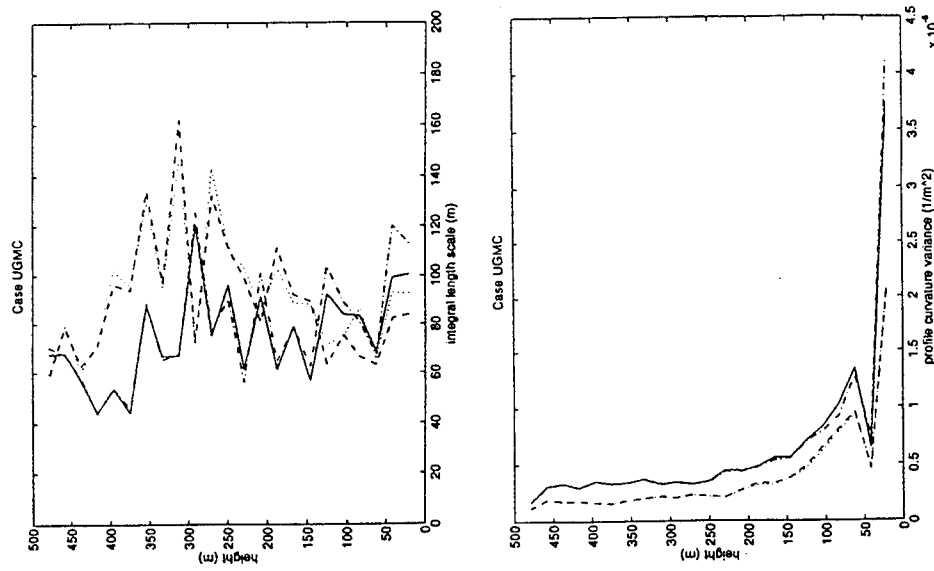


Figure 6: Profile curvature parameters for Case UGMC. (upper) Integral length scale. (lower) Variance. Line types same as Fig. 1.

spatial scales; the phase variance depends primarily on the larger scales, whereas the log-amplitude variance depends on the smaller ones. Moreover, the correlation function of the effective sound speed is extremely anisotropic near the ground.

When the atmosphere is convectively unstable (i.e., the heat flux is from the ground to the air), the strongest eddies have spatial dimensions on the order of the boundary-layer thickness (about 200 m to 2000 m). The structure of these eddies depends on the heat flux and on the wind speed. The statistics of the index of refraction depend, in turn, on the structure of these large eddies. The calculations in this paper suggest that increasing surface heat flux causes increased variability in acoustic signals, although the length scales of the largest eddies actually decrease.

Since local variations in topography and ground albedo have strong effects on large-scale turbulence structure, acoustic phase statistics are probably strongly site dependent. Some evidence of this was given in Ref. [1]. In contrast, log-amplitude fluctuations appear to be driven by small-scale structures in the atmospheric surface layer. The analysis in Ref. [1] suggests that the profile curvature variance $\langle g'^2 \rangle$ scales as $u_*^2/c_0^2 z^4$, and hence diminishes rapidly with height. We also see that, in the geometric acoustics approximation, the relevant length scale for the eddies driving log-amplitude fluctuations is probably z for atmospheric turbulence. Therefore log-amplitude statistics would not be expected to have such a strong a site dependence as phase statistics.

Some of the ideas discussed in this paper are tied together and extended in Fig. 7, which shows a conceptual model for sound propagation through turbulence near the ground. (The figure is intended to provide near-ground detail of the turbulent structures shown, for example, in Fig. 2 of Ref. [6].) The horizontal extent of the depiction is a few hundreds of meters, and the vertical extent is a few tens of meters. A ray tube is shown incident on the bottom edge of a large, boundary-layer scale eddy. Superimposed on the large eddy are smaller-scale bursting and sweeping events [7]. The bursts correspond to upward transport of slowly moving air, whereas the sweeps provide downward transport of fast moving air. (In the atmosphere, the bursts are also associated with heat transport, and are often called surface-layer plumes [8].) The large eddy dominates travel time and phase fluctuations of the acoustic ray, simply because the contributions from smaller scales tend to average out over the ray path. However, as emphasized above, amplitude fluctuations are driven by the smaller scales. Hence I speculate that the surface bursting and sweeping events play the dominant role in altering the area of the acoustic ray tube.

Acknowledgements

The author thanks the Symposium's organizers for providing travel expenses. This work was sponsored by ONR Grant N00014-92-J-1688.

References

- [1] D. K. Wilson and D. W. Thomson, "Propagation through anisotropic, surface-layer turbulence," to appear in *J. Acoust. Soc. Am.*
- [2] C.-H. Moeng, "A large-eddy-simulation model for the study of planetary boundary-layer turbulence," *J. Atmos. Sci.* **45**, 2052-2062 (1984).
- [3] C.-H. Moeng and P. P. Sullivan, "A comparison of shear and buoyancy driven planetary-boundary-layer flows," submitted to *J. Atmos. Sci.*

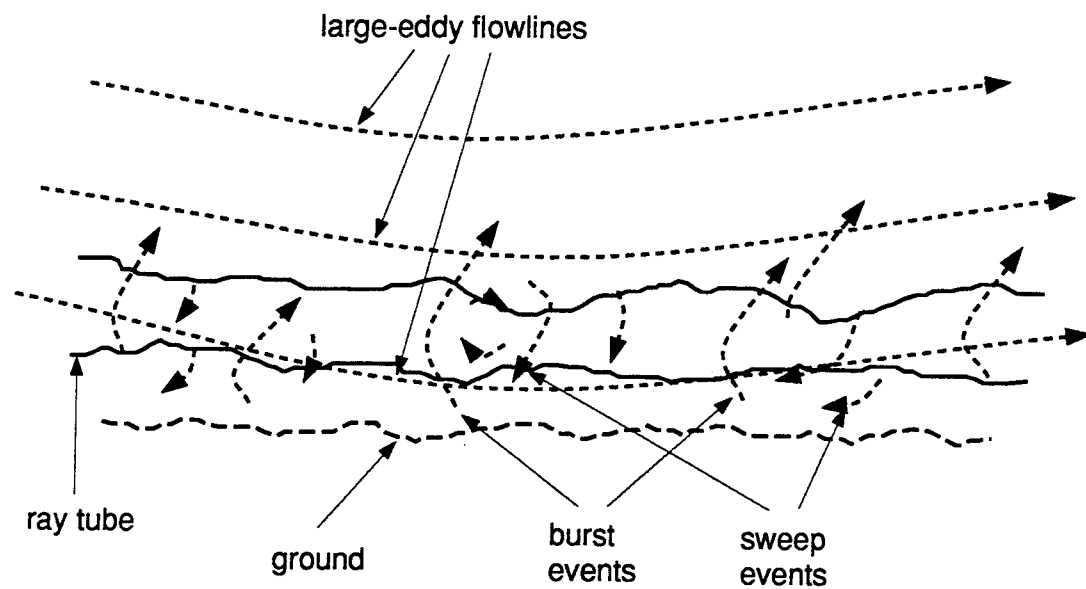


Figure 7: Conceptual model for propagation through turbulence near the ground. The wind field is a superposition of flow lines (dashed lines) from the bottom edge of a large-eddy, and bursting and sweeping events originating at the surface. The width of the ray tube varies in response to the bursts and sweeps.

- [4] L. A. Chernov, *Wave Propagation in a Random Medium* (McGraw-Hill, New York, 1960).
- [5] D. K. Wilson, "Numerical studies of sound propagation in the atmospheric convective boundary layer using a large-eddy simulation," in *Proceedings of NOISE-CON 91*, Tarrytown, New York (1991).
- [6] J. C. Wyngaard, "Atmospheric turbulence," *Ann. Rev. Fluid Mech.* **24**, 205-233 (1992).
- [7] S. K. Robinson, "Coherent motions in the turbulent boundary layer," *Ann. Rev. Fluid Mech.* **23**, 601-639 (1991).
- [8] J. C. Kaimal and J. A. Businger, "Case studies of a convective plume and a dust devil," *J. Appl. Meteor.* **9**, 612-620 (1970).

CONCLUSIONS PERTINENT TO ACOUSTICAL SCATTERING BY ATMOSPHERIC TURBULENCE USING A TURBULE ENSEMBLE MODEL

by

Harry J. Auvermann
U. S. Army Research Laboratory
Battlefield Environment Directorate
White Sands Missile Range, NM 88002-5501

George H. Goedecke and Michael D. DeAntonio
Department of Physics
New Mexico State University
Las Cruces, NM 88003-0001

ABSTRACT

The importance of scattering by atmospheric turbulence as a contributor to acoustic signal levels in shadow zones is widely recognized. Also recognized is the fact that turbulence is neither homogeneous nor isotropic near the ground. The difference in shadow zone signal estimates between the case where the turbulence is considered homogeneous and isotropic and the case where the actual variability of turbulence characteristics is accounted for should be determined. Investigation of scattering from a turbule ensemble model of turbulence was initiated to obtain an answer to this problem. A non-uniform anisotropic turbulence field can be simulated by forming an ensemble of turbules each member of which is suitably oriented, sized and located. The shadow zone signal is then calculated by summing the signals scattered by each member of the ensemble. Besides the distances involved, such a calculation needs the scattering properties and number concentrations of the classes of turbules which make up the ensemble. Expressions for these two quantities have been developed. Important conclusions have been drawn about scattering using the turbule ensemble model of the turbulence field. Examples are: a) velocity turbules have zero scattering amplitude in the forward and backward direction; b) a collection of randomly oriented turbules of arbitrary morphology scatter the same as a collection of rotating spherically symmetric turbules; c) scaling law exponents appropriately chosen lead to a Kolmogorov spectrum within the inertial range independent of turbule morphology. A brief account of these and other results is given in this paper.

1. INTRODUCTION

Scattering by atmospheric turbulence is widely recognized as an important contributor to acoustic signal levels in shadow zones¹. Intuition and experimental evidence suggest that turbulence is neither homogeneous nor isotropic near the ground², a condition applicable to a number of scenarios.

The research reported in this paper was undertaken to determine the difference in shadow zone signal level estimates obtained assuming turbulence is isotropic and homogeneous in contrast to estimates obtained assuming neither isotropy or homogeneity. The final goal has not yet been reached, largely because scattering properties of large sized (relative to the sound wavelength) inhomogeneities are not available. In the course of the investigation to date, however, a number of important discoveries have been made about acoustic scattering from turbulence. These discoveries are discussed below. In section 2, a turbule ensemble model of turbulence is introduced that has the built in flexibility necessary for consideration of the anisotropic inhomogeneous case of interest. In section 3, development of the expressions for scattering from individual temperature and velocity inhomogeneities is covered. In section 4, properties of an ensemble of randomly oriented turbules are presented, bridging to the isotropic case. In section 5, ensembles are further augmented to include uniformly distributed turbules and turbules with a distribution of sizes, showing the connection to homogeneous turbulence. Section 6 concludes the paper with a summary of the results that have been obtained.

2. THE TURBULE ENSEMBLE MODEL

The purpose of the research is to provide acoustic atmospheric turbulence scattering theory applicable to a) wavelengths comparable to the outer scale length, b) inhomogeneous turbulence, and c) anisotropic turbulence. A turbule is defined to be a localized inhomogeneity, either temperature or velocity, with a characteristic size, orientation and position. A turbule ensemble is defined to be a collection of turbules with different sizes, orientations and positions. The flexibility required to model different realizations of a turbulent field results from suitable choice of the mix of size, orientation and position. The energy cascade theory of turbulence³ starts with the assumption of energy flow from large eddies to smaller ones, the smallest size being the one in which energy is dissipated. Because the exact nature and morphology of these eddies are not known, the analysis proceeds using statistical methods. An impressive fund of information about turbulence has been obtained from this statistical model. Experience from the field of optical scattering from atmosphere borne particles or aerosols suggests that morphology may be of limited enough importance that further information can be obtained with inexact morphology knowledge. Good correlation of optical scattering results with experiment has been obtained under the assumption that aerosols are uniform spheres, in spite of the fact that aerosols are generally known to be non-spherical. Below, it is shown that this experience from optics carries over into acoustics. While it is impossible to know the exact expression for a turbulence field that occurs in nature, much information is obtained from assigned specific morphologies and from arbitrary morphologies that have broadly defined orientation and position distributions.

Scattering cross-section results for isotropic, homogeneous turbulence are available³ as a result of a Born approximation derivation. For the most part, the derivations here also employ the Born approximation. Defining the size parameter x to be $(2 \pi a)/\lambda$, Born approximation results fail for very large x . The characteristic size of a scatterer is represented by a and the wavelength by λ . The first step in the implementation of a turbule ensemble model is to find the scattering properties of an individual turbule. It is noted that an exact

scattering cross-section in series form has been obtained⁴ for a uniform solid spherical scatterer with abrupt interface similar to that of a bowling ball. The uniform sphere is analogous to a temperature turbule because the wave speed inside the turbule is different than that of the surrounding medium. The applicability of this theory may be questioned on the grounds that the interface of a turbule may not react to a sound wave in the same way that a solid interface would. Space is too limited here to present all but a few of the steps in the derivations. Those steps included below are intended to show the basic equations and the assumptions made in reaching the useful results.

3. SCATTERING EXPRESSIONS FOR INDIVIDUAL TURBULES

The quantities of importance in scattering are the scattering amplitude f and the scattering cross-section σ . The quantity f relates the incident field amplitude (such as pressure) to the scattered field amplitude. The quantity σ relates the incident field power to the scattered field power. A further quantity Q called the scattering efficiency is often useful, Q being the quotient of σ and an effective physical cross-sectional area of the scatterer. The necessary starting point in developing expressions for these quantities is a suitable wave equation.

In acoustics, the wave equation is deduced from fluid equations. These are:

$$\partial_t \nabla + \nabla \cdot \nabla \nabla + \rho^{-1} \nabla p - \nu_1 \nabla^2 \nabla - \nu_2 \nabla \nabla \cdot \nabla = 0, \quad (1)$$

$$\partial_t \rho + \nabla \cdot (\rho \nabla) = 0, \quad (2)$$

$$p - \rho k_B T / M = 0, \quad (3)$$

$$\partial_t p + \nabla \cdot \nabla p + \gamma p \nabla \cdot \nabla = 0. \quad (4)$$

Equation (1) is the Navier-Stokes equation⁵, equation (2) is the equation of continuity⁵, equation (3) is the perfect gas equation of state⁶, and equation (4) is the heat flow equilibrium equation⁵ without the conduction term. In these equations, ∇ is the velocity vector, ρ is the mass density, p is the pressure, T is the temperature, k_B is the Boltzmann constant, M is the molecular mass, and γ is the ratio of specific heats. ν_1 and ν_2 are viscosity parameters assumed to be zero below. (1) - (4) are a complete set of equations, there being six equations for the six field quantities ν_1 , ν_2 , ν_3 , ρ , p , and T .

The first step in the development of a wave equation is to linearize the field variables. In the following, ∇_0 , ρ_0 , p_0 , and T_0 , the turbulent flow variables, do not vary with time. The acoustic variables, u , ϵ , η , and δ , have time

dependence $\exp(i\omega t)$.

$$\begin{aligned}\bar{\mathbf{v}} &= \bar{\mathbf{v}}_0 + \bar{\mathbf{u}} \\ \rho &= \rho_0(1 + \epsilon) \\ p &= p_0(1 + \eta) \\ T &= T_0(1 + \delta)\end{aligned}\tag{5}$$

Substitution of equation (5) into equations (1) -- (4) along with the assumption that the turbulent flow is solenoidal, or that $\Delta \cdot \bar{\mathbf{v}}_0 = 0$, yields both zero order equations relating to the turbulent fields and equations linear in the acoustic variables.

The acoustic equations may be manipulated under the stipulation that only terms first order in (v_0/c_0) and $(T_0 - T_\infty)/T_\infty$ be retained to obtain the following equation in the relative pressure η :

$$(\nabla^2 + k^2)\eta = \partial_j \{ (\Delta T_0 / T_\infty) \partial_j \eta \} + 2i\omega^{-1} [\partial_j (v_{0j} \partial_l \partial_l \eta)] \tag{6}$$

Tensor notation has been introduced into equation (6) where the convention that repeated indices denotes a summation is understood. Further assumptions are: the turbulence is localized inside a bounded volume V_T ; outside V_T , the pressure, temperature, and mass density take on constant uniform values and the flow velocity is zero; the remote wave speed (outside V_T) is $c_\infty = (\gamma k_B T_\infty / M)^{1/2}$; the local wave speed (inside V_T) is $c_0 = (\gamma k_B T_0 / M)^{1/2}$. The wavenumber is $k = \omega / c_\infty$. The turbulent temperature variation is $\Delta T_0 = T_\infty - T_0$.

The next step is to solve equation (6). The Green's function solution is defined as follows:

Assumptions:

- Incident plane wave $\eta_{in}(\vec{r}) = \exp(i\vec{k} \cdot \vec{r})$
- Incident direction vector $\rightarrow \vec{k}$
- Field position vector $\rightarrow \vec{r}$
- $\vec{r}_{12} = \vec{r}_1 - \vec{r}_2$; $r_{12} = |\vec{r}_1 - \vec{r}_2|$

$$\tag{7}$$

$$(\nabla^2 + k^2)\eta(\vec{r}) = -4\pi S(\vec{r})\eta(\vec{r})$$

Implicit Solution:

$$\eta(\vec{r}_1) = \exp(i\vec{k} \cdot \vec{r}_1) + \int d\vec{r}_2 r_{12}^{-1} \exp(ikr_{12}) S(\vec{r}_2) \eta(\vec{r}_2) \quad (8)$$

Scattered field:

$$\eta_s(\vec{r}_1) = \int d\vec{r}_2 r_{12}^{-1} \exp(ikr_{12}) S(\vec{r}_2) \eta(\vec{r}_2)$$

The expression S in equation (7) represents an operator from the right hand side of equation (6) that operates on the field variable η . The total field η and the scattered field η_s are defined in equation (8). The subscript 1 identifies the observation point while the subscript 2 identifies points within the scattering volume which contribute to the observed field. The following are defined:

Assumptions: \circ Far field $\vec{r}_1 = r\hat{r}$; $r \rightarrow \infty$

$$\eta_s(\hat{r}) = r^{-1} \exp(ikr) f(\hat{r})$$

Scattering amplitude:

$$f(\hat{r}) = \int d\vec{r}_2 \exp(-ik\hat{r} \cdot \vec{r}_2) S(\vec{r}_2) \eta(\vec{r}_2) \quad (9)$$

Differential and total scattering cross-sections:

$$\sigma(\hat{r}) = |f(\hat{r})|^2; \quad \sigma_s = \int d\Omega \sigma(\hat{r})$$

The definitions of the scattering amplitude and scattering cross-section include the specification that the incident field is a plane wave. A further specification of these definitions is that the observation point is sufficiently remote that the amplitude dependence is r^{-1} . Under the latter specification, the scattering quantities depend only on the unit vector in the direction of the observation point and the distance.

Since our main interest is in scattering from velocity inhomogeneities, that part of S in equation (6) associated with velocity is separated out and called S_v . The velocity scattering amplitude is defined as follows:

$$f_v(\hat{r}) = \int d\vec{r}_1 \exp(-ik\hat{r} \cdot \vec{r}_1) S_v(\vec{r}_1) \eta(\vec{r}_1)$$

$$S_v(\vec{r}_1) = (1/2\pi i\omega) [\partial_i (v_{0j} \partial_i \partial_j)]$$

$$\sigma(\hat{r}) = |f(\hat{r})|^2; \quad \sigma_s = \int d\Omega \sigma(\hat{r}) \quad (10)$$

Born approximation:

$$\begin{aligned} f_v(\hat{r}) &= \int d\vec{r}_2 \exp(-ik\hat{r} \cdot \vec{r}_2) S_v(\vec{r}_2) \eta_{in}(\vec{r}_2) \\ &= \int d\vec{r}_2 \exp(-ik\hat{r} \cdot \vec{r}_2) S_v(\vec{r}_2) \exp(i\vec{k} \cdot \vec{r}_2) \end{aligned}$$

Substituting the incident field for the true field in equation (10) constitutes the Born approximation. Equation (10) constitutes the basic equation for determining the Born approximation scattering amplitude f_v for the velocity field whose components are v_{0j} .

It is instructive to calculate the properties of a particular velocity field. The field chosen is referred to here as the Gaussian velocity turbule, where the envelop Gaussian function is modified by a cross product of an angular velocity vector and the field position vector.

Velocity Distribution:

$$v_0(\vec{r}) = \vec{\Omega} \times \vec{r} \exp(r^2/a^2); \quad \vec{k} = k\hat{z}$$

$$\text{where: } \vec{\Omega} = \Omega [\hat{x} \sin(\theta_\alpha) \cos(\phi_\alpha) + \hat{y} \sin(\theta_\alpha) \sin(\phi_\alpha) + \hat{z} \cos(\theta_\alpha)] \quad (11)$$

$$\circ \quad \Omega = \text{angular velocity parameter} = v_a/a$$

$$\circ \quad \hat{r} = r [\hat{x} \sin(\theta) \cos(\phi) + \hat{y} \sin(\theta) \sin(\phi) + \hat{z} \cos(\theta)]$$

$$\circ \quad a = \text{characteristic "radius" of distribution}$$

$$\circ \quad v_a = \Omega a = \text{characteristic velocity of distribution}$$

The result of applying equation (10) to this velocity field⁷ is the differential scattering efficiency as follows:

$$\begin{aligned}
Q(\hat{k}, \hat{r}) &= \sigma(\hat{r})/\pi a^2 \\
&= (v_a/4c_\infty)^2 (ka)^6 [\sin(\theta) \cos(\theta) \sin(\theta_\alpha) \\
&\quad \sin(\phi - \phi_\alpha)]^2 \exp[-(ka)^2(1 - \cos(\theta))]
\end{aligned} \tag{12}$$

In equations (11)-(12), θ_α , ϕ_α are the polar and azimuthal orientation angles respectively of the angular velocity vector. The angles θ , ϕ are the polar and azimuthal angles of the observation direction with respect to the incident field direction, which in this case is along the z-axis. One interesting feature of equation (12) is the presence of the $\sin(\theta)$ factor in the efficiency expression. When θ is zero, that is the observation point is in the exact forward direction, the differential scattering efficiency is zero. It is also zero in the backward direction.

This result can be generalized. If equation (10) is integrated by parts, the divergence theorem will convert certain of the volume integrals into surface integrals. These surface integrals vanish when the velocity distribution is localized. The resulting alternate expression for the scattering amplitude is shown in the following equation:

$$\begin{aligned}
f_v(\hat{r}) &= -(k^2/2\pi c_\infty) \cos(\theta) \hat{k}_j V_{0j}(\vec{K}) \\
\text{where: } \circ \vec{K} &= k(\hat{r} - \hat{k}) \\
\circ V_{0j}(\vec{K}) &\text{ is the Fourier transform of } v_{0j}(\vec{r}_1)
\end{aligned} \tag{13}$$

Forward amplitude: $f_v(\hat{k}) = 0$ if $\nabla \cdot \nabla_0 = 0$

In equation (13), forward scattering occurs when the propagation unit vector is substituted for the observation unit vector. Thus, the forward scattering amplitude is zero for all velocity distributions for which the divergence is zero. It is also true in general in the backward direction³.

An interesting paradox presents itself when the Optical Theorem is considered along side of the results of equation (13). The Optical Theorem states: The total scattering cross-section is equal to the imaginary part of the forward scattering amplitude. The paradox is: How can the scattering amplitude be identically zero from equation (13) when it is known that velocity turbules have a non-zero total scattering cross-section? This paradox is resolved by resort to the Second Born approximation. Substitution of the incident field for η in the integral of the implicit solution of equation (8), and then substitution of the resulting expression again for η in the integral of the implicit solution of equation (8) constitutes the Second Born approximation. When this new field expression is operated on in a similar way as that above, the Second Born approximation scattering amplitude is the product. The imaginary part of the

Second Born scattering amplitude is identically equal to the First Born total scattering cross-section.

4. ISOTROPIC ENSEMBLES OF TURBULES

An isotropic ensemble of turbules of a given scale length a can be approximated by a collection of similar turbules whose orientations are randomly selected. The scattering cross-section for the ensemble is calculated by integration of the orientation angles θ_a, ϕ_a the differential scattering expressions over 4π solid angle with a uniform weighting function. The expressions to integrate are equation (12) for the example velocity distribution and equation (10) for an arbitrary velocity distribution. In the latter, S_v contains the orientation angle dependence. The result for the example distribution is:

$$\begin{aligned} \langle Q_v(\hat{r}) \rangle = & (1/3) (v_a/4c_\infty)^2 (ka)^6 [\sin(\theta) \cos(\theta)]^2 \\ & \exp[-(ka)^2(1 - \cos(\theta))] \end{aligned} \quad (14)$$

The above function is plotted for three different size parameters in Figure 1.

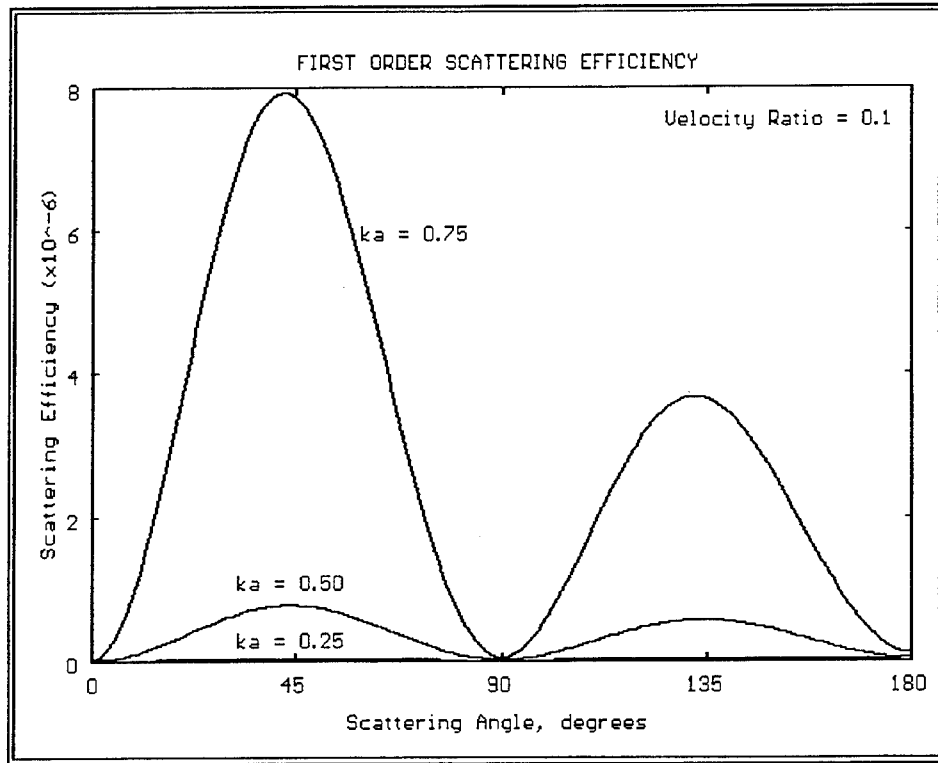


Figure 1. Orientation averaged scattering efficiency

In the above plot of the First Born approximation orientation averaged scattering efficiency of the Gaussian turbule, the quadrupole pattern is clearly apparent. Enhancement of the forward hemisphere lobe caused by the exponential factor is shown for the larger size parameter.

For an arbitrary distribution, averaging over orientation angle gives the following result:

$$\langle Q_v(\hat{r}) \rangle = (1/3) (v_a/2c_\infty)^2 (ka)^4 [\cos(\theta) \cos(\theta/2)]^2 (Ka)^2 B^2(Ka)$$

$$B(Ka) \rightarrow \text{envelop function Fourier transform} \quad (15)$$

$$\text{Examples} \circ \text{Gaussian} \rightarrow B_g(Ka) = \exp[-(Ka)^2/4]$$

$$\circ \text{Exponential} \rightarrow B_e(Ka) = [1 + (Ka)^2/\alpha^2]^{-3}$$

where α is a constant

The presence of the envelop function Fourier transform in equation (15) shows that an ensemble of similar randomly oriented rotating turbules of arbitrary morphology have a scattering pattern with no azimuthal dependence. If B_g is substituted into equation (15), equation (14) is the result. Also given in (14) is the envelop Fourier transform function B_e which will result in a exponential function in coordinate space. When α is chosen to be $(12)^{1/2}$, and the characteristic velocity of the exponential turbule is 0.64 times the characteristic velocity of the Gaussian turbule, then the two turbules are comparable. Comparable means they have the same rms radius and the same average energy content. This comparable concept is used in the next section to insure that the spectra plotted there match in the inertial range.

5. ISOTROPIC AND HOMOGENEOUS ENSEMBLES

In this section, isotropic ensembles of self-similar turbules of many different scale lengths are located at random positions within the scattering volume. The intent is to determine the constraints placed upon the number concentration, and the velocity and temperature difference ratios when the properties of the super ensemble brought into conformance with the properties of naturally occurring turbulence.

The list following contains definitions of the symbols used to describe the homogeneous distribution of isotropic turbules:

- Volume of turbulence region is V_T
- Index of size classes n ; $1 \leq n \leq N_s$
- Number of turbules of each class N_n
- Class size a_n ; Class velocity v_n
- Total number of turbules $N = \sum_n N_n$

- *Individual turbule index* v ; $1 \leq v \leq N$
- *Turbule location* \vec{b}_v
- *Largest size is* a_1 ; *smallest is* a_{N_s}
- *Location probability* $p(\vec{b}_v)$ *uniform* $\in V_T$
- *Temperature differential parameter* δT_n

All turbules in a particular class have the same characteristic size and the same characteristic velocity but have center locations chosen randomly from a uniform distribution. Parameter scaling with turbule size is assumed to be power law according to the following formulas:

$$\frac{N_n}{N_1} = \left(\frac{a_n}{a_1} \right)^{-\beta}, \quad \left(\frac{\delta T_n}{\delta T_1} \right) = \left(\frac{a_n}{a_1} \right)^{\gamma}, \quad \left(\frac{v_n}{v_1} \right) = \left(\frac{a_n}{a_1} \right)^{\zeta} \quad (16)$$

If it is assumed that scaling is fractal (the ratio a_n/a_{n+1} is a constant for $1 \leq n \leq N_s - 1$) and the Kolmogorov energy cascade model is used, the exponents for the separate scaling laws are: $\beta = 3$; $\gamma = (1/3)$; and $\zeta = (1/3)$. The temperature difference and characteristic velocity scale with the expected $(1/3)$ power law exponent. The exponent for the number density scaling being three means that each turbule size class fills an equal percentage of the scattering volume.

These scaling laws allow computation of the spectrum for the isotropic homogeneous turbulence field. This is done by summing the scattering from all size classes according to the following rules:

$$\sum_{n=1}^{N_s} \rightarrow \int_1^{N_s} dn = \mu^{-1} \int_{a_1}^{a_{N_s}} da/a; \quad (17)$$

$$\mu = -\ln(m)/(N_s - 1); \quad m = a_{N_s}/a_1$$

Typically m in equation (17), the ratio of the largest to smallest sizes, is a small number, perhaps 0.0001. In the next equation, the variable x is redefined, the quantity Γ_v is defined, and the integral $J_p(mx, x)$ is defined.

$$\begin{aligned}
\circ \quad x &= 2k a_1 \sin(\theta/2) \\
\circ \quad \Gamma_v &= (1/3) (\pi a_1)^2 (N_1) (ka_1)^4 (v_1/2c_\infty)^2 \\
&\quad [\cos(\theta) \cos(\theta/2)]^2 \\
\circ \quad J_p(mx, x) &= \int_{mx}^x dy y^p B^2(y)
\end{aligned} \tag{18}$$

Using these quantities, the velocity scattering cross-section for the volume V_T is given by the following equation:

$$\bar{\sigma}_v(\hat{r}) = \mu^{-1} \Gamma_v x^{-11/3} J_{14/3}(mx, x) \tag{19}$$

In equation (19), the $x^{-11/3}$ factor is also present in the Tatarskii scattering cross-section formula³. This factor by itself of course diverges for small scattering angle θ . The limits on the integral J_p keep the cross-section finite at the outer scale and cause a more rapid fall off near the inner scale. The integral parameter p is $14/3$ for velocity turbules and $8/3$ for temperature turbules. Figure 2 shows the variation of normalized cross-section, B , with the parameter x for several turbule envelop functions. The figure was calculated for

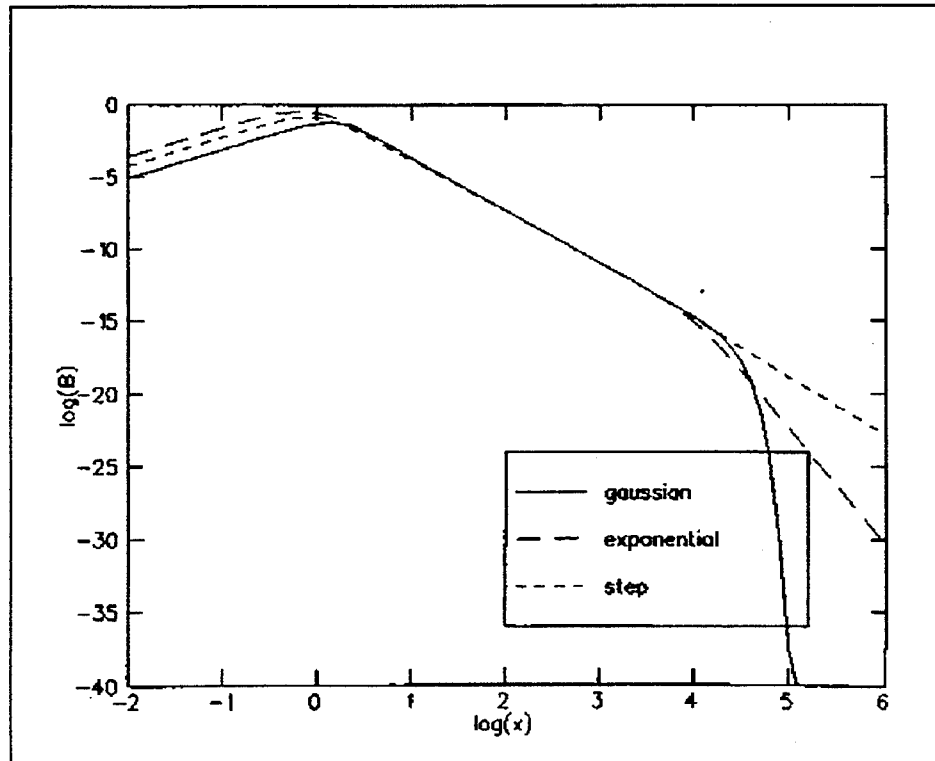


Figure 2. Normalized temperature cross-sections for isotropic turbulence fields made up with tubules of different morphologies

temperature turbules but the behavior has the same character for velocity turbules. The normalization factor in B is $\mu^{-1} \Gamma_v J_p(0, \infty)$.

According to the evidence presented in figure 2, measurements in the mid-range of the variable x will fail to distinguish morphology dependence in a scattering experiment. Measurements at either end of the range of x may be able to distinguish between morphology functions.

The inherent flexibility of the turbule ensemble model of turbulence makes it possible to include the scattering effects of a moderate number of anisotropic inhomogeneities in acoustic propagation models. Under consideration here is the Fast Field Program (FFP). The scheme is to consider turbules as sources when running FFP. The limitation that sources in FFP are spherical radiators is overcome by decomposing the anisotropic scattering pattern into its component multipoles, each component being made up of the appropriate number of spherical radiators appropriately located and phased. The scattered field is then the coherent sum of the fields scattered by the constituent spherical radiators. This scheme was implemented in a computer code called the Acoustical Multi-stream Propagation Program (AMPP). FFP is included in AMPP as a subroutine. The function of code superstructure surrounding FFP is to compute and store the two dimensional fields for a number of sources. Figure 3 shows a simple

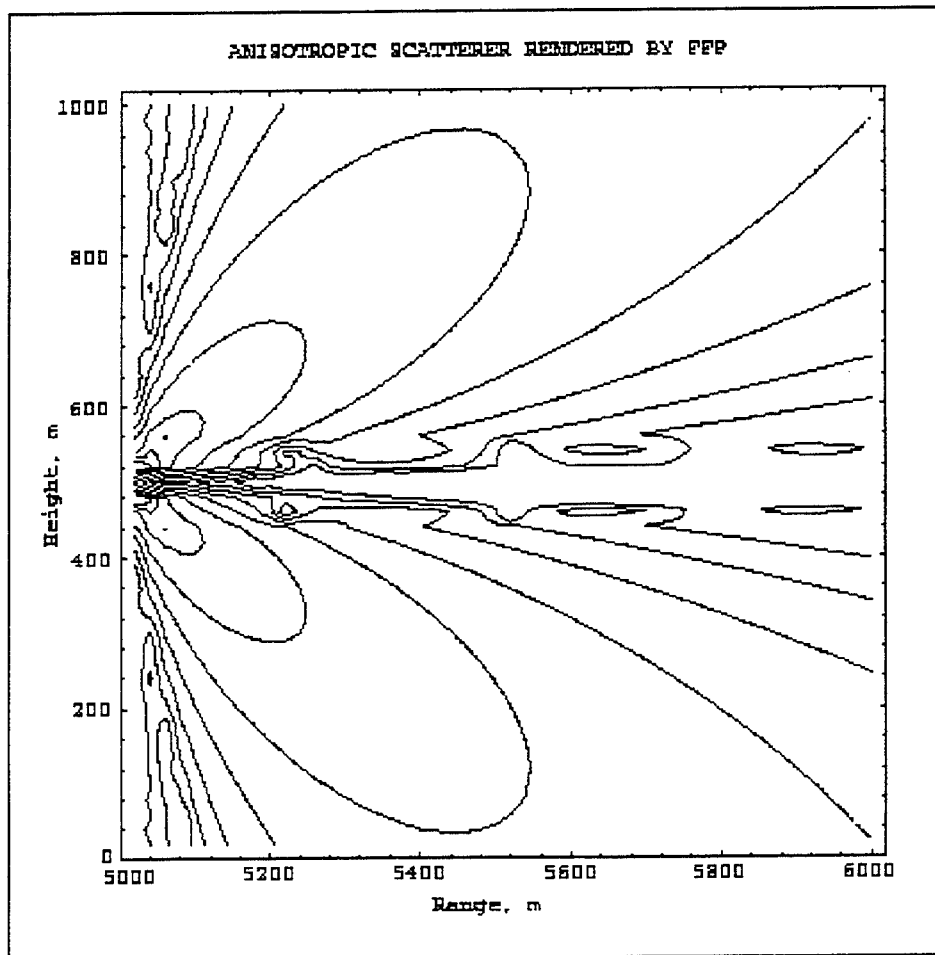


Figure 3. Field of an anisotropic scatterer

example of the field computed by AMPP. For a scattering scenario, the field in the region of interest is first computed and stored in an array for a bonafide source, with the field at all scatterer locations also stored. Then the fields for each component of the multipole decomposition of each of the scatterers are computed and stored in separate arrays. Finally, the fields are coherently added after the scatterer component arrays have been modified by the source field at the scatterer locations. The region of interest is the 1000 meter square beginning 5000 meters from a 170 hertz source located ten meters above ground. The vertical extent of the region begins at ground level. An anisotropic scatterer is located at a range of 5000 meters and a height of 500 meters. The scatterer is a dipole with the two elements separated by approximately one wavelength, with the lower element phased 180 degrees ahead of the upper element. To give clarity in the illustration, the atmospheric parameters were made uniform and the ground reflection coefficient was set to zero. The dipole element separation was made slightly different than one wavelength so that the field computed at the level of the scatterer would not be a computed zero, which is difficult to handle when contours are selected logarithmically. The source field was not included in the summation in this example. This simple case was calculated for illustrative purposes only. AMPP (through FFP) can handle sound speed gradients as well as ground reflections. For example, if an upward refracting atmosphere is modeled, scattering into the shadow zone may be calculated.

6. SUMMARY

The following list is a summary of the conclusions shown in this paper. Using the Born approximation:

- o A velocity turbule has zero scattering in the forward and backward directions
- o The second Born approximation yields agreement with the Optical Theorem
- o Orientation averaging of an arbitrary distribution eliminates azimuthal dependence
- o Fractal scaling and Kolmogorov energy cascade set scaling exponents
- o Cross-section is independent of turbule morphology in the inertial range
- o Turbule morphology influences the scattering data outside the inertial range

It was also shown that anisotropic scattering effects can be calculated using the Fast Field Program by representing the scatterer by a multipole expansion.

REFERENCES

1. Gilbert, K. E., R. Raspet, and X. Di, 1990, "Calculation of Turbulence Effects in an Upward-refracting Atmosphere," *J. Acoust. Soc. Am.*, **87**(6), 2428-2437.
2. Kaimal, J. C., J. C. Wyngaard, D. A. Haugen, O. R. Coté, S. J. Caughey and C. J. Readings, 1976, "Turbulence Structure in the Convective Boundary Layer," *J. Atmos. Sci.*, **33**, 2152-2169.
3. Tatarskii, V. I., 1971, The Effects of the Turbulent Atmosphere on Wave Propagation. TT-68-50464, National Technical Information Service, Springfield, VA 22161.
4. Morse, P. M., and K. U. Ingard, 1968, Theoretical Acoustics, McGraw-Hill Book Company, New York.
5. Landau, L. D., and E. M. Lifshitz, 1987, Fluid Mechanics, Pergamon Press, New York.
6. Menzel, D. H., ed., 1960, Fundamental Formulas of Physics, Dover Publications, Inc., New York.
7. Goedecke, G. H., 1992, "Scattering of Acoustical Waves by a Spinning Atmospheric Turbule," CR-92-0001-2, U. S. Army Research Laboratory, White Sands Missile Range, NM 88002-5501.

PROBLEMS WITH CREEPING WAVES IN A NON-LINEAR SOUND SPEED GRADIENT

C.G. Don

Department of Physics, Monash University
Clayton, Victoria, Australia 3168.

An apparently satisfactory generalized theory for the propagation of sound in an atmosphere supporting a non-linear sound speed gradient will be briefly reviewed. This theory simplifies to the standard creeping wave model for the case of a linear gradient. When the gradient is exponential, however, the solution of the resultant residue series involves confluent hypergeometric functions. If only one or a few terms of the series are used, the results appear to be in excellent agreement with the linear case when an appropriate gradient is chosen. However, there is a problem as the series does not converge. Alas, this is not the only problem. Some of the curious results from the solution will be described and the assumptions of the theory discussed, with the hope that perhaps someone will spot the flaw in the approach.

INTRODUCTION

At the fifth international symposium on long range sound propagation, a theory which allowed an exponential sound speed gradient to be incorporated in creeping wave theory was introduced¹. The following paper contains a more detailed discussion of a generalized theory, which reduces to the specific exponential gradient case discussed in the earlier paper and also simplifies to the linear gradient solution^{2,3}. When numeric solutions are produced for specific exponential gradients, a number of problems arise. These will be discussed in the later sections of this paper. Much of the initial derivation closely follows the discussion found in Pierce², and so will only be briefly indicated in the following work.

GENERALIZED THEORY

The pressure $p(z,r)$ at height z and a horizontal distance r from a point source of strength S above a plane with a normalized impedance Z_n can be expressed as³

$$p(z,r) = -S \int_{-\infty}^{\infty} H_0^1(kr) P(z,k) k dk \quad (1)$$

where k is the wavenumber. Assume that $P(z,k)$ has two solutions of the

inhomogeneous Helmholtz equation, designated $\Psi(z,k)$ and $\Phi(z,k)$, where $\Psi(z,k)$ satisfies the Sommerfeld radiation condition and $\Phi(z,k)$ must comply with the lower boundary condition

$$\left. \frac{d\Phi(z,k)}{dz} \right|_{z=0} + Q \Phi(z,k) \Big|_{z=0} = 0 \quad (2)$$

with $Q = ik_0/Z_n$. The two solutions are linked at the source height h_s by²

$$P(z,k) = \frac{\Psi(z>, k) \Phi(z<, k)}{W_{ron} \Big|_{z=h_s}} \quad (3)$$

where the notation $z>$ means that $\Psi(z>) = \Psi(h_s)$ if the source is above the receiver height, h_r , and $\Phi(z<) = \Phi(h_s)$ if $h_s < h_r$. In the above equation, the Wronskian of Ψ and Φ , designated W_{ron} , is evaluated at the height h_s .

To obtain solutions of the Helmholtz equation,

$$\frac{d^2 P(z,k)}{dz^2} + \left[\left(\frac{\omega}{c(z)} \right)^2 - k^2 \right] P(z,k) = 0 \quad (4)$$

for a particular form of the sound speed $c(z)$ it is, in general, necessary to transform z and k into new variables x and τ in order to obtain an equation with recognized solutions.. Assume the general transform has the form $P(z,k) = M(z,\tau) f(x,\tau)$, and that the transformed version of Eq.(4) has the two solutions $v(x,\tau)$ and $w(x,\tau)$, which correspond to $V(z,k) = M(z,\tau) v(x,\tau)$ and $W(z,k) = M(z,\tau) w(x,\tau)$. Further, let $\Psi(z,k) = W(z,k)$ and $\Phi(z,k) = V(z,k) - \kappa W(z,k)$. Since the latter expression must comply with the boundary condition, Eq.(2), then

$$\kappa = \frac{V_o' + Q V_o}{W_o' + Q W_o} \quad (5)$$

where V_o and W_o are $V(z,k)$ and $W(z,k)$ evaluated at $z=0$. Let v_o and w_o be the transformed quantities corresponding to V_o and W_o , while $V_o' = dV/dz|_{z=0}$, with a similar expression for W_o' . It follows that $V_o' = M_o' v_o + M_o v_o' dx/dz|_{z=0}$, where it is understood that v_o' implies the derivative with respect to x (since v is in the x -domain) and M_o' is the derivative with respect to z . Both derivatives are evaluated when $z = 0$ and Then κ can be

expressed in terms of the transformed quantities as

$$\kappa = \frac{v_o' - q v_o}{w_o' - q w_o} \quad (6)$$

where

$$q = - \frac{Q M_o + M_o'}{M_o \frac{dx}{dz} \Big|_{z=0}} \quad (7)$$

and so the transform of $\Phi(z,k)$ can be written as

$$\Phi(z,k) = M(z,\tau) \{ v(x,\tau) - \kappa w(x,\tau) \} . \quad (8)$$

As the Wronskian of the two solutions of Eq.(4) can be expressed in terms of the Wronskian of the transformed solutions, w_{ron} , by

$$W_{ron} = M(z,\tau)^2 \frac{dx}{dz} w_{ron} , \quad (9)$$

then Eq.(3) becomes

$$P(z,k) = \frac{M(z>,\tau) w(x>,\tau) M(z<,\tau) [v(x<,\tau) - \kappa w(x<,\tau)]}{\left\{ M(z,\tau)^2 \frac{dx}{dz} w_{ron} \right\} \Big|_{z=h_s}} \quad (10)$$

Assume that, in general, τ is related to the wavenumber k by

$$\tau = (k^2 - k_A^2) \ell^2 \quad (11)$$

where k_A and ℓ are constants which will depend on the choice of $c(z)$. Since $d\tau = 2\ell^2 k dk$, then Eq.(1) can be re-written as

$$p(z,r) = -S \int_{-\infty}^{\infty} H_0^1(kr) \frac{M(z>,\tau) M(z<,\tau) w(x>,\tau) [v(x<,\tau) - \kappa w(x<,\tau)]}{\left\{ M(z,\tau)^2 \frac{dx}{dz} \right\} \Big|_{z=h_s} 2\ell^2 w_{ron} \Big|_{z=h_s}} d\tau \quad (12)$$

Assuming that appropriate well behaved solutions for $w(x,\tau)$ and $v(x,\tau)$ can be determined, then there will be no poles in the first term of the above integrand although there will be poles in the second term when the denominator of κ goes to zero. These poles will occur at τ values, designated as τ_n , obtained from Eq.(6), such that

$$w(o,\tau_n) - q w(o,\tau_n) = 0 . \quad (13)$$

Equation (12) can then be evaluated by contour integration, becoming $2\pi i$ times the sum of the residues corresponding to poles in the positive

imaginary half of the τ -plane. Note that by substituting Eq.(13) into the expansion of w_{ron} evaluated at $z = 0$, gives

$$v'(o, \tau_n) - q v(o, \tau_n) = - \frac{w_{ron}|_{z=0}}{w(o, \tau_n)}, \quad (14)$$

which can be used as the numerator of Eq.(6). The poles of Eq.(12) are simple, so the residue series resulting from the second term of Eq.(12) can be written as

$$p(z, r) = - 2\pi i S \sum H_0^1(k_n r) A(\tau) \frac{w(h_s, \tau_n) w(h_r, \tau_n)}{w(o, \tau_n) \frac{d}{d\tau} [w(o, \tau_n) - q w(o, \tau_n)]} \quad (15)$$

where

$$A(\tau) = \frac{1}{2 l^2} \frac{M(h_s, \tau) M(h_r, \tau)}{\{ M(z, \tau) \frac{dx}{dz} \}|_{z=h_s}} \frac{w_{ron}|_o}{w_{ron}|_{h_s}}. \quad (16)$$

The value of k_n required in Eq.(15) is obtained from Eq.(11) as

$$k_n = \sqrt{\frac{\tau_n}{l^2} + k_A^2}. \quad (17)$$

Equations (15) to (17) are the general expressions required to determine the pressure at the receiver, however, an approximate form, avoiding the Hankel function, can be derived as follows. Providing $k_n r$ is large and $\tau_n \ll 2k_A^2 l^2$, then

$$H_0^1(k_n r) \cong \sqrt{\frac{2}{\pi r k_A}} \exp(i [k_A r - \pi/4 + \tau_n r / 2k_A l^2]), \quad (18)$$

and by defining $\xi = r/2k_A l^2$, Eq.(15) becomes

$$p(z, r) = \frac{-2Sl e^{i\pi/4}}{r} \sqrt{4\pi\xi} e^{ik_A r} \sum A(\tau) e^{i\xi\tau_n} \frac{w(h_s, \tau_n) w(h_r, \tau_n)}{w(o, \tau_n) \frac{d}{d\tau} [w(o, \tau_n) - q w(o, \tau_n)]}. \quad (19)$$

Providing the ratio of the Wronskians in Eq.(16) are independent of the particular choice of $v(x, \tau)$ and $w(x, \tau)$, then the residue series represented by either Eqs.(15) or (19) depends only on the single solution $w(x, \tau)$ and it is not necessary to specify the exact nature of $v(x, \tau)$.

LINEAR GRADIENT CASE

Following Pierce², if a linear gradient $1/c(z)^2 = (1/c_0^2)(1-2z/R)$ is assumed, where R is the radius of curvature of the rays in a linear gradient, then Eq.(4) becomes

$$\frac{d^2 P(z,k)}{dz^2} + \left[k_0^2 - k^2 + \left(\frac{2k_0^2}{R} \right) z \right] P(z,k) = 0 \quad (20)$$

By letting $\tau = (k^2 - k_0^2)l^2$ where $l = [R/2k_0^2]^{1/3}$ and applying the transform $x = \tau - z/l$, Eq.(20) is converted into the Airy equation with solutions of the form $Ai(\tau-z/l)$. In this case, $k_A = k_0$, $P(z,k) = P(x,\tau)$, so $M(z,\tau) = 1$ and $M(z,\tau) = 0$ which gives $q = lQ = ik_0 l / Z_n$, as stated by Pierce. The above transform requires $dx/d\tau = 1$, so by noting that the Airy equation gives $w(o,\tau_n) = x w(o,\tau_n)$ and using Eq.(13), there results

$$\frac{d}{d\tau} [w(o,\tau_n) - q w(o,\tau_n)] = (\tau_n - q^2) w(o,\tau_n) \quad (21)$$

For the Airy functions chosen by Pierce, the Wronskian is given by $(1/2\pi)e^{-i\pi/6}$, which is independent of x or z and so $[w_{ron}]_o = [w_{ron}]_{h_s}$.

Consequently, Eq.(19) reduces to

$$p(z,r) = \frac{e^{i\pi/4}}{r} \sqrt{4\pi\xi} S e^{ik_0 r} \int e^{i\xi\tau_n} \frac{Ai(z>) Ai(z<)}{(\tau_n - q^2) Ai(o,\tau_n)^2} \quad (22)$$

which is the form provided by Pierce. By noting that $(\tau_n - q^2)w(o,\tau_n)^2 = -([w(o,\tau_n)]^2 - \tau_n[w(o,\tau_n)]^2)$, then Eq.(15) can be expressed in the form given by Berry and Daigle³. Thus the general residue series, represented by Eq.(15), reduces to the established formulae for the linear gradient situation. Although Pierce specifies the two Airy functions to be used as solutions, only one is actually involved in the final residue series.

AN EXPONENTIAL GRADIENT

Assuming a sound speed $c(z) = c_A / (1 - \beta e^{-\alpha z})$, where $\beta = (c_0 - c_A)/c_0$, then Eq.(4) becomes the confluent hypergeometric equation⁴.

$$x \frac{d^2 f(x,\tau)}{dx^2} + (b-x) \frac{df(x,\tau)}{dx} - af(x,\tau) = 0 \quad (23)$$

if use is made of the transforms

$$P(z,k) = (\beta e^{-\alpha z})^{\sqrt{\tau}} e^{-d\beta e^{-\alpha z}} f(x, \sqrt{\tau}) = M(z, \tau) f(x, \sqrt{\tau}), \quad (24)$$

$$x = 2d\beta e^{-\alpha z} \quad \text{and} \quad \tau = (k^2 - k_A^2) / \alpha^2,$$

where $b = 2\sqrt{\tau} + 1$, $a = \sqrt{\tau} - d + 1/2$, $d = ik_A/\alpha$, and $k_A = \omega/c_A$. The main solution of Eq.(23) considered here is $y_1 = F(a,b;x)/\Gamma(b)$, although another solution $y_2 = x^{1-b}F(a-b+1, 2-b;x)/\Gamma(b)$ will also be considered, where $F(a,b,x)$ is the confluent hypergeometric function^{5,6} and the reasons for invoking $\Gamma(b)$ were discussed in the earlier paper¹.

By comparing the last transform in Eq.(24) with Eq.(17), it is apparent that $l^2 = 1/\alpha^2$ while $z = 0$ implies $x_0 = 2d\beta$ and $dx/dz|_0 = -2\alpha d\beta$. As a consequence, $M_0 = \beta^{\sqrt{\tau}} e^{-d\beta}$ and $M_0' = [-\alpha\sqrt{\tau} + d\beta\alpha]\beta^{\sqrt{\tau}} e^{-d\beta}$, and so Eq.(7) becomes

$$q = \frac{Q - \alpha\sqrt{\tau} + d\beta\alpha}{2d\beta\alpha} \quad (25)$$

which is no longer independent of τ . Equation (16) simplifies to

$$A(\tau) = \frac{-\alpha}{4d\beta} \left[e^{-\alpha\sqrt{\tau}(h_r - h_s) + \alpha h} e^{-d\beta(e^{-\alpha h_r} - e^{-\alpha h_s})} \right] \frac{w_{\text{ron}}|_0}{w_{\text{ron}}|_{h_s}},$$

$$= \frac{-\alpha}{4d\beta} \left[e^{-\alpha\sqrt{\tau}(h_r + h_s)} - d\beta(e^{-\alpha h_r} + e^{-\alpha h_s} - 2) \right], \quad (26)$$

since the ratio of the Wronskians^{5,6} can be expressed as

$$\frac{w_{\text{ron}}|_0}{w_{\text{ron}}|_{h_s}} = e^{-\alpha b h_s} \frac{2d\beta(1 - e^{-\alpha h_s})}{e} \quad (27)$$

for any of the possible pairs of solutions of Eq.(23). [Note that several typographical errors in the equations of Ref.1 have been corrected here.]

PREDICTIONS FOR AN EXPONENTIAL GRADIENT

Figure 1 shows the exponential gradients considered in the following study, assuming $c_0 = 335.0 \text{ ms}^{-1}$ for various α values. It is apparent that $\alpha=0.3$ is a reasonable approximation to the linear gradient of 1.03 s^{-1} and should, therefore, produce attenuations not unlike the linear theory prediction. Figure 2 presents data from the two theories up to 2kHz for the case of a

Fig.1: Exponential sound speed gradients for various α values with $c_0 = 335.0$ m/s and linear gradient assumed in this work.

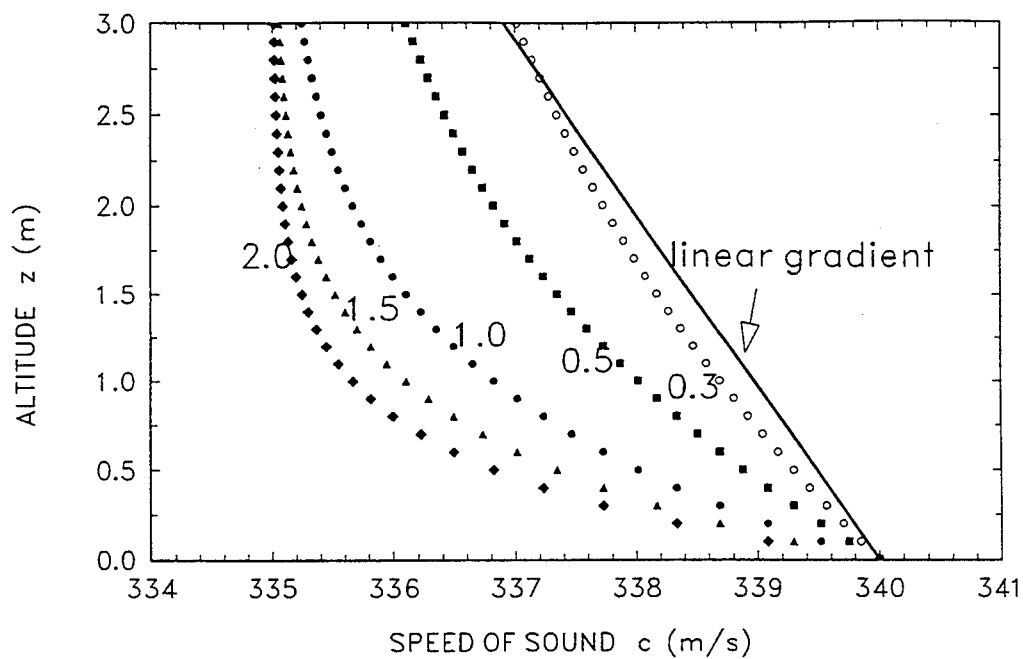
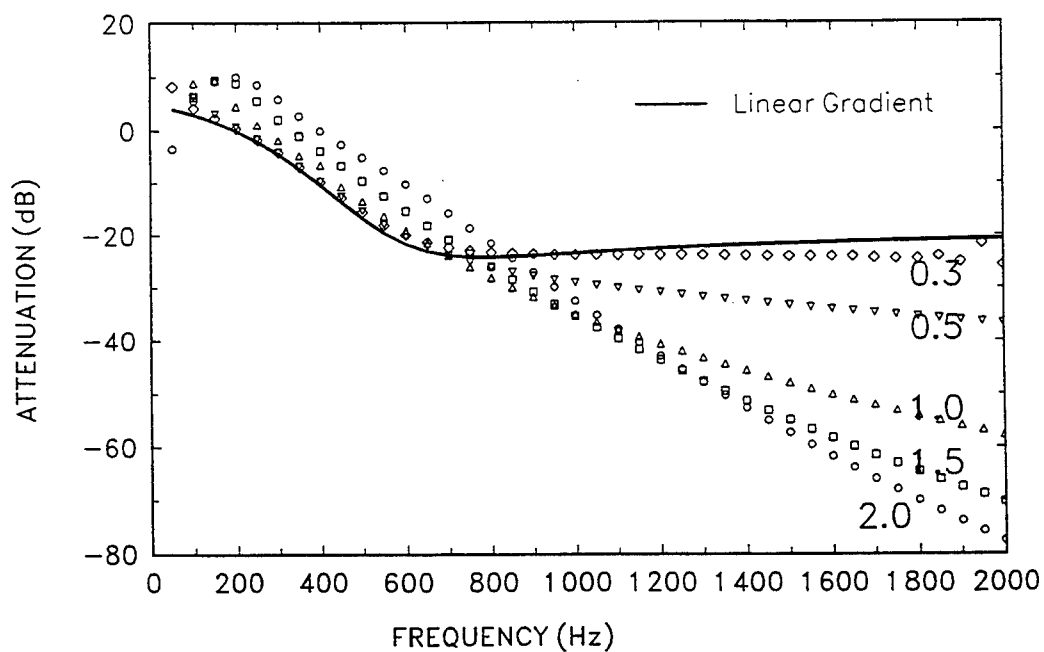


Fig.2: First term predictions for various α values with $h_s = h_r = 0.8$ m, $r = 50$ m.



source and receiver height of 0.8m and a separation of 50m. It is apparent that the curve for $\alpha=0.3$ is indeed closely following the linear gradient prediction. However, several problems have arisen.

Firstly, the non-linear predictions are those obtained using only the *first* term of the residue series. Addition of further residues can cause the predicted attenuation to alter drastically, as indicated in Table 1 for two different source-receiver distances. As a comparison, the table also shows the corresponding linear gradient prediction. It is apparent that the initial sum is in reasonable agreement - considering that $\alpha = 0.3$ is not quite equivalent to the linear case. However, the addition of further terms produces unlikely results; an effect which is especially pronounced at lower frequencies than those tabulated. At even higher frequencies, where perhaps 40 poles occur, the addition of the first thirty or more terms causes only a

Table 1: Excess attenuations calculated from exponential and linear models, showing effect of adding additional terms in residue series. The calculations assume $h_s = h_r = 0.8\text{m}$, $\alpha = 0.3$ and $c_0 = 335\text{m/s}$.

Frequency	Pole No.	τ_n		Attenuation (dB)		Linear Value	
				$r = 50\text{m}$	$r = 200\text{m}$	50m	200m
300 Hz	1	-4.59	3.25	-4.2	-32.2	-4.49	-35.9
	2	0.89	7.07	-3.9	-32.2		
	3	7.27	6.34	-5.2	-32.2		
	4	13.31	4.29	-2.2	-32.5		
	5	19.68	0.85	0.4	-12.6		
	+	-8.23	1.66	9.3	-2.8		
500 Hz	1	-15.13	9.22	-15.6	-67.6	-16.7	-72.3
	2	-6.10	17.01	-15.8	-67.6		
	3	4.27	20.65	-16.2	-67.6		
	4	14.95	21.15	-15.4	-67.6		
	5	25.65	19.40	-16.7	-67.6		
	6	36.28	15.88	-15.4	-67.7		
	7	46.82	10.89	-5.2	-67.7		
	8	57.24	4.67	6.9	-14.0		
	+	-25.06	15.27	7.0	-14.0		

Fig.3: Surface of τ plane at 500Hz, $\alpha = 0.32$, showing location of (a) negative poles and the single positive pole. The pole marked (1) is assumed to be the first pole.

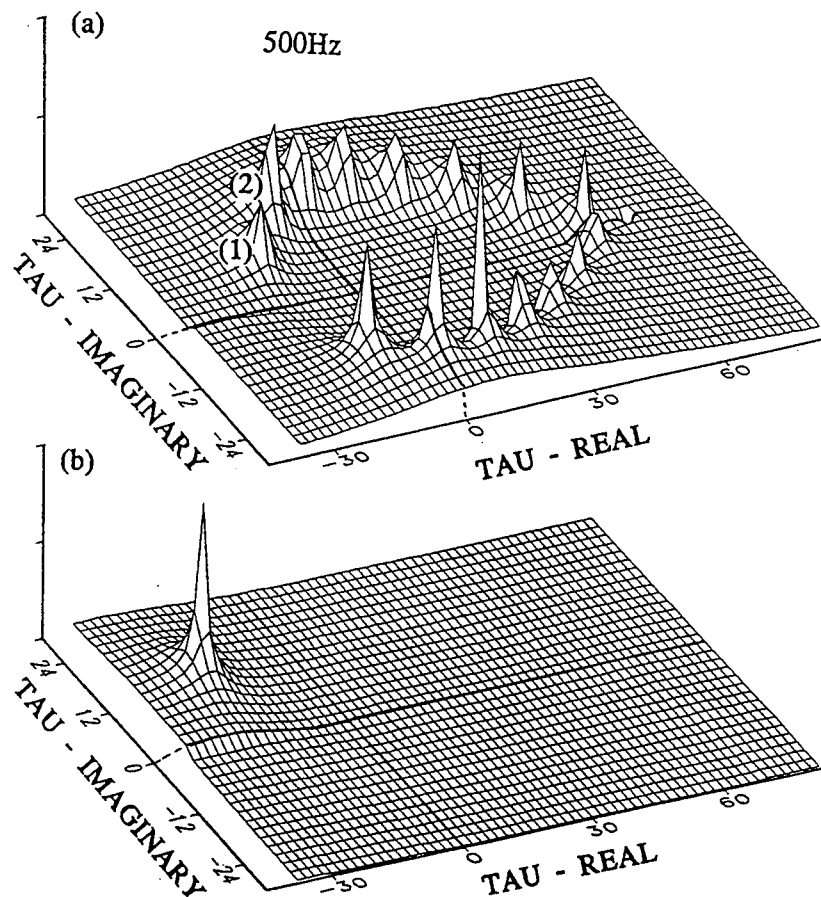
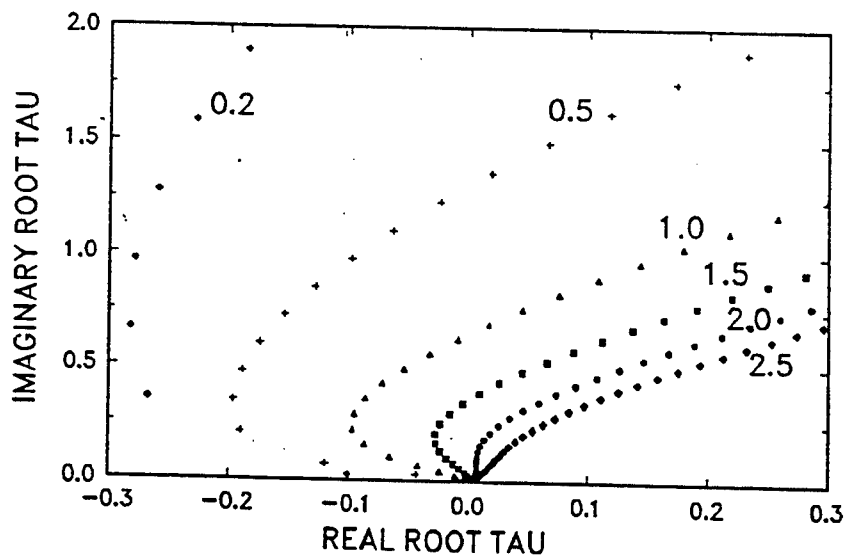


Fig.4: The location of positive poles in 20Hz intervals for various alpha values.



small change to the residue sum, however, addition of the last few terms changes the sum drastically. The problem is caused by the last poles of the series lying near the real τ axis, see Fig.3(a), with small imaginary components, which makes the Hankel function become very large. What flaw in the theory produces this behaviour is unknown.

While the integration is over the τ plane, the calculations involve $\sqrt{\tau}$ so there are two possible solutions. The majority of poles are obtained from the negative square root, however, there is a single "positive pole", Fig.3(b). The last pole for both frequencies in the table is the positive pole, which wanders across the quadrants of the τ plane, as indicated in Fig.4. If included in the residue series, it markedly alters the residue sum at lower frequencies, although its effect becomes negligible beyond 1kHz. The significance of the positive pole is unclear.

There is a regular pattern to the position of the negative poles in the $\sqrt{\tau}$ plane, as shown in Fig.5. When poles for different α values are overlapped, the poles fall on well defined contours. For large α -values, poles have been located out to 10kHz and beyond. However, for an α -value of 0.5 the pole seeking program becomes erratic about 5kHz, or at lower frequencies for smaller α -values. The cause of this behaviour is the presence of thousands of poles, as shown in Fig.6. How does one choose the 'first' pole from such a complicated pole system? This behaviour has prevented testing the theory with a smaller α -value, such as 0.01. This value should be an excellent approximation to the linear gradient case, however, a multitude of poles occur well below 200Hz. The broadening of the pole region begins relatively suddenly as the frequency is increased and appears to happen at all α -values, although the onset does not begin until above 12kHz for $\alpha=2.0$.

The first negative pole produces attenuations which agree very closely with the linear gradient case for small α -values, so it is interesting to consider how the position of these poles vary with frequency. This data are shown in Fig.7 for various α values. It is apparent that for larger α values the trend is quite smooth and it would seem that the results could be extrapolated if it was necessary to locate poles at still higher frequencies. At lower α values the trend is clear until a point where the onset of the broad band of poles causes the values to fluctuate and then become almost random. When the first term is used to calculate attenuations it is again noticeable, Fig.8,

Fig.5: The location of negative poles in 500Hz intervals up to 20kHz. The row with the smallest real $\sqrt{\tau}$ values are the first poles.

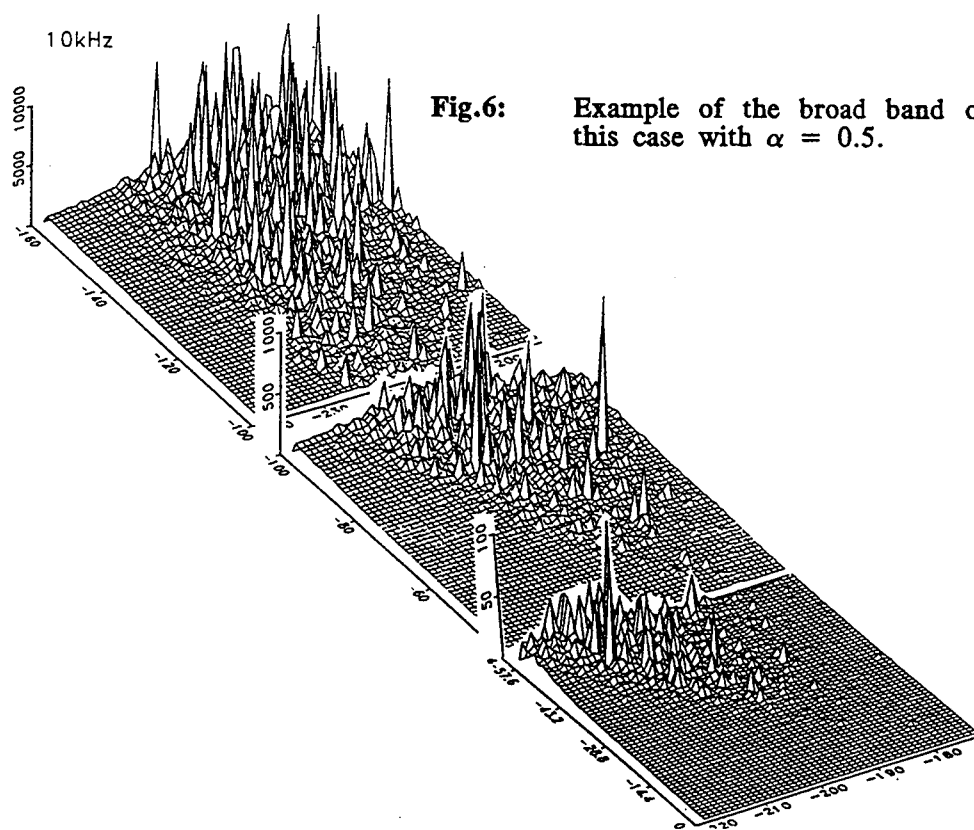
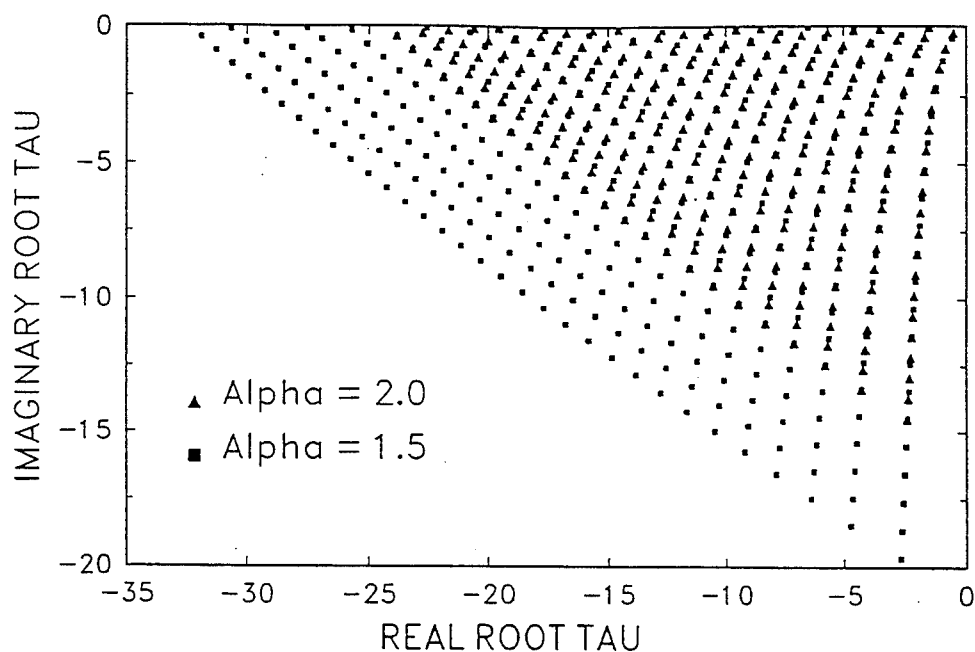


Fig.6: Example of the broad band of poles, this case with $\alpha = 0.5$.

that they follow a smooth trend until some frequency where they become unstable. However, the curious thing is that the frequency at which the break-up occurs is smaller for the attenuation measurements than that observed in the pole locations. In principle, the location of the first poles in the frequency region beyond where broadening starts could be predicted by extrapolating the lower frequency trend. However, this doesn't help as the attenuation calculations will already have failed. Why the calculations of attenuations for the first pole breaks down in this way is another problem yet to be solved.

The work described above used the solution y_1 of the confluent hypergeometric function, however, when the poles for solution y_2 are obtained and used to determine the attenuations, the results are identical to a high accuracy. This is despite the fact that the numbers generated at different stages within the calculation vary markedly between the two solutions.

As the solutions y_1 and y_2 were calculated from a series^{1,4}, it was possible that the series was failing to give correct values and thereby inducing spurious poles. As a check, the results obtained for every pole were substituted into Eq.(23) and also transformed back and used in Eq.(4) along with the appropriate $c(z)$ value. On all occasions, the solutions were valid within an uncertainty which could be ascribed to a small rounding error. This would appear to eliminate this possible source of error.

CONCLUSION

The generalized theory presented here simplifies to the well established solution for a linear gradient. When an exponential gradient is considered, the solution involving confluent hypergeometric functions raises a number of problems. The main fact is that the residue series fails to converge, implying that the assumptions involved in invoking the series are invalid. However, the predictions obtained from just the first pole are tantalizingly in agreement with linear gradient predictions for small α values, suggesting that the overall theory is not too far from being valid.

ACKNOWLEDGEMENT

The author would like to thank Dr A.J.Cramond for the use of his program for calculating the linear gradient predictions used in this work.

Fig.7: Location of first poles for different α values, showing the effect of broadening of the pole pattern at lower α values.

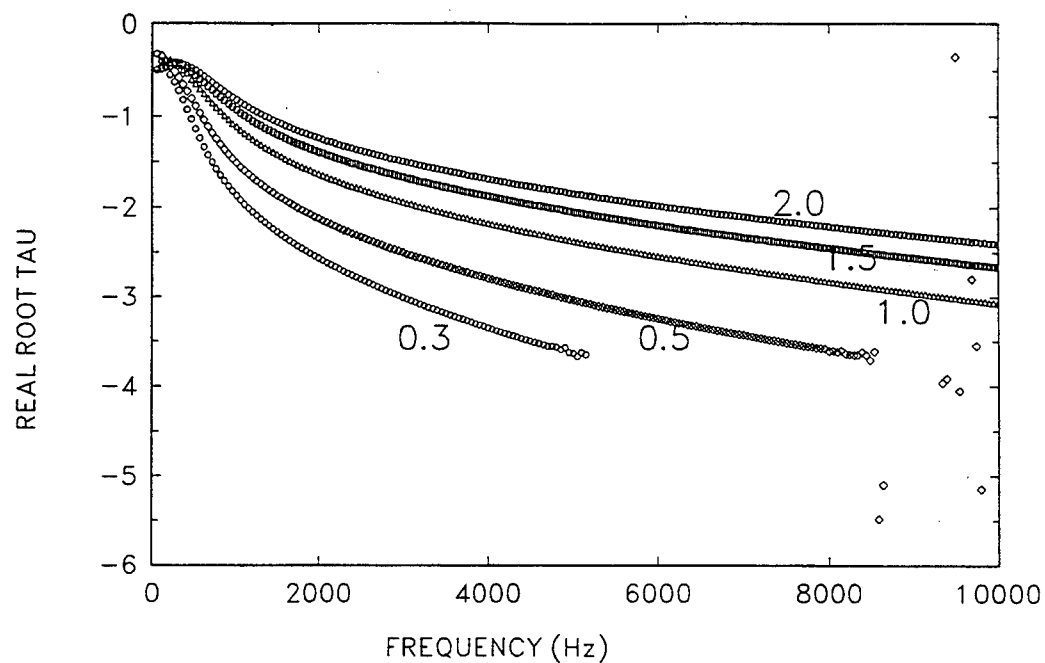
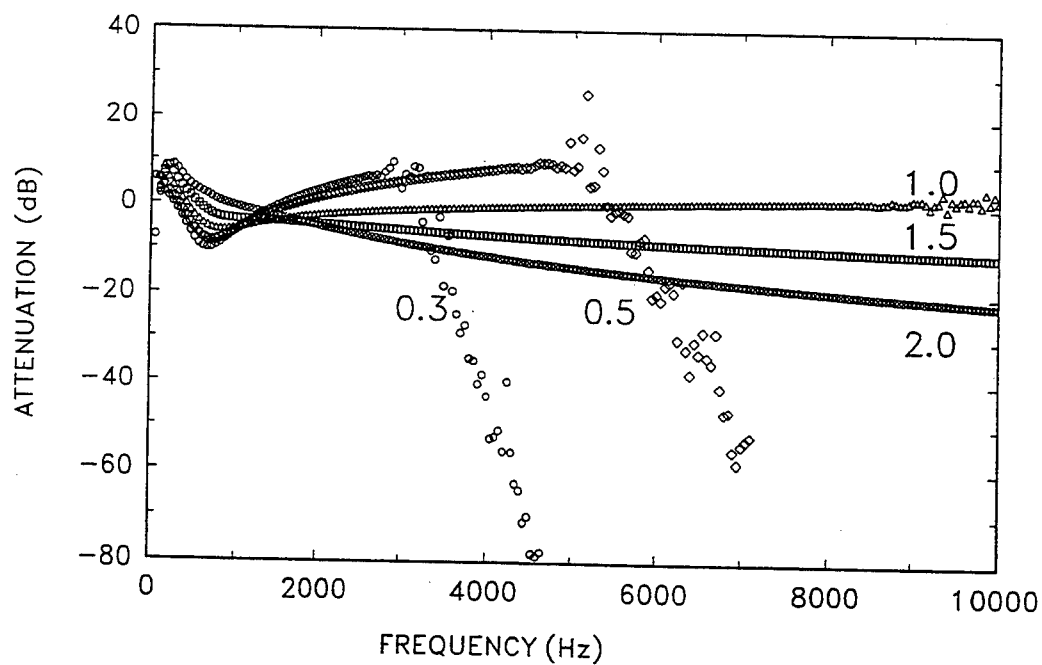


Fig.8: First term predictions for various alpha values. Note that the breakdown occurs at a lower frequency than in Fig.7.



REFERENCES

- (1) C.G.Don. "Creeping waves in an atmosphere supporting a non-linear sound speed gradient", Proc. 5th Int. Symp. on Long Range Sound Prop., p96-102, Milton Keynes 24-26 May (1992).
- (2) A.D.Pierce. "Acoustics: An Introduction to its Physical Principles and Applications" Acoust. Soc. Am., (1989).
- (3) A.Berry and G.A.Daigle. "Controlled experiments of the diffraction of sound by a curved surface", J. Acoust. Soc. Am., 83, 2047-2058 (1988).
- (4) P.M.Morse and H.Feshback. "Methods of Theoretical Physics" McGraw Hill (1953).
- (5) L.J.Slater. "Confluent Hypergeometric Functions" Cambridge University Press (1960).
- (6) M. Abramowitz and I. A. Stegun. "Handbook of Mathematical Functions" Dover (1970).

A New Generalised Terrain Parabolic Equation (GT-PE)

M West and R A Sack

Department of Applied Acoustics
University of Salford, Salford M5 4WT, UK

Abstract

Many of the new PE algorithms for propagation over undulating terrain require a transformation of the computational region such that the transformed domain is rectangular and can be solved by conventional PE algorithms. These methods all have numerical errors arising from the transformation process. In the GT-PE a very simple terrain following transformation is used which does not generate these errors. This paper describes the derivation of the new PE and presents some predictions for propagation over a test hill.

1. Introduction

Predictions of atmospheric sound propagation over *flat* ground have been made successfully using parabolic equation methods¹ for some time. More recently attempts have been made^{2,3} to obtain predictions over undulating terrain. In reference 2 a prediction model for propagation over a simple circular section hill was developed which used a conformal mapping of the piece of atmosphere directly above the hill into a rectangular domain. In reference 3 this model was extended to deal with a more general terrain section broken down into concatenated circular section pieces. The atmosphere above each piece was subject to a separate conformal transformation. This procedure is particularly liable to numerical errors which are described in reference 4.

In this paper a new PE is derived which can give predictions over any smooth terrain profile section without any need for a conformal transformation. The transformation used is known as the "*sigma transformation*" and simply follows the terrain profile at equally incremented heights (Figure 1). The PE algorithm developed allows predictions over undulating terrain which include the effects of ground impedance and meteorology. The model has been tested for propagation over a single test hill.

2. Sigma Transformed Two-Dimensional Helmholtz Equation

The two-dimensional Helmholtz equation for velocity potential ψ in Cartesian coordinates (x,z) is:

$$\frac{\partial^2 \psi}{\partial x^2} + \frac{\partial^2 \psi}{\partial z^2} + k^2 \psi = 0 \quad (2 - 1)$$

This can be written in the sigma transformation coordinates (ξ, η) defined in Figure 1 as follows:

(H' and H'' are the first and second x or ξ derivatives of the terrain profile function H(x).)

$$\frac{\partial^2 \psi}{\partial \xi^2} - 2H' \frac{\partial^2 \psi}{\partial \xi \partial \eta} - H'' \frac{\partial \psi}{\partial \eta} + [(H')^2 + 1] \frac{\partial^2 \psi}{\partial \eta^2} + k^2 \psi = 0 \quad (2 - 2)$$

In the derivation of the flat ground PE¹ we separate the potential ψ into an x (or ξ) dependent exponential term multiplied by a modulator φ :

$$\psi = \exp (ik_0 \xi) \varphi (\xi, \eta) \quad (2 - 3)$$

Using this definition in equation (2.2) we obtain the "*modulator*" wave equation:

$$\begin{aligned} \frac{\partial^2 \varphi}{\partial \xi^2} + 2ik_0 \frac{\partial \varphi}{\partial \xi} - k_0^2 \varphi - 2H' \left\{ \frac{\partial^2 \varphi}{\partial \xi \partial \eta} + ik_0 \frac{\partial \varphi}{\partial \eta} \right\} - H'' \frac{\partial \varphi}{\partial \eta} \\ + \{ 1 + (H')^2 \} \frac{\partial^2 \varphi}{\partial \eta^2} + k^2 \varphi = 0 \end{aligned} \quad (2 - 4)$$

Equation (2 - 4) differs from its flat ground counterpart by the presence of new coefficients which depend on H' and H'' and new terms $\partial^2 \varphi / \partial \xi \partial \eta$, $\partial \varphi / \partial \eta$.

3. "Wide Angle" PE Core

We seek a second order accurate PE which can be obtained by substitution of the narrow angle PE into equation (2 - 4) integrated over one range step following the procedure described in reference 5.

The narrow angle PE obtained by neglection of $\partial^2 \varphi / \partial \xi^2$ and $\partial^2 \varphi / \partial \xi \partial \eta$ in equation (2.4) is:

$$\frac{\partial \varphi}{\partial \xi} = \frac{i}{2k_0} L_1 (\varphi) \quad (3 - 1)$$

where

$$L_1 = \alpha \frac{\partial^2}{\partial \eta^2} - \beta \frac{\partial}{\partial \eta} + \gamma \quad (3 - 2)$$

and

$$\alpha(\xi) = 1 + (H')^2, \quad \beta(\xi) = 2ik_0 H' + H'', \quad \gamma(\eta) = k(\eta)^2 - k_0^2 \quad (3 - 3)$$

Integrating equation (2 - 4) over the range step $\xi = a$ to b gives:

$$\left[\frac{i}{2k_0} L_1(\varphi) + 2ik_0 \varphi - 2H' \frac{\partial \varphi}{\partial \eta} \right]_a^b + I_\alpha + I_\chi + I_\gamma = 0 \quad (3 - 4)$$

where the integrals can each be written in a general form

$$I_n^R = \int_a^b R(\xi) \varphi^{(n)} d\xi \quad (3 - 5)$$

where R is respectively α , χ and γ and n is correspondingly 2, 1 or 0 where

$$\varphi^{(n)} = \frac{\partial^n \varphi}{\partial \eta^n} \quad (3 - 6)$$

and

$$\chi = H'' - 2ik_0 H' \quad (3 - 7)$$

If I_n is replaced by a linear combination of $\varphi^{(n)}$ values at the ends of the interval (see references 4 and 5)

$$I_n = A_n \varphi^{(n)}(a) + B_n \varphi^{(n)}(b) \quad (3 - 8)$$

then we can determine approximate values of the coefficients A_n and B_n assuming a linear variation of R over the interval* $b-a$

$$A_n \approx \Delta \left\{ \frac{R(a)}{3} + \frac{R(b)}{6} \right\} \quad (3 - 9a)$$

$$B_n \approx \Delta \left\{ \frac{R(a)}{6} + \frac{R(b)}{3} \right\} \quad (3 - 9b)$$

The integrals in the PE (equation (3 - 4)) can now be replaced from (3 - 8) and (3 - 9). Discretising all the η derivatives in the resulting equation leads to our wide angle core terrain PE.

*The assumption of linear variation of R over a range step is valid only for terrain profiles with small H' and H'' . A more accurate procedure for evaluating the integrals, applicable to profiles with larger H' and H'' values, will be presented in a future paper.

$$\begin{aligned}
& \left[\frac{1}{\Delta\eta^2} \left[\frac{i \alpha(b)}{2k_0} + B_\alpha \right] \delta^2 - \frac{1}{\Delta\eta} \left[\frac{i}{2k_0} \beta(b) + 2H'(b) - B_x \right] \delta \right. \\
& \quad \left. + \left[\frac{i\gamma}{2k_0} + 2ik_0 + B_\gamma \right] \right] \varphi(b) = \\
& \left[\frac{1}{\Delta\eta^2} \left[\frac{i\alpha(a)}{2k_0} - A_\alpha \right] \delta^2 - \frac{1}{\Delta\eta} \left[\frac{i}{2k_0} \beta(a) + 2H'(a) + A_x \right] \delta \right. \\
& \quad \left. + \left[\frac{i\gamma}{2k_0} + 2ik_0 - A_\gamma \right] \right] \varphi(a)
\end{aligned}
\tag{3 - 10}$$

where

$$\frac{\partial \varphi}{\partial \eta} = \frac{\delta \varphi}{\Delta \eta}, \quad \delta \varphi_m = \frac{(\varphi_{m+1} - \varphi_{m-1})}{2}
\tag{3 - 11a}$$

and

$$\frac{\partial^2 \varphi}{\partial \eta^2} = \frac{\delta^2 \varphi}{\Delta \eta^2}, \quad \delta^2 \varphi_m = (\varphi_{m+1} - 2\varphi_m + \varphi_{m-1})
\tag{3 - 11b}$$

Equation (3 - 10), like its flat ground counterpart, can be written in tridiagonal form inspite of its increased complexity. For non-turbulent conditions all the terms in square brackets in (3 - 10) can be calculated prior to the main range dependent solution. The resulting algorithm is very efficient and its run time is comparable to that of the flat ground CN-PE.

4. The Ground Boundary and Upper Atmosphere Conditions for an Undulating Terrain Profile

4.1 Ground boundary condition

We assume that the normal impedance condition can still be applied at right angles to the undulating ground surface at each range step. The normal impedance condition is

$$\frac{\partial \psi}{\partial n} = - ik_0 \hat{\beta} \psi \quad (4 - 1)$$

where the admittance of the ground is

$$\hat{\beta} = \frac{\rho_0 c}{Z_{GND}} \quad (4 - 2)$$

Z_{GND} being the normal impedance of the ground. The derivative with respect to n is expanded with the chain rule in terms of the derivatives with respect to ξ and η . The velocity potential ψ is replaced by the carrier modulator product given in equation (2 - 3) which gives

$$- ik_0 \hat{\beta} \varphi = \left[\frac{\partial \varphi}{\partial \eta} \right]_{\eta=0} \frac{1}{\cos \alpha_H} - \left[\left[\frac{\partial \varphi}{\partial \xi} \right]_{\eta=0} + ik_0 \varphi_0 \right] \sin \alpha_H \quad (4 - 3)$$

where $\alpha_H(\xi)$ is the angle between the tangent to the terrain section and the horizontal. A second order accurate discretisation of both derivatives of φ in ξ and η is essential to accommodate the logarithmic variation in sound speed close to the ground. The discretised version of equation (4 - 3) can then be written

$$\varphi_0(b) = u \varphi_1(b) + v \varphi_2(b) + w \varphi_0(a) + y \varphi_0(\bar{a}) \quad (4 - 4)$$

where

$$u = \frac{4}{d\epsilon}, \quad v = -\frac{u}{4}, \quad w = \frac{2 \sin \alpha_H}{\Delta \xi d}, \quad y = -\frac{w}{4} \quad (4 - 5)$$

with

$$\epsilon = 2\Delta\eta \cos \alpha_H \quad (4 - 6)$$

and

$$d = - ik_0 \hat{\beta} + 3/\epsilon + \left(\frac{1}{\Delta \xi} + ik_0 \right) \sin \alpha_H \quad (4 - 7)$$

The subscripts on φ refer to the z mesh index, 0 corresponding to the ground. The current range step, as in the core PE, is from $\xi = a$ to b , the new solution being evaluated at $\xi = b$, where $\Delta \xi = b - a$ and $\bar{a} = a - \Delta \xi$.

4.2 Sommerfeld upper boundary condition (SUBC)

A simple and elegant method for treating the upper computational atmospheric boundary which avoids the need for an artificial absorbing layer has been described in reference 6. The method establishes approximate Sommerfeld radiation conditions at the upper boundary. The φ values at the top of the atmosphere are corrected with terms which depend on the angle of ray incidence on the upper boundary. This same method can be applied here with the undulating upper boundary profile which parallels the ground's profile.

5. Test Case with a Simple Hill Profile

The algorithm was tested using a simple hill profile

$$H(x) = a \cos^2 \left[\frac{\pi s}{2} \left(1 - \frac{x}{x_{top}} \right) \right], \quad s = \frac{2x_{top}}{W} \quad (5 - 1)$$

for $w/2 \leq x \leq w$ and elsewhere $H(x) = 0$, with the following values:

height, a	=	200m
width, w	=	1000m
distance to top, x_{top}	=	1000m

The predictions obtained at a 2m height above ground using the GT-PE for still air are compared in Figure 2 with those obtained using Maekawa's procedure, which replaces the hill with an equivalent vertical barrier (see reference 7) located at x_{top} . The agreement is good at distances 700m beyond the hill top. Close to the hill, on the shadow size, the GT-PE predicts a much larger attenuation than the Maekawa model. No predictions from the Maekawa model are given on the bright side of the hill where its errors are significant.

6. Concluding Comments

The new GT-PE has the potential to give predictions for propagation over complicated but smooth terrain profile sections. As the terrain derivatives increase in size the predictions become less reliable and indeed for fairly steep parts of a profile the numerical procedure can break down completely. We have not yet established the limiting H' and H'' values but the accuracy of the whole procedure is clearly dependent on the accuracy of the methods used for the integrals appearing in equation (3 - 4) and the ground boundary condition given in equation (4 - 3). More elaborate procedures which should improve the accuracy of these parts of the computation are being investigated and their implementation should allow steeper profiles to be used.

REFERENCES

1. M West, K Gilbert and R A Sack. A Tutorial on the Parabolic Equation (PE) Model Used for Long Range Sound Propagation in the Atmosphere. *Applied Acoustics* 37, 31- 49 (1992).
2. X Di, K Gilbert and C You. Application of Conformal Mapping for Sound Propagation Over Terrain. NCPA Report #XD1-10-93, January 1993. NCPA, University of Mississippi, University, MS 38677.
3. C You. Doctoral Dissertation, NCPA, University of Mississippi, University MS 38677, 1993.
4. R A Sack and M West. A Parabolic Equation for Sound Propagation in Two Dimensions over ANY Smooth Terrain Profile: The Generalised Terrain Parabolic Equation (GT-PE). *Applied Acoustics* (awaiting publication).
5. R A Sack and M West. Representation of Elliptic by Parabolic Partial Differential Equations with an Application to Axially Symmetric Sound Propagation. *Applied Acoustics*, 37, 141-149 (1992).
6. M West and R A Sack. Development of an Algorithm for Prediction of the Sound Field from a Spherical Acoustic Source Using the Parabolic Approximation. *Proceedings of the 5th International Symposium on Long Range Sound Propagation*. The Open University, Milton Keynes, May 1992, 115-127.
7. D J Saunders and R D Ford. A Study of the Reduction of Explosive Impulses by Finite Sized Barriers. *J Acoust Soc Am* 94(5), 2859-2875, (1993).

ACKNOWLEDGEMENT

The authors wish to thank the Directorate of Defence, Health and Safety, Ministry of Defence for the funding of this work.

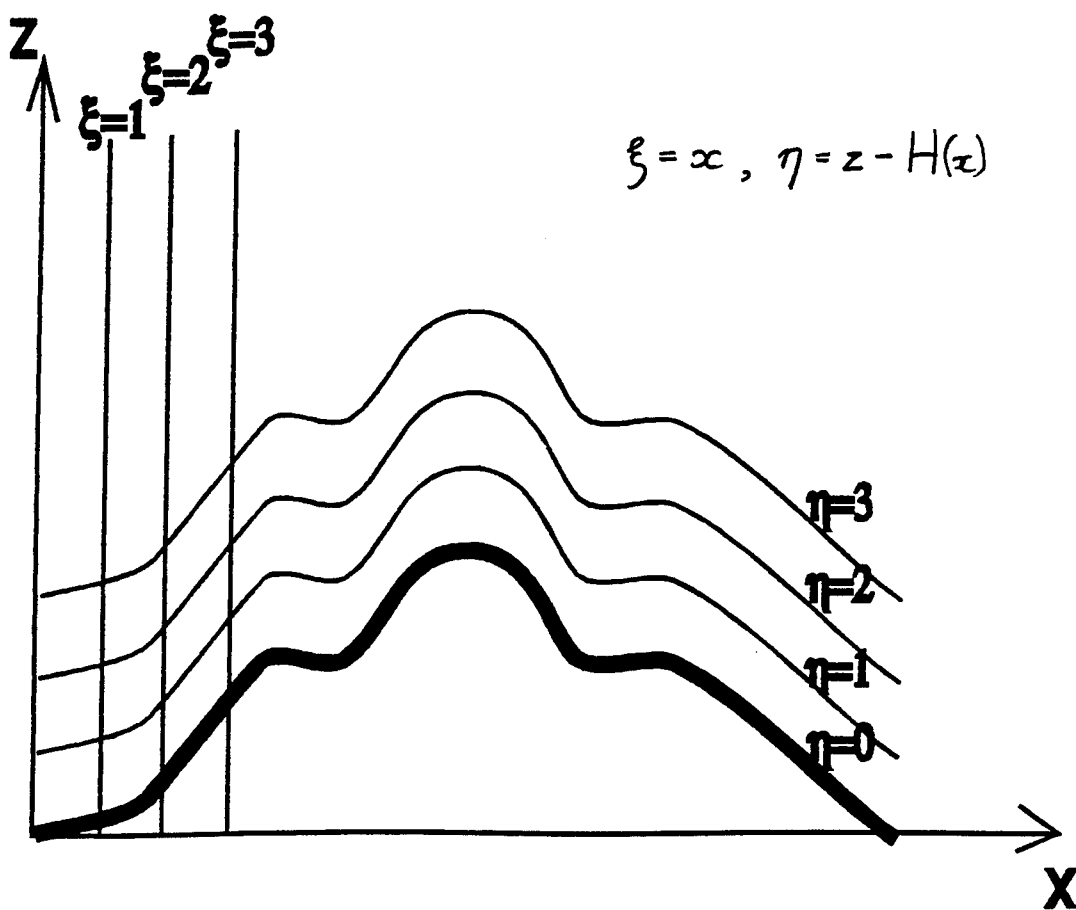


Figure 1. Terrain Following Transformation

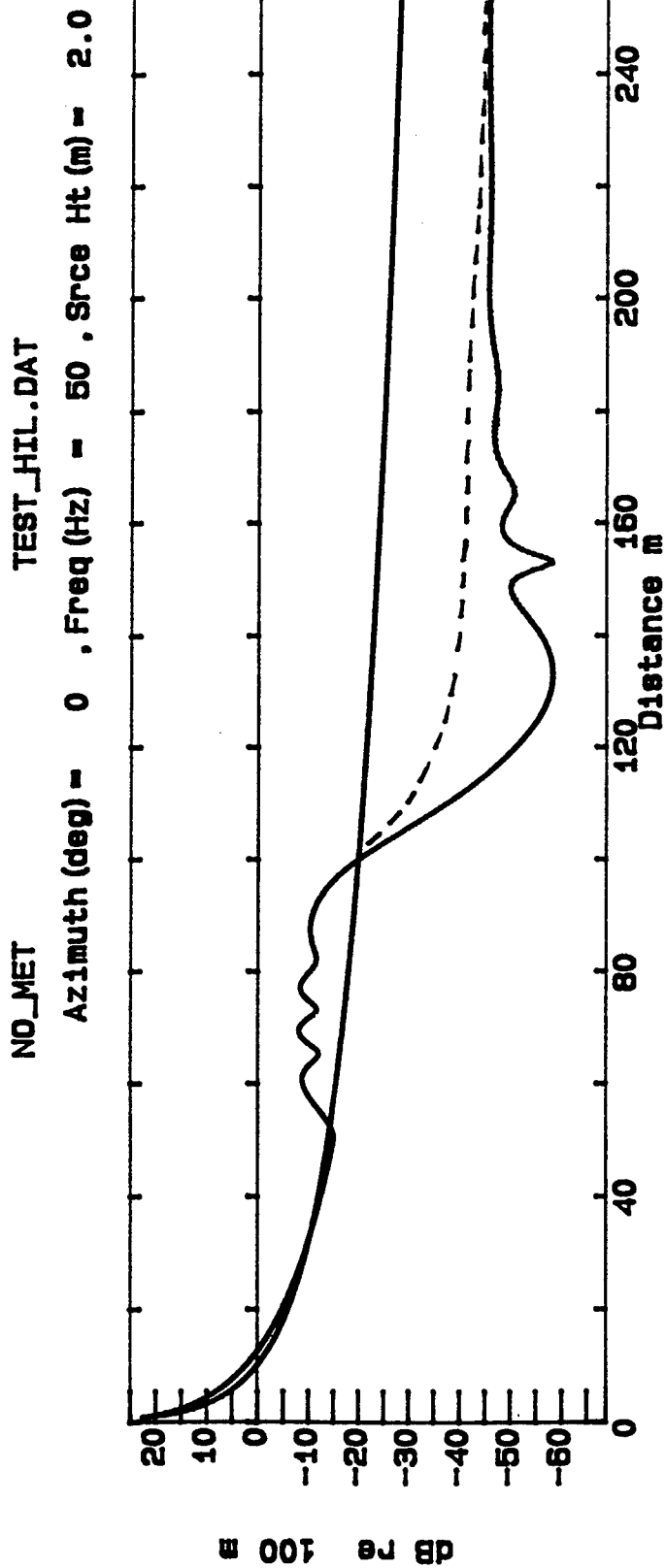


Figure 2. Comparison of Predictions from the GT-PE Model (Solid Line) with those from Maekawa's Procedure (Dashed Line) for the Test Hill (source height, 2m, receiver height 2m, frequency 50Hz, ground impedance, $Z_{GND} = (10.0, -10.0) \rho_c$ units).

APPLICATION OF THE PARABOLIC APPROXIMATION METHOD TO SOUND PROPAGATION ABOVE GROUND WITH IMPEDANCE VARIATIONS

Marta Galindo
The Acoustics Laboratory
Building 352, Technical University of Denmark
DK 2800 Denmark

INTRODUCTION

A wide-angle Parabolic Method (PE) in two dimensions has been developed for sound propagation through a homogeneous atmosphere over a ground with varying acoustic impedance.

In this work, the effects of a strip of soft ground inside a rigid plane is studied. The location of the strip and the amount of soft ground between source and receiver are the parameters under consideration. With the PE method the horizontal propagation is obtained by a marching algorithm, using finite different approximations. The Craddock and White [1] formulation has been included in the method. This allows impedance variations to be taken into account with a very little additional computation time.

The paper is organized in four sections. First the theory behind the parabolic approximations is presented. Then, the numerical implementation of the method is described, including the boundary and initial conditions considered for the study of sound propagation through an homogeneous atmosphere over a ground with impedance jumps. In the next section, the PE calculations are compared with existing prediction models, such as Rasmussen's aperture method [2] over impedance discontinuity. A series of propagation measurements is carried out in a scale model, in order to verify the PE-results. Finally, the conclusion of the investigation shows the PE as an open method for future studies on long range sound propagation in complicated environments.

I. THEORY

In this section the family of parabolic differential wave equations is retrieved. Using the $\exp(-i\omega t)$ time-convention, the Helmholtz wave equation for a harmonic point source in a medium with an azimuthal symmetry takes the form:

$$\frac{\partial^2 p}{\partial r^2} + \frac{1}{r} \frac{\partial p}{\partial r} + \frac{\partial^2 p}{\partial z^2} + k_0^2 n^2 p = 0 \quad , \quad (1)$$

where:

$p(r, z)$	is the acoustic sound pressure,
k_0	is ω/c_0 , where c_0 is the sound speed in the air,
$n(r, z) = c_0/c(r, z)$	is the refraction index.

The solution of Eq.1 can be written as

$$p(r, z) = \phi(r, z) H_0^{(1)}(k_0 r) . \quad (2)$$

This expression represents an outgoing cylindrical wave, the Hankel function, multiplied by an envelope function $\phi(r, z)$ which is assumed to be slowly varying in range. Making use of the fact that the Hankel function satisfies the Bessel differential equation and including the far field approximation for the Hankel function

$$H_0^{(1)} \approx \sqrt{\frac{2}{\pi k_0 r}} e^{i(k_0 r - \frac{\pi}{4})} , \quad (3)$$

the following simplified elliptic wave equation is obtained

$$\frac{\partial^2 \phi}{\partial r^2} + 2ik_0 \frac{\partial \phi}{\partial r} + \frac{\partial^2 \phi}{\partial z^2} + k_0^2 (n^2 - 1) \phi = 0 . \quad (4)$$

Defining the two operators P and Q as

$$P = \frac{\partial}{\partial r} , \quad Q = \sqrt{n^2 + \frac{1}{k_0^2} \frac{\partial^2}{\partial z^2}} , \quad (5)$$

the elliptic wave equation (4) is rewritten as:

$$(P^2 + 2ik_0 P + k_0^2 (Q^2 - 1)) \phi = 0 , \quad (6)$$

where Eq.6 can be separated in two components, an outgoing and an incoming wave

$$[P + ik_0 - ik_0 Q][P + ik_0 + ik_0 Q] \phi - ik_0 [P, Q] \phi = 0 . \quad (7)$$

The first bracket represents the outgoing wave, the second the incoming wave and $[P, Q]$ is the commutator of the operators P and Q, defined as:

$$[P, Q] \phi = PQ \phi - QP \phi . \quad (8)$$

For range-independent media where the refraction index is only a function of the height, $n=n(z)$, the two operators commute and the last term in Eq.7 is equal to zero. In this work it is assumed that the range dependence in $n(r, z)$ is so weak that the commutator term can be ignored. Including the approximation for a one-way wave equation and considering only the outgoing wave component, the family of parabolic partial differential equations is obtained,

$$\frac{\partial \phi}{\partial r} = ik_0 \left(\sqrt{n^2 + \frac{1}{k_0^2} \frac{\partial^2}{\partial z^2}} - 1 \right) \phi \quad (9)$$

Three assumptions are included in the parabolic approximation of the Helmholtz wave equation. These three assumptions limit the applicability of the method to far field solutions, in a medium with a refraction index weak dependence of the range and where backscattered waves are neglected.

To solve Eq.9 by numerical methods a rational approximation of the pseudo-differential operator Q is introduced

$$Q = \sqrt{1+q} \approx \frac{a+bq}{c+dq} \quad , \quad (10)$$

where each set of coefficients gives a different implementation of the PE approximation. The goodness of the parabolic approximation is defined as the accuracy of the angular spectrum of forward propagating plane waves when they are treated by each of the PE's. Following this criterium, the standard parabolic approximation [3] which uses the paraxial approximation is called "the narrow angle parabolic approximation". In the problem under consideration a wide angle parabolic approximation is desired in order to be able to determine the sound field not just in the main propagation direction but also in other directions. The wide angle PE method uses the Claerbout[4] rational approximation which expanded in a power series in q agrees with the Taylor expansion of $(1+q)^{1/2}$ through the quadratic term. Due to the linearity of q , implementing the Claerbout approximation will not be more complicated than using the linear expansion.

II. NUMERICAL IMPLEMENTATION

Discretization in range

Finite-difference (FD) is a numerical scheme which is used for solving partial differential equations. It is based on the concept of discretization of the physical problem and its solution in order to facilitate a numerical evaluation. FD is used in the PE method to advance the solution in range. The operator Q is considered to be independent of the range for short enough range steps, making it possible to integrate Eq.9 with respect to this variable. To solve Eq.9 in range the Crank-Nicolson[5] finite difference scheme, is included and the next equation is obtained

$$\frac{\phi(r+\Delta r) - \phi(r)}{\Delta r} = ik_0(Q-1) \frac{\phi(r+\Delta r) + \phi(r)}{2} , \quad (11)$$

which leads to the following implicit equation

$$\left[1 - \frac{i\Delta r k_0}{2}(Q-1)\right] \phi(r+\Delta r) = \left[1 + \frac{i\Delta r k_0}{2}(Q-1)\right] \phi(r) . \quad (12)$$

The matrix operator equation for advancing ϕ from the range r to $r+\Delta r$ is obtained when the Claerbout rational linear approximation is included into Eq.12

$$C^* \phi(r+\Delta r) = C \phi(r) , \quad (13)$$

where C^* and C are operators which represent the change in ϕ from the range r to $r+\Delta r$,

$$C = C_1 + C_2 n^2 + C_3 \frac{\partial^2}{\partial z^2} , \quad (14)$$

$$C^* = C_1^* + C_2^* n^2 + C_3^* \frac{\partial^2}{\partial z^2} .$$

C_1, C_2 and C_3 are complex constants and $*$ means the conjugate operation. Hence,

$$\begin{aligned} C_1 &= (c-d) + i \frac{k_0 \Delta r}{2} [(a-c) - (b-d)] , \\ C_2 &= d + i \frac{k_0 \Delta r}{2} [b-d] , \\ C_3 &= \frac{d}{k_0^2} + i \frac{\Delta r}{2k_0} [b-d] , \end{aligned} \quad (15)$$

where $a=1, b=0.75, c=1, d=0.25$ are the Claerbout's coefficients.

Discretization in height

The PE method uses linear finite elements (FE) to discretize the vertical dependence on $\phi(r, z)$ [6]. The numerical grid created by FE is nonequidistant, therefore a nonuniform vertical description of the environment can be considered. The next expressions for $\phi(r)$ and $\phi(r+\Delta r)$ are obtained using the linear finite element basis functions to discretize the vertical dependence of the field

$$\begin{aligned} \phi(r, z) &= \sum_j A_j h_j(z) , \\ \phi(r+\Delta r, z) &= \sum_j B_j h_j(z) . \end{aligned} \quad (16)$$

where A_j and B_j are called the expansion coefficients. Due to the nature of the linear basis functions, expanding $\phi(r)$ and $\phi(r+\Delta r)$ in height is equivalent to a linear interpolation between the grid points. Thus, the values for the expansion coefficients are

$$A_j = \phi(r, z_j) \quad , \quad B_j = \phi(r + \Delta r, z_j) \quad . \quad (17)$$

Including the expansion coefficients in Eq.13, multiplying by $h_i(z)$ and integrating over z , the following matrix equation is obtained

$$\begin{aligned} & \sum_n C_n^* \sum_j H_{ij}^n \phi(r + \Delta r, z_j) \\ & = \sum_n C_n \sum_j H_{ij}^n \phi(r, z_j) \end{aligned} \quad n=1, 2, 3. \quad (18)$$

Where the three H_{ij}^n integrals are defined as

$$\begin{aligned} H_{ij}^1 &= \int h_i \frac{1}{\rho} h_j dz \quad , \\ H_{ij}^2 &= \int h_i \frac{n^2}{\rho} h_j dz \quad , \\ H_{ij}^3 &= \int h_i \left(\frac{\partial}{\partial z} \frac{1}{\rho} \frac{\partial}{\partial z} \right) h_j dz \quad . \end{aligned} \quad (19)$$

Following Gilbert and White [7] and considering $(1/\rho)$ and (n^2/ρ) to be linear functions of the height z between two points, and continuous at the grid points z_i simple analytic functions can be found for the H matrices. By definition, the basis functions $h_i(z)$ overlap only with their direct neighbours $h_{i-1}(z)$ and $h_{i+1}(z)$. Therefore only when $j=i, i\pm 1$, the integrals are different from 0 and the H matrices are tridiagonal. Hence with $\phi(r, z_j)$ and $\phi(r + \Delta r, z_j)$ defined as the elements of the vectors $\Phi(r)$ and $\Phi(r + \Delta r)$, respectively, a system of tridiagonal linear algebraic equations is obtained

$$C^* \Phi(r + \Delta r) = C \Phi(r) \quad . \quad (20)$$

The vector $\Phi(r)$ is known and by solving the system of linear equations it is possible to calculate $\Phi(r + \Delta r)$ on each step in range. It is a marching algorithm that calculates for a single frequency a numerical solution in all the steps in range between the source and receiver. To solve the tridiagonal system of linear algebraic equations an alternative Gaussian decomposition proposed by Craddock and White [1] is used. It is called upper-lower (UL) factorization. By this method a jump in the impedance will not require recalculation of the whole matrices C and C^* .

Boundary and initial conditions

The principal advantage of the parabolic wave equation over the elliptic Helmholtz equation is that the PE is a one-way wave equation, which can be solved by a range-marching solution technique. This requires a specification of both initial and boundary conditions to have a well defined problem.

The lower boundary condition is well defined due to the presence of the ground, which is assumed a locally reacting surface. Its properties are characterized by an impedance boundary condition using the Delany and Bazley [8] model. Hence, the characteristic impedance is a function of the ratio of frequency to the specific flow resistance per unit thickness. The boundary condition at $z=0$ is written as

$$\frac{\partial \phi}{\partial z} + \frac{ik_0 \phi}{z^*} = 0 \quad , \quad (21)$$

where:

k_0 is the wave number in the air at $z=0$.

z^* is the complex ground impedance divided by ρc for the air.

It is assumed that $\phi(r, z)$ varies linearly between the grid point, and therefore the derivative can be written as a finite difference in the variable z ,

$$\frac{\phi(z_1) - \phi(z_0)}{z_1 - z_0} + \frac{ik_0 \phi(z_0)}{z^*} = 0 \quad . \quad (22)$$

The point z_0 is located on the ground and the point z_1 is the first one over the ground. The approximation for the partial derivative is a forward differential approximation with a truncation error of the first order. Thus the distance $z_1 - z_0$ over the grid should be chosen a half of step in height. The first boundary condition is included in the marching algorithm when Eq.22 is added to the matrix system Eq.20. The terms in the main diagonal of C are denoted b_i , and the terms in the subdiagonal and superdiagonal are a_i and c_i , respectively. In the case of C^* , the same notation is used but adding *. The first equation in the matrix system Eq.20 is

$$b_0^* \phi(z_0, r + \Delta r) + c_0^* \phi(z_1, r + \Delta r) = b_0 \phi(z_0, r) + c_0 \phi(z_1, r) \quad , \quad (23)$$

and the boundary condition, Eq.21 leads to

$$\left(\frac{ik_0}{z^*} - \frac{1}{z_1 - z_0} \right) \phi(z_0, r + \Delta r) + \frac{1}{z_1 - z_0} \phi(z_1, r + \Delta r) = 0 \quad . \quad (24)$$

To satisfy both equations, b_0 and c_0 are set equal to zero,

and c_0^* remains unchanged from its value at the previous range step. Thus, b_0^* is

$$b_0^* = c_0^* \left(\frac{ik_0(z_1 - z_0)}{z^*} - 1 \right) . \quad (25)$$

Therefore any change in the ground impedance affect only the term b_0^* . No computation time is added due to the impedance jump. Thus, the quality of the terrain can be described precisely through a number of changes in the impedance.

The radiation of the sound at infinity determines the upper boundary condition. As the PE method is solved on a finite-height grid, a simulation of the radiation condition at infinity is required. In order to obtain this condition, an artificial absorption layer is introduced above any possible propagation paths to the receiver. Using this procedure, the computational space is horizontally divided in two: a real domain, from 0 to z_{\max} , where the solution of the differential equation converges and an artificial domain, from z_{\max} to H , where the radiation boundary condition is created.

The artificial absorption layer is modeled according to Jensen et al.[9], with a complex index of refraction of the form

$$n^2 = n^2 + ie^{-\left(\frac{z - z_{\max}}{D}\right)^2 \alpha} , \quad (26)$$

where

$$\alpha = \frac{\text{freq}^2}{1500^2}; \quad D = \frac{z_{\max} - H}{3} ,$$

which results in an exponentially increasing wave attenuation with the height of the absorption layer. The thickness of the artificial absorption layer is one third of the domain. With this sound absorption layer, unwanted reflections from the top are greatly reduced and no significant energy is added to the real domain. At the top of the absorption layer a pressure-release surface condition is implemented.

Since the PE method solves an initial value problem, an initial field has to be specified at a certain range. This is called the starting range of the computation and is generally located at the source position. The appropriate PE starting field can be generated using either numerical or analytical techniques. In the present work an analytical source function is chosen because it can be defined with a minimum of computational effort. The source aperture should be consistent with the angular limitation associated with a particular parabolic approximation. A source with good angle properties is a weighted Gaussian function called Greene's source[10].

III. RESULTS

Several PE calculations for long range propagation over a terrain with an impedance jump have been made to test the accuracy of the method. The values have been compared with Rasmussen's method for an impedance discontinuity[2]. The geometrical configuration of the problem is shown in Fig.1. The source and the receiver are situated 3m and 2m over the ground, respectively. The horizontal distance between them is 100m. Fig.2 shows the calculation of both methods for two different positions of an impedance jump. In set 1 of the calculations the transition between the acoustically soft to the acoustically hard ground is located at 25m from the source while in set 2 a transition from a hard to a soft ground is located at 50m from the source. The flow resistivities are 5×10^4 kNs/m⁴ for a hard surface and 200 kNs/m⁴ for a soft surface, using Delany and Bazley model[8]. The plots represent the sound pressure level relative to a free field as a function of frequency. The solid lines are Rasmussen's predictions and the symbols represent the calculations from the PE method. The calculated values from the PE method show good agreement with the predictions from Rasmussen's method for a range of frequencies from 100 Hz to 2 kHz.

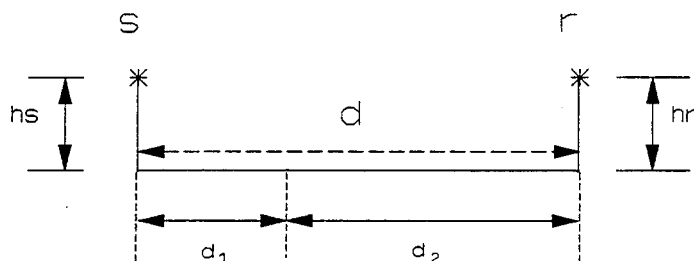


Figure 1. Geometrical parameters for one impedance jump.

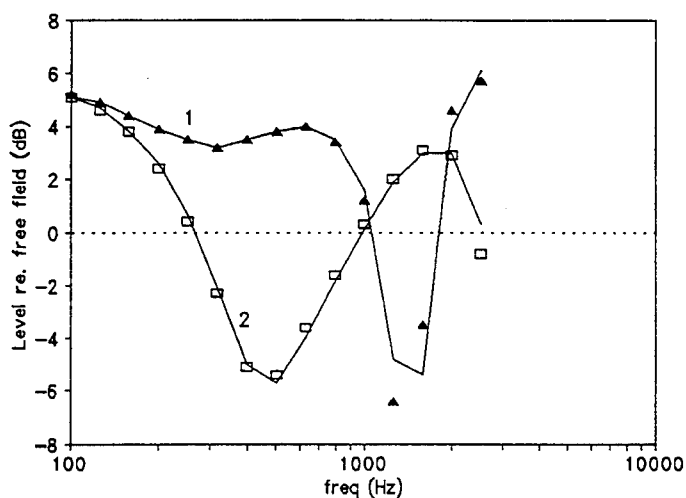


Figure 2. $h_s=3\text{m}$, $h_r=2\text{m}$, $d=100\text{m}$.
 1: $d_1=25\text{m}$, $\sigma_1=200\text{kNsm}^{-4}$, $d_2=75\text{m}$, $\sigma_2=50000\text{kNsm}^{-4}$.
 2: $d_1=50\text{m}$, $\sigma_1=50000\text{kNsm}^{-4}$, $d_2=50\text{m}$, $\sigma_2=200\text{kNsm}^{-4}$.

The PE method can also describe the propagation over different kinds of ground, making it for example possible to study the effects of a strip of soft ground in a rigid plane. The location of the strip and the amount of soft ground between source and receiver are now the parameters under consideration. A sketch defining the geometric parameters of this problem is shown in Fig.3. The source and the receiver are located 1.5m over the ground, the horizontal distance between them is 100m. The porosity of the soft strip is characterized by a flow resistivity of 300 kNs/m^4 and the hard surface is characterized by flow resistivity of $5 \times 10^4 \text{ kNs/m}^4$. The impedance discontinuities are normal to the propagation path. These five parameters are kept constant in all the calculations.

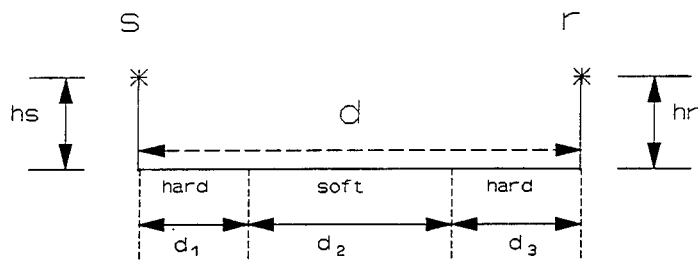


Figure 3. Geometrical parameters for a strip of porous ground in a hard surface.

Fig. 4 and 5 show the results of PE calculations for several strips with different widths. The plots represent the sound pressure level relative to a free field as a function of frequency for different values of d_2 . Thus, a completely porous ground is represented by $d_2=100\text{m}$ and a completely hard ground by $d_2=0\text{m}$. Fig. 4 shows the results where the porous strips are always centred between the source and receiver. Fig. 5 shows the results when the porous strips always begin at 10m distance from the source. The two figures show a similar behaviour for wide strips. As it could be expected, the width of the interference dip gets narrower when the amount of hard surface increases. A significant difference between the two figures appears for narrow strips. The calculations for one narrow strip show different frequency spectra depending on the location.

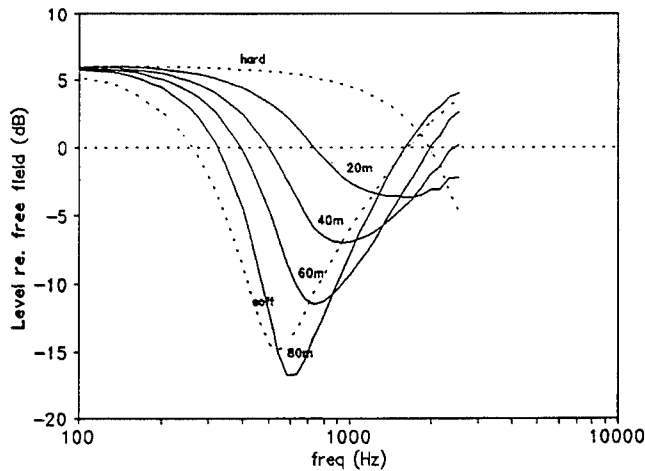


Figure 4. $h_s=h_r=1.5\text{m}$, $d=100\text{m}$. Porous strips, $\sigma=300\text{kNsm}^{-4}$, of different widths located at the centre.

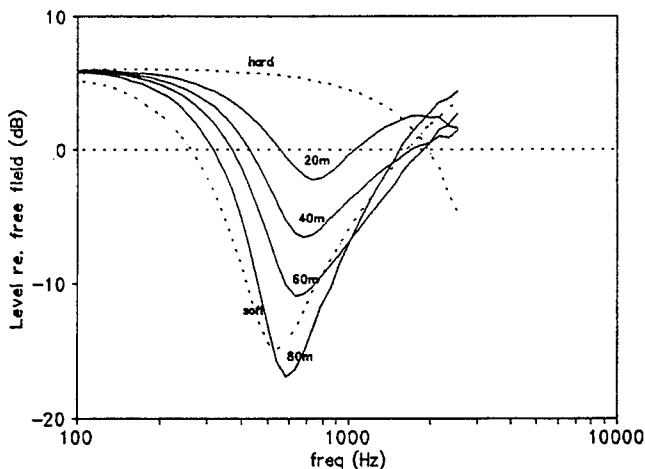


Figure 5. $h_s=h_r=1.5\text{m}$, $d=100\text{m}$. Porous strips, $\sigma=300\text{kNsm}^{-4}$, of different widths beginning at 10m from the source.

Fig. 6 and 7 show the results of the PE calculations for one strip at different positions between source and receiver. Due to the reciprocity principle, the chosen positions for the strip are located in between the source and half of the distance source-receiver. Fig. 6 shows the calculation for a 10m porous strip and Fig. 7 for a 20m porous strip. For a range of frequencies between 900Hz and 2.5kHz the attenuation is higher when the strip is located in the centre. The geometric reflexion point for this configuration of source and receiver falls into the strip area. The PE calculations for this frequency band agree with the ray acoustic theory. The calculations for the frequencies between 500Hz and 900Hz predict higher attenuations when the strips

are located close to the source than when they are located close to the centre. This means that, the quality of the ground near the source and the receiver are very important for the determination of the ground attenuation for these lower frequencies.

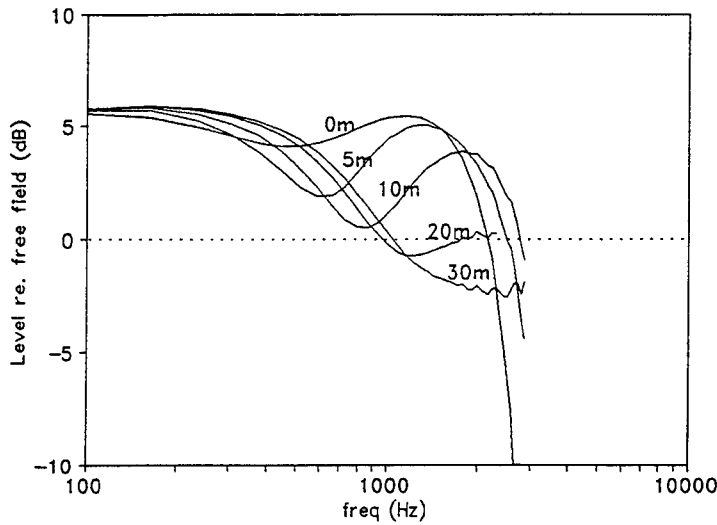


Figure 6. Variations of the 10m wide strip's position. $h_s=h_r=1.5\text{m}$, $d=100\text{m}$, $\sigma=300 \text{ kNsm}^{-4}$. Define parameter: Distance from source to the beginning of the strip.

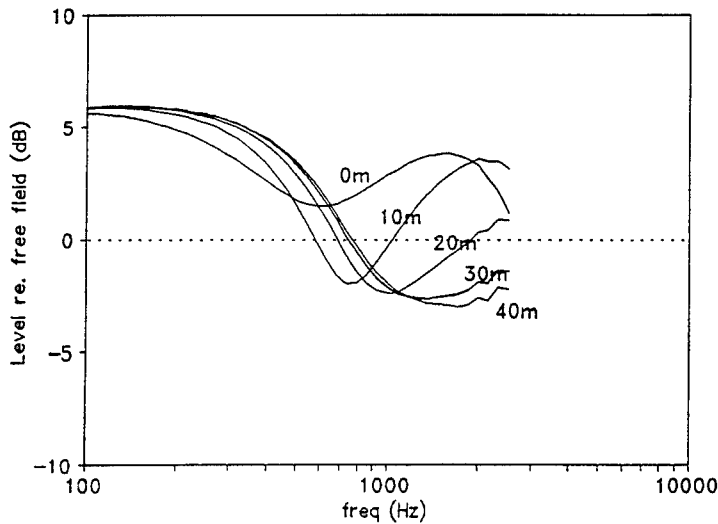


Figure 7. Variations of the 20m wide strip's position. $h_s=h_r=1.5\text{m}$, $d=100\text{m}$, $\sigma=300 \text{ kNsm}^{-4}$. Define parameter: Distance from source to the beginning of the strip.

In order to verify the PE calculations, a series of propagation measurements are carried out in a scale model(1:25). A newly developed scale model facility [11] makes it possible to study one propagation parameter at a time. The position of the strip is the parameter under consideration in the measurements. The strip of porous surface is modeled by a canvas-layer on the top of a hard surface. Using the Delany-Bazley[8] formulation, the material is characterized by a flow resistivity value of 300 kNs/m^4 . The width of the porous strip in real scale corresponds to 10m. The distance between source and receivers is 100m. The location of the strip is changed in the different measurements. In all the cases the edges of the strip are normal to the propagation path. Figs. 8 and 9 show the sound pressure levels relative to a free field against frequency for different position of the strip. The measurements are plotted with dashed lines and the PE predictions with solid lines. In Fig. 8 the strip is located at 5m and 10m from the source and in Fig. 9 at 20m and 30m. The measurements agree quite well with the PE calculations. The slight deviation between measured and calculated values for high frequencies could be caused by measurement inaccuracies. The oscillations of the PE calculations for high frequencies are due to a problem in the convergence of the numerical solution of the parabolic differential equation.

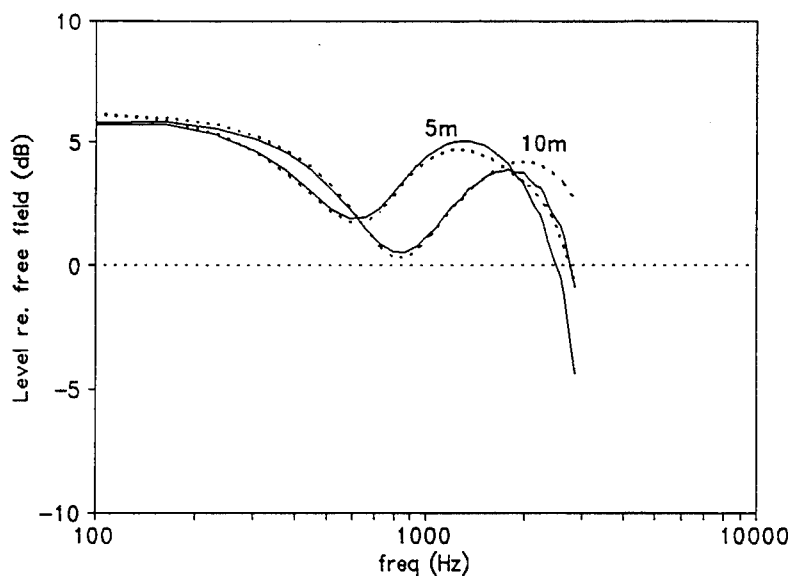


Figure 8. Comparatione between PE calculations (solid lines) and scale model measurements 1:25 (dashed lines), for a 10m porous strip beginning at 5m and 10m from the source. $h_s=h_r=1.5\text{m}$, $d=100\text{m}$, $\sigma=300 \text{ kNsm}^{-4}$.

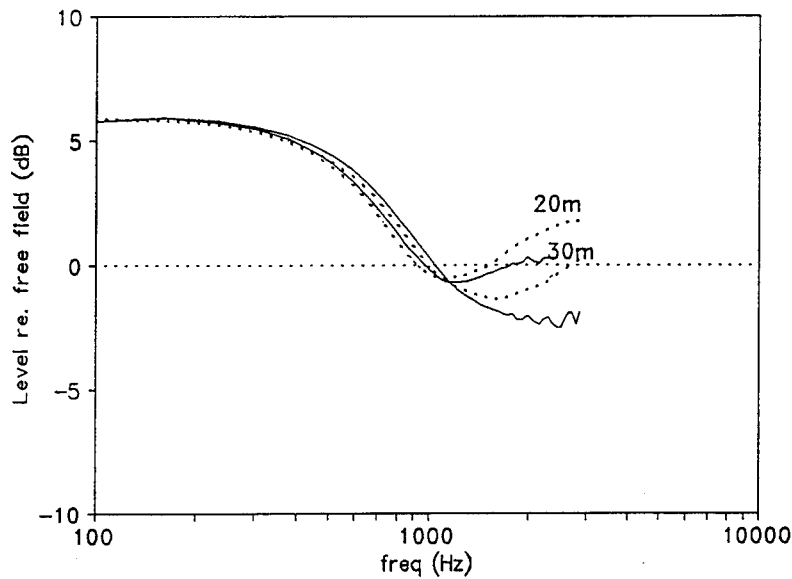


Figure 9. Comparatione between PE calculations (solid lines) and scale model measurements 1:25 (dashed lines), for a 10m porous strip beginning at 20m and 30m from the source. $h_s=h_r=1.5\text{m}$, $d=100\text{m}$, $\sigma=300 \text{ kNsm}^{-4}$.

IV. CONCLUSION

The PE is a numerical method to solve the one-way parabolic wave equation. It represents an alternative to ray-tracing methods. Ray theoretic methods approximately describe the propagation paths in the atmosphere, but do not adequately describe low frequency wave phenomena. In the study of long range sound propagation over a porous strip in a hard surface, the PE method has been confirmed as a powerful tool to predict the sound pressure level in a range of frequencies between 100 Hz and 2.5 kHz. The quality of the ground close to the source or receiver has been shown as an important parameter for frequencies between 400-900 Hz whereas the central area should be considered for frequencies between 900 Hz-2.5 kHz for the parameters in the present work.

REFERENCES

- [1] J.N. Craddock and M.J. White , "Sound propagation over surface with a varying impedance: A parabolic equation approach", J. Acoust. Soc. Am. 91 (6), June 1992.
- [2] K.B.Rasmussen, "A note of on the calculation of sound propagation over impedance jumps and screens" J. Sound and Vib. 84, 598-602 (1982).
- [3] F.D. Tappet "The parabolic approximation method" in Wave Propagation and Underwater Acoustics, edited by J.B. Keller and J.S. Papadakis (Springer, Heidelberg, 1977) Lecture Notes in Physics, Vol 70.
- [4] J.F. Claerbout, "Fundamentals of Geophysical Data Processing" (McGraw-Hill, New York, 1976).
- [5] D.Lee and S.T. McDaniel, "Ocean Acoustic Propagation by Finite Difference Methods" (Pergamon, New York, 1988).
- [6] O. Axelsson and V.A. Barker, "Finite Element Solution of Boundary Value Problems" (Computer Science and Applied Mathematics, Academy Press, INC, 1984)
- [7] K.E. Gilbert and M. White "Application of the parabolic equation to sound propagation in a refracting atmosphere". J.Acoust.Soc.Am. 85(2), Feb 1989 p(630-637).
- [8] M.E. Delany and E. N. Bazley, "Acoustical properties of fibrous absorbent materials", Appl.Acoust. 3, 105-116 (1970).
- [9] F. Jensen, W. Kuperman, M. Porter and H. Schmidt, " Computational Ocean Acoustics", AIP SERIES in modern Acoustics and Signal Processing ,New York, 1994.
- [10] R.R. Greene, "The rational approximation to the acoustic wave equation with bottom interaction," J. Acoust.Soc.Am. 76, 1764-1773 (1984).
- [11] K.B. Rasmussen, "Scale-model simulation of sound propagation over an impedance discontinuity" INTER-NOISE 93 proceedings, Leuven, Belgium (1993).

Influence of Ground Roughness on Outdoor Sound

Keith Attenborough
Engineering Mechanics Discipline,
Faculty of Technology
The Open University
Milton Keynes
MK7 6AA
England

ABSTRACT

Analytical approximations for the field above a finite impedance surface containing arbitrary two or three-dimensional small-scale roughnesses, in the presence of a homogeneous or upward refracting atmosphere, are deduced from modifications to theories by Howe and Tolstoy. These modifications result in expressions for effective admittances of rough finite impedance surfaces.

Some laboratory-based experimental validation of the effective admittance forms of the theory is offered.

Numerical results for the field in the deep shadow zone are presented. It is predicted that roughness-induced surface waves on an acoustically-hard boundary produce considerably higher levels in refractive shadow zones than would be predicted over a smooth hard surface. The effect is predicted to decrease as the surface admittance increases.

INTRODUCTION

Considerable effort has been devoted to the effects of the finite impedance of the ground surface on sound propagation outdoors¹. Less attention has been paid to the possible influences of the roughness of the ground, where the mean roughness height is small compared with a wavelength even though the effects of such surface roughness have been and are being studied intensively by the underwater acoustics community²⁻⁴. In particular the existence of the predicted rough surface boundary wave has been verified experimentally by pulse experiments⁵⁻⁷. It has been suggested³ that there may be interesting aspects of surface roughness effects in atmospheric and room acoustics.

Tolstoy² has distinguished between two theoretical approaches, for predicting the *coherent* field resulting from co-operative forward scatter by boundary roughnesses where the typical roughness height and spacing is small compared to a wavelength. Both of these reduce the rough surface scattering problem to one that uses a suitable boundary condition at a *smoothed* boundary. In particular the *boss* method originally derived by Biot⁸ and Twersky⁹, has the advantages that (i) it is more accurate to first order than *perturbation* methods (ii) it may be used even in conditions where the roughness shapes introduce steep slopes and (iii) it is reasonably accurate even when the roughness size approaches a wavelength. Tolstoy has adapted and extended the Biot theory to deal with pulse propagation over arbitrarily-shaped roughnesses at the

interface between different fluids³ or between a fluid and an elastic solid⁴. He and others have also predicted the possibility that ground roughness enables penetration of underwater sound into the shadow zone formed by an upward refraction^{10,11}.

Howe¹² has considered propagation over a rough finite impedance boundary. Howe laid stress on the prediction of an enhanced surface wave component in the context of long range sound propagation at low frequencies and grazing-incidence over hilly terrain with relatively acoustically-hard surfaces.

An important conclusion of previous work is that the *normal surface impedance or admittance of the boundary is modified by the coherent forward scatter associated with the presence of roughness*. The surface admittance is known to have an influence on the attenuation spectrum due to destructive and constructive interference between direct and ground-reflected sound paths from a point source after allowing for wavefront spreading and atmospheric absorption. This excess attenuation spectrum is known as *ground effect* and is an important factor in studies of outdoor sound, particularly from continuous sources at near-grazing incidence¹.

The effective admittance of a rough acoustically-hard surface is predicted to be a pure reactance. The resulting surface wave at near-grazing incidence is related to that predicted above a comb-like boundary by Brekhovskikh¹³ and that formed during propagation from a point source over the square lattice array formed by a lighting diffuser panel on a hard boundary and studied by Donato¹⁴.

A reconciliation, combination and extension of Howe's and Tolstoy's results^{8,4}, enables predictions of finite impedance ground effect (in the form of excess attenuation spectra) for elevated point source and receiver in the presence of ground surfaces with arbitrary roughness shapes and concentrations, and these predictions have been validated by laboratory measurements¹⁵. In this paper the results of Howe's and Tolstoy's analyses of propagation over acoustically-hard and soft rough boundaries are given and Tolstoy's analysis of propagation into the underwater shadow zone¹⁰ is repeated for the *atmospheric* upward refraction case. Far-field predictions are made for realistic impedances and roughnesses after taking into account incoherent scatter¹⁶.

THEORY

1. Effective admittance theory for homogeneous upper medium

Propagation over a rough rigid-porous boundary where the roughnesses and their spacing are small compared with a wavelength may be predicted from adaptation of the Biot/Tolstoy/Lighthill³ theory for propagation at a rough fluid interface. The rigid-porous lower medium and the (rigid-porous) roughness may be modelled as effective fluids with complex densities and sound speeds.

Given $k_0 h < k_0 \ell \leq 1$, where k_0 is the wave number in the upper half-space h is the mean roughness height and ℓ is the mean centre-to-centre spacing of the roughnesses;

1. The field perturbation due to the presence of a single scatterer is expressed as the sum of monopole and dipole contributions.
2. Force balances with and without the scatterer are solved for monopole and dipole contributions in terms of scatterer volume, density, virtual mass and compressibility at frequencies much less than the scatterer resonance.
3. The reduced dipole effect due to scatterer interaction is determined by nearest neighbour summations.
4. The surface integral representing total field is expressed in terms of a boundary condition (either one-sided or two-sided).

A general (two-sided) boundary condition for the perturbed field potential in the half space $(\rho_1 c_1)$ above the boundary of a fluid (ρ_3, c_3) containing three-dimensional fluid roughnesses (ρ_2, c_2) that is derived in this way³ is given by

$$\frac{\partial \phi_1}{\partial z} - \frac{\partial \phi_3}{\partial z} = ik_0 \beta_3^* \phi_1 + \epsilon_{12} \delta_{12} \frac{\partial^2 \phi_1}{\partial z^2} \quad (1)$$

where ϕ_1 is the perturbed field potential in the upper half-space, ϕ_3 is that in the lower half-space, time dependence $\exp(i\omega t)$ is understood and the effective relative admittance of the rough surface, β_3^* , is given by

$$\beta_3^* = ik_0 \epsilon + \beta \quad (2)$$

$$\epsilon = \epsilon_{12} + \left(\frac{\rho_1 c_1^2}{\rho_3 c_3^2} \right) \epsilon_{32} + \frac{\rho_1}{\rho_3} \left[1 - \frac{c_1^2}{c_3^2} \right] \epsilon_{32} \delta_{32}$$

$$\epsilon_{ij} = a_{ij} - b_{ij} \quad \epsilon_{ij} \delta_{ij} = a_{ij}$$

$$a_{ij} = 3\sigma_v \left[\frac{\rho_j - \rho_i}{\rho_i + \rho_j} \right] \frac{s_{3D}}{v_{3D}} \quad b_{ij} = \sigma_v \left[1 - \frac{\rho_i c_i^2}{\rho_j c_j^2} \right]$$

$$s_{3D} = \left[\frac{\rho_i + 2\rho_j}{\rho_j + K\rho_i} \right] \frac{s_3}{2}$$

$$v_{3D} = 1 + \frac{3\pi\sigma_v}{8N\ell^3} \left[\frac{\rho_j - \rho_i}{\rho_j + \rho_i/2} \right] s_{3D}$$

$$\beta = \frac{\rho_1 c_1}{\rho_2 c_2} \text{ represents the relative normal admittance of the lower half space.}$$

Similarly, the effective relative admittance of a two-dimensionally-rough fluid interface is given by

$$\beta_2^* = ik_1 \cos^2 \theta \epsilon + \beta \quad (3)$$

$$\text{where } a_{ij} \text{ is replaced by } a_{2ij} = 2\sigma_v \left[\frac{\rho_j - \rho_i}{\rho_j + \rho_i} \right] \frac{s_{2D}}{v_{2D}},$$

$$s_{2D} = \frac{\rho_i + \rho_j}{\rho_j + K\rho_i} s_2 \quad \text{and} \quad v_{2D} = 1 + \frac{2\pi\sigma_v}{3N\ell^2} \left[\frac{\rho_j - \rho_i}{\rho_v + \rho_i} \right].$$

For $\rho_2 = \rho_3$, $c_2 = c_3$, $|\rho_3| \gg \rho_1$, the expressions for effective relative admittance of the rough surface may be simplified to

$$\beta_3^* \simeq (1 - ik_g \sigma_v) \beta - ik_0 (\sigma_v / 2) (3s_3 / v_2 - 2) \quad (4)$$

$$\beta_2^* \simeq (1 - ik_g \sigma_v) \beta - ik_0 \cos^2(\theta) \sigma_v (2s_2 / v_2 - 1) \quad (5)$$

where k_g is the complex propagation constant in lower half-space,

Shape Factors s_3 and s_2 are given by,

$$s_3 = \frac{2}{3} (1 + K), \quad s_2 = \frac{1}{2} (1 + K)$$

where $K = \frac{\text{entrained fluid mass}}{\text{mass of fluid displaced by scatterer}}$

and $K = \frac{1}{2}$ for hemispheres, $K = 1$ for semicylinders.

Dipole interaction factors, v_3 and v_2 , are given by

$$v_3 = 1 + \frac{3\pi}{8} \left(\frac{\sigma_v s_3}{N\ell^3} \right), \quad v_2 = 1 + \frac{2\pi}{3} \left(\frac{\sigma_v s_2}{N\ell^2} \right)$$

where N = number of scatterers per unit area

and ℓ = mean spacing of scatterer centres.

In equations (4) and (5) it is interesting to note that²⁰ $k_g \beta \leq \gamma \Omega k_0$ where Ω represents the porosity of the rough surface and γ is the ratio of specific heats in air.

Equivalent forms that may be deduced from the results of Howe¹² are

$$\beta_3^* = (1 + \sigma_A) \beta - ik_0 \frac{\sigma_v}{2} \left(\frac{3s_3}{v_3} - 2 \right) \quad (6)$$

$$\beta_2^* = \left[1 + \left(\frac{\pi}{2} - 1 \right) \sigma_A \right] \beta - ik_0 \sigma_v \cos^2(\theta) \left(\frac{2s_2}{v_2} - 1 \right) \quad (7)$$

where σ_A represents the area of scatterers per unit area of the rough surface.

Given any of these forms for effective relative admittance, it is possible to calculate the excess attenuation (EA) above an arbitrarily rough finite impedance boundary using the classical form for propagation from a point source over an impedance boundary.

$$\text{Hence EA} = 20 \log \left| 1 + Q \left(r_1 / r_2 \right) \exp \left(-ik_0 (r_2 - r_1) \right) \right| \quad (8)$$

where $Q = R_p + (1 - R_p) F(w)$

$$R_p = \frac{\cos \alpha - \beta^*}{\cos \alpha + \beta^*}$$

$$w = (-ik_0 r_2 / 2) (\cos \alpha + \beta^*)^2$$

$$F(w) = 1 - i\sqrt{\pi} w e^{-w^2} \operatorname{erfc}(iw).$$

2. Propagation in a bilinear velocity gradient above a rough impedance surface.

Following Tolstoy¹⁰, we require the solution of

$$\frac{\partial^2 \phi}{\partial z^2} + \gamma^2(z) \phi = 0, \quad z > 0 \quad (9)$$

where $\gamma^2(z) = k^2 - K^2$, K is horizontal wave number
 $k = \omega / c(z)$

$$c(z) = \left(\frac{1}{c_0^2} + qz \right)^{-1/2},$$

$$\text{subject to } \frac{\partial \phi}{\partial z} = -\varepsilon \left(k_0^2 + \delta \frac{\partial^2}{\partial z^2} \right) \phi, \quad z = 0 \quad (10),$$

where

$$\varepsilon = \frac{\sigma_v}{2} \left(\frac{3s}{v} - 2 \right) - i(1 + \sigma_A) \frac{\beta}{k_0} \quad \text{or} \quad \frac{\sigma_v}{2} \left(\frac{3s}{v} - 2 \right) - i(1 + ik_g \sigma_v) \frac{\beta}{k_0}$$

$$\text{and } \delta = \frac{3\sigma_v s}{2\varepsilon v}.$$

If source and receiver are on the boundary, then the solution may be written,

$$\phi = \frac{1}{2\pi} e^{i\alpha} \int_0^\infty \frac{H_{1/3}^{(2)}(S_0)}{H_{-2/3}^{(2)}(S_0) - \varepsilon \left(\delta - k_0^2 / \gamma_0^2 \right) \gamma_0 H_{1/3}^{(2)}(S_0)} \frac{1}{\gamma_0} J_0(Kr) K dK \quad (11)$$

where $S_0 = \frac{2}{3p} \gamma_0^3$, $\gamma_0^2 = k_0^2 - K^2$, $p = \omega^2 q$, and $H^{(2)}(\)$ are Hankel

functions of the second kind.

Note that p may be positive or negative. However in the remainder of this contribution we concentrate on $p \geq 0$, corresponding to a homogeneous or upward refracting atmosphere. If equation (11) is rewritten in the form

$$\phi = \frac{1}{2\pi} \varepsilon^{i\alpha} \int_0^\infty \frac{1}{\gamma_0 \frac{H_{-2/3}^{(2)}(S_0)}{H_{1/3}^{(2)}(S_0)} - \varepsilon(\gamma_0^2 \delta - k_0^2)} J_0(Kr) K dK \quad (12)$$

then it is easier to deduce both the approximate form of solution and the relationship with standard results for special cases. Two of these are given in Table 1.

In particular it should be noted that (12) reduces to the standard integral¹⁷ for propagation over a smooth impedance plane in the absence of a velocity gradient and roughness. The reduced form for $p > 0$, and no roughness may be seen to be related

to the standard integral for this case¹⁸ when the relationships between Hankel functions of one-or two-thirds order and Airy functions are invoked.

Conditions	Reduced form for ϕ
$p \rightarrow 0, S_0 \rightarrow \infty$ $H_{-2/3}^{(2)}(S_0) / H_{1/3}^{(2)}(S_0) \rightarrow -i$ $\sigma_v = \sigma_A = 0$ smooth, finite impedance, isothermal	$-\frac{1}{2\pi} e^{i\alpha x} \int_0^\infty \frac{K J_0(Kr) dK}{\sqrt{k^2 - k_0^2} + i k_0 \beta}$
$p > 0, \sigma_v \sigma_A = 0$ upward refraction, smooth hard	$-\frac{1}{2\pi} e^{i\omega t} \int_0^\infty \frac{H_{1/3}^{(2)}(S_0)}{H_{-2/3}^{(2)}(S_0)} \frac{1}{\gamma_0} J_0(Kr) K dK$
$p \rightarrow 0, \beta = 0$ rough, hard, isovelocity	$-\frac{1}{2\pi} e^{i\alpha x} \int_0^\infty \frac{J_0(Kr)}{i\gamma + \epsilon_1 (\delta\gamma_0^2 - k_0^2)} K dK$ $\epsilon_1 = \frac{\sigma_v}{2} \left(\frac{3s_{3D}}{v} - 2 \right)$

Table 1. Reduced or simplified forms of equation (12) for special cases.

3. Far-field solutions at grazing-incidence over hard boundary.

The integral given in the last row of Table 1 may be evaluated as a residue series sum. One of the poles corresponds to complex value of γ and to a roughness-induced surface wave.

Hence the total field is the sum of the diffracted solution and roughness-induced surface wave.

The diffracted field over a smooth *hard* boundary in shadow zone is given by¹⁰

$$\phi \simeq \frac{p^{1/3}}{2\sqrt{\pi k_0 r}} e^{5i\pi/12} \sum_m k_m^{-1/2} x_m^{-1} e^{-i(k_0 r - \omega t)} e^{-\delta_m r} \quad (13)$$

where $k_m \simeq k_0 - i\delta_m$, $\delta_m = \frac{1}{4\sqrt{3}} X_m q^{2/3} c_0^{4/3} k_0^{1/3}$

and the first three values of X_m are given by

$$X_1 = 1.0188 \quad X_2 = 3.2482 \quad X_3 = 4.8201.$$

The far-field approximation is given simply by the first term, hence

$$\phi_d \simeq \frac{1}{2\sqrt{2\pi k_0 r}} \frac{p^{1/3}}{X_1} e^{5i\pi/12} e^{\delta_1 r} e^{-i(k_0 r - \omega t)}$$

where $\delta_1 = 0.441 q^{2/3} c_0^{4/3} k_0^{1/3}$.

The boundary wave over a *hard rough* surface in the shadow zone, for weak gradients and high frequencies may be calculated from

$$\phi_B \simeq \frac{e^{3i\pi/4}}{\sqrt{2\pi k_0 r}} \epsilon_1 k_0^2 e^{-\delta_B r} e^{-i(k_0 r - \alpha r)} \quad (14)$$

$$\text{where } \delta_B \simeq \epsilon_1^2 k_0^3 \exp\left(-\frac{4\epsilon_1^3 k_0^4}{3q c_0^2}\right).$$

The ratio of the rough surface boundary wave to the first term of the diffracted field in the far-field is given by

$$\left| \frac{\phi_B}{\phi_d} \right| \simeq 2p^{-1/3} \epsilon_1 k_0^2 X_1 \exp(\delta_1 - \delta_B)r \quad (15)$$

where $\epsilon_1 \simeq \frac{1}{2}$ (scatterer volume above plane per unit area).

4. Far-field in shadow zone above a rough impedance boundary

The solution of equation (12) can, in general, be approximated by a residue series summation. Again the total field is given by a diffracted contribution plus a surface wave corresponding complex γ .

Hence $\phi = \phi_d + \phi_B$, where

the diffracted field is given by

$$\phi_d = \frac{ip}{4} \sum_m \frac{H_0^{(2)}(K_m r) e^{i\alpha r}}{\gamma_{0m}^2 + p\epsilon\delta + \epsilon^2(k_0^2 - \delta\gamma_{0m}^2)^2} \quad (16)$$

and the roughness induced surface wave may be approximated by

$$\phi_B \simeq \frac{i\epsilon k_0^2}{\sqrt{2\pi k_0 r}} \left[1 + \frac{0.541}{w_{0B}} \right] \exp(-\alpha_B r) \exp\left[-i\left(k_0 r - \omega t - \frac{\pi}{4}\right)\right] \quad (17)$$

$$\text{where } \alpha_B \simeq \text{Re} \left[\epsilon^2 k_0^3 e^{-2w_{0B}} \left(1 + \frac{7}{36} \frac{1}{w_{0B}} \right) \right]$$

$$\text{and } w_{0B} \simeq \left| \frac{2\epsilon^3 k_0^6}{3p} \right|.$$

$\gamma_{0m}, K_m (= \sqrt{\gamma_{0m}^2 - k_0^2})$ are solutions of

$$\gamma_0 [H_{-2/3}^{(2)}(S_0) / H_{1/3}^{(2)}(S_0)] - \epsilon (\delta\gamma_0^2 - k_0^2) = 0 \quad (18)$$

which requires numerical solution in general.

Raspet et al¹⁹ have shown that, under certain circumstances, the principal far-field contribution in the refractive shadow zone above a *smooth* finite impedance boundary is due to the surface wave associated with propagation from a point source in a homogeneous atmosphere above a finite impedance plane. To estimate the possible effects of roughness, therefore it is interesting to compare the magnitudes of the corresponding surface wave contributions with and without surface roughness.

Under the restrictions,

$k_0 h \ll 1$, $k_0 \ell \leq 1$ (which sets high frequency limit)
and $w_{0BR} > 1$, $w_{0BS} > 1$ (which sets low frequency limit)

The far-field surface wave potentials are given by¹⁰

$$\phi_{BR} = \frac{ik_0^2 \epsilon}{\sqrt{2\pi k_0 r}} \left[1 + \frac{0.541}{w_{0BR}} \right] e^{-\alpha_{BR} r} \exp \left[-i \left(k_0 r - \omega t - \frac{\pi}{4} \right) \right] \quad (19)$$

and

$$\phi_{BS} = \frac{\beta_s k_0}{\sqrt{2\pi k_0 r}} \left[1 + \frac{0.541}{w_{0BS}} \right] e^{-\alpha_{BS} r} \exp \left[-i \left(k_0 r - \omega t - \frac{\pi}{4} \right) \right] \quad (20)$$

for the rough and smooth surface respectively.

$$\text{Hence } \frac{\phi_{BR}}{\phi_{BS}} = \frac{i\epsilon k_0}{\beta_s} \frac{\left[1 + \frac{0.541}{w_{0BR}} \right]}{\left[1 + \frac{0.541}{w_{0BS}} \right]} e^{(\alpha_{BS} - \alpha_{BR})r} \quad (21)$$

where $i\epsilon k_0 = \beta_s$ (effective relative normal admittance of rough surface).

From (21) it is clear that the ratio depends upon the ratio of the effective admittance with roughness to the admittance of the smooth surface. For a given roughness, this ratio decreases as the admittance of the (smooth) surface decreases.

5. Attenuation of boundary wave due to incoherent scatter

The presence of surface roughness leads to incoherent as well as coherent scatter.

Consequently the amplitudes of the roughness-induced boundary waves are decreased. Tolstoy¹⁶ has considered this attenuation for a general rough two-fluid interface.

Hence for a rough two-fluid interface, the attenuation constants are given by

$$\alpha_{3D} = \frac{1}{4\pi N} \frac{g_1 \left(A^2 + \frac{1}{3} b_3^2 \right)}{1 + \rho_1 g_1 / \rho_2 g_2} k_0^4 \quad (22)$$

$$\alpha_{2D} = \frac{1}{2N} \frac{g_1 \left(A^2 + \frac{1}{2} b_2^2 \right)}{1 + \rho_1 g_1 / \rho_2 g_2} k_0^3 \quad (23)$$

where $g_{1,2}$ are roots of characteristic equation for boundary wave,

$$A = \sigma_v (1 - \rho_1 c_1^2 / \rho_2 c_2^2),$$

$$b_3 = \frac{3\sigma_v s_{3D}}{2} (1 - \rho_1 / \rho_2),$$

$$b_2 = 2\sigma_v s_{2D} (1 - \rho_1 / \rho_2),$$

and subscripts 3,2 refer to 3-D and 2-D roughnesses respectively.

In particular for hemispherical or semi cylindrical roughnesses of radius a , in a hard boundary,

$$\alpha_{3D} \simeq \frac{7}{16\pi N} \sigma_v^3 k_0^6, \quad \sigma_v = \frac{2N}{3} \pi a^3$$

and

$$\alpha_{2D} \simeq \frac{3}{4N} \sigma_v^3 k_0^5, \quad \sigma_v = \frac{N\pi a^2}{2}$$

respectively.

RESULTS

1. Comparisons with data

Measurements of excess attenuation above various smooth and artificially-roughened boundaries have been made in an anechoic chamber¹⁵.

A smooth boundary consisted of a varnished-wooden board measuring 1.2 m x 1.2 m x 0.02 m (thick). Forty varnished halves of 1 m long wooden dowel rods (0.006 m radius) were used as two dimensional roughnesses and placed at regular spacing on the board between source and receiver.

Figure 1(b) shows an example comparison between measured and predicted excess attenuation spectra with source and receiver at 0.145 m height and separated by 1 m. The measured influence of these roughnesses is to change the frequency of the primary ground effect dip from 4 kHz to a little more than 3 kHz and to deepen it from 25 to 32 dB. Figure 1(a) shows a prediction obtained by assuming that the (smooth) varnished board has a small but finite admittance corresponding to a rigid-porous medium with triangular pores²¹, porosity 0.1, flow resistivity 500,000 kN s m⁻⁴, tortuosity 1, and that the effect of the roughnesses is modelled by equations (7) and (8) (the curve labelled MH). Also shown is a prediction obtained from equations (2) and (8) using an impedance for the scatterers corresponding to that of a rigid-porous medium with triangular pores²², porosity 0.1, flow resistivity 750 kN s m⁻⁴ tortuosity 1 (the curve labelled MT). The agreement between prediction (MT) and measurement is good.

2. Numerical far-field estimates

Figure 2 shows the estimated ratio of rough to smooth fields as a function of range in the presence of a weak bilinear sound velocity gradient of 0.005 ms⁻¹ m⁻¹ at 500 Hz. Close packed 3-D or 2-D roughnesses of 0.025 m radius are assumed and attenuation due to incoherent scatter is included. Increases of level deep in the shadow zone by more than 20 dB are predicted as a consequence of close packed 3-D ground roughnesses. Incoherent scatter reduces the effect of 2-D roughnesses in comparison. Figures 3 and 4 show predicted roughness effects in the refractive shadow zone above a finite impedance surface. Clearly the influence of a given (3-D) roughness is much reduced if the ground has a small but finite admittance.

CONCLUSIONS

Measurements show that surface roughness has a significant influence on ground effect (homogeneous atmosphere). Predictions of propagation over a rough finite impedance boundary using two alternative models (MH and MT) for the effective surface admittance have been validated by data.

Tolstoy's theory for far-field propagation into the shadow zone caused by a weak velocity gradient in the atmosphere predicts substantial penetration by the rough surface boundary wave over a rough hard ground surface even when attenuation due to incoherent scatter are included.. For a given mean roughness height and close-packing, 3-D roughnesses result in greater penetration than 2-D roughnesses.

Modifications of Tolstoy's theory to account for finite impedance predict that in the far-field and high frequency limits the shadow zone penetration is much less when the ground impedance is finite.

ACKNOWLEDGEMENTS

This work was supported by EPSRC Grant No. GR/J 24052. The measurements reported in this paper were made by Shahram Taherzadeh.

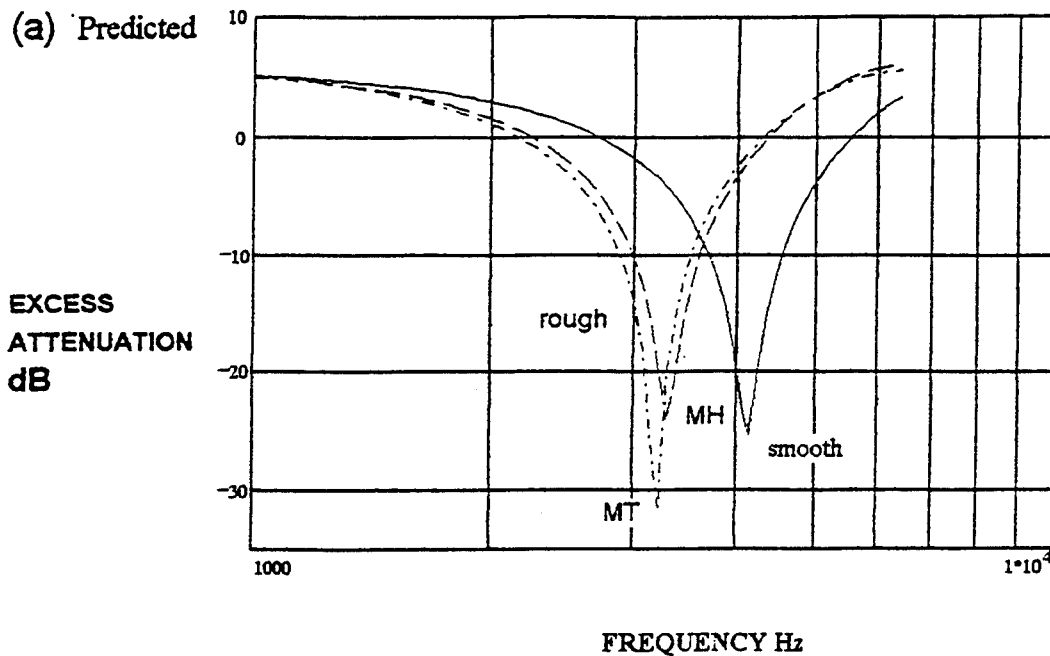
REFERENCES

1. K. Attenborough "Review of ground effects on outdoor sound propagation from continuous broad band sources" *Applied Acoustics* **24** 289-319 (1988).
2. I. Tolstoy "Smoothed boundary conditions, coherent low frequency scatter, and boundary modes" *J. Acoust.Soc.Am.* **75** (1) 1-22 (1984).
3. I. Tolstoy "Coherent sound scatter from a rough interface between arbitrary fluids with particular reference to roughness element shapes and corrugated surfaces" *J.Acoust.Soc.Am.* **72** (3) 960-972 (1982).
4. I. Tolstoy "Acoustic scatter from a slightly rough boundary between a fluid and an elastic solid" *J.Acoust.Soc.Am.* **78** (5) 1727-1734 (1985).
5. H. Medwin, J. Baillie, J. Bremhorst, B.J. Savage and I. Tolstoy "The scattered acoustic boundary wave generated by grazing incidence at a slightly rough rigid surface" *J.Acoust.Soc.Am.* **66**(4) 1131-1134 (1979).
6. H.. Medwin, G.L. D'Spain, E. Childs and S.J. Hollis "Low frequency grazing propagation over periodic steep-sloped rigid roughness elements" *J.Acoust.Soc.Am.* **76** (6) 1774-1791 (1984).
7. H. Medwin and G.L. D'Spain "Near-grazing, low-frequency propagation over randomly-rough rigid surfaces" *J.Acoust.Soc.Am.* **79** (3) 657-665 (1986).

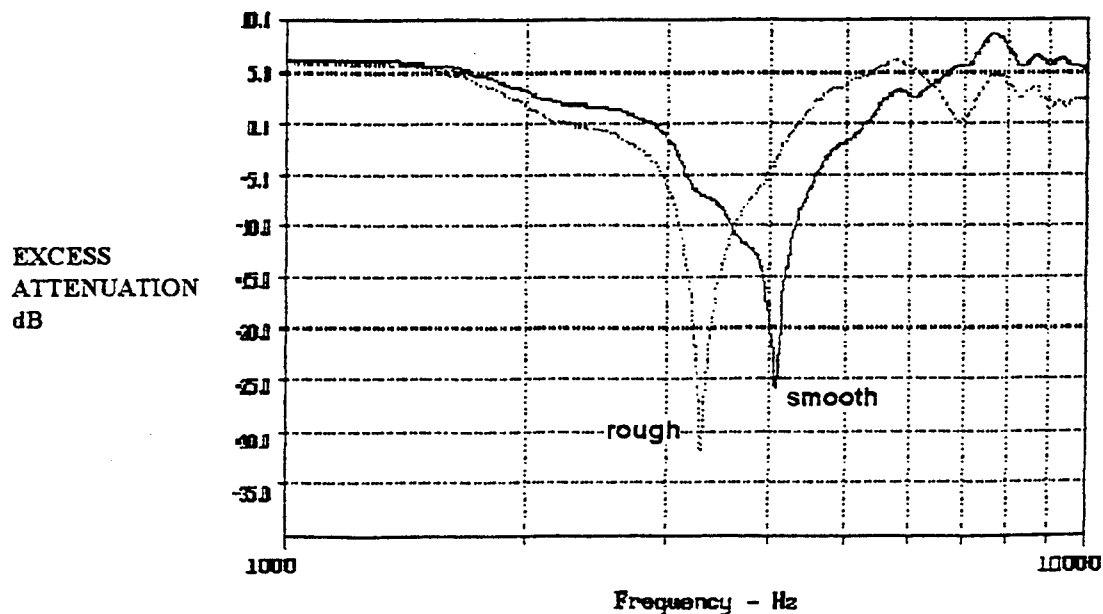
8. M.A. Biot "Reflection on a rough surface from an acoustic point source" *J.Acoust.Soc.Am.* **29** 1192-1200 (1957).
9. V.F. Twersky "On scattering and reflection of sound by rough surfaces" *J.Acoust.Soc.Am.* **29** 209-225 (1957).
10. I. Tolstoy "Energy transmission into shadow zone by rough surface boundary wave" *J.Acoust.Soc.Am.* **69** 1290-1298 (1981).
11. H. Medwin and J.C. Novarini "Modified sound refraction near an ocean bottom" *J.Acoust.Soc.Am.* **76** (6) 1791-1797 (1984).
12. M.S. Howe "On the long range propagation of sound over irregular terrain" *J.Sound Vib.* **98** (1) 83-94 (1985).
13. L.M. Brekhovskikh "Surface waves in Acoustics" *Sov.Phys.Acoust.* **5** 3-12 (1959).
14. R.J. Donato "Model Experiments on Surface Waves" *J.Acoust.Soc.Am.* **63** (3) 700-703 (1978).
15. K. Attenborough and S. Taherzadeh "Propagation of sound over rough finite impedance surfaces" *J.Acoust.Soc.Am.* **95** (5, Pt 2) 2a PA6 (S) 2358 (1994).
16. I. Tolstoy "Rough surface boundary wave attenuation due to incoherent scatter" *J.Acoust.Soc.Am.* **77** (2) 482-488 (1985).
17. K. Attenborough, S.I. Hayek and J.M. Lawther "Propagation from a point source over a porous half space" *J.Acoust.Soc.Am.* **68** (5) 1493-1501 (1980).
18. A. Pierce "Acoustics: an introduction to its physical principles and applications" publ. Acoustical Society of America, American Institute of Physics, New York (1991).
19. R. Raspet, G.E. Baird, W. Wu "The relationship between upward refraction above a complex impedance plane and the spherical wave evaluation for a homogeneous atmosphere" *J.Acoust.Soc.Am.* (1991).
20. K. Attenborough "Acoustical characteristics of rigid absorbents and granular media" *J.Acoust.Soc.Am.* **83** (3) 785-799 (1983).
21. K. Attenborough "Models for the acoustical properties of air-saturated granular materials" *Acta Acustica* **1** 213-226 (1993).

Fig-1

Effects of semicylindrical roughnesses on excess attenuation over wooden boundary



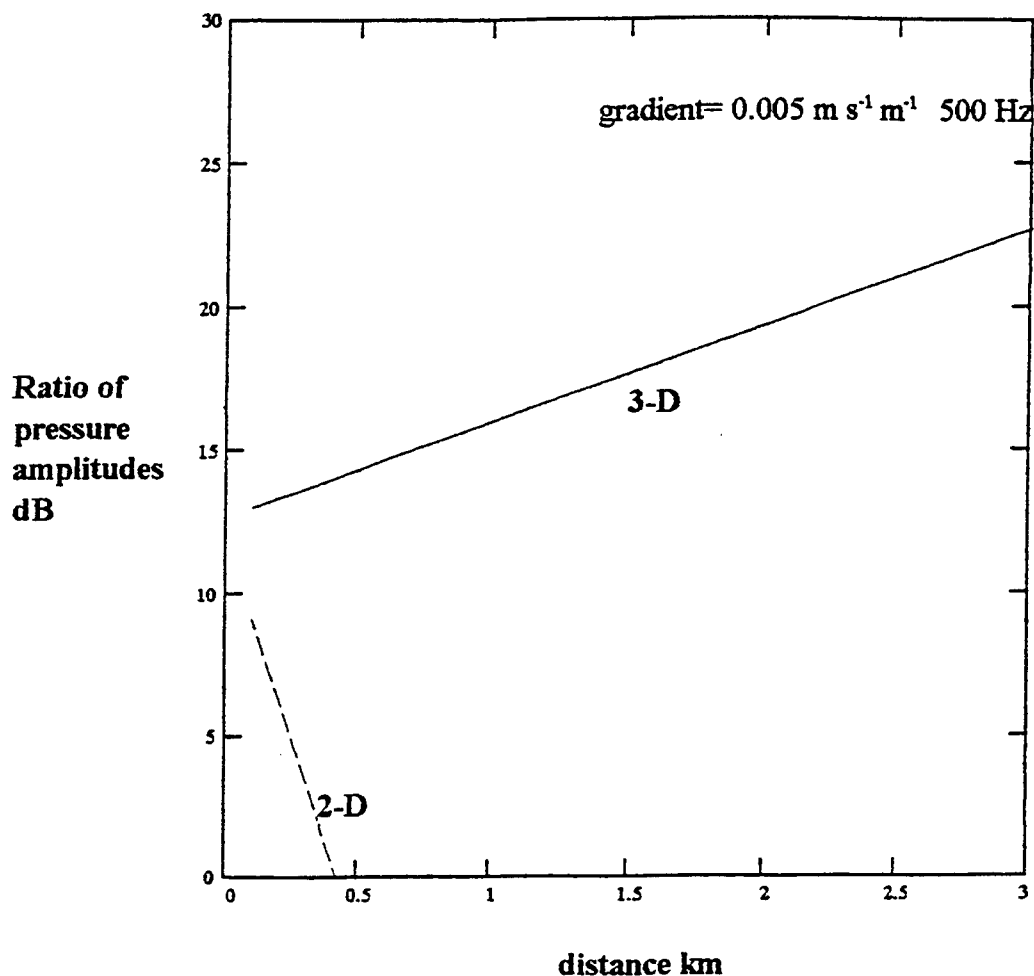
(b) Measured



Predictions for source and receiver at 0.145 m height and 1 m separation with wooden base characterized by flow resistivity $500000 \text{ kN s m}^{-4}$, porosity 0.1, tortuosity 1 and 0.006 mm semicylindrical scatterers characterized by flow resistivity 750 kN s m^{-4} porosity 0.1 and tortuosity 1.

Fig. 2

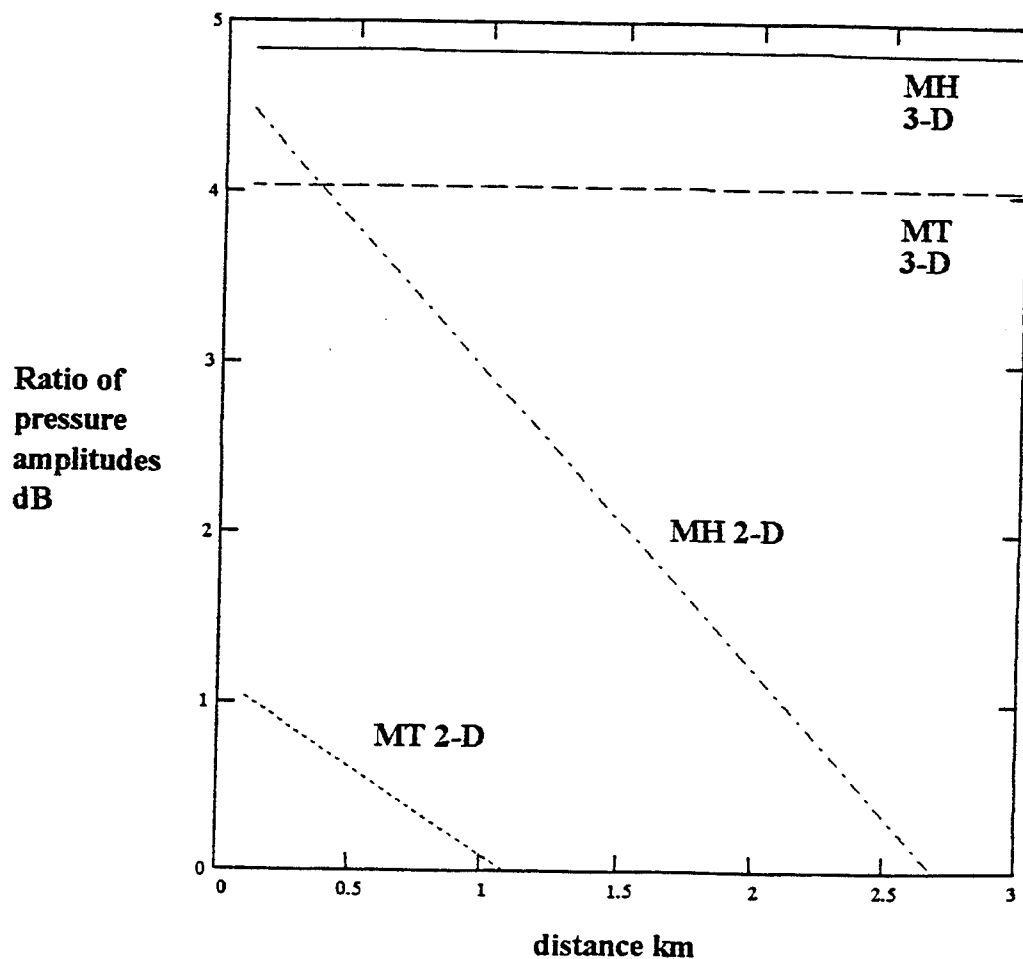
Far-field propagation at grazing incidence into the refractive shadow zone over a rough hard boundary



Predicted ratio of pressure in a rough surface boundary wave to the diffracted field in shadow zone caused by weak upward refracting atmosphere ($-0.005 \text{ m s}^{-1}/\text{m}$) at 500 Hz. Close-packed roughnesses of 0.025 m radius are either hemispherical or cylindrical. Attenuation due to incoherent scatter is included.

Fig. 3

Propagation at grazing incidence into the refractive shadow zone over a rough finite impedance boundary at 200 Hz

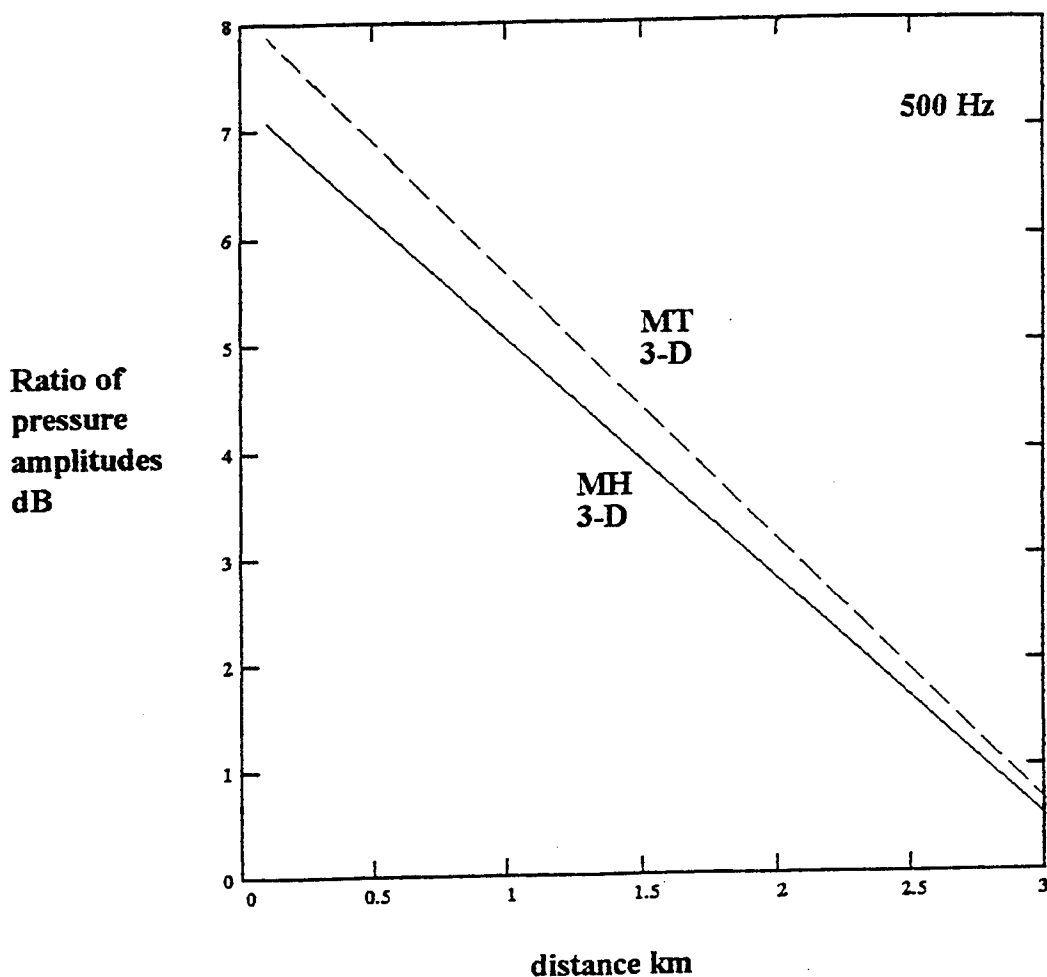


Predicted amplitude ratio of pressure in a rough surface boundary wave to that in the surface wave over smooth finite impedance boundary in shadow zone caused by weak upward refracting atmosphere ($-0.005 \text{ m s}^{-1}/\text{m}$) at 200 Hz. Close-packed roughnesses of 0.025 m radius are assumed. Attenuation due to incoherent scatter is included.

Finite impedance is modelled by flow resistivity $1000 \text{ kPa s m}^{-2}$, porosity 0.2, tortuosity 3.

fig. 4

Propagation at grazing incidence into the refractive shadow zone over a rough finite impedance boundary



Predicted amplitude ratio of pressure in a rough surface boundary wave to that in the surface wave over smooth finite impedance boundary in shadow zone caused by weak upward refracting atmosphere ($-0.005 \text{ m s}^{-1}/\text{m}$) at 500 Hz. Close-packed hemispherical roughnesses of 0.025 m radius are assumed. Attenuation due to incoherent scatter is included. Finite impedance is modelled by flow resistivity $1000 \text{ kPa s m}^{-2}$, porosity 0.2, tortuosity 3.

INVESTIGATIONS INTO POINT SOURCE PROPAGATION IN
THE FREQUENCY DOMAIN AND IN THE TIME DOMAIN

Karsten Bo Rasmussen
The Acoustics Laboratory
Building 352, Technical University of Denmark
DK 2800 Denmark

Stoyan Yotov
The Bulgarian Academy of Sciences
2 Gagarin St.
1113 Sofia Bulgaria

ABSTRACT

Outdoor sound propagation is investigated with emphasis on time domain results and on results from model experiments. Results from model experiments in scale 1:25 are compared with previously published theory for propagation over an impedance discontinuity and for propagation over an earth berm. The influence of the impedance of the earth berm is also studied. It is demonstrated that time domain results provide useful information as a supplement to the frequency spectra.

INTRODUCTION

The present work is an investigation into outdoor propagation with emphasis on time domain results and on results from model experiments. Sound propagation over an impedance jump and over an earth berm is studied. Sound pressure responses are obtained experimentally by means of a 1:25 scale model using a triggered spark source. These results are compared with calculated results based on theories described elsewhere. The theoretical models in question have been developed in the frequency domain but time domain results are obtained by means of inverse Fourier transform.

The use of impulse excitation makes it possible to distinguish contributions from various propagation paths in the scenario. Furthermore the comparison between measured and calculated data in the time domain may reveal phase discrepancies in the theoretical models.

Scale model experiments may introduce a number of errors in comparison with full-scale measurements, since not all physical phenomena involved are transformed according to a linear scaling factor. The influence of atmospheric absorption as well as boundary layer effects are two such examples of phenomena which are not transformed according to scale.

Nevertheless scale modelling makes it possible to investigate one propagation parameter at a time - something which is virtually impossible under full scale conditions.

I. SCALE MODEL MEASUREMENTS

A newly developed scale model facility¹ has been used for the measurements. The facility is based upon a triggered spark source using a spark energy of 0.25 Joule or less. An energy level of 0.25 Joule was found to be sufficiently low to avoid non-linear effects so long as the spark source was 5 cm from the surface. The source is constructed with 40 mm long electrodes in order to reduce unwanted reflection and has a spark gap of 0.5-1 mm. The source is controlled by a PC resident board using two ADSP2101 processors. The board is also used for event recording of the received signal. The receiver chain consists of a B&K 4138 1/8 inch microphone and a battery powered B&K 2804 power supply followed by a battery powered low-noise amplifier and anti-aliasing filter. The set-up is used with a scaling factor of 1:25. This scale factor was the largest possible with the set-up used. The results shown in this work are obtained by time-domain averaging, i.e. the pressure responses from a number of impulses were averaged in the time domain. The sampling frequency used was 600kHz. The

obtained waveform is then edited and Fourier-transformed (FFT with 1024 data points).

Grass-covered ground was modelled by canvas-layers on top of a hard surface. Two types of canvas were used which have been found to represent flow resistivities of 300 kNsm^{-4} and 500 kNsm^{-4} in the well-established Delany-Bazley formulae¹. In the following a case of propagation over a plane surface with a simple impedance variation is studied and propagation over earth berms is also studied. An earth berm model was made of plywood which was assumed to have an infinite impedance. Figure 1 displays the basic earth berm geometry. The internal angle of the wedge representing the earth berm is 90 degrees and the wedge is 240 cm long and 20 cm high in model scale. It effectively represents an infinitely long earth berm with a full scale height of 5 meters.

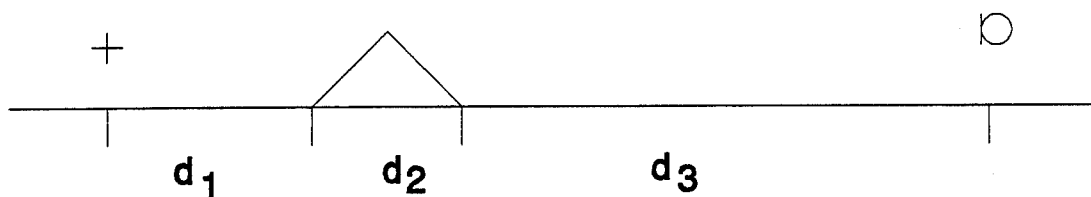


Figure 1. Geometry of earth berm on ground. Full scale source height $h_s=1.25\text{m}$, $d_2=10\text{m}$, berm height 5m in all cases.

II. THEORY FOR SIMPLE IMPEDANCE VARIATION

For studying sound propagation over an impedance discontinuity an aperture method was used². It involves integration over a vertical line located at the impedance discontinuity in the plane containing source and receiver (the horizontal integration has been eliminated by the method of stationary phase).

The expression for the sound pressure p_a is given by Eq. (1) valid for an impedance discontinuity line normal to the line through source and receiver

$$p_a = (k / (2\pi))^{1/2} e^{j\pi/4} \int_0^a \left[\frac{e^{-jk(R_1+R_3)}}{(R_3 R_1 (R_1+R_3))^{1/2}} + \frac{e^{-jk(R_1+R_4)}}{(R_4 R_1 (R_1+R_4))^{1/2}} Q_2 + \frac{e^{-jk(R_2+R_3)}}{(R_3 R_2 (R_2+R_3))^{1/2}} Q_1 + \frac{e^{-jk(R_2+R_4)}}{(R_4 R_2 (R_2+R_4))^{1/2}} Q_1 Q_2 \right] dz \quad (1)$$

Eq. (1) is obtained from Eq. (30) in Rasmussen² after change of sign convention to $e^{j\omega t}$ and after the introduction of the approximation $d_2 \approx R_3 \approx R_4$ valid for low source and receiver heights. The distances R_1 to R_4 are path lengths shown in Figure 2, and the source and receiver heights are given by h_s and h_r . The total horizontal distance is d and the aperture plane is located over the discontinuity at a distance d_1 from source and d_2 from receiver. Q_1 and Q_2 are spherical wave reflection factors which were calculated according to Chien and Soroka³. Theoretically the upper integration limit "a" should be infinity. In practice a suitable order of magnitude for "a" is $d/4$. The numerical integration was performed with a spacing of $\lambda/5$. Formula 1 has been derived and verified in previous work for short ranges.

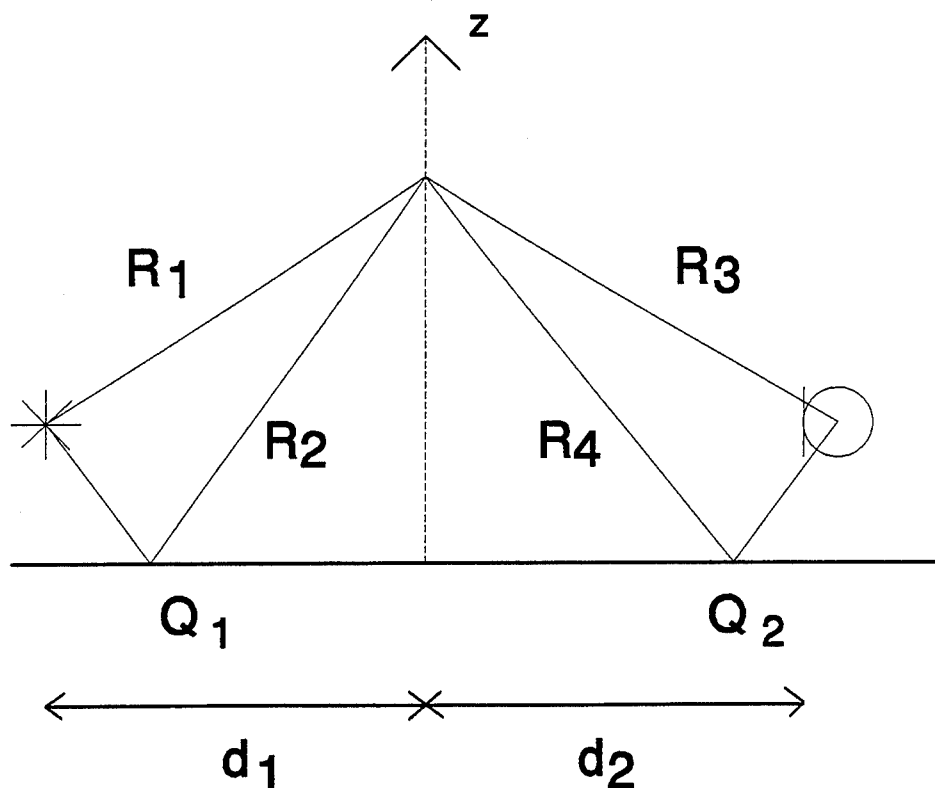


Figure 2. Geometrical parameters for impedance jump.

III. WEDGE THEORY

Previously published theory⁴ was used for comparison with the experimental data obtained. The theory is based upon Uniform Theory of Diffraction⁵ (UTD) in combination with well-established formulae for sound propagation over finite impedance ground.

The UTD calculations are based upon the expressions originally given by Kouyoumjian and Pathak for diffraction by a wedge of infinite impedance. The diffracted sound pressure is (the sound rays being normal to the edge and using $e^{j\omega t}$ notation)

$$p = \frac{e^{-jkR_1}}{4\pi R_1} [V(r_0 r_1 / R_1, 1, \theta_1 - \theta_0) + V(r_0 r_1 / R_1, 1, \theta_1 + \theta_0)], \quad (2)$$

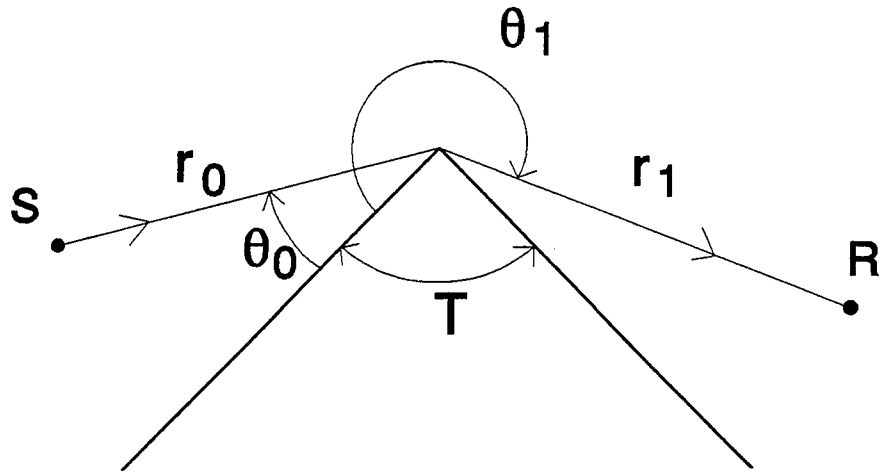


Figure 3. Incident and diffracted ray for a wedge. $R_1=r_0+r_1$.

$$V(A, B, \theta) = V^+(A, B, \theta) + V^-(A, B, \theta), \quad (3)$$

$$V^{\pm}(A, B, \theta) = \frac{-e^{-j\pi/4}}{\sqrt{2\pi kAB}} \frac{1}{2\nu} \cot\left(\frac{\pi \pm \theta}{2\nu}\right) F'(BX^{\pm}(\theta)), \quad (4)$$

$$X^{\pm}(\theta) = 2kA \cos^2((2N^{\pm}\nu\pi - \theta)/2), \quad (5)$$

$$F'(x) = 2j\sqrt{x}e^{jx}F^*(\sqrt{x}). \quad (6)$$

Here $\nu=2-T/\pi$, $R_1=r_0+r_1$ and F^* is the complex conjugate of the Fresnel integral. N^+ and N^- are determined from

$$N^+ = \begin{cases} 0 & \text{for } \theta \leq \pi - T \\ 1 & \text{for } \theta > \pi - T \end{cases} \quad (7)$$

$$N^- = \begin{cases} -1 & \text{for } \theta < T - \pi \\ 0 & \text{for } T - \pi \leq \theta \leq 3\pi - T \\ 1 & \text{for } \theta > 3\pi - T \end{cases} \quad (8)$$

The UTD formulation is believed to be of the same order of accuracy as for instance the formulae developed by Medwin^{6,7} and by Hadden and Pierce⁸. A recent investigation by Saunders and Ford⁹ using explosive sources concludes that the theories of Medwin and Hadden and Pierce are reasonably successful when compared with their experimental data.

The ground below the earth berm is taken into account by means of spherical wave reflection calculations as described in the original reference⁴ as well as in Saunders and Ford⁹.

IV. RESULTS

The outlined theoretical models provide results in the frequency domain. In this section calculated results in the time domain are shown. They are obtained by a convolution of the measured free field time response of the spark source measured at the distance in question in the scale model with the theoretical impulse response of the surface. The convolution was realised as a multiplication in the frequency domain and the result was then transformed into the time domain by means of an inverse Fast Fourier Transform.

The influence of acoustic boundary layer theory on the apparent surface admittance in the scale model has been ignored in all the calculated data in this work.

The Figures 4 and 5 show results for propagation over a plane unobstructed terrain with an impedance jump along a

straight line. The results are seen to agree quite well with the theoretical data in the frequency domain as well as in the time domain.

In Figures 6-7 measured and calculated sound pressure levels are shown for propagation over an earth berm configuration for two different receiver heights. The calculations are made for finite impedance ground (500 kNsm^{-4} in the Delany-Bazley model) and for hard wedge. The theory and experiments are seen to agree very well. The uniform diffraction theory involved is a high frequency approximation and some deviations must therefore be expected at low frequencies.

In Figures 8-10 time domain results are shown for the cases dealt with in Figures 6-7 and for the reference signal corresponding to free field propagation over the same distance as used in the measurements involving ground and earth berm. From the time domain results the specific arrival of the direct (diffracted) ray passing the vertex of the berm is seen followed by arrivals associated with ground reflected ray paths. Hence, the events identified with numbers in the figures are associated with source-vertex-receiver (no.1), source-vertex-mirror receiver (no.2), mirror source-vertex-receiver (no.3), mirror source-vertex-mirror receiver (no.4). The agreement between measured and calculated waveforms is seen to be very good since all major features in the measured curves are reproduced in the calculated ones. The slight deviation between measured and calculated peak heights is believed to be caused by inaccuracies in the calculation model and possibly by a weak non-linearity in the measurements.

Figure 11 shows a comparison between theory and measured data for another slightly different earth berm configuration. In the scale model another type of canvas was used for ground cover representing a flow resistivity of 300 kNsm^{-4} in the Delany and Bazley model. The agreement is satisfactory. This configuration is also used in Figures

12 and 13 but now the influence of the impedance of the berm is investigated. Experimental data for hard versus finite impedance earth berm are shown in the frequency domain and in the time domain. The influence of the impedance of the berm is to increase the attenuation by the berm but also to shift the interference pattern in frequency. The time-domain response reveals an influence of the impedance of the berm which is relatively more pronounced for the part of the signal which is reflected by the ground either on the receiver side of the berm (no.2) or on the source side of the berm (no.3). This is due to the fact that the reflected contributions pass the wedge legs in a grazing fashion.

V. CONCLUSION

Scale model experiments have confirmed the applicability of the calculation models outlined in this work. Time domain representation of results has revealed additional information relating to the phase of the transfer functions and relating to different propagation paths. The influence of the impedance of an earth berm has been illuminated.

REFERENCES

- ¹K.B. Rasmussen, "Scale-model simulation of sound propagation over an impedance discontinuity" INTER-NOISE 93 proceedings, Leuven, Belgium (1993)
- ²K.B. Rasmussen, "A note on the calculation of sound propagation over impedance jumps and screens", J. Sound Vib. 84, 598-602 (1982)
- ³C.F. Chien, W.W. Soroka "A note on the calculation of sound propagation along an impedance surface" Journal of Sound and Vibration 69, 340-343 (1980)
- ⁴K.B. Rasmussen, "On the effect of terrain profile on sound propagation outdoors" Journal of Sound and Vibration 98, 35-44 (1985)
- ⁵R.G. Kouyoumjian and P.H. Pathak, "A uniform geometrical theory of diffraction for an edge in a perfectly conducting surface" Proceedings of the IEEE 62, 1448-1461 (1974)
- ⁶H. Medwin, "Shadowing by finite noise barriers" Journal of the Acoustical Society of America 69, 1060-1064 (1981)
- ⁷H. Medwin, E. Childs and G.M. Jebsen, "Impulse studies of double diffraction: A discrete Huygens interpretation" Journal of the Acoustical Society of America 72, 1005-1013 (1982)
- ⁸W.J. Hadden and A.D. Pierce, "Sound diffraction around screens and wedges for arbitrary source locations" Journal of the Acoustical Society of America 69, 1266-1276 (1981).
- ⁹ D.J. Saunders and R.D. Ford, "A study of the reduction of explosive impulses by finite sized barriers" Journal of the Acoustical Society of America 94, 2859-2875 (1993).

Figure 4. $h_s=1.25\text{m}$
 $h_r=2\text{m}$, $d=112.5\text{m}$.
 1: $d_1=35\text{m}$, $\sigma_1=300\text{kNsm}^{-4}$
 $d_2=77.5\text{m}$, $z_2=\infty$
 2: $d_1=77.5\text{m}$, $z_1=\infty$,
 $d_2=35\text{m}$, $\sigma_2=300\text{kNsm}^{-4}$
 —: Measured
 - - - -: Calculated

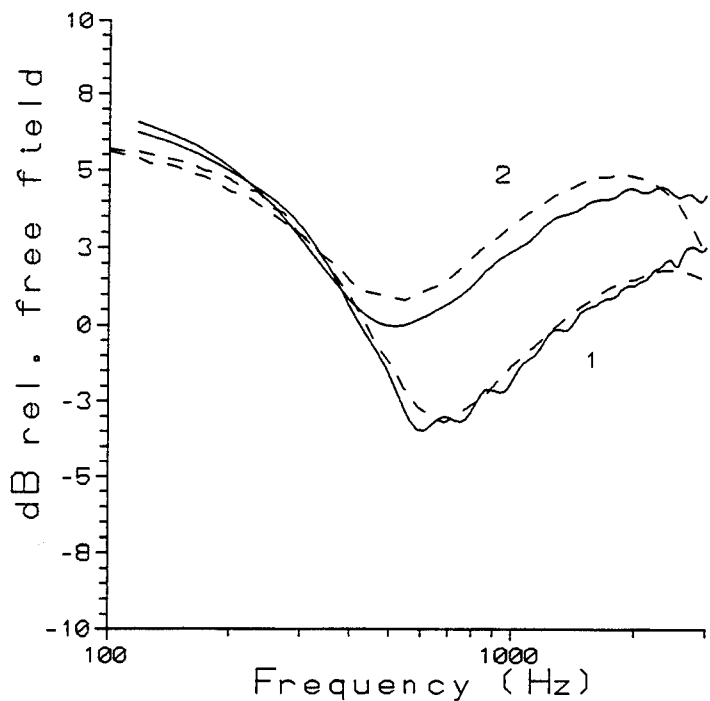


Figure 5. $h_s=1.25\text{m}$
 $h_r=2\text{m}$, $d=112.5\text{m}$.
 $d_1=35\text{m}$, $\sigma_1=300\text{kNsm}^{-4}$
 $d_2=77.5\text{m}$, $z_2=\infty$
 —: Measured
 - - - -: Calculated

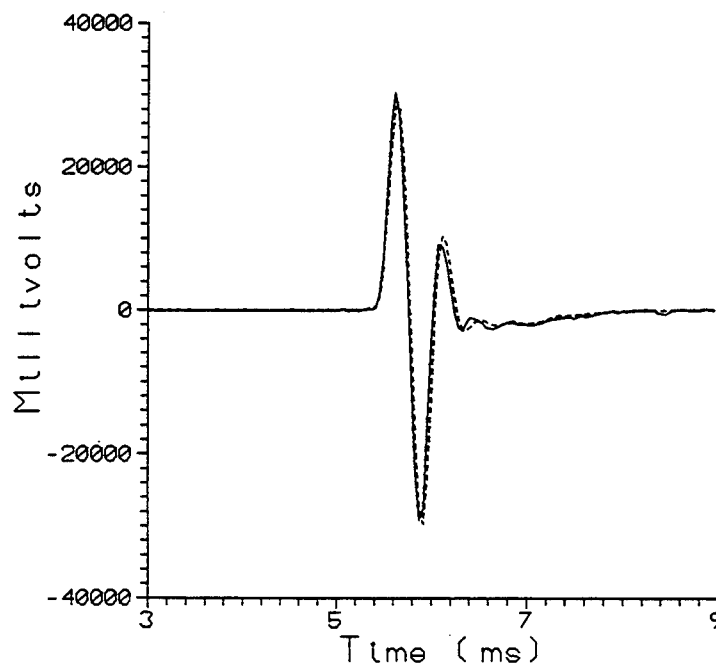


Figure 6. $h_s=1.25\text{m}$

$h_r=0.5\text{m}$, $d=52.5\text{m}$.

$d_1=12.5\text{m}$, $d_2=10$,

$d_3=30\text{m}$,

Ground: 500kNsm^{-4}

Earth berm: $z=\infty$

—: Measured

- - - -: Calculated

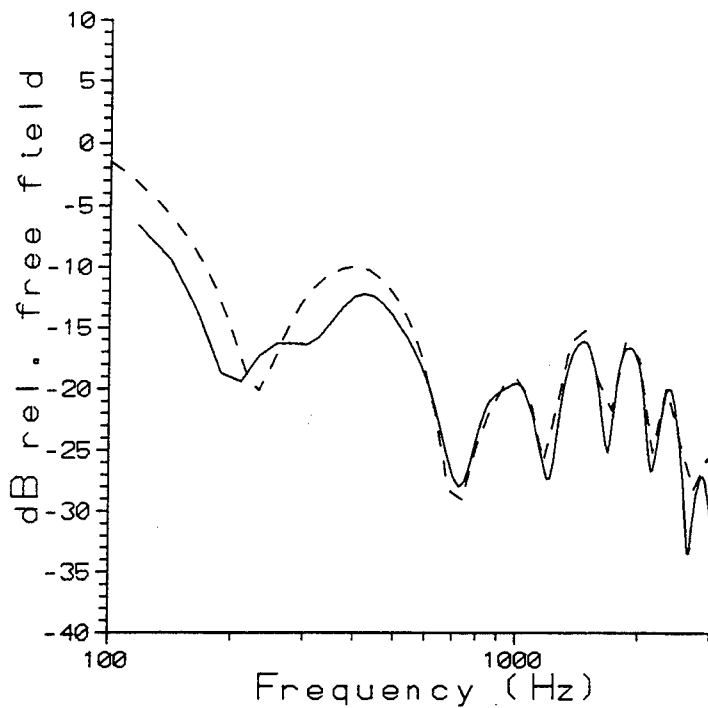


Figure 7. $h_s=1.25\text{m}$

$h_r=1.25\text{m}$, $d=52.5\text{m}$.

$d_1=12.5\text{m}$, $d_2=10$,

$d_3=30\text{m}$,

Ground: 500kNsm^{-4}

Earth berm: $z=\infty$

—: Measured

- - - -: Calculated

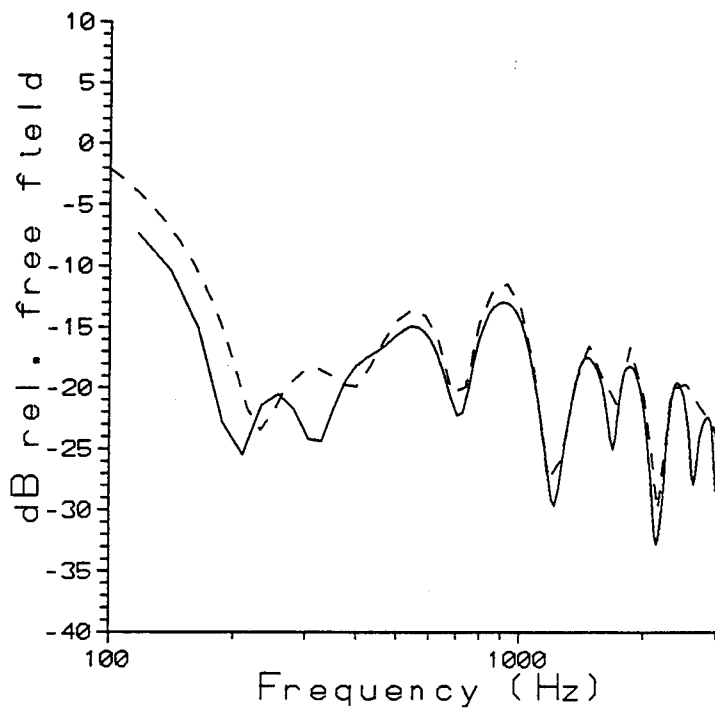


Figure 8. Waveform corresponding to Figure 6.

—: Measured
- - - -: Calculated

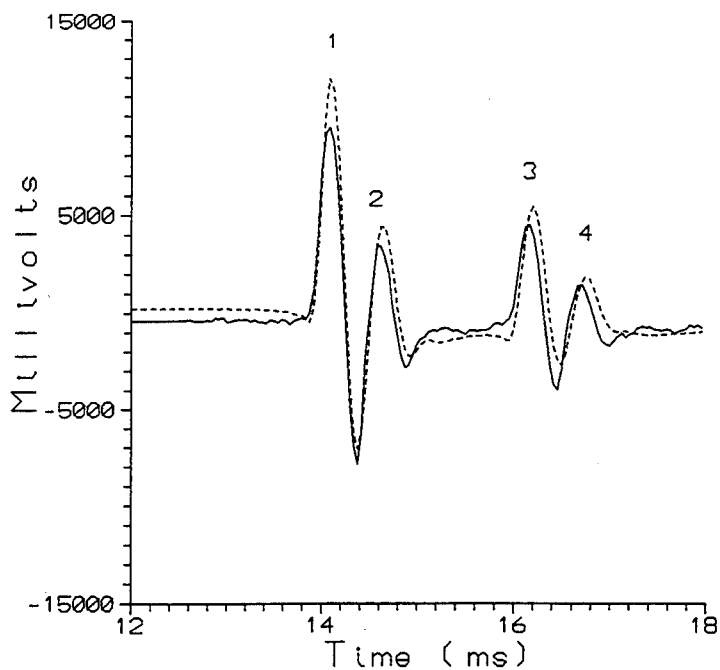


Figure 9. Waveform corresponding to Figure 7.

—: Measured
- - - -: Calculated

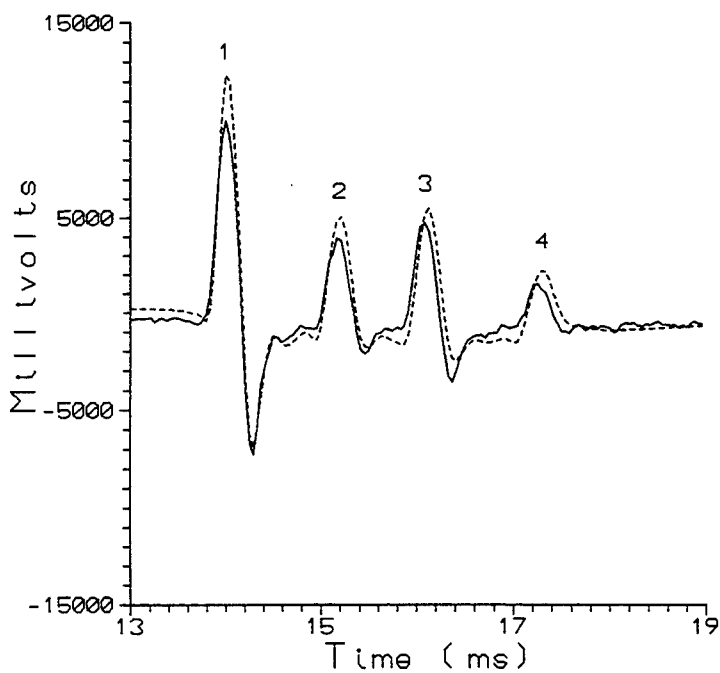


Figure 10. Measured waveform for free field. Response is attenuated 20dB relative to the data in Figures 8-9.

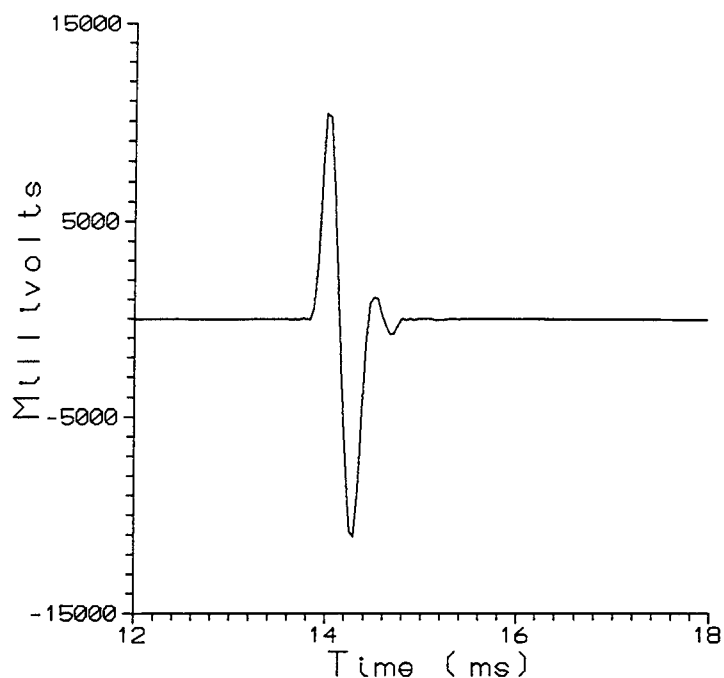


Figure 11. $h_s=1.25m$
 $h_r=1.75m$, $d=50m$.
 $d_1=7.5m$, $d_2=10$,
 $d_3=32.5m$,
Ground: $300kNsm^{-4}$
Earth berm: $z=\infty$
——: Measured
- - - -: Calculated

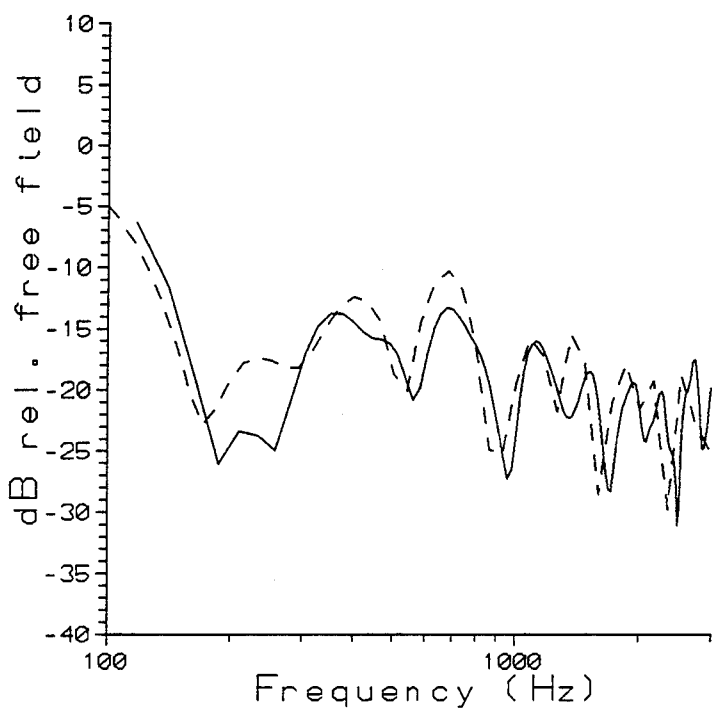


Figure 12. $h_s=1.25\text{m}$
 $h_r=1.75\text{m}$, $d=50\text{m}$.
 $d_1=7.5\text{m}$, $d_2=10$,
 $d_3=32.5\text{m}$,
 Ground: 300kNsm^{-4}
 —: Measured
 for hard berm
 - - - -: Measured
 for 300kNsm^{-4} on
 berm

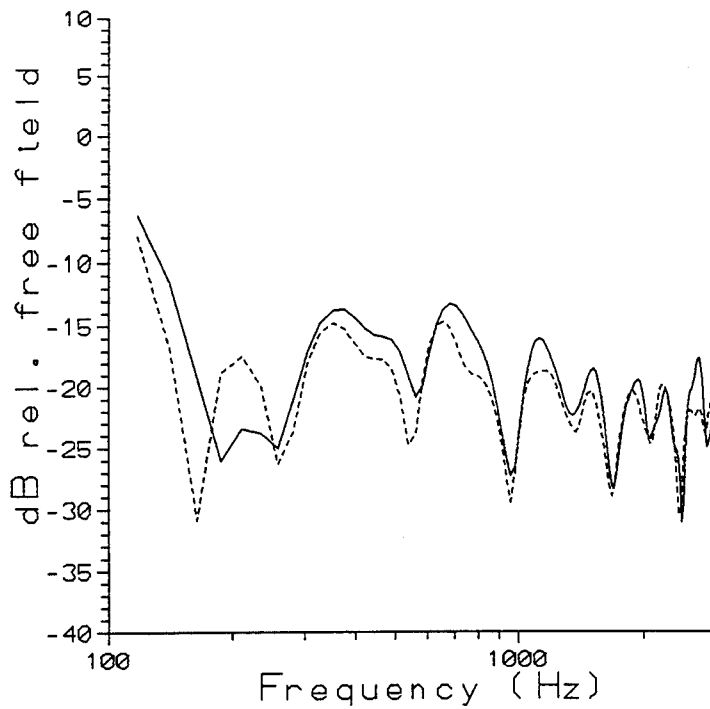
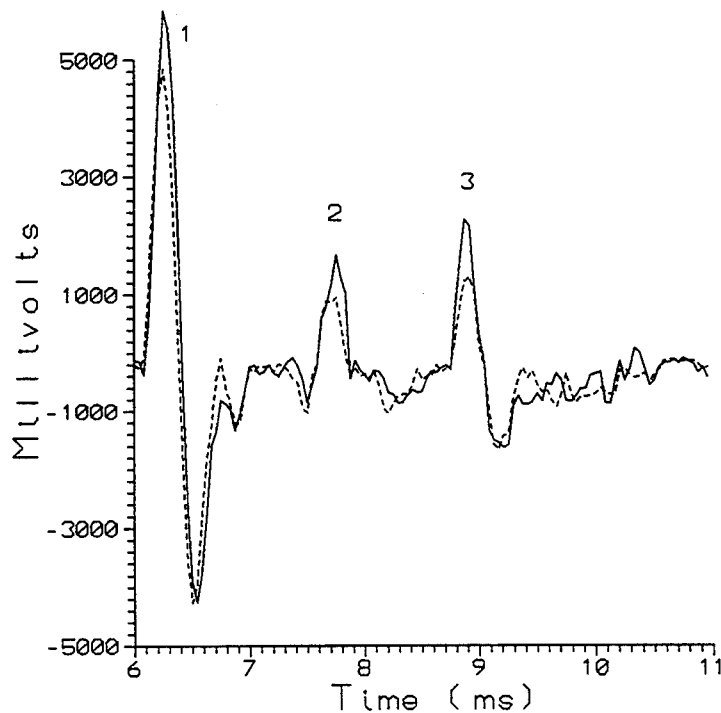


Figure 13. Waveform
 corresponding to
 Figure 12.
 —: Measured
 for hard berm
 - - - -: Measured
 for 300kNsm^{-4} on
 berm



Evaluation of the Noise Assessment and Prediction System (NAPS)

Robert O. Olsen and John M. Noble
U.S. Army Research Laboratory
Battlefield Environment Directorate
White Sands Missile Range, NM 88002

Richard J. Okrasinski
Physical Science Laboratory
New Mexico State University
Las Cruces, NM 88001

Abstract

A system has been designed to predict noise levels that result from testing activities at Aberdeen Proving Ground, Maryland. Meteorological data from surface stations, sodars, and radiosondes are input into an acoustic ray trace model which projects sound level contours onto a two-dimensional display of the surrounding area. This information is provided to the range control office where a decision can be made to proceed with or delay test activity depending upon the noise intensities predicted for nearby communities. To evaluate the system, a series of microphones are located in areas surrounding the reservation to monitor sound intensity for comparison with the model predictions. Some preliminary results of this comparison are presented along with plans for future studies.

1.0 Introduction

The U.S. Army has an active testing program for munitions and weapons at Aberdeen Proving Ground, Maryland (APG). Many of these tests cause high sound levels in the surrounding communities. This problem has existed for a long time, but it has recently become more acute because of increased development in the area. APG is actively engaged in a number of different programs to alleviate the noise problem. One approach is to avoid testing when atmospheric conditions would result in high noise levels in the local communities. To achieve this goal, the Noise Assessment and Prediction System (NAPS) was developed utilizing sensors, models, and computers to predict the noise levels that might be encountered at a off-range site as a result of a particular test.

2.0 System Description and Operation

A diagram of the various components of NAPS is shown in Figure 1. Atmospheric data collected by Doppler sodars, small towers, and radiosondes are linked to a PC at the meteorological office by hardline or RF link. After a meteorologist quality checks the

measurements, they are merged to form vertical profiles of wind, temperature, and humidity between the surface and about 5 km. This information and the 850 mb geostrophic wind from a synoptic chart are optionally input into a one-dimensional (1-D) planetary boundary layer model by Zhang and Anthes (1982) to project the vertical profiles one, two, and three hours into the future. Either these predictions or the measured data are fed into a ray-trace acoustic propagation model to forecast the noise intensities in the areas surrounding APG for a particular test. The results are examined by the meteorologist to verify that the predicted intensities are reasonable and agree with atmospheric conditions. Noise predictions are made available every 15 to 20 minutes. Both the 1-D model and the ray trace model run on the PC. The acoustic propagation model is also installed on another PC in the range control office which receives the necessary input parameters from the meteorological office. Using this information, range control can then decide whether to proceed with or delay the planned test activity. Range control also receives microphone measurements from several locations surrounding the base for comparison with the predicted data and to verify complaints.

2.1 Sensors

APG is located approximately 25 miles northeast of Baltimore near the northern end of the Chesapeake Bay. A map of the area with the sensor sites indicated is shown in Figure 2. The instrumentation consists of eight 2-m masts, two Doppler sodars, a radiosonde station (indicated by the open circle adjacent to the north sodar), and 17 microphones.

A minimum of one radiosonde sounding, released at 0800 local time, is flown for NAPS. When changing synoptic conditions warrant it, the meteorologist will order additional flights.

The two sodars are approximately 12 miles apart at opposite ends of the reservation. Fifteen-minute average wind data at 12 50-m apart heights between 50 m and 600 m above the surface are collected continuously 24 hours a day and are used to supplement the radiosonde wind measurements within the first few hundred meters of the atmosphere.

Temperature, wind, humidity, pressure, and solar radiation are collected by five 2-m meteorological masts at APG and three others in nearby communities. In the future, a 10-m mast will be added to collect data at both 2 m and 10 m. The 2-level configuration will enable meteorologists to utilize similarity theory and other techniques to interpolate between the mast temperature and wind measurements and the lowest upper-air data.

The microphones are set to operate at a threshold of 108 dB. When the unweighted sound intensity exceeds this level, it is transmitted with the time of the occurrence to a computer at range control and from there to the meteorological station.

2.2 Acoustic Propagation Model

The principles used in the ray-trace acoustic propagation model are described in two reports by Gholson (1973 and 1974). Acoustic ray traces are generated for each 5° (or multiples of 5°) between 0° to 360° in azimuth from the blast location for a range of elevations necessary to define the focusing and shadow regions in the area surrounding the blast. The model accounts for spherical spreading, absorption, focusing, shadow zones, reflection from water, interference of multiple rays arriving at the same location, the directional asymmetry of a blast, and the terrain elevation. Essential model inputs are vertical profiles of temperature, wind speed, humidity, and the blast charge weight, blast location, and blast height.

2.3 System Displays

Examples of some of the diagrams NAPS can display on the computer screen are shown in Figures 3 to 9. The meteorological conditions at a sample blast time are presented in Figures 3 to 6 where wind speed, wind direction, temperature, and speed of sound for a selected azimuth are plotted versus height. Figure 7 shows the predicted ray trajectories for a given direction from an explosion with the speed of sound curve superimposed (dashed line), and Figures 8 and 9 shows contour plots of the predicted sound intensities for two blast times. At the Figure 8 time, the NAPS predicts that most of the noise will be confined to a small area around the test site. For the other blast time in Figure 9, the atmospheric conditions are much less favorable, and high noise levels are forecast for the surrounding communities.

3.0 System Evaluation and Future Plans

The accuracy of the NAPS sound intensity predictions can be evaluated by comparing them with the microphone measurements. This has been done on a preliminary basis using 58 firing on three days in February and March, 1992 at APG. Some examples of the data comparisons are shown in Figures 10 and 11 where Grove Point microphone measurements are plotted with predicted sound intensities along the path between the blast site and Grove Point. When all of the matched NAPS predictions and microphone measurements were compared statistically, the mean differences were only .47 dB, but the standard deviations of the differences were a rather large 4.8 dB. These results are inconclusive, however, due to the both the limited sample size and to some problems with the time synchronization among the test sites and the microphones.

A more thorough study using data collected over an entire year at APG with improved time synchronization and atmospheric sensors is planned. It is also proposed to test the NAPS model at White Sands Missile Range (WSMR) in New Mexico which would serve as a prototype development site. Hardware and software will be tested here before integration into the operational NAPS at APG. A diagram of

the proposed NAPS data base management system is shown in Figure 12. The APG and WSMR data will be from markedly different environments. The environment at WSMR is typical of the southwestern U.S. desert with low humidity, high diurnal variation in temperature, and a great deal of solar radiation. The APG site is more maritime with more humidity, clouds, rain, and vegetation. Analyzing data from both sites may make the utilization of NAPS at other locations easier.

4.0 Summary

The NAPS was developed to predict sound level intensities resulting from ordinance testing at APG. A ray trace acoustic model and 1-D planetary boundary layer model are used to predict sound intensities up to 3 hours after the data measurements. A data base is being developed to capture the microphone and meteorological measurements and to utilize this data to evaluate and improve the sound intensity predictions. At least one year of data will be used for this effort to insure that NAPS has been evaluated under a variety of conditions. Information learned from these efforts can be used to install a NAPS at other sites where noise problems can be mitigated by taking into account the effects of the atmosphere on acoustic propagation.

References

- Gholson, N. H. 1973. *An Analysis of Sound Ray Focusing*.
NWL-TR-2834.
- Gholson, N. H. 1974. *Evaluation and Utilization of the NWL Sound Intensity Prediction System*. NWL-TN-T-4/74.
- Zhang, D. and R. A. Anthes 1982. "A High-Resolution Model of the Planetary Boundary Layer - Sensitivity Tests and Comparisons with SESAME-79 Data." *J. Appl. Meteor.*, 21:1594-1609.

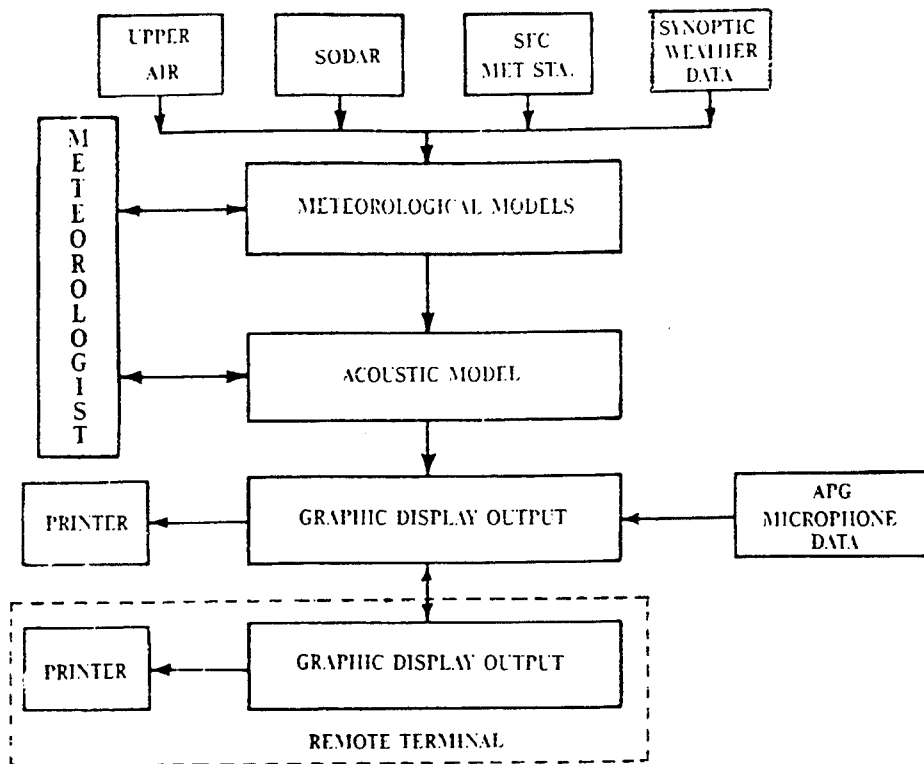


FIGURE 1. NAPS DATA FLOW

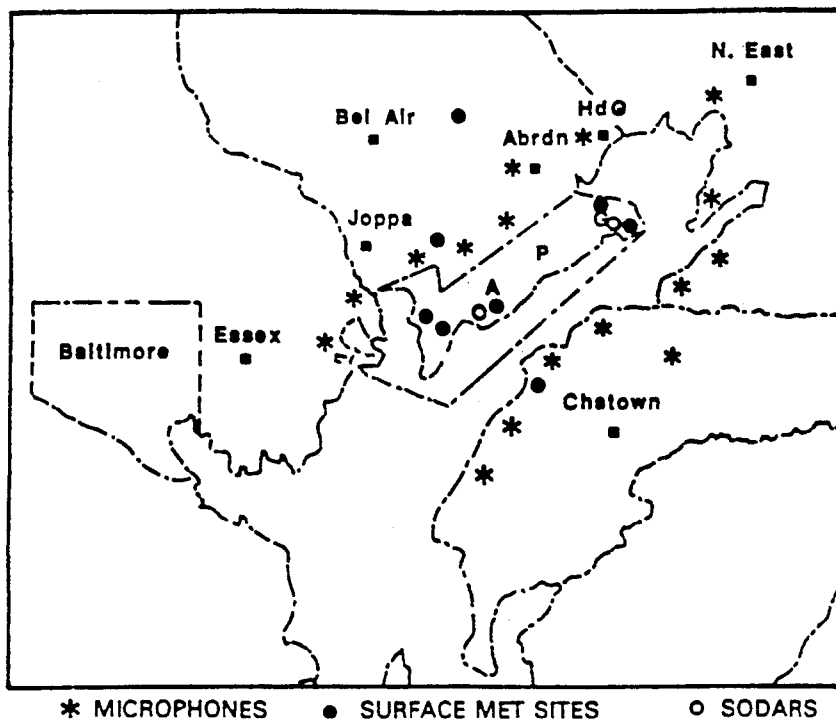


FIGURE 2. ACOUSTIC AND METEOROLOGICAL SENSOR LOCATIONS AT ABERDEEN PROVING GROUND

MET DATA: 03-24-1992 10:21:16

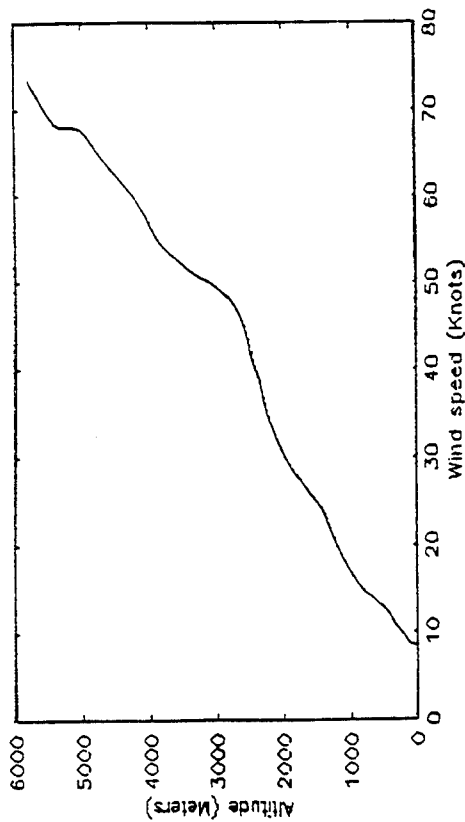


FIGURE 3. NAPS DISPLAY OF WIND SPEED PROFILE

MET DATA: 03-24-1992 10:21:16

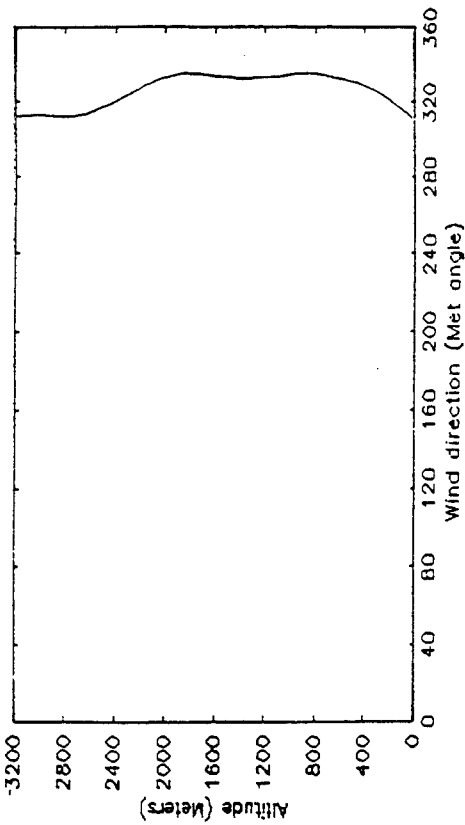


FIGURE 4. NAPS DISPLAY OF WIND DIRECTION PROFILE

MET DATA: 03-24-1992 10:21:16

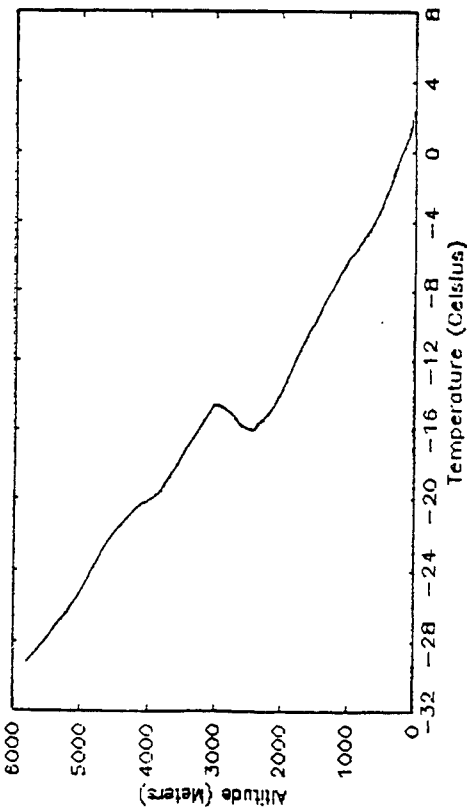


FIGURE 5. NAPS DISPLAY OF TEMPERATURE PROFILE

SPEED OF SOUND AT AZIMUTH 295.

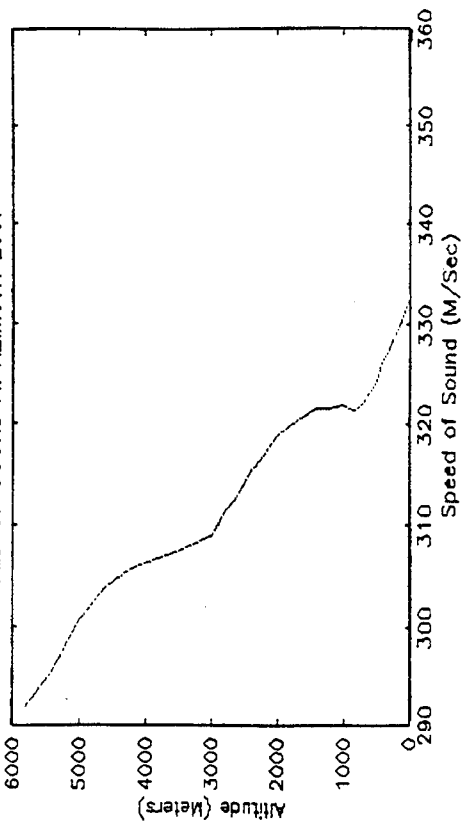


FIGURE 6. NAPS DISPLAY OF SPEED OF SOUND PROFILE

SOUND RAYTRACE PLOT FOR AZIMUTH ANGLE = 150.
 MET: 03-24-1992 10:21:16
 FIRING DATA: PLATE RNG.; 2. M; 18. LBS.

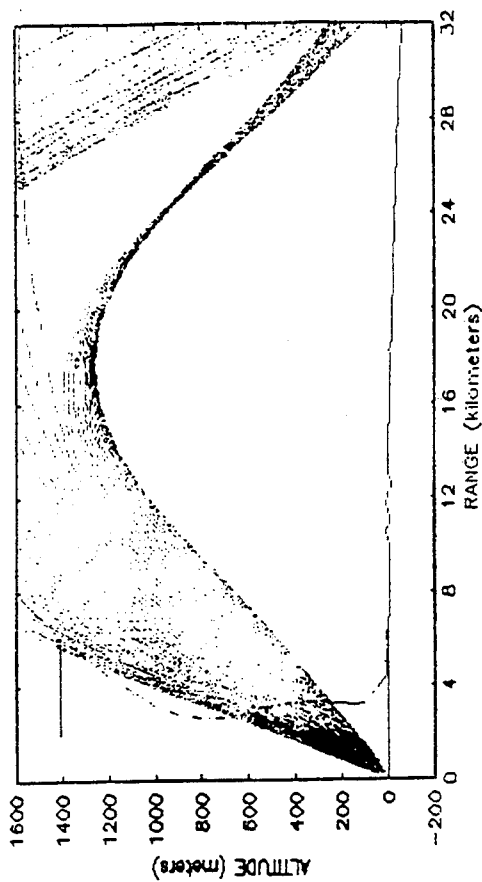


FIGURE 7. NAPS RAY TRACE DISPLAY WITH SPEED OF SOUND PROFILE

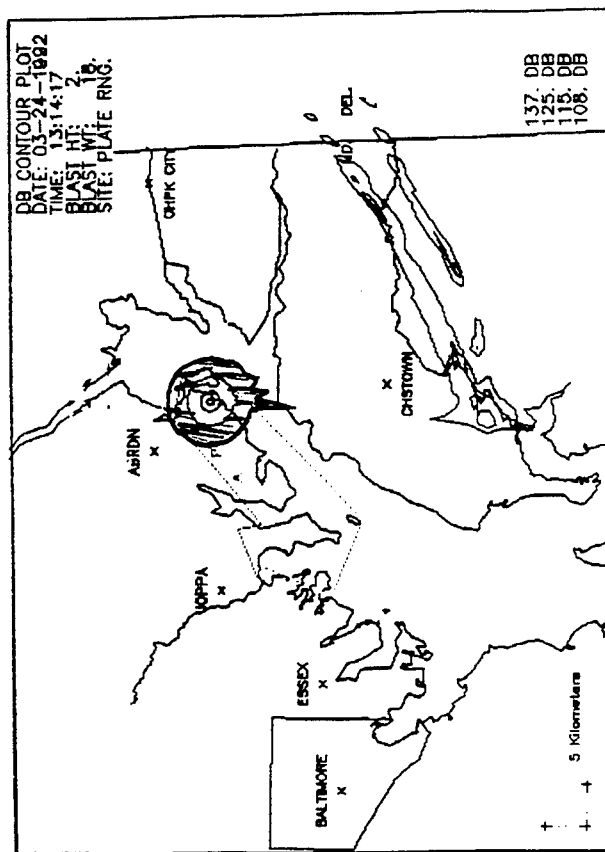


FIGURE 8. SOUND LEVEL CONTOURS PREDICTED BY NAPS

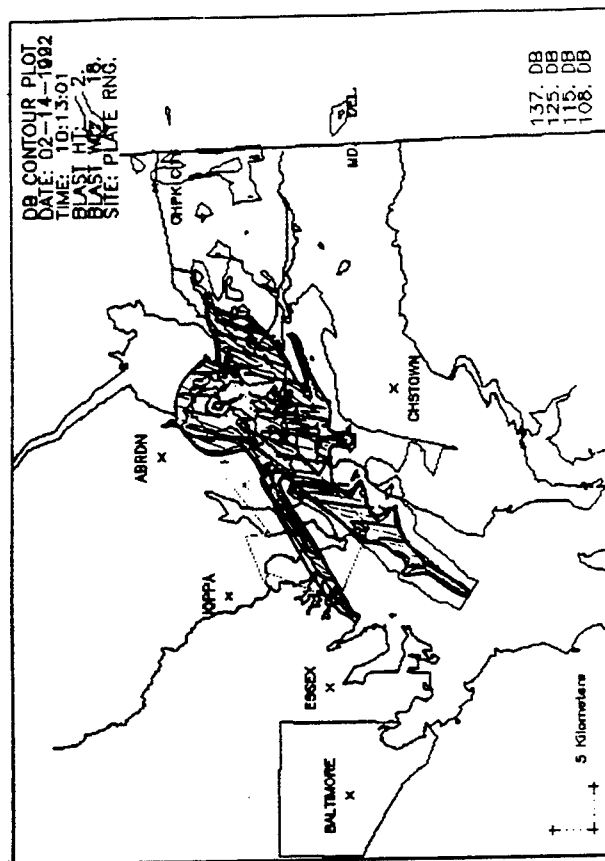


FIGURE 9. SOUND LEVEL CONTOURS PREDICTED BY NAPS

February 14, 1992 10:13
Azimuth 310

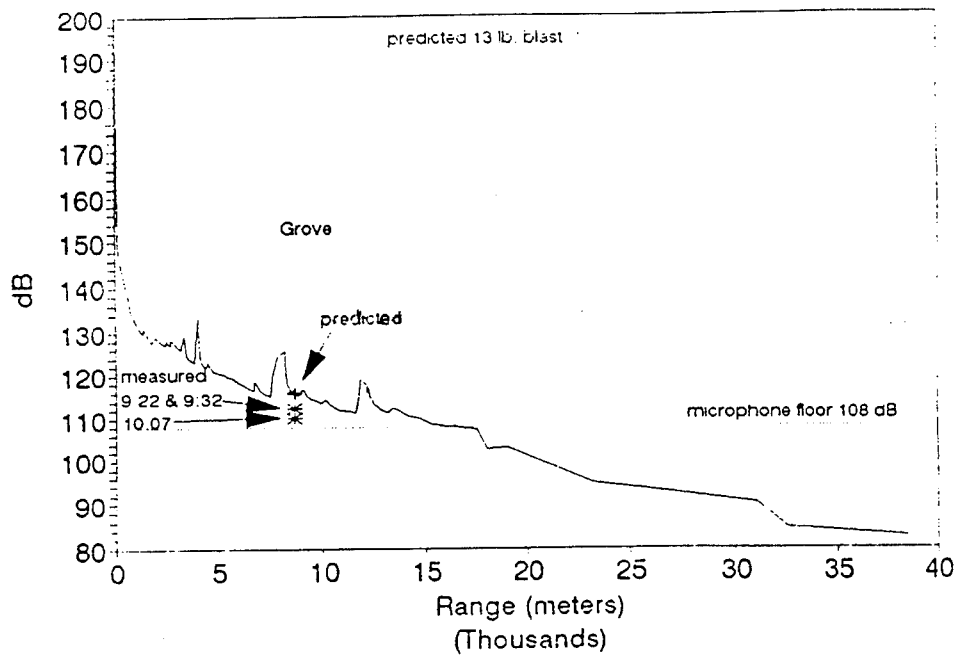


FIGURE 10. NAPS PREDICTED SOUND INTENSITY VERSUS RANGE WITH MICROPHONE MEASUREMENTS

March 24, 1992 14:52
Azimuth 310

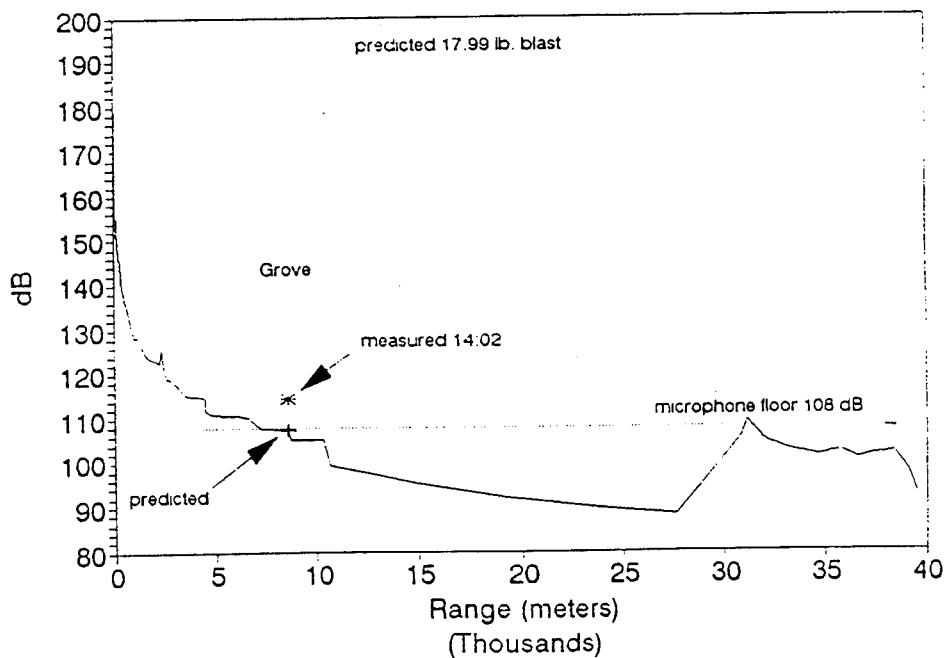


FIGURE 11. NAPS PREDICTED SOUND INTENSITY VERSUS RANGE WITH MICROPHONE MEASUREMENTS

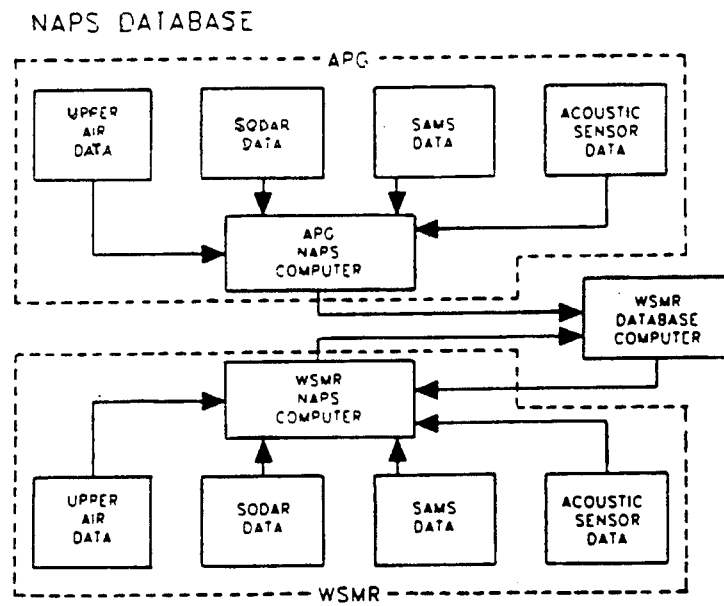


FIGURE 12. NOISE ASSESSMENT AND PREDICTION SYSTEM DATA BASE CONFIGURATION

Methodology of Ground Impedance Measurement Using the Two-Microphone Technique

C Peng and J A Lines

Silsoe Research Institute, Silsoe, Bedford MK45 4HS, U.K.

Abstract

Sound level difference (SLD) measured with two vertically separated microphones can be used to evaluate the acoustic impedance of ground surfaces. Because a measured SLD only provides one independent quantity and the ground impedance is a complex number, at least one other independent measurement is needed. This can be obtained by changing the geometry of the speaker and/or microphones. The geometry of speaker and microphones which should be used for evaluating ground impedance is a compromise between minimizing the effect of meteorological conditions and obtaining the greatest sensitivity to the acoustic properties of the ground surface. In this paper, the variation of the sensitivity of SLD to the ground impedance with the variation in the height of speaker, top microphone height, bottom microphone height and separation of the speaker and microphones is investigated theoretically. The influence of errors in the measurement of SLD on the accuracy of evaluated ground impedance is also considered. A typical numerical result shows that 1 percent error in measured SLD would be expected to produce up to 10 percent error in evaluated impedance. The evaluated impedance may even be scattering if the geometry were chosen without care. The results show that variation in the heights of the top microphone and speaker provide the most sensitive measurement of impedance. The minimization function used for evaluating the impedance converged slowly near the minimum. A logarithmic modification has been introduced to speed up the convergence near the minimum. The results also indicate that changing the height of the bottom microphone is an unsuitable method of obtaining SLD since the function to be minimized then possesses a series of local minima.

Introduction

It is well known that ground effect is the dominant factor of excess attenuation in long range sound propagation and ground impedance is an adequate parameter for representing ground effect. Efforts have been made to develop impedance models to predict acoustic properties of the ground surface. These include single, two and four-parameter models¹⁻⁵.

In order to validate the predictions from the models of ground impedance and to provide measured data of the ground impedance parameters, measurements of acoustic impedance of ground surfaces are necessary. The acoustic impedance of a ground surface can be measured by using an impedance tube or by using two microphones in a free field.

The impedance tube technique involves placing an impedance tube vertically on the ground and pushing the end 12-15 cm below the surface to provide a good seal between the end of the tube and the ground surface. Plane waves of sound are propagated along the tube. Measurements of the standing-wave-ratio (the ratio between maximum and minimum amplitude) and the location of the first minimum with respect to the ground surface are made and used to calculate the ground impedance.

The drawback of the impedance tube technique is that the ground surface is disturbed due to the insertion of the tube into the ground. This may change the physical behaviour of the ground surface. Its usefulness is also doubtful where the surfaces are rough or where they are covered by crops.

The two-microphone techniques were developed in order to avoid some of the difficulties involved in applying impedance tube methods to real ground surfaces. The basic experimental set-up consists of a sound source positioned above the ground, with two vertically separated microphones at appropriate locations, as shown in **Figure 1**.

The two-microphone technique is faster and easier to use. For measurements over agricultural land, such a rapid and simple method has many advantages and allows more samples to be made over a wider range of surface types. This method has been effectively used in the measurement of impedance of ground covered by grass and snow^{4,12}.

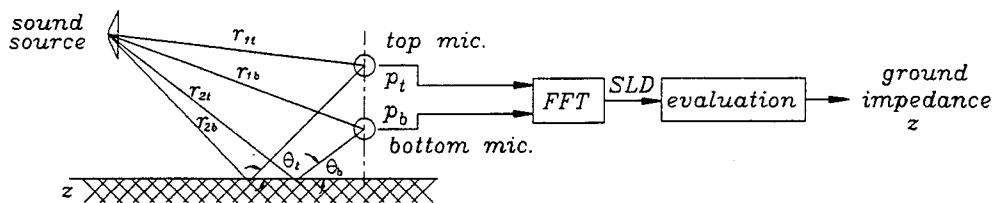


Figure 1 Diagrammatic representation of the two-microphone method.

In this paper the methodologies of measuring ground impedance using the two-microphone technique have been investigated and a recommendation has been made for proper design of the experiments.

Principles of the Two-Microphone Method

Ground impedance is a complex number which consists of two independent components, which could be treated as real and imaginary parts or as amplitude and phase. At least two independent values are required to obtain the ground impedance. Because of that each individual measurement of Sound Level Difference (SLD), obtained from the sound levels at two microphones, only provides one independent quantity. Two or more independent measurements therefore have to be made to evaluate ground impedance. These independent measurements can be made by changing those parameters which not only determine the value of SLD but also reflect the change in the ground impedance.

SLD depends on ground impedance, frequency, speaker-microphone geometry and the speed of sound in the air. Ignoring the influence of meteorological conditions on the short range measurement of SLD and considering the speed of sound as a constant, we could

treat SLD as a function of ground impedance z , frequency f , and speaker-microphone geometry.

Altering frequency is likely to be easier than changing geometry. However, changing frequency will cause changes in ground impedance as it is known that ground impedance is frequency dependent. The measurement with a different frequency would be valuable only if a satisfactory relationship between the ground impedance and frequency has been obtained beforehand.

Changing speaker-microphone geometry can be achieved by altering the speaker height, top microphone height, bottom microphone height, or the separation of the speaker and microphones. With the changes in the geometry, at the same frequency, independent measurements of SLD can be obtained and from them the ground impedance can be evaluated.

The value of SLD at the two vertically separated microphones can be written as:

$$SLD = 20 \times \log_{10} \frac{\frac{e^{ikr_{1t}}}{r_{1t}} + Q_t \frac{e^{ikr_{2t}}}{r_{2t}}}{\frac{e^{ikr_{1b}}}{r_{1b}} + Q_b \frac{e^{ikr_{2b}}}{r_{2b}}} \quad (1)$$

where r_{1t} , r_{2t} are the direct and reflected path lengths of the top microphone, r_{1b} , r_{2b} the direct and reflected path lengths of the bottom microphone, k the wave number, defined as

$$k = \frac{2\pi f}{c} \quad (2)$$

f the frequency (Hz), c the speed of sound in air, Q_t , Q_b the spherical wave reflection coefficients of the top and bottom microphones which are given by

$$\begin{aligned} Q_t &= R_{pt} + (1 - R_{pt})F_t(w) \\ Q_b &= R_{pb} + (1 - R_{pb})F_b(w) \end{aligned} \quad (3)$$

R_{pt} , R_{pb} are the plane wave reflection coefficients of the top and bottom microphone, defined by

$$\begin{aligned} R_{pt} &= \frac{z \sin \theta_t - 1}{z \sin \theta_t + 1}; \\ R_{pb} &= \frac{z \sin \theta_b - 1}{z \sin \theta_b + 1} \end{aligned} \quad (4)$$

$F_t(w)$, $F_b(w)$ the boundary loss factors for the top and bottom microphones, written as

$$F_t = 1 + i\sqrt{\pi}w_t e^{-w_t^2} \operatorname{erfc}(-iw_t) \quad \text{and} \quad w_t^2 = i\frac{k}{2}r_{2t}(\sin\theta_t + \frac{1}{z})^2$$

$$F_b = 1 + i\sqrt{\pi}w_b e^{-w_b^2} \operatorname{erfc}(-iw_b) \quad \text{and} \quad w_b^2 = i\frac{k}{2}r_{2b}(\sin\theta_b + \frac{1}{z})^2$$
(5)

z is the normalized ground impedance, $\operatorname{erfc}()$ the complex error function given by

$$\operatorname{erfc}(x) = \frac{2}{\sqrt{\pi}} \int_x^\infty e^{-u^2} du$$
(6)

For a given geometry, SLD is a spatial surface when plotted against impedance and frequency. An example is given in **Figure 2** where impedance is represented in terms of flow resistance which represents equal real and imaginary parts of the impedance. It shows that at a given frequency SLD changes with impedance. It also shows the frequencies at which maximum variation in SLD is predicted to occur, and which should be chosen for impedance tests.

At a given frequency the change in SLD can be represented by a surface when plotted against the real and imaginary parts of the ground impedance, as shown in **Figure 3**. At a certain value of SLD there is family of complex values of impedance represented by a curve of impedance passing through the expected point. With different geometries we can obtain a set of impedance curves conjoining at the expected point representing the expected value of the impedance.

Numerical Simulations

The infinite integral, $\operatorname{erfc}()$, in the boundary loss factors Q_t and Q_b make it impossible to rearrange SLD for impedance z . A trial and error method has to be implemented to evaluate the impedance from a given SLD based on the following minimizing function

$$(SLD_i(z, \eta)_{meas} - SLD_i(z, \eta)_{pred})^2 < \varepsilon$$
(7)

Figure 4 shows the trend of impedance curves when changing the speaker height, top microphone height, bottom microphone height and separation of speaker and microphone. Apparently the evaluated impedance is more sensitive to the changes in the height of speaker and top microphone than changes in the height of the bottom microphone or the separation of the speaker and the microphone.

It seems that the ground impedance can be obtained simply from the joint point of the impedance curves from two experiments. However in practice the measurement of SLD always comes with some errors due to instrumentation, meteorological effects, etc. These inaccuracies in the measurements shift the impedance curves upwards or downwards. They move the conjoint point away from the expected value and produce error in the evaluated impedance.

A set of simulation tests have been made with different working geometries to determine the effect of the error in SLD measurement on the evaluation of ground impedance. The tests were taken with the working geometry as following:

- test 1: Speaker height 1.1 to 1.3 m;
- test 2: Top microphone height 1.1 to 1.3 m;
- test 3: Bottom microphone height 0 to 0.2 m;
- test 4: Speaker-microphone distance 1.9 to 3.1 m;

The impedance curves corresponding to the numerical tests are shown in **Figure 5**. The two sets of curves represent the conditions of -1% and +1% error in SLD readings respectively. The possible estimated result of impedance would be one of the conjoints. If the measured data of SLD involved +1% or -1% offset error there would be no significant difference in the estimated impedance from all the tests. However, if random measurement error exists in SLD, for instance, -1% in the first measurement and +1% in the second, there would be a significant difference in the estimated results. Tests 1 and 2 would produce 14% and 10% relative error in the real and imaginary parts of estimated impedance; test 4 would produce 28% and 10%. The relative errors generated by test 3 would be more than 100%. This shows that changing the bottom microphone height is the worst case and that the best choice would be to change the height of the top microphone.

Supposing the errors are a normally distributed random series, better estimated impedance can be obtained by averaging the individual evaluated impedances over a large number of measurements. A procedure can be as follows:

$$z = \frac{1}{N} \sum_{i=1}^N z_i \quad (8)$$

where z_i is the conjoint of i^{th} z measurement.

Instead of estimating each individual curve of the ground impedance, statistically, a minimization function can be employed to evaluate the value of the impedance based on the least-square principle. From a set of measurements over a range of frequencies with different geometries, a minimization function can be written (Hutchinson-Howorth et al 1993)

$$F(z) = \sum_{f=f_0}^{f_m} \left[\sum_{i=1}^3 (SLD_i(z, f)_{meas} - SLD_i(z, f)_{pred})^2 \right]^{0.005} \quad (9)$$

Because the summation of the squares at the frequency of interest is less than unity, taking the power of 0.005 will speed up the convergence of the minimization. In this paper, we take the logarithms of the square-summation for reasons of computing speed. **Figure 6** and **Figure 7** show the minimization F plotted against impedance before and after taking the logarithms. They show that taking logarithms speed up the minimum

search and increases the sensitivity of the measurement to ground impedance. This method would be useful for evaluating impedance over a range of frequencies. It should be noted that a model of impedance, $z(f)$, should be involved in the minimization function $F(z)$ to evaluate the ground parameters, such as effective flow resistivity, from the SLD measurements.

In cases where the function $z(f)$ is not available or where the function needs to be validated, the minimization has to be taken at a given frequency, so the minimization function reduces to

$$F(z) = \log \left(\sum_{i=1}^n (SLD_i(z, f)_{meas} - SLD_i(z, f)_{pred})^2 \right) \quad (10)$$

where n is an integer number larger than two.

Numerical simulation of the changes in bottom microphone height shows a series of local minima presented in the minimization function, **Figure 8**. This will increase the difficulty of finding the global minimum or even produce faulty estimation if the global minimum point were missed. This is consistent with the result of previous observations of ground impedance curves in this section.

Considering the effect of error in SLD measurements on ground impedance evaluation, a similar numerical simulation was made with n equals three and assuming each SLD measurement would be one of the three values which contains -1%, 0 and +1% error respectively, **Figure 9**. The results show that the estimated impedances converge well for those tests with changing top microphone height or speaker height. The evaluation of ground impedance from the tests with changing bottom microphone height or changing speaker-microphone distance produces scattered estimates.

Conclusion

A conclusion can be drawn from the above discussions that the measurements of SLD should be undertaken with different top microphone heights at the frequency of the first dip of expected SLD and the **worst** method of obtaining SLD is to change the height of the bottom microphone, because the minimization function possesses a series of local minima.

The ground impedance can be evaluated by either a minimization function or the conjoint of two impedance curves. The logarithmic modification of the minimization function speeds up convergence near the minimum and reduces computing time.

References

- 1 **Attenborough, K.** Acoustical characteristics of rigid fibrous absorbent and granular materials. *Journal of the Acoustical Society of America*, 1983 **73** 785-799

- 2 Attenborough, K.** Acoustical impedance models for outdoor ground surfaces. *Journal of Sound and Vibration* 1985, **99**(4) 521-544
- 3 Attenborough, K.** Review of ground effect on outdoor sound propagation from continuous broadband surfaces. *Applied Acoustics* 1988, **24** 289-319
- 4 Hess, H. M; Attenborough K.; Heap, N. W.** Ground characterization by short-range propagation. *Journal of the Acoustic Society of America* 1990 **87**(5) 1975-1986
- 5 Attenborough, K.** Ground parameter information for propagation modelling. *Journal of the Acoustic Society of America*. 1992 **92**(1) 418-427
- 6 Sabatier, J. M; Rasset, R.; Frederickson, C. K.** An improved procedure for the determination of ground parameters using level difference measurements. *Journal of the Acoustic Society of America* 1993 **94**(1) 96-399
- 7 Glaretas, C.** A new method for measuring the acoustic impedance of the ground. PhD Thesis, The Pennsylvania State University, U.S.A., 1981
- 8 Waddington, D. C.** Acoustical impedance measurement using a two-microphone transfer function technique. PhD Thesis, University of Salford, U.K. 1990
- 9 Seybert, A. F.** Experimental determination of acoustic properties using a two-microphone random-excitation technique. *Journal of the Acoustical Society of America* 1977 **61**(5) 1362-1370
- 10 Heap, N. W.** Sound propagation over mixed impedances. PhD Thesis, The Open University, U.K., 1982.
- 11 Hutchinson-Howorth, C.; Attenborough, K.; Heap, N. W.** Indirect in situ and free-field measurement of impedance model parameters or surface impedance of porous layers. *Applied Acoustics* 1993 **39** 77-117
- 12 Moore, H. M.; Attenborough, K.; Rogers, J.; Lee, S.** In-situ acoustical investigation of deep snow. *Applied Acoustics* 1991 **33** 281-301

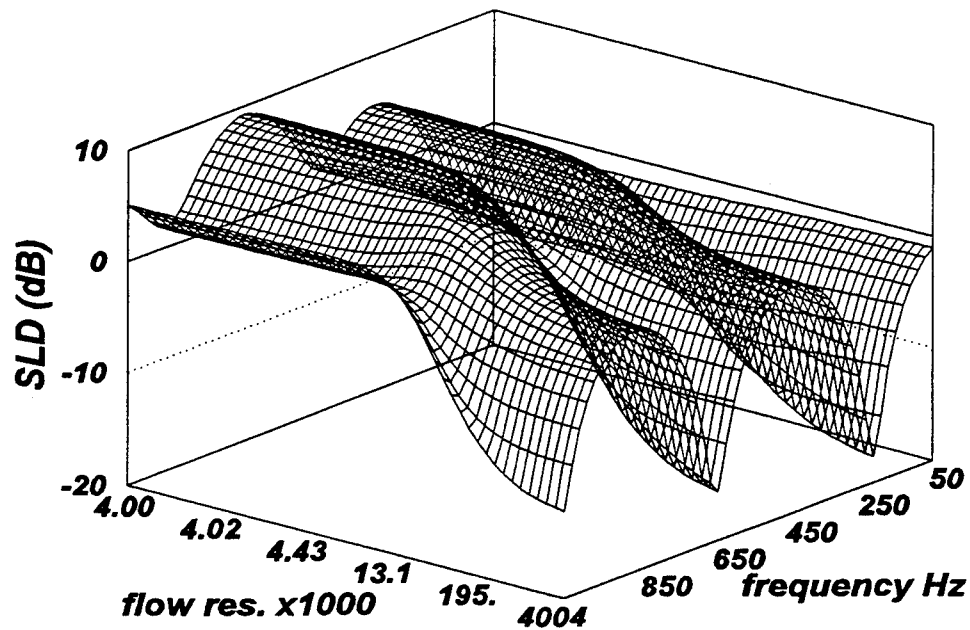


Figure 2 Change in SLD with ground impedance and frequency.

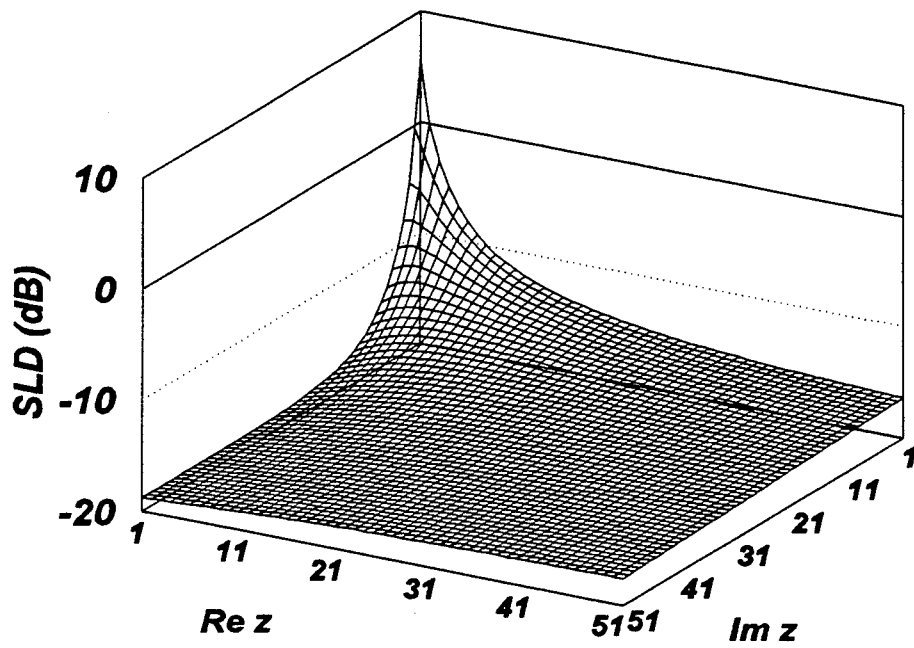
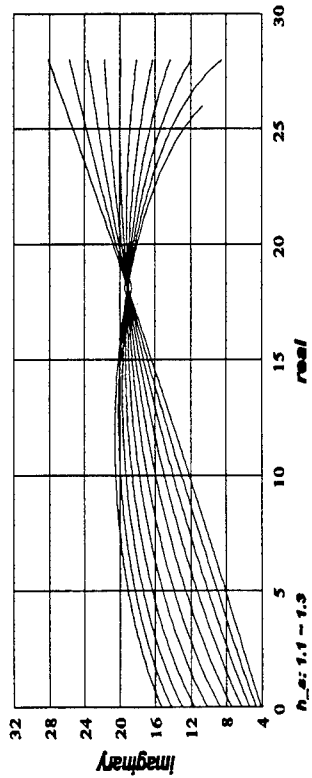
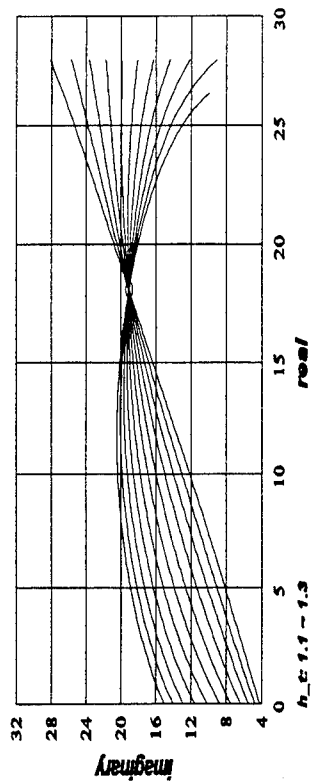


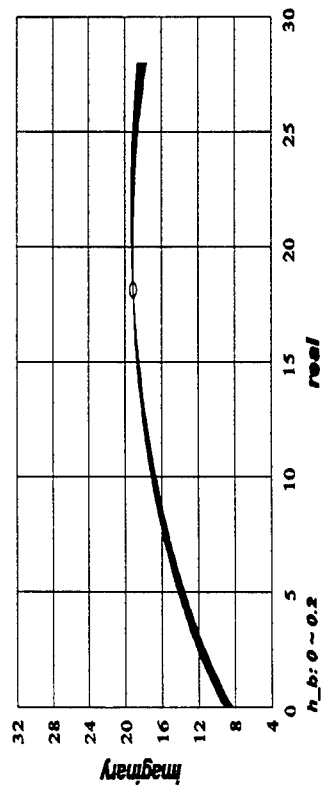
Figure 3 Change in SLD with ground impedance at a given frequency.



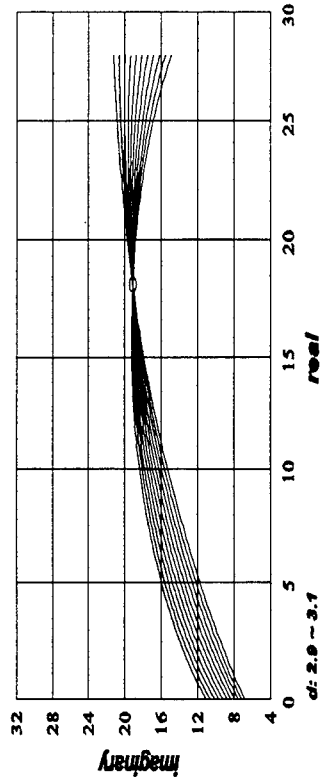
(a)



(b)

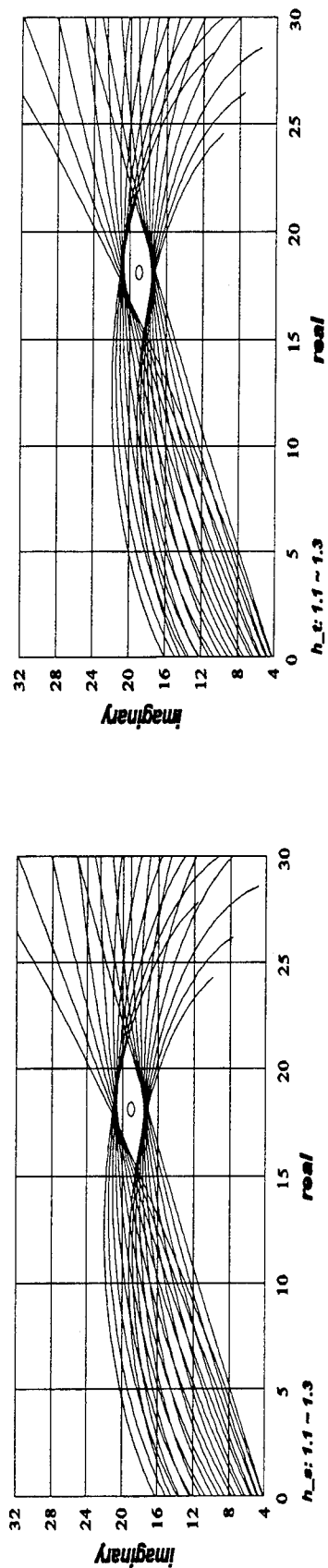


(c)

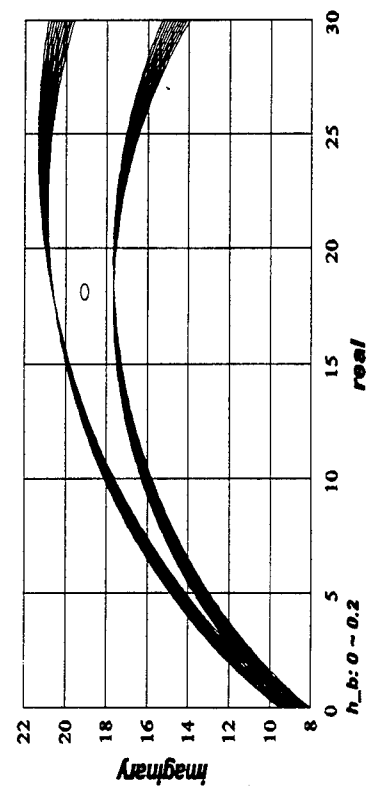


(d)

Figure 4 Ground impedance curves under ideal conditions (zero error in SLD reading) with changes in (a) speaker height; (b) top microphone height; (c) bottom microphone height and (d) speaker-microphone distance.

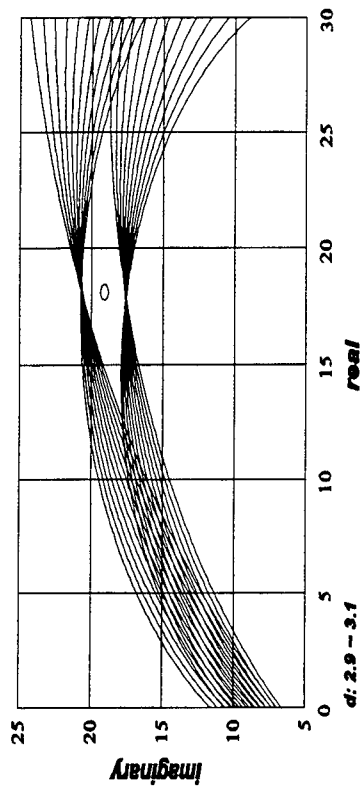


(a)



(c)

(b)



(d)

Figure 5 Ground impedance curves with $\pm 1\%$ error in SLD measurements at different (a) speaker heights; (b) top microphone height; (c) bottom microphone heights and (d) speaker-microphone distances.

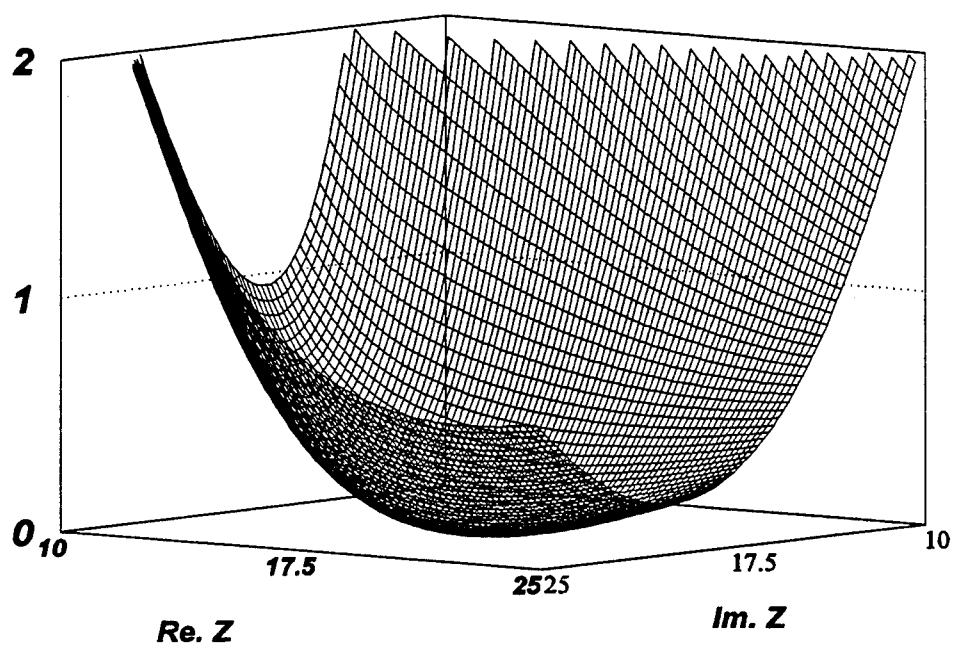


Figure 6 Minimization function F against impedance before taking logarithms.

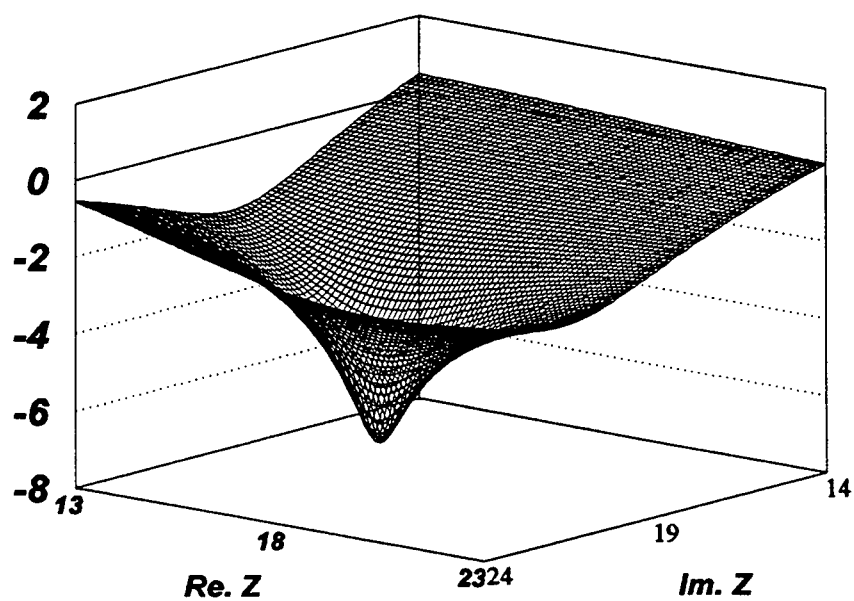


Figure 7 Minimization function F against impedance after taking logarithms.

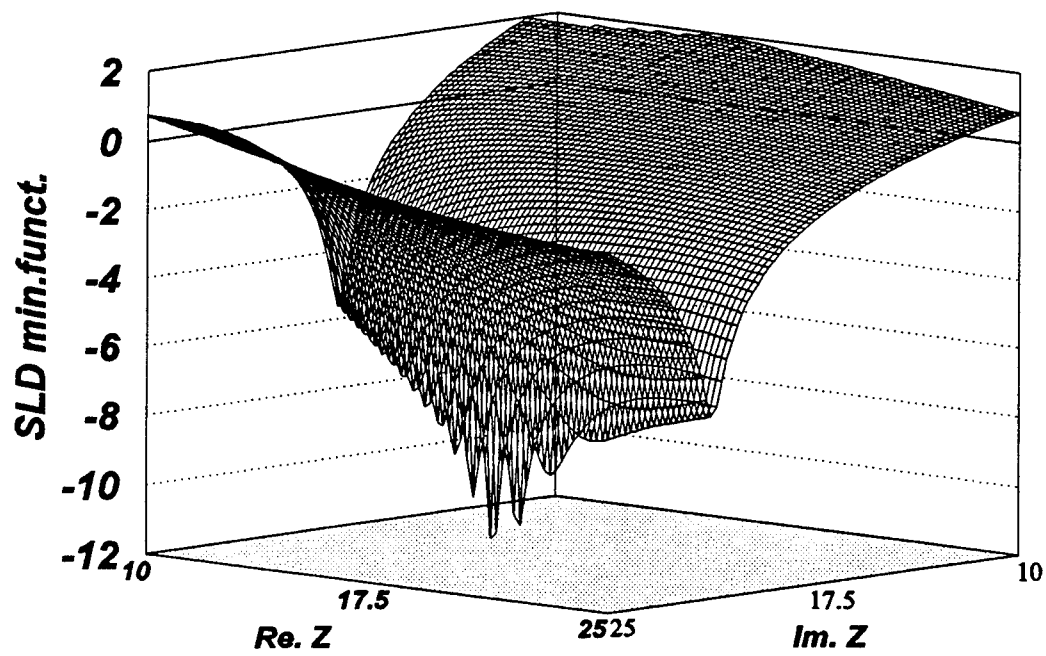


Figure 8 Minimization function F with bottom microphone height against impedance.

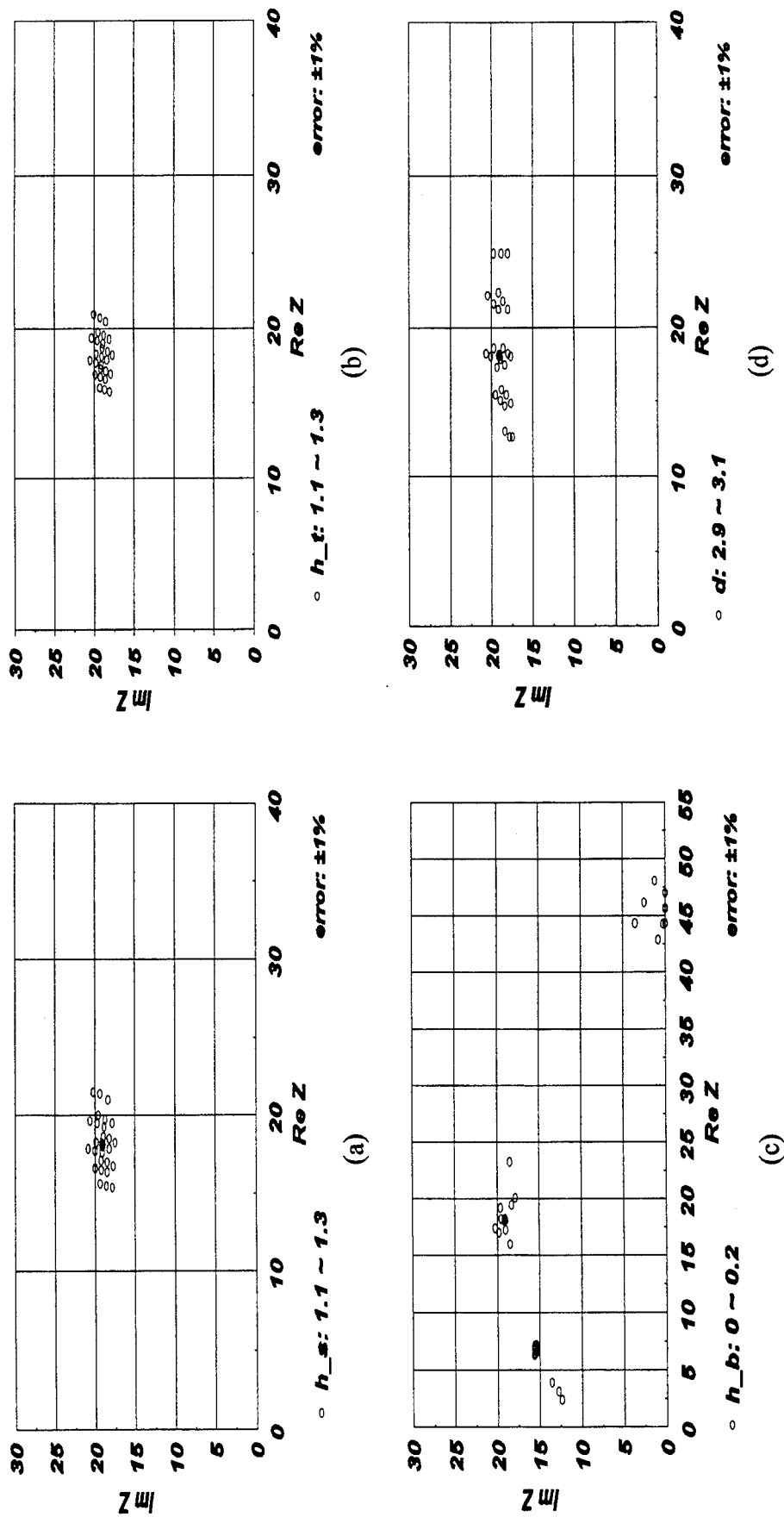


Figure 9 Evaluated ground impedance from SLD with changing (a) speaker height; (b) top microphone height; (c) bottom microphone height and (d) speaker-microphone distance.

REVIEW OF GROUND IMPEDANCE FOR GRASS SURFACES -

DELANY AND BAZLEY REVISITED

by

Louis C. Sutherland, Consultant in Acoustics
27803 Longhill Drive, Rancho Palos Verdes, CA 90275

ABSTRACT

The Delany-Bazley (D-B) model for the characteristic impedance of porous media has been shown by Attenborough and others to be inadequate to explain fine points in the expected acoustic surface impedance of porous and/or layered media. Nevertheless, the model is still commonly applied in many studies of long range sound propagation as a convenient computational approximation for cases where the surface impedance of the ground is only a minor part of the analysis. Based on a review of several published experimental studies of the surface impedance of grass surfaces which used a direct impedance measurement technique, a modified version of the D-B model is proposed which can describe these data in a consistent manner based on selection of a best-fit value for flow resistivity for each data set. The proposed revision to the D-B model for the normalized characteristic acoustic impedance for grass surfaces only changes the resistive term significantly. The revised algorithm indicates an average phase angle that is substantially higher than indicated by the original D-B model for values of the ratio of frequency, in Hz to flow resistivity, in mks rayls/m less than $0.01 \text{ m}^3/\text{Kg}$. This has significant implications for the presence of surface waves at low frequencies.

The ability of alternative models for the impedance of grass surfaces to describe these measured impedance data is also briefly considered. The alternative models considered include a revision to the D-B model recently proposed by Miki and models for impedance of a porous layer with variable porosity or a hard-backed porous layer. Only the latter model appears to show some, but not all, of the general pattern of variation with frequency of the surface impedance for grass surfaces. However, the revision to the D-B model proposed in this paper appears to offer a reasonable single-parameter model to approximate the actual surface impedance of grass surfaces.

1. INTRODUCTION

It is well recognized¹ that the acoustic impedance of the ground is the primary parameter governing the behavior of excess attenuation for sound propagation outdoors in a still, loss-less, homogeneous atmosphere. As Delany points out in his historical review², the first reference to the anomalous effects of sound propagation over an absorbing plane appears to have been by Bekésy in 1933. Following the extensive theoretical work on the problem in the 40's and 50's, the first experimental studies of ground absorption³ and impedance⁴ were followed in 1970 by the benchmark study of Delany and Bazley⁵ on the characteristic acoustic impedance of fibrous materials. Their study, carried out in the laboratory with an impedance tube, was not directed at measurement of ground impedance but rather was intended to provide empirical relations that could:

"prove useful in the general evaluation of absorbents and their application to free-field rooms, room acoustics, noise control measures, the design of linings for ventilation ducts, etc,"

However, the authors soon applied the empirical model that evolved out of their study to the prediction of the acoustic impedance of grass for an evaluation of ground effects on propagation of aircraft noise⁶. They validated this application by showing good agreement between their theoretical predictions with the earlier classic experimental work by Parkin and Scholes.⁸ Subsequently, Chessel⁹ made a similar application of their model to the evaluation of aircraft noise propagation over grass areas.

This paper compares the Delany-Bazley model for the characteristic acoustic impedance of porous media to direct measurements of the surface impedance for grass surfaces. This approach is used in lieu of predicting the ground impedance through curve-fitting of measured sound propagation data. The paper is not intended in any way to suggest that the more detailed multi-parameter studies of ground impedance by Attenborough¹⁰, among others, are not valid. The objective is solely to examine the relative ability of the Delany-Bazley model, or some variation upon this model, to predict directly measured values of the acoustic impedance for grass surfaces.

In the next section, a highly simplified theory for the acoustic impedance of porous media is reviewed to support the form employed in Delany Bazley-type expressions. This is followed by a comparison of data involving direct measurements of the acoustic impedance of grass surfaces with predictions by the D-B model. It is shown that an adjustment, primarily to the resistive term in the model, is desired to more accurately describe the average trend in the data. Included is a comparison of the data with other predictive models¹⁰ and a brief discussion of the implications of the suggested revision relative to surface waves.

2. A SIMPLIFIED THEORY FOR ACOUSTIC IMPEDANCE OF POROUS MEDIA.

The specific normal acoustic impedance, Z_2 , of a ground surface is the complex ratio of the acoustic pressure at the ground surface and the resulting normal component of particle velocity into the ground. For a semi-infinite media, this specific normal acoustic (or simply surface) impedance is the same as the characteristic impedance, Z throughout the medium. (This impedance will be expressed here in terms of its normalized value, $z = Z_2/Z_1$, where Z_1 is the characteristic acoustic impedance of air¹).

The surface impedance of the ground can be conveniently expressed in terms of the characteristic impedance for sound propagation through a medium with a resistance to steady flow - a first approximation to a model for a porous medium with a rigid frame. The equation for propagation of plane waves with a speed c through such a homogeneous medium with a density, p and a steady-state flow resistivity, σ , can be expressed in terms of the particle displacement, $\epsilon(x,t)$ as:

$$\frac{d^2 \epsilon(x,t)}{dt^2} + \frac{\sigma}{p} \frac{d\epsilon(x,t)}{dt} = c^2 \frac{d^2 \epsilon(x,t)}{dx^2} \quad (1)$$

Assuming a solution in the complex form, $\exp[i(kx - 2\pi ft)]$, the normalized characteristic acoustic impedance, z and complex propagation constant, $ik = -\alpha + i\beta$, can be expressed by:

$$z_c = [1 + i(\sigma/2\pi fp)]^{1/2} \quad (2a)$$

and

$$ik = i(2\pi f/c) \cdot [1 + i(\sigma/2\pi fp)]^{1/2} \quad (2b)$$

Transforming the complex roots, Eq. (2) can be expressed in the general form:

$$z_c = ik/(2\pi f/c) = [\frac{1}{2}(A + 1)]^{1/2} + i[\frac{1}{2}(A - 1)]^{1/2} \quad (3a)$$

$$ik = -\alpha + i\beta = -(2\pi f/c) [\frac{1}{2}(A - 1)]^{1/2} + i(2\pi f/c) [\frac{1}{2}(A + 1)]^{1/2} \quad (3b)$$

$$\text{where } A = [1 + (2\pi fp/\sigma)^2]^{1/2}$$

Thus, a dimensionless frequency, fp/σ appears as the key scaling parameter in this first approximation for the characteristic acoustic impedance and complex propagation constant for porous ground. The general form of Eq. (3) is found in other more complex models for propagation through porous media but with other parameters¹⁰ (e.g. - porosity, pore shape factor and tortuosity) included.

Delany and Bazley⁵ found that the measured characteristic acoustic impedance, z and complex propagation constant, ik of a wide range of fibrous, absorbent, porous materials could be expressed, empirically, in terms of this same dimensionless frequency, $(f\rho/\sigma)$. By using a standard value for the density of air, ρ at 20 °C of 1.205 Kg.m³, they developed the following empirical expressions to describe their experimental impedance-tube measurements of the characteristic acoustic impedance, z and propagation constant for the fibrous material in terms of the ratio of frequency, f , in Hz to flow resistivity, σ in Pa·s/m² (mks Rayls/m):

$$z_c = [1 + a (f/\sigma)^b] + i \cdot [c (f/\sigma)^d] \quad (4a)$$

$$ik = - \frac{2\pi f}{c} \left[[p (f/\sigma)^r] + i \cdot [1 + q (f/\sigma)^s] \right] \quad (4b)$$

$$\text{where } a = 0.0511, \quad b = -0.75, \quad c = 0.0768, \quad d = -0.73, \quad (5a)$$

$$p = 0.175, \quad q = 0.0858, \quad r = -0.59 \text{ and } s = -0.70 \quad (5b)$$

As shown in Fig. 1, the experimental data by Delany and Bazley for the characteristic impedance of fibrous materials fit their empirical expression (4a) fairly well over a range for f/σ of 10 to 1,000 cm³/gm, (0.01 to 1.0 m³/Kg in mks units). However, they cautioned that Eq. (4) may not apply outside this range where other power-law relationships would be valid for the impedance of porous materials. For frequencies from 40 to 4,000 Hz and for flow resistivity values representative of a variety of grass surfaces, (i.e. - $\sigma = 60$ to 400 kPa·s/m²), the values of f/σ range from approximately 10⁻⁴ to 0.1 m³/Kg. This range has a low end 2 orders of magnitude below that where Eq. (4) was considered valid by Delany and Bazley but an upper end 1 order of magnitude above this lower limit. Thus, only the upper decade, out of the three decade range in f/σ for grass, overlaps the range in f/σ evaluated by Delany and Bazley and presumably represented by their Eq. (4). It is shown later that this apparent lack of correspondence in the applicable range for f/σ for grass surfaces does not seem to prevent Eq. (4a) from providing a good first approximation to the measured surface impedance for such surfaces. However, this lack may explain, in part, why the resistive term often does not fit the measured impedance data very well for these surfaces.

The dashed lines in Fig. 1 illustrate an alternative model for the resistance and reactance terms for the Delany-Bazley data as proposed by Miki.¹² His modification was intended to eliminate one short-coming of the original Delany-Bazley version which predicts, under some conditions, the physically-unrealizable condition of a negative resistance for the normal impedance of a layered surface. (This issue is considered later in more detail.)

For the modified Eq. (4) proposed by Miki, the constants a - d and p - s are given (for σ in mks Rayls/m) by:

$$a = 0.070, b = -0.632, c = 0.107, d = -0.632 \quad (6a)$$

$$p = 0.160, q = 0.0858, r = -0.618 \text{ and } s = -0.618 \quad (6b)$$

As explained in more detail by Miki¹², these constants meet the following constraints imposed by the requirement that the model describe a physically-realizable porous media with a "positive-real" acoustic impedance. The result of applying these constraints establishes the following relationships:

$$b = d, \quad c = -a \tan[b \cdot \pi/2], \quad -1 < b < 0 \quad (7a)$$

$$r = s, \quad \text{and} \quad p = -q \tan[r \cdot \pi/2]. \quad (7b)$$

(The above version of the relationship between a and c differs from that of Miki due to a change in sign convention and simplification of Miki's form for this relationship.)

Delany and Bazley assumed that their flow resistivity, σ was actually an effective value equal to their measured steady-flow (DC) value, σ_0 , multiplied by the porosity, Ω equal to the ratio of air⁰ to total volume of the porous material. As has been pointed out¹, the porosity, was about 1.0 for the fibrous acoustic materials used by Delany and Bazley to develop Eq. (4). However, since the porosity¹⁷ is typically of the order of 0.4 to 0.7 for grass surfaces, the effective resistivity, σ that would correspond to measured impedance or ground attenuation values would be expected to be about 40% to 70% of the measured "DC" flow resistivity, σ_0 .

Note that for the convention employed here for the complex time variable, $\exp(-i2\pi ft)$, the imaginary or reactive part of the impedance is positive which corresponds to a stiffness or spring reactance.

3. MEASURED ACOUSTIC SURFACE IMPEDANCE OF GRASS SURFACES

The acoustic impedance for ground surfaces have been determined directly or indirectly by at least 4 methods:

- 1) direct measurements using closed impedance tubes placed over a ground surface^{13,14},
- 2) direct calculation from standing wave ratios^{4,13,15-17}, Fourier spectra¹⁸⁻²⁰ or phase gradients²¹ of interference patterns of ground reflected sound measured with vertical, inclined or horizontal microphone arrays,
- 3) indirect calculation by trial and error adjustment of impedance parameters until short-range ground attenuation measurements match theoretically predicted values²²⁻²⁴ or
- 4) indirect calculation by applying measured acoustical properties of the ground (e.g., flow resistivity, etc) to various theoretical models for ground impedance^{10,11}.

The accuracy of the last two methods obviously depends on the validity of the particular models assumed for the ground impedance or corresponding ground attenuation so that, for purposes of this paper, they are not used as primary sources of ground impedance data.

Published ground impedance measurement data for grass surfaces obtained by the first and second (direct) measurement methods cited above are compared in Figure 2 with predicted values based on the above Delany and Bazley model of Eq. (4a), referred to hereinafter as the D-B model. The predicted impedance values, for effective resistivities of 60 and 400 kPa·s/m², provide an approximate lower and upper bound for these measured impedance data from nine different grass site/investigator data sets identified in the figure.^{4,13,14,16,18-21} (For convenience in plotting, the reactance data are shown with negative values for this one figure.)

To more clearly evaluate how the D-B model for the characteristic impedance of porous media might be used to describe these grass surface impedance data, the reactance data are replotted in Fig. 3, but with a log scale for the ordinate values. In this form, the reactance or imaginary part of the impedance predicted by Eq. (4a) is a straight line with a slope of $-\bar{d}$. These predicted values are shown in the figure for the same bounding values for σ of 60 to 400 kPa·s/m². Recall that the D-B model is for the characteristic impedance of an unbounded porous media while the data are for the surface impedance of grass. Nevertheless, the D-B model, or some variation of it, seems to offer promise as a semi-empirical model for this surface impedance. Consider, then, some of these variations.

4. ALTERNATIVE MODELS FOR THE SURFACE IMPEDANCE OF GRASS SURFACES

Fig. 3a and 3b show the characteristic and surface resistance and reactance, respectively, as predicted by the D-B and Miki (identified in the Figure as Delany & Bazley and Delany & Bazley/Miki) models for a grass surface with a flow resistivity of 200 kPa·s/m². The abscissa is shown at the bottom in the normalized form (f/σ) and in Hertz at the top of the figure. For the surface impedance, the ground is assumed to be a 0.02 m thick porous layer of grass turf backed by a rigid surface. The surface impedance, z_s for such a hard-backed layer with a thickness, d is given by^s the well known expression:^{10,11}

$$z_s = z_c \coth[-ikd] \quad (8)$$

For the conditions chosen ($d = 0.02$ m, $\sigma = 200$ kPa·s/m²), the surface resistance, based on either model, approaches the characteristic impedance at high frequencies, as one might expect. However, for the D-B model, the resistance decreases rapidly for frequencies below about 200 Hz and eventually becomes negative. Using the D-B/Miki model, this physically-impossible behavior is absent for this case and

the resistance tends to approach a constant value at low frequencies. However, this low frequency trend in the resistance part of the surface impedance can not be generalized. More complex behavior can occur for other values of flow resistivity and layer thickness.

For both models, the reactance part of the surface impedance again approaches the characteristic impedance at high frequencies but at low frequencies, begins to increase, inversely with frequency, more rapidly. In this case, by evaluation of Eq. (8) for $kd \rightarrow 0$, it can be shown that at low frequencies, the slope of the surface reactance line approaches -1, substantially steeper than predicted by either model for the characteristic impedance.

Considering, for the moment, only the D-B/Miki model, the predicted surface resistance and reactance was evaluated for different thicknesses of a porous (grassy sod) layer using the same flow resistivity of $200 \text{ kPa}\cdot\text{s}/\text{m}^2$. Typical results are shown in Fig. 5a and 5b. For the surface resistance, (Fig. 5a) for a layer thickness of 0.01 m (probably thinner than most sod layers), the resistance again becomes negative for frequencies below about 40 Hz . This behavior was not expected for the D-B/Miki model which was developed, according to the author, to prevent just such behavior.

Eqs. (4-6,8) were used to compute the approximate frequency below which the resistance part of the surface impedance becomes negative according to either the D-B model or the D-B/Miki model for a range of typical flow resistivities and thickness of hard-backed layers. These limited results are given in Table 1.

Table 1. Approximate Frequency, in Hz, below which the surface resistance of a hard-backed porous layer becomes negative according to the: a) Delany-Bazley model⁵ or b) the Delany-Bazley/Miki model.¹²

a) D-B Model

SURFACE	TYPICAL σ $\text{kPa}\cdot\text{s}/\text{m}^2$	Layer Thickness, m					
		0.002	0.005	0.01	0.02	0.05	0.1
Concrete	30,000	<30					
Dirt	3,000	450	45	<30			
Sand	300	1800	630	200	45	<30	
Grass	200	1600	800	250	70	<30	
Snow	30	300	300	250	200	60	<30

b) D-B/Miki Model

Concrete	30,000	<30		
Dirt	3,000	<30		
Sand	300	160	50	<30
Grass	200	120	60	<30
Snow	30	<30		

Clearly, the D-B model is severely handicapped by this anomalous behavior for a significant range of frequencies of

interest for sound propagation studies. The limitation for the D-B/Miki model is less severe but still present. It should be noted, however, that even for the D-B model, this negative surface resistance is not predicted for typical grass sod layer thicknesses expected to be of the order of 0.05 m or more. The point is that, while the D-B model may be flawed as broadly valid model for surface impedance of hard-backed porous layered surfaces, some variation of this model may still be useful for approximating the surface impedance of typical grass surfaces.

For the surface reactance, the dual-slope trend indicated in Fig. 5b that was mentioned earlier can be augmented by the following observations based on the D-B/Miki model. The lower frequency, f_b below which the surface reactance begins to deviate significantly from the characteristic impedance and increase more rapidly (inversely) with frequency, has the following approximate values as a function of a range of flow resistivities typical for grass. A layer thickness of 0.05 m was used to obtain these values.

Flow Resistivity kPa·s/m ²	Frequency, f_b Hz
50	460
100	150
200	50
400	<30

Based on evaluation of the surface impedance for a range of flow resistivities and layer thicknesses, this lower breakpoint frequency seems to decrease approximately exponentially with the layer thickness, d in m. That is, to a first approximation, it was found that $f_b \propto \exp(-d/70)$.

The point is that for typical grass sod thicknesses (e.g. - ≥ 0.05 m), a model for the characteristic reactance of a porous media may provide a good first approximation to the actual surface reactance for grass surfaces for most of the audible frequency range for cases where the surface impedance can be modeled as a hard-backed layer. In any event, for these conditions, one would expect that any deviation from the model for the characteristic reactance, the surface reactance would tend to show a steeper (more negative) slope as a function of frequency than predicted for x_c .

Another possible model for the surface impedance of a grassy surface could be based on a variable porosity model.¹⁰ A limited evaluation of such a model indicated that the surface impedance exhibited a different pattern as compared to that for a hard-backed layer model. In this case, at high frequencies, the slope of the surface reactance vs frequency was similar that for x_c but the absolute values varied monotonically with the decay rate. At low frequencies, in contrast to the trend indicated by the measured data, the slope of the surface reactance tended to decrease slightly below that for x_c .

5. DEVELOPMENT OF A FURTHER VARIATION ON THE DELANY-BAZLEY MODEL FOR GRASS SURFACES.

The preceding results suggest that some variation on the D-B model might be developed to describe the surface impedance data for grass surfaces in a consistent manner and that any such variation may exhibit some of the behavior typical for hard-backed, layered media.

The following steps were taken to develop such a variation of the D-B model.

1. For each data set, regression lines were computed for a best-fit to the surface resistance and reactance data using a general expression of the form given by Eq. (4a) except that the independent variable was frequency, not frequency divided by flow resistivity.

Thus, when plotted on a log-log scale, the normalized resistance and reactance values were assumed to fit straight lines given by:

For r_s for the i_{th} data set,

$$\text{Log}[r_s - 1] = \text{Log } a_i + b_i \cdot \text{Log}[f] \quad (9a)$$

For x_s ,

$$\text{Log}[x_s] = \text{Log } c_i + d_i \cdot \text{Log}[f] \quad (9b)$$

where a_i to d_i are the regression coefficients for these lines.

2. Initial estimates of the effective flow resistivity, σ_i for each data set were then made assuming that the intercept constants, a and c as given by Eq. (5a) for the Delany-Bazley model were valid but that the slope constants (b_i or d_i) derived from the regression lines should be used. Thus, the initial estimates for the effective flow resistivity could be obtained, for example, from the regression figures for the reactance for the i_{th} data set by:

$$x_s = c_i \cdot f_i^{d_i} = c \cdot (f/\sigma_i)^d \quad (10)$$

Solving for σ_i ,

$$\sigma_i = (c/c_i)^{(1/d)} \cdot f_i^{(1-d_i/d)} \quad (11)$$

where the frequency, f_i for each data set was taken to be the logarithmic mean frequency for all the experimental data points considered for each set.

A similar expression could be obtained from the regression line for the surface resistance data to give another estimate for the effective flow resistivity, σ_i as:

$$\sigma_i = (a/a_i)^{(1/b)} \cdot f_i^{(1-b_i/b)} \quad (12)$$

3. These two independent values for the flow resistivity were then averaged to obtain a final estimate for the effective flow resistivity. (These average values for the effective flow resistivity varied from 35 to 310 kPa·s/m² over all of the 7 data sets finally analyzed. The overall average value over all the data, 212 kPa·s/m², is considered a reasonable average effective flow resistivity for grass surfaces.)
4. The experimental data were then replotted on log-log plots but now using the estimated flow resistivity to normalize the frequency scale so that the data from all the data sets could now be combined onto single plots of the normalized surface resistance or reactance versus the normalized frequency (f/σ).
5. A regression line was then constructed in the same manner as before but now the regression coefficients can be directly compared to the corresponding values for the D-B model.

The results of this process are illustrated in Fig. 6a-6c by plots of the normalized surface resistance (6a), normalized surface reactance (6b) and resulting phase (6c) for all the data finally included in the analysis. The results from Ref. 4 and 16 were excluded from the analysis since the surface resistance data from these studies exhibited an unexplained positive slope versus frequency.

The normalized impedance data on these figures are compared to three prediction models: a) the original Delany & Bazley model, b) the version proposed by Miki and c) the version obtained from the regression line through the data as outlined in step 5 above. The regression coefficients, identified here by the subscript "r" have the following values which can be compared to those in Eq. (5a) and (6a). No values are, of course, available for the complex propagation constant, ($ik = -\alpha + i\beta$) since the ground impedance data did not provide such information.

$$a_r = 0.134, \quad b_r = -0.553, \quad c_r = 0.0453, \quad d_r = -0.836 \quad (13)$$

While all of the above values differ substantially from those for the D-B model, it is apparent from Fig. 6b that the net change for the reactance term is rather slight. However, the constants, a , b for the resistance term differ significantly from that of the D-B model and the corresponding regression line in Fig. 6a is substantially different from that of the D-B model. (It should be noted that, just as for the constants for the D-B model, the above values do not conform to the requirements defined by Eq. 7.)

The "agreement" between these normalized, frequency-scaled data and the corresponding three prediction models is best indicated by the rms difference between the data in Fig. 6a - 6c and these models. These rms differences are summarized here.

MODEL	Eq. No.	— rms DIFFERENCE —		
		R_s	X_s	Phase
Delany & Bazley	4a + 5a	31%	27%	31%
Miki	4a + 6a	36%	33%	29%
This paper	4a + 13	29%	25%	22%

It is apparent that the rms differences for the impedance components do not differ substantially between the D-B model and the model developed in this paper. However, the difference is more significant between the measured and predicted phase. As indicated in Fig. 6c, the model proposed herein provides a much better match to the phase based on the measured data at low frequencies.

One obvious approach not evaluated in this paper would have been to compare a predicted surface impedance assuming a hard-backed layer model for the grass surface with the measurements. This approach could use the D-B model (Eq. 4) for the characteristic impedance, z and complex propagation constant, ik and Eq. (8) for the surface impedance given an assumed layer depth. However, for what are considered reasonable values for this depth for typical grass surfaces, (i.e. ≥ 0.05 m), the results of this study would suggest that there would not be very much difference between the surface and characteristic impedance for most of the audible frequency range.

6. SURFACE WAVE CONSIDERATIONS

The apparent greater accuracy of the alternative model given in this paper by the modified constants in Eq. (13) for use in Eq. (4a) for predicting the phase of the surface impedance for grass surfaces has one important implication. As shown in Fig. 7, the Boundary Loss Factor, $F(w)$ for sound propagation over a finite impedance plane in a still, homogeneous atmosphere defines the contribution of a ground and surface wave to the sound field.²⁵ (The algorithms of Chien and Soroka²⁶ were used to compute $F(w)$.) The presence of a surface wave appears as an increase in the Boundary Loss Factor, expressed in decibels, above a value of 0 dB. As indicated in the figure, this only occurs when the phase angle of the ground or surface impedance is greater than 45° - a condition not predicted to occur to any significant degree according to the D-B model for a hard-back layer with a thickness greater than about 0.05 m. In contrast, the modified semi-empirical form proposed in this paper (Eq. 4a, 13 and Fig. 6c) indicates a strong likelihood of the phase substantially exceeding 45° at low frequencies for grass surfaces.

Some evidence of this occurrence is provided by some limited data shown in Fig. 8 taken from ref. 27. For one of the two sites where sound propagation was measured over grass, there is an indication of the presence of a surface wave and the model proposed herein provides a somewhat better

estimate of the resulting sound level variation with distance than is provided by using the D-B model alone as a measure of the surface impedance. Again, it must be acknowledged that had a layered model been used for the surface impedance, the application of the D-B model to this situation might have been more effective. However, the drawback, in this case, is the requirement for a valid estimate of the layer thickness as well as the effective flow resistivity.

7. SUMMARY

Several published sources of data on direct experimental measurements of the surface impedance of grass surfaces have been used to examine the relative ability of three single parameter models (Delany-Bazley model, a variation proposed by Miki and a change developed herein) to predict this surface impedance. The model proposed herein provides a better prediction of the resistive part of the surface impedance than does the D-B model. However, the latter was intended to define the characteristic impedance of a porous media, not the surface impedance.

The data do not show clear evidence of the increasing inverse rate of change of reactance with frequency expected at low frequencies for the surface impedance of a thin porous layer over a hard backing. This may be due to the fact that the layer thickness is great enough so that this change in the reactive term would not be expected to appear.

A variable porosity model does not seem to exhibit the same general trend in impedance versus frequency observed in the measured data.

While refined, multiple parameter models for ground impedance may provide, in some cases, a more accurate basis for prediction of sound propagation losses over an absorbing plane, for grass surfaces, the alternative model outlined herein appears to offer a simple approximation to the measured impedance for such surfaces. It is recommended as a preferred alternate to the use of the Delany-Bazley model alone, especially when there is concern about the presence of surface waves at low frequency.

REFERENCES

1. ATTENBOROUGH, K., "Review of Ground Effects on Outdoor Sound Propagation from Continuous Broadband Sources," Applied Acoust. Vol. 24, 1988, pp. 289-319.
2. DELANY, M.E., "Sound Propagation in the Atmosphere - A Historical Review," Proc. Inst. of Acoustics, 1, 1978, pp 32-72.
3. PROUT, J., "Some Measurements of the Absorption Coefficient of Soil Using the Impedance Tube Technique," Noise Control, 7, 1961, pp 20.

4. DICKINSON, P.J. and DOAK, P.E., "Measurements of the Normal Acoustic Impedance of Ground Surfaces," J. Sound Vib. Vol. 13, 1970, pp.309-322
5. DELANY, M.E. and BAZLEY, E.N. "Acoustical Properties of Fibrous Absorbent Materials," Applied Acoust. Vol. 3, 1970, pp 105-116.
6. DELANY, M.E. and BAZLEY, E.N. "A Note of the Effect of Ground Absorption in the Measurement of Aircraft Noise," J. Sound and Vib. 16, 1971, pp 315-322.
7. DELANY, M.E. and BAZLEY, E.N. "Monopole Radiation in the Presence of an Absorbing Plane," J. Sound Vib. 13, 1970, pp. 269-279.
8. PARKIN, P.H. and SCHOLLES, W.E., "The Horizontal Propagation of Sound from a Jet Engine Close to the Ground at Radlett," J. Sound Vib. Vol 1, 1964, pp. 1-13., "The Horizontal Propagation of Sound from a Jet Engine Close to the Ground at Hatfield," J. Sound Vib. Vol 2, 1965, pp. 353-374.
9. CHESSEL, C.I. "Propagation of Noise Along A Finite Impedance Boundary," J.Acoust. Soc. Am. Vol 62, 1977, pp. 825-834.
10. ATTENBOROUGH, K. "Acoustical Impedance Models for Outdoor Ground Surfaces," J. Sound and Vib. Vol.99, 1985, pp. 521-544.
11. MORSE, P.M. and INGARD, K.U., Theoretical Acoustics, McGraw-Hill, New York, N.,Y., 1968, pp 360-361.
12. MIKI, Y., "Acoustical properties of porous materials - Modifications of Delany-Bazley models," J. Acoust. Soc. Jpn. (E), 1, 19-23 (1990).
13. EMBLETON, T.F.W., PIERCY, J.E. and OLSON, N., "Outdoor Propagation over ground of finite impedance," J. Acoust. Soc. Am., Vol. 59, ,1977, pp. 267-277.
14. ZUCKERWAR, A. "Acoustical Ground Impedance Meter," J. Acoust. Soc. Am.Vol. 73, 1983, pp 2180-2186.
15. JONASSON, H.G. "Sound Reduction by Barriers on the Ground'" J. Sound Vib. Vol. 22, 1972, pp.113-126.
16. BOLTON, J.S. and DOAK, P.E. "Acoustic Modeling of the Ground," Proc. GARTEur 5 Third Specialist Meeting On "Atmospheric and Ground Effects, RAE, Farnborough, (1978).
17. MARTENS, M.J.M, et al "Classification of Soils based on Acoustic Impedance, air flow resistivity, and other physical soil properties," J.Acoust.Soc.Am., Vol.78. 1985, pp. 970-980.

18. CRAMMOND, A.J. and DON, C.G. "Reflection of Impulses as a Method of Determining Acoustic Impedance," J.Acoust.Soc.Am., Vol. 75, 1984, pp 382-389.
 19. DON, C.G. and CRAMMOND, A.J. "Soil Impedance Measurements by an Acoustic Pulse Technique," J.Acoust.Soc.Am, Vol.77, 1985, pp. 1601-1609.
 20. CRAMMOND, A.J. and Don, C.G. "Effects of Moisture Content on Soil Impedance," J.Acoust.Soc.Am, Vol.82, 1987, pp. 293-301.
 21. DAIGLE, G.A. and STINSON, M.R. "Impedance of Grass-covered Ground at Low Frequencies Measured Using a Phase Difference Technique," J.Acoust.Soc.Am, Vol. 81, 1987, pp. 62-68.
 22. EMBLETON, T.F.W., PIERCY, J.E. and DAIGLE, G.A. "Effective Flow Resistivity of Ground Surfaces Determined by Acoustical Measurements," J.Acoust.Soc.Am, Vol. 74, 1983, pp.1283-1244.
 23. BOLEN, L.N. and BASS, H.E. "Effects of Ground Cover on the Propagation of Sound Through the Atmosphere," J.Acoust.Soc.Am, Vol. 69, 1981, pp. 950-954.
 24. HESS, H.M., ATTENBOROUGH, K. and HEAP, N.W. "Ground Characterization by Short Range Propagation Measurements," J.Acoust.Soc.Am, Vol. 87, 1990, pp. 1975-1986.
 25. PIERCY, J.E., EMBLETON, T.F.W. and SUTHERLAND, L.C., "Review of Sound Propagation in the Atmosphere," J. Acoust. Soc. Am. 61, 1977, pp. 1403-1418.
 26. CHIEN, C.F. and SOROKA, W.W., "A Note of the Calculation of Sound Propagation Along an Impedance Surface," J.Sound and Vib. 69, 1980, pp. 340-343.
 27. RASMUSSEN, K.B. "Sound Propagation Over Grass Covered Ground," J.Sound and Vib., Vol. 78, 1981, pp. 247-255.
-

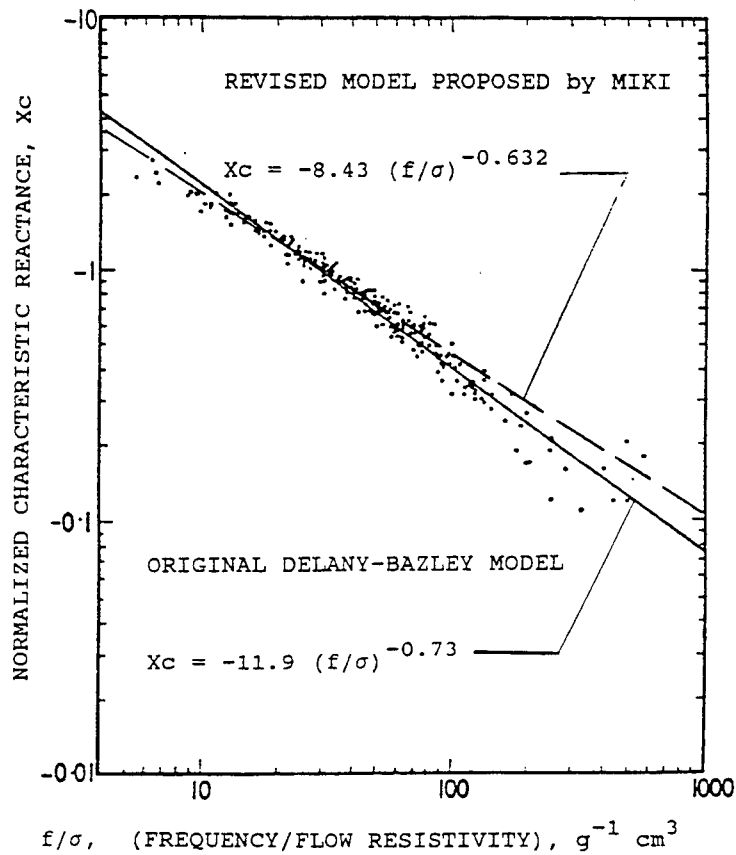
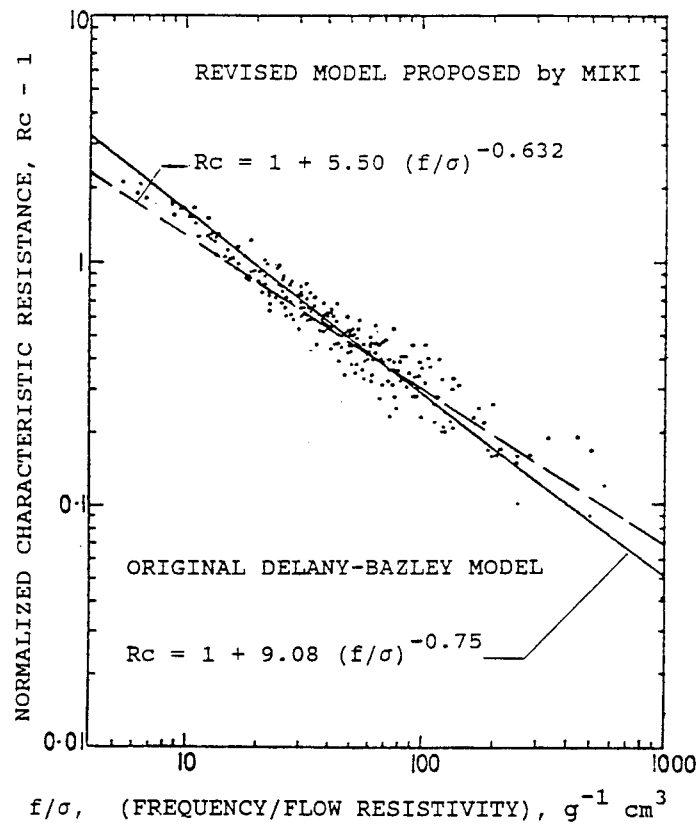


Figure 1. Original data of Delany and Bazley for the normalized resistive and reactive components of the characteristic impedance of fibrous materials compared to their model and a revision proposed by Miki¹². (Adapted from Delany and Bazley⁵).

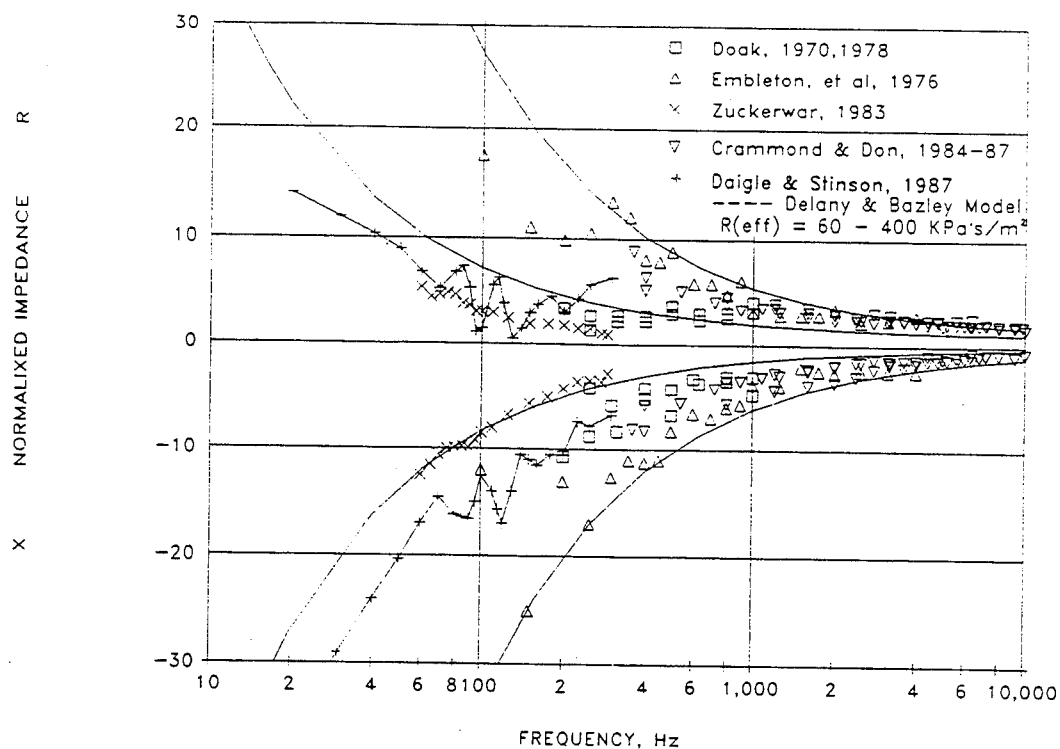


Figure 2. Surface impedance measurements for grass surfaces compared to values predicted by the Delany-Bazley model. Data identified in the figure legend from Ref. 4, 13,14,16,18-21.

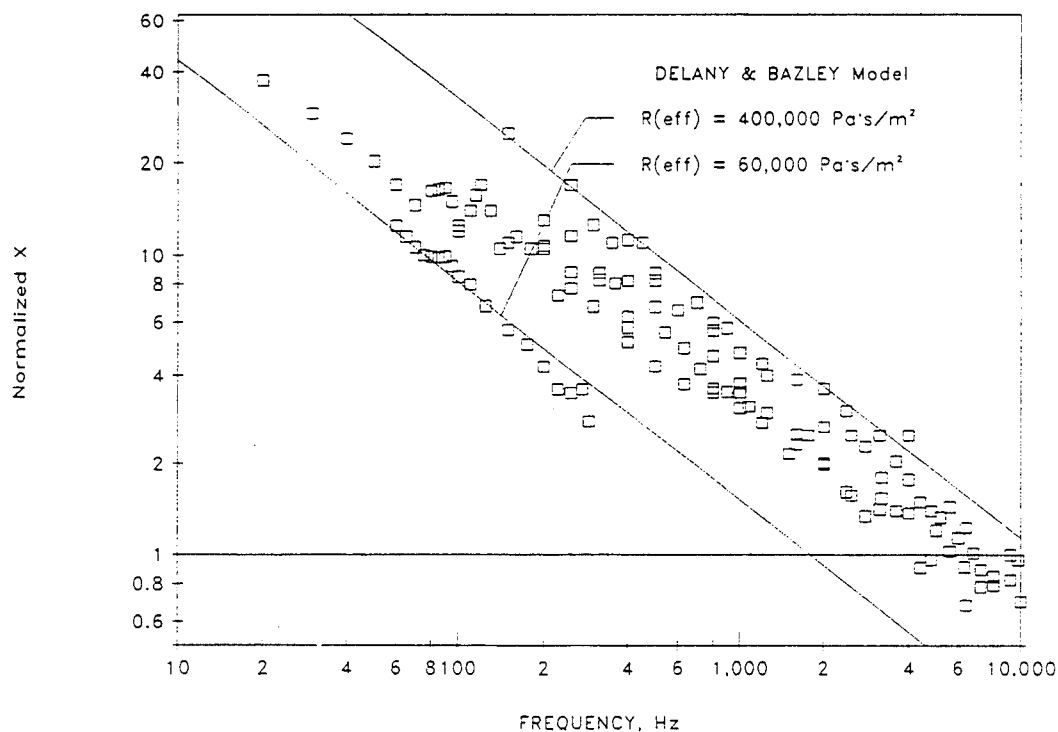


Figure 3. Reactance values from data of Fig. 2 compared with values predicted by the Delany-Bazley model for values of flow resistivity of 60 and 400 kPa's/m².

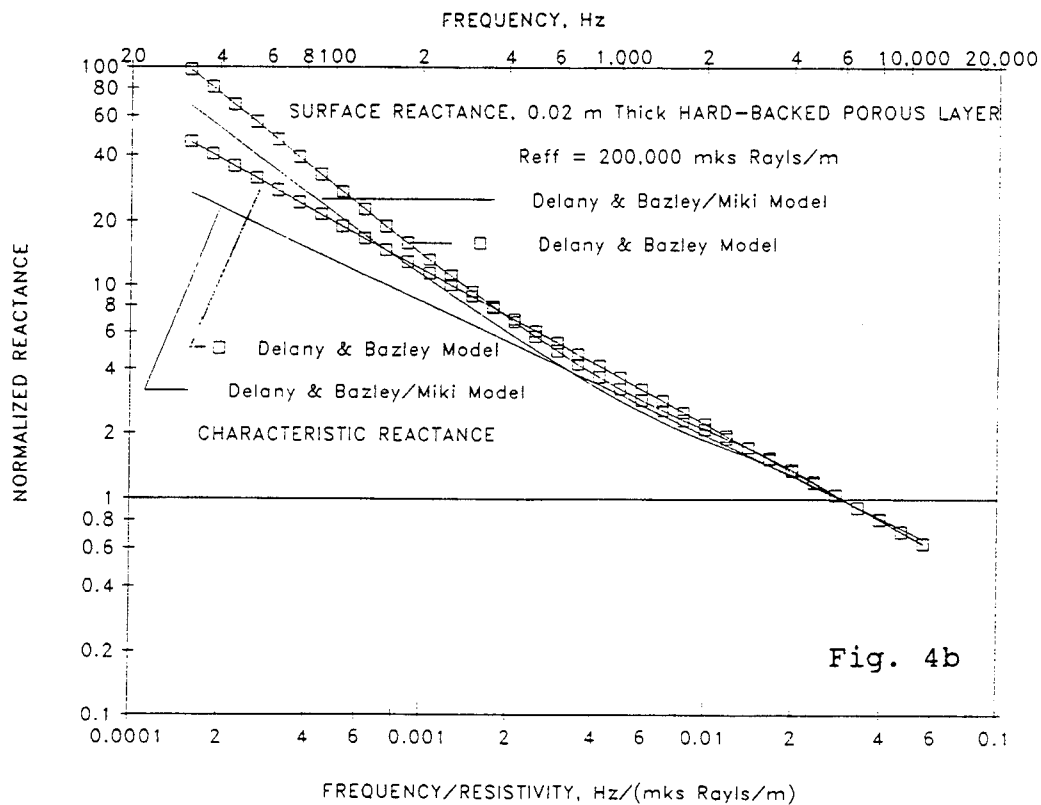
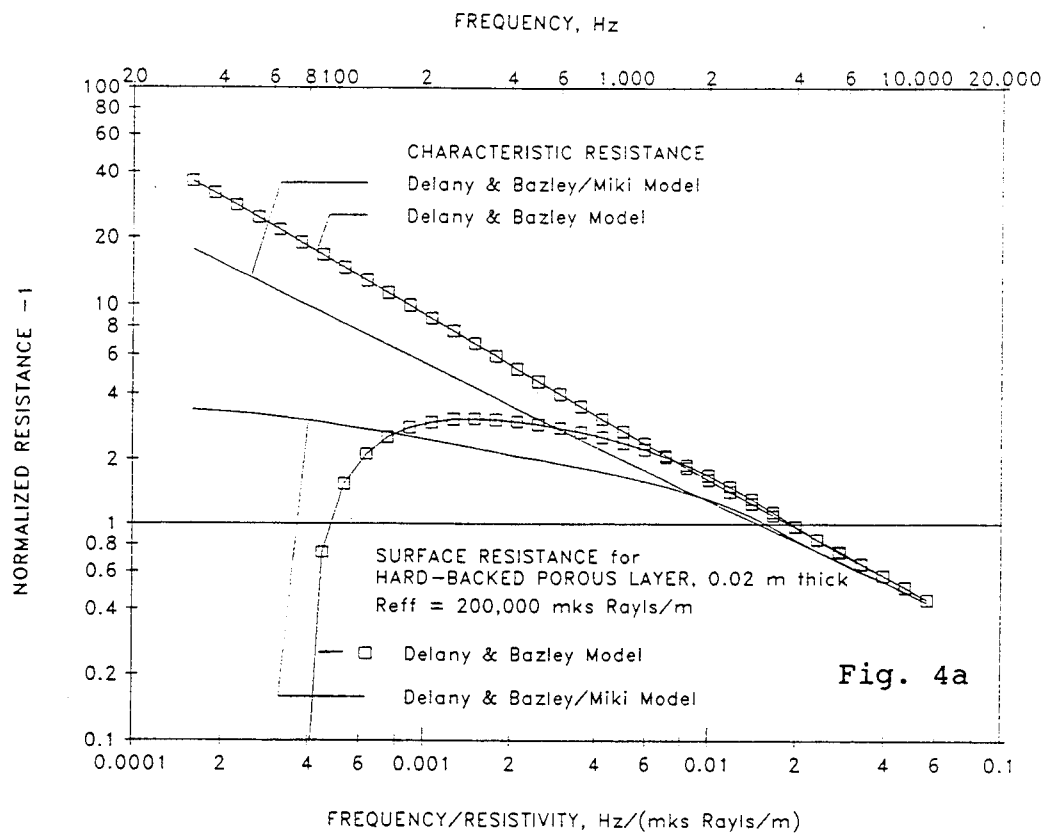


Figure 4. Resistive (part a) and reactive (part b) components of the characteristic and surface impedance as predicted by the Delany-Bazley model and by the model by Miki. Flow resistivity = 200 kPa·s/m².

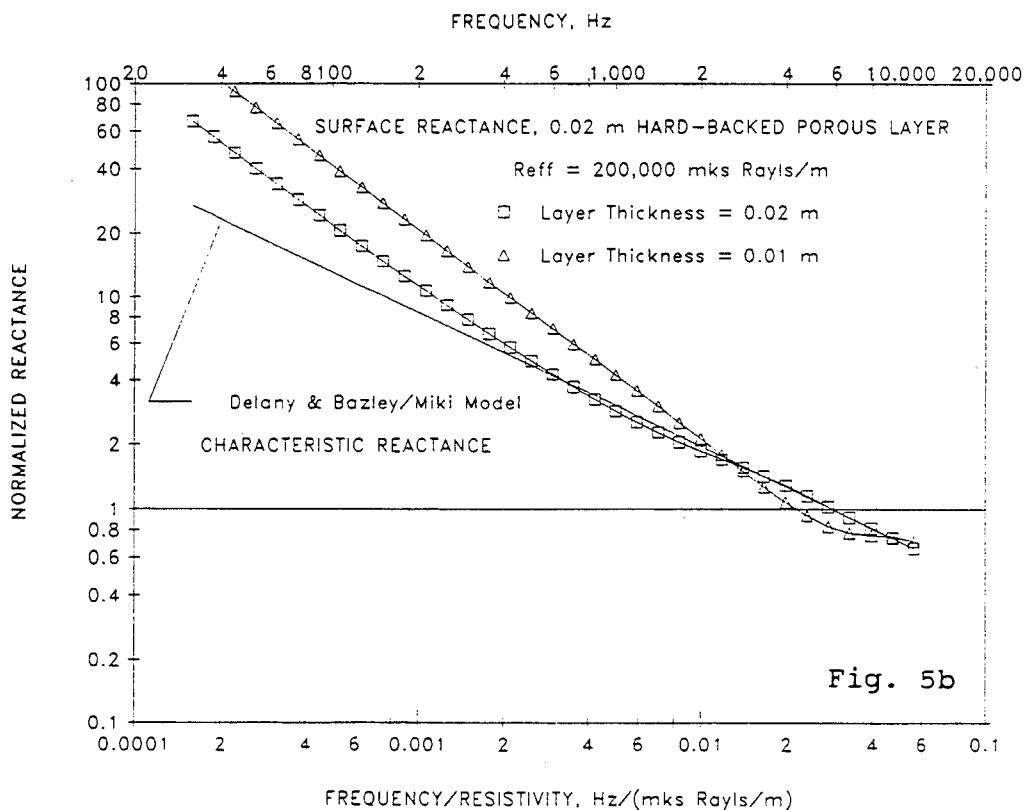
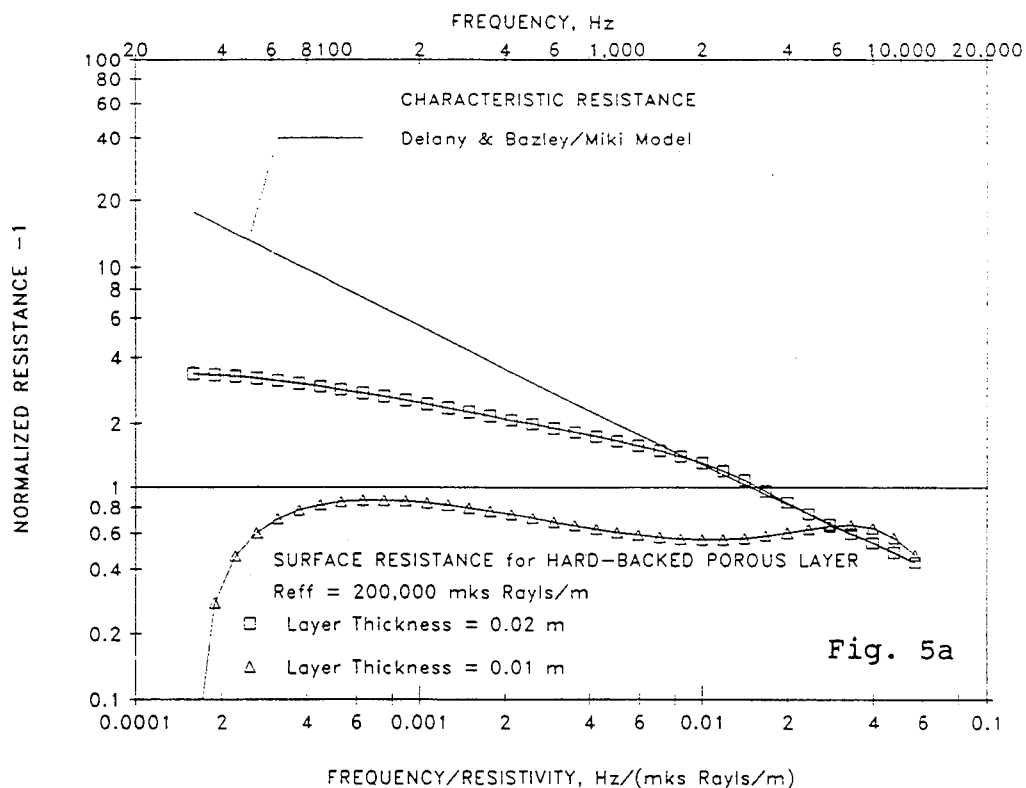


Figure 5. Resistive (part a) and reactive (part b) components of the characteristic and surface impedance as predicted by the model by Miki for two different thicknesses of a hard-backed layer. Flow resistivity = 200 kPa·s/m².

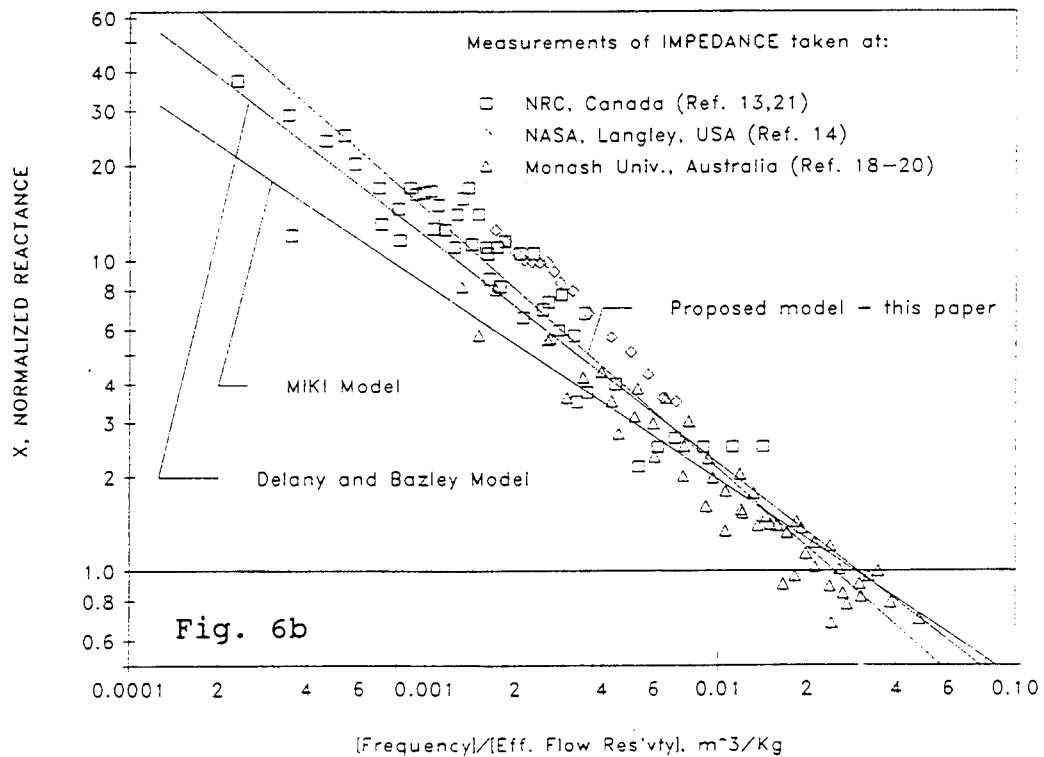
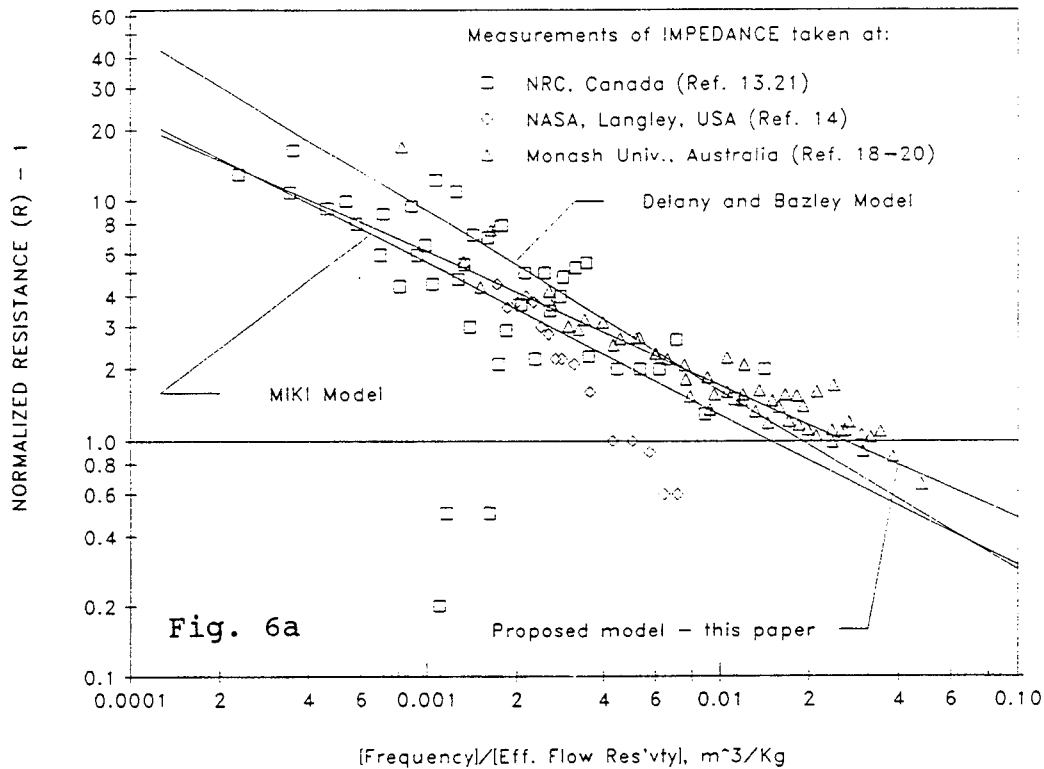


Figure 6. Resistance (part a), reactance (part b) and resulting phase (part c) for the surface impedance data of grass surfaces plotted on a normalized frequency scale compared to three prediction models. Legend identifies the three general locations where data were obtained.

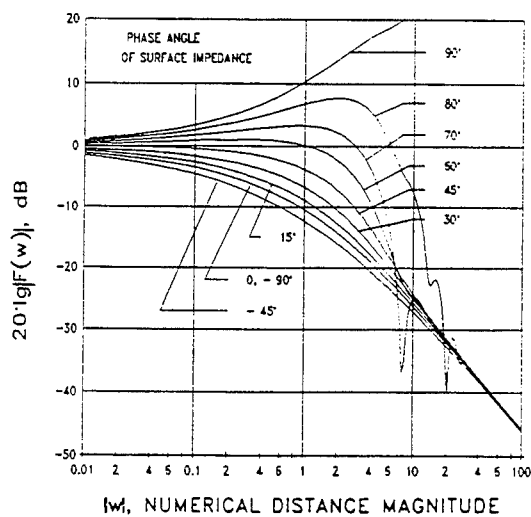
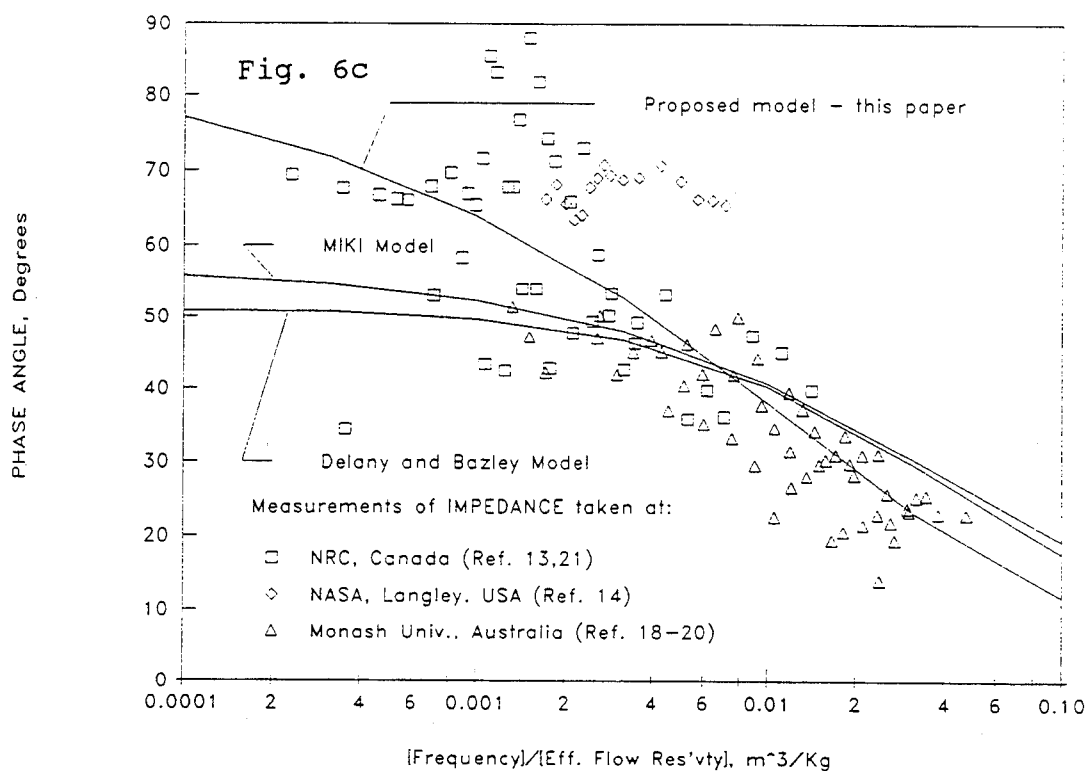


Figure 7. Boundary Loss Factor, in decibels, for sound propagation over an absorbing plane as a function of the numerical distance, w and phase of the surface impedance.

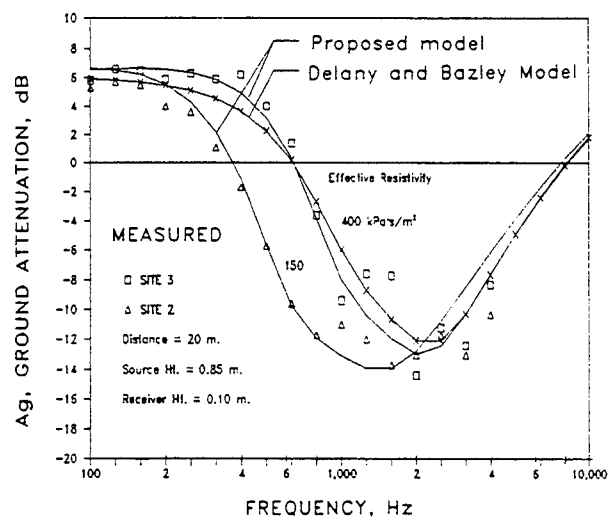


Figure 8. Comparison of measured sound propagation data (from Ref. 27) with predictions according to the Delany-Bazley model and the model proposed in this paper.

Infrasonic Observations and Modeling of the Minor Uncle High Explosive Event

Rodney Whitaker, Susan D. Noel, and Wayne R. Meadows

EES-5 Los Alamos National Laboratory

ABSTRACT

Minor Uncle was a Department of Defense sponsored explosive test of 2440 tons of ammonium nitrate and fuel oil (ANFO) executed on June 10, 1993, at White Sands Missile Range, NM. Los Alamos National Laboratory made infrasonic observations of this event at three stations: Los Alamos, NM, 250 km range; St. George, UT, 750 km range; and the Nevada Test Site, NV, 928 km range. All three stations obtained positive results and had very low background noise levels. Data from all stations will be presented, and normal mode calculations of the wave propagation, including upper atmospheric winds, to St. George will be compared to the data.

BACKGROUND

We present long range, low frequency observations of the Minor Uncle HE detonation. The data are in the infrasonic part of the acoustic spectrum, generally 0.1 Hz to 10.0 Hz, and were recorded at three arrays operated as part of the Los Alamos verification program. Array locations and distances from the event are: Los Alamos, NM, 250 km; St. George, UT, 750 km; and the Nevada Test Site (NTS), NV, 928 km. All three stations had four infrasound microphones in a diamond shaped array. Conditions at all three sites were excellent with low pre-event background levels. Data are processed with standard time-delay and sum beamforming techniques to derive correlation coefficient, trace velocity, and direction to source. Minor Uncle was the eighth large scale DNA experiment we have observed, and a composite summary plot of results is included at the end. Further background information about this series of measurements can be found in Whitaker and Mutschlecner (1988).

Signal energy is propagated to long range via a ducted, multi-hop process, in which the signal may reach 50 to 100 km altitudes. Over these paths, atmospheric winds can influence propagation and we have derived a normalization procedure to account for the seasonal variation of the upper atmospheric wind, Mutschlecner and Whitaker (1988). These normalized pressures are termed wind corrected amplitudes (WCA), and all pressures presented are wind corrected peak to peak amplitudes. With the conditions for Minor Uncle, the largest signals expected would arrive with an average velocity (surface distance divided by travel time) of about 0.29 km/s, representing waves that were refracted at 50 to 60 km altitudes. Larger average velocities indicate lower refraction altitudes; and smaller indicate higher.

Minor Uncle Results

Figures 1 - 3 present summary beamformer output for the three arrays with main signal energy arriving at the following times: Los Alamos -1524 to 1526; St. George- 1548 to 1551; and NTS- 1557 to 1605 (all times are UT). Event zero time was 1510 UT. Each dot represents the beamformer output for a 20 second window of data. Figures 4 -10 show raw channel data (volts) for the signal arrivals at the three sites. Array location is given at the top of each set. Four minutes of data are shown for each channel in each figure. The numbers below or within the "Channel One" panel give the average propagation velocity of the feature. Distinct arrivals are apparent at all stations, have been seen on previous events, and depend on the detailed atmospheric structure at event time. Figures 11 to 12 show the winds at altitude at event time and are normal for this time of year (zonal are east/west, meridional are north /south). These data are from a rocketsonde launched from White Sands Missile Range at event time.

Figure 13 gives the combined results of our observations for Direct Course (DC), Pre-Direct Course (PDC), Mill Race (MR), Minor Scale (MS), Misty Picture (MP), Misers Gold (MG), Distant Image (DI), and Minor Uncle (MU). The peak to peak, wind corrected pressure amplitude is given as a function of scaled range. Here, because of the ducted nature of the propagation, we scale the range by the charge weight raised to the 0.5 power. The least squares fit has a σ (log WCA) of 0.15.

Figure 14 shows the results of a normal mode calculation of the signal at the St. George array. A version of the normal mode propagation code due to Pierce and Posey (1976) was used and included the winds as measured by the WSMR rocketsonde. Fifty modes were used in the calculation with horizontal phase velocities from 0.331 km/s to 0.357 km/s and angular frequencies from 0.01 s^{-1} to 3.6 s^{-1} . These phase velocities span the range appropriate for the wind formed duct from the source to ST. George. A CIRA model atmosphere was used with 2 km thick layers. The main features of the signal are reproduced by the calculation.

Summary

Long range infrasonic observations of the Minor Uncle ANFO explosive test were made at three stations by Los Alamos National Laboratory. These results were added to the data base of previous measurements for such tests. This series of events provides homogeneous sources for the study of long range infrasound propagation in the 1 Hz region of the spectrum. Normal mode calculations, including winds, reproduce the main features of the data recorded at St. George.

This work was supported by the US Department of Energy.

REFERENCES

- Mutschlecner, J. Paul. and Whitaker, Rodney W., 1988, "The Correction of Infrasound Signals for Upper Atmospheric Winds", in Fourth International Symposium on Long Range Sound Propagation, NASA-CP-3101, compiled by William L. Wilshire, Jr.
- Pierce, Allan D., and Kinney, Wayne A., 1976, "Computational Techniques for the Study of Infrasound Propagation in the Atmosphere", AFGL-TR-76-0056.
- Whitaker, Rodney W., Mutschlecner, J. Paul, Davidson, Masha B., and Noel, Susan D., 1988, in Fourth International Symposium on Long Range Sound Propagation, NASA-CP-3101, compiled by William L. Wilshire, Jr.

FIGURE CAPTIONS

Figures 1 -3: Summary plots of beamformer outputs for the three stations. Correlation coefficient, trace velocity, and source azimuth are plotted as functions of time. Station identification and passband are shown in header at the top of each plot.

Figures 4-10: Raw channel data (volts) as function of time for three arrays. Distinct arrivals of larger signal amplitudes are evident. Numbers under these features are the average travel velocities for the features. Station names are in the header information at the top of each plot. Four channels are shown from which the correlation between channels is easily seen.

Figure 11: Zonal (east/west) wind profile from WSMR rocketsonde. Wind speed is in meters per second and altitude is in kilometers.

Figure 12: Same as Figure 12 but for the meridional (north/south) component.

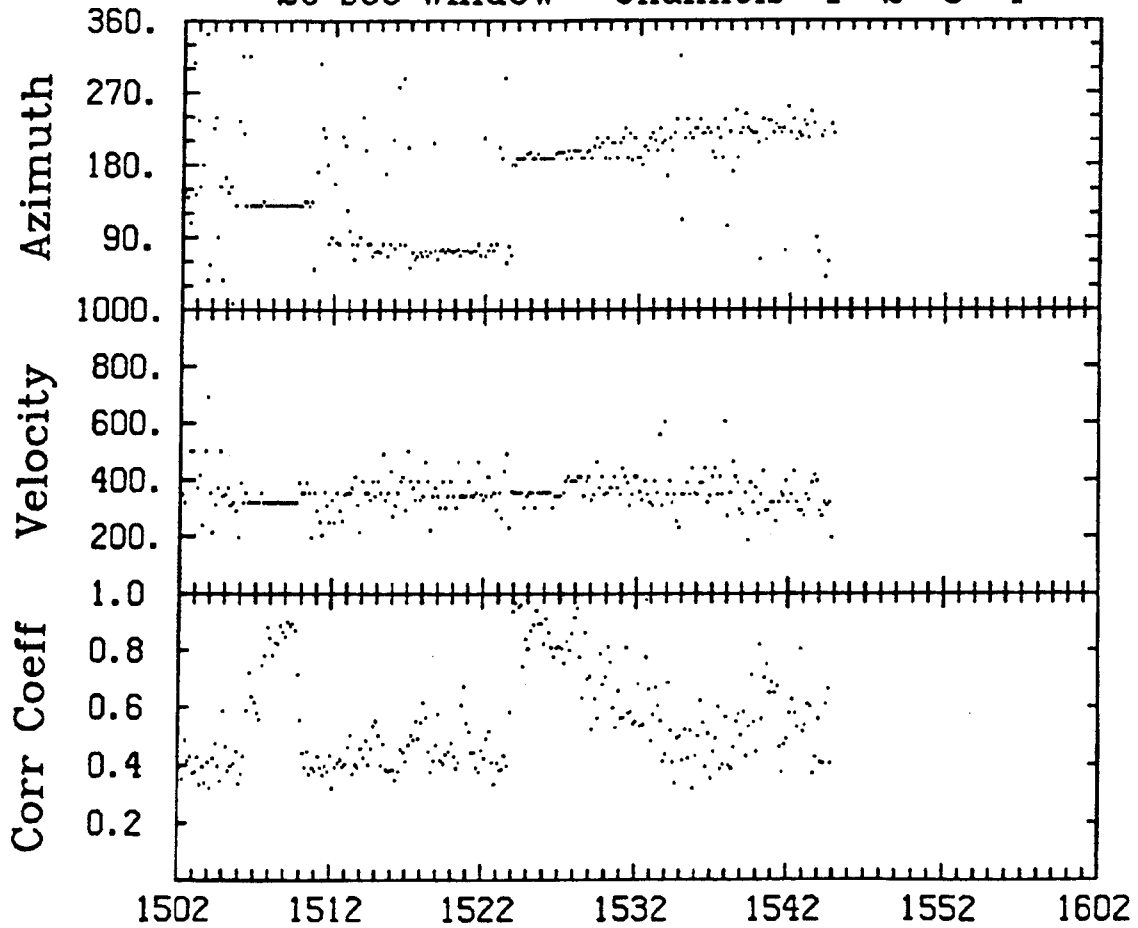
Figure 13: Combined results for all the WSMR explosive tests measured by Los Alamos in terms of WCA versus scaled range.

Figure 14: Calculated waveform at St. George array shown as volts versus time (seconds) after the event zero time. Both segments cover four minutes of data, and the top panel begins at 39 minutes after zero time or at 1549 UT.

LOS ALAMOS ARRAY (PC) DAY Day 161 1993

20 samples/sec 0.49 to 2.99 Hz norm

20 sec window Channels 1 2 3 4



Time (UT)

Figure 1

ST GEORGE PC SETUP DAY Day 161 1993
20 samples/sec 0.49 to 2.99 Hz norm
20 sec window Channels 1 2 3 4

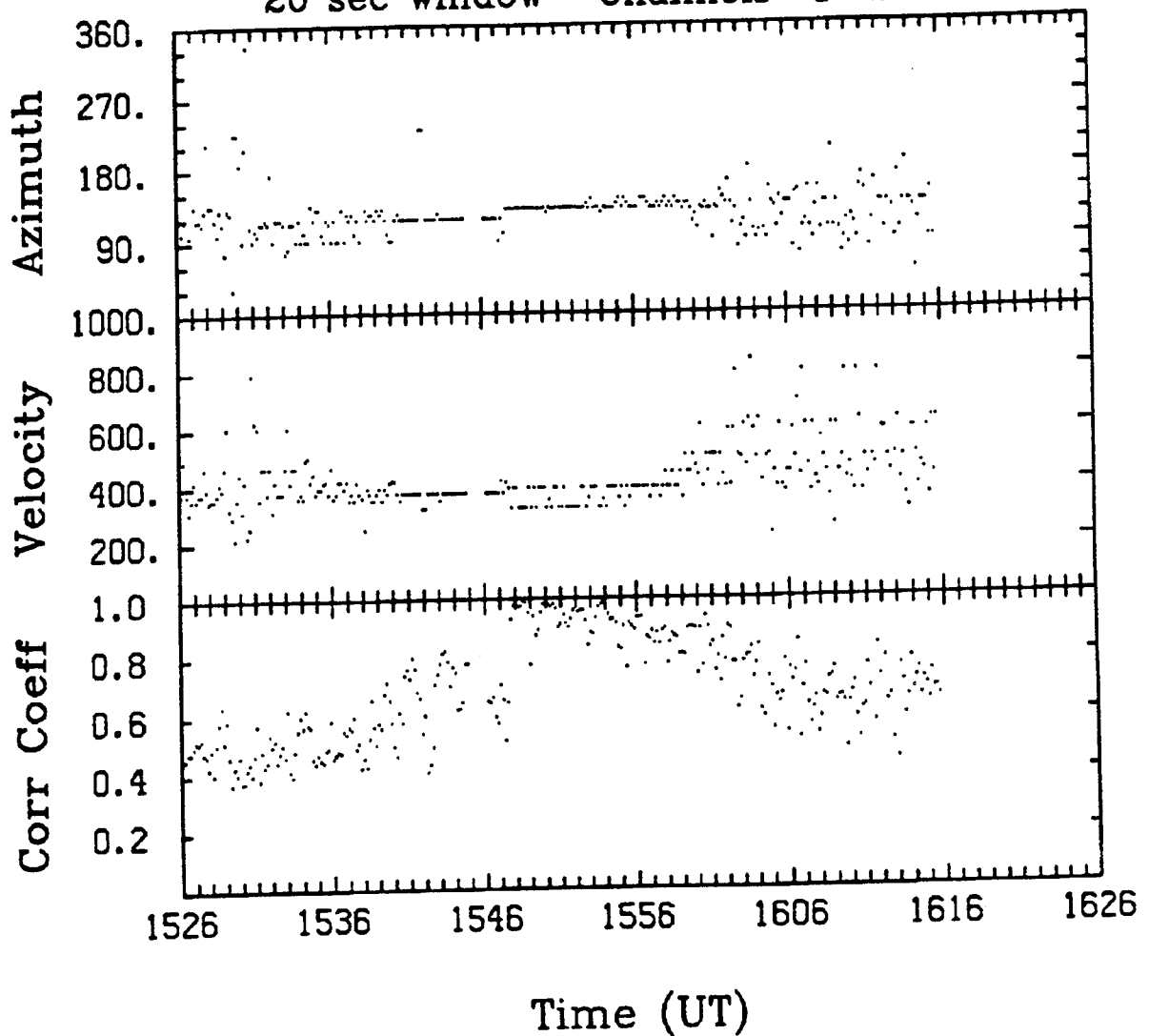


Figure 2

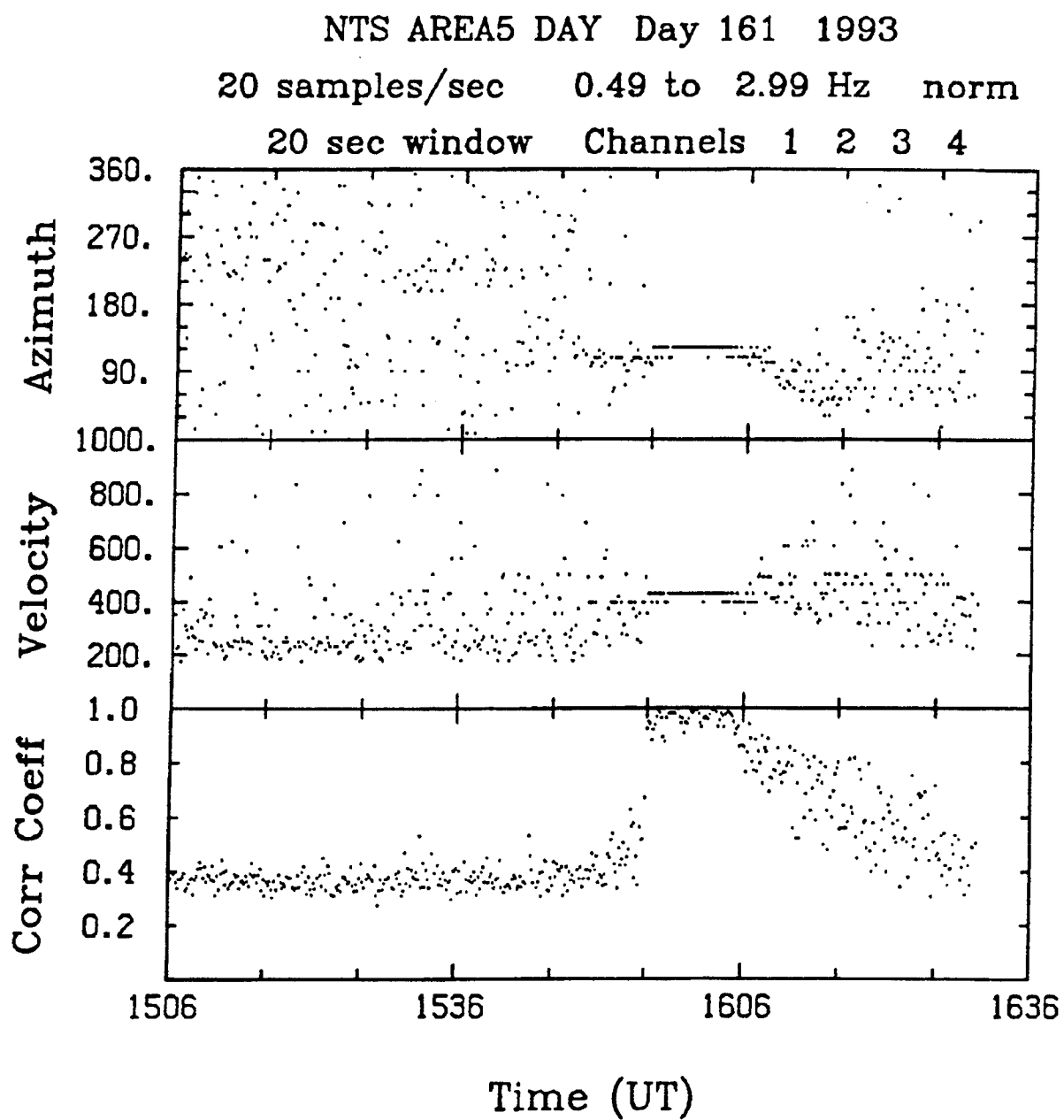


Figure 3

LOS ALAMOS ARRAY
Day 161 1993 1522:00

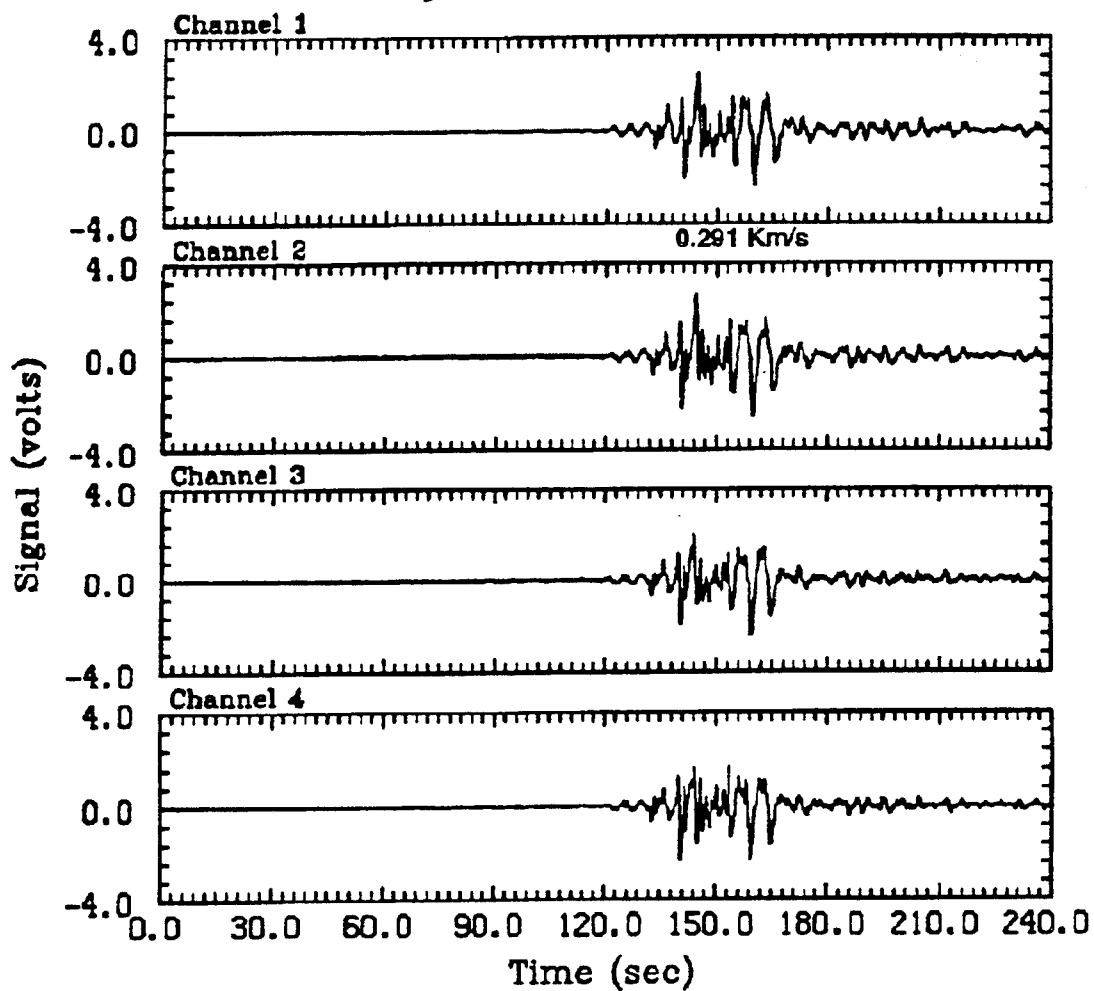


Figure 4

LOS ALAMOS ARRAY
Day 161 1993 1526:00

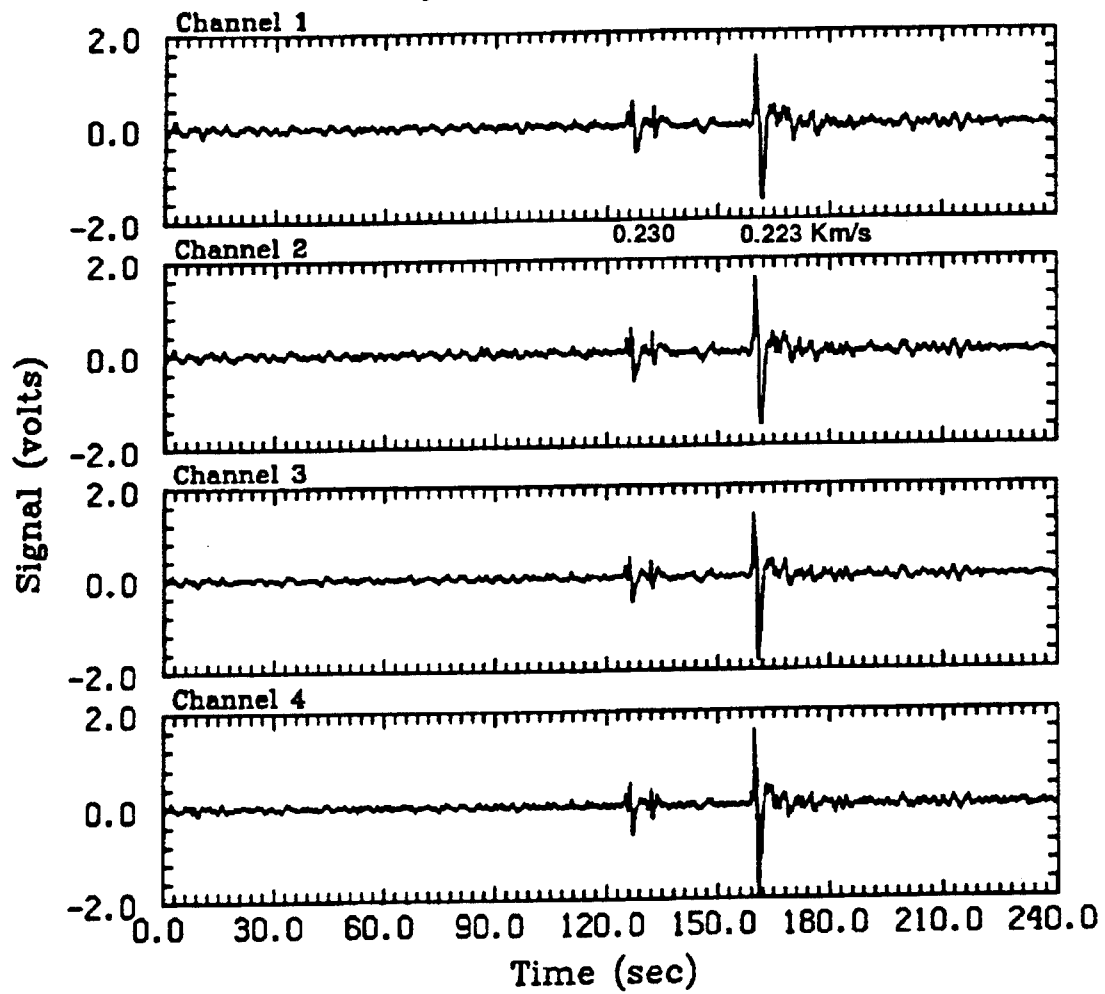


Figure 5

ST GEORGE ARRAY
Day 161 1993 1548:00

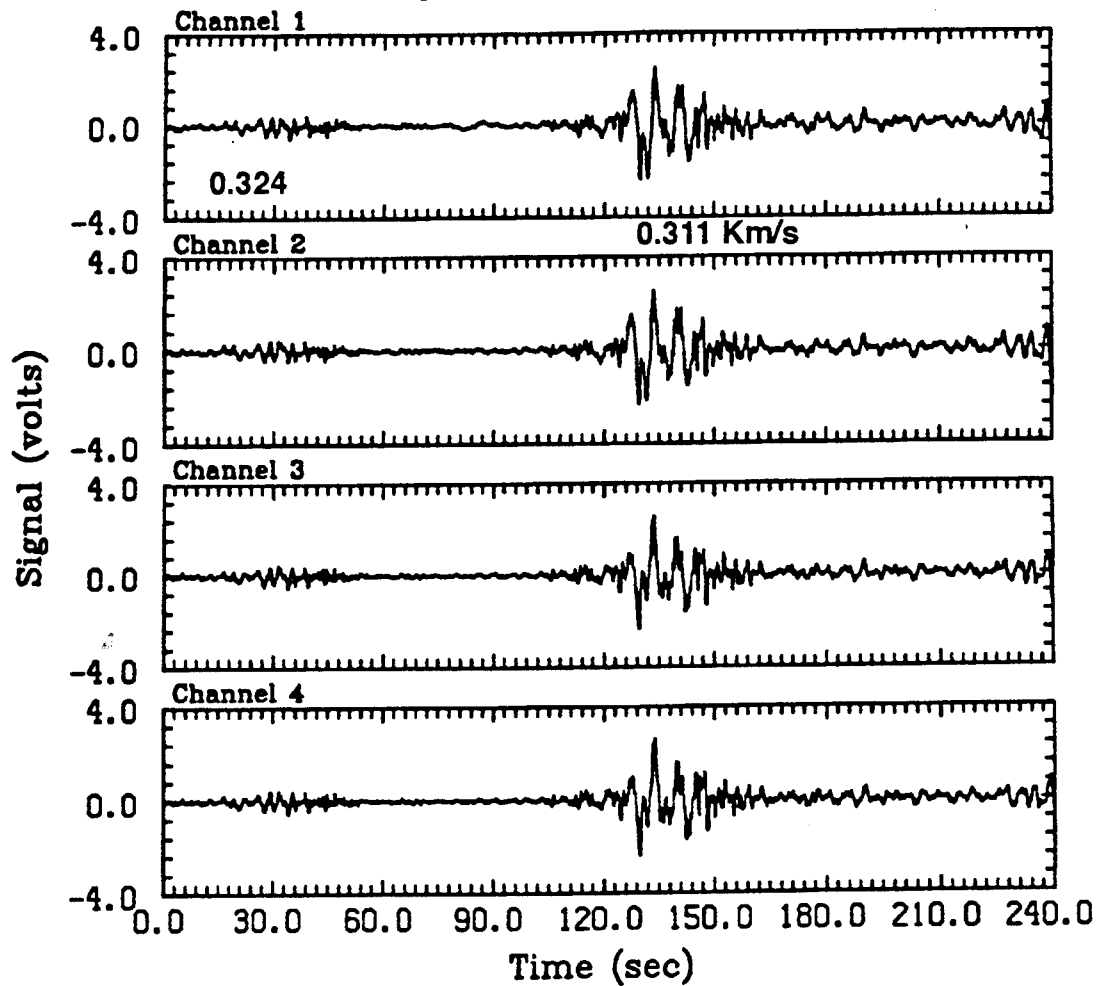


Figure 6

ST GEORGE ARRAY
Day 161 1993 1552:00

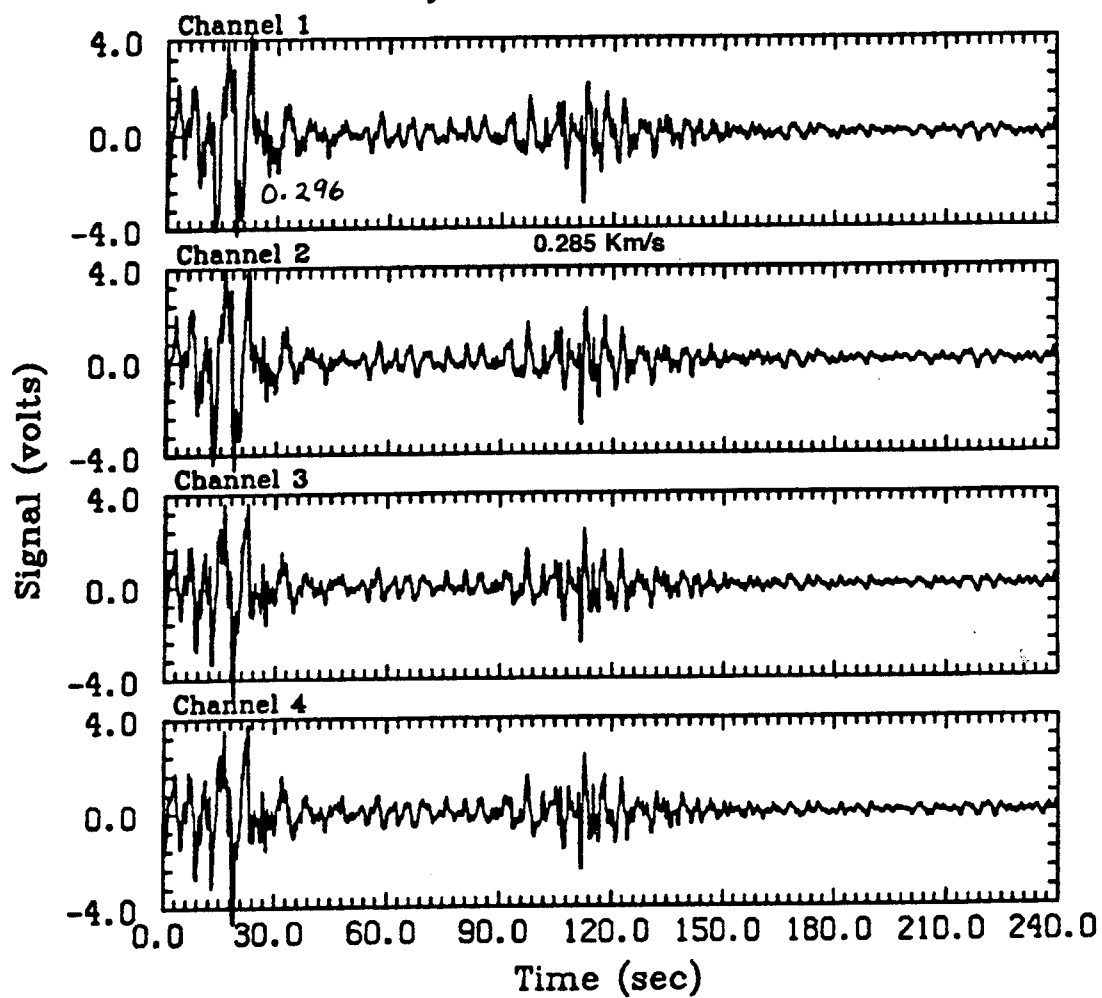


Figure 7

NTS ARRAY

Day 161 1993 1555:00

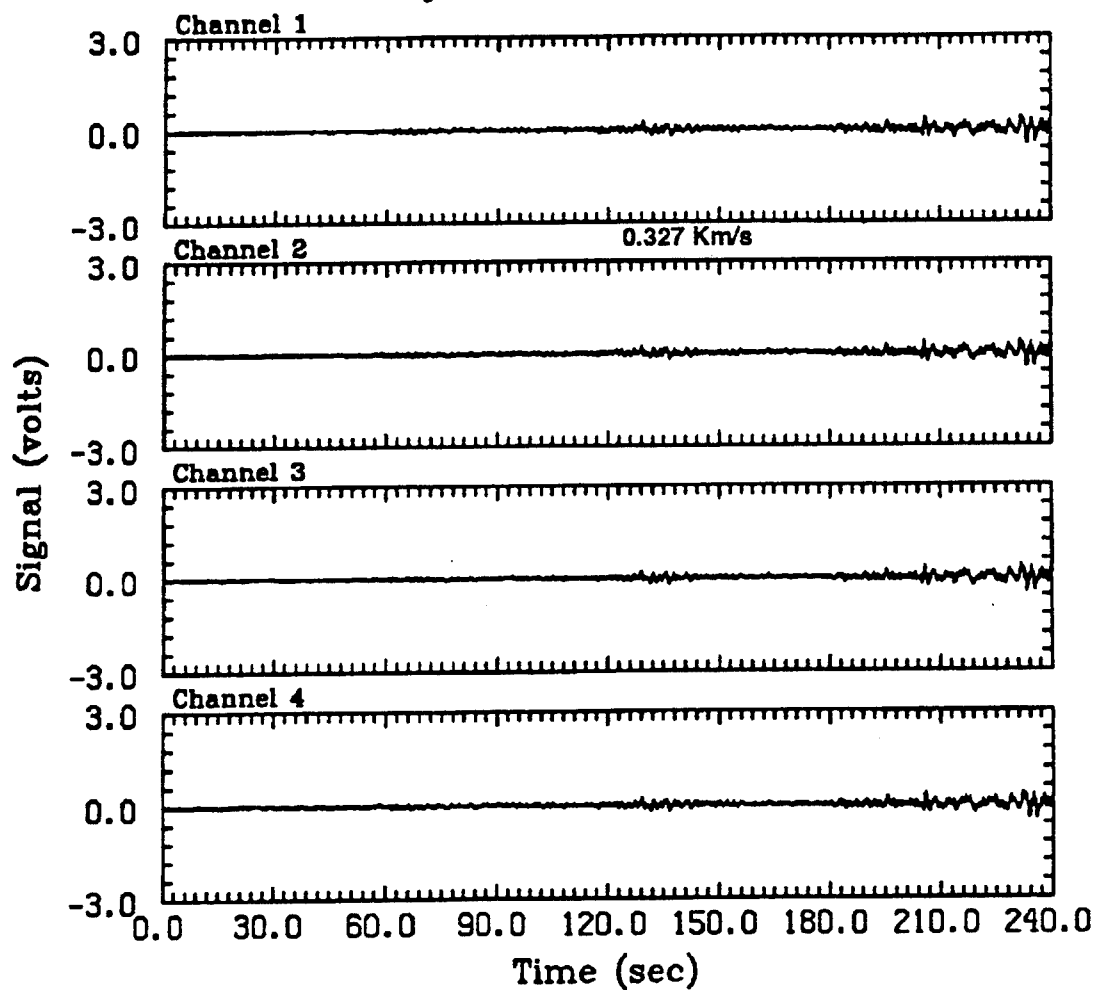


Figure 8

NTS ARRAY

Day 161 1993 1559:00

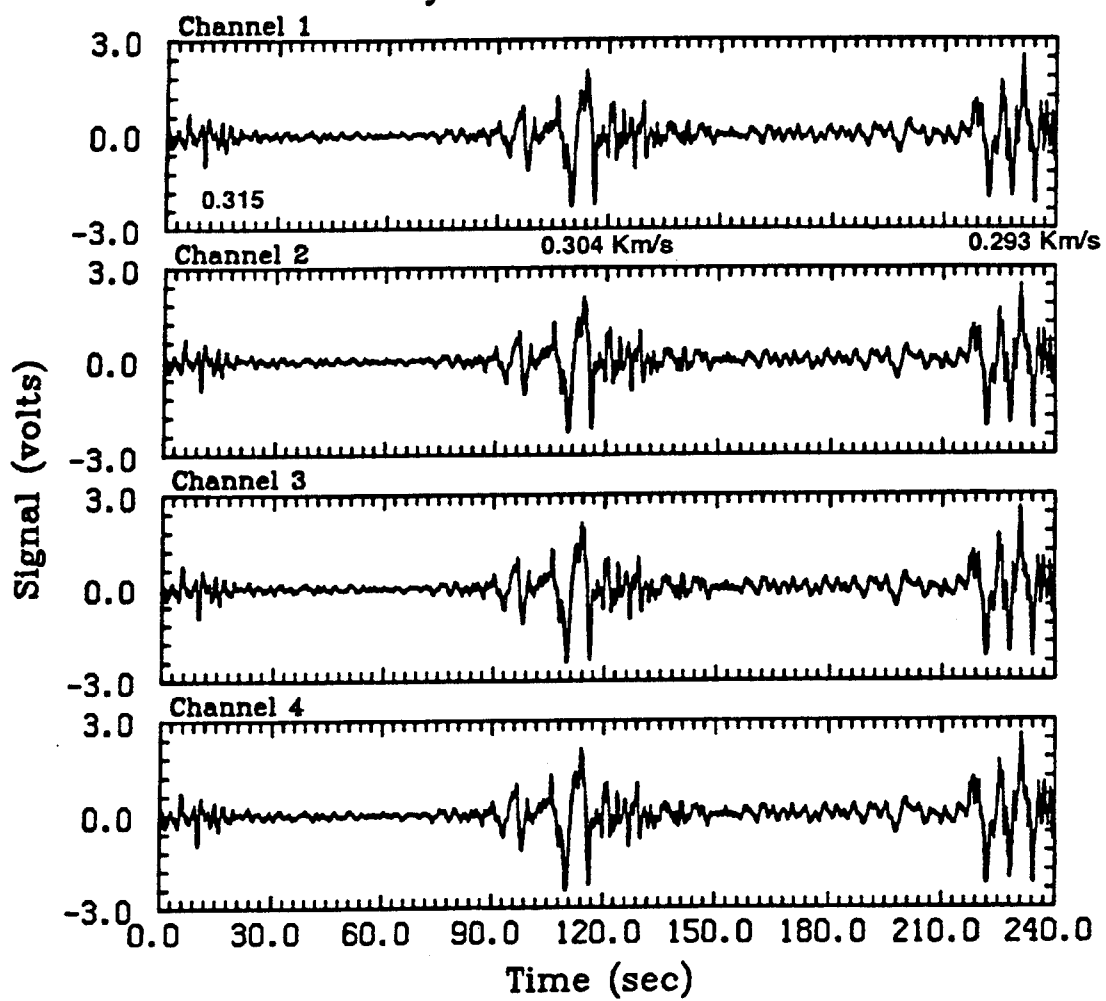


Figure 9

NTS ARRAY

Day 161 1993 1603:00

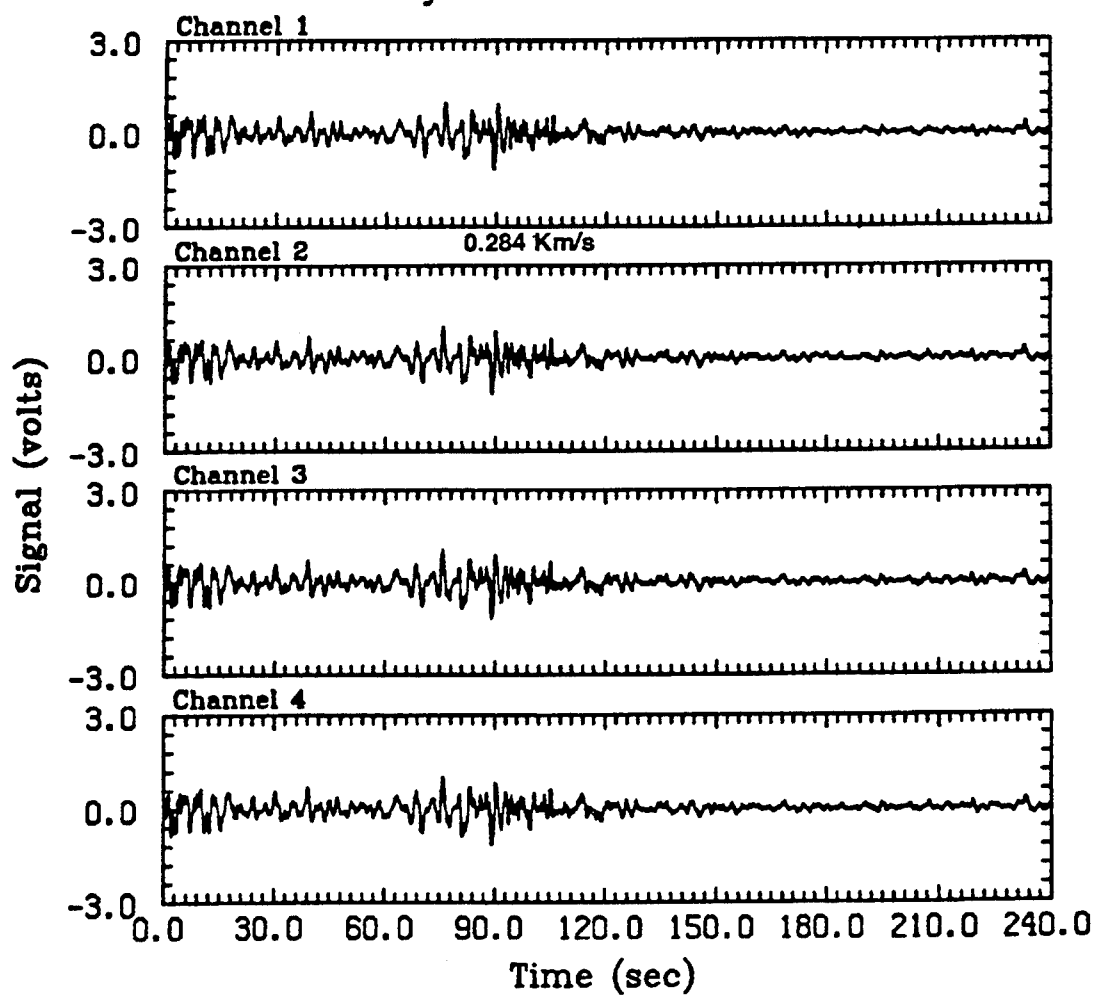


Figure 10

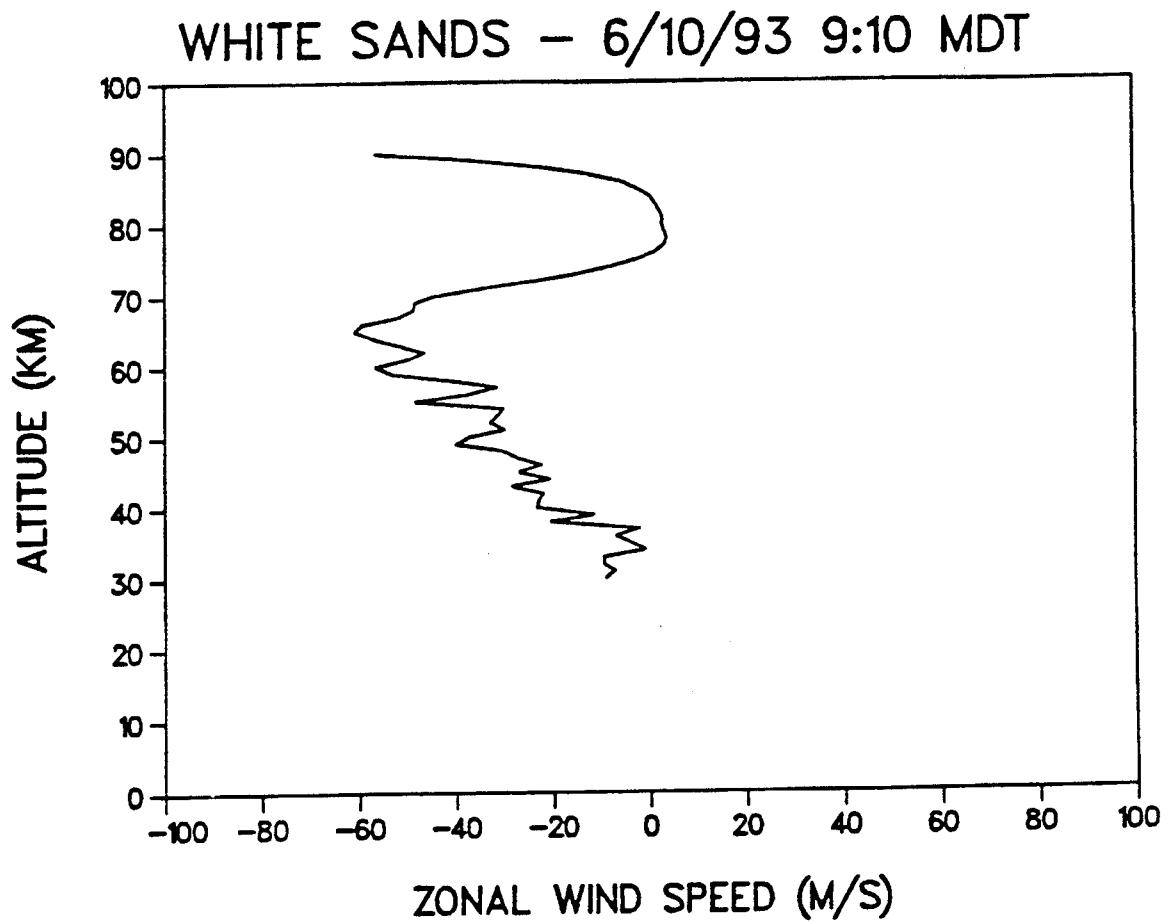


Figure 11

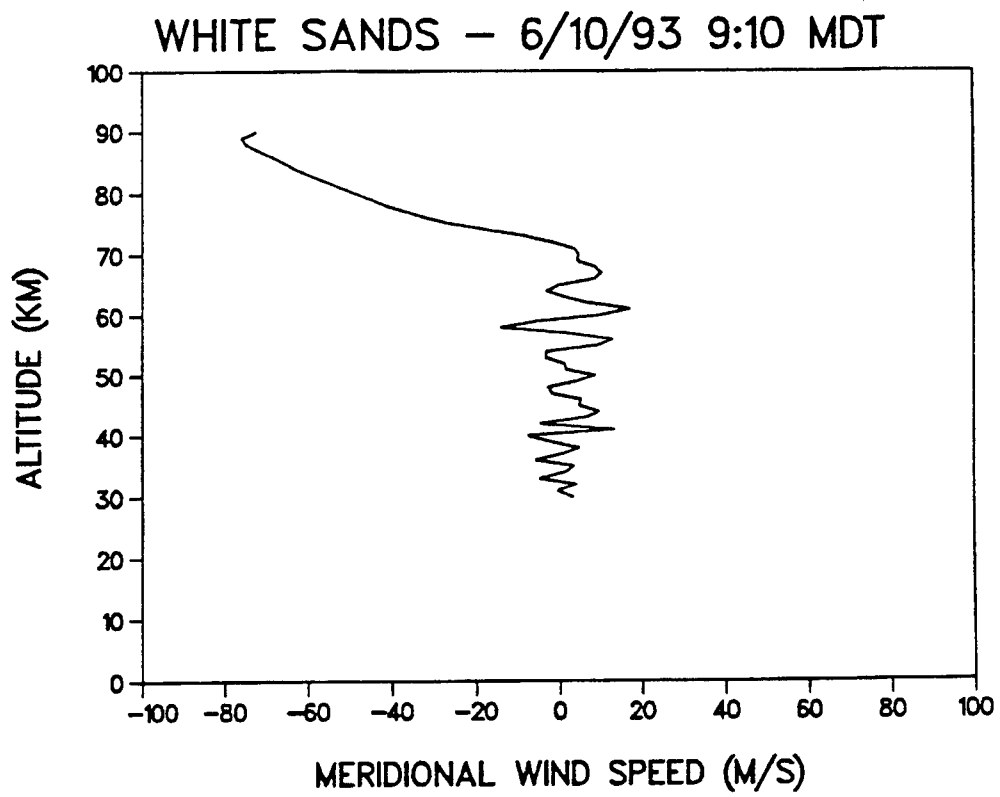


Figure 12

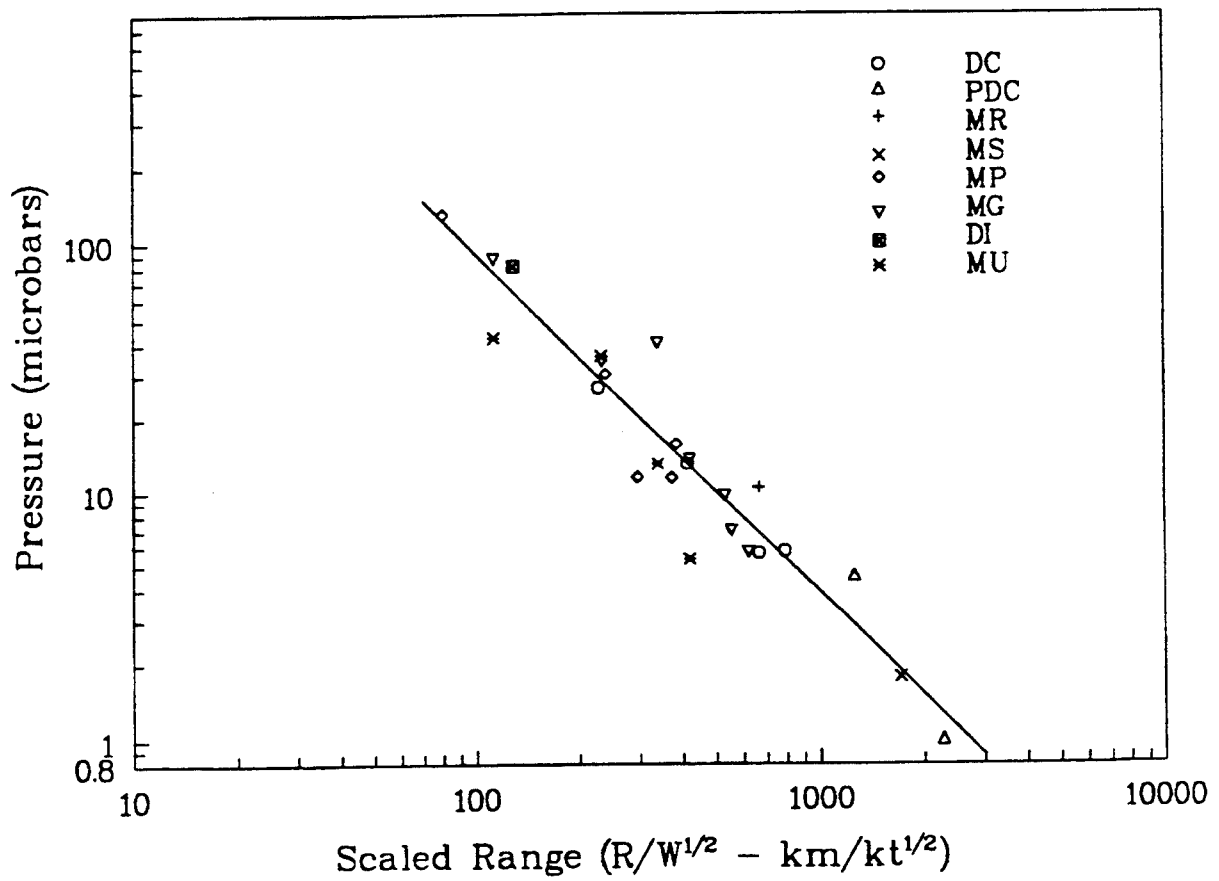


Figure 13

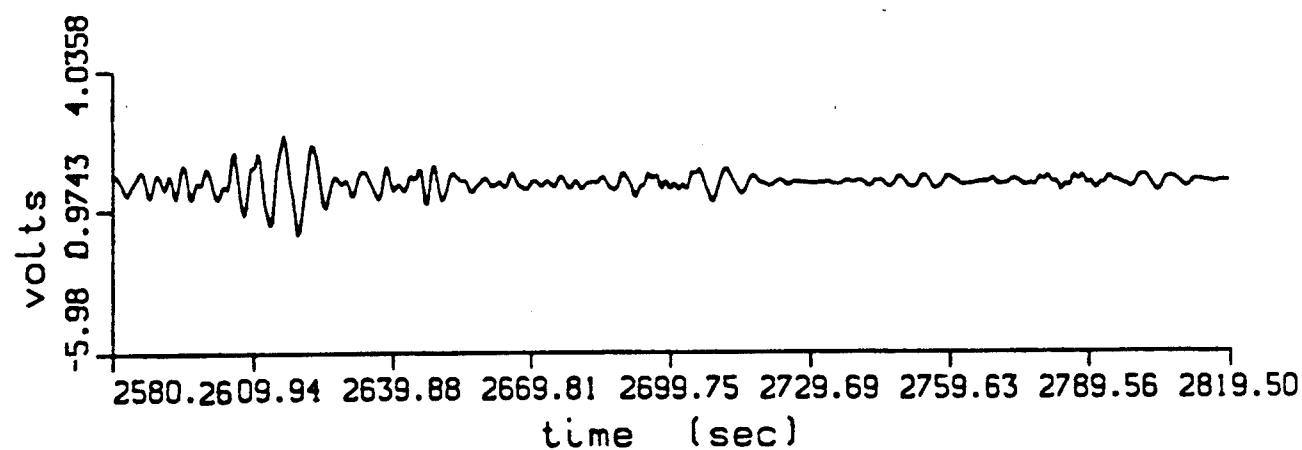
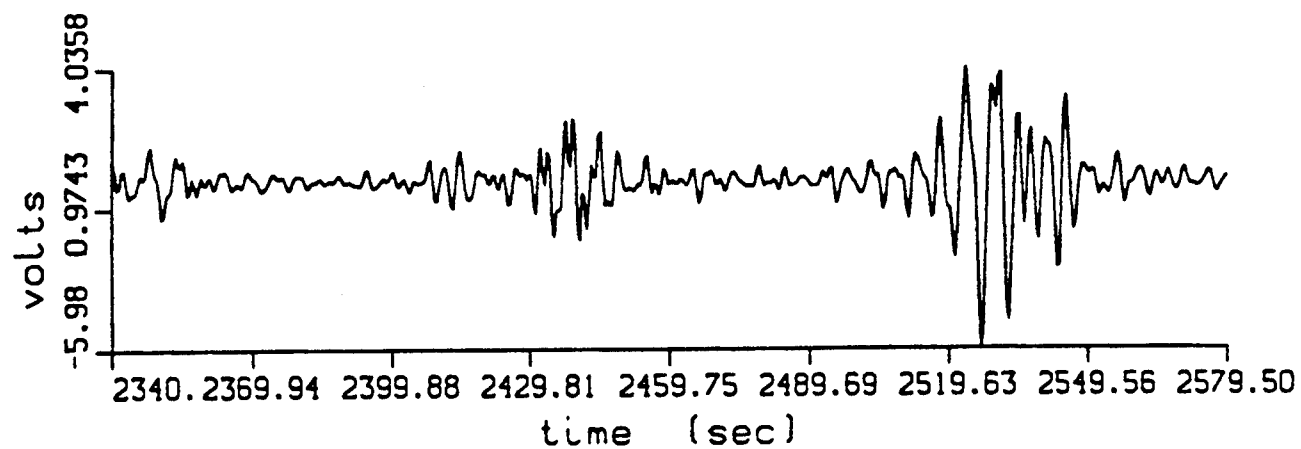


Figure 14

INFRASONIC OBSERVATIONS OF THE NORTHRIDGE, CALIFORNIA, EARTHQUAKE

J. Paul Mutschlecner and Rodney W. Whitaker
Los Alamos National Laboratory
Los Alamos, NM 87545

ABSTRACT

Infrasonic waves from the Northridge, California, earthquake of 17 January 1994 were observed at the St. George, Utah, infrasound array of the Los Alamos National Laboratory. The distance to the epicenter was 543 kilometers. The signal shows a complex character with many peaks and a long duration. An interpretation is given in terms of several modes of signal propagation and generation including a seismic-acoustic secondary source mechanism. A number of signals from aftershocks are also observed.

INTRODUCTION

On 17 January 1994 a large earthquake occurred in Southern California near the town of Northridge in the San Fernando Valley. We report here on the detection of infrasonic waves from the earthquake, which were observed by an array operated by the Los Alamos National Laboratory, near St. George, Utah. The Northridge earthquake was a large, very destructive event with seismic magnitude M_L (local system) = 6.4. The estimated depth of the disturbance was 16.4 km. The principal event (12:30:55 UTC) was followed by many aftershocks; over 400 were observed during the following 8-day period, for example.

OBSERVATIONS

The Los Alamos National Laboratory has for some years operated several infrasound arrays. Some details of these arrays and our operating and analysis procedure have been discussed by Whitaker *et al.* (1988). Because these arrays nominally operate continuously, unanticipated signals, such as those from earthquakes, may be observed. We have, in fact, detected the signals from a number of earthquakes covering a large range in seismic magnitude. Unfortunately, only the St. George array was operating during the Northridge earthquake.

Figure 1 presents results from our analysis for the time period 10:00 to 13:00 (all times herein UTC). The plots, from top to bottom, show the azimuth, trace or horizontal velocity across the array, correlation coefficient, and power resulting from a beam-steering algorithm analysis. The correlation coefficient is essentially an average of pairwise correlations among the channels. The power level is given in relative units; typically

background noise levels are close to, or lower than, 1. Each point represents the result from a twenty-second window of signal with a ten-second overlapping step. The data are recorded at twenty samples/second. In this analysis we have a bandpass of 0.02 to 0.49 Hz to demonstrate the underlying background or "noise" that we believe to be due to microbaroms from an azimuth of about 230° . Typically such microbaroms have a central frequency close to 0.18 Hz. Notice that the trace velocity centers at about 250 m s^{-1} , that the correlation is very high (strong coherence across the array), and that the power level is very low (very weak signals). Microbarom activity, such as this, can be present from many hours or days at a time. During this interval the random noise levels were very low, so that the microbarom signals can be seen well in spite of their low amplitudes.

Because the distance from the epicenter was about 543 km, the direct acoustic earthquake signals can be anticipated to arrive in about 30 minutes or at roughly 13:00. In fact, we see strong activity beginning at about 12:30, with a rise to a peak at about 13:00. In order to filter out the microbarom activity, an analysis was performed for a bandpass of 1.0 to 4.0 Hz (among others), and the results are presented in Fig. 2. Here we see that the background correlation and power are low until a sequence of signals, which are related to the earthquake, begins at about 12:30. This signal activity is strong until a return to approximate background power and correlation at about 13:20. During the strong signal period, the azimuth narrows to a band closely centered on the great circle azimuth to the epicenter: 236° east of north. At the time of the peak signal near 13:03, the azimuth matches the predicted azimuth exactly. The trace velocity data also narrows during the peak signal period to a value close to 350 m s^{-1} —a value typical for stratospheric acoustic refraction. Notice that the strong signal near 12:35 has poorly defined or nearly random values for both azimuth and trace velocity. This is due to the fact that this signal can be identified, as we shall show subsequently, with a wave traveling at a seismic rather than acoustic velocity across the array. The array geometry does not permit azimuth resolution of such high-speed signals. Notice also the general complexity of the signal region. In addition, several signals are seen in the correlation plot following the principal signal. We shall discuss all of this activity in a subsequent section.

Figure 3 shows a portion of the array channel plots during the seismic-coupled signals. The background of microbaroms and other noise is very quiet until some stronger activity begins at about 12:32:30. At about 12:33:50 a larger, nearly sinusoidal, wave is seen followed by a long sequence of moderate amplitude activity; highly correlated activity follows this for several hours. As is easily seen, there is a strong correlation throughout this sequence across the four array channels.

Figure 4 illustrates a portion of the signal train at the time of the peak signal. As can be seen, the signal is highly correlated and has a peak-to-peak amplitude of 10 μbar or more.

Figure 5 presents a sample of power spectra in the band 0.5 to 3.0 Hz during the peak signal. Each power spectrum covers a 20-second sample with 20-second spacings. Note that significant power occurs at the lower frequencies and that there is significant short-term variability.

In Figure 6 we present the correlation survey plot for a 4-hour interval from 12:00 to 16:00. Significant peaks are marked by vertical lines and identifications. Table I presents information on the early portion of the sequence: an identification, arrival time, and an average velocity, \bar{V} . Average velocity means the great circle distance to the source divided by the transit time of the signal measured from event time. We find for the start of the seismic activity a velocity of 5.84 (all \bar{V} in km s^{-1}). This corresponds well with the expected velocity range for a P-wave seismic disturbance arriving from the epicenter. The peak seismic signal has $\bar{V} = 3.02$, corresponding to the arrival of a surface or S-wave. These seismic waves are believed to propagate ground-coupled acoustic waves that are detected by the array. The S-wave disturbances have frequently been seen by us and occasionally the P-wave disturbance.

The primary signal has $\bar{V} = 0.280$ and is clearly identified with a direct acoustic signal from the epicenter. A more typical velocity for infrasonic signals is about 0.29 and it may be that the acoustic signal velocity is affected by high-level winds. Table I and Fig. 6 also indicate three "early" signals, which we shall discuss in a later section.

Figure 6 illustrates signals associated with known aftershocks and shows the seismic magnitude, M_L , of each event. These event-signal identifications are plausible because each signal shows the correct azimuth and has a reasonable value of \bar{V} . In Fig. 7 we see the observed transit time, Δt , and the corresponding \bar{V} for each signal. With a few exceptions, the velocity values cluster tightly around the value of 0.28 observed for the primary signal. It is unique for us to be able to observe aftershocks to these low magnitudes, and we attribute this to excellent propagation conditions and very low background noise. Two signals marked with "?" in Fig. 6 have the correct azimuth but no aftershock identification. The signal at 15:56 is from an azimuth not related to the earthquake.

SEISMIC-ACOUSTIC COUPLING

Several features in the Northridge earthquake signals may be explained by a mechanism of seismic-acoustic coupling. The concept is that surface seismic waves may excite a secondary source at some distance from the epicenter, which then radiates acoustic waves traveling through the atmosphere to the receiver. Possibly a seismic velocity change at the secondary source would be responsible for its radiating characteristics. We have observed strong features in the infrasonic signals of two earlier earthquakes (Coalinga, California, 1983, and Whittier, California, 1987) that appear to be attributable to this mechanism. In addition, the very powerful Alaskan earthquake of 1964 produced a strong secondary

source along much of the Rocky Mountains, as observed by several arrays and reported by Young and Greene (1982).

Figure 8 shows the signal power for the period within a few minutes of peak signal. For comparison, notice that we are showing only the central peak of the main feature in the power survey of Fig. 2 and on a linear rather than logarithmic scale. Two satellite peaks occur at about 13:01 and 13:05. The power also shows a drop close to background levels by about 13:00 and 13:07. In Fig. 9 we present a possible interpretation of these features in terms of seismic-acoustic coupling. The epicenter is shown on a line that passes through the St. George array. The location of the possible secondary sources are determined such that the observed signal transit time matches the sum of the seismic travel time from epicenter to secondary source plus the acoustic travel time from the secondary source to array. We assume a seismic velocity of 3 km s^{-1} . The outer marked rectangles (1 and 4) correspond to the fall of the signal power to low levels, and the two inner rectangles (2 and 3) correspond to the satellite peaks in Fig. 8.

It may be that rectangles 1 and 2 to the west of the epicenter are marking the end of the seismic source area at the ocean interface and a role of the coastal mountains in providing a secondary source. Rectangles 3 and 4 to the east of the epicenter lie in the region of the San Gabriel mountain range, which may be acting as a secondary source and bounding region.

Returning to Table I and Fig. 6, we note the three "early" signals that precede the principal event. These signals may also be considered as possible seismic-acoustic coupled secondary sources and we present the results of this interpretation in Fig. 10. Here we see the epicenter connected with the array location and three possible secondary sources marked 6, 7, and 8. Source 6, corresponding to the signal with $\bar{V} = 0.334$, lies in a desert valley. It is possible that this signal is, in fact, a direct acoustic signal with a very low duct having a high propagation velocity. At this time we do not have the required meteorological records to test this possibility. The area marked 6 ($\bar{V} = 0.389$) lies near the Calico Mountains in California, and the third source, no. 7, ($\bar{V} = 0.683$) lies near the Spring Mountains in Nevada. The Calico Mountains are a rather weak topographical feature.

It is interesting to note that a one-bounce distance for stratospheric return of infrasound waves is about 200 to 250 km. The distance from the array to the Spring Mountains source is about 190 kilometers and to the Calico Mt. source about 370 km; hence, the two locations are respectively about one bounce and two bounces from the array. It may be that a primary factor in determining secondary source location with seismic-acoustic coupling is proper position with respect to an effective bounce distance.

CONCLUSIONS

We have seen that the Northridge earthquake was observed in great detail using infrasound at a large range. The signal is long term and complex because of the presence of seismic, direct acoustic, and seismic-acoustic arrivals. In addition, a number of seismic aftershock signals are observed down to low seismic magnitudes. These will be useful in a future study of the relationship between acoustic amplitude and seismic magnitude. The mechanism for the production of secondary sources by seismic-acoustic coupling is poorly understood and deserves further study.

ACKNOWLEDGMENT

This research was supported by the US Department of Energy. We are grateful to Kay Coen and Andrea Kron for assistance with the graphics.

REFERENCES

Whitaker, Rodney W., Mutschlecner, J. P., Davidson, Masha B., and Noel, Susan D., in Fourth International Symposium on Long Range Sound Propagation, NASA-CP-3101, compiled by William L. Wilshire, Jr., (1988).

Young, Jessie M., and Greene, Gary E. "Anomalous Sound Generated by the Alaskan Earthquake of 28 March 1964", J. Acoust. Soc. Am. 71(2), 334, (1982).

Table I. Signal times and average velocities

EVENT	TIME(UTC)	\bar{V} (km s ⁻¹)
EARTHQUAKE	12:30:55	-----
START SEISMIC	12:32:28	5.84
PEAK SEISMIC	12:33:55	3.02
EARLY SIGNAL	12:44:10	0.683
EARLY SIGNAL	12:54:10	0.389
EARLY SIGNAL	12:58:00	0.334
PRIMARY SIGNAL	13:03:15	0.280

MICROBAROM BACKGROUND

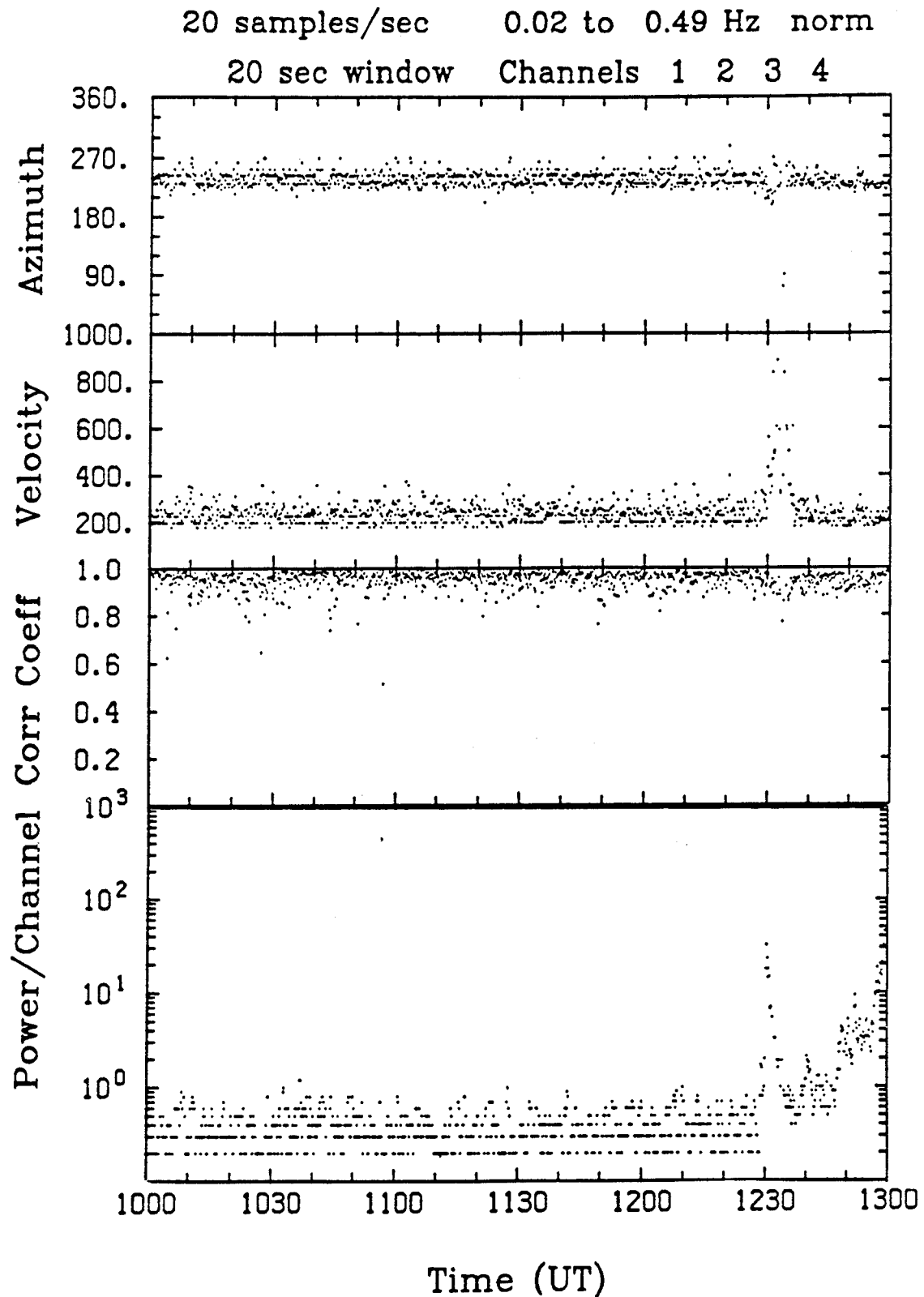


Fig. 1. Survey plots for the bandpass 0.02 to 0.49 Hz showing the microbarom background.

NORTHRIDGE EARTHQUAKE

20 samples/sec 1.00 to 3.98 H unnor

20 sec window Channels 1 2 3 4

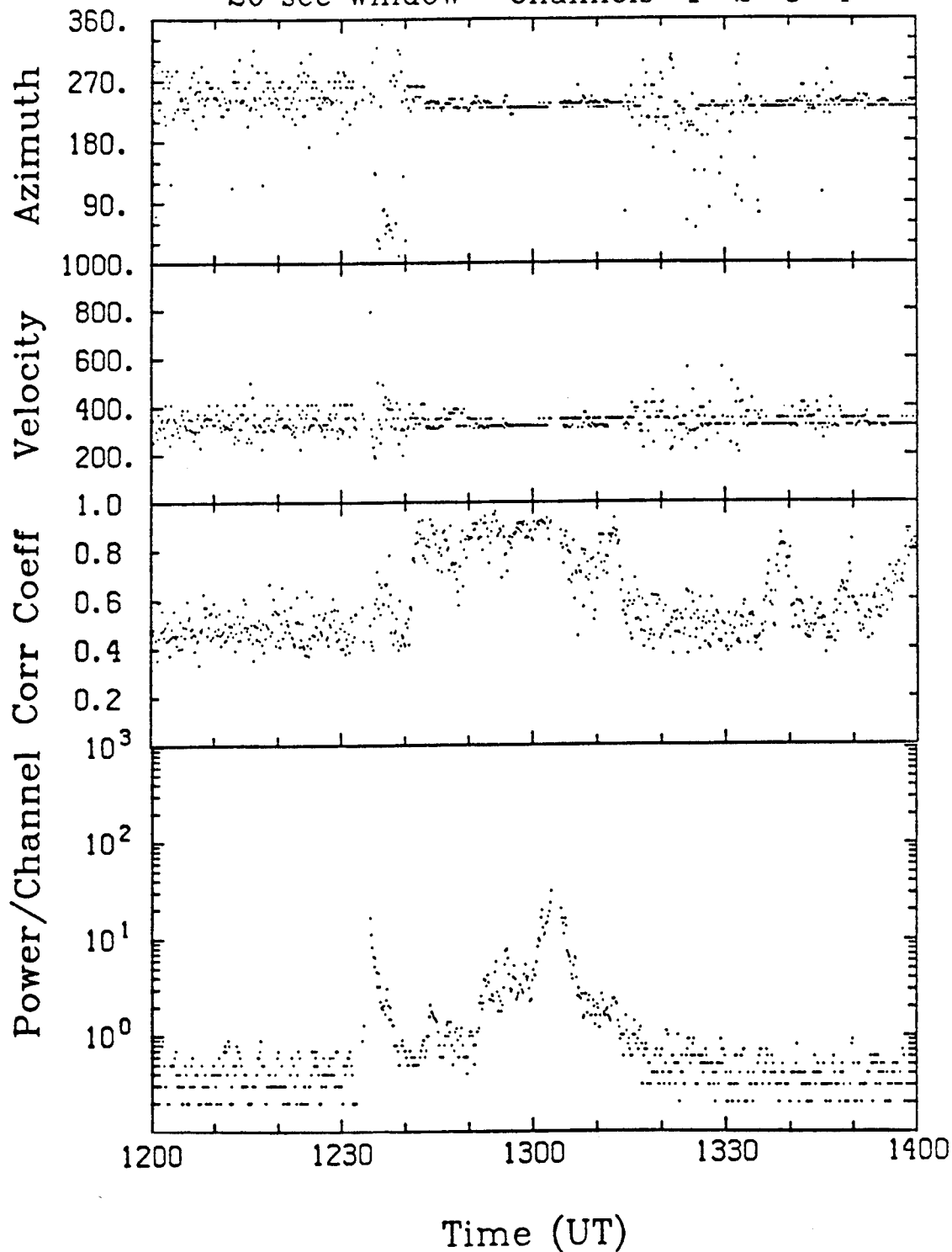


Fig. 2. Survey plots for the same period as Fig. 1 but with a bandpass of 1.0 to 4.0 Hz to emphasize the signals from the earthquake.

SEISMIC SIGNAL REGION

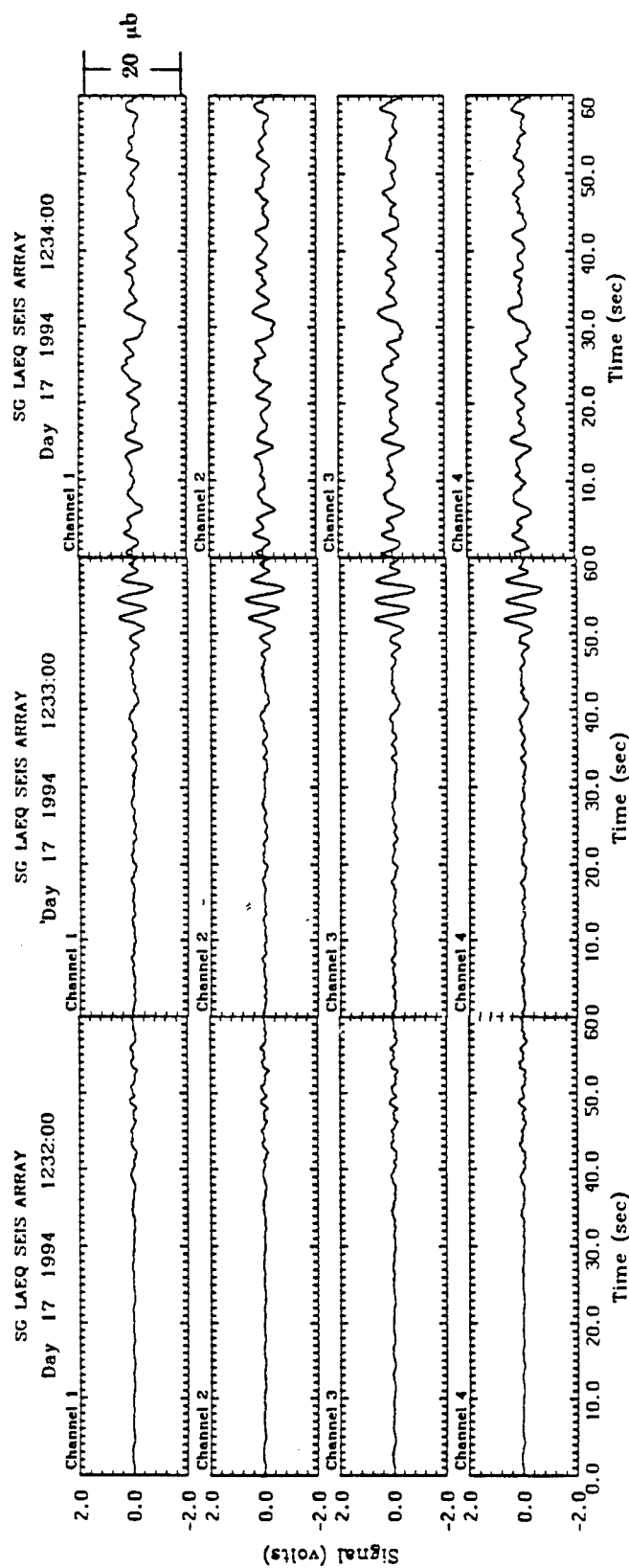


Fig. 3. Channel plots for a three minute interval during the arrival of seismic waves which produce coupled acoustic waves.

PRINCIPAL SIGNAL REGION

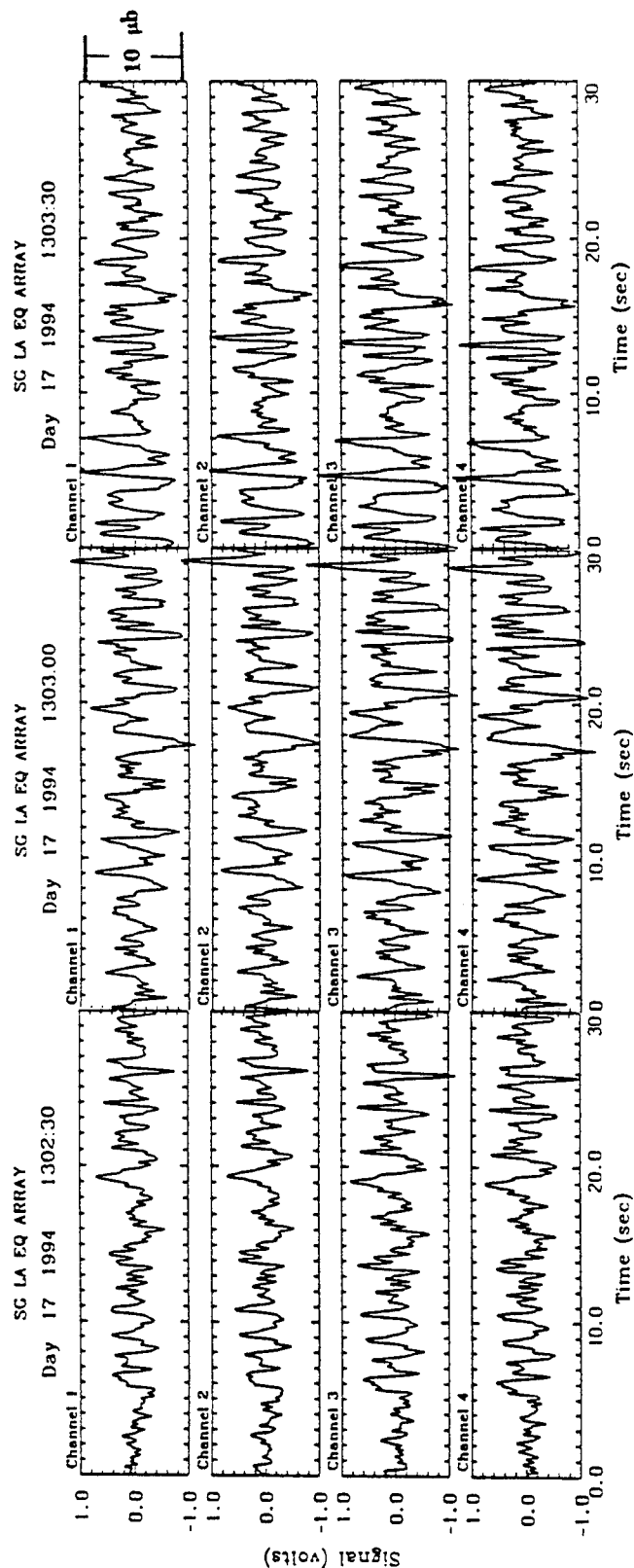


Fig. 4. Channel plots for an interval of 1.5 minutes during the peak acoustic signal from the earthquake.

PEAK REGION POWER SPECTRA

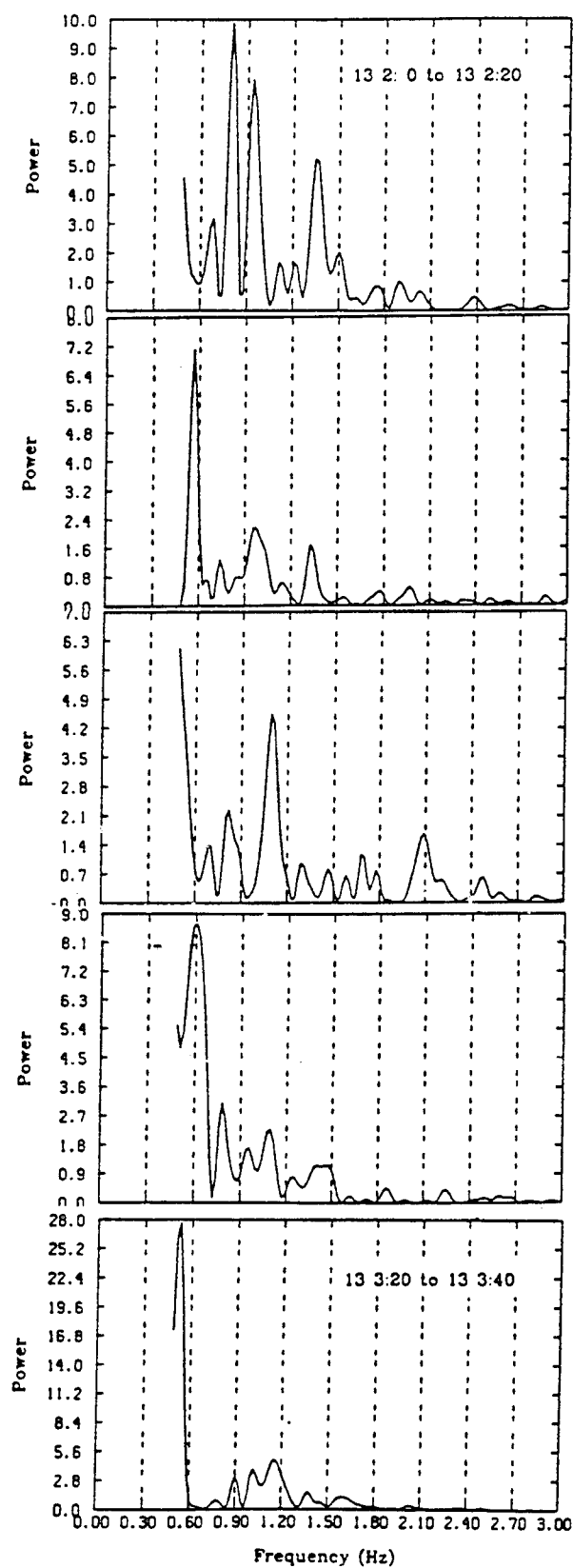


Fig. 5. Power spectra for a series of twenty second windows centered on the time of the peak acoustic signal.

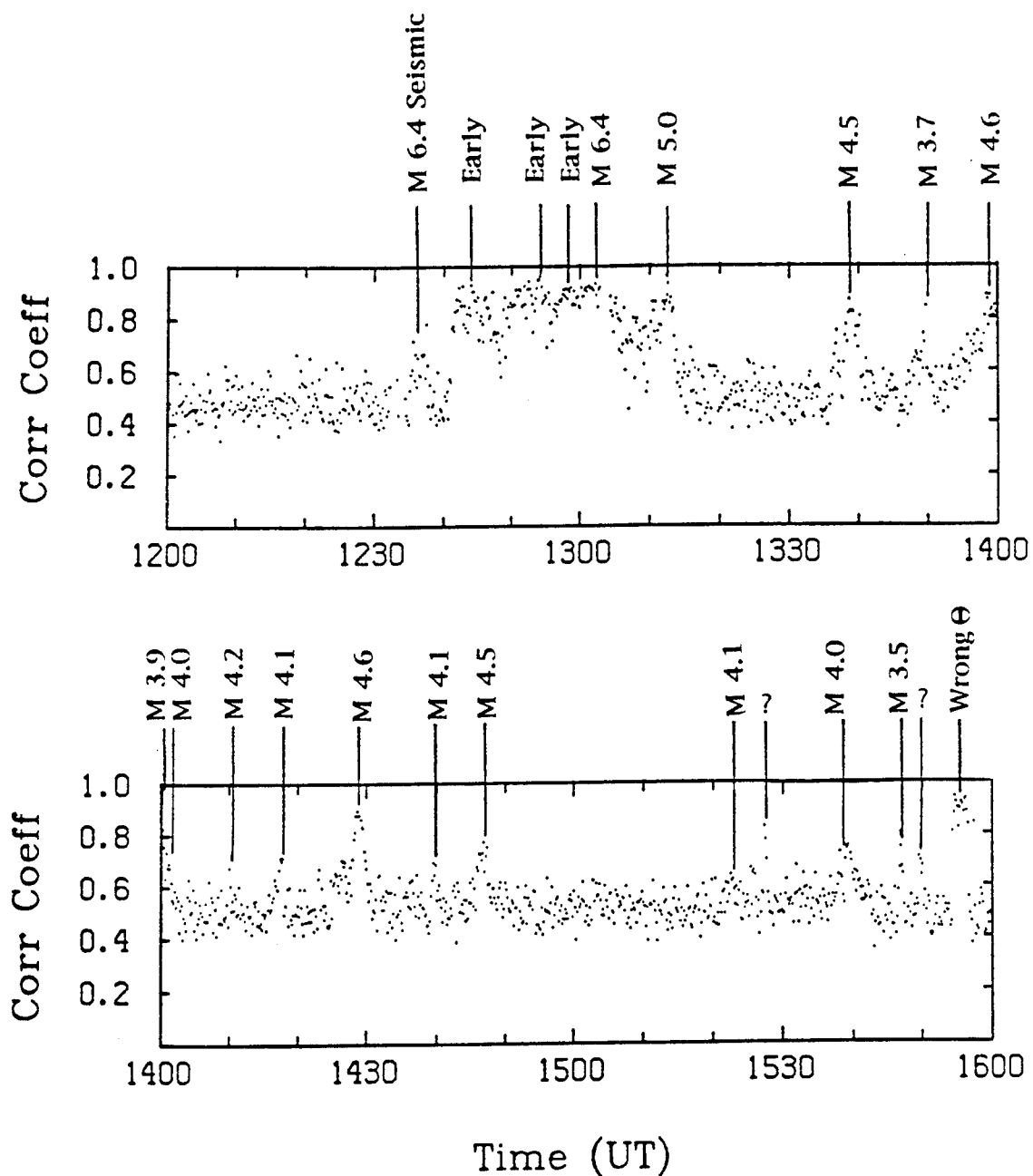
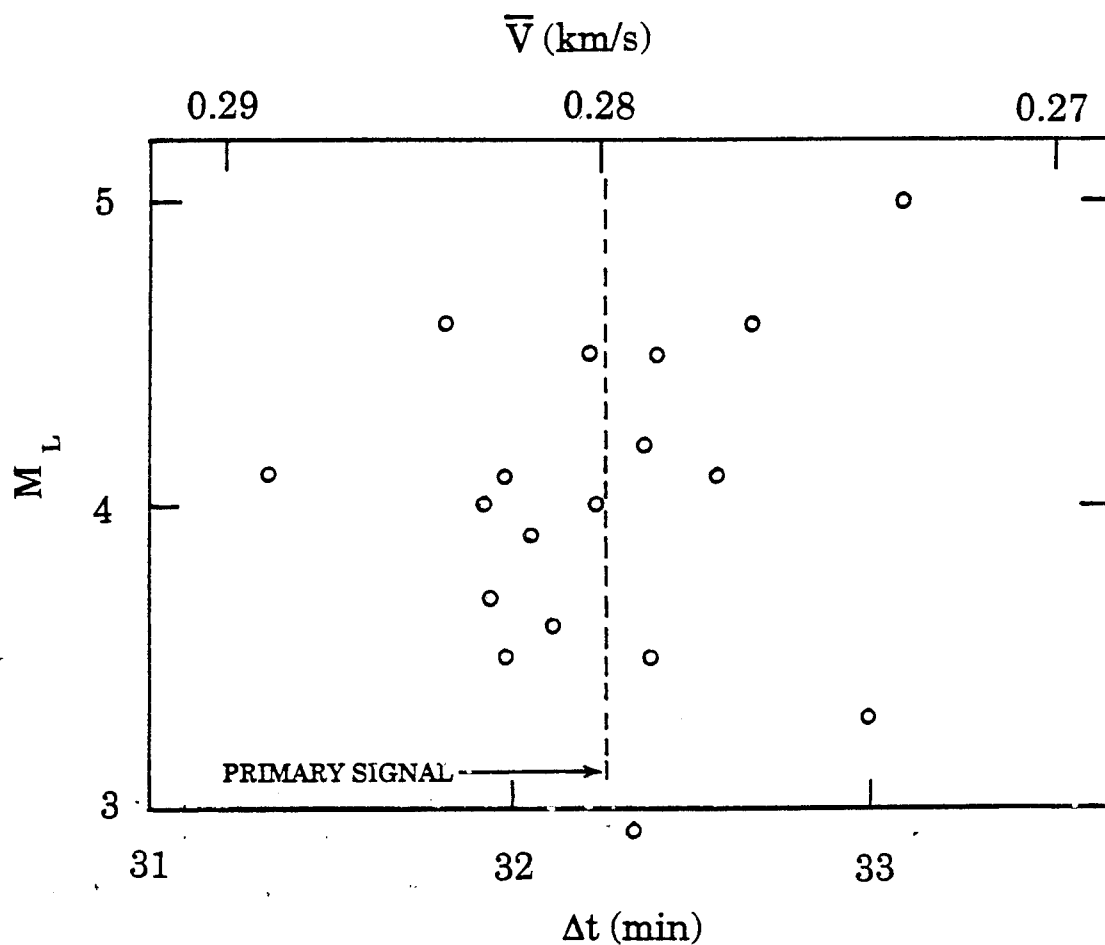


Fig. 6. The correlation coefficient for a four hour period with identifications of signals connected with the earthquake and its aftershocks.

AFTERSHOCK ARRIVAL TIMES



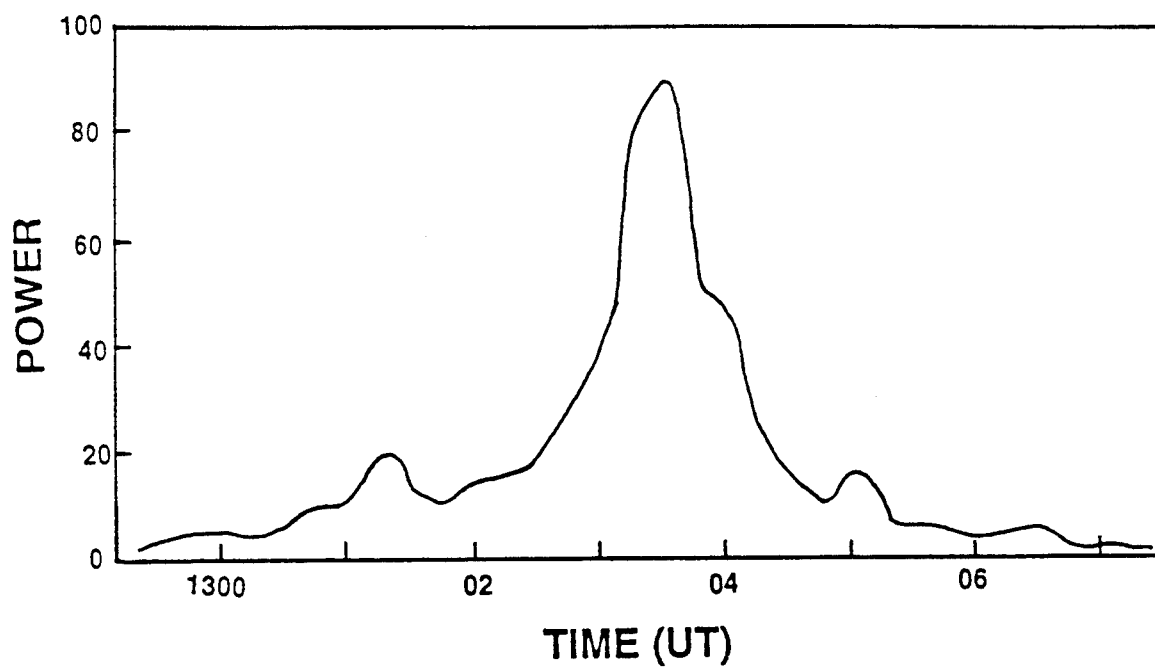


Fig. 8. Signal power near the peak signal time. Power in relative units and time in minutes after 13:00.

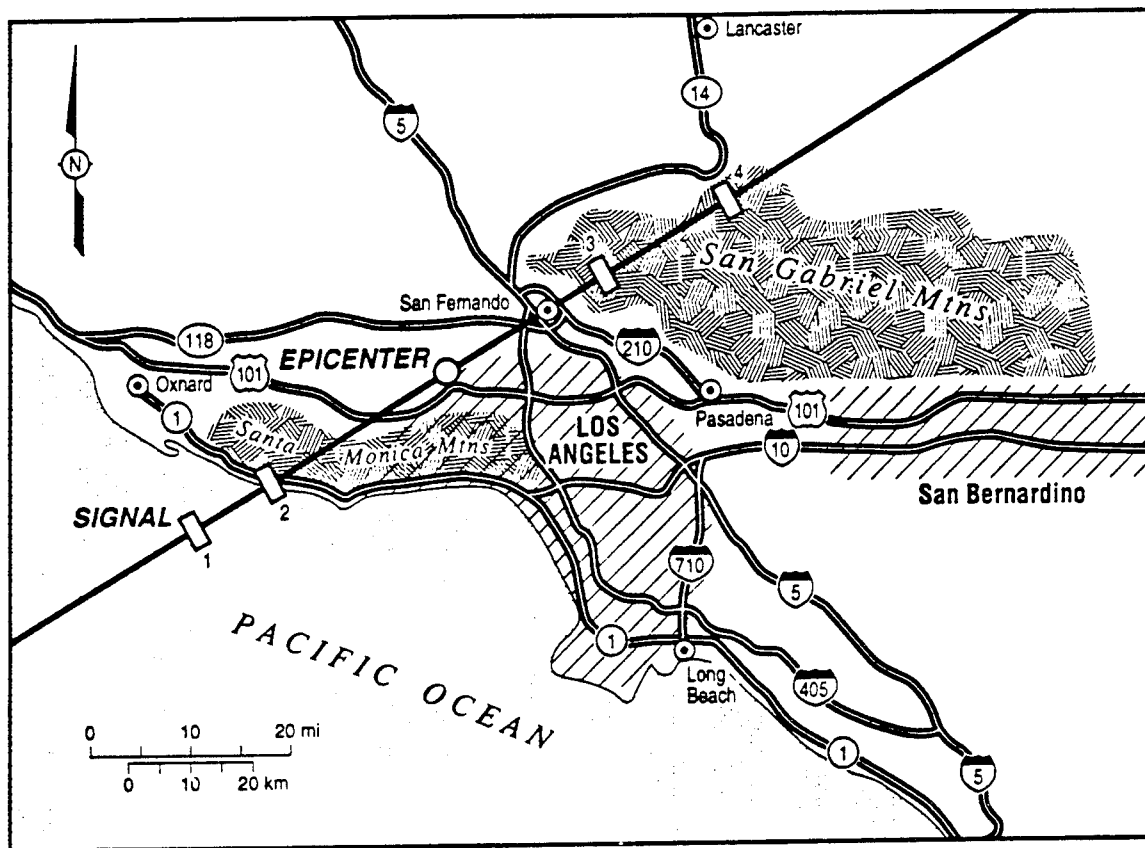


Fig. 9. Geographic region near the epicenter. The line points to the array and the rectangles along the line indicate the location of possible seismic-acoustic coupled secondary sources or source limits.

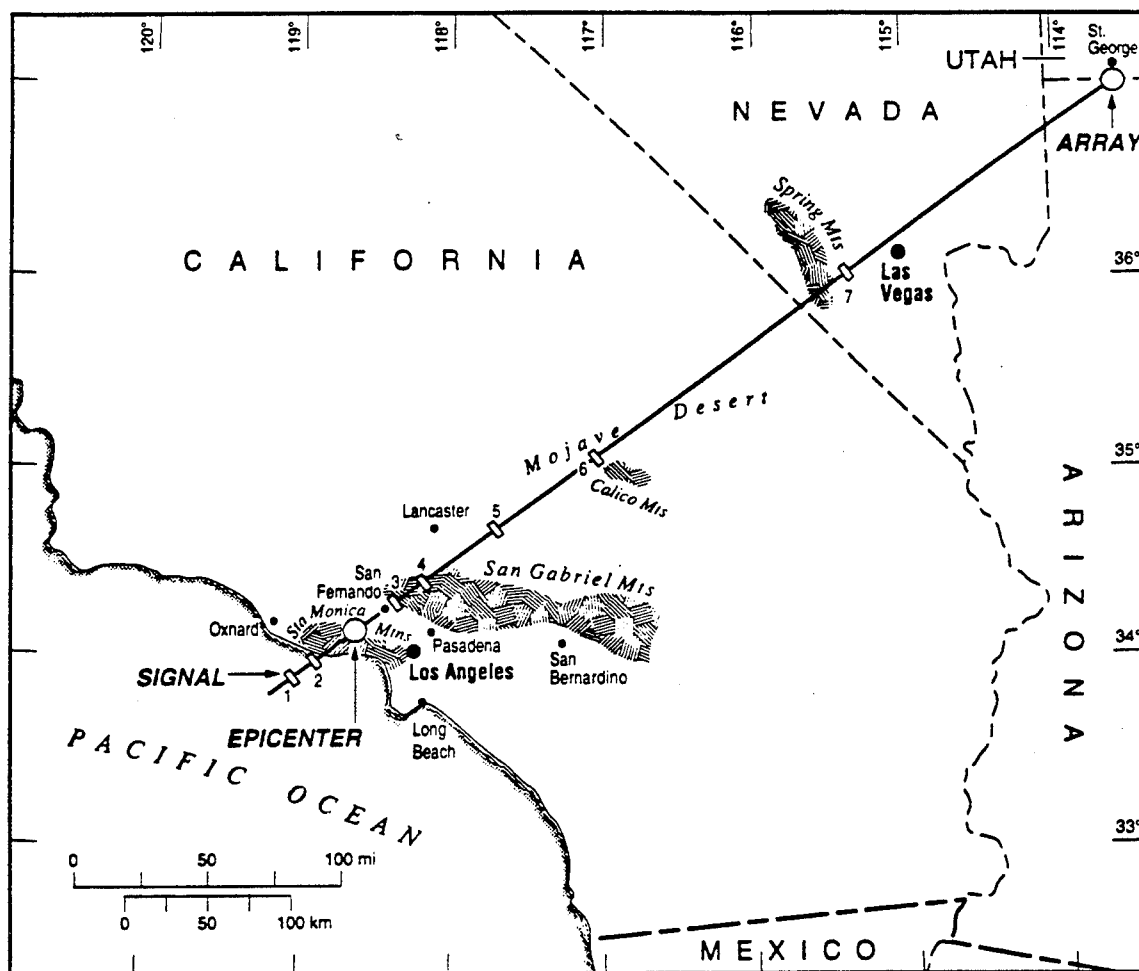


Fig. 10. Geographic region from the epicenter to the array location. Rectangles along the line indicate the position of possible extended region seismic-acoustic coupled secondary sources (6,7, and 8).